UNIVERSIDAD COMPLUTENSE DE MADRID

FACULTAD DE CIENCIAS FÍSICAS

Departamento de Óptica

SOLID STATE DYE LASERS: SCATTERING FEEDBACK AND INTEGRATED DEVICES

MEMORIA PARA OPTAR AL GRADO DE DOCTOR
PRESENTADA POR

Luis Cerdán Pedraza

Bajo la dirección de los doctores

Ángel Costela
Inmaculada García-Moreno

Madrid, 2013

Universidad Complutense de Madrid
Facultad de CC. Físicas
Departamento de Óptica

Láseres de colorante en estado sólido: retroalimentación por dispersión y dispositivos integrados

Tesis Doctoral

Memoria presentada por
Luis Cerdán Pedraza
Para optar al grado de Doctor

Directores: Prof. Ángel Costela y Prof. Inmaculada García-Moreno

Departamento de Sistemas de Baja Dimensionalidad,
Superficies y Materia Condensada
Instituto de Química Física "Rocasolano"
Consejo Superior de Investigaciones Científicas (CSIC)
Madrid. Noviembre 2012

Universidad Complutense de Madrid
Facultad de CC. Físicas
Departamento de Óptica

Solid state dye lasers: scattering feedback and integrated devices

Doctoral Thesis

Thesis report submitted by
Luis Cerdán Pedraza
for the degree of Doctor of Philosophy

Supervisors: Prof. Ángel Costela and Prof. Inmaculada García-Moreno

Departamento de Sistemas de Baja Dimensionalidad,
Superficies y Materia Condensada
Instituto de Química Física "Rocasolano"
Consejo Superior de Investigaciones Científicas (CSIC)
Madrid. November 2012

In my end is my beginning
(Mary, Queen of Scots)

Agradecimientos

El devenir del doctorado debería ser análogo al despegue del vuelo sin motor. Al inicio se necesita ser remolcado porque todavía no se tienen las capacidades necesarias para despegar. Una vez que se ha despegado, se pasa a tener algo de control sobre el vuelo, aunque se sigue necesitando de remolque. Llegado el momento el cable de sujeción se suelta y uno ya puede volar libre siguiendo sus propias corrientes. Angel e Inmaculada se han comportado como unos remolcadores expertos, guiándome y dejándome libertad siempre que ha sido necesario. Este hecho ha contribuido profundamente a mi desarrollo como científico y como persona, lo que siempre les agradeceré y reconoceré.

Siguiendo con la tónica de la ciencia actual, esta tesis no se podría haber llevado a cabo sin la contribución de una red interdisciplinar de científicos de diversas instituciones, ni sin la ayuda inestimable del personal técnico y de gestión del Instituto de Química Física "Rocasolano". A todos ellos estoy agradecido.

Nada de esto hubiese sido lo mismo sin la gente que he conocido a lo largo de todos estos años. Amistades que han estado ahí cuando ha hecho falta y que le han dado alegría y sentido al doctorado. Muchos son los que han contribuido en este aspecto, pero sin duda son Susana y Marien las que merecen una mención especial.

A Nuria.

Índice general

Resumen

Los láseres de colorante en estado sólido (LCES) proporcionan emisión láser eficiente y sintonizable a lo largo de todo el espectro visible siendo, además, económicamente ventajosos dada su flexibilidad, simplicidad y escalabilidad de procesado. Dichas propiedades inducen a desarrollar y fabricar cabezales láser basados en LCES para aplicaciones biomédicas o fuentes de emisión coherente con el fin de ser integradas en dispositivos optoelectrónicos, espectroscópicos o diagnósticos. El mayor reto para estos materiales reside en alargar su vida útil como dispositivos láser (fotoestabilidad), gravemente limitada por la fotodegradación de los colorantes.

En la presente Tesis Doctoral se aborda el problema de la caracterización y mejora de las propiedades láser de LCES en barras láser y dispersiones coloidales, así como en película delgada (dispositivos integrados). Con el fin de alcanzar el objetivo marcado, se han seguido dos aproximaciones diferentes pero complementarias: una aproximación "química", basada en elegir o sintetizar la matriz sólida más adecuada (en términos de compatibilidad química) para cada colorante estudiado, y una aproximación "física", basada en manipular las propiedades de emisión del material activo por medio de modificaciones estructurales a nivel nanométrico con el fin de generar dispersión óptica (scattering). Los resultados incluidos en la presente memoria de Tesis tienen carácter teórico, numérico y experimental, pero con una clara prevalencia de los últimos.

La primera parte de la Memoria de Tesis está dedicada a la evaluación teórica y experimental de LCES en barras láser y dispersiones coloidales con retroalimentación por dispersión. Con anterioridad al inicio de esta tesis, nuestro grupo demostró que la incorporación de nanopartículas de sílice trigonal de 1 nm de tamaño (silsesquioxanos o POSS) a los materiales para LCES dio lugar a las mejores propiedades láser publicadas hasta el momento para distintos tipos de colorantes, tanto polares como no polares. Por ejemplo, la eficiencia láser del pirrometeno 567 (PM567) dopado en una matriz de metacrilato de metilo pasó del 30% al 60% por la simple adición de POSS, manteniéndose esta eficiencia por más de 8.5×10^5 pulsos.

En la presente Memoria de Tesis se demuestra, a través de experimentos específicamente diseñados, así como con extensas simulaciones numéricas (basadas en ecuaciones de balance), que la mejora observada en la eficiencia está ocasionada por la débil dispersión óptica inducida por las nanopartículas de POSS. En este escenario, la retroalimentación no resonante inducida por la dispersión se suma a la retroalimentación resonante debida a la cavidad externa, incrementando la retroalimentación total y, consiguientemente, la eficiencia final. Sin embargo, se muestra que el aumento de la eficiencia sólo puede ser

obtenido para un determinado rango de condiciones experimentales relacionadas con el nivel de dispersión, la intensidad de bombeo y el tamaño temporal del pulso.

Dándole continuidad a la aproximación "física", nuestro grupo tornó su interés de sistemas basados en centros de dispersión pasivos en medios activos (sistemas con POSS), a sistemas basados en centros de dispersión activos en medios pasivos, esto es, suspensiones coloidales de nanopartículas poliméricas con tamaños de decenas de nanómetros dopadas con colorantes láseres. Este último sistema resultó, de nuevo, en la mejora de la eficiencia y fotoestabilidad láser de la Rodamina 6G (Rh6G) con respecto a la solución acuosa. En esta Memoria de Tesis, se demuestra que el uso de esta exitosa solución, en combinación con el conocido proceso de transferencia de energía resonante Förster (FRET por sus siglas en inglés), permite mejorar las "malas" propiedades láser demostradas por el Azul de Nilo (AN), que emite en la región roja del espectro (∼700 nm), siendo de interés para aplicaciones biomédicas y biofotónicas. En este caso, se ha usado la Rh6G como donador para el AN debido al gran solapamiento espectral de la banda de emisión de la primera con la banda de absorción del segundo, un factor clave para conseguir una transferencia de energía eficiente. La evaluación teórica de la fotofísica del proceso FRET se ha llevado a cabo usando modelos existentes adaptados a nuestro sistema, y muestra que las nanopartículas presentan una morfología núcleo/corteza, algo totalmente inesperado. Por último, se ha demostrado que secando las disoluciones coloidales se obtienen muestras sólidas de nanopartículas autoensambladas, las cuales, tras ser excitadas, proporcionan emisión láser aleatoria incoherente asistida por FRET.

La segunda parte de la Memoria de Tesis está dedicada al estudio de dispositivos en película delgada basados en polímeros dopados con colorantes. Los resultados de esta parte de la tesis se han dividido en dos temas bien diferenciados: estudio fundamental de la Emisión Espontánea Amplificada (ASE por sus siglas en inglés) en películas delgadas, y optimización de la eficiencia y fotoestabilidad láser de diferentes colorantes comerciales con emisión del verde al rojo lejano.

Del lado de la caracterización fundamental, se muestra que la modificación del formalismo más utilizado para obtener información sobre la ganancia ASE en guías de onda activas permite tener en cuenta los efectos de saturación en la ganancia. El nuevo formalismo permite obtener nuevos parámetros que caracterizan las propiedades de emisión y que ayudan a optimizar las condiciones de bombeo. Por otro lado, se han evaluado las diferencias en los parámetros ASE de guías de onda (GO) y cuasi-guías de onda (CGO), películas delgadas en las que luz está total o parcialmente confinada, respectivamente. Se muestra que, aunque las CGO presentan mayores pérdidas debido a su menor confinamiento, la ganancia máxima alcanzable es siempre mayor que en las GO, presumiblemente por la mayor restricción de modos de propagación aparejada a las primeras (CGO).

Por último, se han optimizado y caracterizado las propiedades ASE (ganancia, umbral, fotoestabilidad) y láser (longitud de onda de emisión, umbral, fotoestabilidades) de guías de onda poliméricas dopadas con pirrometenos, perilenos, sulforodaminas y hemicianinas, cuya emisión cubre por completo la región espectral entre 570 nm y 730 nm. Para el proceso de optimización, se ha seguido la aproximación "química", esto es, se han elegido específicamente diferentes matrices poliméricas para cada colorante y se ha caracterizado en profundidad la mejor combinación matriz/colorante. Se ha visto que las poliimidas fluoradas, un polímero con una conductividad térmica elevada, es capaz de evitar la fotodegradación de los pirrometenos a la vez que garantiza una ganancia óptica elevada, indicando que estos colorantes son más susceptibles de sufrir fotodegradación térmica. Por el contrario, las propiedades de emisión de los perilenos son optimizadas en poli metacrilato de metilo, un polímero con una baja conductividad térmica pero una bajísima permeabilidad al oxígeno, de lo que se infiere que la fotodegradación química es el principal camino de destrucción de esta familia de colorantes. Sin embargo, las sulforodaminas y las hemicianinas tan sólo se han podido disolver en poli metacrilato de 2-hidroxietilo, ya que no hay muchos polímeros disponibles, y adecuados, compatibles con su naturaleza polar, lo que no ha dejado espacio para la optimización por la vía "química".

Por otro lado, a medida que se utilizan colorantes con emisión más hacia el rojo, la eficiencia comienza a reducirse como consecuencia de la menor absorción del bombeo, así como por sus bajos rendimientos cuánticos de fotoluminiscencia. Para solventar estos problemas, se ha recurrido a la transferencia de energía (FRET) como herramienta para incrementar la absorción total y, consecuentemente, la eficiencia final. Se han elegido los donadores más adecuados para cada uno de los colorantes necesitados de esta solución, y se han optimizado las relaciones donador/aceptor particulares para cada par.

Finalmente, para obtener emisión láser de los pares matriz/colorante ya optimizados, se ha recurrido a dos soluciones diferentes. Para el perileno naranja, con emisión en torno a 570 nm, se han depositado películas delgadas sobre substratos corrugados que proporcionan emisión láser con retroalimentación distribuida. Para el resto de colorantes, se ha usado en su lugar emisión láser aleatoria confinada en la guía de onda, donde la retroalimentación la proporciona la dispersión óptica inducida por la separación de fase que aparece en las mezclas polímero/POSS.

En conclusión, se muestra que el desarrollo de materiales fotónicos avanzados basados en LCES, combinando de un modo sinergético las ventajas de los láseres convencionales y aleatorios, puede resultar en emisión láser optimizada, lo que abre las puertas a la comercialización e industrialización de cabezales láser económicamente competitivos y con prospectivas biomédicas, así como de láseres integrados en laboratorios-en-un-chip de usar y tirar para aplicaciones optoelectrónicas, espectroscópicas o diagnósticas.

Abstract

Solid state dye lasers (SSDL) provide low-cost gain media with tuneable and efficient emission across the whole visible spectrum and beyond, which together with their processing and pumping flexibility, makes them very attractive for the fabrication and development of cost-effective laser heads for biomedical applications or coherent light sources suitable for integration in optoelectronic, spectroscopic or sensing devices. One significant challenge is to address the limited operational lifetime (photostability) of these devices due to dye photodegradation, to enable use of these sources in the aforementioned applications.

In this thesis report, the problem of the optimization and characterization of both the efficiency and photostability of SSDL as laser rods and colloidal suspensions, as well as thin films (integrated devices) is tackled. Two different, but complementary, experimental approaches have been followed in order to achieve this goal: a "chemical" approach, consisting of choosing or synthesizing the most adequate host matrix for a given dye with the aim to improve the dye/host compatibility, and a "physical" approach, consisting of tailoring the emission properties of the active medium by means of optical scattering induced by structural modifications at the nanoscale. The thesis report comprises theoretical, numerical and experimental results, with a clear prevalence of the later.

The first part of the thesis report is devoted to the experimental and theoretical evaluation of SSDL as laser rods and colloidal suspensions with scattering feedback. Prior to the beginning of this thesis, it was shown by our group that the addition of trigonal silica nanoparticles 1 nm in size (silsesquioxanes or POSS) as an additive for SSDL led to the best laser performances reported up to date for different dyes, both polar and non-polar. For example, the laser efficiency of pyrromethene 567 (PM567) dye doped into a matrix of methyl-methacrylate increased from a 30% to a 60% just by adding POSS, with the laser efficiency remaining unchanged after 8.5×10^5 pulses.

In this thesis report, specifically designed experiments and extensive numerical computations (based on rate equations), demonstrate that the observed remarkable efficiency improvements are a direct consequence of the photon path enlargement caused by the weak optical scattering induced by the POSS nanoparticles. In this scenario, the non-resonant feedback resulting from the scattering adds up incoherently to the resonant feedback provided by the external cavity, increasing the overall feedback and, thus, the total efficiency. Nevertheless, it is shown that the efficiency enhancement can only be obtained for a given range of experimental conditions associated to the level of scattering, as well as to the pump intensity and pulse duration.

Keeping on with this "physical" approach, our group interest moved from systems based on passive scatterers in active media (POSS systems) to systems based on active scatterers in passive media, i. e., colloidal suspensions of dye-doped latex nanoparticles (NP) with sizes of tens of nanometres. The use of this system resulted, again, in the enhancement of the laser efficiency and photostability of the laser dye Rhodamine 6G (Rh6G) with respect to those of the same dye in aqueous solution. In this thesis, it is shown that the use of this successful approach, in combination with the well-known Förster resonance energy transfer (FRET) process, allows to solve the problem of the poor laser performance (efficiency and photostability) exhibited by Nile Blue (NB), a long-wavelength emitting (∼700 nm) laser dye of interest in biomedical and biophotonic applications. In the present case, Rh6G has been used as donor for NB due to its high efficiency and the good spectral overlap of the emission band of the former and the absorption band of the later, a key factor for an efficient FRET. A theoretical evaluation of the FRET photophysics is carried out by making use of existing analytical treatments adapted to our system, and it is revealed that the NPs present unexpected core/shell morphology. Finally, it is demonstrated that drying the colloidal suspensions results in the formation of solid samples of self-assembled NPs which, upon photoexcitation, sustain FRET-assisted incoherent random laser emission.

The second part of the thesis report is devoted to the thin film devices based in dye-doped polymers. The thesis results in this part have been divided into two distinguished topics: fundamental understanding of Amplified Spontaneous Emission (ASE) in thin films, and optimization of laser efficiency and photostability of different commercial dyes emitting from the green to nearly the IR.

On the side of the fundamental characterization, it is shown that the modification of the most commonly used ASE gain retrieval formalism for active wave-guides allows to take into account gain saturation effects. The new formalism enables to obtain new parameters that characterize the emission properties and helps to optimize the pumping conditions. In addition, the differences between the ASE parameters of waveguides (WG) and leaky-waveguides (LWG), in which light is totally or partially confined, respectively, are evaluated. It is shown that, although LWGs present higher losses due to its leaky nature, their maximum attainable gain is always higher than that of the WGs, presumably as a consequence of the stronger self-mode restriction capability of the formers.

Finally, the ASE (gain, thresholds, photostabilities) and laser properties (emission wavelength, thresholds, photostabilities) of waveguides doped with pyrromethenes, perylenes, sulforhodamines and hemicyanine dyes, are optimized and characterized. The emission from the chosen dyes covers the whole spectral region between 570 nm and 730 nm. For the optimization process, the "chemical" approach has been followed, i. e., dif-

ferent polymer hosts have been specifically chosen for each dye, and the best dye/host pair has been thoroughly characterized. It has been found that a fluorinated polyimide, a material with a high thermal conductivity, avoids the photodegradation of pyrromethene dyes while maintaining a high optical gain, indicating that pyrromethenes suffer mainly from thermal photodegradation. On the contrary, the emission properties of perylenes are optimized in poly-(methyl methacrylate), a polymer with a low thermal conductivity but a very low oxygen permeability, which helps to infer that chemical photodegradation is the main destruction path in these dyes. Sulforhodamines and hemicyanines, instead, have been solved only in poly(2-hydroxyethyl methacrylate), since their polar nature makes it difficult to find more adequate polymers, and then there has been no room to optimization.

On the other hand, the dyes with emission bands shifted to longer wavelengths are characterized for presenting lower efficiencies, partly as a consequence of the lower pump absorption, partly due to the intrinsic lower photoluminescence quantum yields of these compounds. To overcome this problem, an energy transfer approach (FRET) to increase the overall absorption, and thus the efficiency, has been followed. The most adequate donors have been selected for each of the dyes needing this solution and the particular donor/acceptor ratios have been optimized.

Finally, in order to obtain laser emission in the optimized dye/host pairs, two different approaches have been used. For perylene orange, with emission around 570 nm, the thin films have been deposited onto corrugated substrates sustaining distributed feedback lasing. For the other dyes, instead, waveguided random lasing, in which feedback is provided by the optical scattering induced by the phase separation resulting from the mixtures polymer/POSS, has been used.

In conclusion, it is shown that the development of advanced photonic materials based on SSDL combining synergistically the advantages of both random and conventional lasers, may result in optimized laser emission, boosting the commercialization and industrialization of cost-effective laser heads for biomedical applications, or cheap integrated lasers in disposable lab-on-a-chip platforms for optoelectronic, spectroscopic or sensing applications.

Lista de publicaciones y contribuciones a congresos

El trabajo realizado durante el periodo de tesis ha dado lugar a las siguientes publicaciones y contribuciones a congresos.

Artículos incluidos en la memoria de tesis:

En el Capítulo 1 y ordenados como en la memoria:

1. A. Costela, I. García-Moreno, L. Cerdán, V. Martín, O. García, and R. Sastre, "Dye-Doped POSS solutions: Random Nanomaterials for Laser Emission," Adv. Mater. 21, 4163–4166 (2009)
2. L. Cerdán, A. Costela, I. García-Moreno, V. Martín and M. E. Pérez-Ojeda, "Laser Efficiency Enhancement due to Non-resonant Feedback in Dye-doped Hybrid Materials: Theoretical Insights and Experiment," IEEE J. Quantum Electron. 47, 7, 907–919 (2011)
3. L. Cerdán, E. Enciso, V. Martín, J. Bañuelos, I. López-Arbeloa, A. Costela, and I. García-Moreno, "FRET-assisted laser emission in colloidal suspensions of dye-doped latex nanoparticles," Nature Photonics 6, 621–626 (2012)

En el Capítulo 2 y ordenados como en la memoria:

1. L. Cerdán, A. Costela, and I. García-Moreno, "On the characteristic lengths in the variable stripe length method for optical gain measurements," J. Opt. Soc. Am. B 27, 9, 1874–1877 (2010)
2. A. Costela, O. García, L. Cerdán, I. García-Moreno, and R. Sastre, "Amplified spontaneous emission and optical gain measurements from pyrromethene 567-doped polymer waveguides and quasi-waveguides," Opt. Express 16, 10, 7023–7036 (2008). Erratum: Opt. Express 16, 10, 7587–7587 (2008)
3. L. Cerdán, A. Costela, I. García-Moreno, O. García, and R. Sastre, "Waveguides and Quasi-Waveguides based on pyrromethene 597-doped poly(methyl methacrylate)," Appl. Phys. B 97, 73–83 (2009)
4. L. Cerdán, A. Costela, I. García-Moreno, O. García, R. Sastre, M. Calle, D. Muñoz and J. de Abajo, "High-gain long-lived amplified spontaneous emission from dye-doped fluorinated polyimide planar waveguides," Macromol. Chem. Phys. 210, 1624–1631 (2009)
5. L. Cerdán, A. Costela, I. García-Moreno, O. García and R. Sastre, "Laser emission from mirrorless waveguides based on photosensitized polymers incorporating POSS," Opt. Express 18, 10, 10247–10256 (2010)
6. L. Cerdán, A. Costela, G. Durán-Sampedro, I. García-Moreno, M. Calle, M. Juan-y-Seva, J. de Abajo, and G. A. Turnbull, "New perylene-doped polymeric thin films for efficient and long-lasting lasers," J. Mater. Chem. 22, 8938–8947 (2012)
7. L. Cerdán, A. Costela, G. Durán-Sampedro and I. García-Moreno, "Random lasing from polymer slab waveguides doped with sulforhodamine dyes," Appl. Phys. B 108, 839–850 (2012)

8. L. Cerdán, A. Costela, and I. García-Moreno, "Waveguided random lasing in red-emitting-dye-doped hybrid polymer thin films," Org. Electron. 13, 1463–1469 (2012)

Contribuciones a congresos:

1. L. Cerdán, A. Costela, I. García-Moreno, O. García, R. Sastre and J. de Abajo, "Dye-doped fluorinated polyimides as efficient long-lived wave-guide lasers and amplifiers". CLEO Europe - EQEC 2009, Munich (Germany), 14th-19th June 2009. Oral communication (Luis Cerdán)
2. L. Cerdán, A. Costela, I. García-Moreno, O. García, R. Sastre, M. Calle, D. Muñoz, and J. de Abajo, "Efficient and stable amplified spontaneous emission (ASE) from dye-doped polymeric planar waveguides". IX Congress on Photochemistry. Spanish Royal Chemical Society, Leioa (Vizcaya, Spain), 20th-23rd September 2009. Poster (Luis Cerdán)
3. A. Costela, I. García-Moreno, L. Cerdán, O. García, V. Martín, and R. Sastre, "Nanohybrid POSS-Copolymers as Advanced Solid-State Lasers". Frontiers in Optics 2009/Laser Science XXV, San Jose (California, USA), 11th-15th October 2009. Oral communication (Angel Costela)
4. A. Costela, I. García-Moreno, L. Cerdán, V. Martin, M. E. Pérez-Ojeda, O. García and R. Sastre, "Advanced Solid-State and Scatty Lasers Based on Nanohybrid POSS Composites". International Conference on Nanomaterials: Synrhesis, Characterization and Applications (ICN-2010), Mahatma Gandhi University, Kottayam (Kerala, India), 27th-29th April 2010. Invited Talk (Angel Costela)
5. L. Cerdán, A. Costela, I. García-Moreno, V. Martin, and M. E. Pérez-Ojeda, "Laser efficiency enhancement in dye doped POSS materials via Non-Resonant Feedback Lasing". 6th International ECNP Conference on Nanostructured Polymers and Nanocomposites, Madrid (Spain), 28th-30th April 2010. Oral communication (Luis Cerdán)
6. L. Cerdán, A. Costela, and I. García-Moreno, "Variable Stripe Length method for optical gain measurements: Characteristic Lengths". CLEO Europe - EQEC 2011, Munich (Germany), 22nd-26th May 2011. Poster (Luis Cerdán)
7. L. Cerdán, A. Costela, I. García-Moreno, V. Martin, and M. E. Pérez-Ojeda, "Non-resonant feedback to enhance conventional lasing in advanced materials". CLEO Europe - EQEC 2011, Munich (Germany), 22nd-26th May 2011. Poster (Luis Cerdán)
8. L. Cerdán, G. Durán-Sampedro, I. García-Moreno, A. Costela, and J. de Abajo, "Efficiency and photostability optimization in Perylene-doped polymer Distributed Feedback lasers and amplifiers". CLEO Europe - EQEC 2011, Munich (Germany), 22nd-26th May 2011. Oral communication (Luis Cerdán)
9. L. Cerdán, A. Costela, G. Durán-Sampedro, I. García-Moreno, J. de Abajo, and G. A. Turnbull, "Studies on stimulated emission in dye-doped polymer thin films". III Jornadas Ibéricas en Fotoquímica (III Iberian Conferences on Photochemistry), Granada (Spain), 4th-7th September 2011. Oral communication (Luis Cerdán)
10. L. Cerdán, A. Costela, and I. García-Moreno, "Waveguided random laser emission in dye-doped hybrid polymer thin films". CLEO:2012, San José, CA (USA), 6th-11th May 2012. Poster (Luis Cerdán)
11. E. Enciso, V. Martín, L. Cerdán, A. Costela, I. García-Moreno, J. Bañuelos, and I. López-Arbeloa, "Photophysical and lasing properties of polymeric nanoparticles suspensions". Symposium on Photonics and Optoelectronics (SOPO 2012), Shanghai (China), 21st-23rd May 2012. Oral communication (Eduardo Enciso)
12. I. López-Arbeloa, L. Cerdán, E. Enciso, V. Martín, J. Bañuelos, A. Costela, and I. García-Moreno, "Red emission from oxazine assisted by FRET process from Rhodamine into latex

nanoparticles". XXIVth IUPAC Symposium on Photochemistry, Coimbra (Portugal), 15th-20th July 2012. Poster (I. López-Arbeloa)

Artículos no incluidos en la memoria de tesis:

1. L. Cerdán, R. Weigand, J. M. Guerra Pérez, and H. Crespo, "A simple experiment on slow light in ruby," Am. J. Phys. 76, (9), 826–832 (2008)
2. L. Cerdán, A. Costela, I. García-Moreno, J. Bañuelos, and I. López-Arebeloa, "Singular laser behavior of hemicyanine dyes: unsurpassed efficiency and finely structured spectrum in the near-IR region," Laser Phys. Lett. 9, 6, 426–433 (2012)
3. L. Cerdán, A. Costela, E. Enciso, and I. García-Moreno, "Random lasing in self-assembled dye-doped latex nanoparticles: packing density effects," submitted

Capítulo en libro:

1. A. Costela, I. García-Moreno, L. Cerdán, V. Martín, M. E. Pérez-Ojeda, O. García, and R. Sastre, "Solid-State Scatty Lasers Based on Nanohybrid POSS Composites," in *Polymer procesing and characterization*, S. Thomas, D. Ponnamma, and A. K. Zachariah, eds. (Apple Academic Press, New Jersey (USA), 2012)

Otras contribuciones:

1. L. Cerdán, A. Costela, O. García, I. García-Moreno, and R. Sastre, "Amplified Spontaneous Emission from PM597 dye-doped polymer quasi-waveguides: Thickness effect on optical gain properties and stability". KSOP Summer School 2008, Bad Herrenalb (Germany), 20th-21st August, 2008. Poster (Luis Cerdán)

Introduction

In 1960 Theodor H. Maiman [1] brought to reality what others had predicted [2, 3] and dreamed about since 1917, when Albert Einstein proposed in a seminal work [4] that photons could stimulate emission of identical photons from excited atoms: the optical maser or, as coined by Gordon Gould, LASER, acronym for Light Amplification by Stimulated Emission of Radiation. The laser designed by Maiman was based on a rod of synthetic ruby crystal with reflecting coatings on the ends, surrounded by a helical flash lamp. This demonstration opened the floodgates to the apparition of new laser materials and applications [5].

Maiman published his results in May 1960; by the end of that year the first four-level solid state laser (Uranium in CF_2) and the first continuous-wave laser (the well-known helium-neon), respectively, were already reported [6, 7]. In 1961 the first neodymium laser was announced and the second harmonic of ruby was generated [8], giving birth to the field of non-linear optics. By 1964 the today well-established semiconductor diode laser, the nitrogen laser, the argon ion laser and the CO_2 laser had been demonstrated [5]. Nevertheless, it was not until 1966 that the first organic dye laser was demonstrated independently by Sorokin and Lankard [9] and by Schäfer, Schmidt and Volze [10].

Dyes are organic compounds characterized for possessing several conjugated double bonds (two double bonds separated by a single bond) and, thanks to the degree of delocalization and polarizability of the π electrons in the molecular structure, they present high absorption cross sections in the visible spectral region [11]. In addition, dye molecules show very broad absorption and emission spectra (tens of nanometres) due to the huge number of vibrational and rotational modes existing in a structure with so many atoms and bonds [11]. This last property allows obtaining two of the major achievements of dye lasers, i. e., ultra narrow-linewidth (<1 kHz or $\Delta\lambda \sim 1 \times 10^{-9}$nm) continuous-wave laser emission across tens of nanometres with a single dye, and generation of ultra-short pulses (down to 6 fs after amplification and extracavity compression) in the visible spectrum without the need of using frequency conversion [11, 12].

When analysing the dye laser dynamics, the myriad of electronic and vibrational molecular energy levels of the laser dye can be approximated to a four-level laser system [13] (Fig. 1). The dye molecule is promoted from the ground level L_0 (fundamental electronic, low vibrational) to an excited level L_3 upon photoexcitation (first or higher excited electronic, excited vibrational). By means of internal conversion or vibrational relaxation, the dye molecule ends up in the upper laser level L_2 (first excited electronic, fundamental vibrational), transiting afterwards to the lower laser level L_1 (fundamental

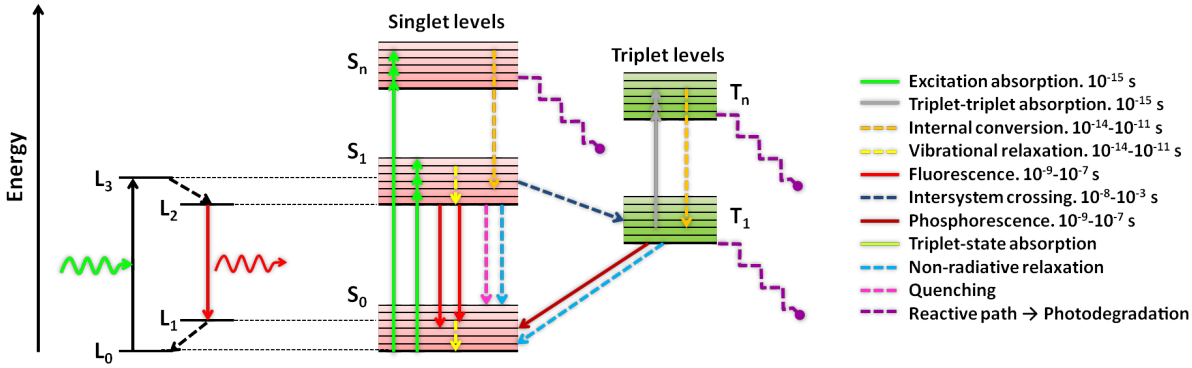

Figure 1: Simplified (four-level laser system approximation) and detailed band-structure and transition paths (and corresponding time scales in the legend) of a dye molecule (Jablonsky energy diagram). Solid and dashed lines represent radiative and non-radiative transitions, respectively.

electronic, excited vibrational), spontaneously or stimulatedly. From the lower laser level the dye molecule relaxes back to the ground state. Although this approximation is used for the theoretical treatment, the real picture is much more complicated (Fig. 1), since once the molecule reaches the upper laser level, it can be deactivated through many paths [11, 12]:

- via non-radiative transitions due to internal conversion or vibrational relaxation
- via quenching due to collisions with other species, formation of excimers and exciplexes, or through dipole-dipole interactions with another dye molecule (resonance energy transfer)
- via intersystem crossing in which a forbidden transition from a singlet to a triplet state takes place

One major drawback of dye lasers is their limited lifetime due to photodegradation. Photodegradation occurs when the dye permanently loses the ability to emit due to photon-induced chemical modifications, which origin may be thermal or reactive (chemical). In the chemical photodegradation, other species take part (oxygen, other dye molecules, free radicals, ...), and is more likely to happen when the dye is promoted to a triplet state, or even to a highly excited singlet state, albeit in a lesser extent (Fig. 1). This is so because singlet states are short-lived (1-5 ns [12]), while triplet states are long-lived (μs to ms [11]) and highly chemically reactive, providing the excited molecule with a long time to undergo chemical reactions leading to its destruction.

On the other hand, thermal destruction also plays a significant role in dye photodegradation, since the heat generated and accumulated during the pumping process, together with the energy of the excited state, may increase the local temperature, understood as the motion energy due to molecular vibrations, promoting the dye above its decomposition threshold. In general, dye photodegradation involves both thermal and chemical

processes, but the partial contribution of each of them varies from dye to dye.

In this sense, although dye lasers can be found in the solid, liquid and gas phases [11], the liquid media (dye in organic solvent) seem, *a priori*, the perfect solution to overcome the dye degradation problems arising from the local heat generated during excitation (pumping). Their fluid nature allows cooling the solution by using flow systems, in such a way that the excess heat is removed and the gain medium is constantly renewed. Thanks to the dye flow, high repetition rate (kHz), high power pumping, as well as continuous wave (CW) operation have been obtained [12].

Nevertheless, the use of liquid solutions in dye lasers entails a number of inconveniences and limitations, mainly related to the employment and disposal of large volumes of organic solutions (flammable and most of them classified as carcinogenic), as well as to the technical complexities of the flow systems. The dye circulation requires the use of pumps, which guarantee a constant flow and avoid turbulences, and the design of complex and bulky cells, increasing the size and cost of the final system and complicating its handling, maintenance and cleaning. For instance, the change of a dye solution to a different one demands an exhaustive cleaning procedure, both for the cell and the circulation circuit, since the presence of impurities, even at the lowest levels, have deleterious effects on the laser performance. These problems have altogether mostly limited the use of dye lasers to laboratory application.

A suggestive alternative to overcome these problems is the use of solid matrices incorporating dye molecules, thereby enabling the design of compact and easy to operate laser devices. Solid matrices avoid the use of complex cells or flow systems and when the samples are degradated, they are simply replaced by new ones. In addition, the problems related to flow fluctuations or solvent leakage and/or evaporation are inexistent, reducing considerably the environmental and health risks and simplifying the security measures, which in turn enables the use of dye lasers by non-highly specialized staff. Taken together, all these advantages decrease the production costs and allow to boost the use of solid-state dye lasers (SSDL) both for industrial (military, medical, telecommunications, ...) and academic (spectroscopy, non-linear optics, ...) applications.

Another advantage of SSDL with respect to liquid dye lasers is that the solid material may be casted as thin films acting as wave-guiding active devices. In fact, there has been significant work over the last few years exploring the development of these type of devices because of their potential applications as coherent light sources suitable for integration in optoelectronic and disposable spectroscopic and sensing devices [14].

Nevertheless, almost since the very first demonstration of a SSDL by Soffer and McFarland [15] in 1967, it was realized that the laser efficiencies of SSDL were lower than those of their liquids counterparts and experienced, on top of that, a faster photodegra-

dation due to the dye immobility, thereby fading rather quickly the laser emission and hindering any application.

Over the following decades, a variety of materials were implemented to avoid as much as possible the dye photodegradation while boosting the efficiency. To achieve this goal, the most of the groups, including ours[1], focused their attention to the particular dye/host interaction and compatibility, specifically choosing already existing hosts for a given dye, synthesizing new dyes and/or matrices, or chemically modifying existing ones; in other words, a "chemical" approach was followed.

Nevertheless, and in spite of having resulted in outstanding SSDL performances, the chemical approach was limited by a simple fact learnt from the experience; there is no universal matrix which optimizes the efficiency and photostability of all dyes. This is an important drawback that had to be overcome if SSDL are to be introduced for industrial and commercial applications.

Hence, it was necessary to survey new approaches in order to overcome this limitation. This could be attained by tailoring the emission properties of the active medium by means of physical and structural modifications of the dye host, i. e., following a "physical", rather than a "chemical", approach.

Thesis goal and report organization

The main goal of the thesis consists of demonstrating that the "physical" approach to change the host material at the nanoscale, supported by a "chemical" approach, might lead to the improvement of both the laser efficiency and photostability of SSDL. More explicitly, the goal consists of studying, both theoretically and experimentally, how, under specific circumstances, optical scattering can be used to improve the laser performance of conventional bulk lasers and, even, to provide an alternative way of obtaining resonant feedback for integrated (thin film) lasers. On the other hand, new host materials have to be explored to optimize the laser efficiency and photostability of integrated devices based in polymers doped with well-known commercial dyes emitting from the green to nearly the IR, a region of interest in telecommunications and biophotonics.

As this thesis report is based on an article compilation, the following chapters will serve to organize, summarize and link the thesis results scattered through the appended papers. For clarity and coherence purposes, extended descriptions or updated discussions of certain aspects of the published works will be provided when needed. With the aim to serve as a quick guide, a chapter just after this introduction has been included in which all the chemical structures of the dyes and polymers used, or mentioned, through the following text, are represented. Following this quick guide, the main chapters are

[1]Chapter 1 gives a thorough account of these results

included, and are organized as follows: i) Introductory text with the state-of-the-art of the subject and chapter goals, ii) methodology section explaining sample preparation and experimental set-ups, iii) summary and discussion of thesis results on the given subject and iv) chapter conclusions. The global conclusions of the thesis report and the appendices with the appended papers are included at the end of the document.

In Chapter 1, the main results on the experimental and theoretical evaluation of SSDL with scattering feedback are presented. The fundamental properties of SSDL based on hybrid materials (polymers doped with inorganic nanoparticles) will be treated in section 1.3.1, beginning with the first experimental evidences of non-resonant feedback enhanced laser emission (section 1.3.1.1), and ending with the numerical and experimental univocal verification of the casted hypothesis (section 1.3.1.2). Section 1.3.2 will describe the properties of SSDL based on colloidal suspensions of dye-doped polymeric nanoparticles (section 1.3.2.1) and solid samples consisting of self-assembled nanoparticles (section 1.3.2.2).

In Chapter 2, the main results on the characterization of thin film emitting devices based on commercial dyes, emitting in the yellow-red spectral range (570-730 nm), incorporated into adequate polymer matrices are presented, evaluated and compared. The contributions to the fundamental characterization of the stimulated emission process in thin films will be treated in section 2.3.1, beginning with the development of the gain parameters retrieval formalism (section 2.3.1.1), and ending with the evaluation of the differences between waveguides and leaky-waveguides (section 2.3.1.2). Sections 2.3.2 to 2.3.5 will summarize the emission properties (gain, thresholds, photostabilities, ...) of the waveguides based on pyrromethenes, perylenes, sulforhodamines and hemicyanines, respectively.

Bibliography

[1] T. H. Maiman. Stimulated optical radiation in ruby. *Nature*, 187:493–494, 1960.

[2] V. A. Fabrikant. Emission mechanism of a gas discharge. *Trudy VEI*, 41:236, 1940.

[3] A. L. Schawlow and C. H. Townes. Infrared and optical masers. *Phys. Rev.*, 112:1940–1949, 1958.

[4] A. Einstein. Zur Quantentheorie der Strahlung. *Physika Zeitschrift*, 18:121–128, 1917.

[5] J. Hetch. A short history of laser development. *Opt. Eng.*, 49(091002):1–23, 2010.

[6] P. P. Sorokin and M. J. Stevenson. Stimulated infrared emission from trivalent uranium. *Phys. Rev. Lett.*, 5:557–559, 1960.

[7] A. Javan, W. R. Bennett Jr., and D. R. Herriott. Population inversion and continuous optical maser oscillation in a gas discharge containing He-Ne mixture. *Phys. Rev. Lett.*, 6(3):106–110, 1961.

[8] P. A. Franken, A. E. Hill, C. W. Peters, and G. Weinreich. Generation of optical harmonics. *Phys. Rev. Lett.*, 7(4):118–119, 1961.

[9] P. P. Sorokin and J. R. Lankard. Stimulated emission observed from an organic dye, chloro-aluminum phthalocyanine. *IBM J. Res. Dev.*, 10(3):162–163, 1966.

[10] F. P. Schäfer, W. Schmidt, and J. Volze. Organic dye solution laser. *Appl. Phys. Lett.*, 9(8):306–309, 1966.

[11] F. P. Schäfer. *Dye Lasers*. Springer-Verlag, Berlin, Germany, 1990.

[12] F. J. Duarte and L. W. Hillman. *Dye Laser Principles*. Academic Press, San Diego, CA, 1990.

[13] A. E. Siegman. *Lasers*. University Science Books, Mill Valley, CA, 1986.

[14] C. Grivas and M. Pollnau. Organic solid-state integrated amplifiers and lasers. *Laser Photonics Rev.*, 6:419–462, 2012.

[15] B. H. Soffer and B. B. McFarland. Continuously tunable, narrow-band organic dye lasers. *Appl. Phys. Lett.*, 10:266–267, 1967.

Guía de estructuras químicas

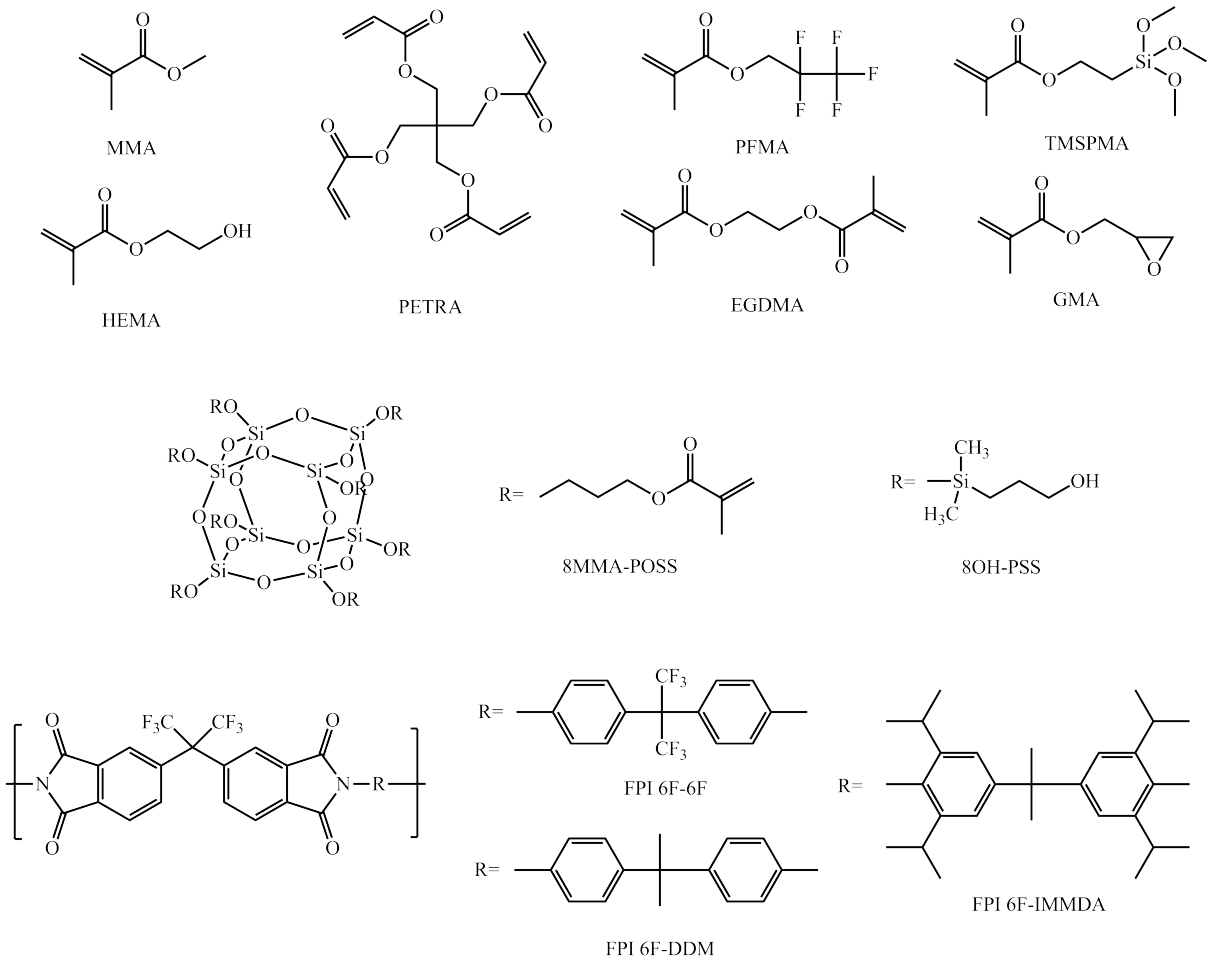

Figure 2: Estructuras químicas de matrices sólidas mencionadas a lo largo de la memoria de tesis. MMA= methyl methacrylate, HEMA= 2-hydroxyethyl methacrylate, PETRA= pentaerythritol tetraacrylate, PFMA= 2,2,3,3,3,-pentafluoropropyl methacrylate, EGDMA= ethylene glycol dimethacrylate, TMSPMA= 3-(trimethoxysilyl)propyl methacrylate, GMA= glycidyl methacrylate, 8MMA-POSS= octa(propyl-methacryl) Polyhedral Oligomeric Silsesquioxane, 8OH-PSS= octa(hydroxypropyldimethylsilyl) Polyhedral Oligomeric Silsesquioxane, FPI= Fluorinated polyimide.

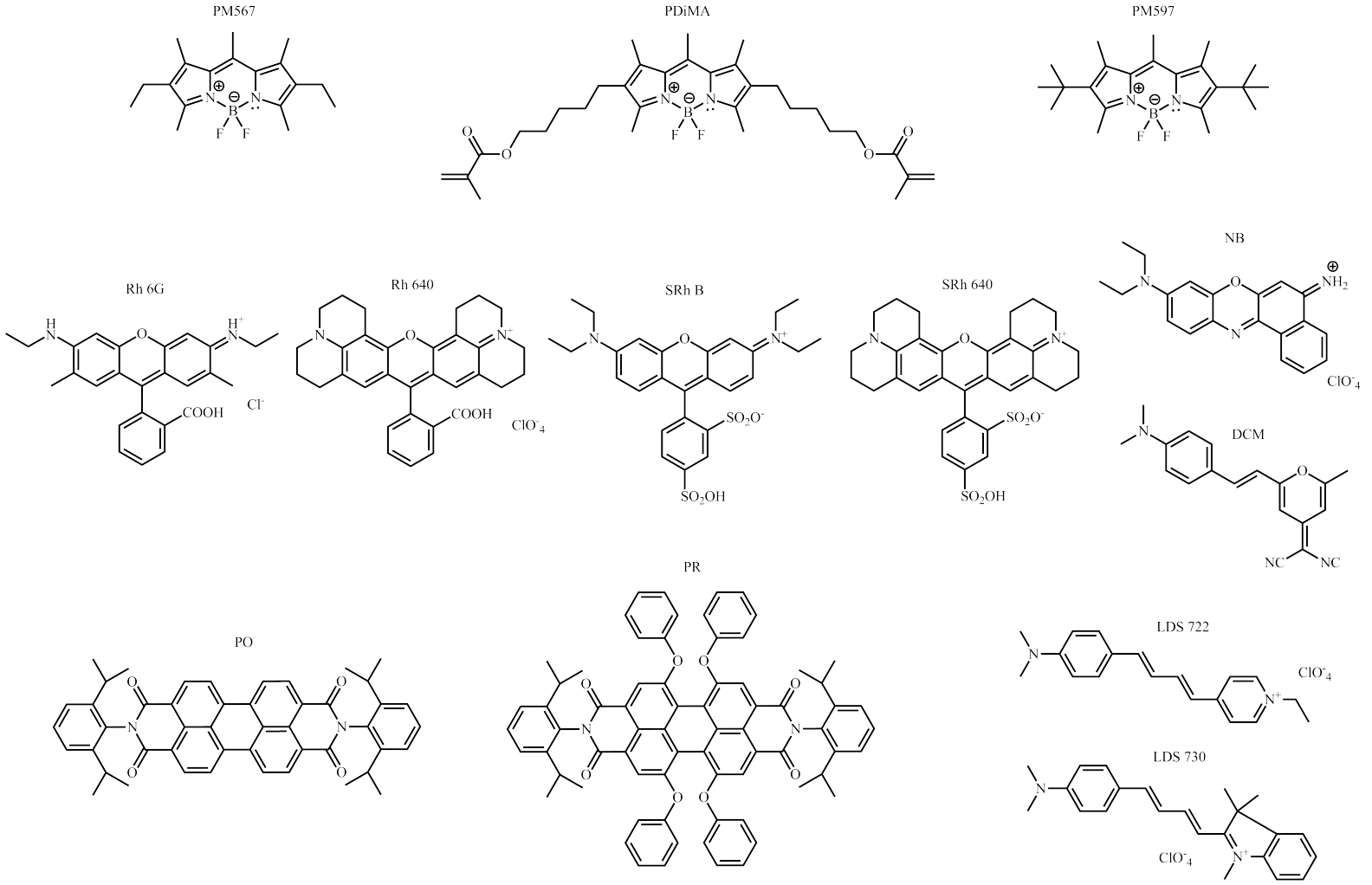

Figure 3: Estructuras químicas de colorantes láseres mencionados a lo largo de la memoria de tesis. PM567= Pyrromethene 567, PDiMA= PM567 derivative compound, PM597= Pyrromethene 597, Rh 6G= Rhodamine 6G, Rh 640= Rhodamine 640, SRh B= Sulforhodamine B, SRh 640= Sulforhodamine 640, NB= Nile Blue, DCM= 4-Dicyanomethylene-2-methyl-6-(p-dimethylaminostyryl)-4H-pyran, PO= Perylene Orange, PR= Perylene Red, LDS 722= Pyridin 2, LDS 730= Styryl 6.

Chapter 1

Solid state dye lasers with scattering feedback

1.1 Introduction

The first solid-state dye laser (SSDL) was demonstrated by Soffer and McFarland [1] in 1967, consisting of a matrix of poly(methyl methacrylate) (PMMA) incorporating Rhodamine 6G (Rh6G, Fig. 3) as laser dye. This work was followed soon after by the work of Peterson and Snavely [2] on the same material but under flash-lamp excitation. Over the next decade a variety of materials were tried as host for laser dyes, but it was soon realized that the laser efficiencies were lower than those of their liquids counterparts, experiencing on top of that a faster photodegradation due to the dye immobility, thereby fading rather quickly the laser emission [3].

It was not until the mid 80's and 90's, when a new bunch of host materials with high damage thresholds and excellent optical properties were synthesized, that the field of SSDL spurred again. Since then, significant advances have been made toward the development of practical, tuneable SSDL. In this regard, our group, in close collaboration with the late Prof. Sastre's group at ICTP-CSIC[1], Prof. Amat-Guerri's group at IQOG-CSIC[2], and Prof. López-Arbeloa's group at UPV-EHU[3], has contributed profusely to the understanding and avoidance of dye photo-degradation in solid matrices. To improve the SSDL performance (efficiency and photostability), two different, but simultaneous, routes were followed: performing structural modifications in the given dye to improve resistance and developing, or synthesizing, new host matrices with better compatibilities. In other words, a "chemical" approach was followed

Among many other dye structural modifications, our group showed that the addition of polymerizable groups to the chromophore (e. g., PDiMA as compared to PM567, Fig. 3) made it possible to bond covalently the dye to the polymer backbone, thereby obtaining higher photostabilities than those of the simply solved parent dye (Group i vs. *ref.* in

[1]Instituto de Ciencia y Tecnología de Polímeros (ICTP). Consejo Superior de Investigaciones Científicas, CSIC (Spain)

[2]Instituto de Química Orgánica General (IQOG). Consejo Superior de Investigaciones Científicas, CSIC (Spain)

[3]Facultad de Ciencias y Tecnologías. Universidad del País Vasco, UPV-EHU (Spain)

Table 1.1), while keeping analogous photophysical properties and laser efficiencies [4, 5]. As one of the main causes of degradation of dyes incorporated into polymeric matrices is the thermal destruction of the dye due to poor thermal dissipation in the polymer host, the above results indicated that the covalent binding of the dye to the polymeric chains provided additional channels for the dissipation along the polymer backbone of the absorbed energy that is not converted into light emission, with a corresponding increase in the laser photostability [6].

In addition, the above results suggested that developing host materials with superior heat dissipation would result, in principle, in improved dye photostabilities. Our group have been trying for some years now different solutions to accomplish this goal.

Attention was paid to the influence of the cross linking degree of the polymer host on the laser action, since caging and immobilizing the chromophores reduces the dynamic interactions with other species (oxygen, other dye molecules, and free radicals), thereby avoiding early photobleaching of the dye [7, 8]. Although the laser photostability of PM567 was somewhat improved (Group ii in Table 1.1), the improvement was not sufficiently satisfactory and, in addition, did not work properly for all dyes. Hence, a different solution was needed.

Moving forward in this direction, the group turned its attention to fluorinated polymers, since they present high thermal stability, high optical damage threshold and enhanced chemical resistance when compared to their non-fluorinated analogues [9]. Using this approach, outstanding photostabilities were obtained [10] (Group iii in Table 1.1). Nevertheless, if too much fluorine atoms were included in the co-monomers, a drastic decrease in the glass transition temperature of these matrices was induced, resulting in soft materials unfitted for subsequent mechanization and proper polishing.

Table 1.1: Laser efficiency and photostability of dye PM567 in different host materials

Group	Laser material	Eff (%)	ΔI (%) (n_{pulses})	Ref.
ref.	PM567 in PMMA	29	70(1×10^5)	[11]
i	PDiMA in PMMA	37	33(4×10^5)	[5]
ii	PM567 in MMA/PETRA 95/5	18	30(1×10^5)	[7]
iii	PM567 in PFMA/EGDMA 80/20	29	5(1×10^5)	[10]
iv	PM567 in SAG/MMA/HEMA 6/47/47	12	10(1×10^6)	[12]
v	PM567 in MMA/TMSPMA 40/60	21	0(1×10^5)	[13]
vi	PM567 in MMA/8MMA-POSS 87/13	60	0(8.5×10^5)	[11]

Eff-Laser efficiency, ΔI-Variation of output energy after n_{pulses} pump pulses. PMMA: poly-(methyl methacrylate). PDiMA: Dye analog of the dye PM567 with two polymerizable methacryloyloxypropyl groups. PETRA: Pentaerythritol tetraacrylate. PFMA: 2,2,3,3,3,-pentafluoropropyl methacrylate. EGDMA: Ethylene glycol dimethacrylate. SAG: Silica AeroGel with 93% porosity. HEMA: 2-hydroxyethyl methacrylate. TMSPMA: 3-(trimethoxysilyl)propyl methacrylate. 8MMA-POSS: octa(propyl-methacryl) Polyhedral Oligomeric Silsesquioxane.

Although organic polymers (linear, cross-linked or fluorinated) had been shown to be capable of improving the dye photostabilities, their practical use was limited by their inherent poor thermal dissipation, as well as by their moderately low laser damage thresholds. Inorganic glasses would be the natural alternative, since they have excellent thermal and optical properties. Nevertheless, there are two main drawbacks which hinder their use as dye host: very low dye solubilities and extremely high synthesis temperatures (which would destroy almost any dye). An intermediate situation was that of organic/inorganic hybrid materials, implemented to combine the excellent thermal properties of inorganic glasses with organic materials properties such as dye solubility, chemical modifications versatility and final sample processability (shaping, cutting, polishing).

With this in mind, the group tackled the synthesis of hybrid materials with the inorganic constituent based on a sol-gel, and the organic one based on a dye-doped polymer [12, 14]. Although very competitive dye photostabilities were obtained (Group iv in Table 1.1), the laser efficiencies remained too low, while the synthesis was too complex and lengthy (up to 2 months), rendering, on top of that, fragile, mechanically unstable (change of morphology over time) and optically heterogeneous samples when using high proportions of inorganic compound. All these facts together hindered the use of these materials as SSDL.

Based on these experiences it was concluded that the chosen matrix should have certain degree of silicon content to increase the thermal conductivity of the polymer and thus reduce the dye degradation. To avoid the synthesis complexity and the optical heterogeneities, organic monomers with silicon atoms in their backbones were used [13, 15]. Although the laser efficiencies were still low, the dye photostabilities were significantly enhanced with respect to those of the non-sililated polymers (Group v in Table 1.1). In this regard, the higher the silicon content in the final matrix was, the higher the photostabilities resulted, although it was accompanied by a decrease in the glass transition temperatures, thereby rendering soft materials inappropriate for polishing.

Hence, the design and synthesis of new materials with silica incorporated at molecular level might overcome all the above mentioned problems. Keeping on with this idea, the group's research interest moved on to study polymer matrices incorporating silica nanoparticles. Polyhedral oligomeric silsesquioxanes (POSS, Fig. 1.1a) were selected as nanoparticles for their reduced size (1 nm), which should avoid, in principle, any optical inhomogeneities. Unlike silica, where the silicon atoms are quadruple-coordinated, in the commercially available POSS the silicon is coordinated with three oxygen atoms. Nevertheless, the similarity between both allows consider POSS compounds like a silica of polyhedrical or prismatic structure, i. e., they can be considered as trigonal silica $(SiO_{1.5})_n$ nanoparticles externally surrounded by non-reactive or reactive polymerizable

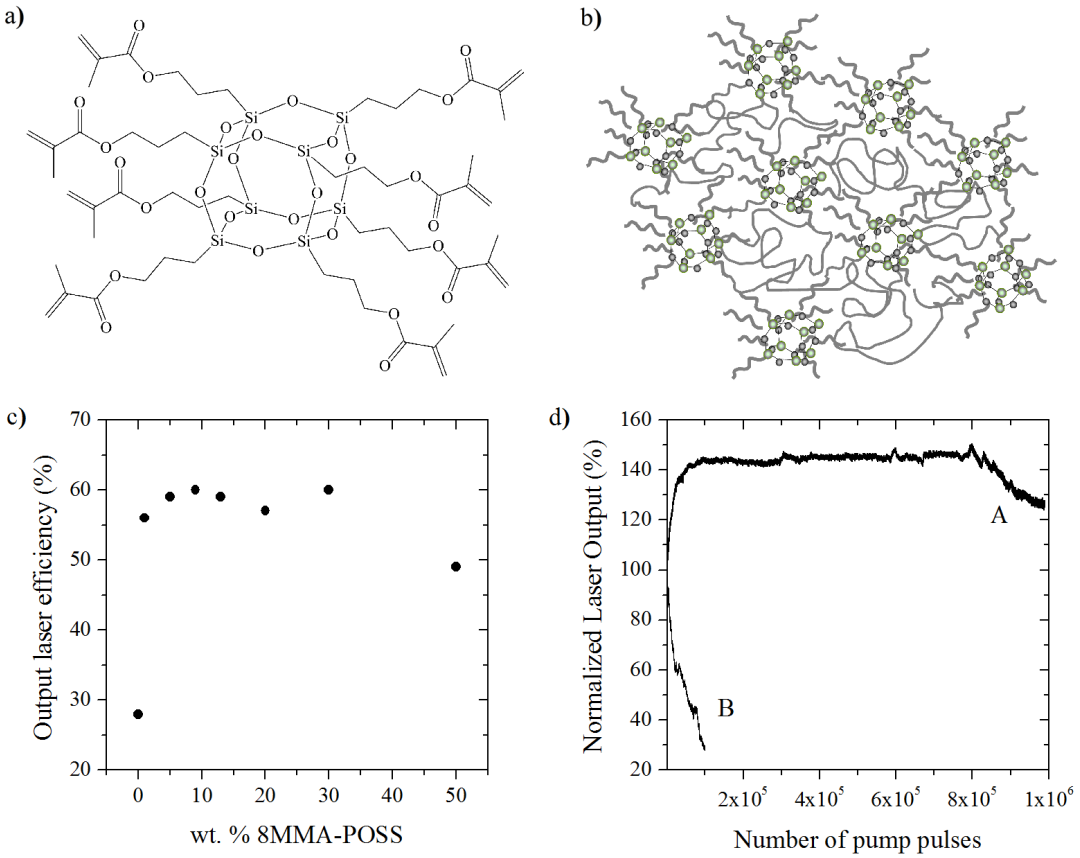

Figure 1.1: a) Chemical structure of octa(propyl-methacryl) Polyhedral Oligomeric Silsesquioxane (8MMA-POSS). b) Sketch of co-polymer network formed by 8MMA-POSS and methyl-methacrylate (MMA). c) Output laser efficiency from dye PM567 (1.5×10^{-3} M) doped into a copolymer cop(MMA/8MMA-POSS) as a function of weight percent of 8MMA-POSS nanoparticles [17]. d) Normalized laser output as a function of the number of pump pulses in the same position of the sample for dye PM567 in a copolymer cop(MMA/8MMA-POSS 87/13) pumped at 30 Hz (A) and pure PMMA pumped at 10 Hz (B) [11].

organic ligands (Fig. 1.1a). If the functional groups are polymerizable, the POSS cages will be bonded directly to the polymer chain, giving place to a organic/inorganic hybrid network (Fig. 1.1b) with enhanced thermal, mechanical and physical properties [16].

Surprisingly, these enhanced properties led to the best laser performance reported up to date for different dye-doped solid matrices (Group vi in Table 1.1), both for polar (Rhodamine 6G, Rhodamine 640, Sulforhodamine B, LDS722 and LDS 730, Fig. 3) and non-polar (Perilene Red, PM567 and PM597, Fig. 3) dyes [11, 17]. With efficiencies as high as 60% for PM567 dye doped into a copolymer cop(MMA/8MMA-POSS 87/13) (Fig. 1.1c), the laser emission remained unchanged after 8.5×10^5 pulses. The 29% laser efficiency with a drop to 30% of the initial value after just 1×10^5 pulses for PM567 in PMMA (Fig. 1.1), or the 21% efficiency with unchanged emission after 1×10^5 pulses in sililated copolymer, testify the importance of the previous results for the development of

SSDL.

It was thought that optical scattering could be taking place in this system, in spite of the small size of the POSS molecules (1 nm), and that this scattering could be the origin of the observed laser behaviour, in spite of the scattering having always been considered detrimental to laser action because it alters the direction, intensity and spatial coherence of the photons from the cavity electromagnetic mode [18]. Although conventional wisdom requires scattering in laser materials being always kept at the lowest possible level, the opposite was surprisingly found to be true in the so-called random lasers (RL), in which feedback is not provided by external means (defined cavity), but by multiple scattering inside the laser medium [19], with the light propagating and being amplified following a random walk resembling that of the Brownian motion of particles suspended in liquids.

The characteristic properties of RL (omnidirectional emission, easy production of samples with arbitrary shapes, unique sample to sample spectral distribution, low spatial coherence) make these light sources ideal for display applications, environmental lightning, remote sensing and identification markers. RL, which has been the subject of extensive research over the last two decades, has been obtained in many different materials and configurations such as dye solutions incorporating scatterers [20] (TiO_2 nanoparticles), semiconductor powders [21], laser crystal powders [22], amorphous photonic structures [23], disordered photonic crystal waveguides [24], fibres [25] and slab waveguides [26] with naturally occurring defects and thin films with induced heterogeneities[4], among many others. As a mere curiosity, the only sources of natural (non-man made) laser emission, the astrophysical lasers, rely on this principle [27].

In RL two different operational regimes may be distinguished. On the one hand, incoherent RLs[5], in which there is only intensity or energy feedback (light phase and interference effects are negligible), show a smooth spectral shape characteristic of Amplified Spontaneous Emission (ASE) with enhanced amplification due to the enlarged optical path induced by the scattering. On the other hand, coherent RLs, in which there is field or amplitude feedback (important phase and interference effects), present similar ASE spectra but superimposed with multiple very narrow spikes associated with spatially extended lasing modes [28]. The transition from one regime to the other depends strongly on both the scattering level and the gain properties. In this sense, high scattering levels and high optical gains, favours the apparition of coherent RL [29].

The characteristic length scales that determine the light transport and RL emission properties in these systems [29] are the scattering mean free path l_{sc}, defined as the average distance the light must travel between two consecutive scattering events, and

[4]In Chapter 2 examples of this last case will be thoroughly described

[5]Also known as non-resonant feedback (NRF) lasers

the transport length l_t (or transport mean free path), defined as the average distance a wave must travel before its direction of propagation is randomized. The calculation of the scattering length is relatively easy when the scatterers are spherical and the scattering is weak (particle-particle interaction vanishes) since

$$l_{sc}(\omega) = \frac{1}{\rho\sigma_{sc}(\omega)} \tag{1.1}$$

where ρ is the volume density of scatterers and $\sigma_{sc}(\omega)$ is the frequency-dependent scattering cross section, which depends on both the size and morphology of the scatterer and the scattered wavelength [30]. On the other hand, l_{sc} and l_t are related by

$$l_t(\omega) = \frac{l_{sc}}{1 - \langle\cos\theta(\omega)\rangle} \tag{1.2}$$

where $\langle\cos\theta(\omega)\rangle$ is the average cosine of the scattering angle, which can be found from the differential scattering cross section [30]. In the Rayleigh scattering regime (size $\ll$ wavelength) $\langle\cos\theta(\omega)\rangle \sim 0$ or $l_t \sim l_{sc}$, while Mie scattering regime may have $\langle\cos\theta(\omega)\rangle \approx 0.5$ or $l_t \approx 2l_{sc}$.

With the idea of proving the existence of RL in the POSS-based system, and to clearly understand the underlying physics of the increased efficiency, I was enrolled in the above described research line. What began as a subsidiary collaboration to explain the efficiency improvement, ended as a full time contribution, becoming, eventually, one of the thesis pillars.

In this chapter, the main results on the experimental and theoretical evaluation of SSDL (laser rods and colloidal suspensions) with scattering feedback are presented. In section 1.2 a brief description of the sample preparation and the emission characterization experimental set-ups will be provided. Section 1.3 will be devoted to the presentation and discussion of the fundamental properties of SSDL based on active media with passive scatterers (polymer/POSS hybrid materials) and active scatterers suspended in passive media (colloidal suspensions). The chapter will be closed with the main conclusion on SSDL with scattering feedback.

As this thesis report is based on an article compilation, the following text will serve as a summary and link between the compiled papers. For clarity and coherence purposes, extended descriptions or updated discussions of certain aspects of the published works will be provided when needed.

The papers used to prepare this chapter has been appended at the end of the thesis report on Appendix A, and will be referred from now on as:

– Paper A1: “Dye-doped POSS solutions: random nanomaterials for laser emission,”

Adv. Mater. 21, 4163–4166 (2009)
- Paper A2: "Laser efficiency enhancement due to non-resonant feedback in dye-doped hybrid materials: theoretical insights and experiment," IEEE J. Quantum Electron. 47, 7, 907–919 (2011)
- Paper A3: "FRET-assisted laser emission in colloidal suspensions of dye-doped latex nanoparticles," Nature Photonics 6, 621–626 (2012)

1.2 Methodology

1.2.1 Sample preparation

1.2.1.1 Laser rods based on POSS

The synthesis route followed to prepare the POSS based laser rods was the block radical polymerization using the initiator azobisisobutyronitrile (AIBN) in an appropriate concentration (1.0 wt.%) with regard to the total amount of monomers in the final mixture. First, adequate amounts of the commercially available methacryl substituted-POSS (8MMA-POSS) (Figs. 1.1a) and the initiator were added to freshly distilled MMA to prepare a number of different weight/weight copolymers proportions of MMA/8MMA-POSS (1 to 50 wt.%). Second, the adequate amount of dye was added to the resulting hybrid mixture, which was then placed in an ultrasonic bath until complete dissolution of the dye. The resulting solution was filtered into appropriate cylindrical polypropylene moulds using 2 μm pore size filters (Fig. 1.2a). Polymerization was performed in a thermal bath at 40 °C over a period of 2 days and then at 45 °C for about 1 day. Afterwards, the temperature was raised to 50 °C and increased slowly up to 80 °C over a period of 1 day, to decompose residual AIBN. Finally, the temperature was reduced in steps of 5 °C per day until room temperature was reached, and only then was the sample unmolded

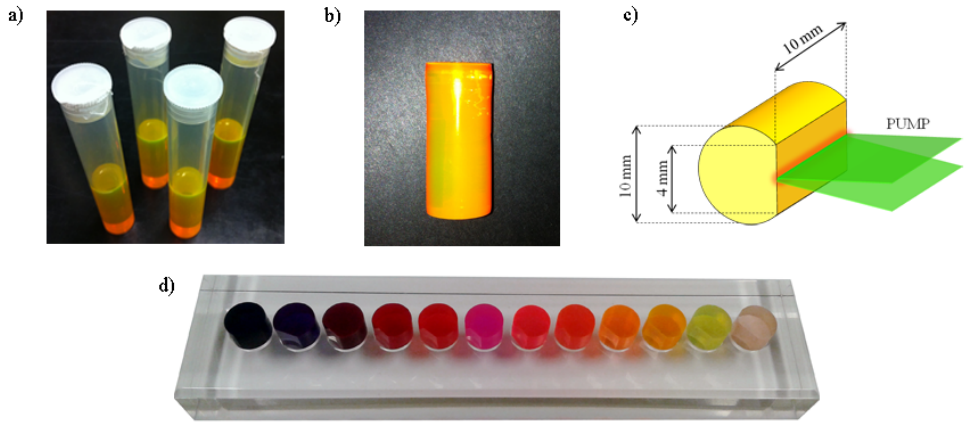

Figure 1.2: a) Polypropylene moulds with dye/monomer/POSS mixture before polymerization. b) Unmolded sample after polymerization. c) Sketch of laser rod after mechanization and polishing and pumping geometry used for SSDL. d) Picture of laser rods doped with different dyes.

(Fig. 1.2b). This procedure was essential to reduce the build-up of stress in the polymer sample due to thermal shock.

The solid samples for laser experiments were cast in cylindrical shape (Fig. 1.2c and d), forming rods of 10 mm diameter and 10 mm length. A cut was made parallel to the axis in order to obtain a lateral flat surface of 4×10 mm^2. All flat surfaces were prepared for laser experiments by conventional grinding and polishing (PhoenixBeta 4000, Buehler) until optical-grade finished. The planar grinding stage was carried out with a CS disc P4000 (Remet) using mineral oil as a lubricant. The final polishing stage was carried out with a G-Tuch Microcloth (Buehler), using a cloth disk Mastertex (Buehler) with diamond crystals of 1 μm in mineral oil as an abrasive type.

1.2.1.2 Colloidal suspensions of latex nanoparticles

The colloidal suspensions of dye-doped latex nanoparticles (NPs) were prepared following the original recipe from Nagao et al. [31] but modified to copolymerize the hydrophobic monomer MMA with more hydrophilic ones such as 2-hydroxylethyl methacrylate (HEMA, Fig. 2) or glycidyl methacrylate (GMA, Fig. 2), introducing in the monomer mixture feed adequate weight ratios of those monomers. Sodium dodecyl sulphate (SDS) was added into the feed mixture as colloidal surfactant stabilizer in order to stabilize large number of NP nuclei and, as a consequence, to control the final NP diameter. The free radical polymerization was initiated with a water soluble initiator such as potassium persulphate (KPS).

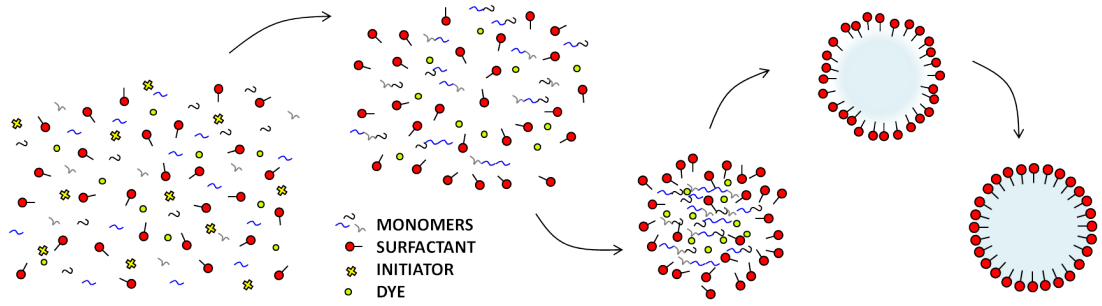

Figure 1.3: Sketch of micelle formation and NP polymerization.

In a standard preparation, surfactant and water were added to a five-necked round-bottom flask equipped with a condenser and a gas inlet. The dye dissolved in the monomer feed mixture was added to the reaction flask with stirring (300 rpm), and the mixture was heated at 65 °C and degassed by nitrogen for 30 min. The reaction was started by introducing the KPS solution, and the polymerization was performed for 3h (Fig. 1.3). The reaction was terminated by introducing air inside the reactor and cooling the reaction flask in ice. The monomer conversion was determined gravimetrically by removing aliquots

after polymerization and drying them in the oven. The obtained dispersions, with a latex content around 5.5 wt.%, were not cleaned, since the centrifugation led to aggregation and dialysis produced a gel after several water changes.

Since the SDS employed concentration was always below the Critical Micelle Concentration (CMC) in water (around 8×10^{-3} M), the monomer polymerization occurs basically in the aqueous phase, until the oligomer concentration reaches the precipitation threshold and the micelle (NP precursor) is established (Fig. 1.3), as it is characteristic in soap free emulsion polymerizations.

The NP size and size polydispersity were measured by dynamic light scattering (DLS) and, when possible, from Scanning Electron Microscopy (SEM) pictures.

1.2.1.3 Self-assembled latex nanoparticles

A poly-(methyl methacrylate) (PMMA) hollow cylinder with a height of 1 cm and inner radius 1 cm was fixed with impermeable silicone to a clean PMMA substrate (Fig. 1.4a). This vessel was then filled with 2 ml of colloidal suspension with a 5 wt.% of NPs previously prepared and the solution was left to dry at room temperature (or oven at 40 °C) until complete water evaporation. Pieces from the centre of the vessel were selected to avoid meniscus effects in the vessel edge, and were stuck to a microscope cover glass (2 cm×2 cm) to allow sample manipulation (Fig. 1.4b).

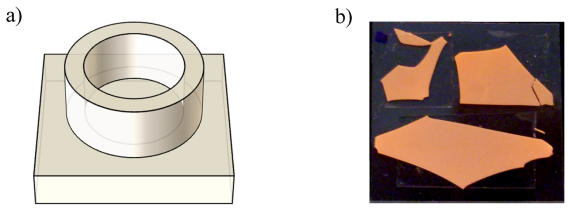

Figure 1.4: a) Vessel used to prepare self-assembled samples. b) Photograph of sample pieces on microscope cover glass.

1.2.2 Experimental Set-ups

Fig. 1.5 shows the experimental set-ups used for the laser experiments. The samples were optically pumped at 532 nm with frequency-doubled Q-switched Nd:YAG lasers operated at 1-15 Hz repetition rate. Two different lasers were used, one emitting 6 ns full width at half maximum (FWHM) pulses (Monocrom STR-2+) and another emitting 20 ns FWHM pulses (Lotis TII SL-2132). The pump radiation was horizontally polarized, which allowed controlling the pulse energy incident on the sample by insertion into the pump beam path of a half-wave plate (HWP) and a linear polarizer (LP) set with its polarization axis horizontal or vertical, depending on the desired final pump polarization. By rotating the HWP, the linear polarization of the input beam is rotated out of the

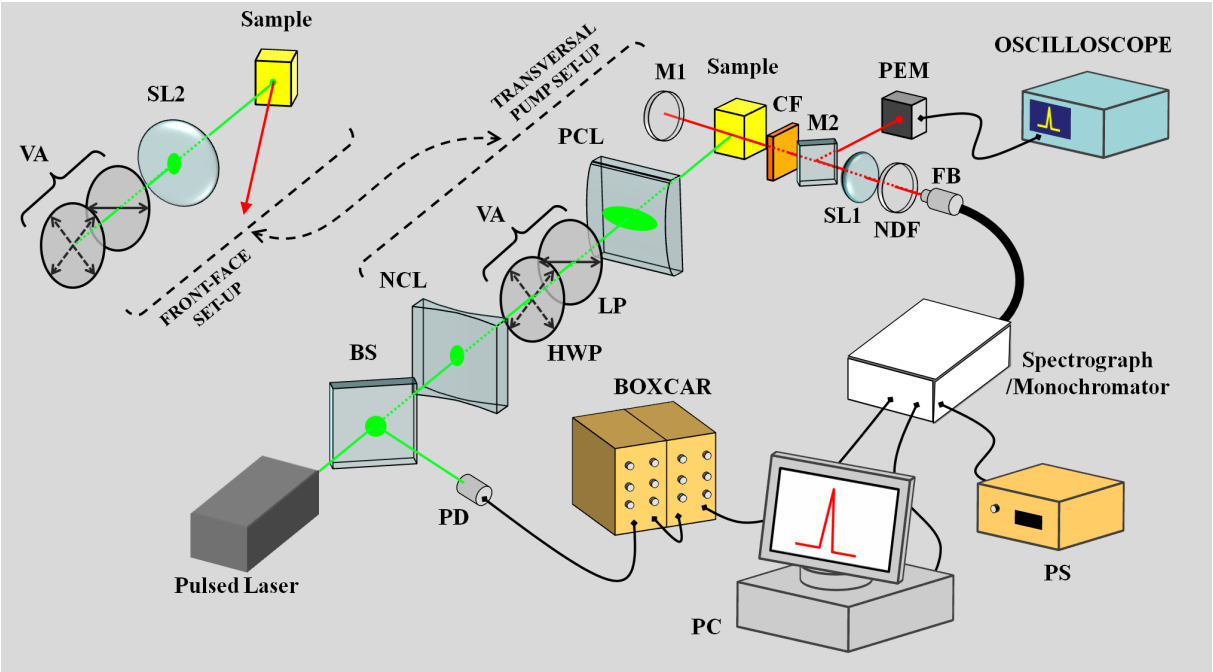

Figure 1.5: Set-ups for laser studies: BS-Beam Splitter, PD-Photo-Diode, NCL-Negative Cylindrical Lens, VA-Variable Attenuator (HWP-Half-Wave Plate and LP-Linear Polarizer), PCL-Positive Cylindrical Lens, M1- Rear-mirror, CF-Cut-off Filter, M2-Mirror in flip-mount, PEM-Pyroelectric Energy Meter, SL1(2)-Spherical Lenses, NDF-Neutral Density Filters, FB-Fibre Bundle, PS-Photomultiplier Power Supply, PC-Computer. The sample may be a rod, a cuvette, etc...

horizontal, and the pump beam is blocked more or less by the LP, depending on the rotation angle introduced by the HWP.

In the transversal pumping configuration measurements, the light incident on the sample was perpendicular to the surface of the sample (cuvette or laser rod) and focused onto that surface in a stripe shape of ∼300 μm width (Fig. 1.2) by a combination of negative (NCL) and positive (PCL) cylindrical quartz lenses (f = -15 and +15 cm, respectively), perpendicularly arranged. The oscillation cavity (2 cm length) consisted of a 90% reflectivity aluminium back mirror (M1) and the end face of the sample as output coupler.

In the front-face configuration measurements, the two cylindrical lenses were substituted by one spherical (SL2) lens (f = +15 cm), and the sample was rotated so that the pump beam arrived to the surface at an angle of about 34º from the normal to that surface. The pumped spot at the surface was elliptical in shape with major and minor axis of about 2 mm and 1.6 mm, respectively.

The laser emission was collected with a 5 cm focal length spherical lens (SL1), focused onto a fibre bundle (FB) and detected with a spectrograph/monochromator (Spectrapro-300i Acton Research) equipped with a thermoelectrically cooled CCD detector (SpectruMM:GS 128B), to acquire the spectra, and a photomultiplier (Hamamatsu R928), for the photostability measurements. A shortwave Cut-off filter (CF) (OptoSigma, cut-off at

540 nm) was placed before the fibre bundle to avoid any scattered pump light entering the spectrograph. Neutral density filters (NDF) were used before the fibre to avoid detectors saturation. For the efficiency measurements, the output laser beam was directed, by means of a mirror (M2), towards pyroelectric energy meters (PEM) (GenTec ED-100A and ED-200).

A beam splitter (BS) was used to send a reflection of the pump beam into a photo-diode (PD) acting as the trigger. The trigger signal was fed to a boxcar (Stanford Research, model 250) to convert it to a delayed TTL pulse to start the CCD or photomultiplier acquisition. The signal from the CCD was sent directly to a PC card, while the signal from the photomultiplier was fed again to the boxcar to be integrated before being digitized and processed by a computer (PC).

1.2.3 Emission properties evaluation

The main laser parameters characterized in this chapter are the laser wavelength, the emission efficiency (percentage of the excitation energy converted into laser emission), the laser threshold (pump energy at which lasing starts) and the emission photostability.

The laser wavelength was measured with the spectrograph/monocromator/CCD system. The emission efficiency was obtained dividing the energy outcoupled from the cavity and the pump energy as measured with a pyroelectric energy meter. For the laser threshold retrieval, the CCD was used to acquire the spectra as a function of the pump intensity (I_p). The threshold was considered to be the point for which there is a change in slope in the light-light curve (I_{out} *vs.* I_p) when plotted in a log-log scale.

Finally, the photostability was assessed by pumping the samples in a fixed position at a pump energy well above threshold and monitoring, with a photomultiplier, the decay of the output intensity as a function of the number of pump pulses received upon the same region.

1.3 Thesis Results

This section will be devoted to the presentation, comparison and discussion of the thesis main results on lasers with scattering feedback. The fundamental properties of SSDL based on POSS hybrid materials will be treated in section 1.3.1, beginning with the first experimental evidences of non-resonant feedback enhanced laser emission (section 1.3.1.1), and ending with the numerical and experimental univocal verification of the casted hypothesis (section 1.3.1.2). Section 1.3.2 will describe the properties of SSDL based on colloidal suspensions (section 1.3.2.1) and self-assembled nanoparticles (section 1.3.2.2).

1.3.1 Hybrid Materials: Passive Scatterers In Active Media

1.3.1.1 First evidences of non-resonant feedback enhanced laser emission (From paper A1)

As mentioned above, the use of 8MMA-POSS as an additive for liquid and solid state dye lasers led to the best laser performance reported to date for different dyes, both polar and non-polar. In order to assess whether the laser emission improvements were inherent to the dye, i. e., whether they were the result of changes in the dye properties induced by dye-POSS interaction, we evaluated the photophysical properties of the new system. Nevertheless, it was found that the photophysics (molar absorption coefficient, absorption and fluorescence wavelengths, fluorescence quantum yields, lifetime, etc.) of PM567 was not as strongly affected by the presence of increased weight proportions of 8MMA-POSS as to account for the observed performance enhancement.

Taking into account that the radiative properties of molecular systems are altered significantly in the presence of optical scattering, given place to the already mentioned random lasers (RL), the question that immediately arose was whether the POSS nanoparticles could act as passive scatterers when they were present in the dye-gain media in spite of the bulk material showing high optical homogeneity.

In order to prove the existence of RL in the present system, the rear mirror was removed and the sample was pumped in front-face configuration (Fig. 1.5). This way, coherent effects due to the external cavity would be avoided and information about the internal (scattering) feedback, if present, would be gathered.

The excitation of PM567, both in liquids and solids, with no POSS resulted in a broad photoluminescence spectrum centred at 564 nm (Fig. 1.6), which remained unchanged for the entire range of pumping energies. In the presence of POSS, even at the lowest (1%) weight proportion selected, a narrow stimulated emission band centred at 561 nm increased as the pump energy increased (Fig. 1.6). This was a clear indication that non-resonant feedback due to scattering was unexpectedly taking place in this particular system.

Since for an amplifying random medium, the overall scattering properties depend strongly on the particle size (Eq. 1.1), the spatial structure of liquid solutions with POSS was examined by dynamic light scattering (DLS), and we found that the 8MMA-POSS size distribution by volume was centred at 1.2 nm.

Such small nanoparticles would scatter light in the Rayleigh regime ($2\pi r/\lambda < 10$, with r the scatterer radius and λ the scattered wavelength). Hence, the characteristic length scale that determines the light transport and RL emission properties in these systems is the scattering mean free path l_{sc}, defined as the average distance the light must travel

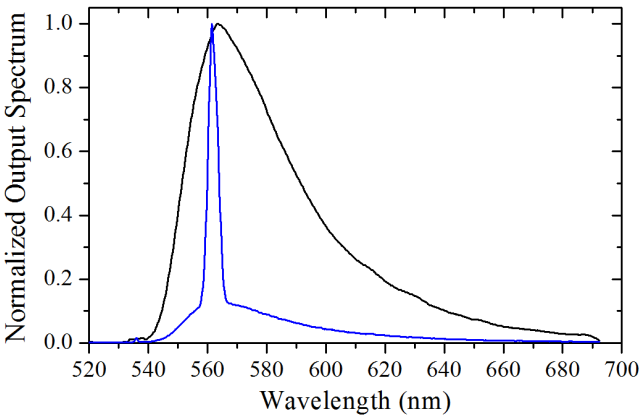

Figure 1.6: Front-face emission spectra from an ethyl acetate solution of PM567 dye (1.5×10^{-3} M) containing 0 (black line) and 50 wt.% (blue line) of 8MMA-POSS nanoparticles.

between two consecutive scattering events. Alternatively, l_{sc} is the distance a beam must travel within a random medium to reduce its intensity in a factor e.

We calculated this parameter by performing a ballistic transmission experiment, in which a reference beam with certain wavelength traverses the scattering medium, and the output intensity is measured as a function of the length of the medium. The output intensity will then follow a monoexponential decay, which decay constant is l_{sc}. Following this approach, we found that for an ethyl acetate solution with 50 wt.% of 8MMA-POSS, $l_{sc} \sim 55$ cm at the emission wavelength 560 nm, testifying the reduced level of scattering that this system sustained.

Another relevant parameter is the scattering time, t_{sc}, defined as the average time between two scattering events, $t_{sc} = nl_{sc}/c$, where n is the refractive index of the media and c is the speed of light in vacuum. Using $n = 1.435$ for ethyl acetate, a minimum t_{sc} value of 2.62 ns at 560nm is required for scattering events to take place. This means that the POSS nanoparticles can only act as efficient scattering centres in the nanosecond, or longer, pumping regime, independently of the pumping geometry.

The above discussion led to the hypothesis that the remarkable improvement observed in the laser performance of dye-doped POSS systems was a direct consequence of scattering processes. Under the defined experimental conditions, the dye-laser action was enhanced by the stimulated emission built up in the gain direction as a consequence of the elongated photon path length induced by the scattering inside the gain medium. This non-resonant feedback laser emission would be added up to the usual resonant feedback provided by the external cavity. Once certain parameters (scatterer density, sample size, pumping fluence) reach a critical value, the stimulated emission is effectively scrambled due to the high losses resulting from the scattering, and the system becomes unstable with a decrease in intensity.

1.3.1.2 Numerical verification of non-resonant feedback enhanced laser emission (From paper A2)

In order to confirm this hypothesis, more evidences, both experimental and theoretical, were needed. This motivation led us to develop a theoretical model to simulate the behaviour of gain media with very weak scattering. In addition, the fundamental understanding of the physics underlying the interaction of light with nanometric scatterers embedded in active media, which could be gathered from this model, could allow moving forward in the development of new optical materials for advanced photonic applications.

To model the effect of scattering events on the emission processes involved in transversely pumped dye laser systems with nanometre-size scatterers we made use of a rate equation formalism with spectral, temporal and spatial resolution [32]. Rate equations can be used to study a wide variety of light-matter interaction problems in which the phase and quantum nature of the interaction is not strictly needed [18], therefore being adequate for the present system.

As active medium, we assumed a solution of PM567 in ethyl acetate incorporating dielectric nanoparticles (POSS) in the Rayleigh scattering regime (size≪scattered wavelength). The geometry of the system consisted of a transversely pump excited region of length L, width b ($L \ll b$) and depth d, determined by the pump focusing and penetration depth, respectively (Fig. 1.7a).

Fig. 1.7b depicts the different processes taken into account in the simulation. Due to the pumping geometry, the emission grows preferentially in the direction defined by the axis of the excited region, which is perpendicular to the pump direction. Two counter

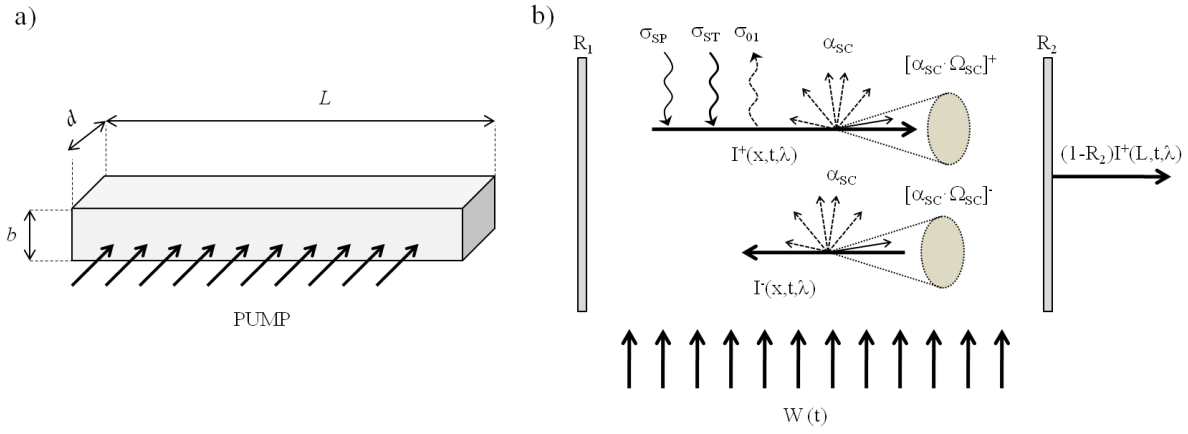

Figure 1.7: a) Active region geometry: L=1.4 cm, b=150 μm and d=180 μm. b) Processes considered in simulation: W(t) pump rate, $I^+(x,t,\lambda)$ and $I^-(x,t,\lambda)$ forward and backward photon fluxes, σ_{SP} spontaneous emission, σ_{ST} stimulated emission, σ_{01} losses due to absorption, α_{SC} scattering losses, $[\alpha_{SC} \cdot \Omega_{SC}]^+$ recovered forward scattering, $[\alpha_{SC} \cdot \Omega_{SC}]^-$ recovered backscattering. R_1 and R_2 possible cavity reflectivities.

propagating waves along the axis of the excited region were considered: the forward ($I^+(x,t,\lambda)$) and backward ($I^-(x,t,\lambda)$) photon fluxes. The contributions to $I^+(x,t,\lambda)$ were: the spontaneous emission as the seed, which is amplified by stimulated emission, reabsorbed by the ground state population and dispersed due to scattering, as well as the forward scattering of $I^+(x,t,\lambda)$ and the backscattering of $I^-(x,t,\lambda)$ within a certain solid angle, which are added up to $I^+(x,t,\lambda)$. Finally, a small contribution of an external feedback was considered.

The rate equations for the photon fluxes (I^+ and I^-) and population densities of the upper and lower laser levels (N_1 and N_0, respectively) describing all these processes read[6]:

$$\begin{aligned}\frac{\partial N_1(x,t)}{\partial t} = W(x,t)N_0(x,t) - \tau^{-1}N_1(x,t) - \\ N_1(x,t)\int \sigma_{st}(\lambda)\left(I^+(x,t,\lambda) + I^-(x,t,\lambda)d\lambda\right) + \\ N_0(x,t)\int \sigma_{01}(\lambda)\left(I^+(x,t,\lambda) + I^-(x,t,\lambda)d\lambda\right)\end{aligned} \tag{1.3}$$

$$N_0(x,t) + N_1(x,t) = N \tag{1.4}$$

$$\begin{aligned}\frac{d}{dx}I^{\pm}(x,t,\lambda) = \tau^{-1}N_1(x,t)\Omega + N_1(x,t)\sigma_{ST}(\lambda)I^{\pm}(x,t,\lambda) \\ -\sigma_{01}(\lambda)N_0(x,t)I^{\pm}(x,t,\lambda) - \alpha_{SC}(\lambda)I^{\pm}(x,t,\lambda) \\ +\alpha_{SC}(\lambda)\Omega_{SC}\left(I^{\pm}(x,t,\lambda) + I^{\mp}(x,t,\lambda)\right)\end{aligned} \tag{1.5}$$

$$W(x,t) = W_0 \exp\left(-\frac{(t-t_0)^2}{(\sigma_t/2)^2}\ln 2\right)\exp\left(-\frac{(x-L/2)^2}{(\sigma_x/2)^2}\ln 2\right) \tag{1.6}$$

$$\frac{d}{dx}I^{\pm} = \left(\frac{\eta}{c}\right)\left(\frac{\partial}{\partial t}\right)I^{\pm} \pm \left(\frac{\partial}{\partial x}\right)I^{\pm} \tag{1.7}$$

With initial and boundary conditions:

$$\begin{aligned}&I^+(x,t=0,\lambda) = I^-(x,t=0,\lambda) = N_1(x,t=0) = 0 \\ &N_0(x,t=0) = N \\ &I^+(x=0,t,\lambda) = R_1 I^-(x=0,t,\lambda) \\ &I^-(x=L,t,\lambda) = R_2 I^+(x=L,t,\lambda)\end{aligned} \tag{1.8}$$

The spectroscopic parameters needed for the computation were obtained from pho-

[6]The details on the notation can be found in Paper A2

tophysical measurements performed by Prof. López Arbeloa's group at UPV-EHU. The system of equations 1.3-1.8 were solved numerically with a specifically written MATLAB code. Both population and photon fluxes equations were integrated using Euler's method, whereas the spectral integrals were performed by the midpoint rule. The spatial, temporal and spectral integration steps were, respectively, $\Delta x = L/200$, $\Delta t = \eta x/c$ and $\Delta\lambda = 1$ nm, where c is the speed of light in vacuum and η the medium refractive index. These steps ensured numerical stability in all cases.

The predictions of the model were compared with experimental results obtained under pumping conditions analogous to those of the simulation. In order to prevent resonant laser effects as much as possible and to study pure non-resonant feedback lasing, the mirrors of the cavity were removed. In addition, the solutions were placed in triangular quartz cuvettes to avoid feedback from the windows of the usual rectangular cells.

Variation of output efficiency with POSS content and pump energy

To better compare the influence of the scattering feedback on the output energy when changing the experimental conditions, we defined the output relative efficiency enhancement ΔE as the ratio of the output energy when there are scatterers (E_{OUT}) and the one extracted from a system without scatterers in the same pumping conditions (E^0_{OUT}), i. e., $\Delta E = E_{OUT}/E^0_{OUT} \times 100\%$.

The solution of equations 1.3-1.8, increasing in every run the scattering feedback (α_{SC}), showed that the presence of scatterers in the system might result in an important increase (up to 10 times, $\Delta E \sim 1000\%$) in the output energy with respect to that extracted from a system without losses (Fig. 1.8a). The experimental results, obtained under experimental conditions analogous to the simulation ones, showed that the output energy increased as the density of nanoscatterers was increased (inset Fig. 1.8a). The quantitative differences between the experimental results and the simulation were due to the simplified nature of our 1D model.

This behaviour was explained by the photon path enlargement caused by the back scattering, which acts as non-resonant feedback. In this way, the longer the photon path is, the bigger the amplification becomes and, consequently, the higher the output energy is. For certain range of scattering, this "extra" amplification can compensate the increase in losses but, once a critical limit has been reached, in which gain saturation sets in, the losing rate exceeds the extra amplification rate and the system becomes unstable with a decrease in the output energy (Fig. 1.8a). These results confirmed the hypothesis about the improvement in laser efficiencies stated previously (section 1.3.1.1). That is, the non-resonant feedback lasing due to scattering is added up incoherently to the conventional resonant laser emission provided by the external cavity, thereby increasing the total efficiency (Fig. 1.1c).

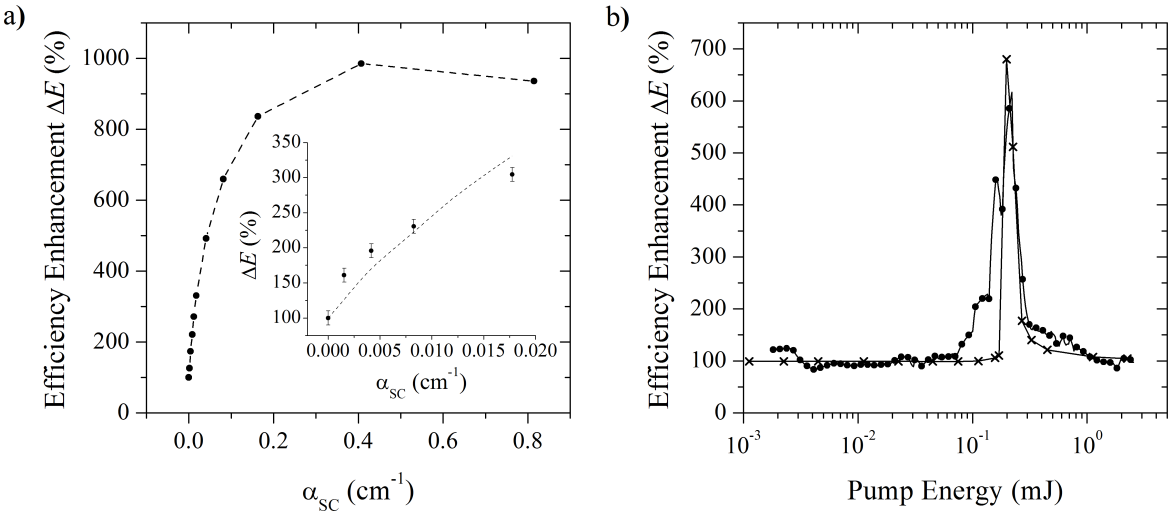

Figure 1.8: a) Calculated relative emission improvement ΔE for increasing scattering ($E_p = 0.25$ mJ). Inset: comparison of calculated (dashed line) and experimental (circles) ΔE corresponding to the scattering losses physically achievable with 8MMA-POSS molecules. b) Comparison of calculated (crosses) and experimental (dots) ΔE as a function of the pump energy for a PM567 solution in EtOAc with 50 wt.% 8MMA-POSS ($\alpha_{SC} = 1.8 \times 10^{-2}$ cm^{-1}).

When the system of equations 1.3-1.8 was solved increasing in every run the pump energy (E_p), it was obtained that the efficiency enhancement was very dependent on the given pump energy, with theory and experiment being again in good agreement (Fig. 1.8b). The most important feature of this dependency was the resonance-like behaviour of ΔE when approaching certain "resonant energy", reaching a sevenfold enhancement ($\Delta E \sim$ 700%), but only within a narrow pump energy range. Moving away from this resonance resulted in the decrease in the efficiency improvement, with no enhancement at all for very low and very high pump energies (Fig. 1.8b). This fact showed the importance of choosing adequately the experimental conditions in order to optimize the final NRF enhanced laser emission.

Then, the developed model provided a theoretical explanation of the previously observed enhanced conventional two-mirror cavity laser emission in gain media when doped with nanoscatterers, and established the limits for the region where gain dominates over scattering losses. At the same time, the model and the experimental evidences, showed that scattering is not always detrimental to conventional laser emission as thought so far.

As a final remark, a very interesting fact is that, provided the Rayleigh regime is fulfilled, the above results are kind of universal ones, independently of the scatterer nature and of the active medium. In this sense, given certain scattering cross section σ_{SC}, the scatterer density ρ could be chosen adequately to tailor the scattering level ($\alpha_{SC} = \rho\sigma_{SC}$) in order to be in the region of maximum amplification. For this effect to occur only nanometric-sized scatterers (Rayleigh regime) should be used in order to have enough

backscattering as to provide the needed feedback while simultaneously avoiding most of the undesirable effect of scattering losses. Hence, the nanometric size of the scatterers is then the critical factor which allows the emission improvement and governs the physics of the emission.

1.3.2 All-Organic Materials: Active Scatterers In Passive Media

The above reasoning led our group to work with a different system based on colloidal suspensions of dye-doped latex nanoparticles (NPs) synthesized, as described in section 1.2.1.2, by Prof. Enciso at UCM[7], with sizes of tens of nanometres, therefore being significantly larger than the POSS molecules but still within the Rayleigh scattering regime ($2\pi r/\lambda < 10$). As a result of this work, it was shown [33, 34] that the laser efficiency and photostability of the laser dye Rhodamine 6G (Rh6G, Fig. 3) was greatly enhanced when incorporated into latex NPs 20 nm wide as compared with the performance of the same dye in solution.

Since the photophysical properties of the dye were not very affected by the encapsulation in the nanoparticle, the emission improvement had to come from the non-resonant feedback due to the scattering induced by the nanoparticles theirselves. As a further evidence of this fact, the encapsulation of Rh6G in latexes with diameters higher than 70 nm had a deleterious effect on both the photophysics and the laser action of the system [34], since the light scattering started dominating its optical properties, therefore resulting in overall loss of emission capability.

1.3.2.1 FRET assisted laser emission in colloidal suspensions of dye-doped latex nanoparticles (From paper A3)

Given the success of this approach to improve both the efficiency and photostability of laser dyes, we decided to tackle the problem of the poor laser performance exhibited by long-wavelength emitting ($\sim$ 700 nm) laser dyes, of interest in biomedical and biophotonic applications due to the capability of this wavelength to penetrate deeper into tissues, which facilitates their use in surgical and photodynamic therapy treatments [35]. The main problem of these dyes is the low absorption at the standard pump wavelength of 532 nm and/or rather poor photostability. The former might be avoided by making use of mixtures of dyes in a system based on Förster resonance energy transfer (FRET). FRET is a physical phenomenon where excitation energy from an excited donor is non-radiatively transferred via dipole-dipole interaction to a proximal ground-state acceptor [36]. A system is required that consists of two dyes; one efficiently absorbs the pump radiation

[7]Facultad de Ciencias Químicas. Universidad Complutense de Madrid, UCM (Spain)

at 532 nm and is able to transfer the excitation energy to the second, long-wavelength emitting dye of interest. The energy transfer process in a FRET system requires good overlap between donor emission and acceptor absorption bands, and it depends strongly on the distance between donor and acceptor molecules [36].

Consequently, it naturally arose the thought of using dye confinement in latex nanoparticles in combination with the FRET process as a strategy to overcome simultaneously the low absorption, low laser efficiency and photostability problems of long-wavelength emitting dyes, for example, Nile Blue (NB, Fig. 3). This dye, which is quite efficient but rather unstable under pumping at 532 nm, seemed an ideal candidate to prove this approach, as there is a good overlap between its absorption band and the emission band of Rh6G, whose laser performance in colloidal suspensions had been already optimized [34].

Laser performance

A systematic study was carried out regarding the laser performance of samples with different dye loadings and ratios and nanoparticle content in the suspension. The optimized laser emission, obtained for the sample with a ratio Rh6G/NB 1.5/1 (Fig. 1.9a), was centred at 700 nm (Fig. 1.9b), with just some residual emission from the Rh6G, and reached an efficiency of 13%. The sample without donor (Rh6G), instead, showed no sign of laser emission, testifying the goodness of the energy transfer approach. Nevertheless, when both dyes were solved in ethanol at the same dye ratio and concentration and under the same pumping conditions, the laser efficiency was slightly higher (18%) than that of the colloidal suspensions, but only because of the higher affinity of NB for ethanol than for the polymer.

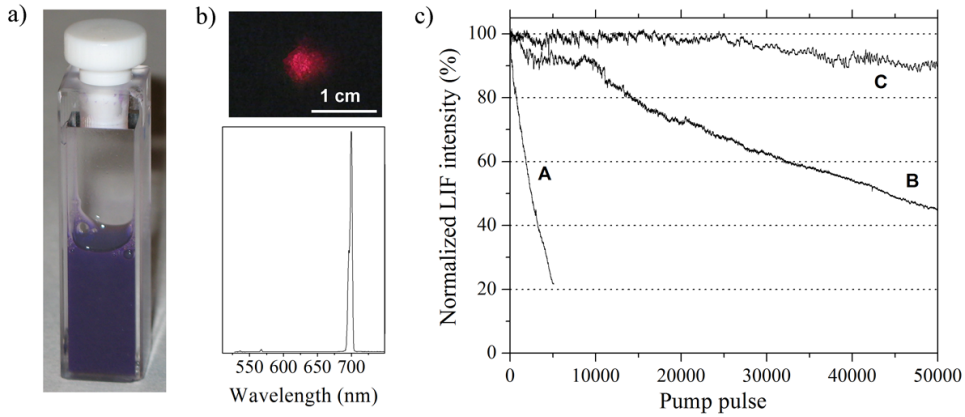

Figure 1.9: a) Colloidal suspension with a Rh6G/NB proportion 1.5/1 (0.28/0.19 wt.% with respect to monomer). b) Laser emission spectrum from colloidal suspension in a). Photograph over the spectrum shows the actual laser spot on a black screen placed 30 cm away from the laser cavity. c) Normalized laser-induced fluorescence emission as a function of the number of pump pulses for NB in ethanol (A), a mixture of 0.024/0.016 wt.% of Rh6G/NB in ethanol (B), and colloidal suspension a) (C).

The true extent of the importance of dye confinement was revealed by the emission photostability under laser operation (Fig. 1.9c). As mentioned earlier, NB is a rather unstable dye under laser irradiation with its laser-induced fluorescence (LIF) emission in ethanol solution dropping by 80% from its initial value after just 5×10^3 pump pulses (Fig. 1.9c, curve A). The addition of Rh6G donor to the ethanol solution significantly increased the NB stability, with the emission at 695 nm dropping by 55% from its initial value after 5×10^4 pump pulses (Fig. 1.9c, curve B). In contrast, when the dyes were confined in nanoparticles, the emission of NB dropped by less than 10% after 5×10^4 pump pulses (Fig. 1.9c, curve C). Thus, the FRET process, together with the confinement of the dye molecules in the reduced space of the nanoparticles, significantly enhanced the photostability of the laser system under consideration.

Photophysical characterization

The photophysical study of the nanoparticles revealed that the encapsulation of each of the dyes alone into the NPs did not significantly alter their absorption and emission bands with respect to those of the diluted solutions in ethanol, indicating the absence of aggregates. Nevertheless, the fluorescence lifetimes (τ) exhibited a slight enlargement when the dyes were incorporated into the NPs, which in our previous work [34] was ascribed to the spontaneous emission inhibition experienced by emitters confined in subwavelength cavities, i. e., the dyes are subjected to the so-called Purcell's effect.

It has been theoretically shown [37] and experimentally proved [38] that when the dimensions of the cavity (NPs in our case) are reduced well below the emission wavelength (Rayleigh regime), the spontaneous emission decay rate ($\gamma = 1/\tau$) decreases smoothly, tending to a limiting value $\gamma_{NP} = [9/((n_1/n_2)^2 + 2)^2](\gamma_{bulk} n_2/n_1)$, where n_1 and n_2 are the refractive indices of the cavity and the surrounding media, respectively, and γ_{bulk} is the decay rate of the emitter in the bulk dielectric medium [37]. Taking into account the refractive indices of the NP and surrounding medium (water), $\gamma_{NP} \sim 0.76\gamma_{bulk}$, that is, $\tau_{NP} \sim \tau_{bulk}/0.76$, which agreed well with the experimental results (τ_{20nm}=4.54 ns, τ_{bulk}=3.60 ns, $\tau_{20nm} = \tau_{bulk}/0.79$) [34].

In a similar way, we carried out the photophysical characterization of the NP which optimized the laser emission (Rh6G/NB 1.5/1). Both the absorption, fluorescence (excitation of Rh6G in a region where NB does not absorb) and excitation spectra revealed the presence of both dyes (Fig. 1.10a), demonstrating an efficient energy transfer from the donor Rh6G to the acceptor NB. These results indicated that the NB excited state was populated by means of the donor, via an energy transfer process, as was nicely reproduced in the time-resolved emission spectra of Fig. 1.10b. Accordingly, this process affected the fluorescence decay curve of the confined donor Rh6G in the presence of NB, characterized by a faster decay than that observed for Rh6G encapsulated alone in the

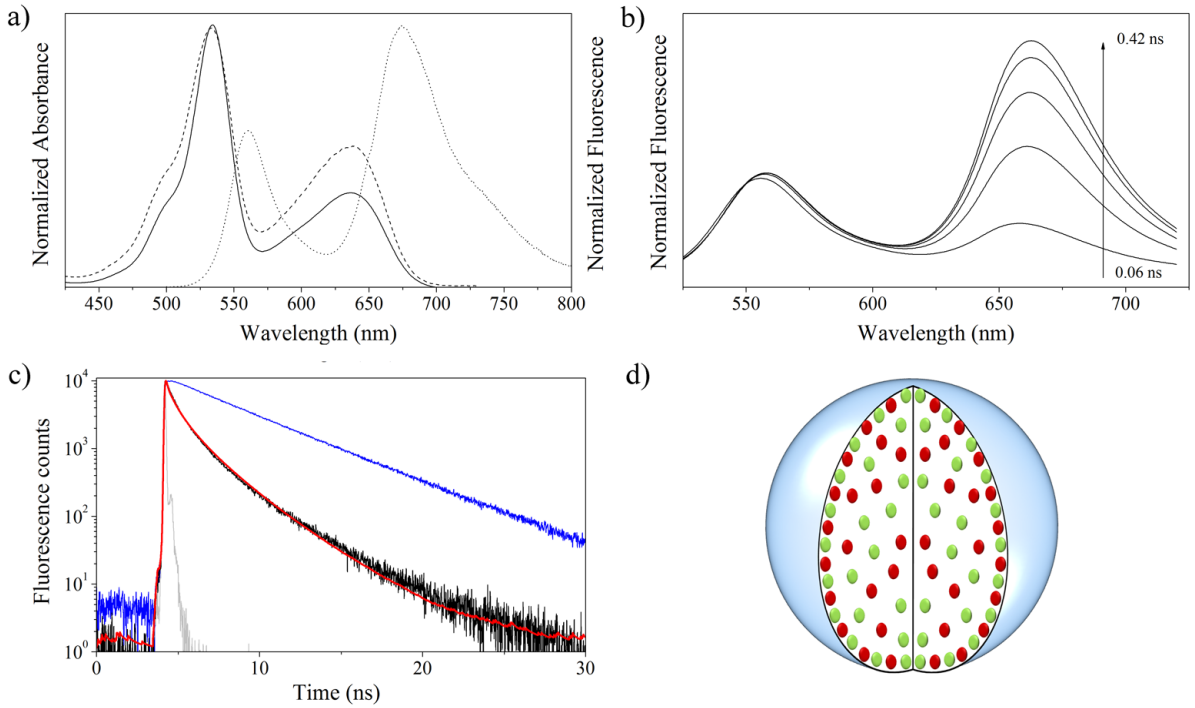

Figure 1.10: a) Normalized absorption (solid line), fluorescence (dotted line) and excitation (dashed line) spectra of a colloidal suspension with a Rh6G/NB proportion 1.5/1 (0.28/0.19 wt.% with respect to monomer). b) Fluorescence spectra (normalized at the donor emission) at different delay times after donor excitation (0.06, 0.12, 0.18, 0.30 and 0.42 ns) of the same sample. c) Experimental fluorescence decay curve of Rh6G in latexes in the absence (blue line) and presence (black line) of NB, exciting at 470 nm and monitoring at 560 nm. The red line is the best fit to the experimental data. d) Sketch of dye distribution (Rh6G in green dots and NB in red dots) assumed for best fit to experimental data.

latex nanoparticles (Fig. 1.10c).

The built up of NB emission entails different energy transfer mechanisms, both radiative (photon interchange) and non-radiative (dipole-dipole interactions), as has been depicted in Fig. 1.11. Once a Rh6G molecule is excited and prepared in an emitting state, it may undergo several decay pathways. If a NB molecule is sufficiently close (e. g., inside the NP), the excited Rh6G molecule can transfer non-radiatively its energy to the NB molecule (hetero-FRET). This very same process may happen as well when a Rh6G molecule in the ground state is close enough (homo-FRET). When the later occurs, the excitation energy will be finally transfered to a NB molecule, but only after several energy hops among the donors coexisting in the nanoparticle. Furthermore, photons emitted by an excited Rh6G molecule surviving the FRET processes in a NP could be absorbed (by undergoing a radiative energy transfer, RET, process) by another Rh6G molecule (homo-RET) or a NB acceptor (hetero-RET) located in a distant nanoparticle (Fig. 1.11). Finally, the excited Rh6G molecule has a certain probability of emitting a photon capable of leaving the system and reaching the detector.

The efficiency of the FRET process (quantum yield ϕ_{FRET}) was calculated from the

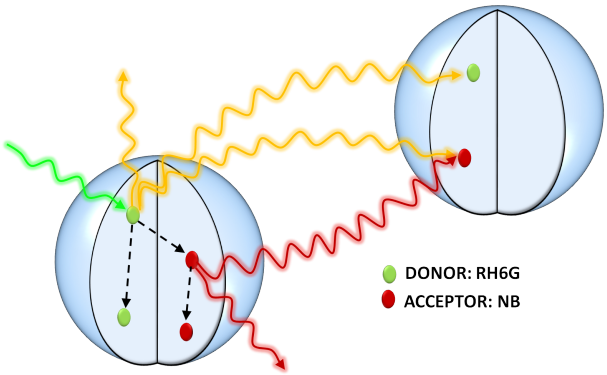

Figure 1.11: Sketch of energy transfer mechanisms present in the colloidal suspensions. Solid and dashed arrows represent, respectively, radiative and non-radiative energy transfers. Green arrow=pump, Yellow arrows=Rh6G emission, Red arrows=NB emission.

comparison of the fluorescence decay curves of the donor in the absence ($I_f^D(t)$) and presence ($I_f^{D+A}(t)$) of acceptors with the equation [36]

$$\phi_{FRET} = 1 - \frac{\int I_f^{D+A}(t)dt}{\int I_f^D(t)dt}, \tag{1.9}$$

and reached a value as high as ϕ_{FRET}=0.77. The influence of the RET processes was avoided in the photophysical measurements by diluting the suspensions, but it was very important at the high optical densities required to record laser action. In fact, the laser spectra (Fig. 1.9) suggested that the total energy transfer efficiency was much higher (0.98) than the ϕ_{FRET} obtained with Eq. 1.9. Taking into account these results, we concluded that the energy transfer in the confined Rh6G/NB system under laser operation took place mainly via a FRET mechanism reinforced by RET processes.

In addition, the fluorescence decay curve of the donor not only serves to obtain the transfer efficiency, but it can be used as a tool to determine the dye distribution within a nanoparticle, because the energy transfer is highly dependent on the particular donor-acceptor distance distribution [39]. The fluorescence decay curve of the donor in the presence of acceptors in our latex nanoparticles were theoretically analyzed following (and modifying when needed) the expressions developed by Martinho's group[8] for FRET processes in systems with spherical symmetry [39, 40].

As we had carried out a synthesis in which all the ingredients were mixed before polymerization, and not in a sequential route, we began by assuming that the nanoparticle consisted of a homogeneous polymer and that the dye distributions were therefore uniform. The fluorescence decay curve computed with this assumption fitted quite accurately for short times, but deviated from the experimental points for longer times, predicting a

[8]Centro de Química-Física Molecular and IN-Institute of Nanoscience and Nanotechnology. Instituto Superior Técnico (Portugal)

quicker deactivation. This result indicated that the dye distribution had to be, unexpectedly, inhomogeneous.

Our initial interpretation of this inhomogeneity was that there were two different domains, because the monomer HEMA is more polar than MMA and GMA, and would therefore tend to be closer to the aqueous solution (closer to the surface) than the MMA and GMA. Because Rh6G and NB are more soluble in HEMA than in MMA and GMA, both dyes would consequently lie closer to the surface than to the centre of the nanoparticle. Hence, the latexes would demonstrate a core/shell morphology with a smooth transition from core to shell.

Following a trial-and-error approach with different core/shell morphologies, and in view of the fit shown in Fig. 1.10c, we concluded that the actual distribution of dyes within the nanoparticle was intermediate between a core/shell distribution and a core/surface one (Fig. 1.10d). In other words, the nanoparticles would have a core/thin shell morphology, consistent with the following interpretation: (i) the core consists of a homogeneous tertpolymer of MMA/HEMA/GMA, in which both dyes are homogeneously solved; (ii) the thin shell is formed of a so-called nanoparticle 'hairy layer' (surface roughness or fuzziness), in which both dyes are adsorbed with a concentration different to that of the core. As we used an anionic surfactant (SDS) in the synthesis, the 'hairy layer' (tertpolymer/surfactant/water interface) would have a certain negative charge distribution. Hence, cationic dyes such as Rh6G (donor) and NB (acceptor) would be adsorbed on, or electrostatically attracted to, the anionic surface with the very same distribution. Of course, more work would be needed to confirm this hypothesis.

1.3.2.2 Random lasing in self-assembled dye-doped latex nanoparticles (From paper A3)

As mentioned above, RL has been observed in many different materials and configurations. In this regard, the so-called photonic glasses [41–44] (Fig. 1.12), which are formed by randomly self-assembled monodispersed spherical micro or nanoparticles and that thus constitute the antithesis of the well known photonic crystals (Fig. 1.12), have attracted interest due to the possibility to tailor their RL emission properties by modifying the nanoparticle size.

Given the good laser performance shown by the previously presented colloidal suspensions of latex nanoparticles, we wondered whether the high efficiency of the energy transfer process in these systems would be maintained when the nanoparticles were not contained in the suspension but were casted instead as photonic glasses. The solid samples, obtained as described in section 1.2.1.3, gave place, as a proof of concept, to FRET-assisted stimulated emission around 710 nm when pumped in front-face (Fig. 1.13), thereby rep-

Figure 1.12: Nanoparticle packing in colloidal photonic crystal (a) and photonic glass (b).

resenting the first demonstration of FRET assisted incoherent RL from solid samples of dye-doped latex NPs.

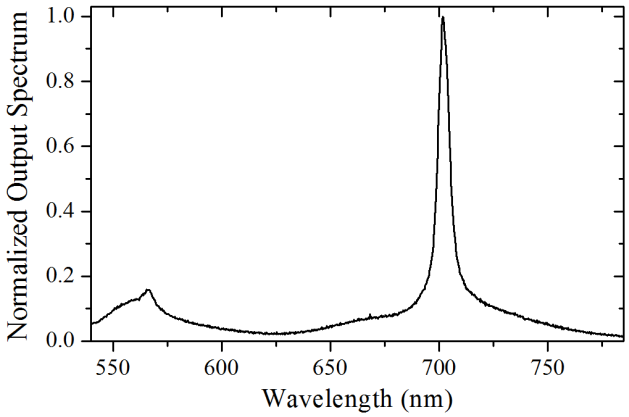

Figure 1.13: Normalized emission spectra from a solid sample of NPs containing a mixture of Rh6G/NB (0.28/0.19 wt.%) when pumped in front-face at 490 kW/cm^2.

In view of this result, it was clear that a deeper study of the random laser properties of this type of sample was needed. Although this work has been already done, it has not been included in the thesis report since it will be published after this thesis report is presented.

1.4 Conclusion on SSDL with scattering feedback

The experimental and theoretical results presented in this chapter demonstrate conclusively that optical scattering is not always detrimental to conventional lasers, as is commonly believed, but may give place, on the contrary, to dramatic improvements in the output efficiencies. If the scattering level is adequately selected, the non-resonant feedback induced by the back scattering adds up incoherently to the resonant feedback provided by the external cavity, increasing the overall feedback and, thus, the total efficiency. This phenomenon has been demonstrated to be present in laser materials based both on passive scatterers embedded in active media (POSS based systems) and on active scatterers suspended in passive media (colloidal systems). With this last system, we have

demonstrated, for the first time, that the confinement into subwavelength nanoparticles of laser dyes undergoing FRET may significantly enhance the laser efficiency and photostability of red-emitting laser dyes of interest in biomedical and biophotonic applications.

In conclusion, we have shown that the development of advanced photonic materials combining synergistically the advantages of both random and conventional laser may result in optimized laser emission, paving the way to the commercialization and industrialization of laser heads based on SSDL.

Bibliography

[1] B. H. Soffer and B. B. McFarland, "Continuously tunable, narrow-band organic dye lasers," *Appl. Phys. Lett.*, vol. 10, pp. 266–267, 1967.

[2] O. G. Peterson and B. B. Snavely, "Stimulated emission from flashlamp-excited organic dyes in polymethylmethacrylate," *Appl. Phys. Lett.*, vol. 12, pp. 238–240, 1968.

[3] R. M. O'Connell and T. T. Saito, "Plastics for high-power laser applications: a review," *Opt. Eng.*, vol. 22, pp. 393–399, 1983.

[4] A. Costela, I. García-Moreno, J. M. Figuera, F. Amat-Guerri, R. Mallavía, M. D. Santa-María, and R. Sastre, "Solid-state dye lasers based on modified rhodamine 6G copolymerized methacrylic monomers," *J. Appl. Phys.*, vol. 80, pp. 3167–3173, 1996.

[5] I. García-Moreno, F. Amat-Guerri, M. Liras, A. Costela, L. Infantes, R. Sastre, F. L. Arbeloa, J. Bañuelos, and I. L. Arbeloa, "Structural changes in the BODIPY dye PM567 enhancing the laser action in liquid and solid media," *Adv. Funct. Mat.*, vol. 17, no. 16, pp. 3088–3098, 2007.

[6] A. Costela, I. García-Moreno, and R. Sastre, "Materials for solid-state dye lasers," in *Handbook of advanced electronic and photonic materials and devices, edited by H. S. Nalwa, Volume 7: Liquid crystals, display and laser materials*, pp. 161–208, Academic Press, 2001.

[7] A. Costela, I. García-Moreno, C. Gómez, O. García, and R. Sastre, "Laser performance of pyrromethene 567 dye in solid polymeric matrices with different cross-linking degrees," *J. Appl. Phys.*, vol. 90, pp. 3159–3166, 2001.

[8] V. Martín, A. Costela, M. Pintado-Sierra, and I. García-Moreno, "Sulforhodamine B doped polymeric matrices: a high efficient and stable solid-state laser," *J. Photochem. Photobiol. A: Chem.*, vol. 219, pp. 265–272, 2011.

[9] J. J. Reisinger and M. A. Hillmyer, "Synthesis of fluorinated polymers by chemical modifications," *Prog. Polym. Sci.*, vol. 27, pp. 971–1005, 2002.

[10] O. García, R. Sastre, D. del Agua, A. Costela, I. García-Moreno, F. L. Arbeloa, J. Bañuelos, and I. L. Arbeloa, "Laser and physical properties of BODIPY chromophores in new fluorinated polymeric materials," *J. Phys. Chem. C*, vol. 111, pp. 1508–1516, 2007.

[11] O. García, R. Sastre, I. García-Moreno, V. Martín, and A. Costela, "New laser hybrid materials based on POSS copolymers," *J. Phys. Chem. C*, vol. 112, pp. 14710–14713, 2008.

[12] A. Costela, I. García-Moreno, C. Gómez, O. García, R. Sastre, A. Roig, and E. Molins, "Polymer-filled nanoporous silica Aerogels as host for highly stable solid-state dye lasers," *J. Phys. Chem. B*, vol. 109, pp. 4475–4480, 2005.

[13] A. Costela, I. García-Moreno, D. del Agua, O. García, and R. Sastre, "Highly photostable solid-state dye lasers based on silicon-modified organic matrices," *J. Appl. Phys.*, vol. 101, no. 073110, pp. 1–11, 2007.

[14] A. Costela, I. García-Moreno, C. Gómez, O. García, and R. Sastre, "Enhancement of laser properties of pyrromethene 567 dye incorporated into new organic-inorganic hybrid materials," *Chem. Phys. Lett.*, vol. 369, pp. 656–661, 2003.

[15] A. Costela, I. García-Moreno, D. del Agua, O. García, and R. Sastre, "Silicon-containing organic matrices as hosts for highly photostable solid-state dye lasers," *Appl. Phys. Lett.*, vol. 85, pp. 2160–2162, 2004.

[16] D. B. Cordes, P. D. Lickiss, and F. Rataboul, "Recent developments in the chemistry of cubic polyhedral oligosilsesquioxanes," *Chem. Rev.*, vol. 110, no. 4, pp. 2081–2173, 2010.

[17] R. Sastre, V. Martín, L. Garrido, J. L. Chiara, B. Trastoy, O. García, A. Costela, and I. García-Moreno, "Dye-doped polyhedral oligomeric silsesquioxane (POSS)-modified polymeric matrices for highly efficient and photostable solid-state lasers," *Adv. Funct. Mat.*, vol. 19, pp. 3307–3316, 2009.

[18] A. E. Siegman, *Lasers.* Mill Valley, CA: University Science Books, 1986.

[19] D. S. Wiersma, "The physics and applications of random lasers," *Nat. Physics*, vol. 4, pp. 359–367, 2008.

[20] M. N. Lawandy, R. M. Balachandran, A. S. L. Gomes, and E. Sauvain, "Laser action in strongly scattering media," *Nature*, vol. 368, pp. 436–438, 1994.

[21] H. Cao, Y. G. Zhao, S. T. Ho, E. W. Seelig, Q. H. Wang, and R. P. H. Chang, "Random laser action in semiconductor powder," *Phys. Rev. Lett.*, vol. 82, pp. 2278–2281, 1999.

[22] M. A. Noginov, *Solid-state random lasers.* New York: Springer, 2005.

[23] H. Noh, J. K. Yang, S. F. Liew, M. J. Rooks, G. S. Solomon, and H. Cao, "Control of lasing in biomimetic structures with short-range order," *Phys. Rev. Lett.*, vol. 106, no. 183901, pp. 1–4, 2011.

[24] L. Sapienza, H. Thyrrestrup, S. Stobbe, P. G. García, S. Smolka, and P. Lodahl, "Cavity quantum electrodynamics with Anderson-localized modes," *Science*, vol. 327, pp. 1352–1355, 2010.

[25] S. K. Turitsyn, S. A. Babin, A. E. El-Taher, P. Harper, D. V. Churkin, S. I. Kablukov, J. D. Ania-Castañón, V. Karalekas, and E. Podivilov, "Random distributed feedback fibre laser," *Nature Photon.*, vol. 4, pp. 231–235, 2010.

[26] A. Tulek, R. C. Polson, and Z. V. Vardeny, "Naturally occurring resonantors in random lasing of π-conjugated polymer films," *Nature Physics*, vol. 6, pp. 303–310, 2010.

[27] S. Johannson and V. S. Letokhov, "Astrophysical lasers and nonlinear optical effects in space," *New Astron. Rev.*, vol. 51, pp. 443–523, 2007.

[28] J. Andreasen, A. A. Asatryan, L. C. Botten, M. A. Byrne, H. Cao, L. Ge, L. Labonté, P. Sebbah, A. D. Stone, H. E. Türeci, and C. Vanneste, "Modes in random lasers," *Adv. Opt. Photon.*, vol. 3, pp. 88–127, 2010.

[29] H. Cao, "Review on lates developments in random lasers with coherent feedback," *J. Phys. A: Math. Gen.*, vol. 38, pp. 10497–10535, 2005.

[30] C. F. Bohren and D. R. Huffman, *Absorption and scattering of light by small particles.* Weinheim, Germany: Wiley-VCH, 2004.

[31] T. D. Nagao, N. Anzai, Y. Kobayashi, S. Gu, and M. Konno, "Preparation of highly monodispersed poly(methyl mathacrylate) particles incorporating fluorescence Rhodamine 6G for colloidal crystals," *J. Colloid Interface Sci.*, vol. 298, pp. 232–237, 2006.

[32] U. Ganiel, A. Hardy, G. Neumann, and D. Treves, "Amplified spontaneous emission and sigal amplification in dye-laser systems," *IEEE J. Quantum Electron.*, vol. QE-11, no. 11, pp. 881–892, 1975.

[33] E. Enciso, A. Costela, I. García-Moreno, V. Martín, and R. Sastre, "Conventional unidirectional laser action enhanced by dye confined in nanoparticle scatters," *Langmuir*, vol. 26, no. 9, pp. 6154–6157, 2010.

[34] V. Martín, J. Bañuelos, E. Enciso, I. López-Arbeloa, A. Costela, and I. García-Moreno, "Photophysical and lasing properties of rhodamine 6G confined in polymeric nanoparticles," *J. Phys. Chem. C*, vol. 115, no. 10, pp. 3926–3933, 2011.

[35] F. J. Duarte, *Tunable laser applications.* Boca Raton, FL: CRC Press, 2009.

[36] B. Valeur, *Molecular fluorescence.* Weinhaim, Germany: Wiley-VCH, 2002.

[37] H. Chew, "Radiation and lifetimes of atoms inside dielectric particles," *Phys. Rev. A*,

vol. 38, pp. 3410–3416, 1988.

[38] H. Schniepp and V. Sandoghdar, "Spontaneous emission of europium ions embedded in dielectric nanospheres," *Phys. Rev. Lett.*, vol. 89, no. 257403, pp. 1–4, 2002.

[39] J. P. S. Farinha and J. M. G. Martinho, "Resonance energy transfer in polymer nanodomains," *J. Phys. Chem. C*, vol. 112, pp. 10591–10601, 2008.

[40] A. Yekta, M. A. Winnik, J. P. S. Farinha, and J. M. G. Martinho, "Dipole-dipole electronic energy transfer. fluorescence decay functions for arbitrary distributions of donors and acceptors. ii. systems with spherical symmetry," *J. Phys. Chem. A*, vol. 101, pp. 1787–1792, 1997.

[41] P. D. García, R. Sapienza, A. Blanco, and C. López, "Photonic glass: a novel random material for light," *Adv. Mater.*, vol. 19, pp. 2597–2602, 2007.

[42] P. D. García, R. Sapienza, and C. López, "Photonic glass: a step beyond white paint," *Adv. Mater.*, vol. 22, pp. 12–19, 2010.

[43] S. Gottardo, R. Sapienza, P. D. García, A. Blanco, D. S. Wiersma, and C. López, "Resonance-driven random lasing," *Nat. Photonics*, vol. 2, pp. 429–432, 2008.

[44] Y. Chen, J. Herrnsdorf, B. Guilhabert, Y. Zhang, A. L. Kanibolotsky, P. J. Skabara, E. Gu, N. Laurand, and M. D. Dawson, "Modification of emission wavelength in organic random lasers based on photonic glass," *Org. Electron.*, vol. 13, pp. 1126–1135, 2012.

Chapter 2

Solid state dye lasers as integrated devices

2.1 Introduction

Over the last few years there has been significant work exploring the development of organic thin film lasers based on dye doped polymers because of their potential applications as integrated devices. Organic materials provide low-cost gain media with high emission efficiency across the whole visible spectrum and beyond, which, together with their processing and pumping flexibility, makes them very attractive for the fabrication and development of coherent light sources suitable for integration in optoelectronic and disposable spectroscopic and sensing devices [1].

One of the most characteristic properties of organic materials, either dyes or polymers, is the almost limitless amount of compositions and structures that can be attained through chemical modifications, with its optical and mechanical properties relatively easily tuneable [2]. This is translated into a vast amount of available dyes with emission expanding the whole visible spectrum, many of them being commercial[1]. Leaving apart specifically synthesized emitters, many commercial dyes have been used in dye-doped integrated devices emitting from the blue region [3, 4] to the near-IR [5–13], and passing through the green [5, 14–17], but with an special emphasis on the yellow-red spectral region.

A huge advantage of organic thin film lasers is that they can be deposited from solution, fact that enables the use of many different deposition techniques such as spin coating [18], dip coating [19], pen drawing [20], extender-roller [21] and drop casting [22]. Thanks to this full solution processability, many different resonator types may be used with the aim to integrate these devices into small footprint platforms such as photonic circuits and lab-on-chips. The commonly used cavities can be divided into diffractive resonators, making use of Bragg scattering, and reflective resonators making use of Fresnel or total internal reflection. In the former type one can find in-plane Distributed Bragg Reflectors (DBR) [23, 24], stacked DBRs [25, 26], Distributed Feedback (DFB) resonators (1D, 2D or circular [27]), in 1^{st} [27], 2^{nd} [27] or higher [22] diffraction orders, and photonic crystals

[1] See for example: Exciton, Radiant Dyes, Coherent, Sigma-Aldrich, American Dyes

[28, 29], among others. With respect to reflective resonators one could use Fabry-Perot waveguides [30, 31], circular [32] and deformed [33] microdisks, stadium-shape [34] and spiral [35] microcavities and many others.

The rich selection of available cavity configurations has been made possible thanks to the proliferation of resonator fabrication techniques, which may be arranged in two general groups: active film modification techniques and substrate modification techniques, depending on where the resonator is "written". The substrate structuring is, the most of the times, performed by making use of Reactive Ion Beam Etching (RIBE) to transfer to the substrate a pattern recorded on a resist by means of photolithography [36] or electron beam lithography [37]. Nevertheless, other techniques such as lithographical laser ablation [38, 39] or Laser Induced Backside Wet Etching (LIBWE) [40] could be used. On the other hand, the "soft" nature of the organic materials and their solution processability enable the use of many processing techniques in order to "write" the resonator in the active film: electron beam lithography [23, 41], UV-lithography [42], Nano-Imprint Lithography (NIL) [28], thermal-NIL [43], solvent assisted micromolding (SaMiM) [44], replica molding [16, 45], holographic polymerization [29], holographic writing [6] or compression-molding [25], among others.

The versatility of resonator designs for organic thin film lasers is enriched, in addition, by a variety of pumping configurations, as they have been excited transversally [6], longitudinally [46], quasi-longitudinally [25], and by using a "Quasi-end-fire" scheme, as coined by Oki and colleagues [47]. On the other hand, these devices are pumped, the most of the times, with nanosecond pulses, but picosecond [6] and femtosecond [48] pulses have been used as well. But an even more relevant fact is that the pumping sources have been reduced in size to the point of using diode lasers [46] and, more recently, simple light emitting diodes [49]. Unfortunately, the long sought-after milestone of continuous wave (CW) operation in organic thin film laser has not come true yet, albeit some results on Amplified Spontaneous Emission under CW pumping have been already reported [50, 51].

Another desirable property for this family of devices is the emission wavelength tunability. The laser peak wavelength can be controlled by changing the cavity parameters. For example, in DFB lasers the emission wavelength is tuned either by a change in the periodic structure period [52] or in the film thickness [53]. Nevertheless, most of the times, the tuning capabilities are proven fabricating different devices, each one of them presenting different cavity parameters [43, 54], which hinders the applicability of this technique to the fabrication of integrated tuneable devices. Some approaches have been reported in which the emission wavelength is tuned without involving sample substitution or displacement: two-beam holographic pumping with intensity [55] or polarization [13] modulation in which there is a variation on the periodic structure due to the change in the

interference pattern, temperature tuning [56, 57] due to a thermoelastic expansion of the cavity and a thermally induced change in the refractive index [58], and mechanical tuning [59] of a flexible device by stretching the grating area. The holographic and mechanical methods can provide more than 60 nm tuning range, whereas the temperature method is restricted to only some nanometres (1-5 nm). Another attractive approach consists of obtaining simultaneous multiwavelength emission (RGB lasing) from a single chip [60].

A major concern in organic materials is the device durability, which is limited by the emitter (dye, quantum dot, semiconductor polymer) degradation upon optical excitation by means of thermal processes and/or photochemical reactions. Surprisingly, in spite of the vast amount of works on the characterization of dye-doped organic thin film lasers, only a few groups have shown a serious interest on the device operational life-time evaluation [17, 41, 43, 54]. A special mention must be made of Oki's group, which have studied extensively the dye photostability in thin film polymer lasers [5, 6, 20, 47, 56, 61–64].

In this regard, our group has been working extensively, for more than two decades now, on the optimization of the efficiency and photostability of dye-doped polymer laser rods (Chapter 1), with an special emphasis on the chemical and physical compatibility of dyes and hosts and the correspondence of structural properties with photophysical and laser emission properties, i. e., following the "chemical" approach. This expertise led us to turn our interests towards the optimization of both efficiency and photostability in thin film dye-doped polymer lasers by applying our knowledge on the specific dye/host chemical and physical compatibilities. To our surprise, the survey of the existing literature revealed a shortage of works studying in a systematic way the stimulated emission properties, in general, and the emission photostability in particular, of very well known commercial dyes such as pyrromethenes, perylenes, sulforhodamines or hemicyanines (Fig. 3), in spite of them having shown outstanding laser characteristic as bulk materials. Hence, one of the objectives of the presented thesis was to fill in this gap as much as possible.

In this chapter, the main results on the characterization of thin film emitting devices based on commercial dyes, emitting in the yellow-red spectral range (570-730 nm), incorporated into adequate polymer matrices are presented, evaluated and compared. In section 2.2 an extended description of the thin film fabrication techniques and the emission characterization experimental set-ups and measurements will be provided. Section 2.3 will be devoted to the presentation, comparison and discussion of the thesis main results on SSDL based on thin films. The chapter will be closed with the main conclusion on dye-doped polymer thin film devices.

As this thesis report is based on an article compilation, the following text will serve as a summary and link between the compiled papers. The results will not be presented in a chronologic order, but in a more natural and fluid way with the aim to help to

better understand the obtained results. For clarity and coherence purposes, extended descriptions or updated discussions of certain aspects of the published works will be provided when needed.

The papers used to prepare this chapter have been appended at the end of the thesis report on Appendix B, and will be referred from now on as:

- Paper B1: "On the characteristic lengths in the variable stripe length method for optical gain measurements," J. Opt. Soc. Am. B 27, 9, 1874–1877 (2010)
- Paper B2: "Amplified spontaneous emission and optical gain measurements from pyrromethene 567-doped polymer waveguides and quasi-waveguides," Opt. Express 16, 10, 7023–7036 (2008). Erratum: Opt. Express 16, 10, 7587–7587 (2008)
- Paper B3: "Waveguides and Quasi-Waveguides based on pyrromethene 597-doped poly(methyl methacrylate)," Appl. Phys. B 97, 73–83 (2009)
- Paper B4: "High-gain long-lived amplified spontaneous emission from dye-doped fluorinated polyimide planar waveguides," Macromol. Chem. Phys. 210, 1624–1631 (2009)
- Paper B5: "Laser emission from mirrorless waveguides based on photosensitized polymers incorporating POSS," Opt. Express 18, 10, 10247–10256 (2010)
- Paper B6: "New perylene-doped polymeric thin films for efficient and long-lasting lasers," J. Mater. Chem. 22, 8938–8947 (2012)
- Paper B7: "Random lasing from sulforhodamine dye doped polymer films with high surface roughness," Appl. Phys. B 108, 839–850 (2012)
- Paper B8: "Waveguided random lasing in red-emitting-dye-doped hybrid polymer thin films," Org. Electron. 13, 1463–1469 (2012)

2.2 Methodology

Section 2.2.1 presents an extended description of the fabrication techniques used to prepare the films evaluated through the report. Section 2.2.2 shows the road-map followed to obtain laser emission from the active thin films. In section 2.2.3 the experimental set-ups used for the Amplified Spontaneous Emission (ASE), Random Laser (RL) and Distributed Feedback (DFB) lasing experiments are presented, including some details not described on the compiled papers. Some aspects on the ASE experimental set-up evolution along the thesis years and on failed set-ups will be provided. Finally, the kind of experiments performed for the emission characterization will be described.

2.2.1 Film deposition techniques

Depending on the desired thickness, two different deposition techniques were used to prepare the thin films: Extender-roller technique [21] and spin coating [18]. The solutions used for both methods are equally prepared: dye, polymer and additives (when used) are incorporated into the solvent in adequate proportions and gently stirred. Once the solution is well mixed, it is ready to be casted.

2.2.1.1 Extender-roller technique

This technique owes its name to the nature of the film preparation [21], which consists of extending the dye/polymer solution over the substrate by means of a threaded rod with a particular thread (Fig. 2.1a). In our experimental set-up the procedure is as follows: a quartz or glass slide (substrate) is surrounded by slides of the same thickness to hold the substrate tight and to obtain an even surface to extend the solution over the desired substrate homogeneously (Fig. 2.1b). Sufficient dye/polymer solution is dropped onto the adjacent slide (Fig. 2.1c), and is extended over the substrate with one quick rod slide (Fig. 2.1d), trying to maintain the rod as perpendicular to the movement as possible. Before complete solvent evaporation the adjacent slides are removed (Fig. 2.1e) and the coated substrate is placed in a oven at 50 °C for 15 minutes. Once the solvent is completely evaporated the substrate is removed from the oven and the sample is ready to be measured (Fig. 2.1f).

By changing the size of the thread groove the initial wet film thickness will vary [21]. On the other hand, depending on the polymer concentration with respect to solvent a thinner (diluted solution) or thicker (concentrated solution) dry film will be obtained. In these experiments the rod thread was kept fixed, and the thicknesses were controlled with the polymer concentration. With this technique films from 3-4 μm to 20 μm have been obtained for the papers in this thesis.

The main drawback of this technique is that the thickness and sample quality depends on the speed and pressure applied to the rod when extending the solution. As the rod is

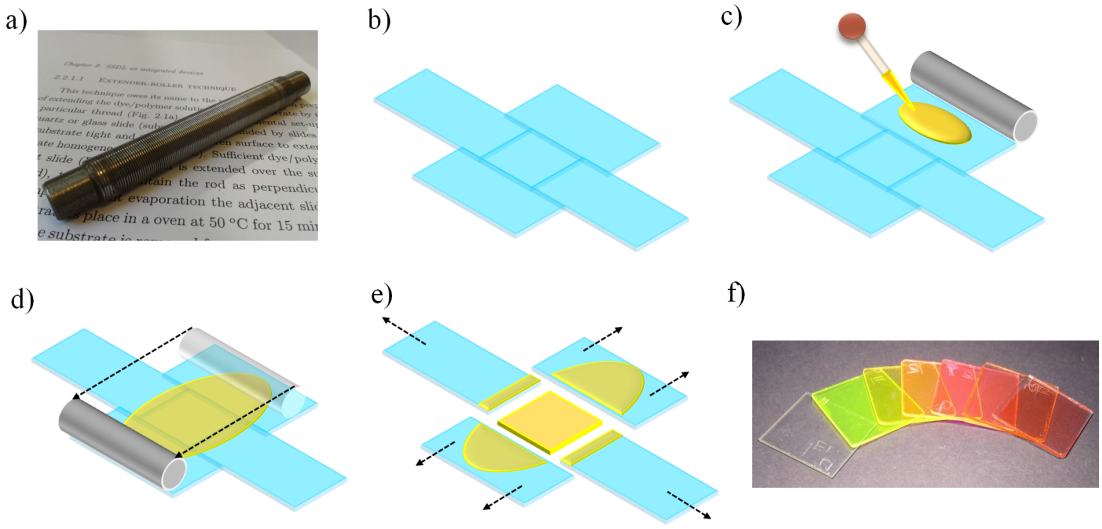

Figure 2.1: Extender-roller technique: a) Picture of extending rod, b) substrate positioning and holding, c) solution drop casting, d) solution extension, e) sample unmolding and f) picture of as-prepared samples.

manually manipulated, the final film thickness will vary from person to person and even from sample to sample, although to a lesser extent. This means that the film thickness has to be checked for every sample.

2.2.1.2 Spin coating

The spin coating technique is by far the most commonly used method to deposit thin films. In this case the substrate is place on top of a chuck which applies vacuum to hold the sample fixed and which is able to spin at a prefixed speed and time. A small amount of solution is dropped onto the centre of the substrate and then the substrate is spinned at high speed. The solution is consequently spread to the edge of the substrate, and eventually off, by means of the centripetal acceleration. In the spinning process the solvent evaporates and a thin polymer film remains on top of the substrate. With this technique, films down to a few nanometres thick can be obtained. The film thickness is controlled with the spin speed and time, and the polymer concentration. In this sense, the higher the speed, the longer the time and the lower the concentration are, the thinner the film is obtained. With this technique, films from 1 μm to 4 μm have been obtained for the papers in this thesis.

2.2.2 Roadmap to obtain laser emission

In this section the methodology followed to obtain laser emission from the active thin films is described.

2.2.2.1 Amplified Spontaneous Emission (ASE)

When dealing with a new material intended to be the active medium for an integrated device, one has to ensure that it is susceptible of emitting laser light prior to tackle the difficulties entailed by the cavity design and implementation. One way to ensure this viability is to probe that the material presents sufficiently efficient Amplified Spontaneous Emission (ASE) in the absence of any resonant structure (cavity).

ASE is a type of emission obtained when spontaneously emitted photons (fluorescence) are amplified while propagating in an excited region (e. g., thin film in integrated devices). The ASE is characterized for having spectra few nanometres wide (2-10 nm), which confers the light a moderately low temporal coherence, and a high directionality, with divergences in the order of a few mrads [65], despite the absence of any cavity. The ASE spectral narrowing is not caused by frequency selective cavity resonances, but rather by the preferential amplification of frequencies close to the maximum of the amplification line. In addition, despite the lack of a resonant cavity and the subsequent mode selection, the ASE possesses a fair amount of spatial coherence [65], although it is more a property

of the geometry of the medium (gas tube, waveguide, ...) rather than of the medium itself or the radiation process [65]. With these properties ASE devices lay between truly coherent laser oscillators and completely incoherent thermal sources [66].

The characteristic parameter that accounts for the ASE properties is the optical gain (or negative absorption), expressed in units of cm^{-1}, which is, roughly speaking, defined as the distance the light must travel in an inverted (excited) medium to be amplified by a factor e. A more rigorous definition will be shown in sections 2.2.4.2 and 2.3.1.1, together with the role of the optical gain on the amplification and emission saturation processes. In the frame of thin film devices, the gain will depend on the spectroscopic properties of the given medium, the thin film properties (thickness, effective refractive index) and the pump intensity, as will be seen in section 2.3.

Then, if a positive gain is measured, the particular material is susceptible of emitting laser light and, thus, it is worth to tackle the design and implementation of an adequate cavity. On the contrary, if the gain is never positive under any circumstances, the material will not be a good candidate as a laser medium.

2.2.2.2 Distributed Feedback (DFB) lasing

Provided that a sufficiently high optical gain has been proven, the active medium should be incorporated into an integrated cavity. The most common approach to solve this problem in organic thin film lasers is to use Distributed Feedback (DFB) [22, 27, 43, 55, 64].

In DFB lasers (Fig. 2.2a), light propagating in a waveguide mode of the organic film is Bragg-scattered by a wavelength-scale periodic modulation of the refractive index in the film, substrate, or both, to create a diffracted wave propagating in the counterpropagating waveguide mode. The propagating and counterpropagating modes will destructively interfere with each other to create a photonic stopband at which light propagation is forbidden. This optical gap, which width depends on the refractive index contrast of the periodic modulation, is centred at a wavelength λ_B satisfying the Bragg condition,

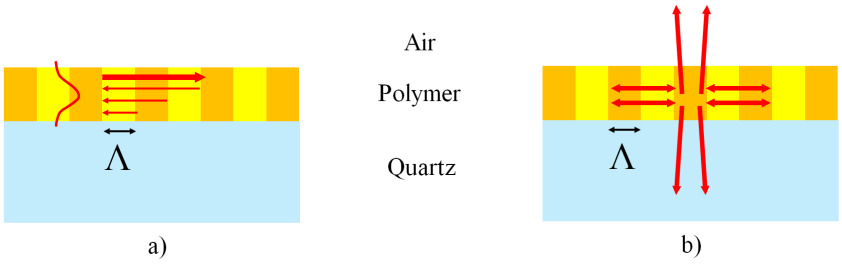

Figure 2.2: a) Ray picture of Bragg scattering in DFB laser, b) Feedback and output coupling in a 2^{nd} order DFB laser.

$m\lambda_B = 2n_{eff}\Lambda$, where m is an integer that represents the order of the diffraction, n_{eff} is the effective refractive index of the waveguide, which represents a geometrical average of the refractive indices of the three layers of the waveguide, and Λ is the period of the modulation (Fig. 2.2). In such photonic crystal structures the laser emission will not take place at λ_B, but at the edges of the photonic stopband, since the photon group velocity at these wavelengths approaches zero. This effect implies an exceedingly long optical path length in the structure, which leads to extreme gain enhancements [67]. It has been shown that, in fact, the laser emission takes place preferentially at the long-wavelength photonic stopband edge thanks to the weaker coupling between the waveguide modes and the free space radiation at this edge [68], as compared with that of the short-wavelength band-edge.

Working with the second order $m = 2$, the Bragg wavelength is equal to $n_{eff}\Lambda$, and light is diffracted out of the surface of the film perpendicular to the plane of the waveguide (Fig. 2.2b). That is, the second-order structure provides a surface-emitted output coupling of the laser light via first-order diffraction while providing in-plane feedback via second-order diffraction [27].

2.2.2.3 Random Lasing (RL)

The main drawback of DFB lasers is that the fabrication of the resonant structure requires techniques such as photolithography [36], electron beam lithography [37] or interferometric pumping geometries [55] (Section 2.2.3.1), which are not readily available in every laboratory. An alternative approach to prove that the active material under study is capable of sustaining laser emission is to implement a waveguide Random Laser (RL), in which feedback is provided by light scattering (Fig. 2.3). In such a device the active material must present structural heterogeneities, which can be obtained either by doping the active material with passive nanoparticles (for example, SiO_2 [69]), by inducing phase separation in polymer mixtures [70] or by naturally ocurring structural inhomogeneities in the neat films [71], to mention some. Of course, if RL can be excited, conventional DFB lasing could be obtained if the proper resonant structure is included.

Since the feedback mechanism is governed by light scattering, the obtained laser emis-

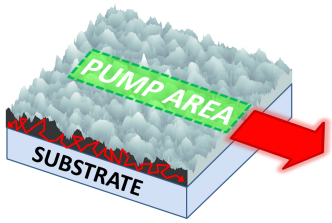

Figure 2.3: Sketch of a waveguide Random Laser.

sion is characterized by presenting multimode spectra, with the intensity of each mode fluctuating randomly from shot to shot thanks to the stochastic nature of the mode selection. Unfortunately, the light scattering not only provides feedback, but it contributes to increase the cavity losses, fact that increases the lasing threshold. Nevertheless, RL waveguide devices could find a place in disposable lab-on-chip applications in which there is not a need of high spectral purity, for example for organic (biological, analytical, ...) samples, thanks to the smooth and broad absorption spectra of these compounds. On the other hand, for applications requiring a laser source with high spectral purity and a reduced threshold, a DFB laser or similar should be chosen.

2.2.3 Set-ups for ASE, RL and DFB experiments

The experimental set-up for the ASE, RL and DFB lasing experiments is almost the same as that described in the previous chapter (section 1.2.2 and Fig. 1.5), only differing in the pumping geometry (Fig. 2.4).

In the ASE and RL measurements, the light incident on the sample was perpendicular to the film surface and focused onto that surface in stripe shape of ∼150 μm width by a combination of negative (NCL) and positive (PCL) cylindrical quartz lenses (f = -15 and +15 cm, respectively), perpendicularly arranged. An adjustable slit was used to select only the central portion of the pump beam to obtain an homogeneous pump spot. A micrometer screw allowed selecting precisely the width of the slit. Excitation stripes of up to 3 mm length were used, with an end placed right up to the edge of the film. Sample and adjustable slit were placed on vertical and horizontal, respectively, motorized translation stages (MTS50, Thorlabs), computer controlled, to allow precise positioning.

In the DFB laser measurements, the two cylindrical lenses were substituted by one spherical (SL) lens (f = +15 cm), the adjustable slit was removed, and the sample was

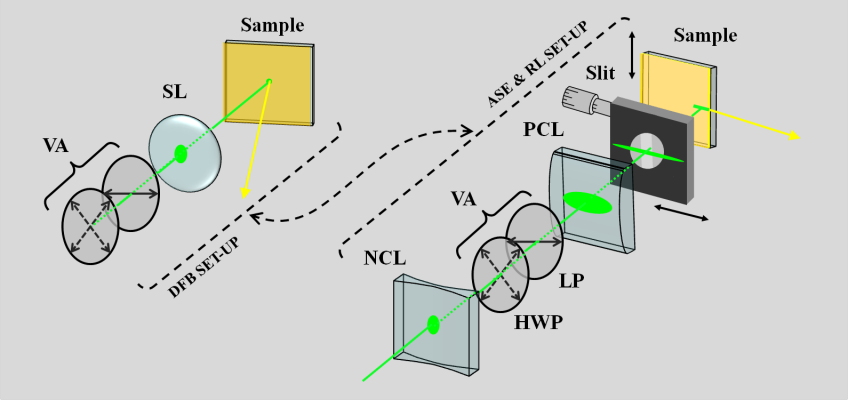

Figure 2.4: Pump spot shaping system for ASE, RL and DFB studies: NCL-Negative Cylindrical Lens, VA-Variable Attenuator (HWP-Half-Wave Plate and LP-Linear Polarizer), SL-Spherical Lens.

rotated so that the pump beam arrived to the surface at an angle of about 34° from the normal to that surface. The pumped spot at the surface was elliptical in shape with major and minor axis of about 245 μm and 185 μm, respectively.

During the thesis period the ASE experimental set-up evolved and this evolution may be traced down by looking chronologically at the experimental sections of the compiled papers. The changes, which are summarized in Table 2.1, were carried out in the pump energy control, the sample and slit positioning and the sample orientation.

Table 2.1: Changes performed on ASE experimental set-up

Paper	Pump Energy Control	Slit Positioning	Sample Positioning/Orientation
B2 & B3	NDF	Fixed	XY Manual/Horizontal
B4 & B5	HWP+LP	Fixed	XZ Motorized/Vertical
B6, B7 & B8	HWP+LP	X Motorized	Z Motorized & X Manual/Vertical

NDF: Neutral Density Filters, HWP: Half-Wave Plate, LP: Linear Polarizer

2.2.3.1 Holographic pumping set-up

We tried to implement an holographic pumping set-up [55, 72] to obtain laser emission without the need of using corrugated substrates, which are difficult to obtain and have a very limited range of resonant wavelengths, a fact that hinders the emission tunability and its use for the evaluation of dyes emitting in different spectral regions. The aim of this set-up (Fig. 2.5a) is to form a two-beam interference pattern in the active film (Fig. 2.5b), in such a way that the spatially modulated pump generates a faint refractive index variation with the very same pattern (Fig. 2.5c). In this way, an holographic distributed feedback resonator is created in which feedback is provided by backward Bragg scattering.

The period Λ of the refractive index variation is determined by the beam interference

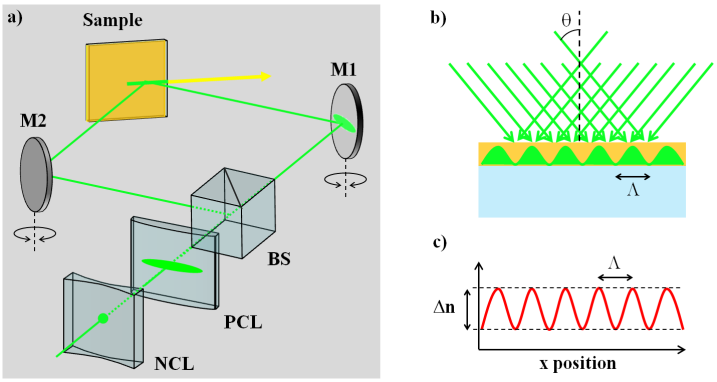

Figure 2.5: a) Sketch of holographic pumping set-up: NCL-Negative Cylindrical Lens, PCL-Positive Cylindrical Lens, BS-50/50 Beam Splitter, M1 and M2- Plane mirror. b) Two beam interference pattern. c) Variation of refractive index through pumped area.

angle θ, in such a way that:

$$\Lambda = \frac{\lambda_p}{sin\theta}$$

where λ_p is the pump wavelength. In this set-up the alignment is critical to obtain the correct pattern period and orientation. Unfortunately we were unable to align the system correctly and laser emission was not obtained.

2.2.4 Emission properties evaluation

With the experimental set-ups shown in section 2.2.3 four different types of measurements have been carried out. In these experiments only spectral properties have been acquired, whereas temporal behaviour and absolute efficiencies measurements were not considered. From the emission spectra one can retrieve valuable information such as the output relative intensity integrated over the whole spectral range (I_{out}), the relative peak intensity (I_{peak}), the peak wavelength (λ_{peak}) and the full width at half maximum (FWHM). The evaluation of these parameters as a function of the experimental conditions allows gathering in much information on the emission properties of the studied samples, as can be seen in Table 2.2 (at the end of chapter)

2.2.4.1 Variation of pump intensity

In these measurements, the CCD is used to acquire the data, and the spectral properties are evaluated as a function of the pump intensity (I_p), leaving the pump spot dimensions unchanged. This type of experiment has been carried out both for ASE, RL and DFB studies, and the most important parameter obtained in these measurements is the ASE, RL or DFB threshold intensity (Table 2.2). In the ASE and RL experiments the threshold is considered to be the point for which there is a change in slope in the light-light curve (I_{out} *vs.* I_p) when plotted in a log-log scale (Fig. 2.6a). In the DFB measurements the change in slope in the light-light curve is not smooth at threshold, but is characterized by a stepped region (Fig. 2.6b). The middle point of this step is considered the laser threshold, coinciding with the point at which the laser line is clearly emerging

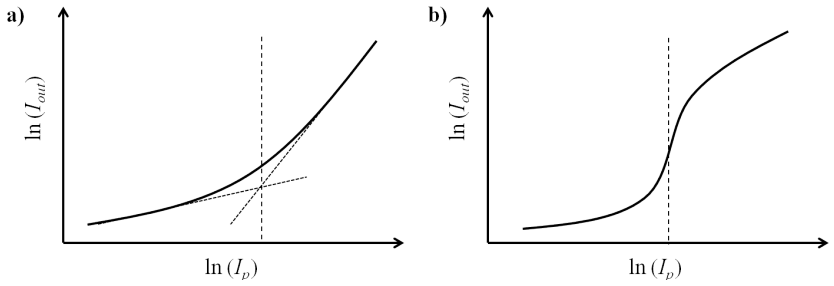

Figure 2.6: Light-light curves in a) ASE and RL and b) DFB. The dashed lines mark the threshold.

from the fluorescence background. In addition, the minimum emission linewidth (FWHM or $\Delta\lambda$) is as well obtained from these experiments (Table 2.2).

2.2.4.2 Variable Stripe Length (VSL) method: Gain measurements

To measure the ASE optical gain we have made use of the Variable Stripe Length (VSL) method, which consists of varying the pump stripe length (hence its name) without changing the pump intensity, and evaluating the output emission, as acquired with the CCD, as a function of this variation. A simple fit of an appropriate expression to the resulting data gives the optical gain as an output parameter. It will be shown that the relationship between pumped stripe length and edge-emitted ASE intensity in the absence of gain saturation, at a given wavelength, can be written as:

$$I_{ASE}(L) = \frac{\Omega}{g}\left(e^{gL} - 1\right)$$

where L is the stripe length, g is the net optical gain and Ω is a parameter related to the fluorescence growing. If $g > 0$ (gain higher than losses), the emission will grow superlinearly along the excited region, whereas if $g < 0$ (losses higher than gain), it will do it sublinearly. When gain saturation is significant, the above expression is no longer valid and has to be accordingly modified, as will be discussed in section 2.3.1.1.

2.2.4.3 Shifting Excitation Spot (SES) method: Losses measurements

The waveguide losses α can be characterized by using the Shifting Excitation Spot (SES) method. The SES method consists of exciting the sample with a constant stripe length (2 or 3 mm), which is gradually translated away from the edge of the sample, and detecting the ASE (with the CCD) as a function of the distance between the end of the pump stripe and the edge of the sample. Since the emitted light travels along a region which is not photo-excited, the collected intensity as a function of the separation z decreases, in principle, according to the Lambert-Beer's law:

$$I_{ASE}(z) = I_0 e^{-\alpha z}$$

where α includes the scattering losses and the reabsorption losses.

2.2.4.4 Photostability measurements

From a practical point of view, an important parameter in the behaviour of the waveguides is the photostability of the emission under long time operation, which implies high resistance to dye degradation under repeated pumping. This information is assessed by pumping the samples at a fixed position at a pump intensity well above threshold and

monitoring, with the photomultiplier, the decay of the output intensity as a function of the number of pump pulses received upon the same region. The slit of the monochromator was set to detect the signal corresponding to 4-5 nm around the peak wavelength. This spectral width allows taking into account possible peak displacements during photodegradation.

The proper comparison of photostability results obtained in different samples and/or materials is a difficult task because of the substantial differences in the experimental conditions, such as pump intensity, pump repetition rate, dye concentration or excited volume. In order to facilitate comparisons independently of the experimental set-up and sample, Rahn and King [73] introduced a normalized photostability defined as the accumulated pump energy absorbed by the system per mol of dye molecules before the output energy falls to one-half its initial value. In terms of experimental parameters, this energy dose, in units of GJ/mol, can be expressed as:

$$E_{Dose}(GJ/mol) = 10^{-8} \times (n_{pulses}) \times \frac{I_p(kW/cm^2)\tau(ns)}{C_{Dye}(M)t(\mu m)}$$

where n_{pulses} is the number of pump pulses received, τ is the pump pulse FWHM (20 ns), C_{Dye} is the dye concentration and t is the thin film thickness.

Given the high photostabilities shown by some of the samples evaluated in this thesis, a slightly different criterion has been used to define the normalized photostability, since not all the photostability measurements resulted in an intensity decrease below half the initial value. The limiting case corresponds to the sample based on Perylene Orange doped PMMA, which emission decreased only to an 83% of the initial intensity. For this reason, the photostability data shown in Table 2.2 are referred to this value, i. e., n_{pulses} and E_{Dose} represent, respectively, the number of pulses and the energy dose needed to reduce the output intensity to a 83% of the initial value at the given pump intensity. It must be noticed that this parameter has not been used in the published papers, but has been introduced in this report in order to better compare the global results.

2.3 Thesis results

This section will be devoted to the presentation, comparison and discussion of the thesis main results on dye doped polymer thin film lasers. The contributions to the fundamental characterization of the ASE process in waveguides will be treated in section 2.3.1, beginning with the development of the gain parameters retrieval formalism (section 2.3.1.1), and ending with the evaluation of the differences between waveguides and leaky-waveguides (section 2.3.1.2). Sections 2.3.2 to 2.3.5 will summarize the emission properties (gain, thresholds, photostabilities, ...) of the waveguides based on pyrrometh-

enes, perylenes, sulforhodamines and hemicyanines, respectively.

2.3.1 Fundamental insights into ASE in thin films

2.3.1.1 Optical gain analysis (From papers B1, B2 & B3)

It has been aforementioned that the characteristic parameter that determines the ASE properties is the optical gain. There are different methods to infer this gain but, in the context of waveguides, the VSL method (Section 2.2.4.2) is preferred due to the simplicity in its experimental implementation and theoretical analysis.

For the theoretical analysis, the system is treated as a time-independent one dimensional amplifier[2] (i. e., light propagating in only one direction in a excited region whose length is much longer than its width) in which there is no gain saturation (small-signal regime). This implies that the excited state population is always the same, regardless of the ASE intensity propagating in the waveguide. In this situation, the growth of the ASE intensity ($I_{ASE}(\lambda, z)$) in the propagation direction z reads[3]:

$$\frac{dI_{ASE}(\lambda, z)}{dz} = \Omega(\lambda) + \gamma(\lambda) I_{ASE}(\lambda, z) - \alpha(\lambda) I_{ASE}(\lambda, z) \tag{2.1}$$

where $\gamma(\lambda) = \sigma_{st}(\lambda)\Delta n$ is the gain coefficient, $\sigma_{st}(\lambda)$ is the stimulated emission cross section, Δn is the population inversion density, $\alpha(\lambda)$ is the loss coefficient, and $\Omega(\lambda) = \Gamma(\lambda)\Delta n \tau^{-1} E(\lambda)$ is the fluorescence growing parameter, where $\Gamma(\lambda)$ is a confinement factor which determines the amount of light trapped in the waveguide, τ is the fluorescence lifetime, and $E(\lambda)$ is the fluorescence spectrum normalized so that $\int E(\lambda) d\lambda = \phi$, with ϕ being the fluorescence quantum yield. Since the VSL method is applied for a single wavelength, generally the one corresponding to the peak emission, and for the sake of notation's simplicity, the λ dependence will be ignored from now on. The integration of this equation, with boundary conditions $I_{ASE}(z = 0) = 0$ and $I_{ASE}(z = L) = I_{ASE}(L)$, being L the stripe length, leads to:

$$I_{ASE}(L) = \frac{\Omega}{g}\left(e^{gL} - 1\right) \tag{2.2}$$

where $g = \gamma - \alpha$ is the net gain coefficient. This is the expression that it is used, the most of the times, for the gain retrieval.

Unfortunately, for long excitation stripes or high pump intensities, gain saturation cannot be avoided and then Eq. (2.2) is no longer valid, since it predicts a higher amplification rate than the one seen in the experimental data (blue line in Fig. 2.7). Gain

[2]It is indeed a rough approximation since the process is pulsed, light propagates in both directions and the excited region is far from being one-dimensional. Even so, it is used profusely.

[3]The notation of Paper B1 will be followed

saturation occurs because the light travelling in the sample is so strongly amplified that it depletes a substantial fraction of the population in the upper laser level. As gain saturation sets in, the gain coefficient is reduced and light is not exponentially amplified further as the length of the pumped stripe is increased. What it is usually done is to select only the data set in which, apparently, gain saturation is not still present, and fit Eq. (2.2) to this set. Nevertheless, this means that the unused data have been acquired pointlessly, not to talk about the inherent subjectivity in the selection of the non-saturated points.

The influence of the gain saturation on the VSL measurements had been previously treated theoretically [74], but none, as far as we know, had published an expression accounting for ASE gain saturation which could be fitted to the experimental data. Surveying the literature we found that, back in 1972, Casperson and Yariv [75] had investigated the effects of gain saturation on the spectral narrowing in high-gain gas lasers. They found that the depletion of the excitation density (population inversion), which is responsible of the gain saturation, could be expressed as:

$$\Delta n = \frac{\Delta n_0}{1 + \frac{I_{ASE}}{I_s}} \tag{2.3}$$

where Δn_0 is the population inversion in the absence of depletion, and $I_s = h\nu/(\sigma_{st}\tau)$ is the saturation intensity, with h the Planck's constant and ν the frequency of the ASE emission.

Constituting a novel result of the thesis, we made use of this expression to reformulate

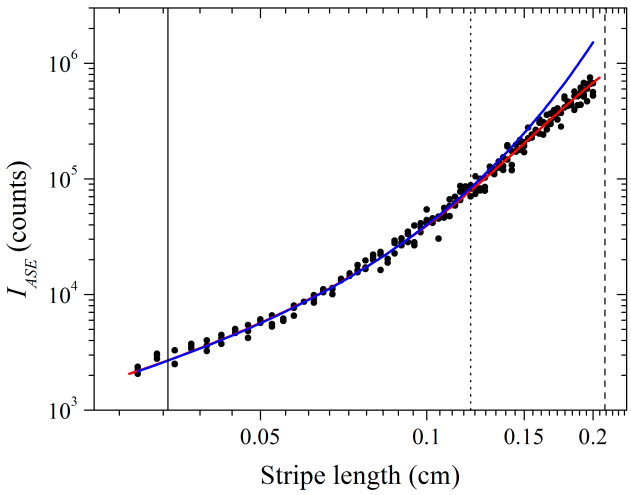

Figure 2.7: Dots are VSL data obtained for a waveguide based on Perylene Orange doped into PMMA deposited on quartz and pumped at 190 kW/cm^2. The blue and red lines are fits to the data using Eq. (2.2) and Eq. (2.5), respectively. The black solid line marks the ASE threshold length as calculated with Eq. (2.7). Dashed and dotted lines mark the saturation points using Eq. (2.6) and visual inspection ($gL_{sat} \approx 4.4$), respectively. $g = 36.5 \pm 0.6$ cm^{-1}, $\Omega = (4.0 \pm 0.2) \times 10^4$ counts, $I_s = (7.6 \pm 0.8) \times 10^5$ counts, $L_{th} = 0.034$ cm and $L_{sat} = 0.21$ cm.

the differential equation describing the growth of the ASE intensity in the excitation direction z (Eq. (2.1)) taking gain saturation effects into account, which now was read:

$$\frac{dI_{ASE}(\lambda, z)}{dz} = \Omega + \frac{\gamma I_{ASE}(z)}{1 + I_{ASE}(z)/I_s} - \alpha I_{ASE}(z) \tag{2.4}$$

The integration of this equation, with boundary conditions $I_{ASE}(z = 0) = 0$ and $I_{ASE}(z = L) = I_{ASE}(L)$, and assuming that $\alpha I_{ASE}/I_s \ll \gamma$, led to:

$$L = \frac{I_{ASE}(L)/I_s}{g + \Omega/I_s} + \frac{g}{(g + \Omega/I_s)^2} ln \left| \frac{\Omega + (g + \Omega/I_s) I_{ASE}(L)}{\Omega} \right| \tag{2.5}$$

Eq. (2.5) is implicit in $I_{ASE}(L)$ and, hence, it cannot be fitted to an $I_{ASE}(L)$ versus L plot as it is done with Eq. (2.2). Fortunately, Eq. (2.5) is explicit in L and, consequently, g, Ω and I_s can be calculated by means of a least squares fit of Eq. (2.5) to a L versus $I_{ASE}(L)$ plot.

Then, this new formalism allowed using the whole range of measured values in the fitting procedure, as can be seen in Fig. 2.7 (red line), and it paved the way to obtain new information on the sample ASE properties, as will be seen in what follows.

Another concern in the VSL measurements was the determination of the threshold and saturation lengths, L_{th} and L_{sat}, defined as the stripe lengths for which the ASE threshold and gain saturation set in, respectively. These lengths establish the range for which the pump to ASE conversion rate is most efficient and the optical gain values are more accurately calculated. Strangely enough, L_{th} is a parameter that, to the best of our knowledge, nobody had cared about, and L_{sat}, which had received much more attention, was mostly determined by means of a visual estimation of the point at which the experimental saturated emission points depart from the ones estimated by the small-signal approximation (Eq. (2.2)). By using the visual inspection, many works had claimed that gain saturation sets in when the gain-length product $gL_{sat} \approx 4$. Applying this criterion to the data in Fig. 2.7 we find a gain-length product $gL_{sat} \approx 4.4$ (dotted line in Fig. 2.7).

In our opinion, there was a lack of analytical expressions for L_{th} and L_{sat} because the criteria for the ASE threshold and saturation were not univocally established. The deduction of Eq. (2.5) helped to find an analytical expression for L_{sat} by simply assuming the following criterion: at the saturation length the ASE intensity equals the saturation intensity (I_s). Thus, substitution in Eq. (2.5) of $L = L_{sat}$ and $I_{ASE}(L_{sat}) = I_s$ leads to

$$gL_{sat} \approx 1 + ln \left| \frac{gI_s}{\Omega} \right| \tag{2.6}$$

Nevertheless, the establishment of an expression for the onset of ASE emission (threshold) was not that straightforward. We found that the most accurate criterion for the onset

of ASE was established by Peters and Allen [76], who stated that "the threshold condition for ASE is realized when a spontaneously emitted photon at one end of the column just induces another at the other end". We reformulated this statement for not just one but many photons in such a way that the criterion was considered to be: the threshold condition for ASE is realized when the stimulated and the spontaneously emitted photon fluxes are, after losses, equal at the edge of the excitation region. Applying this criterion, we found that at threshold

$$gL_{th} \approx 1.256, \tag{2.7}$$

being a surprisingly simple analytical expression that provided an easy and universal way to objectively calculate the threshold length (L_{th}).

In Fig. 2.7 the values of L_{th} and L_{sat} as calculated with Eqs. (2.7) and (2.6), respectively, have been represented. It is worth noticing the differences between the saturation length analytically calculated and the one obtained via visual inspection. In fact, the analytical expression casts a gain-length product $gL_{sat} \approx 7.7$, far from the commonly used $gL_{sat} \approx 4$.

Then, Eqs. (2.6) and (2.7) showed that the characteristic lengths L_{th} and L_{sat} could then be easily calculated from the fitting parameters (g, Ω and I_s) obtained applying the VSL method (Eqs. (2.2) or (2.5)), preventing errors arising from visual estimations.

2.3.1.2 Waveguides vs. Leaky-waveguides (From papers B2 & B3)

The substrate/film/air structures used through the thesis report define asymmetric slab optical waveguides (WG) [77], which light propagation properties depend on the thin film thickness and on the refractive indices of the thin film, substrate and upper layer (air in our case). When the refractive index of the thin film is higher than that of the substrate, total internal reflection (TIR) at the film/substrate and film/air interfaces confines and guides the light along the film (Fig. 2.8). On the contrary, when the substrate refractive index is higher than that of the active film, no TIR takes place at the film/substrate interface and the propagating light leaks into the substrate (Fig. 2.8). Then, a leaky waveguide (LWG) or quasi-waveguide is obtained, where light is confined by the film/air interface by TIR while the reflection at the film/substrate boundary is leaked. Nevertheless, not all of the emission is leaked into the substrate, since the large Fresnel reflectivity [78] occurring at grazing incidence at the film/substrate interface leads to significant confinement of the light [79].

Both types of structures, WG and LWG, had been shown to present highly efficient ASE and even DFB lasing [80]. Nevertheless, their particular ASE properties may differ from one another and we were unaware of published works dealing with this issue. In

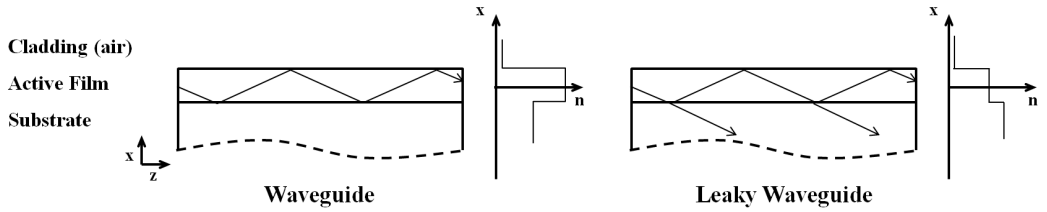

Figure 2.8: Ray picture and refractive index profile of optical slab waveguide and leaky waveguide.

order to clarify this point, we performed systematic measurements of the ASE properties of active thin films deposited on substrates which refractive indices enabled either WG or LWG confinement. For those studies, we used active thin films based on poly(methyl methacrylate) (PMMA), with $n_{PMMA} = 1.49$, doped with pyrromethene dyes (Fig. 3 and Section 2.3.2) and deposited on glass ($n_{glass} = 1.52$), to obtain LWG confinement, and quartz ($n_{quartz} = 1.456$), to obtain WG confinement. The experimental parameters (film thickness, dye concentration and pumping conditions) were kept as similar as possible for both type of samples with the aim to evaluate the sole effect of the light confinement mechanism.

We observed that, although the leaky nature of the LWGs made them present higher losses (α), the maximum attainable gain (g), which already accounts for α, was always higher in the LWGs than in the WGs. Furthermore, the peak emission wavelength (λ_{peak}) in the WGs was consistently redshifted with respect to λ_{peak} in the LWGs, with a gap between them of up to 15 nm. This behaviour was independent on the dye used or the film thickness, at least in the range we evaluated (5-13 μm).

We do not know the exact origin of the observed redshift in the emission of the WGs with respect to the LWGs but, since both samples are exactly equal in dye concentration, film thickness and pump conditions, one could, in principle, rule out photophysical effects such as reabsorption/reemission processes to be responsible for the redshift. Nevertheless, the part of the emission that is leaked into the substrate in the LWG stops suffering reabsorption processes, thereby reducing somewhat the overall redshift. We suspect that it is as well related to the differences in the resonant wavelengths propagating in the WGs and LWGs [81]. Further studies should be carried out in order to clarify this point.

On the other hand, the origin of the gain differences between WGs and LWGs may be found in the number of propagating modes that are amplified in both structures. In the LWG, the different transverse modes propagating within the gain layer have different reflectivity losses due to the Fresnel reflection [78]. Although several low-loss leaky modes may exist when the thickness of the gain layer is large compared with the wavelength of the propagating light, the fundamental mode is the one with the lowest losses (highest reflectivity) and, thus, light is amplified preferentially in this mode. On the other hand,

the differences in the losses of the different modes propagating in the WG are not as pronounced as in the case of the LWG, whereupon all the existing modes in the WG compete for the available population inversion, considerably reducing the attainable gain. As a result, LWGs provide a much stronger self-mode restriction capability than conventional WGs, hence a higher gain is obtained in the formers.

This interpretation is backed up by the fact that the modifications in the optical gain when changing the active film thickness are much more pronounced in the WG that in the LWG. In fact, for the WG based on PM597 doped PMMA, changing the thickness from 5 μm (6 waveguided modes) to 13 μm (15 waveguided modes) supposed a reduction in the optical gain from 60 cm^{-1} to a mere 10 cm^{-1}, while the same change in the LWG configuration implied a reduction from 83 cm^{-1} to 53 cm^{-1}.

Nevertheless, both LWGs and WGs did present features in common, related to how the gain behaves when the active film thickness is modified. As has been shown above, the thicker the film is, the lower the optical gain becomes. This behaviour suggests that the dependency of the gain on the film thickness is not only determined by the confinement mechanism, but by the film properties itself. This dependency could have its origin in the pump inhomogeneity along the thickness, since the incident pump is being absorbed as it travels down the thickness of the sample, which implies that the population inversion, and consequently the gain, is not the same in the film/air interface, where the pump firstly impinges, than in the film/substrate one, where there is no longer pump light to be absorbed. In order to verify this extent, the average population inversion (Δn) along the sample was numerically calculated as a function of both pump intensity and film thickness, assuming that gain saturation was not yet set in. It was found that Δn, as seen experimentally by means of the gain, was reduced as the film thickness was increased, confirming that the pump inhomogeneity along the film thickness was responsible for the observed gain behaviour.

2.3.2 Waveguides based on Pyrromethene dyes

Laser dyes belonging to the pyrromethene family (4,4-difluor-3a,4a-diaza-4-boro-s-indacene or dipyrromethene.BF_2 (PM) dyes), are highly efficient and photostable laser dyes, with emission from the blue to the red spectral region, which outperform the laser behaviour of the well known rhodamine dyes, both in liquid and solid gain media. In spite of this, reports on the optical gain and photostability properties of pyrromethene dyes in waveguides were scarcely found. To fill this gap we characterized thoroughly two different members of the pyrromethene family, namely, PM567 and PM597 (Fig. 3), which emit close to 570 nm and 590 nm, respectively.

2.3.2.1 Amplified Spontaneous Emission (From papers B2, B3 & B4)

We begun by incorporating these dyes into the common polymer poly(methyl methacrylate) (PMMA) (Fig. 2), in which both dyes had presented very good laser properties as bulk materials [82]. As they where our first attempts working with thin film emitters, we proved different experimental conditions such us dye concentration, film thickness and substrate material. Table 2.2 summarizes the best ASE results obtained for both PM567 and PM597 doped into PMMA.

Remarkably, both dyes showed very high optical gains when casted as 5 μm thick films, reaching 53 cm^{-1} (PM567) and 83 cm^{-1} (PM597) when pumping at 1 MW/cm^2 and 410 kW/cm^2, respectively, surpassing the gains obtained for other materials in similar conditions.

The emission photostability was measured on the sample PM597/PMMA but the results were far from being impressive. Pumping at 200 kW/cm^2 the output emission was reduced to an 83% of the initial value after only 58 pulses, which suppose an energy dose of a mere 9×10^{-3} GJ/mol. Since both the emission efficiency and photostability are highly dependent on the chosen polymer matrix, as has been shown many times before by our group, we decided to prove different polymer materials in order to optimize the pyrromethene photostabilities without compromising the needed efficiency. In this regard, it was known that the improvement in polymer thermal conductivity reduced pyrromethene dyes degradation and could increase the device's lifetime.

Following this approach to increase the dye photostability, we doped PM597 into two different fluorinated polyimides (FPI) synthesized by Prof. de Abajo's group at ICTP-CSIC[4]. FPIs combine excellent thermal properties, with a thermal conductivity doubling that of the PMMA, and good optical transparency at the wavelengths of interest. In addition, the FPIs are soluble in common non-polar organic solvents, e.g., chloroform, tetrahydrofuran or dioxane, so that films doped with non-polar dyes can be readily fabricated by casting and controlled elimination of solvent.

It was found that the FPI 6F-6F (Fig. 2) not only increased the photostability of PM597 by orders of magnitude with respect to that in PMMA, 0.51 GJ/mol against 9×10^{-3} GJ/mol, but it improved as well the optical gain, with an outstanding value of 93 cm^{-1} when pumped at nearly the same pump intensity, i. e., 500 kW/cm^2 (Table 2.2). The second FPI used (FPI 6F-IMMDA, Fig. 2) did as well increase both the photostability and the optical gain of PM597 with respect to those of PMMA, but in a lesser extent than the FPI 6F-6F.

The improvement in photostability of the two FPI films with respect to the PMMA

[4]Instituto de Ciencia y Tecnología de Polímeros (ICTP). Consejo Superior de Investigaciones Científicas, CSIC (Spain)

waveguide can be attributed mostly to differences in thermal properties between both polymer families, while the origin of the increase in the optical gain can be found in the fluorinated composition of FPIs. The thermal stability of the FPIs at least doubles that of the PMMA; hence, the heat transferred from the dye molecule to the matrix is more rapidly dissipated in the FPI films, avoiding early thermal degradation of the dye. We had already seen this effect in bulk solid state dye lasers, where the laser action, both efficiency and photostability, of pyrromethene chromophores incorporated into methacrylic and acrylic polymers was greatly enhanced by the presence of fluorine atoms into the structure of the organic monomers.

To explain the differences between the two FPIs, additional aspects such as polymer chain density and fluorine content must be considered. The polyimide 6F-6F is denser than 6F-IMMDA, thus, the polymeric free volume is lower in the former and the average distance between dye molecules and polymeric chains is shorter in 6F-6F than in 6F-IMMDA. A higher proximity to the polymeric chains facilitates nonradiative energy transfer from the dye molecules to the polymeric chains decreasing thermal and photochemical (dye molecule radicalization via triplet states) degradation. On the other hand, pyrromethene dyes incorporate fluorine atoms in their structure, fact that increases the compatibility of the dye molecules with the fluorinated matrix and favours the emission properties of the dye molecules. Polyimide 6F-6F incorporates more fluorine atoms than polyimide 6F-IMMDA, which should favour the stability of PM597 in 6F-6F. Taken together, these mechanisms could explain the better performance of PM597 when incorporated into polyimide 6F-6F.

With these ASE properties it was evident that the dye PM597 was definitively susceptible and very suitable to emit laser light if provided with the adequate cavity.

2.3.2.2 Random Lasing (From paper B5)

The most adequate solution to achieve laser emission would have been to deposit a thin film doped with PM597 onto a substrate with a DFB structure engraved on it which resonant wavelength matched the corresponding emission window. Unfortunately we lacked such structure but found serendipitously that the addition of polyhedral oligomeric silsesquioxanes (Fig. 2) to PMMA allowed obtaining, under certain circumstances, laser emission without the need of using structured substrates. Indeed, our original idea was to dope PMMA with silsesquioxanes in order to improve the ASE properties by means of a non-resonant feedback mechanism (Chapter 1).

The samples under study consisted of 5.5 μm thick films of PMMA/8MMA-POSS mixtures doped with PM597 (2.5×10^{-2} M) deposited onto a glass substrate (Table 2.2). As the refractive index of the polymer layer ($1.488<n<1.499$) was lower than that of the

substrate, a leaky waveguide was obtained (Section 2.3.1.2).

Following the same procedure as when studying ASE (Section 2.2.3), we pumped the samples with the stripe (2 mm long) placed right up to the edge of the film. The samples were pumped at 550 kW/cm^2 to ensure well above threshold emission. In the leaky waveguide with no 8MMA-POSS, the emission was just ASE with a linewidth of 16 nm (Fig. 2.9a). The presence of 8MMA-POSS in 13 wt.% proportion resulted in a slight decrease in the emission linewidth, now of 13 nm, a moderate increase in the intensity, and a faint red shift of the peak wavelength. Increasing the proportion of 8MMA-POSS in the material to 20 wt.% resulted in a further increase of the intensity, narrowing of the emission to 10 nm, and a red shift of the peak wavelength of about 2 nm with respect to that of the material with no POSS. The characteristics of the emission changed dramatically when the content of 8MMA-POSS in the polymer increased to 50 wt.%. In this case, multimode emission with narrow peaks on top of a globally narrowed ASE spectrum did appear (Fig. 2.9a).

Interestingly, moving the stripe away from the edge did not result in a worsening of the emission properties in spite of the increase in the emission losses (Section 2.2.4.3). On the contrary, as the stripe was separated from the edge, the FWHM was reduced monotonically to 11 nm, 7 nm and 4 nm for the samples with 0%, 13% and 20% 8MMA-POSS, respectively, when the stripe-edge separation reached 6 mm (Fig. 2.9b). For higher separations the FWHM increased again. Moving away the stripe from the edge in the sample with 50 wt.% 8MMA-POSS resulted in even more drastic changes, with the emission spikes being much more pronounced (Fig. 2.9b) and the intensity increasing tenfold. In addition a surprisingly bright spot, associated with a beam with divergence 10 mrad and 6 mrad in the planes parallel and perpendicular to the film, did appear in the centre of the fringe-shaped spot characteristic of slab waveguides (Fig. 2.10).

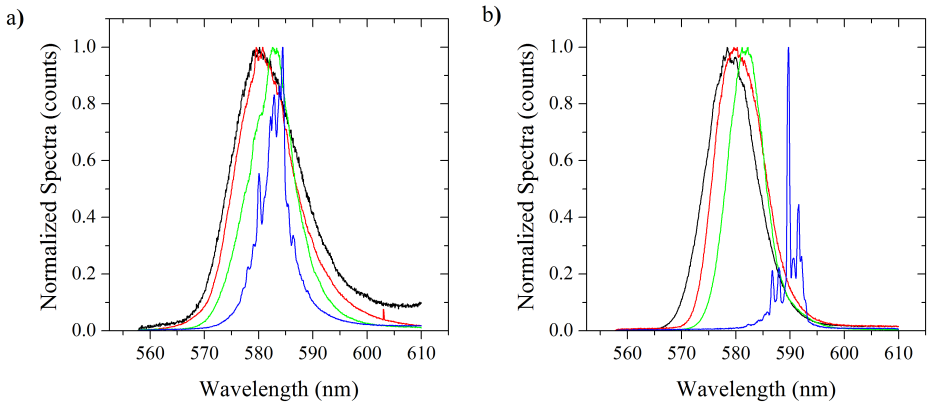

Figure 2.9: Emission spectra of samples PM597/PMMA doped with 0 (black line), 13 (red line), 20 (green line) and 50 (blue line) wt.% 8MMA-POSS pumped at the sample edge (a) and at 4 mm from the sample edge (b).

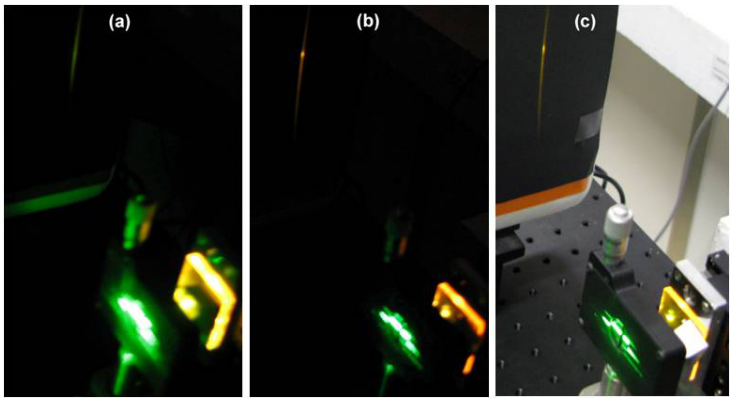

Figure 2.10: Emission spot from a sample without POSS (a) and with 50 wt.% 8MMA-POSS (b) at 20 cm from the waveguide edge. (c) Same as (b) but with the lab fully lighted.

The spectral narrowing observed in the samples with 13% and 20% 8MMA-POSS with respect to that of the sample with 0% 8MMA-POSS was ascribed to a mechanism of non-resonant feedback (Chapter 1), where the photon path enlargement caused by multiple scattering provides an intensity feedback which enhances incoherently the magnitude of the amplification process. On the other hand, the presence of multimode laser emission in the samples with 50% 8MMA-POSS, without the need to modulate the substrate to obtain feedback, was understood in terms of coherent random lasing (RL).

At the time of this work publication we were unaware of the exact origin of the scattering feedback. Nevertheless, an Atomic Force Microscopy (AFM) analysis performed later to similar samples concluded that the RL emission originates due to the scattering induced by the high surface roughness coming from the polymer/silsesquioxane phase separation (Section 2.3.4.4).

In conclusion, the previous results show that efficient and photostable laser emission in the range 560-590 nm can be obtained when using pyrromethene doped polymers as active media, assuming that the adequate integrated feedback is provided.

2.3.3 Waveguides based on Perylene dyes

Perylenediimide dyes, perylene for simplicity, constitute a dye family emitting in the yellow-red spectral region which have demonstrated laser emission with reasonable efficiency and very good photostability both in liquid and solid media. Nevertheless, dye doped polymer thin film lasers based on commercial perylene dyes or perylenediimide derivatives had not received much attention. In addition, the predominant photodegradation mechanism in these dyes had not been clearly identified. To fill this gap we characterized thoroughly two commercially available perylene dyes, namely, perylene orange (PO) and perylene red (PR) (Fig. 3), with emission close to 580 nm and 620 nm, respectively.

2.3.3.1 Photodegradation mechanism identification (From paper B6)

For most laser dyes, the dominant mechanism, or even the partial contribution of various mechanisms, to their final photodegradation is not well-established. As was explained in the introduction, dye degradation is generally caused by thermal and/or chemical (photooxidation) processes, and different routes must be followed in order to avoid each of them while keeping the desired efficiency in the final device. It is known that an improvement in the polymer thermal conductivity reduces dye thermal degradation through a more efficient dye-to-polymer heat transfer, as seen in the case of PM597 (Section 2.3.2.1). Chemical photodegradation, meanwhile, can be reduced by decreasing the amount of oxygen dissolved in the polymer matrix, which can be responsible for dye photooxidation. Hence, polymers with a low permeability and solubility to oxygen should be used as host materials for these laser dyes.

In this sense, we showed that an efficient strategy to optimize the performance of dye-doped polymers consisted of analyzing the dependence of its Amplified Spontaneous Emission (ASE) efficiency and photostability on the composition and structure of the given polymer, selected to specifically avoid one or another mechanisms. If the photostability increases when the oxygen permeability is reduced, then the photodegradation mechanism may be considered mainly chemical, but if the photostability improves when the thermal stability increases, the dominant mechanism will be thermal.

As a preliminary study on the photodegradation mechanism involved in perylene dyes, we first proceeded to evaluate the thermal stability of PO by Thermogravimetric Analyses (TGA) and compared it with that of PM597. This analysis indicated that PO is much more thermostable that PM597, decomposing at about 390 ^{o}C, 170 degrees above the temperature at which PM597 is destroyed. This fact implied that PO is a thermally robust dye and that, *a priori*, would be mainly affected by chemical photodegradation.

To confirm this statement, ASE photostability experiments were performed on waveguides based on PO doped into PMMA (low O_2 permeability but low thermal conductivity) and fluorinated polyimides, FPIs, (high thermal conductivity but high O_2 permeability), polymers selected for their capabilities to avoid the chemical and thermal photodegradation mechanisms, respectively. The sample based on PMMA showed a higher dye photostability than the samples based on FPIs (E_{dose}=16.9 GJ/mol against E_{dose}=5.91 GJ/mol), which presented between them very similar photodegradation rates. Thus, the fact that the lower photodegradation was achieved in PMMA, which is the material with lower permeability to oxygen and lower thermal conductivity, indicated that in perylenes photodegradation is mainly caused by photooxidation processes, as was foreseen from the TGA measurements.

2.3.3.2 Amplified Spontaneous Emission (From paper B6)

Apart from the ASE photostability measurements, light-light curve experiments to retrieve the ASE threshold were performed for PO doped into the different polymers (PMMA and FPIs). These experiments revealed that the sample PO/6F-DDM (Fig. 2) presented the lowest ASE threshold (67 kW/cm^2) and the highest relative output intensity, while the sample PO/PMMA threshold reached a value of 98 kW/cm^2. Both samples showed very similar gains but the one of the waveguide based on 6F-DDM was slightly higher (38 cm^{-1} against 34 cm^{-1}), in agreement with the tendency observed when measuring the ASE threshold. Nevertheless, taking into account that the waveguide based on PMMA rendered the highest photostability, which in turn is the most important property, together with the fact that PMMA is much cheaper than FPIs, which would reduce the future production costs, we considered PO/PMMA as the best combination that guaranteed both high efficiency and photostability.

Since PO and PR are very similar in nature and chemical structure, we extrapolated the previous results to PR and chose PMMA as its polymer matrix. Nevertheless, high gain ASE was not obtained at any of the dye concentrations tried, since the absorption at 532 nm is weak (maximum absorption at 580 nm), and when trying to increase the absorption through an increase in the dye concentration, the apparition of dye aggregates hindered the excitation of efficient ASE. Trying to overcome these problems, we proceeded to prepare mixtures of PO and PR in PMMA, with the idea of using the process of energy transfer from PO to PR, favoured by the overlapping between the emission band of PO (donor) and the absorption band of PR (acceptor) [83]. We found that the PO/PR molar proportion 1/1 provided the best compromise between pump absorption and ASE efficiency, giving place to ASE centred at 620 nm with a threshold of 115 kW/cm^2, slightly higher than the one obtained for PO, but much lower than the one corresponding to PR alone. The sample photostability was much higher than that of the sample PO/PMMA, with an energy dose needed to reduced the emission to an 83% of the initial value of E_{dose}=189 GJ/mol.

As a final remark on the ASE properties, it is worth carrying out a comparison between PO and PM597 (or PM567), since both have similar emission windows. The energy dose needed to reduce the emission to an 83% of the initial value for the sample PO/PMMA (E_{dose}=16.9 GJ/mol) is at least 30 higher than that for the sample PM597/6F-6F (E_{dose}=0.51 GJ/mol). Nevertheless, the ASE threshold intensity in the sample PM597/6F-6F is lower than the one in the sample PO/PMMA, and the attainable gain is much higher in the former (Table 2.2). This comparison indicates that the samples based on PO are much more photostable, but much less efficient, than the ones based on pyrromethene dyes. If a dye should be chosen, pyrromethenes would be better

candidates, since it is easier to improve the photostability in these dyes than to improve the efficiency of perylene ones, which is limited by their lower photoluminescence quantum yield.

Nevertheless, the ASE properties shown here for the perylenes demonstrate that they are suitable to emit laser light if provided with the adequate cavity.

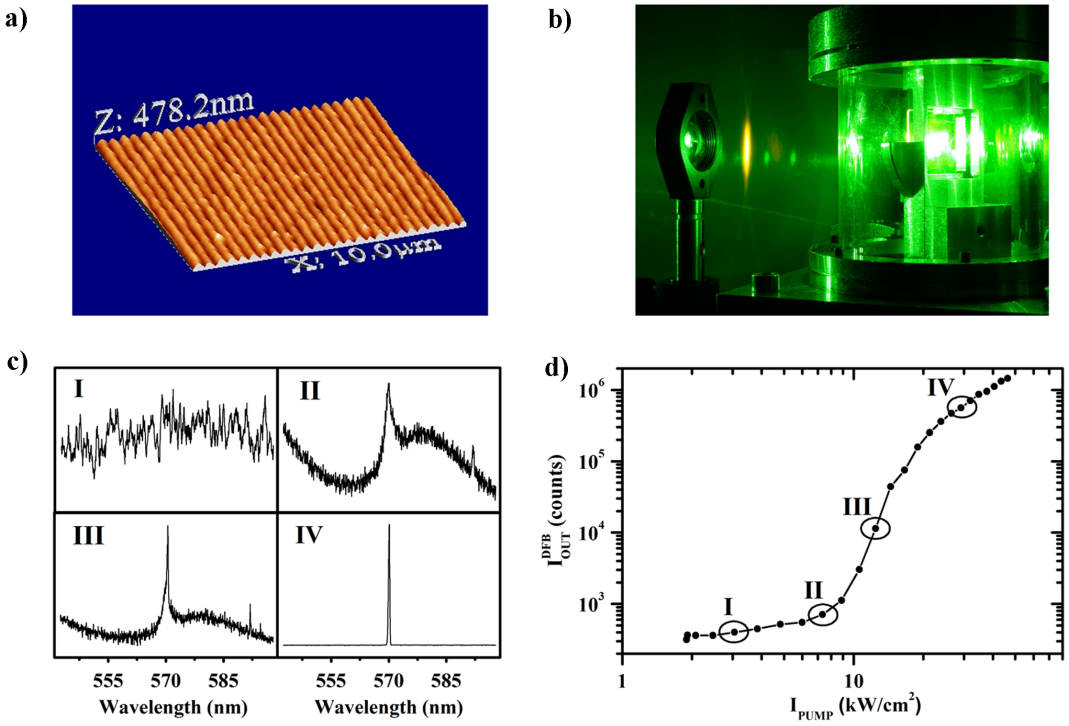

Figure 2.11: a) AFM topography of the 1D corrugated substrate with period Λ=386 nm used to obtain DFB lasing in sample PO/PMMA. b) Characteristic laser spot of a 2^{nd} order 1D DFB laser. c) Evolution of the DFB laser emission spectrum as the pump intensity is increased (spectra I to IV correspond to points I-IV in d)). d) Dependence of the DFB laser output intensity on pump intensity (light-light curve).

2.3.3.3 Distributed Feedback Lasing (From paper B6)

To demonstrate laser emission a 1 μm thick thin film of PO/PMMA (1×10^{-2} M) was deposited onto a quartz substrate (Fig. 2.11a) with a 1D sinusoidal DFB structure with period Λ=386 nm engraved on it, which resonant wavelength matched the corresponding PO emission window (kindly provided by Dr. G. A. Turnbull[5]). By using the pumping set-up shown in Fig. 2.4, DFB laser emission, with its characteristic diffractive spot (Fig. 2.11b), was obtained at a wavelength of 570.1 nm (Fig. 2.11c). The output emission vs. input pump curve, characterized for having a steepy trend near threshold (Point III in Fig. 2.11d), casted a threshold value as low as 12 kW/cm^2, much lower than the ASE

[5]Organic Semiconductor Centre, SUPA School of Physics & Astronomy, University of St. Andrews, (UK)

threshold of the same sample, as expected.

As an additional remark, taking into account the Bragg condition in second order ($\lambda_B = n_{eff}\Lambda$) and the substrate modulation period Λ=386 nm, an effective refractive index n_{eff}=1.477 is calculated. This value is consistent with the effective refractive index "seen" by the fundamental transverse electric (TE_0) propagating mode (as calculated with a waveguide mode solver[6]).

Finally, laser emission could not be obtained for the sample with Perylene Red, since we lacked a DFB substrate with the adequate modulation period as to match the resonant wavelength with the PR emission window.

In conclusion, the previous results show that efficient and photostable laser emission in the range 570-620 nm can be obtained when using perylene doped polymers as active media, assuming that the adequate integrated feedback is provided.

2.3.4 Waveguides based on Sulforhodamine dyes

Sulforhodamine dyes, which are sulfonated derivatives of the very well known rhodamine dyes, have demonstrated laser emission in the long-wavelength spectral region (>600 nm) with high efficiency and very good photostability, both in liquid and solid media. This spectral region is of interest for biophotonic applications, since these wavelengths can penetrate deeper into tissues and can excite, for example, fluorescence markers within biological samples. Dyes such as DCM, Rhodamine B or Rhodamine 640 had been used as dopants for thin film organic lasers in this spectral region. Surprisingly, very few works, if any, could be found in which sulforhodamine dyes were used in dye doped polymer thin film lasers. To fill this gap, we characterized thoroughly two commercially available sulforhodamine dyes, namely, Sulforhodamine B (SRhB) and Sulforhodamine 640 (SRh640) (Fig. 3), with emission close to 610 nm and 630 nm, respectively.

2.3.4.1 Amplified Spontaneous Emission (From paper B7)

Sulforhodamines can only be solved into highly polar media, whereupon the polymer availability for these dyes is limited. We had shown before that both dyes presented high lasing efficiency when doped into the polymer host poly(2-hydroxyethyl methacrylate) (pHEMA, Fig. 2) and, hence, we decided to use this polymer as the host for the sulforhodamine dyes in the thin film devices.

Once the dye concentrations were optimized, efficient ASE emission was obtained for both dyes (Table 2.2). The ASE peak wavelengths were centred around 610 nm and 630 nm for SRhB and SRh640, respectively, and the ASE thresholds were 90 kW/cm^2

[6]On-line 1-D multilayer slab waveguide mode solver by Dr. Manfred Hammer. URL: http://wwwhome.math.utwente.nl/~hammer/oms.html

(SRhB) and 106 kW/cm^2 (SRh640), very similar to the ones obtained for perylenes or pyrromethenes. Nevertheless, the optical gains of SRhB and SRh640 were well below the ones of their counterparts pyrromethenes and perylenes, since the formers only reached 26 cm^{-1} and 14 cm^{-1} when pumped with intensities as high as 400 kW/cm^2 (Table 2.2).

Anyhow, these ASE properties were an indicative of the suitability of SRhB and SRh640 to emit laser light if provided with the adequate cavity.

2.3.4.2 Non-Resonant Feedback Lasing (From paper B7)

Unfortunately, we lacked again a DFB substrate with the adequate modulation period as to match its resonant wavelength with the sulforhodamines emission windows. Then, we followed an analogous approach as with PM597 (Section 2.3.2.2) and incorporated 8MMA-POSS (Fig. 2) to the pHEMA matrix. Nevertheless, we found that pHEMA and 8MMA-POSS were not miscible, since the later was exuded from the thin film and a wet layer (8MMA-POSS) remained on top of the pHEMA. To overcome the solubility problem we purchased a POSS compound soluble in polar solvents, 8OH-PSS (Fig. 2), which avoided the exudation problems, as long as it did not surpass a 25 wt.% in the matrix.

The thickness for the thin films was chosen to be 4.5 μm because in films of about the same thickness laser emission in PM597 was demonstrated. Although coherent random laser emission was not excited for the sample doped with SRhB, a clear change in the emission properties did occur when increasing the amount of 8OH-PSS in the final matrix. Fig. 2.12a shows that the FWHM was reduced as the amount of 8OH-PSS increased, passing from 17 nm to a mere 5 nm, a fact that revealed the transition from ASE to broadband laser emission caused by non-resonant feedback (NRF), as was seen before for the samples PM597/PMMA/8MMA-POSS (Section 2.3.2.2).

Even more interesting was the fact that bichromatic NRF emission was obtained in the sample with 25 wt.% when excited with longer stripes (Fig. 2.12b). When the pump region was increased to 1 cm in length, simultaneous emission at 611 nm and 635 nm with FWHM of 5 nm and 7 nm, respectively, was observed. Moreover, the relative intensity of the two peaks could be varied by decreasing or increasing the length of the pumped region, in such a way that shortening the stripe did result in an increase of the 611 nm peak and a decrease of the 635 nm one, whereas a longer pump stripe resulted in a decrease of the 611 nm peak and an increase of the one at 635 nm. Eventually, when the length of the pumped region reached 1.5 cm the peak at 611 nm did completely disappear (Fig. 2.12b).

The band at 611 nm corresponded to emission from SRhB monomers, whereas the band at 635 nm was ascribed to the presence of dimers, which at the high dye concentrations used (1×10^{-2} M) were expected to appear. In this scenario, the emission from the dimers

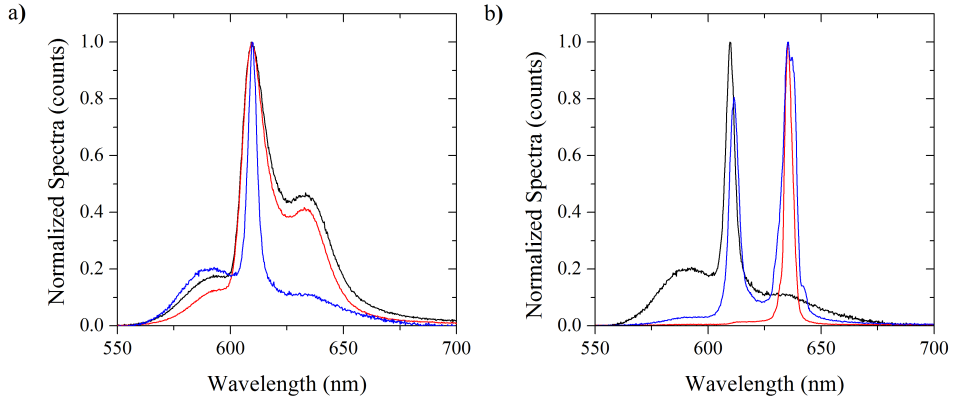

Figure 2.12: Emission spectra of (a) samples SRhB/pHEMA doped with 0% (black line), 10% (red line) and 25% (blue line) 8OH-PSS pumped with a stripe 2 mm long and b) sample SRhB/pHEMA doped with 25% 8OH-PSS pumped with stripe lengths 2 mm (black line), 1 cm (blue line) and 1.5 cm (red line).

was excited through an energy transfer process from the monomers due to the partial overlap of the dimer absorption band with the monomer emission window. The change in the relative emission intensities of both bands with the variation in the pump length is a clear indication that the energy transfer from monomer to dimer was mainly radiative. When the whole length of the sample (1.5 cm) is pumped, the optical path is long enough as to let the dimers absorb all the emission from the monomers and, hence, the emission from the dimers dominates (635 nm). When the pumped region is shortened to 1 cm, not all the emission from the monomers is absorbed by the dimers, and the peaks of both species are observed. Finally, when the length of the pumped region is shortened to 2 mm, there is no enough optical length as to transfer energy to the dimers, and the emission from the monomers (611 nm) dominates.

2.3.4.3 Random Lasing (From paper B7)

In the previous results we did not observe coherent random lasing (RL), probably due to the lack of sufficient optical gain. As we had already seen that decreasing the thickness of the film increased the gain (Section 2.3.1.2), we decided to prepare films 1 μm thick and with 25 wt.% content in weight of 8OH-PSS.

Under these conditions, RL emission centred at 610 nm and 630 nm, with multiple laser spikes less than 0.3 nm wide, was excited in the samples with SRhB and SRh640, respectively (Fig. 2.13a). With laser thresholds of 50 kW/cm^2 (SRhB) and 70 kW/cm^2 (SRh640), the energy dose needed to reduce the emission intensity to an 83% of the initial value reached 35 GJ/mol for SRhB and 74 GJ/mol for SRh640, which is a considerably high emission photostability, as compared with the rest of the samples evaluated through the thesis (Table 2.2).

To increase the laser efficiency of SRh640, which is limited by its lower absorption

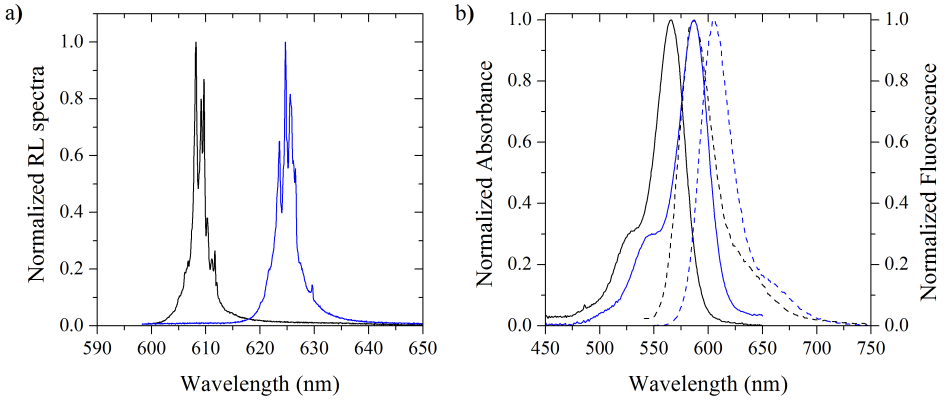

Figure 2.13: a) Random Laser emission spectra for samples SRhB/pHEMA/8OH-PSS(25 wt.%) (black line) and SRhB:SRh640(1:1)/pHEMA/8OH-PSS(25 wt.%) (blue line) pumped at I_p=380 kW/cm^2. b) Spectral overlap of SRhB bands (black lines) and SRh640 bands (blue lines). Absorbance in solid lines and fluorescence (λ_{ex}=532 nm) in dashed lines.

at 532 nm, we made use of the perfect overlap of the emission spectrum of SRhB with the absorption spectrum of SRh640 (Fig. 2.13b), in such a way that the pump radiation absorbed by SRhB is transferred to the SRh640 molecules by means of Förster resonance energy transfer (FRET) and/or via radiative energy transfer [83]. It was found that the SRhB:SRh640 molar proportion 1:1 provided the best compromise between pump absorption and laser efficiency. The spectrum in Fig. 2.13a and the peak wavelength, RL threshold and photostability values of SRh640 provided in the previous paragraph do correspond to the doped sample, i. e., SRhB:SRh640(1:1)/pHEMA/8OH-PSS(25 wt.%).

Then, these results demonstrate that it is possible to excite efficient and photostable laser emission from sulforhodamine doped polymer thin films in a wavelength region (>600 nm) interesting for biophotonic applications.

2.3.4.4 The origin of the scattering feedback (From paper B7)

An Atomic Force Microscopy (AFM), in tapping mode, analysis of the samples revealed that the roughness of the film surfaces was highly affected by the addition of 8OH-PSS. The sample without 8OH-PSS (Fig. 2.14a) presented a rather smooth surface, whereas the topography of the sample with 8OH-PSS showed a much rougher surface (Fig. 2.14b) with island type nanostructures. The phase image[7] of the sample with 8OH-PSS (Fig. 2.14c) showed a clear superficial phase separation that, when compared with the topography in 2D (Fig. 2.14d), helped conclude that the island nanostructures in the surface corresponded to pHEMA, while the valleys contained principally 8OH-PSS. This is because pHEMA would have a higher solubility in the solvent than 8OH-PSS and, then,

[7]The AFM phase image gives information about the material composition, whereupon the differences in the phase image are associated with differences in the surface composition

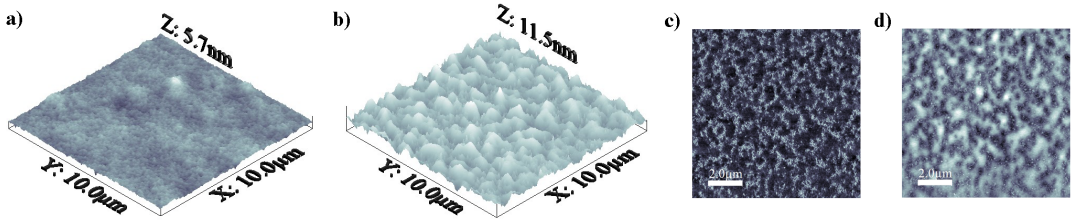

Figure 2.14: Topography images (3D-view, 10 μm $\times$ 10 μm) of samples without (a) and with (b) 8OH-PSS (25%). Phase (c) and topography (d) images (top view, 10 μm $\times$ 10 μm) of the sample with 25 wt.% 8OH-PSS. The scale bars in c) and d) represent 2 μm.

the later would be more quickly depleted from the solvent than the former, thus giving place to the granular surface structure.

Then, the scattering feedback in the samples with 8OH-PSS (or the ones with 8MMA-POSS, section 2.3.2.2) has its origin in the high surface roughness induced by the polymer/silsesquioxane phase separation. Nevertheless, and as a final remark, there is no way (or we have no way) to know whether the phase separation takes place in the whole volume of the sample or just in the surface. This uncertainty leaves the following question open: Is the feedback taking place only at the surface or simultaneously at the surface and within the waveguide?

2.3.5 Waveguides based on Hemicyanine dyes

As it was already mentioned in the Introduction of this chapter, the most of the work on dye doped polymer thin film lasers had been carried out with dyes emitting in the green-yellow spectral region, and, very scarce results could be found on thin film devices emitting in the deep red part of the visible spectrum (660-740 nm), even though this spectral region is of interest in biophotonic applications, just as happened with the spectral window of sulforhodamine dyes.

Leaving apart specifically synthesized dyes, commercial dyes such as Rhodamine 640, Nile Blue or hemicyanines had been used as dopants for active polymer waveguides with emission in the red. Surprisingly, the well known hemicyanine dyes LDS 722 and LDS 730 (Fig. 3), with emission close to 670 nm and 730 nm, respectively, and characterized for having very broad absorption and emission bands and huge Stokes shifts, had not received much attention, if any, in this context. To fill this gap we characterized these two commercially available hemicyanine dyes as Random Laser (RL) emitters.

2.3.5.1 Random Lasing (From paper B8)

Following the approach to obtain RL emission in sulforhodamines, we deposited onto quartz substrates 1 μm thick films of pHEMA/8OH-PSS(25 wt.%) doped with LDS 722

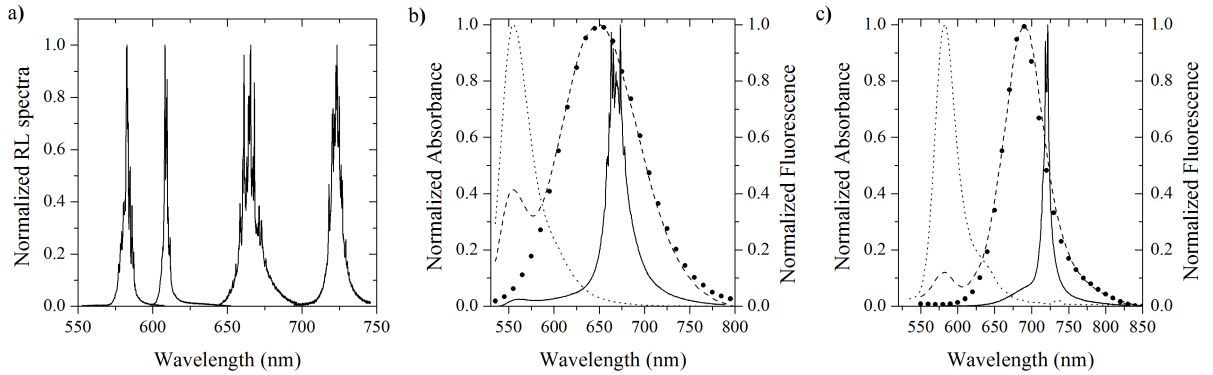

Figure 2.15: a) (From left to right) Normalized RL output spectra at I_p=380 kW/cm^2 from Rh6G, SRhB, Rh6G/LDS 722 and SRhB/LDS 730. b) Front-face fluorescence (λ_{exc}=532 nm) from Rh6G (dotted line), LDS 722 (thick dots), Rh6G/LDS 722 (dashed line) and RL spectrum of the later pumped at 380 kW/cm^2 (solid line). c) Front-face fluorescence (λ_{exc}=532 nm) from SRhB (dotted line), LDS 730 (thick dots), SRhB/LDS 730 (dashed line) and RL spectrum of the later pumped at 380 kW/cm^2 (solid line).

and LDS 730. Both samples presented RL emission, but with a lower intensity than that of the sulforhodamines in the same matrix. The later occurs because both dyes present low absorption at the pump wavelength (532 nm), and so we made use again of the energy transfer mechanism to increase the net efficiency. Several donors were proven, but it was shown that the best donor for LDS 722 was Rhodamine 6G (Rh6G) in a Rh6G:LDS 722 molar proportion 3.3:6.6 (sample Rh6G/LDS 722), while SRhB was the best donor for LDS 730, in SRhB:LDS 730 molar proportion 1:9 (sample SRhB/LDS 730).

In these conditions, RL emission centred at 665 nm and 730 nm was obtained in the samples Rh6G/LDS 722 and SRhB/LDS 730, respectively (Fig. 2.15a). The RL spectra from Rh6G/LDS 722 and SRhB/LDS 730 were seen to be overall much less collapsed that the RL spectra from samples with Rh6G and SRhB alone (Fig. 2.15a). This happens because the fluorescence FWHM of LDS 722 and LDS 730, 100 nm and 63 nm, respectively, is much broader than those of Rh6G (41 nm) and SRhB (37 nm). Finally, with laser thresholds of nearly 100 kW/cm^2 for both samples Rh6G/LDS 722 and SRhB/LDS 730, the energy dose needed to reduce the emission intensity to an 83% of the initial value reached 13 GJ/mol for the sample Rh6G/LDS 722 and 43 GJ/mol for the sample SRhB/LDS 730. The lower photostability of LDS 722 can somewhat be the result of by the low photostability of its donor, i. e., Rh6G, which energy dose was close to 14 GJ/mol, not being an impressive resistance if compared with that of its relatives SRhB and SRh640 (Table 2.2).

These results show that it is possible to obtain efficient and photostable laser emission at the red edge of the visible spectrum by using hemicyanine dyes doped into hybrid matrices.

2.3.5.2 Photophysical characterization of FRET (From paper B8)

As mentioned before, the excitation transfer between donor and acceptor takes place by means of Förster resonance energy transfer (FRET) and/or via radiative energy transfer. In order to estimate the weight of the FRET on the overall energy transfer efficiency, we had to study the system photophysics trying to minimize the effects of the radiative transfer processes. This was achieved by using steady-state fluorimetry in front face configuration, in which the short optical path (film thickness) reduced significantly the re-absorption/re-emission phenomena.

The fluorescence spectra of the donors alone, the acceptors alone and of the optimized mixtures from the pairs Rh6G/LDS 722 and SRhB/LDS 730, are represented in Figs. 2.15b and 2.15c, respectively. From Fig. 2.15b (dashed line) it is evident that the energy transfer from Rh6G to LDS 722 was not complete, since there was still residual emission from Rh6G. On the other hand, the energy transfer was more favourable in the pair SRhB/LDS 730, since the emission corresponding to SRhB was much weaker (dashed line in Fig. 2.15c). From these spectra it was possible to obtain an estimation of the FRET quantum yield, which is given by

$$\phi_{FRET} = 1 - \frac{I_F^{D+A}(\lambda_D^{peak})}{I_F^{D}(\lambda_D^{peak})} \tag{2.8}$$

where $I_F^{D+A}(\lambda_D^{peak})$ and $I_F^{D}(\lambda_D^{peak})$ are the fluorescence intensity at the donor emission peak in the presence and absence of acceptors, respectively. Introducing the data obtained from the spectra shown in Figs. 2.15b and 2.15c (without normalization) into Eq. 2.8, it was found that $\phi_{FRET}^{Rh6G/LDS722} \leq 0.9$ and $\phi_{FRET}^{ShB/LDS730} \leq 0.98$. Such a high transfer efficiencies were obtained, apart from the good spectral overlaps, thanks to the high dye concentrations in the samples, which made the donor and acceptor molecules being in very close proximity, a fact that favours the energy transfer [83].

As a final remark, in the RL measurements the radiative transfer processes were activated thanks to the length travelled by the photons in the active medium (2 mm) and by the population inversion situation, fact that was translated into a less pronounced contribution of the donor emission to the final spectra, as can be observed in Figs. 2.15b and 2.15c (solid lines). Then, we concluded that the energy transfer in these systems is dominated by FRET, but is reinforced by radiative transfer processes.

2.4 Conclusion on SSDL as integrated devices

The studies on the stimulated emission of thin polymer films doped with different commercial dyes belonging to the pyrromethene, perylene, sulforhodamine and hemicya-

nine families, which have been summarized in this chapter, demonstrate that it is possible to obtain efficient (high gains and low thresholds) laser emission from the yellow to the red edge of the visible spectrum (570-730 nm, Fig. 2.16) with a moderate photostability. Although some of these devices would not be very suitable for applications requiring extensive and long-term operation, they could find a place as cheap integrated lasers in disposable lab-on-a-chip applications for the evaluation of biological or organic samples, in which high spectral purity would not be strictly needed. Thanks to this requirements relaxation random lasing could be used, allowing the integration of devices which would be, technologically and economically, more favourable than those based on nanopatterning (DFB).

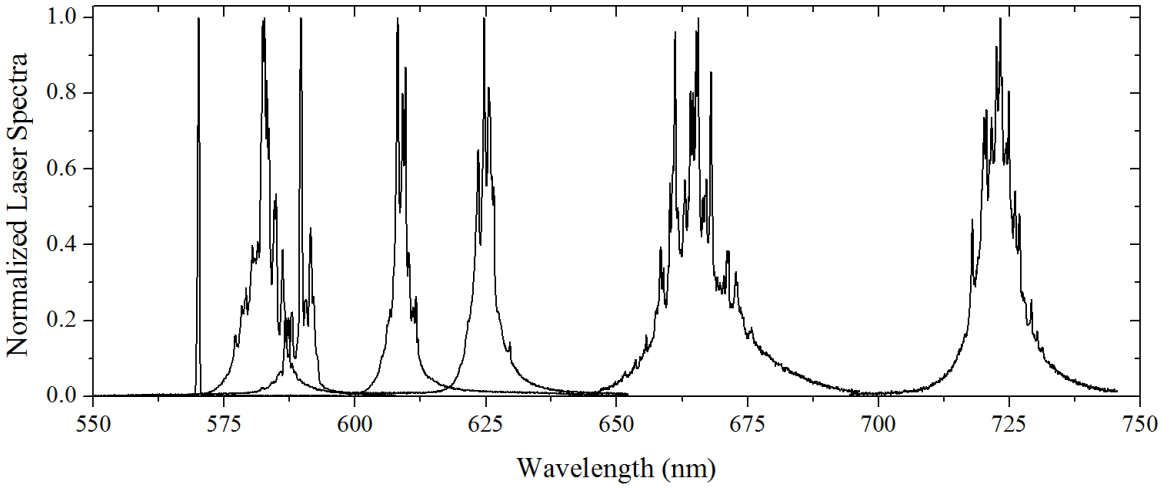

Figure 2.16: (From left to right) Normalized laser spectra of samples PO/PMMA, PM597/pMMA/8MMA-PSS(50 wt.%), Rh6G/pHEMA/8OH-PSS(25 wt.%), SRhB/pHEMA/8OH-PSS(25 wt.%), SRhB:SRh640(1:1)/pHEMA/8OH-PSS(25 wt.%), Rh6G:LDS 722(3.3:6.6)/pHEMA/8OH-PSS(25 wt.%) and SRhB:LDS 730(1:9)/pHEMA/8OH-PSS(25 wt.%).

Table 2.2: Summary of structural and emission properties of best dye/host pairs in each work

Dye	PM567	Per Or	Rh6G	PM597			SRhB	Per Red	SRh640	LDS 722	LDS 730
Paper #	B2	B6	B8	B3	B4	B5	B7	B6	B7	B8	B8
C_{Dye} ($\times 10^{-2}$M)	5	1	1	5	2.5	2.5	1	0.75	1	1	1
Donor	-	-	-	-	-	-	-	Per Or	-	-	-
Host	PMMA	PMMA	pHEMA +PSS	PMMA	6F-6F	PMMA +POSS	pHEMA (+PSS)	PMMA	pHEMA (+PSS)	pHEMA +PSS	pHEMA +PSS
n_{host}	1.49	1.49	1.51	1.49	1.56	1.50	1.51	1.49	1.51	1.51	1.51
n_{subs}	1.52(G)	1.45(Q)	1.45(Q)	1.52(G)	1.52(G)	1.52(G)	1.45(Q)	1.45(Q)	1.45(Q)	1.45(Q)	1.45(Q)
Confinement	LWG	WG	WG	LWG	WG	LWG	WG	WG	WG	WG	WG
ASE properties											
t (μm)	6	9	-	5	9	-	9	1.5	9	-	-
λ_{ASE}^{peak} (nm)	572	581	-	585	593	-	609	620	631	-	-
$\Delta\lambda_{ASE}$ (nm)	18	3.4	-	10	8	-	15	8	14	-	-
I_{ASE}^{th} (kW/cm^2)	10^3	98	-	70	80	-	90	115	106	-	-
g (cm^{-1})	56	34	-	83	93	-	26	-	14.2	-	-
(I_p (kW/cm^2))	(5.3 $\times 10^3$)	(190)		(410)	(500)		(395)		(395)		
n_{pulses}	-	40000	-	58	2600	-	-	56000	-	-	-
(I_p (kW/cm^2))		(190)		(200)	(220)			(190)			
E_{Dose} (GJ/mol)	-	16.9	-	9×10^{-3}	0.51	-	-	189.1	-	-	-
Laser properties											
t (μm)	-	1.5	1	-	-	5	1	-	1	1	1
Donor	-	-	-	-	-	-	-	-	SRhB	Rh6G	SRhB
Laser type	-	DFB	RL	-	-	RL	RL	-	RL	RL	RL
λ_L (nm)	-	570	582	-	-	590	608	-	625	665	725
$\Delta\lambda_L$ (nm)	-	0.38	0.4	-	-	0.56	0.4	-	0.4	0.4	0.4
I_L^{th} (kW/cm^2)	-	12.5	60	-	-	140	50	-	70	100	100
n_{pulses}	-	8400	1300	-	-	-	3200	-	6700	1200	3900
(I_p (kW/cm^2))	-	(51)	(550)	-	-	-	(550)	-	(550)	(550)	(550)
E_{Dose} (GJ/mol)	-	5.7	14.3	-	-	-	35	-	73.7	13.2	42.9

C_{Dye}-Dye concentration, n_{host}-Host refractive index, n_{subs}-Substrate refractive index (Quartz(Q) or Glass(G)), Confinement-Leaky-waveguide (LWG) or waveguide (WG), t-Film thickness, λ_{ASE}^{peak}-ASE peak wavelength, $\Delta\lambda_{ASE}$-ASE Full width at half maximum, I_{ASE}^{th}- ASE pump threshold intensity, g-Maximum gain [at pump intensity (I_p)], n_{pulses}-$I_{out} = 0.83 * I_{in}$ after n pulses [at pump intensity (I_p)], E_{Dose}-Energy dose per mol after # Pulses, Donor-Dye when energy transfer is involved, λ_L-Laser wavelength, $\Delta\lambda L$-Laser linewidth, I_L^{th}-Laser threshold intensity.

Bibliography

[1] C. Grivas and M. Pollnau, "Organic solid-state integrated amplifiers and lasers," *Laser Photonics Rev.*, vol. 6, pp. 419–462, 2012.

[2] A. Costela, I. García-Moreno, and R. Sastre, "Materials for solid-state dye lasers," in *Handbook of advanced electronic and photonic materials and devices, edited by H. S. Nalwa, Volume 7: Liquid crystals, display and laser materials*, pp. 161–208, Academic Press, 2001.

[3] X.-L. Zhu and D. Lo, "Distributed-feedback sol-gel dye laser tunable in the near ultraviolet," *Appl. Phys. Lett.*, vol. 77, pp. 2647–2649, 2000.

[4] T. Saraidarov, R. Reisfeld, M. Kazes, and U. Banin, "Blue laser dye spectroscopic properties in solgel inorganic-organic hybrid films," *Opt. Lett.*, vol. 31, pp. 356–358, 2006.

[5] Y. Oki, K. Aso, D. Zuo, N. J. Vasa, and M. Maeda, "Wide-wavelength-range operation of a distributed-feedback dye laser with a plastic waveguide," *Jpn. J. Appl. Phys*, vol. 41, pp. 6370–6374, 2002.

[6] Y. Oki, S. Miyamoto, M. Tanaka, D. Zuo, and M. Maeda, "Long lifetime and high repetition rate operation from distributed feedback plastic waveguided dye lasers," *Opt. Commun.*, vol. 214, pp. 277–283, 2002.

[7] M. Casalboni, F. D. Matteis, V. Merlo, P. Prosposito, and R. Russo, "1.3 μm light amplification in dye-doped hybrid sol-gel channel waveguides," *Appl. Phys. Lett.*, vol. 83, no. 3, pp. 416–418, 2003.

[8] C. Ye, J. Wang, L. Shi, and D. Lo, "Polarization and threshold energy variation of distributed feedback lasing of oxazine dye in zirconia waveguides and in solutions," *Appl. Phys. B*, vol. 78, pp. 189–194, 2004.

[9] F. Chen, J. Wang, C. Ye, W. Ni, J. Chan, Y. Yang, and D. Lo, "Near infrared distributed feedback lasers based on LDS dye-doped zirconia-organically modified silicate channe waveguides," *Opt. Express*, vol. 13, pp. 1643–1650, 2005.

[10] K. Yamashita, T. Kuro, K. Oe, and H. Yanagi, "Low threshold amplified spontaneous emission from near-infrared dye-doped polymeric waveguide," *Appl. Phys. Lett.*, vol. 88, no. 241110, pp. 1–3, 2006.

[11] M. Djiango, T. Kobayashi, W. J. Blau, B. Cai, K. Komatsu, and T. Kaino, "Near-infrared luminiscent polymer waveguide with a 20 dB small-signal gain," *Appl. Phys. Lett.*, vol. 92, no. 083306, pp. 1–3, 2008.

[12] S. Yuyama, T. Nakajima, K. Yamashita, and K. Oe, "Solid state organic laser emission at 970 nm from dye-doped fluorinated-polyimide planar waveguides," *Appl. Phys. Lett.*, vol. 93, no. 023306, pp. 1–3, 2008.

[13] J. Wang, H. Dong, J. Fan, R. Li, L. Zhang, and K. Y. Wong, "Near-infrared distributed feedback solgel lasers by intensity modulation and polarization modulation," *Appl. Opt.*, vol. 50, pp. 6248–6253, 2012.

[14] G. Jordan, M. Flämmich, M. Ruther, T. Kobayashi, and W. J. Blau, "Light amplification at 501 nm and large nanosecond optical gain in organic dye-doped polymeric waveguides," *Appl. Phys. Lett.*, vol. 88, no. 161114, pp. 1–3, 2006.

[15] I. Sakata, S. Fujimoto, and H. Yanagi, "Stimulated resonance Raman scattering from dye-doped polymer waveguides," *Appl. Phys. Lett.*, vol. 88, no. 191104, pp. 1–3, 2006.

[16] M. Lu, B. T. Cunningham, S.-J. Park, and J. G. Eden, "Vertically emitting, dye-doped polymer laser in the green ($\lambda \sim 536$nm) with a second order distributed feedback grating

fabricated by replica molding," *Opt. Commun.*, vol. 281, pp. 3159–3162, 2008.

[17] M. Fukuda, H. Matsuura, E. Yamazaki, and H. Sakata, "Expansion of emission band based on energy transfer in diode-pumped microcavity dye lasers," *Appl. Opt.*, vol. 49, no. 14, pp. 2552–2556, 2010.

[18] K. Norrman, A. Ghanbari-Siahkali, and N. B. Larsen, "6 studies of spin-coated polymer films," *Annu. Rep. Prog. Chem., Sect. C*, vol. 101, pp. 174–201, 2005.

[19] S. S. Gaur, K. Ghawana, , V. K. Sharma, and K. Tripathi, "Dye-doped polymeric waveguides for integrated optics," *J. Opt. A: Pure Appl. Opt.*, vol. 6, pp. 312–314, 2004.

[20] Y. Yang, R. Goto, S. Omi, K. Yamashita, H. Watanabe, M. Miyazaki, and Y. Oki, "Highly photo-stable dye doped solid-state distributed-feedback (DFB) channeled waveguide lasers by a pen-drawing technique," *Opt. Express*, vol. 18, pp. 22080–22089, 2010.

[21] C. Lowe, *Test Methods for UV & EB Curable Systems*, vol. VI of *Surface Coatings Technology*. John Wiley in association with SITA Technology Limited, 2007.

[22] Y. Chen, J. Herrnsdorf, B. Guilhabert, A. L. Kanibolotsky, A. R. Mackintosh, Y. Wang, R. A. Pethrick, E. Gu, G. A. Turnbull, P. J. Skabara, I. D. W. Samuel, N. Laurand, and M. D. Dawson, "Laser action in surface-structured free-standing membrane based on a π-conjugated polymer-composite," *Org. Electron.*, vol. 12, pp. 62–69, 2011.

[23] A. Büttner and U. D. Zeitner, "Experimental realization of monolithic diffractive broad-area polymeric waveguide dye lasers," *IEEE J. Quantum Electron.*, vol. QE-43, no. 7, pp. 545–551, 2007.

[24] N. Tsutsumi and T. Ishibashi, "Organic dye lasers with distributed Bragg reflector grating and distributed feedback resonator," *Opt. Express*, vol. 17, no. 24, pp. 21698–21703, 2009.

[25] K. D. Singer, T. Kazmierczak, J. Lott, H. Song, Y. Wu, J. Andrews, E. Baer, A. Hiltner, and C. Weder, "Melt-processed all-polymer distributed Bragg reflector laser," *Opt. Express*, vol. 16, no. 14, pp. 10358–10363, 2008.

[26] K. Yamashita, H. Yanagi, and K. Oe, "Array of a dye-doped polymer-based microlaser with multiwavelength emission," *Opt. Lett.*, vol. 36, pp. 1875–1877, 2011.

[27] I. D. W. Samuel and G. A. Turnbull, "Organic semiconductor lasers," *Chem. Rev.*, vol. 107, pp. 1272–1295, 2007.

[28] M. B. Christiansen, A. Kristensen, S. Xiao, and N. A. Mortensen, "Photonic integration in k-space: Enhancing the performance of photonic crystal dye lasers," *Appl. Phys. Lett.*, vol. 93, no. 231101, pp. 1–3, 2008.

[29] D. Luo, X. W. Sun, H. T. Dai, Y. J. Liu, H. Z. Yang, and W. Ji, "Two-directional lasing from a dye-doped two-dimensional hexagonal photonic crystal made of holographic polymer-dispersed liquid crystals," *Appl. Phys. Lett.*, vol. 95, no. 151115, pp. 1–3, 2009.

[30] V. G. Kozlov, V. Bulovic, P. E. Burrows, and S. R. Forrest, "Laser action in organic semiconductor waveguide and double-heterostructure devices," *Nature*, vol. 389, pp. 362–364, 1997.

[31] K. Yamashita, A. Kitanobou, M. Ito, E. Fukuzawa, and K. Oe, "Solid-state organic laser using self-written active waveguide with in-line Fabry-Pérot cavity," *Appl. Phys. Lett.*, vol. 92, no. 143305, pp. 1–3, 2008.

[32] M. Kuwata-Gonokami, R. H. Jordan, A. Dodabalapur, H. E. Katz, M. L. Shilling, R. E. Slusher, and S. Ozawa, "Polymer microdisk and microring lasers," *Opt. Lett.*, vol. 20, no. 20, pp. 2093–2095, 1995.

[33] J. Wiersig, J. Unterhinninghofen, Q. Song, H. Cao, M. Hentschel, and S. Shinohara, "Review on unidirectional light emission from ultralow-loss modes in deformed microdisks," in *Trends in Nano- and Micro-Cavities (Editors: O. Kwon, B. Lee, K. An)*, pp. 109–152, Bentham Science Publishers Ltd., 2011.

[34] M. Lebental, J. S. Lauret, R. Hierle, and J. Zyss, "Highly directional stadium-shaped polymer microlasers," *Appl. Phys. Lett.*, vol. 88, no. 031108, pp. 1–3, 2006.

[35] T. Ben-Messaoud and J. Zyss, "Unidirectional laser emission from polymer-based spiral microdisks," *Appl. Phys. Lett.*, vol. 86, no. 241110, pp. 1–3, 2005.

[36] B. J. Lin, *Optical Lithography.* Bellingham, WA: SPIE Press Books, 2010.

[37] G. A. Turnbull, A. Carleton, G. F. Barlow, A. Tahraouhi, T. F. Krauss, K. A. Shore, and I. D. W. Samuel, "Influence of grating characteristics on the operation of circular-grating distributed-feedback polymer lasers," *J. Appl. Phys.*, vol. 98, no. 023105, pp. 1–7, 2005.

[38] Y. Nakata, T. Okada, and M. Maeda, "Lithographical laser ablation using femtosecond laser," *Appl. Phys. A*, vol. 79, pp. 1481–1483, 2004.

[39] T. Zhai, X. Zhang, Z. Pang, and F. Dou, "Direct writing of polymer lasers using interference ablation," *Adv. Mater.*, vol. 23, no. 16, pp. 1860–1864, 2011.

[40] C. Vass, K. Osvay, T. Veso, B. Hopp, and Z. Bor, "Submicrometer grating fabrication in fused silica by interferometric laser-induced backside wet etching technique," *Appl. Phys. A*, vol. 93, pp. 69–73, 2008.

[41] S. Balslev, T. Rasmussen, P. Shi, and A. Kristensen, "Single mode solid state distributed feedback dye laser fabricated by gray scale electron beam lithography on a dye doped SU-8 resist," *J. Micromech. Microeng.*, vol. 15, pp. 2456–2460, 2005.

[42] S. Balslev, A. Mironov, D. Nilsson, and A. Kristensen, "Micro-fabricated single mode polymer dye laser," *Opt. Express*, vol. 14, no. 6, pp. 2170–2177, 2006.

[43] M. G. Ramírez, P. G. Boj, V. Navarro-Fuster, I. Vragovic, J. M. Villalvilla, I. Alonso, V. Trabadelo, S. Merino, and M. A. Díaz-García, "Efficient organic distributed feedback lasers with imprinted active films," *Opt. Express*, vol. 19, no. 23, pp. 22443–22454, 2011.

[44] J. R. Lawrence, G. A. Turnbull, and I. D. W. Samuel, "Polymer laser fabricated by a simple micromolding process," *Appl. Phys. Lett.*, vol. 82, no. 23, pp. 4023–4025, 2003.

[45] J. Herrnsdorf, B. Guilhabert, Y. Chen, A. L. Kanibolotsky, A. R. Mackintosh, R. A. Pethrick, P. J. Skabara, E. Gu, N. Laurand, and M. D. Dawson, "Flexible blue-emitting encapsulated organic semiconductor DFB laser," *Opt. Express*, vol. 18, no. 25, pp. 25535–25545, 2010.

[46] I. Sakata, K. Yamashita, H. Takeuchi, and M. Tomiki, "Diode-pumped distributed-feedback dye laser with an organic-inorganic microcavity," *Appl. Phys. B*, vol. 92, pp. 243–246, 2008.

[47] Y. Oki, M. Tanaka, Y. Ogawa, H. Watanabe, and M. Maeda, "Development of quasi-end-fire waveguide plastic dye laser," *IEEE J. Quantum. Electron.*, vol. 42, no. 4, pp. 389–396, 2005.

[48] N. Tsutsumi and M. Takeuchi, "Ti-sapphire femtosecond pulse pumped laser emission from all-plastic organic waveguide with distributed feedback resonator," *Opt. Commun.*, vol. 281, pp. 2179–2183, 2008.

[49] Y. Yang, G. A. Turnbull, and I. D. W. Samuel, "Hybrid optoelectronics: A polymer laser pumped by a nitride light-emitting diode," *Appl. Phys. Lett.*, vol. 92, no. 163306, pp. 1–3, 2008.

[50] K. Yamashita, K. Hase, H. Yanagi, and K. Oe, "Optical amplification in organic dye-doped polymeric channel waveguide under CW optical pumping," *Jap. J. Appl. Phys.*, vol. 46, no. 28, pp. L688–L690, 2007.

[51] H. Nakanotani, C. Adachi, S. Watanabe, and R. Katoh, "Spectrally narrow emission from organic films under continuous-wave excitation," *Appl. Phys. Lett.*, vol. 90, no. 231109, pp. 1–3, 2007.

[52] Y. Huang, L.-P. Chen, C. Doyle, Y. Zhou, and S.-T. Wu, "Spatially tunable laser emission in dye-doped cholesteric polymer films," *Appl. Phys. Lett.*, vol. 89, no. 111106, pp. 1–3,

2006.

[53] S. Klinkhammer, X. Liu, K. Huska, Y. Shen, S. Vanderheiden, S. Valouch, C. Vannahme, S. Bräse, T. Mappes, and U. Lemmer, "Continuously tunable solution-processed organic semiconductor DFB lasers pumped by laser diode," *Opt. Express*, vol. 20, no. 6, pp. 6357–6364, 2012.

[54] C. Vannahme, S. Klinkhammer, M. B. Christiansen, A. Kolew, A. Kristensen, U. Lemmer, and T. Mappes, "All-polymer organic semiconductor laser chips: Parallel fabrication and encapsulation," *Opt. Express*, vol. 18, no. 24, pp. 24881–24887, 2010.

[55] Y. Yang, G. Lin, H. Xu, M. Wang, and G. Qian, "Distributed-feedback laser actions in zirconia-ORMOSIL waveguides based on energy transfer between co-doped laser dyes," *Opt. Commun.*, vol. 281, pp. 5218–5221, 2008.

[56] Y. Oki, T. Yoshiura, Y. Chisaki, and M. Maeda, "Fabrication of a distributed-feedback dye laser with a grating structure in its plastic waveguide," *Appl. Opt.*, vol. 41, pp. 5030–5035, 2002.

[57] T. Voss, D. Scheel, and W. Schade, "A microchip-laser-pumped DFB-polymer-dye laser," *Appl. Phys. B*, vol. 73, pp. 105–109, 2001.

[58] S. Ricciardi, S. Popov, A. T. Friberg, and S. Sergeyev, "Thermally induced wavelength tunability of microcavity solid-state lasers," *Opt. Express*, vol. 15, no. 20, pp. 12971–12978, 2007.

[59] Z. Li, Z. Zhang, A. Scherer, and D. Psaltis, "Mechanically tunable optofluidic distributed feedback dye laser," *Opt. Express*, vol. 14, no. 22, pp. 10494–10499, 2006.

[60] K. Yamashita, N. Takeuchi, K. Oe, and H. Yanagi, "Simultaneous RGB lasing from a single-chip polymer device," *Opt. Lett.*, vol. 35, pp. 2451–2453, 2010.

[61] Y. Oki, S. Miyamoto, M. Maeda, and N. J. Vasa, "Multiwavelength distributed-feedback dye laser array and its application to spectroscopy," *Opt. Lett.*, vol. 27, no. 14, pp. 1220–1222, 2002.

[62] Y. Oki, S. Miyawaki, M. Maeda, and M. Tanaka, "Spectroscopic applications of integrated tunable solid-state dye laser," *Opt. Rev.*, vol. 12, no. 4, pp. 301–306, 2005.

[63] H. Watanabe, Y. Oki, and T. Omatsu, "Highly efficient long-lifetime dual-layered waveguide dye laser containing SiO_2 nanoparticles-dispersed random scattering active media," *Jap. J. Appl. Phys.*, vol. 48, no. 112503, pp. 1–3, 2009.

[64] H. Yoshioka, Y. Yang, H. Watanabe, and Y. Oki, "Fundamental characteristics of degradation-recoverable solid-state DFB polymer laser," *Opt. Express*, vol. 20, pp. 4690–4696, 2012.

[65] G. I. Peters and L. Allen, "Amplified spontaneous emission IV. beam divergence and spatial coherence," *J. Phys. A: Gen. Phys.*, vol. 5, pp. 546–554, 1972.

[66] A. E. Siegman, *Lasers.* Mill Valley, CA: University Science Books, 1986.

[67] J. P. Dowling, M. Scalora, M. J. Bloemer, and C. M. Bowden, "The photonic band edge laser: a new approach to gain enhancement," *J. Appl. Phys.*, vol. 75, pp. 1896–1899, 1994.

[68] G. A. Turnbull, P. Andrew, M. J. Jory, W. L. Barnes, and I. D. W. Samuel, "Relationship between photonic band structure and emission characteristics of a polymer distributed feedback laser," *Phys. Rev. B*, vol. 64, no. 125122, pp. 1–6, 2001.

[69] D. Zhang, Y. Wang, and D. Ma, "SiO_2 nanoparticles as scatterers for random organic laser action in red fluorescent dye 4-(dicyanomethylene)-2-tert-butyl-6(1,1,7,7-tetramethyljulolidyl-9-enyl)-4 H-pyran doped polystyrene films," *J. Appl. Phys.*, vol. 103, no. 123107, pp. 1–4, 2008.

[70] X. Zhao, Z. Wu, S. Ning, S. Liang, D. Wang, and X. Hou, "Random lasing from granular surface of waveguide with blends of ps and pmma," *Opt. Express*, vol. 19, no. 17, pp. 16126–

16131, 2011.

[71] A. Tulek, R. C. Polson, and Z. V. Vardeny, "Naturally occurring resonantors in random lasing of π-conjugated polymer films," *Nature Physics*, vol. 6, pp. 303–310, 2010.

[72] H. Kogelnik and C. V. Shank, "Stimulated emission in a periodic structure," *Appl. Phys. Lett.*, vol. 18, no. 4, pp. 152–154, 1971.

[73] M. D. Rahn and T. A. King, "Comparison of laser performance of dye molecules in sol-gel, polycom, ormosil, and poly(methyl methacrylate) host media," *Appl. Opt.*, vol. 34, no. 36, pp. 8260–8271, 1995.

[74] L. D. Negro, P. Bettotti, M. Cazzanelli, D. Pacifici, and L. Pavesi, "Applicability conditions and experimental analysis of the variable stripe length method for gain measurements," *Opt. Commun.*, vol. 229, pp. 337–348, 2004.

[75] L. W. Casperson and A. Yariv, "Spectral narrowing in high-gain lasers," *IEEE J. Quantum Electron.*, vol. QE-8, no. 2, pp. 80–85, 1972.

[76] G. I. Peters and L. Allen, "Amplified spontaneous emission I. the threshold condition," *J. Phys. A: Gen. Phys.*, vol. 4, pp. 238–243, 1971.

[77] K. Okamoto, *Fundamentals of optical waveguides*. Burlington, MA: Academic Press, 2006.

[78] M. Born and E. Wolf, *Principles of Optics*. Oxford, UK: Pergamon Press, 1975.

[79] T.-N. Ding and E. Garmire, "Measuring refractive index and thickness on thin films: a new technique," *Appl. Opt.*, vol. 22, no. 20, pp. 3177–3181, 1983.

[80] L. Chen, F. Gao, Y. Bu, F. Jia, C. Liu, and Z. Cai, "Tunable distributed feedback lasing from leaky waveguides based on gel-glass dispersed liquid crystal thin films," *Mat. Lett.*, vol. 65, pp. 3476–3478, 2011.

[81] J.-H. Kang and Q.-H. Park, "Spectral property of leaky waves from planar dielectric waveguide," *J. Opt. Soc. Am. B*, vol. 28, no. 9, pp. 2248–2252, 2011.

[82] R. Sastre, V. Martín, L. Garrido, J. L. Chiara, B. Trastoy, O. García, A. Costela, and I. García-Moreno, "Dye-doped polyhedral oligomeric silsesquioxane (POSS)-modified polymeric matrices for highly efficient and photostable solid-state lasers," *Adv. Funct. Mat.*, vol. 19, pp. 3307–3316, 2009.

[83] B. Valeur, *Molecular fluorescence*. Weinhaim, Germany: Wiley-VCH, 2002.

Global Conclusion

The experimental and theoretical results presented in this thesis report demonstrate conclusively that following a simultaneous "physical" and "chemical" approach to tailor the emission properties of the host materials for solid state dye lasers, may lead, under specific circumstances, to the improvement of both the laser efficiency and photostability of commercially available laser dyes emitting from the green to nearly the IR, a region of interest in telecommunications and biophotonics.

In this sense, it has been demonstrated, both theoretically and experimentally, that optical scattering is not always detrimental either to conventional bulk lasers (laser rods or colloidal suspensions) or to integrated devices, but may give place, on the contrary, to dramatic improvements in the output efficiencies and photostabilities of organic (hybrid) laser rods, and to alternative ways of obtaining laser light from integrated devices more favourable, technologically and economically, than those based on nanopatterning.

In conclusion, it has been shown that the development of advanced photonic materials based on solid state dye lasers combining synergistically the advantages of both random and conventional lasers, may result in optimized laser emission, which, together with their processing and pumping flexibility, paves the way to the commercialization and industrialization of cost-effective laser heads for biomedical applications, or cheap integrated lasers in disposable lab-on-a-chip platforms for optoelectronic, spectroscopic or sensing applications.

Conclusión General

Los resultados, experimentales y teóricos, expuestos en esta memoria demuestran convincentemente que la aplicación simultánea de estrategias "físicas" y "químicas", con la idea de manipular las propiedades de emisión de las matrices utilizadas en láseres de colorante en estado sólido, puede llevar, bajo determinadas circunstancias, a la mejora en la eficiencia y fotoestabilidad de colorantes comerciales con emisión desde el verde hasta casi el IR, una región espectral apta para aplicaciones biofotónicas y en telecomunicación.

En este sentido, se ha demostrado, tanto teórica como experimentalmente, que la dispersión óptica no siempre es perjudicial para los láseres convencionales (barras láser o suspensiones coloidales) ni para los dispositivos integrados, sino que, muy al contrario, puede propiciar mejoras importantes tanto en la eficiencia como en la fotoestabilidad láser de barras láseres orgánicas (o híbridas), así como abrir la puerta a vías alternativas para obtener emisión láser en dispositivos integrados, lo que presenta ventajas, tanto económicas como tecnológicas, frente a los dispositivos basados en nanoescritura.

En conclusión, se ha mostrado que el desarrollo de materiales fotónicos avanzados basados en láseres de colorante en estado sólido, combinando de un modo sinergético las ventajas de los láseres convencionales y 'aleatorios', puede resultar en emisión láser optimizada, lo que, junto con la flexibilidad de procesado y bombeo intrínseca a estos materiales, abre las puertas a la comercialización e industrialización de cabezales láser económicamente competitivos y con prospectivas biomédicas, así como de láseres integrados en laboratorios-en-un-chip de usar y tirar para aplicaciones optoelectrónicas, espectroscópicas o diagnósticas.

Apéndice A

Artículos sobre láseres de colorante en estado sólido con retroalimentación por dispersión

Este apéndice contiene todos los artículos utilizados para la discusión del Capítulo 1. Los artículos están ordenados como siguen:

1. A. Costela, I. García-Moreno, L. Cerdán, V. Martín, O. García, and R. Sastre, "Dye-doped POSS solutions: random nanomaterials for laser emission," Adv. Mater. 21, 4163–4166 (2009)

2. L. Cerdán, A. Costela, I. García-Moreno, V. Martín and M. E. Pérez-Ojeda, "Laser efficiency enhancement due to non-resonant feedback in dye-doped hybrid materials: theoretical insights and experiment," IEEE J. Quantum Electron. 47, 7, 907–919 (2011)

3. L. Cerdán, E. Enciso, V. Martín, J. Bañuelos, I. López-Arbeloa, A. Costela, and I. García-Moreno, "FRET assisted laser emission in colloidal suspensions of dye-doped latex nanoparticles," Nature Photonics 6, 621–626 (2012)

Paper A1: Adv. Mater. 21, 4163–4166 (2009)

Dye-doped POSS solutions: random nanomaterials for laser emission

A. Costela, I. Garcia-Moreno, L. Cerdán, V. Martin, O. Garcia, and R. Sastre

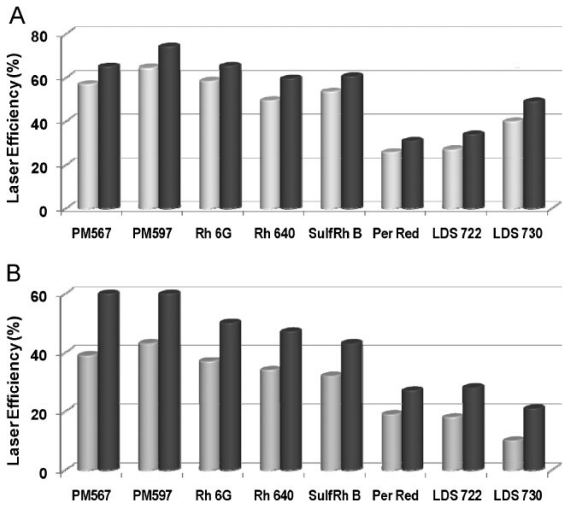

Laser efficiency of different dyes in the presence (black) and absence (grey) of POSS nanoparticles in liquid solutions (A) and in solid samples (B) transversely pumped at 532 with 5.5 mJ pulse^{-1}.

ADVANCED MATERIALS

Dye-Doped POSS Solutions: Random Nanomaterials for Laser Emission

By *Angel Costela, Inmaculada Garcia-Moreno,* Luis Cerdan, Virginia Martin, Olga Garcia,* and *Roberto Sastre*

Optical properties of new materials based on nanometer-sized polyhedral oligomeric silsesquioxanes (POSS) have been of increasing interest for both fundamental and practical reasons, largely because of their novel applications in photonics and electronic devices.[1] The presence of POSS enhances significantly the thermal, mechanical, and physical properties of the final materials, opening the challenge to synthesize new luminescent hybrid matrices with optoelectronic properties comparable to dendronized or grafted conjugated polymers.[2,3] POSS has a compact hybrid structure with an inorganic core made up of silicon and oxygen $(SiO_{1.5})_n$ externally surrounded by non-reactive or reactive polymerizable organic ligands, R. The type and number of substituents control the interactions between the organic ligand and the medium defining the compatibility, and thus the final properties of the POSS-modified systems. Thus, POSS nanoparticles can be dispersed at a molecular level (1–3 nm)[4] and, because of their synthetically well-controlled functionalization, can be incorporated into polymers by different polymerization techniques with minimal processing disruption.[5–7] This excellent dispersion at the molecular scale prevents phase separation and assures the macroscopic homogeneity of the materials.[8] In this way, new optical hybrid materials based on POSS nanoparticles as the inorganic part overcome some of the most important limitations intrinsic to sol–gel hybrid composites while maintaining the physical, chemical, and mechanical combined advantages of organic–inorganic systems.[9]

In this contribution, we propose and demonstrate, for the first time to the best of our knowledge, the behaviour of POSS-doped systems as random materials, a possibility never before considered. The dispersion of POSS nanoparticles at a molecular level defines highly homogeneous materials that, when doped with lasing dyes, allow coherent laser emission but, in addition and in spite of their nanometer size, the POSS particulates sustain an incoherent feedback into the coherent emission by multiple scattering. Multiple scattering is a well-known phenomenon that occurs in nearly all optical materials that appear opaque. Thus, it was difficult to predict that such a homogeneous material with nanoparticles with a size in the range 0.5–4 nm could sustain a scattering phenomenon. In addition, optical scattering has always been considered as detrimental to laser action, representing a source of loss. However, the nanosized POSS particulates allow a weak optical scattering of the emission that helps lasing by elongating the light path inside the gain media and providing an extra feedback, a phenomenum central to the process called 'incoherent random laser' or 'lasing with intensity feedback'.[10] In this way, the laser action in systems based on dye-doped POSS materials is significantly enhanced.[9]

An ethyl acetate solution of PM567 (1.5×10^{-3} M), contained in a 1 cm optical-path quartz cell, was transversely pumped at 532 nm with 5.5 mJ pulse^{-1} in a simple plane–plane non-tunable resonator,[8] and a laser spot area at the incident surface of 3×10^{-2} cm^2 with about 300 μm penetration depth. Under these experimental conditions, the PM567 dye, considered to be a benchmark for laser emission in the visible spectroscopic region, emitted broad-line-width laser light at 567 nm, with a laser efficiency (percentage of the excitation energy converted into laser emission) of 57%. Under the same pumping conditions, the presence of octa(methyl methacryl)-POSS (8MMAPOSS) nanoparticles, in just 1 wt %, improved the dye laser efficiency up to 65% and decreased the emission threshold from 0.3 to 0.18 mJ. An increase of the 8MMAPOSS weight proportion from 1 to 13%, corresponded to an increase of the weight content of silicon from 0.2 to 2%, which led to laser efficiencies of around 70%. Further increases of POSS content up to 50 wt % resulted in a decrease of laser efficiency down to 64% but preserved the threshold (∼0.18 mJ), pulse duration (∼5 ns FWHM), and peak of the laser emission.

In a previous work we characterized in detail the lasing behaviour of PM567-doped copolymers of methyl methacrylate (MMA) with 8MMAPOSS added in weight proportions from 1% up to 50% and pumped under otherwise identical experimental conditions to those selected in the liquid phase.[9] Once again, the presence of POSS nanoparticles allowed PM567 to reach a lasing efficiency of 60% with a high photostability, since no sign of degradation in the laser output was observed after 100 000 pump pulses in the same position of the sample at a 10 Hz repetition rate.[9] The new dye-doped POSS-based materials improved remarkably the lasing performance of this dye incorporated into pure poly(methyl methacrylate) (PMMA), where a lasing efficiency of 39%, with a 70% drop in its initial laser output after 100 000 pump pulses, was recorded within the same experimental set-up. In addition, the presence of POSS led to the

[*] Dr. A. Costela, Dr. I. Garcia-Moreno, L. Cerdan, Dr. V. Martin
Dpto. Quimica Laser
Instituto de Quimica-Fisica 'Rocasolano' (CSIC)
28006 Madrid (Spain)
E-mail: i.garcia-moreno@iqfr.csic.es
Dr. O. Garcia, Prof. R. Sastre
Dpto. Fotoquimica de Polimeros
Instituto de Ciencia y Tecnologia de Polimeros (CSIC)
28006 Madrid (Spain)

DOI: 10.1002/adma.200900799

ADVANCED MATERIALS www.advmat.de

best laser parameters achieved to date for PM567-doped organic, inorganic, and sol–gel hybrid materials, without rotating or translating the medium to distribute the thermal load over a large volume.[9,11,12]

For all the 8MMAPOSS weight proportions selected herein, the gain media exhibited a high degree of optical homogeneity, which indicates that nanosized POSS monomers were dispersed in liquid solutions at the molecular scale and copolymerized with MMA in a fairly uniform manner in the solid matrices. This prevented internal interference that would lead to macroscopic manifestations of spatial inhomogeneities in the laser spot, clearly evident in early samples of organic–inorganic composites.[13] This feature allowed the attainment of high efficiency laser emissions with low beam divergence (~1.5 mrad).

In order to understand the process involved in the enhancement of laser action induced by POSS, some photophysical and thermal properties of the new systems were analyzed (Supporting Information). It was found that the photophysics (molar absorption coefficient, absorption and fluorescence wavelengths, fluorescence quantum yields, lifetime, etc.) of PM567 are not strongly affected by the presence of increased weight proportions of 8MMAPOSS. Thus, a change in the photophysics can be ruled out as being responsible for the exhibited lasing properties. In addition, in the POSS-modified copolymers the thermal conductivity was enhanced from 0.182 W m^{-1} K^{-1} in pure PMMA to 0.2333 W m^{-1} K^{-1} for the material with 50 wt % of 8MMAPOSS. However, this is neither the only nor the main cause of the improved lasing properties in these POSS-based materials, since other PM567-doped silicon-containing organic matrices[11] and sol–gel hybrid materials[9] with similar thermal properties exhibited a worse laser action when pumped under identical experimental conditions.

Taking into account that radiative properties of molecular systems are altered significantly in the presence of optical scattering, the question that immediately arises is whether the POSS nanoparticles could act as passive scatterers when they are present in the dye-gain media in spite of their high optical homogeneity. Scattering has always been considered detrimental to laser action because it alters the direction and spatial coherence of the photons from the lasing mode of a conventional cavity. However, under suitable circumstances, the density of scattering particles allows an increase in the path length travelled by diffusive photons, and a large gain can occur in photoexcited media, which gives rise to scattering laser-like emission.[10]

To asses this question in the present case, we characterized in detail the laser-induced spectroscopy of PM567 both in liquid solutions and in solid matrices pumped under the same experimental conditions. The pump pulses were now incident on the samples at a 30° angle and the laser excitation energy was gradually increased from 0.9 to 6 mJ $pulse^{-1}$. The emission from the front-face of the sample was collected into an optical fiber and sent to a 0.3 m spectrometer with a grating of 1200 grooves per mm and a 0.1 nm spectroscopic resolution, detected with a CCD camera and recorded with a PC. A long-pass filter (OptoSigma, cutoff at 534 nm) was used to remove the pumping light.

The excitation of the pure dye solution resulted in a broad photoluminescence spectrum centred at 556 nm, which remained constant for the entire range of pumping energies.

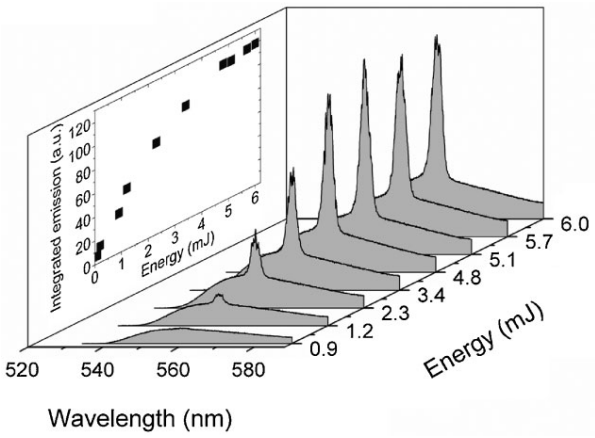

Figure 1. Front-face emission spectra as a function of the pumping energy at 532 nm from an ethyl acetate solution of a PM567 dye that contains 13 wt % of 8MMAPOSS nanoparticles. Inset: output emission intensity integrated over all wavelengths.

In the presence of POSS, even at the lowest (1%) weight proportion selected, a narrow stimulated emission band centred at 559 nm increased as the pump energy increased. Figure 1 shows the evolution of the emission spectra from PM567-doped liquid solutions with 13 wt % of 8MMAPOSS at different pump energies above the threshold for the onset of the amplified stimulated emission (1.0 mJ). This behaviour became independent of both the POSS proportion and the phase of the gain media. However, the increase of the scattering particle density led to the gain-narrowed band predominance over the emission spectra with the broad tails of the photoluminescence being progressively suppressed. In the liquid phase, a multimode emission with narrow peaks emerged at a low pump energy, which became sharper, with a linewidth as small as 0.1 nm on top of a globally narrowed spectrum, for further increases of the pump energy. It was found that the wavelengths and heights of the narrow spikes in the emission spectra changed in a random fashion from one excitation pulse to another. The emission spectra were then completely uncorrelated from shot to shot since each excitation pulse illuminated a different configuration of scatters in a random walk motion inside the solutions. On the contrary, in the emission spectra recorded from dye-doped solid-state POSS matrices, where the scattering particles were not moving and all other experimental conditions remained constant, narrow peaks were apparently lost and the sample front-face emission spectra became highly reproducible.

To gain more insight into the actual effect of the scatter POSS proportion in the spectroscopic characteristics of the media, the wavelength-integrated emission was analyzed as a function of both the nanoparticle concentrations and the pump pulse energy (inset Fig. 1). The pure dye solution exhibited a constant emission while the POSS-doped media followed a different behaviour: first, the emission increased rapidly, with a higher slope for a higher POSS proportion, and with pump energies up to ~5 mJ, to reach a plateau or slightly decrease for further increases in the incident energy. The same behaviour was followed by the intensity of the wavelength peak of the emission (559 nm) as a function of the

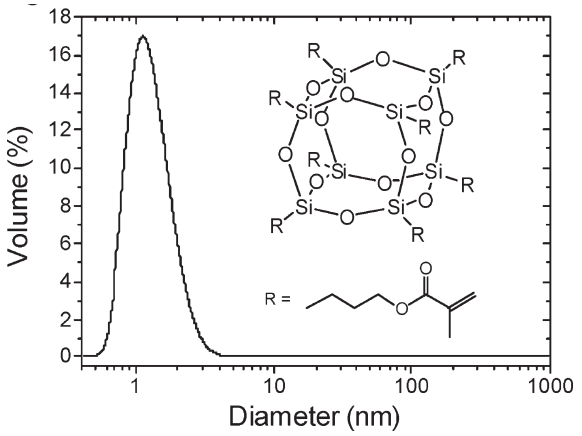

Figure 2. Analysis by DLS of the size distribution by volume of 8MMA-POSS nanoparticles incorporated in a 13 wt % proportion to a MMA solution.

pump energy for the increased scatter densities, which was mirrored in the corresponding linewidth collapse.

Since for an amplifying random medium, the overall scattering properties depend strongly on the particle size, the spatial structure of liquid solutions with POSS was examined by dynamic light scattering (DLS) on a Malvern Zetasizer NS with a measurement diameter size range from 0.4 to 1000 nm. The 8MMAPOSS size distribution by volume was centred at 1.17 nm with an approximate range from 0.5 to 4 nm (see Fig. 2). In addition, nanographs from transmission electron microscopy (TEM), atomic force microscopy (AFM), and scanning electron microscopy (SEM) of thin-film sections of the gain media used in the laser experiments revealed a homogeneous distribution of POSS in the polymer, and depict a continuous phase that corresponds to the organic matrix which incorporates these nanosized POSS crosslinkers at a molecular level, which is in agreement with the transparency of the samples (Fig. 3).

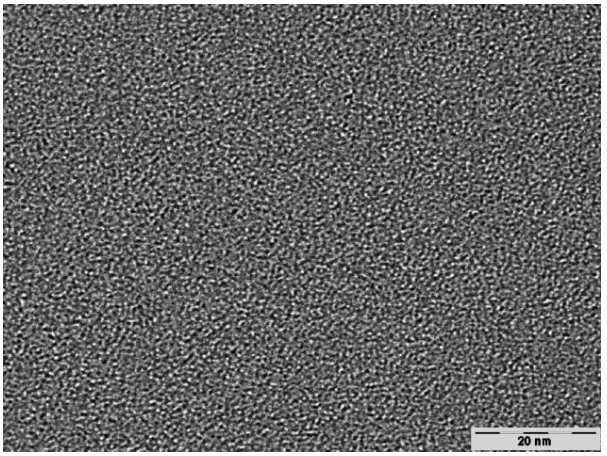

Figure 3. TEM imagess of the MMA + 13 wt % 8MMAPOSS copolymer network.

For a quantitative understanding of the origin and features observed in the sample front-face emission spectra as a result of the system acting as weak scattering gain media, a relevant length scale is the scattering mean free path, l_{sc}, defined as the average distance between two scattering events. In the Rayleigh limit,[14] this parameter depends on both the scattering cross section and the particle density ρ in the solutions. Thus, for the highest ρ utilized in our case, $2.17 \times 10^{20}\,cm^{-3}$, which corresponds to a 50 wt % proportion of POSS, and for a value of a scattering cross section of $(1.0 \pm 0.2) \times 10^{-23}\,cm^2$, calculated according equation (3) of ref. [14], a minimum l_{sc} value of 54 cm at 560 nm describes the scattering process. Because the scattering mean free path is much longer than the optical wavelength, the drastic spectroscopic narrowing observed can be understood in terms of the light diffusion model with gain, where the phase of light wave and interference effects are neglected.[15] According to this model, there is gain in the medium because of a mere increase in the path length of light in the region, but the model cannot provide coherent feedback into discrete lasing modes.

Another relevant parameter is the scattering time, t_{sc}, defined as the average time between two scattering events, $t_{sc} = nl_{sc}/c$, where n is the refractive index of the media and c is the speed of light in a vacuum. Using $n = 1.435$ for ethyl acetate, a minimum t_{sc} value of 2.62 ns at 560 nm is required for scattering events to take place. Thus, the POSS nanoparticles could act as efficient scatter centres only under nanosecond laser pulses independent of the pumping geometry. This implies that the time-resolved spectroscopy after excitation with picosecond pulses, often utilized as a technique to study random lasing media to separate the narrow laser-like contribution of the scatters from the usual spontaneous emission under irradiation above the threshold, cannot be applied in the present case because both processes take place in the same time scale.

The above discussion allows the conclusion that the remarkable improvement observed in the laser performance of dye-doped POSS systems is a direct consequence of scattering processes. Under defined experimental conditions, the dye-laser action is enhanced by stimulated emission built up in the gain direction by the elongated photon path length inside the random system. The laser-like emission adds up to the usual stimulated emission as long as the gain exceeds the losses in the scattering media. Once certain parameters (scatter density, sample size, pumping fluence) reach a critical value, the stimulated emission is effectively scrambled and the spectroscopically narrowed laser-like emission appears in all directions. Consequently, the optical losses that result from this leakage become larger than the optical gain, and the system become unstable with a decrease in intensity.

The physics of the laser emission induced by the presence of POSS nanoparticles is independent of both the photophysics of the dye molecules and the functionalization of the POSS core. Thus, both octa(methyl methacrylate)- and octa(isobutyl)-POSS nanoparticles enhance the laser action of polar (Rhodamine 6G, Rhodamine 640, Sulforhodamine B, LDS722 and LDS 730) and non-polar (Perilene Red, PM567 and PM 597) dyes, with respect to the effectiveness recorded in pure organic solvents and polymeric solutions pumped under the same experimental conditions (Fig. 4). In this way, dye-doped POSS solutions could be defined as a kind of universal gain media to optimize the laser

ADVANCED MATERIALS www.advmat.de

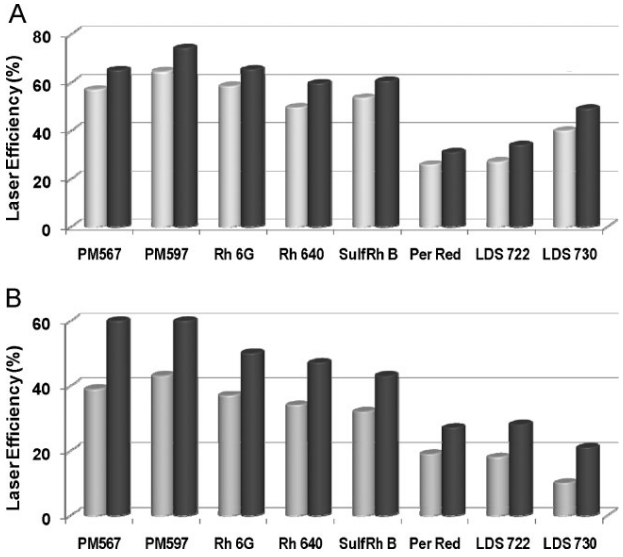

Figure 4. Laser efficiency of different dyes in the presence (black) and absence (grey) of POSS nanoparticles in liquid solutions (A) and in solid samples (B) transversely pumped at 532 with 5.5 mJ pulse^{-1}. The compositions of these dye-doped systems are detailed in the Supporting Information.

action that overcomes the dye/host specificity imposed up to date, which represents one of the most important limitations of these laser systems.

In conclusion, we report, for the first time to the best of our knowledge, the scattering action of POSS-based materials as an efficient and easy novel strategy to enhance the laser performance of dye-doped systems, which is actually demanded in the framework of optoelectronic research. The present hybrid disordered nanomaterials represent an important improvement over those dye-doped optical materials obtained by an empirically pursued synthetic route, which proceed with low yields or lead to undesired properties for specific applications, and also over those materials obtained by their rational design, which is made difficult by the complexity of the underlying photophysical phenomena. The ease of the synthesis of dye-doped POSS liquid solutions and solid matrices, their significantly improved physical, thermal, and optical properties, together with their nanofabrication capability, open up the possibility of using these new hybrid materials as an alternative source for photonic devices.

Experimental

Experimental details are given in the Supporting Information.

Acknowledgements

This research was financed by the Spanish MICINN under Project MAT2007–65778-C02–01. V.M. thanks Spanish CSIC for her JAE-Doc postdoctoral contract and L.C. thanks MICINN for a predoctoral scholarship (cofinanced by Fondo Social Europeo). Supporting Information is available online at Wiley InterScience or from the author.

Received: March 5, 2009
Revised: April 20, 2009
Published online:

[1] K. Pielichowski, J. Njuguna, B. Janowski, J. Pielichowski, *Adv. Polym. Sci.* **2006**, *201*, 225.
[2] E. Markovic, S. Clarke, J. Matisons, G. P. Simon, *Macromolecules* **2008**, *41*, 1685.
[3] C. Zhao, X. Yang, X. Wu, X. Liu, X. Wang, L. Lu, *Polym. Bull.* **2008**, *60*, 495.
[4] S. Bizet, J. Galy, J. F. Gerard, *Macromolecules* **2006**, *39*, 2574.
[5] L. Zheng, A. J. Waddon, R. J. Farris, E. B. Coughlin, *Macromolecules* **2002**, *35*, 2375.
[6] E. T. Kopesky, T. S. Haddad, R. E. Cohen, G. H. McKinley, *Macromolecules* **2004**, *37*, 8992.
[7] K. Y. Pu, B. Zhang, Z. Ma, P. Wang, X. Y. Qi, R. F. Chen, L. H. Wang, Q. L. Fan, W. Huang, *Polymer* **2006**, *47*, 1970.
[8] S. Bizet, J. Galy, J. F. Gerard, *Polymer* **2006**, *47*, 8219.
[9] O. Garcia, R. Sastre, I. Garcia-Moreno, V. Martin, A. Costela, *J. Phys. Chem. C* **2008**, *112*, 14 710.
[10] S. Takeda, M. Obara, *Appl. Phys. B* **2009**, *94*, 443.
[11] A. Costela, I. Garcia-Moreno, D. del Agua, O. Garcia, R. Sastre, *J. Appl. Phys.* **2007**, *101*, 073 110.
[12] O. Garcia, R. Sastre, D. del Agua, A. Costela, I. Garcia-Moreno, F. Lopez Arbeloa, F. Bañuelos Prieto, J. Lopez Arbeloa, *J. Phys. Chem. C* **2007**, *111*, 1508.
[13] F. J. Duarte, R. O. James, *Appl. Opt.* **2004**, *43*, 4088.
[14] X. H. Wu, A. Yamilov, H. Noh, H. Cao, E. W. Seelig, R. P. H. Chang, *J. Opt. Soc. Am. B* **2004**, *21*, 159.
[15] D. S. Wiesrma, A. Lagendijk, *Phys. Rev. E* **1996**, *54*, 4256.

Supporting Information

Dye-Doped POSS solutions: Random Nanomaterials for Laser Emission**

By *Angel Costela, Inmaculada Garcia-Moreno*, Luis Cerdan, Virginia Martin, Olga Garcia, and Roberto Sastre*

[*] Dr. A. Costela, Dr. I. Garcia-Moreno, Luis Cerdan, Dr. V. Martin
Dpto. Quimica Laser, Instituto de Quimica-Fisica "Rocasolano", (CSIC)
C/ Serrano, 119. 28006 Madrid
E-mail: i.garcia-moreno@iqfr.csic.es
Dr. O. Garcia, Prof. R. Sastre
Dpto. Fotoquimica de Polimeros, Instituto de Ciencia y Tecnologia de Polimeros, (CSIC)
C/ Juan de la Cierva, 3. 28006 Madrid

Materials

Most of the dyes selected in this work (PM567, PM597, Rhodamine 6G, Rhodamine 640, and Sulforhodamine B, LDS722 and LDS 730) were laser grade and purchased from Exciton. Perylene Red (generously gifted by BASF, Red 305) was first used as received with a purity of only 90% (checked by spectroscopic and chromatographic methods). The dye purity was improved up to a 99% through a flash column chromatography based on silica with hexane/ethyl acetate 95/5 v/v proportion as eluent, to remove the N-methyl-2-pyrrolidone, identified by NMR-^{1}H as the principal impurity. Octa(methyl methacrylate)-POSS and octa(isobutyl)-POSS purchased from Hybrid Plastics^{TM} were used as received. The methyl methacrylate (MMA) and 2-hydroxyethyl methacrylate (HEMA) monomers (Aldrich) as well as the initiator 2,2´-azobis(isobutyronitrile) (AIBN) (Acros), were purified before use. All solvents (Merck) were spectroscopic grade and were used without purification.

The compositions of the dye-doped systems are detailed in Table 1. Solvents and monomers were selected to assure total solubility of dye at the concentration selected in the present work. The synthesis route followed to prepare the materials studied in this work was the block radical polymerization of the above monomers using AIBN in an appropriate

concentration (1.0% wt.), with regard to the total amount of monomers in the polymerization mixture. AIBN is the thermal polymerization initiator of choice, since it leaves ultraviolet-transparent end groups on the copolymer.

First, adequate amounts of the substituted-POSS® (8MMAPOSS) and the initiator were added to freshly distilled MMA or HEMA or copolymers of (MMA/HEMA 1/1) in order to prepare polymers with a 13% weight proportion of 8MMAPOSS nanoparticles. Secondly, the adequate amount of the dye was added to the resulting mixture and was placed in an ultrasonic bath until complete dissolution of the dye. The resulting solution was filtered into appropriate cylindrical polypropylene molds using a 0.2 μm pore size filter (Whatman Lab, PTFE disposable filters). Polymerization was performed in a thermal bath at 40 ºC over a period of two days and then at 45 ºC for about one day. Afterwards the temperature was raised to 50 ºC and increased slowly up to 80 ºC over a period of one day, in order to decompose residual AIBN. Finally, the temperature was reduced in steps of 5 ºC per day until room temperature was reached, and only then the sample was unmolded. This procedure was essential in order to reduce the build up of stress in the polymer sample due the thermal shock.

Laser Evaluation

Liquid solutions of dye were contained in 1 cm optical-path quartz cells that were carefully sealed to avoid solvent evaporation during the experiments. The solid samples for laser experiments were cast in a cylindrical shape, forming rods of 10 mm diameter and 10 mm length. A cut was made parallel to the axis in order to obtain a lateral flat surface of ~4×10 mm^2. All flat surfaces were prepared for laser experiments by conventional grinding and polishing machine (PhoenixBeta 4000, Buehler) until optical-grade finished. The planar grinding stage was carried out with a CS disc P4000 (Remet) using mineral oil as a lubricant. The final polishing stage was carried out with a G-Tuch Microcloth (Buehler), using a cloth disk Mastertex (Buehler) with diamond of 1 μm in mineral oil as an abrasive type.

The samples were transversely pumped at 532 nm with 5.5 mJ, 6 ns FWHM pulses from a frequency-doubled *Q*-switched Nd:YAG laser (Monocrom STR-2+) laser at 10 Hz repetition rate. The exciting pulses were line-focused onto the lateral flat surface of the solid samples, providing pump fluences on the active medium of 180 mJ/cm^2. The oscillation cavity (2 cm length) consisted of a 90% reflectivity aluminum back mirror and the end face of the sample as output coupler. Details of the experimental setup can be found elsewhere.[1]

The dye and pump laser pulses were characterized with the following instruments: GenTec ED-100A and ED-200 pyroelectric energy meters, ITL TF1850 fast rise time photodiode, Tektronix 7974 storage oscilloscope and TDS3032 digital phosphore oscilloscope, SpectraPro-300i spectrograph/monochromator (Acton research Corporation) with charge-coupled device (CCD) (SpectruMM:GS128B) and Hamamatsu R928 photomultiplier. Dye and pump laser signals were sampled with boxcar (Stanford Research, model 250), and all the integrated signals were digitized and processed using a PC via a Computerboard DASH-8 interface.[2]

Characterization

Photophysical properties of dyes in diluted solutions (2×10^{-6} M) were measured in 1 cm optical pathlength quartz cuvettes. Absorption and fluorescence (after excitation at 490 nm) spectra were recorded on a Cary 4E spectrophotometer and on a SPEX Fluorolog 3-22 spectrofluorimeter, respectively. Fluorescence quantum yields (ϕ) were determined using a diluted solution of PM567 in methanol as reference ($\phi = 0.91$).[3] Radiative decay curves were recorded by the time-correlated single photon counting technique (Edinburgh Instruments model FL920) after excitation at 410 nm by means of a laser diode (pico Quant, model LDH410) operating with 150 ps FWHM pulses. The fluorescence decay time (τ) was obtained from the slope of the deconvoluted curves. The time resolution after the deconvolution procedure was estimated around 30 ps.

Thermal conductivity of the solid samples was measured by using a Differential Scanning Calorimeter (DSC-6, Perkin Elmer).[4]

Topographical and lateral Atomic Force Microscopic (AFM) images were recorded simultaneously in the contact mode with a Topometrix TMX2010 Discoverer scanning probe microscope by using commercial silicon nitride (Si_3N_4) probe tips placed at the end of a V-type cantilever. Environmental Scanning Electron Microscopy (ESEM) images were obtained in a Philips XL-30 microscope using an accelerator voltage of 15 kV. The fractured surfaces of nanocomposites were prepared by cryogenic fracturing in liquid nitrogen. Transmission Electron Microscopy (TEM) analysis of the samples was carried out in a Philips Tecnai 20 with an accelerator voltage of 200 kV. Ultrathin sections of the composites with a thickness of approximately 50 nm were prepared in a Metkon ultramicrotome Finocut equipped with a diamond knife.

Table 1

		Liquid solution			Solid matrices		
Dye[a]	Conc. (M)	Solvent[b]	Eff[c] (%)	Eff[d] (%)	Material[e]	Eff[f] (%)	Eff[g] (%)
PM567	1.5×10^{-3}	AcOEt	65	57	MMA	60	39
PM597	6×10^{-4}	AcOEt	74	64	MMA	62	43
Rh6G	4×10^{-4}	AcOEt/EtOH (1/1)	65	58	MMA/HEMA (1/1)	50	37
Rh640	5×10^{-4}	AcOEt/EtOH (1/1)	60	50	MMA/HEMA (1/1)	47	34
SulRhB	4×10^{-4}	AcOEt/EtOH (3/7)	61	54	MMA/HEMA (1/1)	43	32
PerRed	5×10^{-4}	AcOEt	31	26	MMA	27	19
LDS722	4×10^{-4}	EtOH	34	27	HEMA	28	18
LDS730	8×10^{-4}	EtOH	49	40	HEMA	21	10

[a] Rh6G: Rhodamine 6G; Rh640: Rhodamine 640; SulRhB: SulfoRhodamine B; PerRed: Perylene Red
[b] AcOEt: Ethyl acetate; EtOH: ethanol
[c] In presence of octa(isobutyl)-POSS particles added in equimolecular proportions with respect to the dye concentration
[d] In absence of octa(isobutyl)-POSS particles
[e] MMA: methyl methacrylate; HEMA:2-hydroxy-ethyl methacrylate
[f] In presence of 13% wt. proportion of 8MMAPOSS nanoparticles
[g] In absence of 13% wt. proportion of 8MMAPOSS nanoparticles

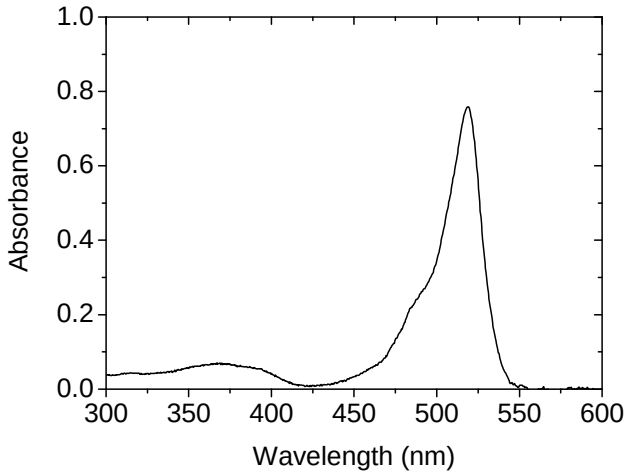

Absorption spectrum of PM567 (1.1×10^{-4} M) doped a copolymer (MMA+13%wt.8MMAPOSS) with a thickness of 1 mm.

(1) I. Garcia-Moreno, A. Costela, A. Cuesta, O. Garcia, D. del Agua, R. Sastre, *J. Phys. Chem. B* **2005**, *109*, 21618.

(2) M. Rodríguez, A. Costela, I. Garcia-Moreno, F. Florido, J. M. Figuera, R. Sastre, *Meas. Sci. Technol*. **1995**, *6*, 971.

(3) F. Lopez Arbeloa, T. Lopez Arbeloa, I. Lopez Arbeloa, I. Garcia-Moreno, A. Costela, R. Sastre, F. Amat-Guerri, *Chem. Phys.* **1998**, *236*, 331.

(4) R. Riesen, *UserCom* **2005**, 2, 19.

Paper A2: IEEE J. Quantum Electron. 47, 7, 907–919 (2011)

Laser efficiency enhancement due to non-resonant feedback in dye-doped hybrid materials: theoretical insights and experiment

L. Cerdán, A. Costela, I. García-Moreno, V. Martín and M. E. Pérez-Ojeda

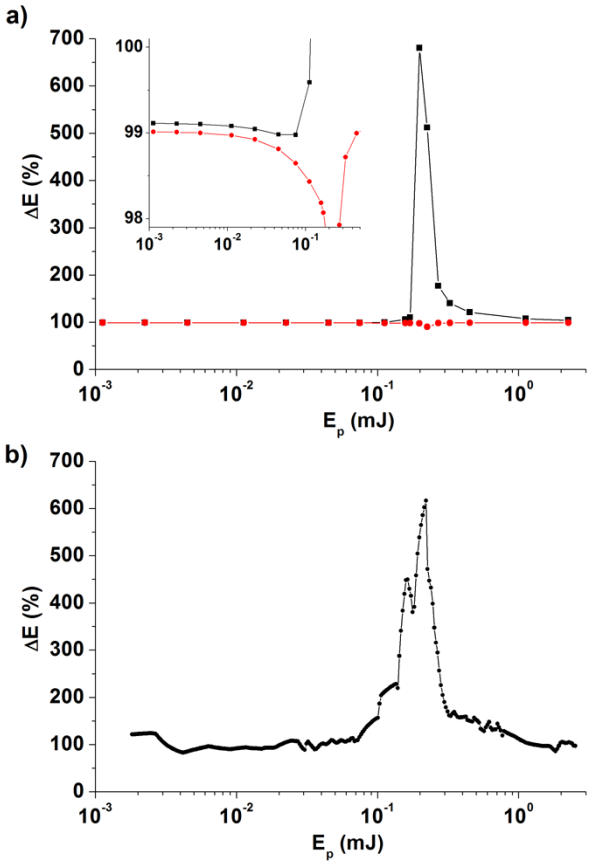

(a) Calculated relative emission improvement as a function of the pump energy for $\alpha_{SC} = 1{,}8 \times 10^{-2}$ cm^{-1} with (squares) and without (circles) scattering feedback. Inset in (a): detail of the region corresponding to transition from losses to gain. b) Experimental relative emission improvement as a function of the pump energy for a dye solution in EtOAc with 50 % wt. 8MMAPOSS ($\alpha_{SC} = 1{,}8 \times 10^{-2}$ cm^{-1}).

Laser Efficiency Enhancement Due to Non-Resonant Feedback in Dye-Doped Hybrid Materials: Theoretical Insights and Experiment

Luis Cerdán, Angel Costela, Inmaculada García-Moreno, Virginia Martín, and María E. Pérez-Ojeda

***Abstract*— It has been recently shown that the presence of nanoscatterers up to a certain density, homogeneously distributed in gain media, instead of being detrimental to conventional two-mirror cavity laser efficiency and directionality, may result in an increase of the output energy due to an enlargement in the effective optical path. Here we present a theoretical model for the stimulated emission in very weak scattering active media and show that the aforementioned laser efficiency improvement owes to a contribution of non-resonant feedback due to Rayleigh scattering. The model reveals that a critical factor in the physics of the emission is the nanometric size of the scattering particles irrespective of their nature. Experiments are carried out and the results are shown to be in agreement with the predictions of the model.**

***Index Terms*— Hybrid materials, lasers, rate equations, scattering.**

I. Introduction

SCATTERING has always been considered detrimental to conventional lasers, being a source of losses which scramble the directionality and intensity of the output emission [1], [2]. Hence, conventional wisdom requires scattering in laser materials being always kept at the lowest possible level.

The opposite is true in the so-called random lasers, which have received much attention in recent years [3], [4]. In a random laser feedback is provided by light scattering inside a laser gain medium, eliminating the need for an external cavity, like in regular lasers [4]. The characteristic properties of random lasers (omnidirectional emission, easy production of samples with arbitrary shapes, unique sample to sample spectral distribution) make these light sources ideal for display applications, environmental lightning, remote sensing and identification markers.

A challenge of modern laser science is to develop advanced materials which combine synergistically the advantages of both random and conventional lasers [5], advancing lasing performance and thus boosting their industrial applications.

Manuscript received January 12, 2011; revised March 16, 2011; accepted March 27, 2011. Date of current version May 17, 2011. This work was supported in part by the Spanish Ministerio de Ciencia e Innovación under Project MAT2010-20646-C04-01 and Project TRA2009-0144.

The authors are with the Instituto de Química Física Rocasolano, Consejo Superior de Investigaciones Científicas, Madrid 28006, Spain (e-mail: lcerdan@iqfr.csic.es; acostela@iqfr.csic.es; i.garcia-moreno@iqfr.csic.es; vmartin@iqfr.csic.es; elma@iqfr.csic.es).

Color versions of one or more of the figures in this paper are available online at http://ieeexplore.ieee.org.

Digital Object Identifier 10.1109/JQE.2011.2138118

In this regard, in a recent paper [6], we reported on experimental evidence of enhanced conventional two mirror cavity laser performance in liquid and solid solutions of organic dyes containing nanometer-sized polyhedral oligomeric silsesquioxanes (POSS). We demonstrated that if the particles are small enough and randomly distributed, the transparency of the material (both in liquid and solid solutions) was not affected and the laser efficiency was actually enhanced. The POSS particles, with sizes below 5 nanometers, acted as weak scattering centers in the Rayleigh limit (particle size much smaller than the emission wavelength), increasing the effective optical path inside the gain medium in the process known as intensity or non-resonant feedback (NRF) lasing, which added up incoherently to the conventional laser action in a way that increased the efficiency of the laser material. It should be remarked that at this weak level of scattering the system behaves neither as a conventional laser nor as a very weak random laser, but as a conventional laser enhanced by weak scattering feedback.

More recently [7], it has been shown that the weak Rayleigh scattering induced by glass inhomogeneities in optical fibers with Raman amplification may lead to the generation of laser emission with near-Gaussian beams, narrow spectra, and with efficiency and performance comparable to regular fiber lasers.

The fundamental understanding of the physics underlying the interaction of light with nanometric scatterers embedded in active media will allow moving forward in the development of new optical materials for advanced photonic applications. With this in mind, in this paper we develop a theoretical approach, which models the behavior of gain media with very weak scattering, to understand the role of the NRF mechanism in the aforementioned laser efficiency enhancement. By using a formalism of rate equations properly modified, the main spectral, temporal and spatial features of the observed NRF emission in gain media with POSS nanoscatterers are evaluated as a function of the amount of scattering feedback and the excitation level. The predictions of the model are compared with experimental results. The model provides inklings to understand the physics responsible for the enhanced emission in these rather complex systems, and reveals that a key factor in the process is the nanometer size of the scatterers. The paper is organized as follows: in Section II the theoretical aspects of the model are explained in detail and the experimental aspects for the model verification are presented; in Section III the numerical and experimental results are presented and

discussed, beginning with the output efficiency of these systems and following with the spectral, temporal and spatial properties of the NRF enhanced laser light. The paper closes with a brief summary and relevant conclusions.

II. Theoretical and Experimental Aspects

In our previous paper [6] both resonant (due to the external cavity) and non-resonant (due to the scatterers) laser mechanisms were competing and the true extend of NRF lasing could not be clearly distinguished. In order to study the NRF lasing in depth the resonant contribution should be avoided and, thus, the external feedback be kept at the lowest level.

Since laser dyes are high gain media, any residual reflection may give place to feedback and consequently to laser emission. This possible effect will be taken into account both in the experimental results interpretation and the simulation boundary conditions.

A. Theoretical Model

The active medium will consist of a solution of dye Pyrromethene 567 (PM567) in ethyl acetate incorporating dielectric nanoparticles in the Rayleigh scattering regime (size $<<$scattered wavelength). The geometry of the system will consist of a transversely pump excited region of length L, width b ($L>>b$) and depth d, determined by the pump focusing and penetration depth, respectively. The pump polarization is parallel to the plane containing the exciting and output beams and thus, the emitted light will be unpolarized [8].[1]

Since the size of the scatterers (*ca*. 1.2 nm) is much smaller than the scattered wavelength (560 nm), the Rayleigh scattering formalism can be used. A fingerprint of the Rayleigh regimen is the omnidirectional deflection of light, which means that not all of the scattered light will leave the system. Thus, the forward and backward scattered light within a certain solid angle is recovered by the system. In this sense, the presence of scatterers in the medium provides intensity feedback, albeit it produces additional losses.

The losses due to scattering are $\alpha_{SC}(\lambda) = \rho\sigma_{SC}(\lambda)$, where ρ is the density of scatterers and $\sigma_{SC}(\lambda)$ is the wavelength dependent scattering cross section. For the sake of simplicity we consider the scatterer (e. g., POSS molecule) to be a dielectric sphere. Thus, $\sigma_{SC}(\lambda)$ can be readily calculated knowing the radius and refractive index of the scatterer [9], and the contribution of the forward and back scattering can be considered the same.

Fig. 1 shows a scheme with the different processes taken into account in the simulation. Due to the pumping geometry, the emission grows preferentially in the direction defined by the axis of the excited region, which is perpendicular to the pump direction. Two counter propagating waves along the axis of the excited region are considered: the forward ($I^+(x,t,\lambda)$) and backward ($I^-(x,t,\lambda)$) photon fluxes. The contributions to $I^+(x,t,\lambda)$ are: the spontaneous emission as the seed, which is amplified by stimulated emission, reabsorbed by the ground state population and dispersed due to scattering; The forward scattering of $I^+(x,t,\lambda)$ and the backscattering of $I^-(x,t,\lambda)$ within a certain solid angle is then added up to $I^+(x,t,\lambda)$. Finally, there is a small contribution of an external feedback.[2]

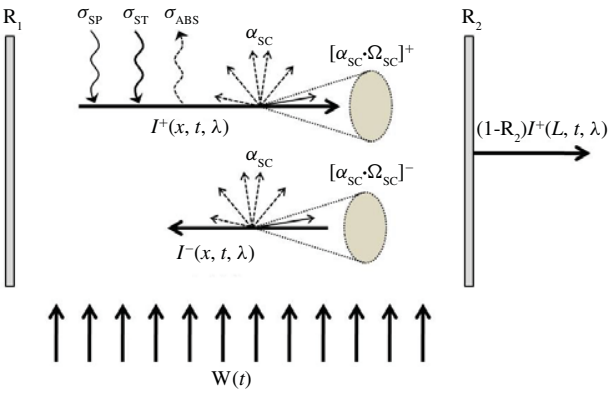

Fig. 1. Processes considered in simulation: W(t) pump rate, $I^+(x,t,\lambda)$ and $I^-(x,t,\lambda)$ forward and backward photon fluxes, σ_{SP} spontaneous emission, σ_{ST} stimulated emission, σ_{ABS} losses due to absorption, α_{SC} scattering losses, $[\alpha_{SC}\cdot\Omega_{SC}]^+$ recovered forward scattering, $[\alpha_{SC}\cdot\Omega_{SC}]^-$ recovered backscattering. R_1 and R_2 possible cavity reflectivities.[2]

To model the effect of scattering events on the emission processes involved in transversely pumped dye laser systems with nanometer-size scatterers we have modified rate equations to consider weak scattering effects. Rate equations can be used to study a wide variety of light-matter interaction problems in which the quantum nature of the interaction is not strictly needed [2]. In particular, they have been extensively used to describe a number of laser systems, including those with non-resonant feedback [4], [10] and other regimes of random lasing [11], [12]. We have developed an extension of the model that Ganiel *et al*. [13] proposed to analyze theoretically and experimentally Amplified Spontaneous Emission (ASE) and signal amplification in dye laser systems. We will make use of the same formalism and notation employed in [13], but with some added terms to take scattering and external feedback effects into account. Since the scattering length $\ell_{SC} = \alpha_{SC}^{-1}$ in our problem is much larger than any of the amplifier dimensions (subdiffusive or ballistic domain), the diffusion approximation [14] for the photon flux propagation is no longer valid [15]. Thus, the scattering contribution will be considered as Lambert-Beer law terms [10]. With these assumptions, the modified set of equations reads:

$$\frac{\partial N_1(x,t)}{\partial t} = W(x,t)N_0(x,t) - \tau^{-1}N_1(x,t) - N_1(x,t)\int \sigma_{ST}(\lambda)\left(I^+(x,t,\lambda) + I^-(x,t,\lambda)\right)d\lambda + N_0(x,t)\int \sigma_{01}(\lambda)\left(I^+(x,t,\lambda) + I^-(x,t,\lambda)\right)d\lambda \quad (1)$$

[1]The model is valid both for liquid and solid solutions, and the unpolarization condition is fulfilled in both of the cases as long as the pump polarization is parallel to the plane containing the exciting and output beams.

[2]Through the investigation we found mismatches between the experimental and theoretical results. We concluded that, even using the triangular cuvette, a very low reflection cavity mode was excited inside the cuvette, and some laser emission was still present. This fact had to be taken into account in the simulation in order to obtain fair results.

$$N_0(x,t) + N_1(x,t) = N \tag{2}$$

$$\frac{\mathrm{d}}{\mathrm{d}x} I^{\pm}(x,t,\lambda) = \tau^{-1} N_1(x,t) E(\lambda) \Omega + N_1(x,t)\sigma_{ST}(\lambda) I^{\pm}(x,t,\lambda) - \sigma_{01}(\lambda) N_0(x,t) I^{\pm}(x,t,\lambda) - \alpha_{SC}(\lambda) I^{\pm}(x,t,\lambda) + \alpha_{SC}(\lambda)\Omega_{SC}(I^{\pm}(x,t,\lambda) + I^{\mp}(x,t,\lambda)). \tag{3}$$

The initial conditions will be $I^+(x, t = 0, \lambda) = I^-(x, t = 0, \lambda) = N_1\ (x, t = 0) = 0$ and $N_0\ (x, t = 0) = N$, where N is the density of dye molecules. As boundary conditions we will use

$$I^+(x = 0, t, \lambda) = R_1 I^-(x = 0, t, \lambda)$$
$$I^-(x = L, t, \lambda) = R_2 I^+(x = L, t, \lambda). \tag{4}$$

Finally, the system is transversely pumped with Gaussian pulses:

$$W(x,t) = W_0 \exp\left(-\frac{(t - t_0)^2}{(\sigma_t/2)^2} \ln 2\right) \exp\left(-\frac{(x - L/2)^2}{(\sigma_x/2)^2} \ln 2\right). \tag{5}$$

The quantities in (1)–(5) are defined as follows: $N_i(x,t)$ $(i = 0, 1)$ is the population density (molecules$\times$cm^{-3}) in the ground state S_0 and first excited (electronic) singlet manifold S_1, respectively, $\sigma_{01}(\lambda)$ is the absorption cross section (cm^2) from S_0 to S_1 at wavelength λ, τ is the lifetime of the S_1 state in the absence of stimulated emission, $\sigma_{ST}(\lambda)$ is the stimulated emission cross section, given by $\sigma_{ST}(\lambda) = [\lambda^4 E(\lambda)]/8\pi c\eta^2\tau$, where $E(\lambda)$ is the $S_1 \rightarrow S_0$ fluorescence spectrum normalized so that $\int E(\lambda) d\lambda = \phi$, ϕ being the fluorescence quantum yield, and η is the refractive index of the dye solution.

$W(x,t)$ is the pumping rate, and due to experimental constrains is considered to be spatially inhomogeneous along the excitation axis, $W_0 = 4 \cdot ln(1) \cdot \sigma_{01}(\lambda_p) \cdot E_p \cdot \lambda_p / (\sigma_t \cdot \sigma_x \pi \cdot h \cdot c)$ is a scale parameter to take into account the total pump energy E_p, $t_0 = 1.5 \cdot \sigma_t$ is the pump pulse delay, and $\sigma_t = 20$ ns and $\sigma_x = 0.8$ cm are the temporal and spatial full width at half maximum (FWHM), respectively. An offset, not shown here, has been added to (5) to avoid discontinuities at $t = 0$.

Ω is a geometrical factor which determines the solid angle subtended by the aperture of the active volume (Fig. 1), and is estimated as the transversal section of the active zone/(length of the active medium)^2. The transversal section of the active zone depends on the penetration depth d and pump focusing b. d can be calculated using the Lambert-Beer law ($d = 1/(\sigma_{01}(\lambda_p) \cdot N)$), and hence:

$$\Omega = \frac{1}{4\pi} \frac{b}{\sigma_{01}(\lambda_p) \cdot N \cdot L^2}, \tag{6}$$

N being the volume concentration of the dye molecules, $\sigma_{01}(\lambda_p)$ the absorption cross section at the pumping wavelength, and L the active medium length.

Ω_{SC} is a factor which determines the strength of the scattering feedback and should be equal to Ω. But due to the simplifying nature of our 1D model presented here, there are feedback contributions which cannot be explicitly taken into account within this model. e.g., the light scattered off the excitation axis, which would be further amplified, could be recovered later on in a consecutive scattering process, acting as a further feedback. This feedback would contribute positively to the output energy, increasing the emission enhancement. Then, the use of $\Omega_{SC} = \Omega$ in (4) would lead to underestimated results. Nevertheless, these feedback terms can be approximately taken into account in an implicit way by artificially increasing the value of Ω_{SC}. The quantitative value of Ω_{SC} has been obtained by fitting the numerical results to the experimental data in the presence of scattering particles. As far as we are concerned, a 3D model would be more accurate but also would require much more computational power and it would not provide more useful information.

Finally, R_1 and R_2 are the effective reflectivities of the excited cavity inside the cuvette[2] which, unknown for us, will be assume to be a Fabry-Perot type cavity with reflectivities $R_1 = R_2 = R << 1$. Once again, the quantitative value of R has been obtained by fitting the numerical results to the experimental data in the absence of scattering.

In the excited state population equation (1) the terms are described as follows: The first term describes the absorption of the pumping flux. The second term accounts for spontaneous decay through all available channels. The third term describes the depletion of the excited state due to stimulated emission of radiation in all wavelengths, and the last term describes the recovery of population due to self-absorption of the photon flux. The build-up of photon flux in the forward ($I^+(x,t,\lambda)$) and backward ($I^-(x,t,\lambda)$) directions is given by (3), which has been modified with respect to that of Ganiel *et al.* [13], where $(\mathrm{d}/\mathrm{dx})I^{\pm} = (\eta/\mathrm{c})(\partial/\partial \mathrm{t})I^{\pm} \pm (\partial/\partial \mathrm{x})I^{\pm}$. The right hand terms in (3) are interpreted as follows: The spontaneous emission within the solid angle Ω around the axial coordinate x (first term) is amplified by stimulated emission (second term) and reabsorbed by the ground state population (third term). The fourth term takes into account the overall losses associated with scattering, while the fifth and sixth terms are the contributions of the forward scattering of $I^+(I^-)$ and the back scattering of $I^-(I^+)$ within the solid angle Ω_{SC}, respectively. These contributions are expressed as the total amount of flux in the corresponding direction lost due to scattering weighted by the corresponding solid angle. In order to facilitate the calculations we have assumed that the scattering is isotropic and unpolarized, which, for the unpolarized emitted light, guaranteed by the pumping polarization [8], and for the solid angles involved, is a reasonable approximation [9]. Finally, triplet state population terms have been neglected due to the short pulse pumping conditions.

The scattering feedback terms as expressed in (3), are only valid if the amount of forward and backward scattering equals, which is a fact that only happens in the Rayleigh limit, i.e., whenever the size of the scatterer is much smaller than the scattered wavelength. Thus, the size of the scatterers must be in the few nanometer range, which is a condition that the POSS particles fulfill.

For the sake of completeness we will simulate as well a system where scattering does not provide feedback, but only acts as a source of losses, i.e., (1), (1), (4) and (5) are kept

TABLE I
PARAMETERS USED IN THE COMPUTATION

PARAMETER	Numerical Value
τ(ns)	5.78[a]
ϕ	0.80 [a]
$\sigma_{01}(\lambda)$ (cm^2)	*b*
$E(\lambda)$	*b*
$\sigma_{01}(\lambda_P)$(cm^2)	6.07×10^{-17}
λ_P (nm) (pump wavelength)	532
N (cm^{-3})	9×10^{17} (1.5 mM)
η (ethyl acetate)	1.37
L (cm)	1.4
b (μm)	150
d (μm)	183
Ω	1.1×10^{-5}
R (%)	0.01[c]
α_{SC} (cm^{-1}) [at $\lambda = 560$ nm]	0-0.8
Ω_{SC}	5×10^3 Ω[c]
Pump energy (mJ)	1×10^{-3}-2.5

[a] [16]
[b] In [16], we studied the photophysics of PM567 and other dyes in six different solvents and only published as an example the curves corresponding to solutions of PM567 in methanol. For the calculations here reported the unpublished but similar curves of PM567 in ethyl acetate have been utilized.
[c] Chosen to fit the experimental data

the same, whereas (3) is substituted by

$$\frac{\mathrm{d}}{\mathrm{d}x} I^{\pm}(x,t,\lambda) = \tau^{-1} N_1(x,t) E(\lambda)\Omega + \sigma_{ST}(\lambda) N_1(x,t) I^{\pm}(x,t,\lambda) - \sigma_{01}(\lambda) N_0(x,t) I^{\pm}(x,t,\lambda) - \alpha_{SC} I^{\pm}(x,t,\lambda), \quad (7)$$

where the forward and back scattering terms have been neglected. This will help to better understand the effects observed when simulating the original system of equations (1)–(5).

The parameters needed for the computation are given in Table I. Both systems of equations were solved numerically with a specifically written MATLAB code on a Toshiba laptop with an Intel® Core 2 duo P8700 (2.53 GHz) processor for a large variety of practical situations. MATLAB R2009a was used to run the programs. Both population and photon fluxes equations were integrated using Euler's method, whereas the spectral integrals were performed by the midpoint rule. The spatial, temporal and spectral integration steps were, respectively, $\Delta x = L/200$, $\Delta t = \eta \Delta x/c$ and $\Delta\lambda = 1$ nm, where c is the speed of light in vacuum and η the medium refractive index. These steps ensured numerical stability in all cases.

B. Experimental Verification

The predictions of the model have been compared with experimental results obtained under pumping conditions analogous to those of the simulation. The influence of the nanoscatterers on the emission was studied by preparing solutions of dye PM567 (1.5×10^{-3} M) in ethyl acetate incorporating octa(methyl methacryl)-POSS (8MMAPOSS) nanoparticles with an average nominal size of 1.2 nm [6], in weight proportions from 0% up to 50%. In order to prevent resonant laser effects as much as possible and to study pure NRF lasing, the mirrors of the cavity were removed. In addition, the solutions were placed in triangular quartz cuvettes with 1.4 cm wide front-faces to avoid the feedback in the cell's windows present in the usual rectangular cells (Fig. 2). The cuvettes were carefully sealed to avoid solvent evaporation during the experiments. The cuvettes were pumped at 532 nm with 20 ns full width at half maximum (FWHM) pulses from a frequency-doubled Q-switched Nd:YAG laser (Lotis TII SL-2132). The pump radiation was horizontally polarized and the pulse energy incident onto the sample was controlled by insertion in the beam path of a half-wave plate (HWP) and a linear polarizer (LP) set with its polarization axis horizontal. By rotating the HWP the linear polarization of the input beam is rotated out of the horizontal, and the pump beam is blocked more or less by the LP, depending on the rotation angle introduced by the HWP. A combination of negative and positive cylindrical quartz lenses ($f = -15$ and $+15$ cm, respectively), perpendicularly arranged, focused the pump beam to a narrow horizontal line onto the surface of the cuvette, defining a Gaussian excitation stripe of $\sim$150 μm $\times$ 0.8 cm FWHM. The edge emission from the cuvette was collected with a 5 cm focal length spherical lens, focused onto a fibre bundle and detected with a spectrograph/monochromator (SpectraPro-300i Acton Research) equipped with a thermoelectrically cooled CCD detector (SpectruMM:GS 128B). The pump energies were measured with a calibrated Laser Energy Meter (QE 12LP-S-MB-DO, Gentec). A diaphragm was placed in front of the collecting lens in order to remove fluorescence spurious effects.

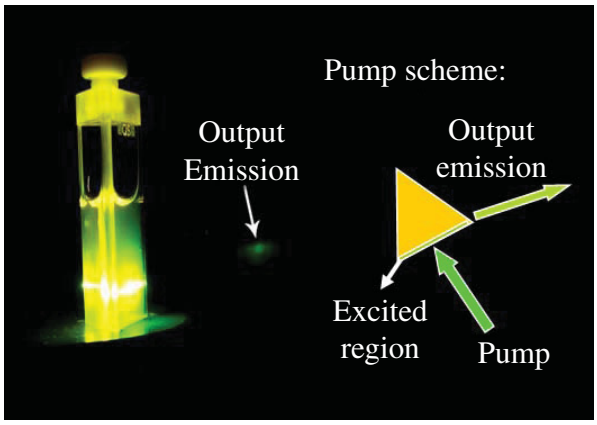

Fig. 2. Emission spot from a solution of dye PM567 in ethyl acetate containing 50% wt. 8MMAPOSS nanoparticles. In the scheme is shown the top-view of the pumping geometry in the experiment.

III. RESULTS AND DISCUSSION

A. Output Energy

To better compare the influence of the scattering feedback on the output energy integrated for all wavelengths when

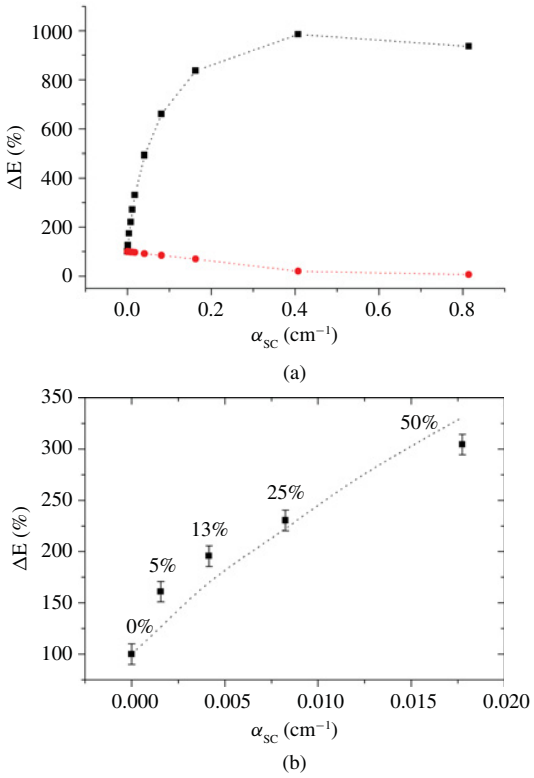

Fig. 3. (a) Calculated relative emission improvement for increasing scattering with (squares) and without (circles) considering scattering feedback. E_p = 0.25 mJ. (b) Calculated (dotted line) and experimental (squares) relative emission improvement corresponding to the scattering losses (8MMAPOSS densities) physically achievable with 8MMAPOSS molecules. Labels adjacent to experimental points indicate % wt. of 8MMAPOSS molecules in the solution.

changing the pumping conditions, we will define the output efficiency ΔE as the output energy when there are scatterers (E_{OUT}) normalized to the one extracted from a system without scatterers in the same pumping conditions (E^0_{OUT}), i.e., $\Delta E = E_{OUT}/E^0_{OUT} \times 100\%$. For the sake of simplicity, we will use in the plots the scattering losses α_{SC}(560nm) as a parameter to state the scattering feedback strength. α_{SC} is evaluated at 560 nm since the peak emission for PM567 is close to this wavelength.

1) Dependence on Scattering Losses: Fig. 3 shows the effect of increasing scattering centers in the emission output intensity for pump energy of 0.25 mJ. From a *naïve* point of view, one would expect a decrease in the output energy ($\Delta E < 100\%$) along the cylinder axis as the density of scatterers in the system increases (which is equivalent to say that the losses in the system increase). Nevertheless, the model predicts [Fig. 3(a)], and the experiment shows [Fig. 3(b)], that the presence of scatterers in the system results in an increase in the output energy with respect to that extracted from a system without losses. The variation of ΔE with the density of scatterers indicates that there is a competition between the losses and the feedback provided simultaneously by the scattering processes. First, gain dominates and ΔE follows a logarithmic increase until it reaches a maximum improvement. Afterwards, the NRF enhanced laser emission decreases smoothly as the losses begin to dominate. This behavior was observed in our previous works [6], [17]. It is worth noticing that these results are consistent with the ones presented by other authors [12], [18], [19] in different scattering regimes and pumping geometries.

Fig. 3(a) also shows the calculated relative emission improvement ΔE as a function of the scattering losses for pump energy of 0.25 mJ when the scattering feedback is not considered (Eq. (7)). As expected, the scattering acts as a source of losses and the output energy decreases up to a barely 5%, following a exponential decay, when the scattering losses are increased.

Fig. 3(b) shows the superimposed experimental and calculated results of the effects of the presence of increasing amounts of 8MMAPOSS on the relative emission improvement of the PM567 dye solution. As predicted in the simulation, and previously seen in laser measurements [6], [17] the output energy increases as the density of nanoscatterers is increased. There is good agreement with the predictions of the model, as shown in Fig. 3(b). The quantitative differences between the experimental results and the simulation are due to the simplified nature of our 1D model presented here.

The above apparently counterintuitive behavior can be explained by the photon path enlargement caused by the back scattering, which acts as non-resonant feedback. In this way, the longer the photon path is, the bigger the amplification becomes and, consequently, the higher the output energy is. For certain range of scattering this "extra" amplification can compensate the increase in losses but, once a critic limit has been reached, in which gain saturation sets in, the losing rate exceeds the extra amplification rate and the system becomes unstable with a decrease in the output energy. These results confirm the hypothesis about the improvement in laser efficiencies stated in our previous work [6]. That is, the NRF lasing due to scattering adds up incoherently to the conventional resonant laser emission provided by the external cavity. Hence, the total efficiency increases.

A very interesting fact is that, provided we are in the Rayleigh regime, the above results are kind of universal ones, independently of the scatterer nature and the medium. In this sense, given certain scattering cross section σ_{SC}, we could choose the generic scatterer density ρ to tailor the losses ($\alpha_{SC} = \rho\sigma_{SC}$) in order to be in the region of maximum amplification. For this effect to occur only nanometric-sized scatters (Rayleigh regime) can be used in order to have enough backscattering as to provide the needed feedback while simultaneously avoiding most of the undesirable effect of scattering losses. The nanometric size of the scatterers is the critical factor which allows the emission improvement and governs the physics of the emission.

As a final remark, 8MMAPOSS is not soluble at weight proportions higher than 50% wt. This corresponds to a particle density $\rho \sim 2.5\times10^{20}$ cm^{-3} and scattering losses of $\alpha_{SC} \sim 0.02$ cm^{-1}, which is one order of magnitude lower than the density of scatterers required to be in the region of maximum amplification. Thus, as seen in Fig. 3(b), within the range of 8MMAPOSS concentrations physically achievable, we are always in the growing section of the extra amplifi-

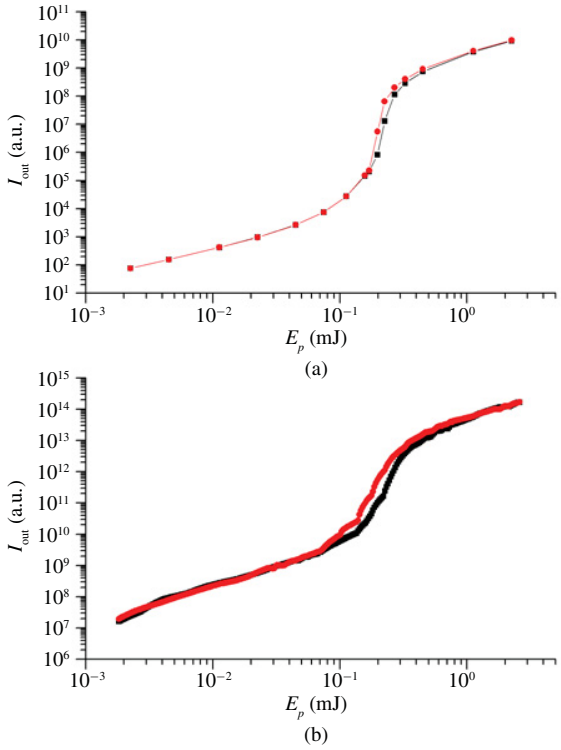

Fig. 4. (a) Calculated output intensity as a function of pump energy for $\alpha_{SC} = 0$ cm^{-1} (squares) and $\alpha_{SC} = 1.8 \times 10^{-2}$ cm^{-1} (circles). (b) Experimental output intensity as a function of the pump energy for a dye solution in EtOAc with 0% (squares) and 50% (circles) wt. 8MMAPOSS, corresponding to $\alpha_{SC} = 0$ cm^{-1} and $\alpha_{SC} = 1.8 \times 10^{-2}$ cm^{-1}, respectively.

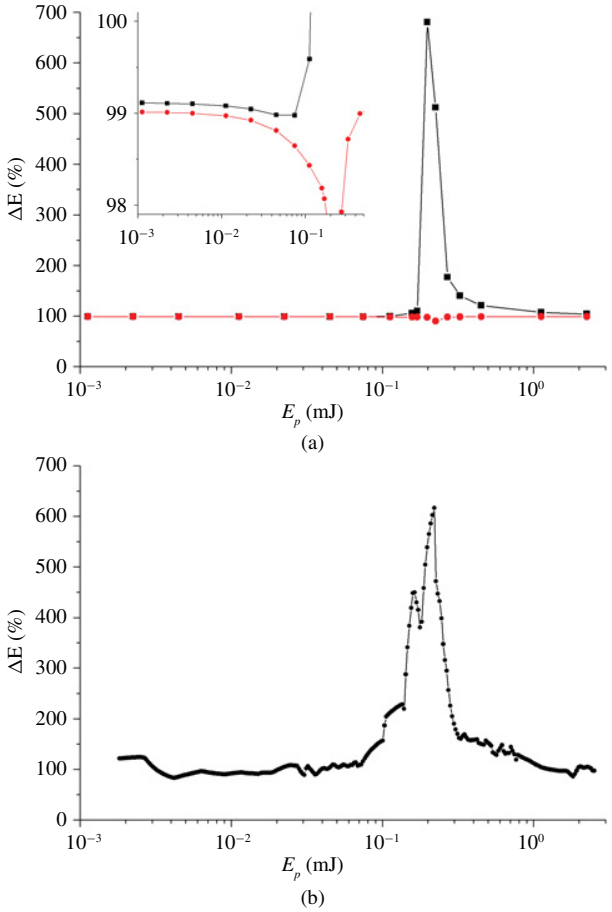

Fig. 5. (a) Calculated relative emission improvement as a function of the pump energy for $\alpha_{SC} = 1.8 \times 10^{-2}$ cm^{-1} with (squares) and without (circles) scattering feedback. Inset in (a): detail of the region corresponding to transition from losses to gain. b) Experimental relative emission improvement as a function of the pump energy for a dye solution in EtOAc with 50% wt. 8MMAPOSS ($\alpha_{SC} = 1.8 \times 10^{-2}$ cm^{-1}).

cation regime. Although some signs of saturation could be appreciated in Fig. 3(b), the limited solubility of 8MMAPOSS does not allow reaching the region where the losses begin to dominate and, consequently, the emission begins to decrease [scattering losses of about 0.4 cm^{-1} in Fig. 3(a)]. In order to prove this region, studies are in progress where a different scattering system, based on latex or Aerosil particles with sizes below the Rayleigh limit $\lambda/10$, are being used.

2) Dependence on Pump Energy: Once the effect of the scattering losses in ΔE is known, the question arises naturally whether the emission improvement is the same for different pumping conditions. With the aim of answering this question, the calculated output photon flux as a function of the pump energy with and without scattering losses is plotted in Fig. 4. For low pump energies there are no appreciable differences on the output emission, but once certain threshold is reached these differences become important. At threshold, the emission starts a superlinear growth, and higher growing rates and slightly lower thresholds are observed for increasing scattering losses. When further increasing the pump energy, the emission improvement due to scattering tends to vanish again.

In order to evaluate these differences more objectively, Fig. 5 shows the evolution of ΔE as a function of the pump energy for $\alpha_{SC} = 1.8 \times 10^{-2}$ cm^{-1}. There is again good agreement between theory and experiment. It is clearly seen that ΔE is extremely dependent on the pump energy. Several features must be highlighted. The first, and most eye-catching one, is the resonance like behavior of ΔE when approaching certain "resonant pump energy". It is worth noticing that for this level of scattering a sevenfold ($\Delta E \sim 700\%$) enhancement can be achieved, but only within a narrow pump energy range.

Moving away from this "resonance", two different behaviors are found. As can be seen in Fig. 5, in the high pump energy region, ΔE simply tends to 100% monotonically, i.e., neither gain nor losses. On the other hand, although for the lowest pump energies ΔE seems to follow the same tendency, a closer inspection [inset in Fig. 5(a)] reveals that in fact ΔE does not approach 100%, but that it tends to a slightly lower value, meaning that the system is in a regime of losses. Furthermore, the tendency of the variation of ΔE is not monotonic, and presents a dip defining a minimum. This minimum marks the point for which the amplification process due to scattering starts compensating the scattering losses. This dip cannot be observed in the experimental data of Fig. 5(b) since they are quite noisy.

In addition, as the scattering losses are increased the output emission in the low pumping range decreases (not shown

here). In other words, in this pumping region any level of scattering effectively scrambles the output emission, being detrimental to the emission process.

All these features can be explained by analyzing how the system makes use of the available gain, or, more precisely, the population inversion. At very low pump energies, the population inversion is not high enough as to provide a considerable amount of amplification, and the presence of feedback due to scattering is not noticed. This behavior can be observed in the inset in Fig. 5(a), where the evolution of ΔE as a function of the pump energy for scattering losses $\alpha_{SC} = 1.8 \times 10^{-2}$ cm^{-1} is shown for the cases when scattering feedback is considered [Eq. (3)] and neglected [Eq. (7)]. It can be seen that in both cases a similar behavior is followed at low pump energies, which indicates that the scattering feedback is not being effective and the scattering losses govern the emission processes. In the case with no scattering feedback the dip is due to the distributed nature of the scattering losses and the way the photon fluxes are distributed along the excited region (see subsection *E*), which affects the final output emission. In addition, as the feedback is negligible in this pumping range, an increase in the scattering losses lowers the final output emission, as was shown in Fig. 3(a).

When the pump energy reaches certain level, the population inversion becomes high enough as to provide the necessary amount of amplification to make the scattering feedback more efficient than the losses. This change in tendency gives place to the sharp emission improvement observed in Fig. 5. When the pump energy is further increased, gain saturation becomes important, and the use of population inversion by the scattering feedback stops being efficient. In other words, since the contributions of the scattering losses and feedback are compensated, the emission improvement smoothly vanishes (Fig. 5) and eventually reaches a regime of losses ($\Delta E < 100\%$).

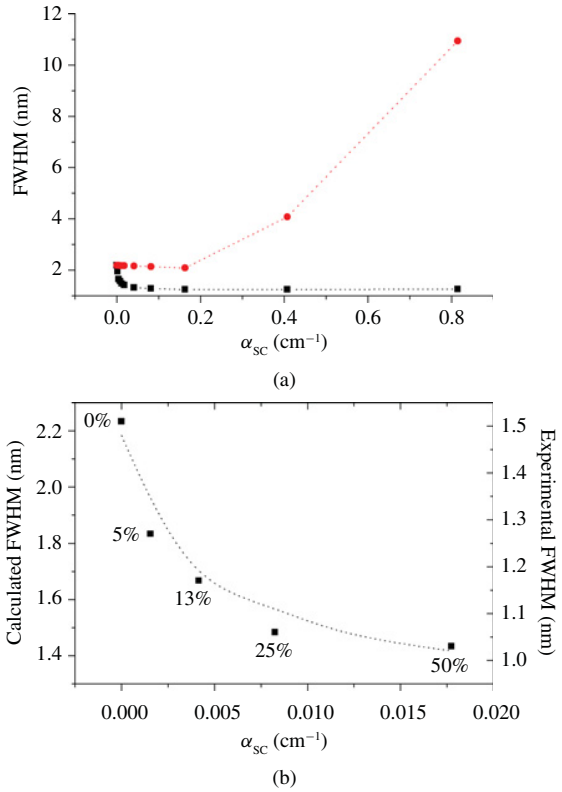

Fig. 6. (a) Calculated spectral narrowing for increasing scattering with (squares) and without (circles) considering scattering feedback. $E_p = 0.25$ mJ. (b) Calculated (dotted line) and experimental (squares) spectral narrowing corresponding to the scattering losses (8MMAPOSS densities) physically achievable with 8MMAPOSS molecules. Labels adjacent to experimental points indicate % wt. of 8MMAPOSS molecules in the solution.

B. Spectral Narrowing

A characteristic feature of laser emission is the large spectral narrowing of the emission in comparison with fluorescence or ASE. In the case of non-resonant feedback this narrowing is not caused by frequency selective cavity resonances, but rather by the preferential amplification of frequencies close to the maximum of the amplification line [10]. Nevertheless, as has been explained above, our system must have a weak reflecting cavity (R$\sim$0.01%), and consequently the spectral narrowing will be somehow determined by the cavity resonance. We will see that the effect of the scattering will be mirrored in the threshold for the onset of the spectral narrowing.

1) Dependence on Scattering Losses: Fig. 6(a) shows the calculated FWHM of the emission spectrum for different densities of scatterers depending on the scattering feedback being taken into account or neglected for a pump energy of 0.25 mJ. The first point, which corresponds to no scattering losses, gives a FWHM mainly determined by the cuvette cavity resonance. As the scatterer density is increased, an additional collapse in the emission linewidth is observed in the presence of scattering feedback. For high enough scattering losses the FWHM stops collapsing and a steady broadening begins, indicating that for that amount of losses the system starts being less efficient, as was observed in Fig. 3(a). On the other hand, the absence of scattering feedback results in an extremely spectral broadening with respect to the pure lasing case, indicating that the system would be in a regime of high losses, as was shown in Fig. 3(a). This fact indicates that the additional collapse is due to the elongated optical path traveled by the photons within the excited medium caused by the scattering feedback.

In Fig. 6(b) it is represented the superimposed experimental and calculated effects of the presence of increased amounts of 8MMAPOSS on the FWHM of the emission spectra of the PM567 dye. As expected, and predicted in the simulation, the FWHM of the emission decreases consistently as the density of nanoscatterers is increased. It is worth noticing that this effect has been observed by other authors when studying incoherent random lasers [20]. Again, the quantitative differences must be ascribed to the simplifying nature of our model.

It is important to say that no spikes were observed in the measured spectra for any of the pumping energies and scatterers densities used in the experiments, indicating that the transition from non-resonant to coherent feedback [20] is not taking place in the present system.

2) Dependence on Pump Energy: Fig. 7 shows the dependence on the pump energy of the emission FWHM with

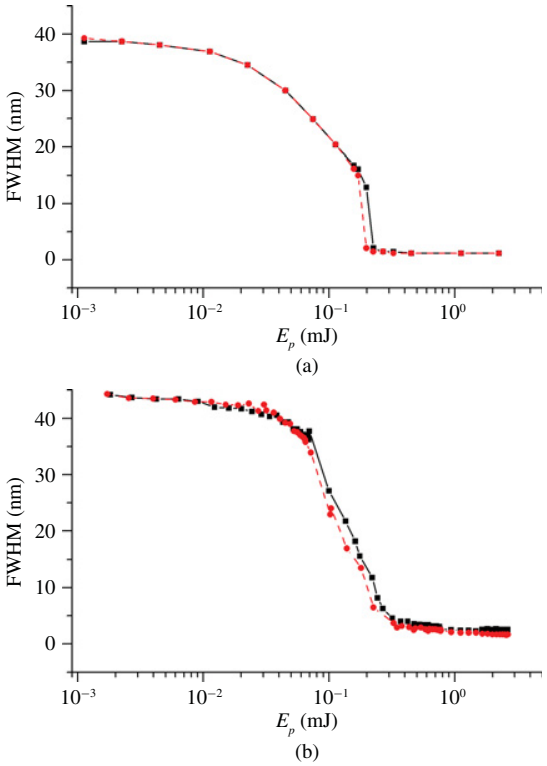

Fig. 7. (a) Calculated spectral narrowing as a function of the pump energy for $\alpha_{SC} = 0$ cm^{-1} (squares) and $\alpha_{SC} = 1.8 \times 10^{-2}$ cm^{-1} (circles). (b) Experimental spectral narrowing as a function of the pump energy for a dye solution in EtOAc with 0% (squares) and 50% (circles) wt. 8MMAPOSS, corresponding to $\alpha_{SC} = 0$ cm^{-1} and $\alpha_{SC} = 1.8 \times 10^{-2}$ cm^{-1}, respectively.

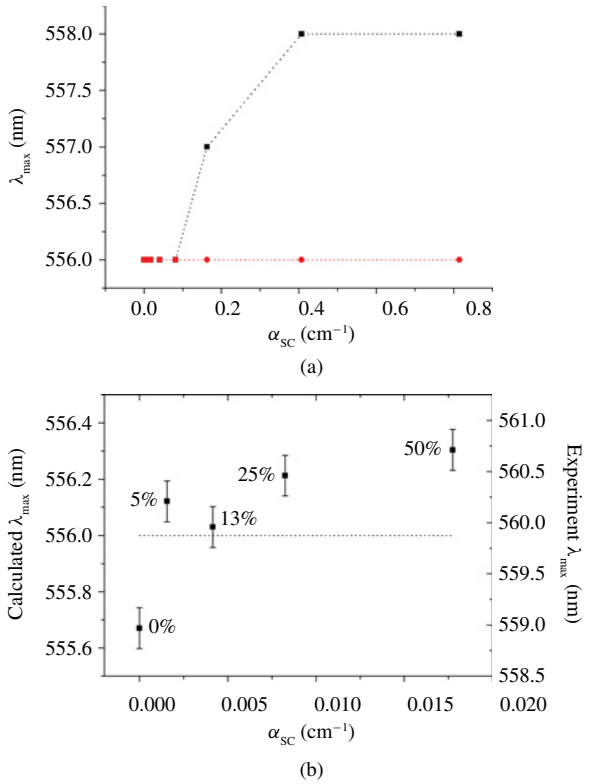

Fig. 8. (a) Calculated maximum emission wavelength for increasing scattering with (squares) and without (circles) considering scattering feedback. $E_p = 0.25$ mJ. (b) Calculated (dotted line) and experimental (squares) maximum emission wavelength corresponding to the scattering losses (8MMAPOSS densities) physically achievable with 8MMAPOSS molecules. Labels adjacent to experimental points indicate % wt. of 8MMAPOSS molecules in the solution.

($\alpha_{SC} = 1.8 \times 10^{-2}$ cm^{-1}) and without ($\alpha_{SC} = 0$ cm^{-1}) scattering losses. At this level of scattering losses the FWHM is somehow determined by the cavity resonance. Consequently, the dependence with the pump energy is similar in both cases: At low pump energies just fluorescence is emitted, characterized by broadband emission, and then, at certain "threshold" pump energy, an abrupt drop to narrow linewidths takes place. At high pump energies the system is saturated in both cases and the FWHM is mainly determined by the weak cavity resonance. In addition, Fig. 7 shows that an increase in the scattering losses leads to a slightly lower threshold, defined as the pump energy for which the FWHM starts collapsing. This fact was previously observed in Fig. 4. Once more, it should be pointed out that the quantitative differences observed between numerical and experimental results can be, to some extend, ascribed to the limited spectral accuracy ($\Delta\lambda = 1$ nm) and the 1D approximation of the model.

C. Emission Wavelength

1) Dependence on Scattering Losses: A redshift in the maximum emission wavelength as the scattering losses are increased can be observed [Fig. 8(a)]. This shift can be ascribed to two different effects: on the one hand, the self-absorption of the emitted radiation due to the increased photon path and, on the other hand, the higher scattering losses experienced by the shorter wavelengths. In order to assess the weight of each of the possible contributions we calculated the maximum emission wavelength as a function of the scattering losses in the absence of scattering feedback [Eq. (7)]. It can be seen in Fig. 8(a) that in this case the wavelength does not change within the scattering losses range inspected and the simulation spectral accuracy, indicating that the observed redshift is due to a process of self-absorption (and reemission) of the emitted radiation. In other words, the scattering feedback tends to trap the light in the excited region, increasing its probability of being reabsorbed; thus, the higher the scattering losses (feedback) are, the higher the observed redshift is.

Fig. 8(b) represents the experimental effects of the presence of increased amounts of 8MMAPOSS on the maximum emission wavelength of the emission spectra of the PM567 dye. It can be clearly seen that the peak of the emission is consistently redshifted as the density of nanoscatterers is increased. It is necessary to say that at this level of scattering losses the model predicts no change in the emission wavelength. This has to be ascribed to the fact that the change is smaller than the spectral accuracy ($\Delta\lambda = 1$nm) of the model, which is not able to resolve the spectral shift.

2) Dependence on Pump Energy: Fig. 9 shows the maximum emission wavelength as a function of the pump energy for different amounts of scattering losses. In both cases the behavior is very similar. At low pump energies the emission

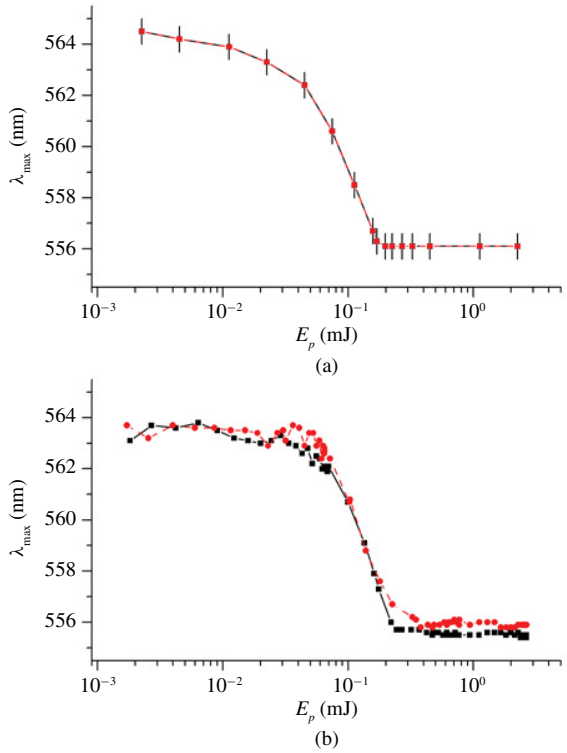

Fig. 9. (a) Calculated maximum emission wavelength as a function of the pump energy for $\alpha_{SC} = 0$ (squares) and 1.8×10^{-2} cm^{-1} (circles). The simulation error is added for comparison. (b) Experimental maximum emission wavelength as a function of the pump energy for a dye solution in EtOAc with 0% (squares) and 50% (circles) wt. 8MMAPOSS, corresponding to $\alpha_{SC} = 0$ and 1.8×10^{-2} cm^{-1}, respectively. The apparent bump close to 0.05 mJ in the experimental data corresponding to 50% wt. 8MMAPOSS is not an emission instability but experimental noise

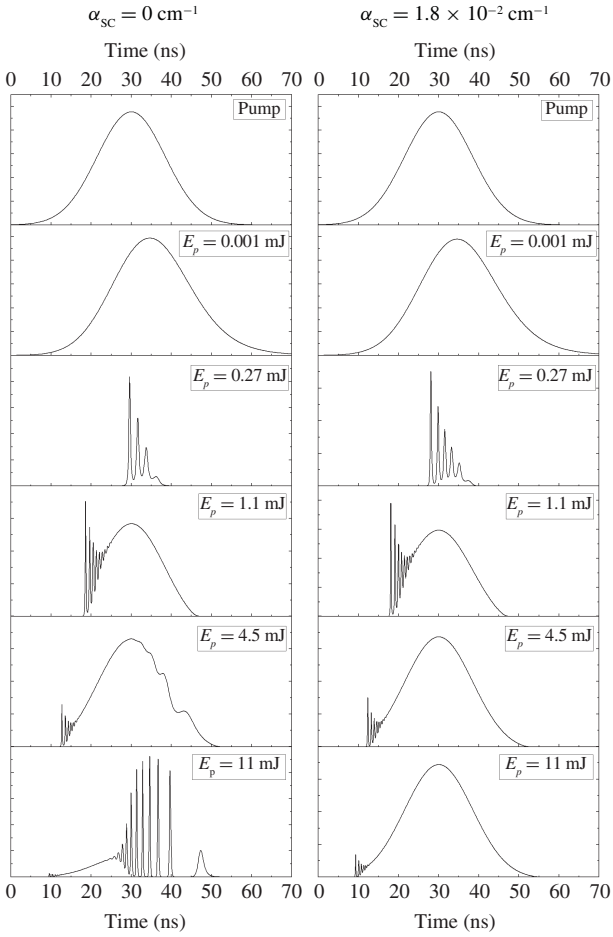

Fig. 10. Calculated temporal evolution as a function of pump energy for $\alpha_{SC} = 0$ cm^{-1} (left column) and $\alpha_{SC} = 1.8 \times 10^{-2}$ cm^{-1} (right column).

wavelength is highly redshifted with respect to the fluorescence maximum emission wavelength (534 nm). Once certain threshold is reached, the emission is abruptly shifted to shorter wavelengths. As higher pump energies are applied, the wavelength remains unchanged.

It can be experimentally observed that there is a slight redshift when scattering losses are present [Figs. 8(b) and 9(b)]. Nevertheless, the model does not predict any change in the emission wavelength when the scattering losses are increased. This discrepancy is due to the model spectral accuracy, as explained above. The simulation error is plot in Fig. 9(a) for comparison.

The observed behaviors can be explained as follows: At low pump energies the ground state population N_0 is hardly depleted and the reabsorption/reemission processes dominate, which results in a redshift of the emission wavelength. As the pump energy is increased above certain threshold the ground state population is more and more depleted, which makes the reabsorption/reemission processes to be less efficient and the emission wavelength to be shifted towards the fluorescence peak. At high pump intensities the system is already saturated, which means that the ground state cannot be further depleted, and so the wavelength cannot be further shifted towards shorter wavelengths.

D. Temporal Behavior

1) Dependence on Pump Energy: The temporal evolution of the output emission follows the expected laser behavior (Fig. 10): For low pump energies, there is not enough population inversion as to provide amplification and the system emits fluorescence or ASE, which is delayed with respect to the pump pulse. When the pump energy is raised above the threshold, there is sufficient population inversion as to provide amplification and the output emission starts a spiking behavior [1]. These pulsations may appear whenever the photon-cavity decay time t_c (time the photon stays within the cavity) is smaller than the fluorescence lifetime. This condition is fulfilled in the low reflectivity cavity we are dealing with. The spiking follows the typical behavior observed in dye systems [21]: 1) the frequency and number of spikes scales with the pump energy, 2) despite that each spike in the damped relaxation oscillation has a different duration (increasing with time and decreasing with the pump energy), which is smaller than the spike spacing, there is a fairly constant (slightly decreasing with time) spacing between peaks which can be designated as the period of oscillation, 3) the initial spike and the dumping become smaller in amplitude and stronger, respectively, as the pumping level is increased, and 4) in

certain range of pumping levels the time variation of the pulse subsequent to the relaxation oscillations is similar to that of the pumping pulse. At high enough pump energies, approximately ten times the first threshold pump energy, the laser crosses its second threshold [22], which is manifested in the apparition of a second set of spikes of irregular nature. A more thorough stability analysis would be necessary to determine the exact nature of this instability, albeit this analysis is beyond the scope of this work.

The temporal behavior when scattering losses are included does not change dramatically with respect to the pure laser case (Fig. 10). Since the scattering induces a further feedback, both the effective reflectivity and the cavity life-time of the laser are increased. This increase is mirrored in a slightly higher spiking frequency and a lower threshold for the appearance of spiking. Furthermore, the system with losses does not seem to cross the second threshold. Although at the present time we can only speculate on the exact reason for this behavior, it could be due to the scattering feedback distributed nature.

Experimental measurements of these effects could not be done due to lack of adequate equipment.

E. Spatial Distribution

1) Dependence on Scattering Losses: Another interesting feature of the studied system is the spatial distribution of the photon flux and gain (population inversion) along the excited medium, which, albeit is not a direct experimental observable, can give theoretical insights into the scattering problem and will help understand other emission properties. Fig. 11(a) shows a snapshot of the spatial distribution of the forward (I^+), backward (I^-) and total (I_T) photon fluxes along the gain medium for different amounts of scattering losses. The forward and backward distributions show a characteristic S-shape. As a consequence, the total photon flux, understood as the sum of I^+ and I^-, shows a characteristic gap in the middle of the gain medium. This gap gives rise to a peak-shape distribution of the excited state population, since the strong photon flux in the extremes quenches the population inversion at the edges [13], as can be seen in Fig. 11(b).

As the scattering losses are increased the total photon flux grows and is homogenized [Fig. 11(a)], i.e., the gap in the middle becomes less prominent. This is due to the fact that the scattering feedback is becoming stronger and is "trapping" the light within the gain medium. This change in the spatial distribution allows the system to make better use of the available population inversion [Fig. 11(b)], which is translated into a more efficient amplification process. This constitutes a further explanation to the efficiency improvement observed when scattering feedback is added to the system.

F. Beam Divergence

Since we are dealing with scattering processes capable of dispersing light, an important parameter to assess is the beam divergence. Given the nature of the reflective cavity we are dealing with, the beam divergence will be mostly determined not by the cavity mode but by the amplification process. Thus,

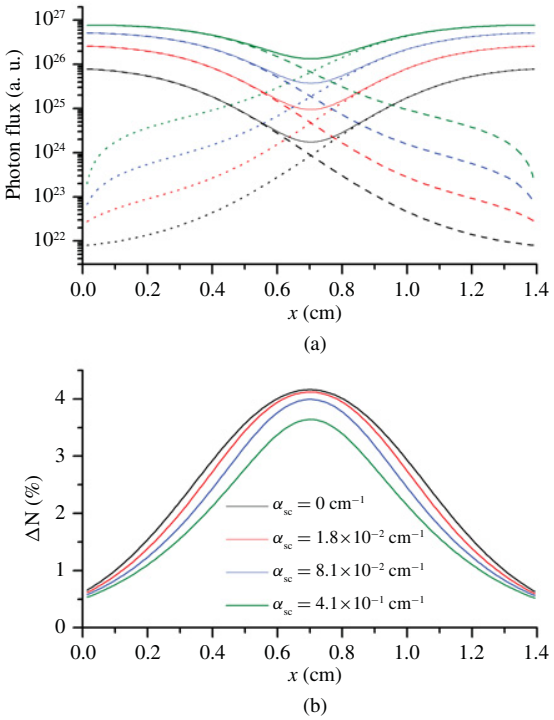

Fig. 11. Spatial distribution snapshot of: (a) calculated photon flux (I^+ dotted line, I^- dashed line, $I_T = I^+ + I^-$ solid line) and (b) population inversion $\Delta N = N_1/N$ 100% as a function of scattering feedback strength α_{SC}. Traces from bottom to top in (a) and (b) correspond, respectively, to increasing and decreasing α_{SC}.

to calculate this parameter we use an approach similar to the one used in [23], referred as to ASE-geometric theory. The geometric theory considers the beam divergence in ASE experiments to be the angle subtended by the exit window, i.e., $\theta_B^{geo} = \arctan(r/L)$, being r and L the excited region radius and length, respectively. Nevertheless, in actual experiments, only the photons traveling a distance $\ell = L$ would give place to this divergence, while the photons traveling $L > \ell > 0$, would subtend a wider divergence $\theta_B = \arctan(r/\ell)$. In addition, the photons traveling $\ell = L$ would be more amplified than the photons traveling $\ell \sim 0$. These differences in contributions must be taken into account in order to properly calculate the beam divergence. To this end, the ASE-geometric theory considers a weighted mean divergence, in which the weight will be determined by the value of the photon flux after traveling a distance ℓ. Thus, the photons traveling a distance ℓ will contribute with a divergence $\theta_B(\ell) = \arctan(r/\ell)$ with weight $I^+(\ell)$. Averaging over the whole length of the excited region, the beam divergence can be defined as

$$\theta_B = \int_0^L I^+(\ell) \arctan\left(\frac{r}{\ell}\right) d\ell \Big/ \int_0^L I^+(\ell) d\ell, \qquad (8)$$

where

$$I^+(\ell) = \int d\lambda \int I^+(\ell, t, \lambda) dt. \qquad (9)$$

In the present case, the excited region has two different transversal sizes, i.e., the width b and the depth d. Consequently, the divergence will be different in the horizontal

(d) and the vertical (b) exit planes. Thus, in (8) r will be substituted by $d/2$ or $b/2$, to give θ_B^H and θ_B^V, which are the divergences in the horizontal and vertical planes, respectively.

1) Dependence on Scattering Losses: Proceeding as explained above, we calculated the beam divergence as a function of the scattering losses. θ_B effectively increases when α_{SC} is increased [Fig. 12(a)], as was expected. It has to be stressed that this divergence increase is not due to the photon deviation induced by the scattering, but to the way we have calculated θ_B, which takes into account the photon flux distribution within the excited medium. This effect can be better observed by computing the beam divergence dependence when the scattering feedback is not considered [Eq. (7)]. In this case θ_B hardly changes in all the range of scattering losses considered in the simulation [Fig. 12(a)]. This is because the photon flux distribution in the gain medium is not much affected when there is no scattering feedback.

Hence, the beam divergence increase can be understood as follows: for low scattering losses, the photon flux distribution is quite inhomogeneous [Fig. 11(a)]. This inhomogeneity makes the photons travelling a distance $\ell \sim$L contribute more effectively to the beam divergence than the photons travelling a distance $\ell <<$L. Thus, θ_B is close to the pure ASE divergence value, but a little widened. When the scattering losses are further increased, the photon flux distribution within the excited medium is homogenized [Fig. 11(a)], compensating the contribution of the photons travelling distances $\ell \sim$L and $\ell <<$L, which leads to an increase in the final beam divergence.

The observed directional emission, generated due to the pumping geometry (Fig. 2), had a coarsely measured divergence close to 10 mrad, and was not apparently affected by the addition of any of the available nanoscatterer concentrations. More accurate measurements could not be done due to lack of adequate equipment.

2) Dependence on Pump Energy: When the pump energy is changed, the behavior of θ_B varies. Fig. 12(b) shows the calculated beam divergence as a function of the pump energy for different amounts of scattering losses. Three different regimes can be distinguished. At low pump energies, the beam divergence stays almost unchanged. At certain threshold energy, θ_B drops abruptly to a value slightly higher than the geometrical divergence. For high enough pump energies the beam divergence starts a steady growing. This behavior is due to the fact that we have defined the beam divergence as a function of the photon flux distribution within the excited medium, and can be understood by a similar reasoning to that in the previous section. At low pump energies the intensity distribution is quite homogeneous and all the photons coming along the excited medium contribute to effectively widen the beam divergence. At certain threshold, the intensity distribution becomes quite inhomogeneous, which makes the photons travelling a distance $\ell \sim$L contribute more effectively to the beam divergence than the photons travelling a distance $\ell <<$L, making θ_B to drop abruptly. When further increasing the pump energy the system saturates and the intensity distribution is again homogenized, increasing again the beam divergence. The increase in the beam divergence above threshold is consistent with the results observed by Peters and Allen [23]. In addition, Fig. 12(b) shows that above certain pump energy, the higher the scattering losses are, the higher the beam divergence is, as was seen in Fig. 12(a), confirming that the scattering feedback is beneficial only for certain range of energies, as has been shown along the entire paper.

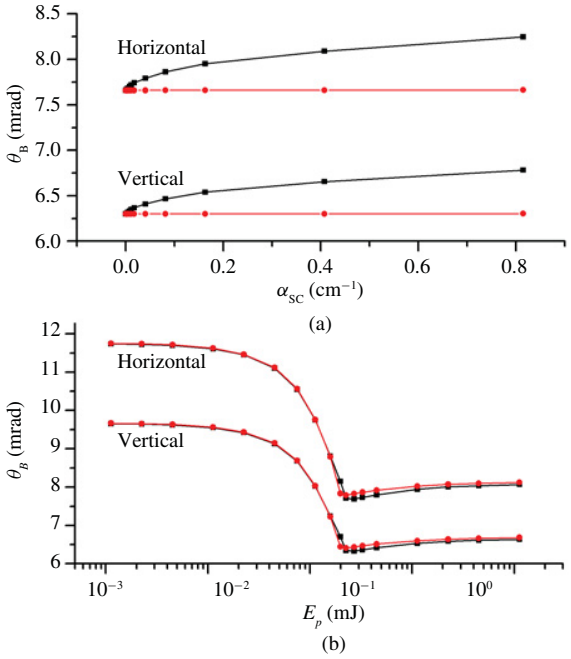

Fig. 12. Calculated beam divergences. (a) For increasing α_{SC} with (squares) and without (circles) considering scattering feedback. $E_{pump} = 0.25$ mJ. (b) As a function of pump energy for $\alpha_{SC} = 0$ cm^{-1} (squares) and $\alpha_{SC} = 1.8 \times 10^{-2}$ cm^{-1} (circles).

IV. Conclusion

In summary, we have presented in this paper extensive numerical results on NRF processes in laser dye systems doped with Rayleigh scatterers. We have evaluated the output efficiency, the spectral, temporal and spatial properties of these NRF systems as a function of both the scattering and excitation levels. The results can be summarized as follows.

1) The NRF enhanced laser efficiency increases with the scattering losses, improvement that is only possible if scattering feedback is taken into account. Furthermore, ΔE is highly dependent on the selected pumping conditions. This fact shows the importance of choosing adequately the experimental conditions in order to optimize the final NRF enhanced laser emission.
2) For this effect to occur, only nanometric-sized scatterers (Rayleigh regime) can be used in order to have enough backscattering as to provide the needed feedback while simultaneously avoiding most of the undesirable effect of scattering losses. The nanometric size of the scatterers is the critical factor which allows the emission improvement and governs the physics of the emission.
3) As the scattering feedback becomes stronger the light is trapped within the gain medium and, thus, the total photon flux is more homogeneously distributed. This allows the system to make better use of the available

population inversion. This constitutes a further explanation to the efficiency improvement observed in NRF enhanced lasers.

4) The scattering feedback induces an additional collapse in the FWHM due to the elongated photon path within the excited medium, as well as a redshift in the maximum emission wavelength due to the trapping of the light in the excited region, which increases the probability of being reabsorbed. Furthermore, no spikes were observed in the emission spectra for any of the measurements, indicating that the transition from non-resonant to coherent feedback is not taking place in this kind of system.
5) The presence of scattering feedback in the medium gives rise to an increase in the spiking frequency and leads to the disappearance of the laser second threshold.
6) The beam divergence depends on both the scattering losses and the pump energy. The observed beam divergence increase is not due to the photon deviation induced by the scattering, but to the photon flux distribution within the excited medium.

In conclusion, the proposed model provides a theoretical explanation of the previously observed enhanced conventional two-mirror cavity laser emission in gain media when doped with nanoscatterers, and establishes the limits for the region where gain dominates over scattering losses. At the same time the model, and the experimental evidences, show that scattering is not always detrimental to conventional laser emission as thought so far. Finally, we have shown that the development of advanced photonic materials combining synergistically the advantages of both random and conventional laser results in optimized laser emission.

ACKNOWLEDGMENT

V. Martín and M. E. Pérez-Ojeda would like to thank Spanish Consejo Superior de Investigaciones Científicas for their Junta para la Ampliación de Estudios, post-doctoral and pre-doctoral contracts, respectively, and L. Cerdán also thanks Ministerio de Ciencia e Innovación for a pre-doctoral scholarship (cofinanced by Fondo Social Europeo). L. Cerdán thanks J. M. Guerra and N. Fonseca for fruitful discussion on the model.

REFERENCES

[1] A. Siegman, *Lasers*. Mill Valley, CA: University Science, 1986.
[2] O. Svelto, *Principles of Lasers*. New York: Springer-Verlag, 1998.
[3] D. S. Wiersma, "The physics and applications of random lasers," *Nature Phys.*, vol. 4, pp. 359–367, May 2008.
[4] M. A. Noginov, *Solid-State Random Lasers*. New York: Springer-Verlag, 2005.
[5] H. Watanabe, Y. Oki, M. Maeda, and T. Omatsu, "Waveguide dye laser including a SiO_2 nanoparticle-dispersed random scattering active layer," *Appl. Phys. Lett.*, vol. 86, no. 15, pp. 151123-1–151123-3, Apr. 2005.
[6] A. Costela, I. García-Moreno, L. Cerdán, V. Martín, O. García, and R. Sastre, "Dye-doped POSS solutions: Random nanomaterials for laser emission," *Adv. Mater.*, vol. 21, no. 41, pp. 4163–4166, Nov. 2009.
[7] S. K. Turitsyn, S. A. Babin, A. E. El-Taher, P. Harper, D. V. Churkin, S. I. Kablukov, J. D. Ania-Castañón, V. Karalekas, and E. V. Podivilov, "Random distributed feedback fibre laser," *Nature Photon.*, vol. 4, pp. 231–235, Apr. 2010.
[8] F. P. Schäfer, "Principles of dye laser operation," in *Dye Lasers* (Applied Physics), vol. 1, F. P. Schäfer, Ed., 3rd ed. Berlin, Germany: Springer-Verlag, 1990, pp. 40–42.
[9] H. C. Hulst, *Light Scattering by Small Particles*. New York: Dover, 1981.
[10] R. V. Ambartsumyan, N. G. Basov, P. G. Kryukov, and V. S. Letokhov, "Non-resonant feedback in lasers," *Prog. Quantum Electron.*, vol. 1, no. 3, pp. 107–120, 1970.
[11] D. S. Wiersma and A. Lagendijk, "Light diffusion with gain and random lasers," *Phys. Rev. E*, vol. 54, no. 4, pp. 4256–4265, Oct. 1996.
[12] R. Pierrat and R. Carminati, "Threshold of random lasers in the incoherent transport regime," *Phys. Rev. A*, vol. 76, no. 2, pp. 023821-1–023821-6, Aug. 2007.
[13] U. Ganiel, A. Hardy, G. Neumann, and D. Treves, "Amplified spontaneous emission and signal amplification in dye-laser systems," *IEEE J. Quantum Electron.*, vol. 11, no. 11, pp. 881–892, Nov. 1975.
[14] V. S. Letokhov, "Generation of light by a scattering medium with negative resonance absorption," *Sov. Phys. JETP*, vol. 26, no. 4, pp. 835–840, Apr. 1968.
[15] B. R. Prasad, H. Ramachandran, A. K. Sood, C. K. Subramanian, and N. Kumar, "Lasing in active, sub-mean-free path-sized systems with dense, random, weak scatterers," *Appl. Opt.*, vol. 36, no. 30, pp. 7718–7724, Oct. 1997.
[16] A. Costela, I. García-Moreno, C. Gómez, R. Sastre, F. Amat-Guerri, M. Liras, F. L. Arbeloa, J. Bañuelos, and I. L. Arbeloa, "Photophysical and lasing properties of new analogs of the boron-dipyrromethene laser dye PM567 in liquid solution," *J. Phys. Chem. A*, vol. 106, no. 34, pp. 7736–7742, Aug. 2002.
[17] R. Sastre, V. Martín, L. Garrido, J. L. Chiara, B. Trastoy, O. García, A. Costela, and I. García-Moreno, "Dye-doped polyhedral oligomeric silsesquioxane (POSS)-modified polymeric matrices for highly efficient and photostable solid-state lasers," *Adv. Funct. Mater.*, vol. 19, no. 20, pp. 3307–3316, Oct. 2009.
[18] S. John and G. Pang, "Theory of lasing in a multiple-scattering medium," *Phys. Rev. A*, vol. 54, no. 4, pp. 3642–3652, Oct. 1996.
[19] P. C. Oliveira, J. A. McGreevy, and N. M. Lawandy, "External-feedback effects in high-gain scattering media," *Opt. Lett.*, vol. 22, no. 12, pp. 895–897, Jun. 1997.
[20] H. Cao, "Lasing in random media," *Waves Random Media*, vol. 13, no. 3, pp. R1–R39, 2003.
[21] C. Lin, "Studies of relaxation oscillations in organic dye lasers," *IEEE J. Quantum Electron.*, vol. 11, no. 8, pp. 602–609, Aug. 1975.
[22] H. Haken, *Light*, vol. 2. Amsterdam, The Netherlands: North Holland, 1986.
[23] G. I. Peters and L. Allen, "Amplified spontaneous emission. IV. Beam divergence and spatial coherence," *J. Phys. A: General Phys.*, vol. 5, no. 4, pp. 546–554, Apr. 1972.

Luis Cerdán received the Licenciatura degree in physics and the M.S. degree in fundamental physics from the Universidad Complutense de Madrid, Madrid, Spain, in 2006 and 2007, respectively. He is currently pursuing the Ph.D. degree in solid state dye lasers at the Instituto de Química Física Rocasolano, Consejo Superior de Investigaciones Cientificas, Madrid, under the supervision of Prof. Costela and Prof. García-Moreno.

He spent three months working on organic distributed feedback lasers at the School of Physics and Astronomy, University of St. Andrews, St. Andrews, Scotland, in 2009, under the supervision of Dr. Turnbull. His current research interests include simulation and experimental characterization of integrated laser systems.

Angel Costela received the Ph.D. degree in physics from the Universidad Complutense de Madrid, Madrid, Spain, in 1980, for studies on fundamental processes in the photochemical iodine laser.

He has been a Visiting Scientist at the Clarendon Laboratory, University of Oxford, Oxford, U.K., where he carried out research on frequency up-conversion by resonantly enhanced sum-frequency mixing in metallic vapors. He is a Professor of Research at the Instituto Rocasolano, Consejo Superior de Investigaciones Científicas, Madrid. His current research interests include study and development of solid state dye lasers, laser ablation of materials, nonlinear optics, and nanostructured materials for advanced biophotonic and laser applications.

Prof. Costela is a Fellow of the Optical Society of America.

Inmaculada García-Moreno received the Ph.D. degree in chemistry from the Universidad Complutense de Madrid, Madrid, Spain, in 1989, for studies on fundamental processes in photochemistry and molecular dynamics.

She has been a Visiting Scientist at the Chemistry College, University of California at Berkeley, Berkeley, where she carried out research on molecular beams, photofragment excitation spectroscopy, and laser-induced photochemistry. She currently holds the position of Professor of Research at the Instituto Rocasolano, Consejo Superior de Investigaciones Científicas, Madrid. Her current research interests include study and development of solid state dye lasers, laser ablation of materials, nonlinear optics and nanostructured materials for advanced biophotonic and laser applications.

Virginia Martín received the Ph.D. degree in chemistry from the Universidad Autónoma de Madrid, Madrid, Spain, in 2005, for the development of new 4-in-dimethylaminostyryldiazines and their application as fluorescent probes to monitoring of photoinitiated radical polymerization reactions.

She has been working on the development of solid state dye lasers at the Instituto de Química Física Rocasolano, Consejo Superior de Investigaciones Científicas, Madrid. In 2010, she spent 10 months at the Institut de Chimie de la Matière Condensée de Bordeaux, Centre National de la Recherche Scientifique, Paris, France, where she carried out the synthesis and characterization of noble metal and semiconductor nanoparticles, under the supervision of Dr. Delville. Her current research interests include the development of new nanostructured hybrid materials for biophotonic and laser applications.

María E. Pérez-Ojeda received the B.S. degree in chemistry from the Universidad Complutense of Madrid, Madrid, Spain, in 2008, and the M.S. degree in high specialization in plastics and rubber from the International University Menéndez Pelayo, Madrid, in 2009. She is currently pursuing the Ph.D. degree in the development of new hybrid nanomaterials for biophotonic applications at the Instituto de Química Física Rocasolano and the Instituto de Química Orgánica, both at the Consejo Superior de Investigaciones Científicas (CSIC), Madrid, under the supervision of Prof. García-Moreno and Dr. Chiara.

She joined the Institito de Ciencia y Tecnología de Polímeros, CSIC, under the supervision of Prof. Sastre working on polymers functionalized with laser dyes.

Paper A3: Nature Photonics 6, 621–626 (2012)

FRET-assisted laser emission in colloidal suspensions of dye-doped latex nanoparticles

L. Cerdán, E. Enciso, V. Martín, J. Bañuelos, I. López-Arbeloa, A. Costela, and I. García-Moreno

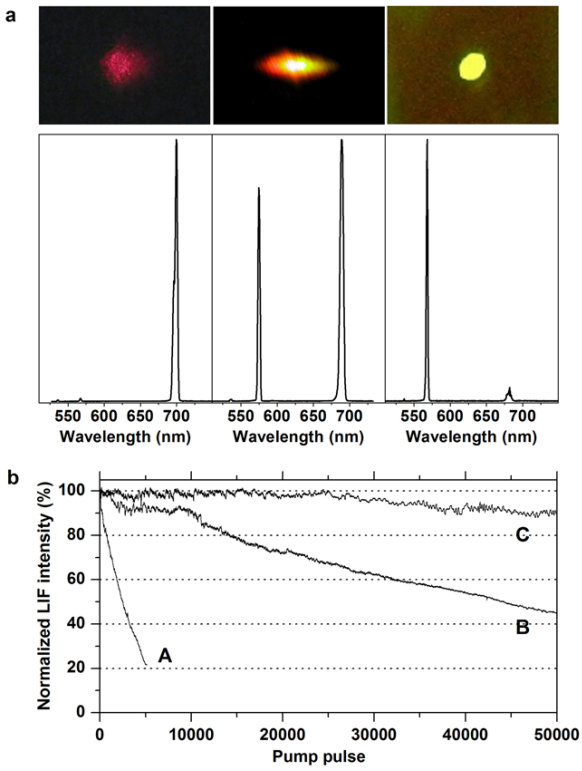

a) Lasing emission spectra from colloidal suspensions of poly(MMA-HEMA-GMA) nanoparticles with different relative proportions of Rh6G/NB: From left to right: 1.5/1 (0.28/0.19 wt %), 3/1 (0.36/0.12 wt %) and 1/1 (0.09/0.09 wt %). Photographs over spectra show the actual laser spot on a black screen placed at 30 cm from the laser cavity. b) Normalized laser-induced fluorescence emission as a function of the number of pump pulses for: (A) NB in ethanol; (B) mixture 0.024/0.016 wt % of Rh6G/NB in ethanol; (C) colloidal suspension of nanoparticles with 1.5/1 (0.28/0.19 wt %) Rh6G/NB proportion.

nature photonics

ARTICLES

PUBLISHED ONLINE: 19 AUGUST 2012 | DOI: 10.1038/NPHOTON.2012.201

FRET-assisted laser emission in colloidal suspensions of dye-doped latex nanoparticles

Luis Cerdán[1]*, Eduardo Enciso[2], Virginia Martín[1], Jorge Bañuelos[3], Iñigo López-Arbeloa[3], Angel Costela[1] and Inmaculada García-Moreno[1]

The use of commercial long-wavelength (>650 nm) laser dyes in many biophotonic applications has several important limitations, including low absorption at the standard pump wavelength (532 nm) and poor photostability. Here, we demonstrate that the use of Förster type (FRET) energy transfer can overcome these problems to enable efficient, stable near-infrared lasing in a colloidal suspension of latex nanoparticles containing a mixture of Rhodamine 6G and Nile Blue dyes. Experimental and theoretical analyses of the photophysics suggest that the dominant energy transfer mechanism is Förster type via dipole–dipole coupling, and also reveal an unexpected core/shell morphology in the dye-doped nanoparticles. FRET-assisted incoherent random lasing is also demonstrated in solid samples obtained by evaporation of colloidal suspensions.

Tunable dye lasers have been demonstrated to be an important tool in a wide variety of fields, from spectroscopy to isotope separation, photochemistry, material diagnosis and medicine[1–3]. In biomedical and biophotonic applications, long-wavelength (>650 nm) fluorescent dyes have some distinct advantages linked to the fact that long-wavelength light can penetrate deeper into tissue[4], which facilitates their use in surgical and photodynamic therapy treatments[3]. Although a number of long-wavelength-emitting commercial dyes are available that have reasonable efficiency[5], these dyes have two important drawbacks: low absorption at the standard pump wavelength of 532 nm and/or rather poor photostability. One approach to overcoming these drawbacks is to use mixtures of dyes in a system based on Förster resonance energy transfer (FRET). FRET is a physical phenomenon where excitation energy from an excited donor is non-radiatively transferred to a proximal ground-state acceptor[6–14]. A system is required that consists of two dyes; one efficiently absorbs the pump radiation at 532 nm and is able to transfer the excitation energy to a second, long-wavelength emitting dye. The energy transfer process in a FRET system requires good overlap between donor emission and acceptor absorption bands; it depends strongly on the distance between donor and acceptor molecules, and, as recently reported, on the conservation or not of the angular momentum in the transfer process[15]. One way to ensure the proximity of the dye molecules and thus favour the energy transfer process is to confine donor and acceptor molecules within nanoparticles[11,16,17]. We have also recently demonstrated significant improvements in the lasing efficiency and photostability of the dye Rhodamine 6G (Rh6G) by confining it in polymeric nanoparticles (latexes) homogeneously dispersed in aqueous suspensions[18,19]. Consequently, we thought of using dye confinement in latex nanoparticles in combination with the FRET process as a strategy to overcome simultaneously the low absorption, low laser efficiency and photostability problems of long-wavelength emitting dyes. The red emitting dye Nile Blue (NB), which is quite efficient but rather unstable under pumping at 532 nm, seemed an ideal candidate to prove this approach, as there is a good overlap between the emission band of Rh6G and its absorption band (Supplementary Fig. S1), a necessary condition for an efficient non-radiative energy transfer.

In this Article, we report, for the first time, efficient and photostable FRET-assisted laser emission in colloidal suspensions of latex nanoparticles containing mixtures of Rh6G and NB (see Methods). The mechanism of energy transfer in this system is properly assessed by analysing the photophysical properties of the donor, acceptor and mixtures of donor and acceptor encapsulated inside the nanoparticles. A thorough theoretical analysis of the FRET process allows us to infer that the inner morphology of the latex nanoparticles is of a core–shell type. Finally, unprecedented FRET-assisted incoherent random lasing is also obtained in solid samples deposited by evaporation of the colloidal suspensions.

Laser characterization

A systematic study was carried out regarding the laser performance of samples with different dye loadings and ratios and nanoparticle content in the suspension. The best compromise between laser and transfer efficiency was obtained from a colloidal suspension of 6.7 wt% of nanoparticles with a Rh6G/NB proportion of 1.5/1 (0.28/0.19 wt% with respect to monomer, respectively). The optimized laser emission (Fig. 1a) was centred at 700 nm (typical of NB), with just some residual emission from the Rh6G, and reached an efficiency (percentage of the excitation energy converted into laser emission) of 13% under transversal pumping at 532 nm. The laser output energy and spectrum suggest that the energy transfer efficiency reaches 98%, because the efficiency of a suspension containing only Rh6G is 30%, and the contribution of the Rh6G emission to the efficiency of the suspension with both Rh6G and NB is just 0.6%. (This is determined as $\int I_L(\lambda)hc/\lambda \, d\lambda$, integrated over the Rh6G contribution to the laser spectrum $I_L(\lambda)$, normalized so that $\int I_L(\lambda)hc/\lambda \, d\lambda$, integrated over all wavelengths, is 13%, where h is Planck's constant and c is the speed of light in vacuum.) In comparison, and indicative of this efficient energy transfer, no laser emission was obtained when the nanoparticles contained only NB at the concentration that optimized lasing in the donor/acceptor mixtures.

[1]Instituto de Química Física 'Rocasolano', CSIC-Consejo Superior de Investigaciones Científicas, Serrano 119, 28006, Madrid, Spain, [2]Facultad de Ciencias Químicas, Universidad Complutense de Madrid, Av. Complutense s/n, 28040, Madrid, Spain, [3]Facultad de Ciencias y Tecnologías, Universidad del País Vasco/EHU, Apdo 644, 48080, Bilbao, Spain. *e-mail: lcerdan@iqfr.csic.es

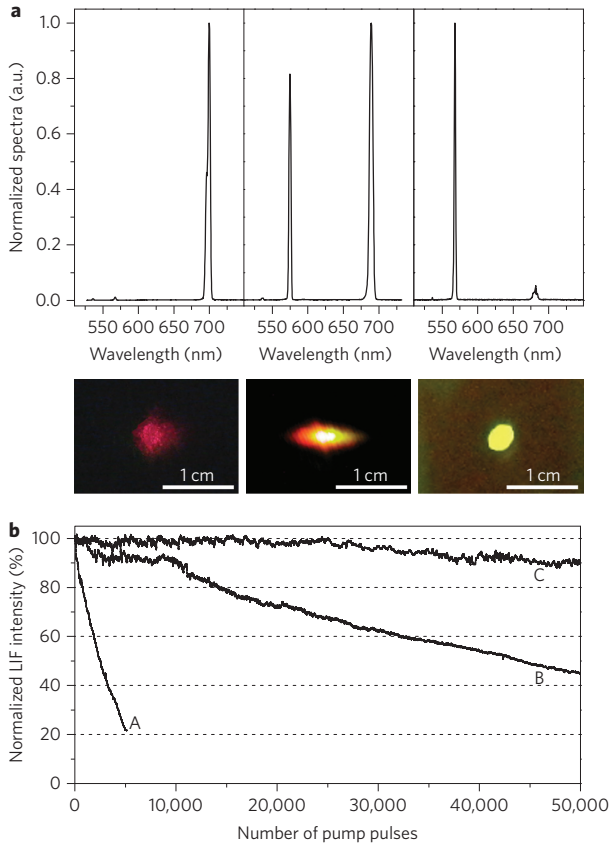

Figure 1 | FRET-assisted laser emission measurements. a, Lasing emission spectra from colloidal suspensions of poly(MMA-HEMA-GMA) nanoparticles with different relative proportions of Rh6G/NB: (from left to right) 1.5/1 (0.28/0.19 wt%), 3/1 (0.36/0.12 wt%) and 1/1 (0.09/0.09 wt%). Photographs below the spectra show the actual laser spot on a black screen placed 30 cm from the laser cavity. **b**, Normalized laser-induced fluorescence emission as a function of the number of pump pulses for NB in ethanol (A), a mixture of 0.024/0.016 wt% of Rh6G/NB in ethanol (B), a colloidal suspension of nanoparticles with 1.5/1 (0.28/0.19 wt%) Rh6G/NB (C).

This lack of laser emission from NB alone can be understood as being a result of a combination of two factors. First, it is well known that the composition of the material containing the dye is most important in ensuring laser emission from organic dyes[20]. In this regard, methyl methacrylate (MMA)/2-hydroxylethylmethacrylate (HEMA) copolymers are not the best environment for the laser action of NB, because this dye lases more efficiently in protic solvents such as ethanol (which is mimicked by the HEMA monomer) than in aprotic solvents such as ethyl acetate (which is mimicked by the MMA monomer). Thus, the presence of MMA in the nanoparticle composition does not favour laser emission from NB when this dye is alone in the nanoparticle. Second, under transversal excitation, dye concentration becomes a critical factor, because the dye samples require an optical density of ~20 to assure that the incoming pump radiation is absorbed within a depth similar to the cross-section of that pump radiation at the input face of the cell onto which the exciting pulses are line-focused (~0.3 mm). Then, the concentration of NB that optimizes its emission from the confined donor/acceptor mixtures is lower than that required for efficient laser emission when the NB is alone within the nanoparticle. These two factors, taken together, prevent laser emission from NB when included in nanoparticles, alone, at the concentration that is optimal for the Rh6G/NB mixtures.

The lasing efficiency and spectrum depend strongly on donor/acceptor proportion (Fig. 1). When this is increased to 2/1, lasing efficiency is slightly reduced (11%), but Rh6G residual emission increases. Higher amounts of Rh6G result in a reduced efficiency, with progressively growing Rh6G emission (Fig. 1a). If the donor/acceptor proportion is changed to 1/1 (0.27/0.27 wt%) or 1/1.5 (0.23/0.35 wt%), only the 700 nm emission from NB appears, but lasing efficiency is reduced to 7%. Reducing the concentrations of dyes in the nanoparticles and/or the proportion of nanoparticles in the suspension progressively reduces the lasing efficiency down to 5%, when emission at 570 nm is observed from the Rh6G (Fig. 1a).

For comparison purposes we determined the lasing properties in an ethanolic solution of both dyes while maintaining the pumping conditions, the relative proportion of donor/acceptor, as well as keeping the dye concentrations equal to those used in the colloidal suspensions. An effective energy transfer was again observed, leading to laser emission from NB, centred at 695 nm, with an efficiency of 18%, which is somewhat higher than that obtained in the colloidal suspension due to the higher affinity of NB for ethanol than for the polymer.

The true extent of the importance of dye confinement is revealed by the emission photostability under laser operation (Fig. 1b); this is an important parameter of any laser dye, because it determines the usefulness of the dye when used in practical applications. NB is a rather unstable dye under laser irradiation. In fact, its laser-induced fluorescence (LIF) emission in ethanol solution (see Methods for a detailed description of the procedure used to assess the photostability of the dyes) dropped by 80% from its initial value after just 5,000 pump pulses (Fig. 1b, curve A). The addition of Rh6G donor to the ethanol solution significantly increased NB stability, with the emission at 695 nm dropping by 55% from its initial value after 50,000 pump pulses (Fig. 1b, curve B). In contrast, when the dyes were confined in nanoparticles, the emission of NB dropped by less than 10% after 50,000 pump pulses (Fig. 1b, curve C). Thus, the FRET process, together with confinement of the dye molecules in the reduced space of the nanoparticles, significantly enhances the photostability of the laser system under consideration, in an approach that is extendable to other donor/acceptor pairs. In fact, preliminary studies in our group are showing that the improvement in lasing performance can be even higher when NB is replaced by Oxazine 720 (Ox720). This dye is very unstable, and in an ethanol solution loses its LIF emission after just 3,000 pump pulses. In contrast, a mixture of Rh6G/Ox720 (0.16/0.16 wt%), confined in the same latex nanoparticles as described above, results in laser emission at 674 nm with an efficiency of 15% (similar to that obtained in the liquid phase) and demonstrates high photostability, maintaining 100% of its initial emission after 60,000 pump pulses. The complete results will be published elsewhere.

Photophysical characterization

The mechanisms of energy transfer in this system were assessed by analysing the photophysical properties of confined donor/acceptor suspensions with respect to the photophysics of each of these dyes when encapsulated alone in the nanoparticles. Encapsulation of Rh6G or NB into nanoparticles did not significantly alter their photophysical properties. The shape of their absorption spectra matched those obtained in the corresponding diluted solution, and the fluorescence quantum yields (ϕ) and lifetimes (τ) of the Rh6G ($\phi = 0.60$, $\tau = 4.47$ ns) and NB ($\phi = 0.47$, $\tau = 2.53$ ns) were also similar to those recorded in diluted solutions ($\phi = 0.77$, $\tau = 3.85$ ns for Rh6G and $\phi = 0.43$, $\tau = 2.07$ ns for NB in ethanol). In spite of the dye confinement, there was no sign of aggregation, even at the high dye concentrations reached inside the latex nanoparticles. The slight fluorescence lifetime enlargement observed in the colloidal suspensions with respect to the diluted

solutions can be ascribed to the spontaneous emission inhibition experienced by emitters confined in subwavelength cavities (Purcell's effect)[19].

In a similar way, we carried out photophysical characterization of the latex nanoparticles containing a mixture of Rh6G and NB in a 1.5/1 weight proportion. The absorption spectrum revealed the presence of both dyes (Rh6G at 533 nm and NB at 636 nm); excitation of Rh6G in a region where NB does not absorb gave rise to fluorescence emission at 560 nm, and this was followed by strong emission at 670 nm, assigned to the fluorescence of NB (Supplementary Fig. S2). Moreover, the excitation spectrum monitored at the NB emission also showed the presence of two bands, in agreement with the corresponding absorption spectrum, revealing an efficient energy transfer from the donor Rh6G to the acceptor NB. Accordingly, this process affected the fluorescence decay curve of the confined donor Rh6G (Fig. 2a) in the presence of NB, which became multiexponential and characterized by new more dominant and faster components (0.29 and 1.05 ns) than observed for Rh6G encapsulated alone in the latex nanoparticles (4.47 ns). In fact, it will be seen later that the fluorescence decay curve cannot be described simply by a multiexponential; the relation is more complex. The NB fluorescence decay curve induced by exciting the donor molecules revealed a growing component (0.33 ns), then a decay (2.63 ns), matching the curve for the NB alone inside latex nanoparticles (2.53 ns). These results indicate that the acceptor NB excited state is populated by means of the donor, via an energy transfer process, as is nicely reproduced in the time-resolved emission spectra of Fig. 2b. Taking into account the high spectral overlap between the dyes (Supplementary Fig. S1) and their photophysical behaviour, as described above, the energy transfer mechanism from Rh6G to NB inside latex nanoparticles should be Förster type via dipole–dipole coupling. As further evidence, the FRET quantum yield $\phi_{FRET} = 0.77$ was calculated from a comparison of the fluorescence decay curves of the donor in the absence and presence of acceptors (Supplementary equation (3)).

On the other hand, there are different ways in which NB emission could be built up: by direct energy transfer from excited Rh6G molecules (hetero-FRET) or after several energy hops among the donors coexisting in the nanoparticle (homo-FRET). Furthermore, photons emitted by an excited Rh6G molecule surviving the FRET process in a distant nanoparticle could be absorbed (by undergoing a radiative energy transfer, RET, process) by another Rh6G molecule (homo-RET) or a NB acceptor (hetero-RET). The influence of such RET processes is very important at the high optical densities required to record laser action. As evidence for this, the laser spectra suggest that the total energy transfer efficiency is much higher (0.98) than the ϕ_{FRET} value. The presence of RET was assessed photophysically by changing the suspension net dye concentration and the recording pathway. In diluted solutions (2 μM and 1 cm pathway), where such effects are usually negligible, the influence of reabsorption–re-emission (that is, RET) was detected in the fluorescence spectra (bathochromic shift), but RET effects were insignificant when using a 0.1 cm optical pathlength in a front-face configuration. As expected, concentrated suspensions presented higher energy transfers than diluted ones, but, once the reabsorption/re-emission phenomena were mathematically corrected, the differences vanished (Supplementary Fig. S3). In view of these results, we concluded that the energy transfer in this confined Rh6G/NB system under laser operation takes place mainly via a FRET mechanism reinforced by RET processes. Nonetheless, it has to be considered that in confined systems the emission of the donor could also be quenched, to some extent, by the sole presence of an acceptor in the 'active sphere' of the donor[21].

Theoretical analysis of FRET

From the photophysical characterization, very interesting and useful information may be obtained about the FRET process within latex nanoparticles, as well as about their thus far imprecisely known inner morphology. This latter fact is important because of its influence on dye distribution, which may deeply affect laser performance because every monomer has a different polarity and, consequently, a different affinity for the dyes.

The fluorescence decay curve of the donor in the presence of acceptors (Fig. 2a) can be used as a tool to determine the dye distribution within a nanoparticle, because the energy transfer is highly dependent on the distribution of donor–acceptor distance[11]. It was therefore analysed theoretically following (but modifying where needed) the treatment developed by Martinho's group[11,22,23] for FRET processes in systems with spherical symmetry (see Supplementary Section S2 for a detailed description of the treatment used). We began by assuming that the nanoparticle consists of a homogeneous tert-polymer of MMA/HEMA/glycidylmethacrylate (GMA) and that the dye distributions are therefore uniform. As seen in Fig. 2c (curve I), the fluorescence decay curve computed with this assumption fits quite accurately for short times, but deviates from the experimental points for longer times, and in fact predicts a quicker deactivation. This result indicates that the dye distribution must be, to some extent, inhomogeneous.

Our initial interpretation of this inhomegeneity was that there were two different domains, because HEMA is more polar than MMA and GMA, and would therefore tend to be closer to the aqueous solution (closer to the surface) than the MMA and GMA. Because Rh6G and NB are more soluble in HEMA than in

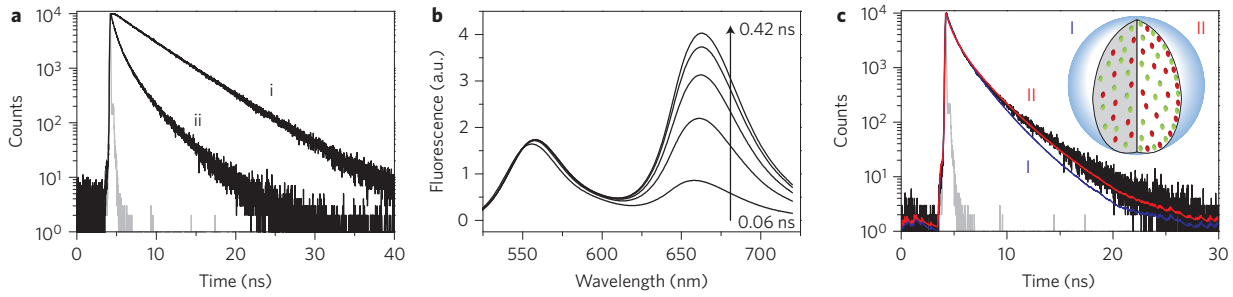

Figure 2 | Photophysical study of colloidal suspensions. a, Fluorescence decay curve of Rh6G in latexes in the absence (i) and presence (ii) of NB, with excitation at 470 nm and monitoring at 560 nm. **b**, Fluorescence spectra (normalized at the donor emission) at different delay times after donor excitation (0.06, 0.12, 0.18, 0.30 and 0.42 ns) in latex doped with Rh6G and NB. **c**, Experimental (dots) and modelled (lines) fluorescence decay curves of Rh6G in the presence of NB. Fits of curve I (blue) and II (red) assume homogeneous and core/surface distributions, respectively. Inset: sketch of dye distributions (Rh6G in green dots and NB in red dots) used for curves I and II.

MMA and GMA, both dyes would consequently lie closer to the surface than to the centre of the nanoparticle. Hence, the latexes would demonstrate a somewhat core/shell morphology with a smooth transition from core to shell. Following a trial-and-error approach with different core/shell morphologies (Supplementary Section S2), and in view of the fit shown in Fig. 2c (curve II), we concluded that the actual distribution of dyes within the nanoparticle is intermediate between a core/shell distribution and a core/surface one. In other words, the nanoparticles have a core/thin shell morphology, consistent with the following interpretation: (i) the core consists of a homogeneous tert-polymer of MMA/HEMA/GMA, in which both dyes are homogeneously solved; (ii) the thin shell is formed of a so-called nanoparticle 'hairy layer' (surface roughness or fuzziness[23]), in which both dyes are adsorbed with a concentration different to that of the core. As we used an anionic surfactant (SDS) in the synthesis, the 'hairy layer' (tert-polymer/surfactant/water interface) would have a certain negative charge distribution. Hence, cationic dyes such as Rh6G (donor) and NB (acceptor) would be adsorbed on the anionic surface with the very same distribution. Experimental and theoretical studies are currently under way to gain more insights into the inner morphology of the dye-doped latex nanoparticles and its correlation with FRET-assisted laser emission.

As a final remark, one might wonder how the presence of homo-RET, hetero-RET or homo-FRET would affect the analysis and interpretation of the decay curve. The presence of homo-RET lengthens the fluorescence decay lifetime; however, hetero-RET does not modify this decay rate, but instead modifies the output donor intensity[21]. These effects were avoided by carefully selecting the experimental conditions (front-face configuration and diluted solutions with a 0.1 cm pathlength, or concentrated solutions with 0.001 cm pathlength). On the other hand, the presence of homo-FRET decreases the ensemble fluorescence polarization anisotropy and leads to a possible energy spread due to excitation migration[24], whereupon a change in the distribution of the excited molecules could, consequently, appear. The fluorescence anisotropy measurements (Supplementary Section S3) reveal the presence of hetero-FRET, which is somewhat reduced by the presence of the acceptor, because both homo-FRET and hetero-FRET compete for the same excitation with similar transfer probabilities (Supplementary Fig. S4). Consequently, there will be an energy migration. However, because the donor molecules are confined within the nanoparticle and the excitation spread (before being absorbed by the acceptor) will not exceed a few Förster radii[24], the energy will stay in the nanoparticle. In addition, given the stochastic nature of this process, the excitation distribution will be randomized, a fact that in turn justifies the assumption of a homogeneous and spherically symmetric distribution. Hence, all of the aforementioned processes have already been taken into account in the decay curve analysis and do not call into question the reasoning about the core/shell distribution of the dyes in the nanoparticles.

Random lasing in solid samples

As a proof of concept, we show that the high efficiency of the energy transfer process in these systems is maintained when the nanoparticles are not contained in a suspension but are cast instead as solid monoliths. The solid samples, with a thickness of ~100 μm, were obtained by drying 2 ml of suspension in an oven at 40 °C. Under front-face irradiation (see Methods), FRET-assisted stimulated emission was observed at 710 nm (Fig. 3a). However, when the solid sample was obtained by drying the suspension at room temperature, the efficiency of the energy transfer decreased dramatically, with only a small emission corresponding to fluorescence of Rh6G and NB (Fig. 3a).

To assess whether the differences in the emission from the two samples were related to structural changes induced by the drying method, we carried out scanning electron microscopy (SEM) analysis of the monoliths prepared by the two different approaches. This analysis revealed that the slow drying (at room temperature) induces a very homogeneous structure (Fig. 3b), whereas the faster drying (evaporation at 40 °C) leads to nanoparticle agglomeration and a nanostructured and heterogeneous system (Fig. 3c). Better quality and higher-resolution SEM images could not be obtained because the voltage required to do so led to clear sample degradation and modification as a result of the 'soft' nature of the polymeric nanoparticles.

This correlation can be understood in a random lasing picture. In random lasers, feedback is not provided by external means (defined cavity), but by multiple scattering inside the laser medium[25]. Incoherent random lasers, in which there is only intensity or energy feedback[26], demonstrate a smooth spectral shape that is characteristic of amplified spontaneous emission (ASE) reinforced by the enlarged optical path induced by the scattering. Coherent random lasers, in which there is field or amplitude feedback[26], have similar ASE spectra, but superimposed with multiple very narrow spikes associated with spatially extended lasing modes[27]. In our fast-dried sample, the scattering strength due to induced disorder is much higher than in the ambient-dried one due to the presence of nanoparticle aggregation; accordingly, the stimulated emission in the fast-dried sample will be reinforced by light scattering, with random lasing taking place. Taking into account that the emission spectra of this sample show no spikes, the random

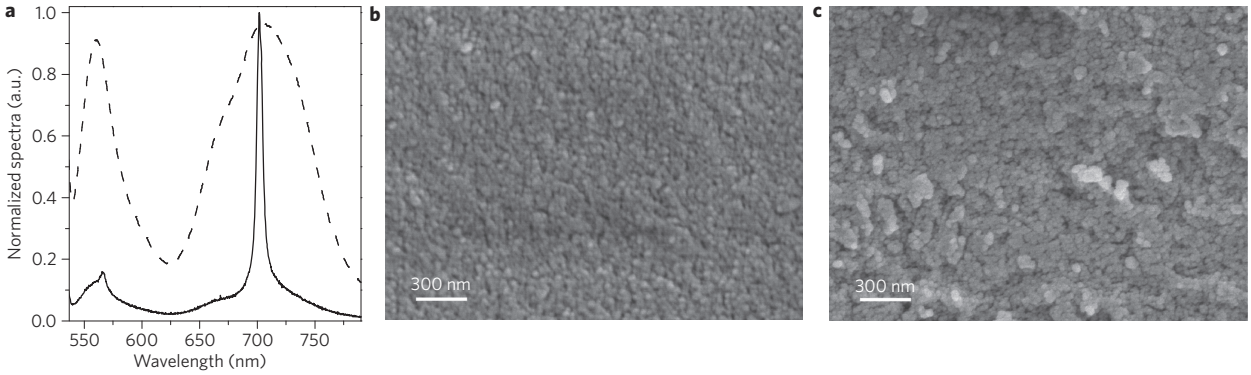

Figure 3 | FRET-assisted incoherent random lasing. a, Normalized emission spectra from oven-dried (solid line) and ambient-dried (dashed line) latex nanoparticle thin films containing a mixture of Rh6G/NB (0.28/0.19 wt%) with front-face pumping at 490 kW cm^{-2}. **b**, FESEM photograph of ambient-dried sample. **c**, FESEM photograph of oven-dried sample.

system would be acting in an incoherent regime. This result represents the first demonstration of FRET-assisted incoherent random lasing from solid samples of dye-doped latex nanoparticles, and shows the importance of the drying process in influencing emission properties.

In view of these results it is clear that a deeper study of the random laser properties of this type of sample, as well as the influence of structural properties, is needed. This work is under way in our laboratories and will be published elsewhere.

Conclusion

For the first time, we have demonstrated that the confinement into subwavelength nanoparticles of laser dyes undergoing FRET may significantly enhance the laser efficiency and photostability of red-emitting laser dyes pumped at 532 nm. Carefully selected mixtures of Rh6G and NB have been used in the present study, but this approach may be extended to other donor/acceptor pairs, as has been proved with Rh6G and Ox720. A thorough photophysical study has shown that the energy transfer in the confined Rh6G/NB system takes place predominantly via FRET, but backed up by RET processes. It has also revealed that the latex nanoparticles have an unexpected core/thin shell morphology. Finally, unprecedented FRET-assisted incoherent random lasing has been observed in solid samples obtained by evaporation of the colloidal suspensions. In conclusion, our approach provides a facile and cost-effective strategy to overcome the inherent low visible absorption and poor photostability problems associated with commercial red-emitting laser dyes, avoiding the need to resort to specially engineered expensive dyes.

Methods

Materials and synthesis procedures. MMA (Aldrich, 99%) was purified with a 0.1 M sodium hydroxide solution to remove inhibitor. HEMA (Aldrich, 97%), GMA (Fluka, 97%), potassium persulfate (Sigma, 99%), sodium dodecylsulphate (SDS) (Sigma, 99%), Rhodamine 6G and Nile Blue (Exciton, laser grade) were used without further purification. Deionized water was obtained from Direct QTM 5 Millipore. Dye-doped polymeric nanoparticles were prepared by batch dispersion polymerization of MMA:HEMA:GMA monomers[18], introducing a monomer mixture feed with a weight ratio 67:22:11 of those monomers into the reactor, together with dye and sodium dodecylsulphate (SDS) as colloidal stabilizer. The polymerization temperature was 65 °C and the monomer content in the feed was 7% wt of the total mass of the suspension. Free radical polymerization was initiated by a water-soluble initiator, by adding 0.5% wt of potassium persulphate (KPS) with respect to the monomer present in the feed. The donor/acceptor wt% loadings in the nanoparticles against monomer feed ranged from 0.36/0.12 wt% (3/1) to 0.23/0.35 wt% (1/1.5) for the Rh6G/NB system. For comparison purposes, nanoparticles doped with only donor (Rh6G, 0.24 wt%) and only acceptor (NB, 0.15 wt%) were also prepared.

Analytical methodology. The hydrodynamic diameters of the nanoparticles were measured by dynamic light scattering (DLS) with a 90 Plus particle analyser (Brookhaven Instruments). A qualitative indicator of particle size distribution is the relative standard deviation; values smaller than 0.1 were indicative of a fairly monodisperse samples, as verified by calibration latexes. The size distribution by volume of the sensitized nanospheres was centred at 48–50 nm and had a relative standard deviation of 0.11–0.12. The morphology and microscopic structures of the latex monoliths were observed using field-emission scanning electron microscopy (FESEM, JEOL, JSM-6700F) with an acceleration voltage of 5 kV and an emission current of 10 mA. The samples were fragments of thin films obtained after drying the suspension in an oven at 40 °C and at room temperature.

Photophysical properties. The photophysical properties were registered both in diluted aqueous suspensions (optical pathway, 1 cm; right angle) and in concentrated aqueous suspensions (optical pathway, 0.1, 0.01 and 0.001 cm; front-face configuration) of latex nanoparticles doped with only Rh6G, only NB, and with a mixture of both dyes in a 1.5:1 ratio. The diluted suspensions ($\sim 3 \times 10^{-6}$ M) were obtained by diluting the original suspensions ($\sim 3 \times 10^{-4}$ M) to a latex content of 0.03–0.04 wt%. UV–vis absorption and fluorescence spectra were recorded on a Cary 4E spectrophotometer and on a SPEX Fluorolog 3-22 spectrofluorimeter, respectively. The absorption spectra were recorded using a blank suspension of latex in water as reference. Fluorescence quantum yields (ϕ) were evaluated from corrected spectra, using a diluted solution (1×10^{-6} M) of Rh6G dye in water ($\phi = 0.59$) as reference[28]. Radiative decay curves were registered using the time-correlated single-photon timing technique (Edinburgh Instruments, model FL920), provided with a microchannel plate (Hamamatsu C4878). Fluorescence emission was monitored at the maximum emission wavelength after excitation at 470 nm by means of a diode laser (PicoQuant, model LDH470) for Rh6G and a 600 nm LED for NB. The corrected fluorescence spectra from reabsorption/re-emission phenomena were obtained by means of a mathematical method as detailed in ref. 29. The fluorescence lifetime τ was obtained from the slope after deconvolution of the instrumental response signal from the recorded decay curves using an iterative method. The goodness of the exponential fit was controlled by statistical parameters (χ^2, Durbin–Watson and analysis of the residuals).

Laser properties. Colloidal suspensions of nanoparticles incorporating dyes as well as solutions of dyes in ethanol were contained in quartz cells (optical path, 1 cm), which were carefully sealed to avoid solvent evaporation. The samples were transversely pumped at 532 nm with 5.5 mJ, 6 ns FWHM pulses from a frequency-doubled Q-switched Nd:YAG laser (Monocrom STR-2+) at a repetition rate of 10 Hz. The exciting pulses were line-focused onto the front face of the cell, providing pump fluences on the active medium of 180 mJ cm^{-2}. The oscillation cavity (length, 2 cm) consisted of a 90% reflectivity aluminium plane mirror, with the end lateral face of the cell as output coupler. Details of the experimental set-up can be found elsewhere[20]. The photostability of the gain medium was evaluated by irradiating (under lasing conditions) 10 μl of the colloidal suspension of nanoparticles incorporating the dyes or 10 μl of the dye solution in ethanol. The solutions and suspensions were contained in cylindrical Pyrex tubes (height, 1 cm; inner diameter, 1 mm) that were carefully sealed. Sample photolysis was monitored by recording the LIF emission from the dye solutions and suspensions in the tubes; these were placed horizontally and excited along the axis using the same pump pulses from the Nd:YAG laser used for producing dye laser emission, as a function of the pump pulses, at a repetition rate of 10 Hz. LIF was monitored perpendicular to the exciting beam, collected by an optical fibre, imaged onto the input slit of a monochromator (Acton Research), and detected using a charge-coupled device (CCD) (SpectruMM:GS128B) and/or a photomultiplier (Hamamatsu R928). LIF was recorded by feeding the signal to a boxcar (Stanford Research, model 250) to be integrated before being digitized and processed by a computer. Each measurement was repeated at least three times. The estimated error of the energy measurements was 10% and the experimental error in the photostability measurements was estimated to be on the order of 7%. The solid samples were pumped at 532 nm with 20 ns FWHM pulses from a frequency-doubled Q-switched Nd:YAG laser (Lotis TII SL-2132) at a repetition rate of 15 Hz. The pump radiation was horizontally polarized and focused onto the sample with a spherical quartz lens ($f = 15$ cm), at an angle of incidence of 34° with respect to the normal to the surface of the film. The spot on the surface of the sample was elliptical, with major and minor axis of 2 mm and 1.6 mm, respectively, resulting in a pump intensity of 490 kW cm^{-2}. An optical fibre, placed normal to the sample, collected the surface emission, which was detected and analysed with the same monochromator/CCD/boxcar system described above.

Received 13 February 2012; accepted 4 July 2012; published online 19 August 2012

References

1. Duarte, F. J. & Hillman, L. W. (eds) *Dye Laser Principles* (Academic, 1990).
2. Duarte, F. J. (ed.) *Tunable Lasers Handbook* (Academic, 1995).
3. Duarte, F. J. (ed.) *Tunable Lasers Applications* (CRC, 2009).
4. Steiner R. in *Applied Laser Medicine* (eds Berlien, H. P. & Müller, G. H.) 101–106 (Springer-Verlag, 2003).
5. Backmann, U. (ed.) *Lambdachorme Laser Dyes* (Lambda Physik, 2000).
6. Förster, T. Zwischenmolekulare energiewanderung und fluoreszenz. *Ann. Phys. (Leipz.)* **2,** 55–75 (1948).
7. Förster, T. Experimentelle und theoretische Untersuchung des zwischenmolecularen Uebergangs von Electronenanregungsenergie. *Z. Naturforsch.* **4A,** 321–327 (1949).
8. Tcherkasskaya, O., Spiro, J. S., Ni, S. & Winnick, A. Energy transfer in restricted geometry: polyisoprene-poly(methyl methacrylate) block copolymer. *J. Phys. Chem.* **100,** 7114–7121 (1996).
9. Scott, B. J., Bartl, M. H., Wirnsberger, G. & Stucky, G. D. Energy transfer in dye-doped mesostructured composites. *J. Phys. Chem. A* **107,** 5499–5502 (2003).
10. Li, K. J., Oh, J. H., Kim, Y. & Jang, J. Macroscopic parallel nanocylinder array fabrication using a simple rubbing technique. *Adv. Mater.* **18,** 2213–2215 (2006).
11. Farinha, J. P. S. & Martinho, J. M. G. Resonance energy transfer in polymer nanodomains. *J. Phys. Chem. C* **112,** 10591–10601 (2008).
12. Lei, J., Wang, L. & Zhang, J. Radiometric pH sensor based on mesoporous silicananoparticles and Förster resonance energy transfer. *Chem. Commun.* **46,** 8445–8447 (2010).
13. Sen, T., Jana, S., Koner, S. & Patra, A. Efficient energy transfer between confined dye and Y-zeolite functionalized Au nanoparticles. *J. Phys. Chem. C* **114,** 19667–19672 (2010).
14. Ma, C., Zeng, F., Huang, L. & Wu, S. FRET-based radiometric detection system for mercury ions in water with polymeric particles as scaffolds. *J. Phys. Chem. B* **115,** 874–882 (2011).

15. Guo, D., Knight, T. E. & McCusker, J. K. Angular momentum conservation in dipolar energy transfer. *Science* **334,** 1684–1687 (2011).
16. Wang, L., Liu, Y., Chen, F., Zhang, J. & Anpo, M. Manipulating energy transfer processes between rhodamine 6G and rhodamine B in different mesoporous hosts. *J. Phys. Chem. C* **111,** 5541–5548 (2007).
17. Wu, C., Zheng, Y., Szymanski, C. & McNeill, J. Energy transfer in a nanoscale multichromophoric system: fluorescent dye-doped conjugated polymer nanoparticles. *J. Phys. Chem. C* **112,** 1772–1781 (2008).
18. Enciso, E., Costela, A., García-Moreno, I., Martín, V. & Sastre, R. Conventional unidirectional laser action enhanced by eye confined in nanoparticles scatters. *Langmuir* **26,** 6154–6157 (2010).
19. Martín, V. *et al.* Photophysical and lasing properties of rhodamine 6G confined in polymeric nanoparticles. *J. Phys. Chem. C* **115,** 3926–3933 (2011).
20. Costela, A., García-Moreno, I. & Sastre, R. Polymeric solid-state dye lasers: recent developments. *Phys. Chem. Chem. Phys.* **5,** 4745–4763 (2003).
21. Lakowicz, J. R. (ed.) *Principles of Fluorescence Spectroscopy* (Kluwer Academic/Plenum, 1999).
22. Yekta, A., Winnik, M. A., Farinha, J. P. S. & Martinho, J. M. G. Dipole–dipole electronic energy transfer. Fluorescence decay functions for arbitrary distributions of donors and acceptors. II. Systems with spherical symmetry. *J. Phys. Chem. A* **101,** 1787–1792 (1997).
23. Farinha, J. P. S., Charreyre, M-T., Martinho, J. M. G., Winnik, M. A. & Pichot, C. Picosecond fluorescence studies of the surface morphology of charged polystyrene latex particles. *Langmuir* **17,** 2617–2623 (2001).
24. Barberan-Santos, M. N., Nunes Pereira, E. J. & Martinho, J. M. G. Stochastic theory of combined radiative and nonradiative transport. *J. Chem. Phys.* **107,** 10480–10484 (1997).
25. Wiersma, D. S. The physics and applications of random lasers. *Nature Phys.* **4,** 359–367 (2008).
26. Cao, H. Lasing in random media. *Waves Random Media* **13,** R1–R39 (2003).
27. Andreasen, J. *et al.* Modes of random lasers. *Adv. Opt. Photon.* **3,** 88–127 (2011).
28. Lopez Arbeloa, F., Lopez Arbeloa, T. & Lopez Arbeloa, I. in *Handbook of Advances Electronic and Photonic Materials and Devices* Ch. 5 (Academic, 2001).
29. López Arbeloa, I. Fluorescence quantum yield evaluation: corrections for re-absorption and re-emission. *J. Photochem.* **14,** 97–105 (1980).

Acknowledgements

This work was supported by the Spanish MICINN (projects TRACE2009-0144, MAT2010-20646-C04-01, MAT2010-20646-C04-04 and MAT2007-65711-C04-02). The authors thank Gobierno Vasco (IT339-10) and Universidad Complutense/Banco Santander (grant no. 921556) for financial support. L.C. thanks MICINN for a predoctoral scholarship (FPI, co-financed by Fondo Social Europeo). The authors also acknowledge technical assistance from the ICTS Microscopy National Center (UCM).

Author contributions

L.C. conducted the theoretical FRET analysis and solid sample measurements. E.E. proposed the study of FRET phenomenology in nanoparticles, synthesized the particles and helped with the theoretical FRET analysis. V.M. contributed with sample preparation. J.B. and I.L.-A. conducted the photophysical studies. A.C. supervised and coordinated the project. I.G.-M. conducted the laser measurements and supervised and coordinated the project. L.C. and I.G.-M. coordinated the manuscript preparation. All authors contributed to writing the paper.

Additional information

Supplementary information is available in the online version of the paper. Reprints and permission information is available online at http://www.nature.com/reprints. Correspondence and requests for materials should be addressed to L.C.

Competing financial interests

The authors declare no competing financial interests.

nature photonics

SUPPLEMENTARY INFORMATION

DOI: 10.1038/NPHOTON.2012.201

Supplementary Information

to

FRET Assisted Laser Emission in Colloidal Suspensions of Dye-Doped Latex Nanoparticles

Luis Cerdán[1], Eduardo Enciso[2], Virginia Martín[1], Jorge Bañuelos[3], Iñigo López-Arbeloa[3], Angel Costela[1], and Inmaculada García-Moreno[1]*

[1] *Instituto de Química Física "Rocasolano", CSIC-Consejo Superior de Investigaciones Científicas, Serrano 119, 28006, Madrid, Spain.*

[2] *Facultad de Ciencias Químicas, Universidad Complutense de Madrid, Av. Complutense s/n, 28040, Madrid, Spain.*

[3] *Facultad de Ciencias y Tecnologías, Universidad del País Vasco/EHU,. Apdo. 644, 48080, Bilbao, Spain.*

**e-mail: lcerdan@iqfr.csic.es*

Supplementary Figures to 'Photophysical study of colloidal suspensions'

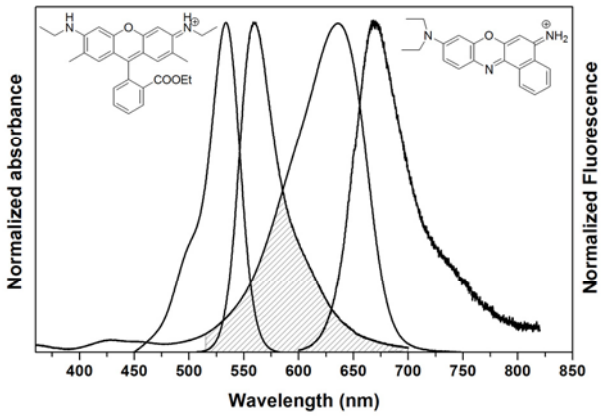

Figure S1.- Spectral overlap of donor and acceptor Absorption and fluorescence spectra of colloidal suspensions of latex nanoparticles doped with Rh6G alone (0.34 wt % against monomer) and NB alone (0.15 wt % against monomer). The stripped region accounts for the spectral overlap between the Rh6G emission and the NB absorption.

DOI: 10.1038/NPHOTON.2012.201

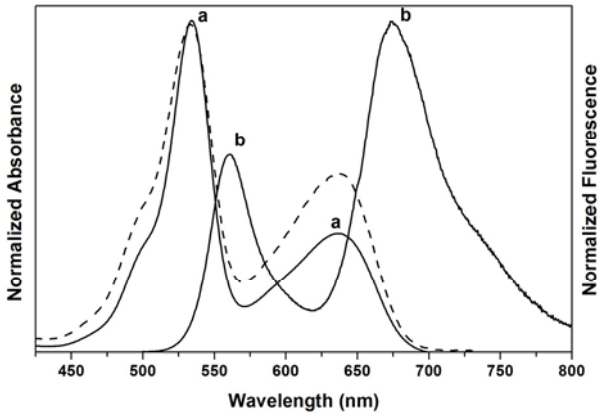

Figure S2.- Spectral response of mixed donor and acceptor Normalized absorption (a), fluorescence (b) and excitation (dashed) spectra of a colloidal suspension of Rh6G and NB (0.28 and 0.19 wt % against monomer, respectively) enclosed in latex nanoparticles (6.7 wt %).

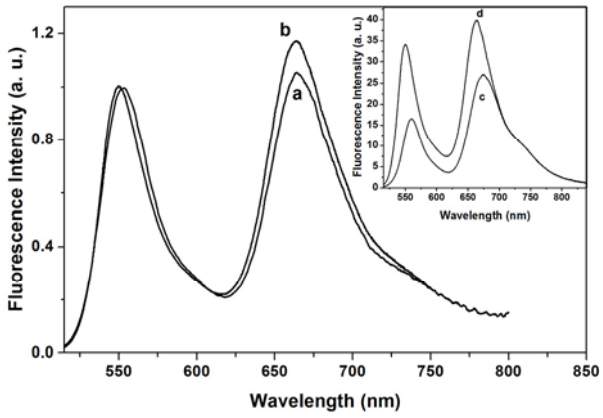

Figure S3.- Effect of radiative transfer processes on fluorescence emission Normalized fluorescence (to the donor emission) of the latex suspension of Rh6G and NB at low (a, 3×10^{-6} M) and high (b, 3×10^{-4} M) dye concentration, recorded with a 0.1 cm optical pathway cuvette and corrected from the reabsorption/reemission phenomena processes. Inset; fluorescence spectra of the concentrated sample before (c) and after (d) the mathematical correction.

Supplementary Text to 'Theoretical analysis of FRET decay curves'

From the previous photophysical characterization very interesting and useful information may be obtained about the FRET process within the latex nanoparticles and on the particular inner morphology of these nanoparticles. The FRET rate from an electronically excited donor (D*) to an acceptor (A) separated by a distance *r* is given by [1,2]

$$w(r) = \frac{1}{\tau_D}\left(\frac{R_0}{r}\right)^6 \tag{S1}$$

where τ_D is the donor lifetime in the absence of acceptors and R_0 is the most characteristic FRET parameter, known as Förster radius and defined as the donor-acceptor separation for which the donor emits and transfers (to the acceptor) its energy with the same probability. R_0 depends on the photophysical properties of donor and acceptor and is given by [3]

$$R_0{}^6 = \frac{9000(\ln 10)\kappa^2\phi_f}{128\pi^5 N_A n^4}\int_0^\infty F_D(\lambda)\varepsilon_A(\lambda)\lambda^4 \mathrm{d}\lambda \tag{S2}$$

In Eq. (S2) the integral accounts for the spectral overlap of the normalized donor fluorescence spectrum $F_D(\lambda)$, with the absorption spectrum of the acceptor $\varepsilon_A(\lambda)$ ($M^{-1}cm^{-1}$). ϕ_f and *n* are the fluorescence quantum yield of the donor in the absence of acceptors and the refractive index of the host medium, respectively, and κ^2 is the orientation factor which accounts for the relative orientation of donor and acceptor transition dipole moments in the host medium.

On the other hand, the efficiency of the FRET process in the latex nanoparticles can be obtained from the comparison of the fluorescence decay curves of the donor in the absence ($I_f^D(t)$) and presence ($I_f^{D+A}(t)$) of acceptors as [4]

$$\phi_{FRET} = 1 - \frac{\int_0^\infty I_f^{D+A}(t)\mathrm{d}t}{\int_0^\infty I_f^{D}(t)\mathrm{d}t} \tag{S3}$$

In the photophysical characterization of the latex nanoparticles, $I_f{}^D(t)$, $I_f{}^{D+A}(t)$, $F_D(\lambda)$, $\varepsilon_A(\lambda)$, τ_D and ϕ_f have been obtained. Taking into account that the mixture MMA/HEMA/GMA has a refractive index n~1.5 and assuming κ^2~2/3 (isotropic dynamic averaging), one obtains a Förster radius R_0 = 33 Å and a FRET quantum yield ϕ_{FRET} = 0.77, both data being consistent with an efficient FRET system.

In spite of this, the laser spectra in these samples (Fig. 1a) suggest that the energy transfer efficiency is much higher (0.98) than this value of ϕ_{FRET}, since the efficiency of the suspension containing only Rh6G is 30%, whereas the contribution of the Rh6G emission to the efficiency of the suspension with both Rh6G and NB (13%) is just a 0.6% (determined as $\int I_L(\lambda)hc/\lambda \mathrm{d}\lambda$, integrated over the Rh6G contribution to the laser spectrum $I_L(\lambda)$ normalized so that $\int I_L(\lambda)hc/\lambda \mathrm{d}\lambda$, integrated over all wavelengths, is 13%, with *h* being the Plank constant and *c* the speed of light in vacuum). This fact agrees with the conclusion from the photophysical dependence of the confined donor/acceptor system on the dye concentration in the suspensions. Since both FRET and RET processes are taking place simultaneously, the final energy transfer efficiency is increased.

The donor and acceptor distributions within the latexes may affect the lasing performance in these systems. Thus, it is important to determine these particular distributions in order to correlate nanoparticle morphology with laser performance. As mentioned above, the latexes are composed by a mixture of polymers (MMA/HEMA/GMA), whose proportion across the nanoparticle is unknown. This inner morphology determines the dye distribution within the nanoparticle, since every monomer has a different polarity and, subsequently, a different affinity for the dyes. The fluorescence decay curve of the donor in the presence of acceptors (Fig. 2a) can be used as a tool to determine the distribution of donors and acceptors within the nanoparticle, since the resonance energy transfer is highly dependent on the donor-acceptor distance distribution.[3]

DOI: 10.1038/NPHOTON.2012.201

To have a reference and starting point, the fluorescence decay measurements in our latex nanoparticles were theoretically analyzed following the expressions developed by Martinho's group [3,5,6] for FRET processes in systems with spherical symmetry. In their theoretical treatment,[5] the fluorescence decay curve depends on R_0, τ_D, nanoparticle radius R_S and the candidate donor and acceptor radial distributions along the nanoparticle radius, $C_D(R)$ and $C_A(R)$, respectively (Eqs. SA1 in Appendix SA). In these equations all parameters are known with the exception of $C_D(R)$ and $C_A(R)$, which should be guessed approximately from the synthesis route.

It is important to state at this point that the slight nanoparticle size polydispersity in the colloidal suspension influenced the results and so it was taken into account in the theoretical simulations by properly modifying all of the models computed in this paper (see Appendix SA).

We began by computing the fluorescence decay curve of the simpler case of a uniform distribution of both donor and acceptor inside the nanoparticles (case F in [5]). This assumption would imply that the nanoparticle consists of a homogeneous and uniform tertpolymer of MMA/HEMA/GMA. Mathematically, $C_D(R) = C_D H(R-R_S)$ and $C_A(R) = C_A H(R-R_S)$, with C_D and C_A the number volume density of donors and acceptors, respectively, $H(R-R_S)$ the Heavyside function and R_S the nanoparticle radius. In this 'Homogeneous Model' the fitting parameter is C_A. As seen in Fig. 2c (Curve I), the fluorescence decay curve computed with the 'Homogeneous Model', considering C_A = 0.0095 nm^{-3}, fitted quite accurately at short times, but deviated from the experimental points for longer times, predicting a quicker deactivation. The lack of agreement of the theoretical predictions with experiment when assuming a homogeneous model indicated that the dye distribution had to be at some extent inhomogeneous.

Our initial guess on the inhomogeneity, taking into account the latex components and synthesis route, was that there would be two different domains within the nanoparticle due to the fact that HEMA is more polar than MMA and GMA, and thus HEMA would tend to be closer to the aqueous solution, i. e., closer to the nanoparticle surface. Since Rh6G and NB are more soluble in HEMA than in MMA and GMA, both dyes would be, consequently, closer to the surface than to the center of the nanoparticle. Then the latexes could be described by a kind of core/shell morphology with a smooth transition from core to shell. Since we still lacked information on the exact $C_D(R)$ and $C_A(R)$ in our latex nanoparticles, a trial and error approach with different core/shell situations had to be followed to simulate the experimental results.

Core/shell type dye distributions were not developed in the followed approach,[5] and so we had to reformulate the treatment with new expressions for $C_D(R)$ and $C_A(R)$. To model FRET in a core/shell nanoparticle with a smooth transition from core to shell is a difficult task, since the particular transition function is completely unknown. But for our purposes it was enough to consider core/shell models with step functions for the distributions of donors and acceptors. The most general distribution functions for this type of systems would be $C_{D,A}(R) = C^S_{D,A}H(R-R_S) - (C^S_{D,A}-C^C_{D,A})H(R-R_C)$, where $C^S_{D,A}$ and $C^C_{D,A}$ are the number density of donor and acceptor in the shell (S) and the core (C), respectively, and R_C is the core radius. In fact, it is simply a combination of two homogeneous models, one with nanoparticle radius R_S and concentration $C_{D,A}{}^S$, and the other with nanoparticle radius R_C and concentration $(C^S_{D,A}-C^C_{D,A})$. We substituted the new expressions for $C_D(R)$ and $C_A(R)$ into Eqs. A1, and found that the fluorescence decay curve in a core/shell nanoparticle is given by

$$I_D(R_S,t) \propto \exp\left\{-\frac{t}{\tau_D}\right\}\left[\int_0^{R_S} \mathrm{d}R\, R^2 \exp\{-g_1(R,t)\} - \left(1-\frac{C_D^C}{C_D^S}\right)\int_0^{R_C} \mathrm{d}R\, R^2 \exp\{-g_2(R,t)\}\right] \quad \text{(S4)}$$

The expressions for the functions $g_1(R,t)$ and $g_2(R,t)$ in Eq. (S4) can be found in Appendix SB. Interestingly, Eq. (S4) does not depend on the exact value of C_D, $C_D{}^S$ or $C_D{}^C$, but on the particular ratio C^C_D/C^S_D. Then, Eq. (S4) (together with Eqs. SB1b and c) has four fitting parameters (C^C_D/C^S_D, C^S_A, C^C_A, and $f = (R_S-R_C)/R_S$). For simplicity we considered that the shell/core concentration ratio is the same for both dyes, i. e., $C^C_A/C^S_A = C^C_D/C^S_D$, which implies that both dyes have similar affinities for a given monomer. This is, actually, a fair assumption, since both dyes are cationic. This constraint leads to a system with three degrees of freedom. On the other hand, the total acceptor number density C_A within the nanoparticle is given by $C_A = C^C_A V_C/V_T + C^S_A V_S/V_T$, where V_C, V_S and V_T are the core, shell and whole nanoparticle volumes,

respectively. For convenience we chose C^C_A, f and C_A, instead of C^S_A, as degrees of freedom. Once C^C_A, f and C_A are known C^S_A is calculated as

$$C_A^S = \frac{C_A - C_A^C(1-f)^3}{1-(1-f)^3} \tag{S5}$$

It is worth noticing that when f exactly equals 0 or 1, one recovers the 'Homogeneous Model' (Case F in [5]).

To fit Eq. S4 to the experimental data is too computationally expensive as to perform the optimization process, since the problem has three degrees of freedom. We tried some particular cases to see how the predicted fluorescence decay curve behaved when changing C_A, C^C_A, and f in a controlled way. In this trial and error procedure we observed that the 'Core/Shell Model' fitted better and better as $f\to 0$, but the integration steps needed to accomplice the desired accuracy should be shortened, increasing even more the computational time.

In order to avoid this extensive computation we tried a different approach in the integration. As $f\to 0$ the shell might be approximated by a surface. Surface distributions were worked in [5] (Cases B, C and E), under the following considerations: a) both donor and acceptor only in the surface (surface-to-surface FRET), b) donor in the surface and acceptor inside (surface-to-inside FRET) and c) acceptor in the surface and donor inside (inside-to-surface FRET). However, the particular case in which both donors and acceptors are present simultaneously, albeit in different proportions, in the surface and inside the nanoparticle (core/surface model) was not treated, and hence it had to be reformulated by us. To work this problem the distributions of dyes in the nanoparticle were considered to be $C_{D,A}(R) = C^S_{D,A}\delta(R-R_S) + C^C_{D,A}H(R-R_S)$, where $\delta(R-R_S)$ is the Dirac delta function. These distributions imply, in certain way, a combination of cases B, C, E and F in reference 5. We substituted $C_D(R)$ and $C_A(R)$ into Eqs. SA1 and found that the expression for the fluorescence decay curve in a core/surface nanoparticle is given by

$$I_D(R_S,t) \propto \exp\left\{-\frac{t}{\tau_D}\right\}\left[\exp\left\{-\left(g_1(t)+g_2(t)\right)\right\}+ \right.$$
$$\left. + \frac{C_D^C}{C_D^S}\int_0^{R_S} \mathrm{d}R\, R^2 \exp\left\{-\left(g_3(R,t)+g_4(R,t)\right)\right\}\right] \tag{S6}$$

where $g_1(t)$ corresponds to the $g(t)$ in the surface-to-surface FRET (Case B in [5]), $g_2(t)$ to the surface-to-inside FRET (Case C in [5]), $g_3(R,t)$ to the inside-to-surface FRET (Case E in [5]), and finally $g_4(R,t)$ to the inside-to-inside FRET (Case F in [5]). In this 'Core/Surface Model' expression $C^S_{D,A}$ are the number surface density of dyes in the nanoparticle, whereas $C^C_{D,A}$ are still number volume densities. Eq. S6 (together with the g functions shown in [5]) has three degrees of freedom (C^C_D/C^S_D, C^S_A, and C^C_A). We observed that the fit was almost independent on C^C_D/C^S_D and, hence, we considered again $C^C_A/C^S_A = C^C_D/C^S_D$ without loss of generality. This constraint leaves the system with two degrees of freedom. On the other hand, the total acceptor concentration is given by $C_A = C^C_A V_C/V_T + C^S_A S_S/V_T$, where V_C and V_T are the core and whole nanoparticle volumes, respectively, and S_S is the nanoparticle surface area. We assumed that all of the nanoparticles have the same morphology independently of their size, i. e., they have the same C^S_A, and C^C_A. Then we chose C^S_A and C^C_A as degrees of freedom, leaving C_A constrained as

$$C_A = \frac{3C_A^S}{R_S} + C_A^C \tag{S7}$$

As we have mentioned above, the suspensions had a certain nanoparticle size (R_S) distribution with a mean radius $R_S^{mean} = 24.6$ nm, meaning that, according to Eq. (S7), they have a C_A distribution with mean $C_A^{mean} = C_A(R_S^{mean})$.

As seen in Fig. 2c (Curve II), the fluorescence decay curve computed with this 'Core/Surface Model', with fitting parameters $C_A^{mean}\sim 0.0064$ nm^{-3}, $C^C_A\sim 0.0028$ nm^{-3}, and $C^S_A\sim 0.029$ nm^{-2}, gave a much better fit to the experimental data than the 'Homogeneous Model' (Curve I). The predicted value for the total acceptor concentration within the nanoparticle $C_A^{fit} = C_A^{mean}\sim 0.0064$ nm^{-3} is somewhat higher than the expected (experimental) one $C_A^{exp}\sim 0.0043$ nm^{-3}. We are currently unaware of the exact origin of this discrepancy, but it might come from an artifact in the core/surface

DOI: 10.1038/NPHOTON.2012.201

approximation and/or, most probably, from an underestimation of C_A^{exp}, which would imply an overestimation of C_A^{fit}, giving place to the observed discrepancy. The exact C_A^{exp} cannot be extracted directly from the synthesis route, but it has to be roughly estimated indirectly from the absorption spectra and the nanoparticle content in the colloidal suspension. Thus, an underestimated C_A^{exp} would lead to an underestimated $\varepsilon_A(\lambda)$ and, according to Eq. (S2), to an underestimated R_0, which would be directly translated into the overestimated C_A^{fit}. It is worth noticing that a change in R_0 from 33 Å to 38 Å, just a 14%, could account for the observed discrepancy. The fit would be probably much better and discrepancy much lower with the more rigorous 'Core/Shell Model'.

The above discussion indicates that the actual distribution of donor and acceptor within the nanoparticle is an intermediate situation in between a core/shell distribution and a core/surface one, i. e., the nanoparticles would possess a core/shell type morphology with a very thin shell. The 'Core/Surface Model' (or 'Core/Very Thin Shell Model') interpretation would be consistent with the following nanoparticle morphology: a) the core would consist of a homogeneous tertpolymer of MMA/HEMA/GMA, in which both donors and acceptors are homogeneously and uniformly solved with densities C^C_D and C^C_A. b) The surface (or very thin shell) would be formed by the so-called nanoparticle 'hairy layer' (surface roughness or fuzziness [6]), in which both donors and acceptors would be adsorbed with surface densities C^S_D and C^S_A. Since we have used an anionic surfactant (SDS) in the synthesis, the 'hairy layer', formed by the tertpolymer/surfactant/water interfacial layer, would have a certain negative charge distribution. Hence, cationic dyes such as Rh6G (donor) and NB (acceptor) would be adsorbed on the anionic surface with the very same distribution.

Appendix SA: FRET general analysis and polydispersity treatment

The general expression for the fluorescence decay curve of a donor (Rh6G) in the presence of acceptors (NB) in systems with spherical symmetry (latex nanoparticles of radius R_S) undergoing FRET processes is given by [13]

$$I_D(R_S,t) \propto \exp\left\{-\frac{t}{\tau_D}\right\}\int_0^\infty \mathrm{d}R\, R^2 C_D(R) \exp\{-g(R,t)\} \tag{SA1a}$$

$$g(R,t) = 4\pi\int_0^\infty \mathrm{d}r\, r^2 \langle C_A(R,r)\rangle \left[1-\exp\left\{-\frac{t}{\tau_D}\left(\frac{R_0}{r}\right)^6\right\}\right] \tag{SA1b}$$

$$\langle C_A(R,r)\rangle = \frac{1}{2rR}\int_{|R-r|}^{(R+r)} \mathrm{d}R'\, R'\, C_A(R') \tag{SA1c}$$

For details on notation refer to [5].

Our samples have a slight nanoparticle size polydispersity given by the log-normal distribution

$$\varphi(R_s) = \frac{2.43}{\sqrt{2\pi}R_S w}\exp\left\{-\frac{\left(\ln\left(R_S / R_S^{mean}\right)\right)^2}{2w^2}\right\} \tag{SA2}$$

with R_S^{mean} = 24.6 nm and w = 0.3. $\varphi(R_S)$ is normalized so that $\Sigma\varphi(R_S)$= 1. The nanoparticles with a size R_S have a contribution to the total fluorescence decay curve $I_D(t)$ of $I_D(R_S,t)$ weighted by $\varphi(R_S)$. Then, $I_D(t)$ is calculated as:

$$I_D(t) = \sum_1^n \varphi(R_S) I_D(R_S,t) \tag{SA3}$$

For our purposes it is enough to use $\varphi(R_S)$ divided into n=20 segments with 9nm<R_S<55nm and, so that $\varphi(R_S$=9nm$)$=0.0013 and $\varphi(R_S$=9nm$)$=0.0015, as compared to max[$\varphi(R_S)$]=0.136.

In order to compare the theoretical predictions on the fluorescence decay curves $I_D(t)$, with the experimental ones $I_{exp}(t)$, $I_D(t)$ was convoluted with the instrument response function $L(t)$, so that:

$$I_{\exp}(t) = L(t) \otimes I_D(t) \tag{SA4}$$

Appendix SB: Core/Shell Model FRET expressions

The dye distribution in a generic Core/Shell nanoparticle is given by $C_{D,A}(R) = C^S_{D,A}H(R-R_S)-(C^S_{D,A}-C^C_{D,A})H(R-R_C)$, where $C^S_{D,A}$ and $C^C_{D,A}$ are the number density of donor and acceptor in the shell (S) and the core (C), respectively, and R_C is the core radius. Substitution of this expression into Eqs. SA1 leads to:

$$I_D(R_S,t) \propto \exp\left\{-\frac{t}{\tau_D}\right\}\left[C_D^S \int_0^{R_S} \mathrm{d}R\, R^2 \exp\left\{-\left(g_1(R,t)-g_2(R,t)\right)\right\} - \left(C_D^S - C_D^C\right)\int_0^{R_C} \mathrm{d}R\, R^2 \exp\left\{-\left(g_1(R,t)-g_2(R,t)\right)\right\}\right] \tag{SB1a}$$

$$g_1(R,t) = 4\pi C_A^S \int_0^{R_S-R} \mathrm{d}r\, r^2\left[1-\exp\left\{-\frac{t}{\tau_D}\left(\frac{R_0}{r}\right)^6\right\}\right] + \frac{\pi C_A^S}{R}\int_{(R_S-R)}^{(R_S+R)} \mathrm{d}r\, r\left(R_S^2-(R-r)^2\right)\left[1-\exp\left\{-\frac{t}{\tau_D}\left(\frac{R_0}{r}\right)^6\right\}\right] \tag{SB1b}$$

$$g_2(R,t) = 4\pi\left(C_A^S - C_A^C\right)\int_0^{R_C-R} \mathrm{d}r\, r^2\left[1-\exp\left\{-\frac{t}{\tau_D}\left(\frac{R_0}{r}\right)^6\right\}\right] + \frac{\pi\left(C_A^S - C_A^C\right)}{R}\int_{(R_C-R)}^{(R_C+R)} \mathrm{d}r\, r\left(R_C^2-(R-r)^2\right)\left[1-\exp\left\{-\frac{t}{\tau_D}\left(\frac{R_0}{r}\right)^6\right\}\right] \tag{SB1c}$$

Supplementary text and figures on fluorescence anisotropy measurements

With the aim to assess whether the Rh6G molecules present homo-FRET within the nanoparticles, we have performed fluorescence anisotropy measurements, since it is known that the non-radiative transfer decreases this anisotropy [4]. We have made use of the experimental set-up and treatment used in ref. [7]. According to this formalism, if the emission is isotropic then D_{HV}=1, with D_{HV} being the dichroic ratio (r anisotropy in ref. [4]). If the emission is fully anisotropic D_{HV} will tend to 0 or ∞, depending on the output polarization. We have evaluated two different samples, one with donor alone (Rh6G) to avoid the influence of hetero-FRET (Fig. S4a), and one with both donor (Rh6G) and acceptor (NB) to assess the influence of hetero-FRET on the homo-FRET (Fig. S4b). From Fig. S4a it is evident that the system with only donor indeed presents homo-FRET, since D_{HV} ~1 for the whole range of wavelengths evaluated. Nevertheless, when the acceptor is included, both homo-FRET and hetero-FRET compete, and the contribution of the homo-FRET to the depolarization is somewhat reduced (Fig. S4b), since D_{HV} is significantly lower than 1. The occurrence of this competition is backed up by the fact that the Förster radius (Eq. S2) for homo-FRET and

DOI: 10.1038/NPHOTON.2012.201

hetero-FRET is quite similar, being R_0=3.8 nm and R_0=3.3 nm, respectively, which confer both processes a similar probability to occur. As a final remark on these measurements, to avoid the scattering effects on the anisotropy measurements we have used very dilute colloidal suspensions, in such a way that the scattering is negligible and the environment within the nanoparticle, where the homo-FRET takes place, is kept unchanged.

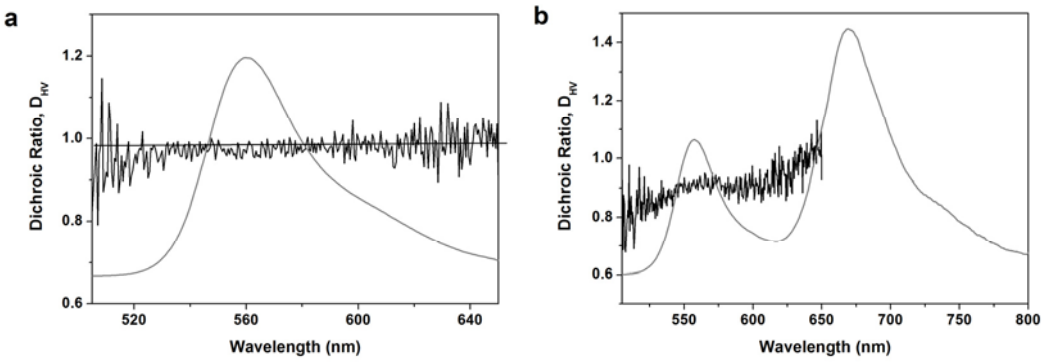

Figure S4.- Fluorescence anisotropy measurements Fluorescence dichroic ratio (corrected for the instrumental isotropic responce) and emission spectrum of colloidal suspensions of latex nanoparticles doped with **a** Rh6G alone (0.34 wt % against monomer) and **b** Rh6G and NB (0.28 and 0.19 wt % against monomer, respectively).

References

[1] Förster, T. Zwischenmolekulare Energiewanderung und Fluoreszenz. *Ann. Phys.* **2**, 55-75 (1948).

[2] Förster, T. Experimentelle und Theoretische Untersuchung des Zwischenmolecularen Uebergangs von Electronenanregungsenergie. *Z. Naturforsch.* **4A**, 321-327 (1949).

[3] Farinha, J. P. S., Martinho, J. M. G. Resonance Energy Transfer in Polymer Nanodomains. *J. Phys. Chem. C* **112**, 10591-10601 (2008).

[4] Lakowicz, J. R., Ed. *Principles of Fluorescence Spectroscopy* (Kluwer Academic/Plenum Publishers, New York, 1999)

[5] Yekta, A., Winnik, M. A., Farinha, J. P. S., Martinho, J. M. G. Dipole-Dipole Electronic Energy Transfer. Fluorescence Decay Functions for Arbitrary Distributions of Donors and Acceptors. II. Systems with Spherical Symmetry. *J. Phys. Chem. A* **101**, 1787-1792 (1997).

[6] Farinha, J. P. S., Charreyre, M.-T., Martinho, J. M. G., Winnik, M. A., Pichot, C. Picosecond Fluorescence Studies of the Surface Morphology of Charged Polystyrene Latex Particles. *Langmuir* **17**, 2617-2623 (2001).

[7] Martínez, V., Salleres, S., Bañuelos, J., López Arbeloa, F. Application of fluorescence with polarized light to evaluate the orientation of dyes adsorbed in layered materials. *J. Fluoresc.* **16**, 233-240 (2006)

Apéndice B

Artículos sobre láseres de colorante en estado sólido como dispositivos integrados

En este apéndice se han incluido todos los artículos utilizados para la discusión del Capítulo 2. Los artículos están ordenados como siguen:

1. L. Cerdán, A. Costela, and I. García-Moreno, "On the characteristic lengths in the variable stripe length method for optical gain measurements," J. Opt. Soc. Am. B 27, 9, 1874–1877 (2010)
2. A. Costela, O. García, L. Cerdán, I. García-Moreno, and R. Sastre, "Amplified spontaneous emission and optical gain measurements from pyrromethene 567-doped polymer waveguides and quasi-waveguides," Opt. Express 16, 10, 7023–7036 (2008). Erratum: Opt. Express 16, 10, 7587–7587 (2008)
3. L. Cerdán, A. Costela, I. García-Moreno, O. García, and R. Sastre, "Waveguides and Quasi-Waveguides based on pyrromethene 597-doped poly(methyl methacrylate)," Appl. Phys. B 97, 73–83 (2009)
4. L. Cerdán, A. Costela, I. García-Moreno, O. García, R. Sastre, M. Calle, D. Muñoz and J. de Abajo, "High-gain long-lived amplified spontaneous emission from dye-doped fluorinated polyimide planar waveguides," Macromol. Chem. Phys. 210, 1624–1631 (2009)
5. L. Cerdán, A. Costela, I. García-Moreno, O. García and R. Sastre, "Laser emission from mirrorless waveguides based on photosensitized polymers incorporating POSS," Opt. Express 18, 10, 10247–10256 (2010)
6. L. Cerdán, A. Costela, G. Durán-Sampedro, I. García-Moreno, M. Calle, M. Juan-y-Seva, J. de Abajo, and G. A. Turnbull, "New perylene-doped polymeric thin films for efficient and long-lasting lasers," J. Mater. Chem. 22, 8938–8947 (2012)
7. L. Cerdán, A. Costela, G. Durán-Sampedro and I. García-Moreno, "Random lasing from sulforhodamine dye doped polymer films with high surface roughness," Appl. Phys. B 108, 839–850 (2012)
8. L. Cerdán, A. Costela, and I. García-Moreno, "Waveguided random lasing in red-emitting-dye-doped hybrid polymer thin films," Org. Electron. 13, 1463–1469 (2012)

Paper B1: J. Opt. Soc. Am. B 27, 9, 1874–1877 (2010)

On the characteristic lengths in the variable stripe length method for optical gain measurements

L. Cerdán, A. Costela, and I. García-Moreno

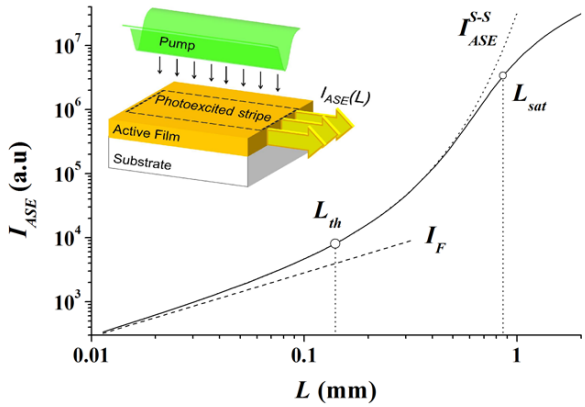

Dependence of ASE intensity (I_{ASE}) on stripe length (L) as described by Eq. (2). I_F and I_{ASE}^{S-S} are representations of Eqs. (4) and (3), respectively. The corresponding lengths L_{th} and L_{sat} are indicated in the graph with hollow points. Inset: Sketch of the VSL method.

On the characteristic lengths in the variable stripe length method for optical gain measurements

L. Cerdán,* A. Costela, and I. García-Moreno

Instituto de Química Física "Rocasolano," CSIC, Serrano 119, 28006 Madrid, Spain
**Corresponding author: lcerdan@iqfr.csic.es*

Received May 3, 2010; revised July 14, 2010; accepted July 15, 2010;
posted July 16, 2010 (Doc. ID 127926); published August 23, 2010

Although the variable stripe length (VSL) method has been widely used to measure the optical gain in thin film active media, different nor totally rigorous criteria have yet been used to estimate two important characterization parameters, namely, threshold and saturation lengths, on which the method critically depends. Here we present a formalism which leads to analytical expressions to rigorously calculate these characteristic lengths from VSL data, providing a unique criterion for the estimation of the amplified spontaneous emission threshold and saturation points. © 2010 Optical Society of America

OCIS codes: 130.2790, 140.3380, 310.6805, 310.6860.

1. INTRODUCTION

The variable stripe length (VSL) method has been revealed in the last few years to be a very useful tool to measure the optical gain in thin film active media [1–4]. Basically the sample is optically pumped with a stripe-shape beam of variable length at constant intensity and the intensity of the edge-emitted amplified spontaneous emission (ASE) is measured as a function of the excitation stripe length. A simple fit of an appropriate expression to the resulting data gives the optical gain as an output parameter. In recent years some works have appeared in which different improvements for the fitting procedure have been suggested [1,2,5–8].

When performing VSL measurements it is very important to properly characterize ASE. In this regard, two important parameters are the threshold (L_{th}) and saturation (L_{sat}) lengths, defined as the stripe lengths for which the ASE threshold and ASE saturation set in, respectively. These lengths establish the range for which the pump to the ASE conversion rate is most efficient and the optical gain values are more accurately calculated.

Many ways of estimating the ASE intensity and length thresholds can be found in the literature, but most of them rely on the visual estimation of a certain change in the emission behavior. The most usual approach has been looking for a change in slope in input-output intensity traces, in which the edge-emitted light is displayed as a function of the pumping intensity [9,10]. In some works the threshold of ASE is considered to set in when the full width at half-maximum (FWHM) of the emission spectrum just begins to drop from the fluorescence one [11]. In other works, it is not until the ASE FWHM reaches half the value of the fluorescence FWHM that it is considered that the threshold for the onset of ASE has been reached [12,13]. In a previous work we have introduced a different approach which relies on a more objective criterion, considering the threshold intensity to be that which makes the net gain $g=0$ [14].

Different strategies have also been used to estimate saturation lengths and intensities. In most previous works the criterion has been looking for the length for which the experimental saturated emission points depart from the ones estimated by the small-signal approximation [9,15]. By using this visual estimation it has been claimed that saturation sets in when the gain-length product $gL_{\mathrm{sat}} \approx 4$. Based on a theoretical analysis Dal Negro *et al.* [7] proposed the criterion $gL_{\mathrm{sat}} \approx 10$ for the onset of saturation. We have recently proposed [14] an objective method for calculating L_{sat}, showing that the gain-length product depends on the pump intensity and tends to reach the value of 8–10 for the higher pump values.

In order to establish a unique criterion for the estimation of the ASE threshold and saturation point, we present in this paper a formalism based on the VSL method which leads to analytical expressions to objectively calculate the characteristic lengths L_{th} and L_{sat}, preventing errors arising from subjective visual estimations, and we show that they depend only on data obtained applying the VSL method. We apply these expressions to appropriate experimental data reported in a previous paper and interpret the obtained results.

2. DERIVATION OF EQUATIONS

We begin by evaluating the propagation of light within an excited region (inset in Fig. 1) whose length is much longer than its width, i.e., it can be treated as a one dimensional amplifier. The growth of the ASE intensity in the excitation direction z taking saturation effects into account reads [1,2]

$$\frac{\mathrm{d}I(\lambda)}{\mathrm{d}z} = \Omega(\lambda) + \frac{\gamma(\lambda)I(\lambda)}{1 + I(\lambda)/I_s(\lambda)} - \alpha(\lambda)I(\lambda), \qquad (1)$$

where $\gamma(\lambda)$ is the gain coefficient, $I_s(\lambda)$ is the saturation

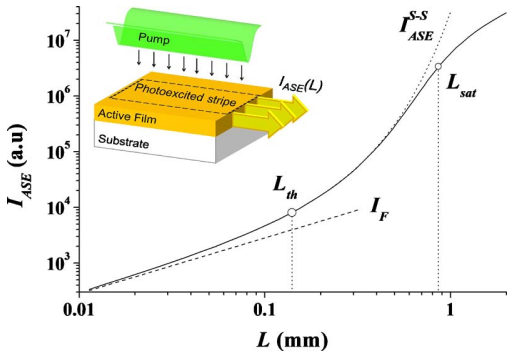

Fig. 1. (Color online) Dependence of ASE intensity (I_{ASE}) on stripe length (L) as described by Eq. (2). I_F and $I_{\mathrm{ASE}}^{\mathrm{S\text{-}S}}$ are representations of Eqs. (4) and (3), respectively. The corresponding lengths L_{th} and L_{sat} are indicated in the graph with hollow points. Inset: Sketch of the VSL method.

intensity, $\alpha(\lambda)$ is the loss coefficient, and $\Omega(\lambda) = \Gamma(\lambda) n \tau^{-1} E(\lambda)$ is the fluorescence growing parameter, where $\Gamma(\lambda)$ is a confinement factor which determines the amount of light trapped in the waveguide, n is the population inversion density, τ is the fluorescence lifetime, and $E(\lambda)$ is the fluorescence spectrum normalized so that $\int E(\lambda)\mathrm{d}\lambda = \varphi$, with φ being the fluorescence quantum yield. Since the VSL method is applied for a single wavelength, generally the one corresponding to the peak emission, and for the sake of notation's simplicity, the λ dependence will be ignored from now on. The integration of this equation, with boundary conditions $I(z=0)=0$ and $I(z=L)=I_{\mathrm{ASE}}(L)$, leads to [1,2]

$$L = \frac{I_{\mathrm{ASE}}(L)/I_s}{g + \Omega/I_s} + \frac{g}{(g + \Omega/I_s)^2} \ln \left| \frac{\Omega + (g + \Omega/I_s) I_{\mathrm{ASE}}(L)}{\Omega} \right|, \tag{2}$$

where L is the stripe length and $g = \gamma - \alpha$ is the net gain. Equation (2) describes the growth of ASE even when saturation sets in. In the small-signal regime ($I_{\mathrm{ASE}}/I_s \ll 1$) Eq. (2) becomes the well-known expression [1,2]

$$I_{\mathrm{ASE}}^{\mathrm{S\text{-}S}}(L) = \frac{\Omega}{g}(e^{gL} - 1). \tag{3}$$

Fluorescence dominates over ASE when the pump length is very short. Then, in the limit of Eq. (3) when $L \to 0$, expanding the exponential term in a Taylor series up to first order in L, it is obtained for the growth of fluorescence that

$$I_F(L) \approx \Omega L. \tag{4}$$

Thus, once one has performed the VSL measurements, g, Ω, and I_s for a fixed wavelength can be determined by plotting the pumped stripe length as a function of the ASE peak intensity and fitting Eq. (2) to the resulting curve. If the gain saturation is not present in the VSL measurements ($I_{\mathrm{ASE}}(L) \ll I_s$), $1/I_s$ can be fixed to zero to facilitate the fitting procedure [16]. Figure 1 shows a log-log plot of the typical behavior of the ASE intensity as a function of the stripe length as described by Eq. (2). For small stripe lengths fluorescence (I_F), characterized by a linear increase [Eq. (4)], dominates the emission. As the excitation length increases, stimulated emission begins to gain weight, and the ASE intensity departs from the behavior of I_F following a superlinear growth [Eq. (3)]. For big enough stripe lengths, saturation sets in and the growing rate diminishes, tending to a linear increase.

Once the equations governing ASE are known, a threshold and saturation criterion must be established. The most accurate criterion for the onset of ASE was established by Peters and Allen [17] who stated "the threshold condition for ASE is realized when a spontaneously emitted photon at one end of the column just induces another at the other end," and defined the threshold length for this to happen as

$$L_{th} = \frac{8\pi\Delta\nu\tau}{n\lambda^2\varphi}, \tag{5}$$

where $\Delta\nu$ is the bandwidth of the fluorescence spectrum, τ is the fluorescence lifetime, λ is the photon wavelength, n is the population inversion density, and φ is the fluorescence quantum yield. Taking into account the dependence of the population inversion on the pump intensity [14], it is seen that L_{th} decreases as the pump intensity increases following a hyperbola. This behavior will be recalled later on in the discussion. It must be stressed that, according to this dependence, it makes no sense to give a value of I_{th} (or L_{th}) without stating the corresponding pumping length (or intensity), as it is usually done in the literature.

In an actual experiment, not just one but many photons do participate, and losses due to scattering or reabsorption are present; thus, the above criterion has to be reinterpreted in the following way: The threshold condition for ASE is realized when the stimulated and the spontaneously emitted photon fluxes are, after losses, equal at the edge of the excitation region. In other words, at threshold the ASE output intensity must be twice the fluorescence:

$$I_{\mathrm{ASE}}^{\mathrm{S\text{-}S}}(L_{th}) = 2I_F(L_{th}). \tag{6}$$

On the other hand, saturation sets in whenever the ASE intensity equals the saturation intensity I_s [14]; hence,

$$I_{\mathrm{ASE}}(L_{\mathrm{sat}}) = I_s. \tag{7}$$

Equations (2)–(4) together with the threshold and saturation criteria given by Eqs. (6) and (7) allow calculating the ASE characteristic lengths. Since saturation is negligible at the ASE threshold, Eq. (3) can be used instead of Eq. (2) in determining L_{th}. Substitution of Eqs. (3) and (4) into Eq. (6) gives the transcendental equation $2gL_{th} = (\exp(gL_{th}) - 1)$, whose only possible solution is

$$gL_{th} \approx 1.256, \tag{8}$$

which provides an easy and universal way to objectively calculate the threshold length L_{th} by simply determining the net gain g by means of Eq. (2) or Eq. (3). Regarding the saturation length, substitution of $L = L_{\mathrm{sat}}$ and $I_{\mathrm{ASE}} = I_s$ into Eq. (2), and taking into account that $gI_s \gg \Omega$, leads to

$$gL_{\mathrm{sat}} \approx 1 + \ln\left(\frac{gI_s}{\Omega}\right), \tag{9}$$

which allows one to objectively obtain L_{sat}, by simply determining g, Ω, and I_s by means of Eq. (2). Hence, Eqs. (8) and (9) show that the characteristic lengths L_{th} and L_{sat} can be easily calculated from the fitting parameters (g, Ω, and I_s) obtained applying the VSL method [Eq. (2) or Eq. (3)], preventing errors arising from visual estimations.

3. APPLICATION TO EXPERIMENTAL DATA

We applied the above treatment to experimental results reported in a previous paper [18], in which gain measurements were carried out in a fluorinated polyimide (6F-6F) waveguide doped with laser dye Pyrromethene 597. VSL measurements were performed at different pump intensities with stripe lengths ranging from 0.5 to 2 mm. The stripe width was fixed at 150 μm to guarantee the accuracy in the application of the one-dimensional model [Eq. (2)]. Accordingly, the VSL parameters g, Ω, and I_s, calculated for the peak emission (gain) wavelength using Eq. (2) and its corresponding fitting procedure, are known. Hence, the threshold and saturation lengths for each of the pump intensities can be calculated using Eqs. (8) and (9). Figure 2 shows the variation of the net gain g, obtained in [18], with the pump intensity [Fig. 2(a)] and the corresponding threshold [Fig. 2(b)] and saturation [Fig. 2(c)] lengths calculated using Eqs. (8) and (9), respectively, with the VSL parameters obtained from [18]. Several features must be highlighted in these plots. Firstly, and the most eye-catching one, is the characteristic behavior of L_{th} [Fig. 2(b)], which follows a shifted hyperbola, indicating that the threshold intensity and length are linked. Consequently, it makes no sense to give a value of I_{th} (or L_{th}) in an ASE experiment without stating the corresponding pumping length (or intensity).

Although Eq. (5) imposes L_{th} to have an asymptote at $I_{\mathrm{pump}}=0$, Fig. 2(b) shows that this vertical asymptote is shifted to 67 kW/cm^2. This discrepancy appears because in Eq. (5) losses are not taken into account, which effectively rise the pump intensity needed for ASE to set in. The negative values of L_{th}, owed to negative gain values, have no physical meaning and indicate that the ASE threshold will be never reached for those pump intensities.

Obviously the asymptote in Fig. 2(b) coincides with the point in which the net gain $g=0$ [Fig. 2(a)]. This point has been previously defined as the ASE threshold [14] (since for $g>0$ ASE was observed, while for $g<0$ it was not), and its interpretation, which at first sight could be thought of as superfluous, can now be clarified. This value indicates the pump intensity for which the ASE intensity growth as a function of the stripe length, defined by Eq. (3), changes from sublinear (losses higher than gain) to superlinear (gain higher than losses). In other words, it is the minimum pump intensity for which the ASE threshold can be reached and corresponds to $L_{th}\to\infty$ [Fig. 2(b)].

The so-obtained threshold lengths can be compared to the ones estimated by other approaches. In [18] a threshold intensity of 80 kW/cm^2 was obtained via visual inspection of the change in slope in the input-output intensity trace with a pumped stripe 2 mm long or, which is the same thing, at 80 kW/cm^2 the threshold length equals 2 mm. The point (80 kW/cm^2, 2 mm) is plotted in Fig. 2(b) and exhibits good agreement, within the experimental error, with the value predicted by Eq. (8). This coincidence implies that both methods render similar threshold lengths, but the formalism presented here avoids errors arising from visual estimations and makes this approach more accurate.

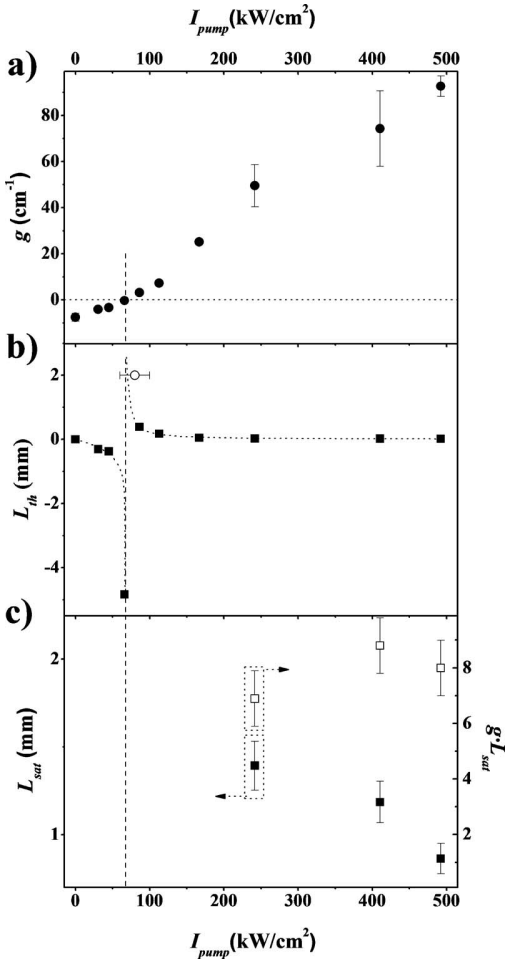

Fig. 2. Variation with pump intensity of (a) g, (b) L_{th}, and (c) L_{sat} and gL_{sat}. Points in (a) correspond to a fluorinated polyimide (6F-6F) waveguide doped with laser dye Pyrromethene 597 [18]. Points in (b) and (c) are calculated using Eqs. (8) and (9), respectively. The hollow point in plot (b) is the value of I_{th} obtained from the input-output trace and corresponds to an excitation stripe $L_{th}=2$ mm. Dashed lines are vertical asymptotes. Dotted lines in (b) are a guide to the eye.

In Fig. 2(c) values of L_{sat} and gL_{sat}, calculated using Eq. (9), have been presented as functions of the pump intensity. When increasing the pump intensity the saturation length shortens since the high amplification level allows the photon flux to deplete the population inversion in shorter stripe lengths. At pump intensities lower than 200 kW/cm^2, L_{sat} could not be calculated since no sign of saturation appeared in the fitting ($1/I_s=0$). For intensities below the asymptote no values of L_{sat} can be attained because there is no ASE to saturate. The gain-length

product gL_{sat} it is seen to depend on the pump intensity, although with a tendency to settle around the value of 8. In [14] we found a similar behavior, albeit there the gL_{sat} value settled at a value of about 10. This discrepancy owes to the fact that g and L_{sat} depend on the spectroscopic parameters of the active medium, which are different in [14,18].

As a final remark, it is worth noticing that, with the present method, a circular dependence may arise when highly accurate optical gain and characteristic lengths are desired: the gain cannot be determined without evaluating the experimental data which, in order to be accurate, already require the knowledge of the characteristic lengths, which in turn depend on the gain. This vicious circle could be circumvented by means of an iterative approach to minimize the overall error. In this sense the strategy to follow would be: (i) Acquisition of experimental data for a wide range of stripe lengths, (ii) gain and subsequent characteristic length calculation for that stripe length range, (iii) recalculation of gain and characteristic lengths in the range between L_{th} and L_{sat} previously calculated, and (iv) repeating (iii) until convergence or the desired accuracy is achieved.

4. CONCLUSION

In summary, the formalism developed in this paper allows for the rigorous calculation of the characteristic threshold and saturation lengths in an easy and straightforward way from parameters obtained applying the VSL method. We have shown that the lengths obtained with the present formalism compare well with the ones estimated by other approaches. However, this method prevents errors arising from visual estimations, making this approach more accurate. The correct estimation of these lengths is essential for the proper characterization of optical gains in thin film active media.

ACKNOWLEDGMENTS

This work was supported by Projects MAT2007-65778-C02-01 and TRA2009-0144 of the Spanish Ministerio de Ciencia e Innovación (MICINN). L. Cerdán acknowledges MICINN for a Predoctoral scholarship (FPI, cofinanced by Fondo Social Europeo). The authors thank the reviewers for their useful comments and suggestions, which have allowed improving the quality of the final manuscript.

REFERENCES AND NOTES

1. A. Costela, O. García, L. Cerdán, I. García-Moreno, and R. Sastre, "Amplified spontaneous emission and optical gain measurements from pyrromethene 567–doped polymer waveguides and quasi-waveguides," Opt. Express **16**, 7023–7036 (2008).
2. A. Costela, O. García, L. Cerdán, I. García-Moreno, and R. Sastre, "Amplified spontaneous emission and optical gain measurements from pyrromethene 567–doped polymer waveguides and quasi-waveguides: erratum," Opt. Express **16**, 7587–7587 (2008).
3. L. Pavesi, L. Dal Negro, C. Mazzoleni, G. Franzò, and F. Priolo, "Optical gain in silicon nanocrystals," Nature **408**, 440–444 (2000).
4. J. Mickevičius, G. Tamulaitis, M. S. Shur, Q. Fareed, J. P. Zhang, and R. Gaska, "Saturated gain in GaN epilayers studied by variable stripe length technique," J. Appl. Phys. **99**, 103513 (2006).
5. M. Vehse, J. Meinertz, O. Lange, P. Michler, J. Gutowski, S. Bader, A. Lell, and V. Härle, "Analysis of gain saturation behavior in GaN based quantum well lasers," Phys. Status Solidi C **0**, 43–47 (2002).
6. J. Valenta, I. Pelant, and J. Linnros, "Waveguiding effects in the measurement of optical gain in a layer of Si nanocrystals," Appl. Phys. Lett. **81**, 1396–1398 (2002).
7. L. Dal Negro, P. Bettotti, M. Cazzanelli, D. Pacifici, and L. Pavesi, "Applicability conditions and experimental analysis of the variable stripe length method for gain measurements," Opt. Commun. **229**, 337–348 (2004).
8. C. Lange, M. Schwalm, S. Chatterjee, W. W. Rühle, N. C. Gerhardt, S. R. Johnson, J.-B. Wang, and Y.-H. Zhang, "The variable stripe-length method revisited: Improved analysis," Appl. Phys. Lett. **91**, 191107 (2007).
9. M. D. McGehee, R. Gupta, S. Veenstra, E. K. Miller, M. A. Díaz-García, and A. J. Heeger, "Amplified spontaneous emission from photopumped films of a conjugated polymer," Phys. Rev. B **58**, 7035–7039 (1998).
10. K. Yamashita, T. Kuro, K. Oe, and H. Yanagi, "Low threshold amplified spontaneous emission from near-infrared dye-doped polymeric waveguide," Appl. Phys. Lett. **88**, 241110 (2006).
11. H. Azuma, T. Kobayashi, Y. Shim, N. Mamedov, and H. Naito, "Amplified spontaneous emission in α-phase and α-phase polyfluorene waveguides," Org. Electron. **8**, 184–188 (2007).
12. W. Holzer A. Penzkofer, T. Schmitt, A. Hartmann, C. Bader, H. Tillmann, D. Raabe, R. Stockmann, and H.-H. Hörnhold, "Amplified spontaneous emission in neat films of arylene-vinylene polymers," Opt. Quantum Electron. **33**, 121–150 (2001).
13. F. Lahoz, C. J. Oton, N. Capuj, M. Ferrer-González, S. Cheylan, and D. Navarro-Urrios, "Reduction of the amplified spontaneous emission threshold in semiconducting polymer waveguides on porous silica," Opt. Express **17**, 16766–16775 (2009).
14. L. Cerdán, A. Costela, I. García-Moreno, O. García, and R. Sastre, "Waveguides and quasi-waveguides based on pyrromethene 597-doped poly(methyl methacrylate)," Appl. Phys. B **97**, 73–83 (2009).
15. T. Kobayashi, M. Flämmich, G. Jordan, R. D'Arcy, M. Rüther, W. J. Blau, Y. Suzuki, and T. Kaino, "Blue-green small-signal gain and saturation in a luminescent polymer gain medium," Appl. Phys. Lett. **89**, 131119 (2006).
16. Equation (2) is implicit in $I_{ASE}(L)$ and, hence, it cannot be fitted to an $I_{ASE}(L)$ versus L plot as is done with Eq. (3). Fortunately Eq. (2) is explicit in L and, consequently, g, Ω, and $s=1/I_s$ can be calculated by means of a least squares fit of Eq. (2) to a L versus $I_{ASE}(L)$ plot. When saturation is not evident (low pump intensity or short L) and the data dispersion is significant, the fit may render negative values of s (and so incorrect g and Ω values). In that case $s=1/I_s$ is fixed to zero, which is equivalent to saying that there is no gain saturation. Alternatively, Eq. (3) can be fitted to the usual $I_{ASE}(L)$ versus L plot. These two last fits will lead to slightly different g and Ω values since the former minimizes the sum of squared residuals in L, while the last minimizes the ones in $I_{ASE}(L)$. Nevertheless, both fits are statistically significant.
17. G. I. Peters and L. Allen, "Amplified spontaneous emission I. The threshold condition," J. Phys. A **4**, 238–243 (1971).
18. L. Cerdán, A. Costela, I. García-Moreno, O. García, R. Sastre, M. Calle, D. Muñoz, and J. de Abajo, "High-gain long-lived amplified spontaneous emission from dye-doped fluorinated polyimide planar waveguides," Macromol. Chem. Phys. **210**, 1624–1631 (2009).

Paper B2: Opt. Express 16, 10, 7023–7036 (2008)

Amplified spontaneous emission and optical gain measurements from pyrromethene 567-doped polymer waveguides and quasi-waveguides

A. Costela, O. García, L. Cerdán, I. García-Moreno, and R. Sastre

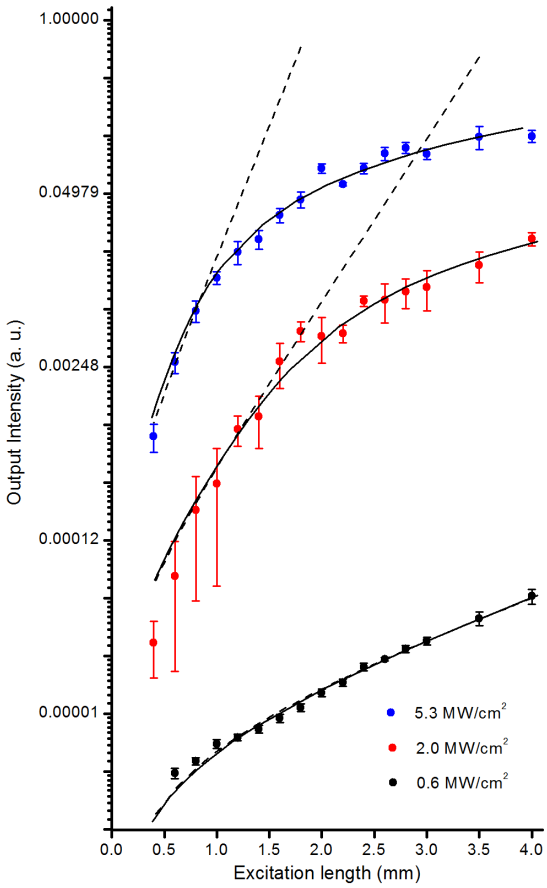

Dependence of the emission intensity on excitation length at various pump intensities for sample 4. the dashed lines are fits to the data using Eq. (2). The solid lines are fits to the data using Eq. (6).

Amplified spontaneous emission and optical gain measurements from pyrromethene 567 – doped polymer waveguides and quasi-waveguides

A. Costela [1,*], O. García [2], L. Cerdán [1], I. García-Moreno [1], and R. Sastre [1]

[1] Instituto de Química Física "Rocasolano", C.S.I.C., Serrano 119, 28006 Madrid, Spain
[2] Instituto de Ciencia y Tecnología de Polímeros, C.S.I.C., Juan de la Cierva 3, 28006 Madrid, Spain
[*] *Corresponding author: acostela@iqfr.csic.es*

Abstract: Amplified spontaneous emission from planar waveguides and quasi-waveguides based on Pyrromethene 567-doped poly(methyl methacrylate) thin films deposited onto quartz and glass substrates is investigated. Films with different thickness were prepared and pumped optically at 532 nm with pulses of up to 8 MW/cm^2. Pump thresholds for the onset of ASE emission, optical gains and losses were assessed. Net gain coefficients were estimated by fitting the data provided by variable stripe length measurements with a theoretical expression which takes into account saturation. In this way, net gain coefficients of up to 56 ± 9 cm^{-1} at a pump intensity of 5.3 MW/cm^2 for quasi-waveguides and up to 20.6 ± 2.7 cm^{-1} at a pump intensity of 3.4 MW/cm^2 for waveguides, were obtained. Loss coefficients in the waveguides were estimated to be 3.8 ± 0.4 cm^{-1} and 6.1 ± 1.3 cm^{-1} for 15 μm and 5 μm thick films, respectively. The results obtained seem to indicate a stronger self-mode-restriction capability in the quasi-waveguides than in conventional total internal-reflection waveguides.

OCIS codes: (140.2050) Dye lasers; (140.3380) laser materials; (230.7390) Waveguides, planar; (230.310) Thin films; (250.2080) Polymer active devices; (250.5460) Polymer waveguides.

References and links

1. A. Costela, I. García-Moreno, and R. Sastre, "Materials for solid-state dye lasers," in *Handbook of Advanced Electronic and Photonic Materials and Devices*, H.S. Nalwa, ed. (Academic, San Diego, Ca., 2001), vol. 7, Chap. 4, p.161.
2. A. Costela, I. García-Moreno, and R. Sastre, "Polymeric solid-state dye lasers: recent developments," Phys. Chem. Chem. Phys. **5**, 4745-4763 (2003).
3. K. P. Kretsch, C. Belton, S. Lipson, W. J. Blau, F. Z. Henari, H. Rost, S. Pfeiffer, A. Teuschel, H. Tillmann, and H.-H. Hörhold, "Amplified spontaneous emission and optical gain spectra from stilbenoid and phenylene detrivative model compounds," J. Appl. Phys. **86**, 6155-6159 (1999).
4. H. Manaa and S. M. Al-Alawi, "Optical gain measurements in polymethyl methacrylate plastic doped with perylimide dyes," J. Lumin. **94-95**, 55-58 (2001).
5. M. C. Castex, C. Olivero, A. Fischer, S. Mousel, J. Michelon, D. Adês, and A. Siove, "Polycarbazoles microcavities: towards plastic blue lasers," Appl. Surf. Sci. **197-198**, 822-825 (2002).
6. Y. Kawabe, L. Wang, T. Nakamura, and N. Ogata, "Thin-film lasers based on dye-deoxyribonucleic acid-lipid complexes," Appl. Phys. Lett. **81**, 1372-1374 (2002).
7. A. K. Sheridan, A. R. Buckley, A. M. Fox, A. Bacher, D. D. C. Bradley, and I. D. W. Samuel, "Efficient energy-transfer in organic thin films-implications for organic laser," J. Appl. Phys. **92**, 6367-6371 (2002).
8. S.-S. Yap, W.-O. Siew, T.-Y. Tou, and S.-W. Ng, "Red-green-blue laser emission from dye-doped poly(vinyl alcohol) films," Appl. Opt. **41**, 1725-1728 (2002).
9. Y. Oki, S. Miyamoto, M. Maeda, and N. J. Vasa, "Multiwavelength distributed-feedback dye laser array and its application to spectroscopy," Opt. Lett. **27**, 1220-1222 (2002).
10. Y. Oki, T. Yoshiura, Y. Chisaki, and M. Maeda, "Fabrication of a distributed-feedback dye laser with a grating structure in its plastic waveguide," Appl. Opt. **41**, 5030-5035 (2002).
11. Y. Oki, S. Miyamoto, M. Tanaka, D. Zuo, and M. Maeda, "Long lifetime and high repetition rate operation from distributed feedback plastic waveguided dye lasers," Opt. Commun. **214,** 277-383 (2002).

#93332 - $15.00 USD Received 29 Feb 2008; revised 7 Apr 2008; accepted 15 Apr 2008; published 1 May 2008

12. Y. Oki, M. Tanaka, Y. Ogawa, H. Watanabe, and M. Maeda, "Development of Quasi-End-Fired Waveguide Plastic Dye Laser," IEEE J. Quantum Electron. **42,** 389-396 (2006).
13. N. Tsutsumi, T. Kawahira, and W. Sakai, "Amplified spontaneous emission and distributed feedback lasing from a conjugated compound in various polymer matrices,"Appl. Phys. Lett. **83**, 2533-2535 (2003).
14. N. Tsutsumi, A. Fujihara, and D. Hayashi, "Tunable distributed feedback lasing with a threshold in the nanojoule range in an organic guest-host polymeric waveguide," Appl. Opt. **45,** 5748-5751 (2006).
15. M. A. Reilly, C. Marinelli, C. N. Morgan, R. V. Penty, I. H. White, M. Ramon, M. Ariu, R. Xia, and D. D. C. Bradley, "Rib waveguide dye-doped polymer amplifier with up to 26 dB optical gain at 625 nm," Appl. Phys. Lett. **85,** 5137-5139 (2004).
16. M. A. Reilly, B. Coleman, E. Y. B. Pun, R. V. Penty, I. H. White, M. Ramon, R. Xia, and D. D. C. Bradley, "Optical gain at 650 nm from a polymer waveguide with dye-doped cladding," Appl. Phys. Lett. **87,** (2005) 231116 (2005).
17. W. Lu, B. Zhong, and D. Ma, "Amplified spontaneous emission and gain from optically pumped films of dye-doped polymers," Appl. Opt. **43**, 5074-5078 (2004).
18. D. Zhang and D. Ma, "Improved amplified spontaneous emission by doping of green fluorescent dye C545T in red fluorescent dye DCJTB:PS polymer films," Appl. Opt. **46**, 2996-3000 (2007).
19. E. V. Calzado, J. M. Villalvilla, P. G. Boj, J. A. Quintana, and M. A. Díaz García, "Tuneability of amplified spontaneous emission through control of the thickness in organic-based waveguides," J. Appl. Phys. **7**, 093103 (2005).
20. E. V. Calzado, J. M. Villalvilla, P. G. Boj, J. A. Quintana, R. Gómez, J. L. Segura, and M. A. Díaz García, "Effect of structural Modifications in the Spectral and Laser properties of Perylendiimide Derivatives," J. Phys Chem. **111**, 13595-13605 (2007).
21. E. V. Calzado, J. M. Villalvilla, P. G. Boj, J. A. Quintana, R. Gómez, J. L. Segura, and M. A. Díaz García, "Amplified spontaneous emission in polymer films doped with a perylenediimide derivative," Appl. Opt. **46,** 3836-3842 (2007).
22. R. Kumar, A. P. Singh, A. Kapoor, and K. N. Tripathi, "Effect of dye doping in poly(vinyl alcohol) waveguides," J. Mod. Opt. **10**, 1471-1483 (2005).
23. K. Sakai, T. Tsuzuki, Y. Itoh, M. Ichikawa, and Y. Taniguchi, "Using proton-transfer dyes for organic laser diodes," Appl. Phys. Lett. **86**, 081103 (2005).
24. K. Geetha, M. Rajesh, V. P. N. Nampoori, C. P. G. Vallabhan, and P. Radhakrishnan, "Laser emission from transversely pumped dye-doped free-standimg polymer film," J. Opt. A: Pure Appl. Opt. **8**, 189-193 (2006).
25. G. Jordan, M. Flämmich, M. Rüther, T. Kobayashi, and W. J. Blau, "Light amplification at 501 nm and large nanosecond optical gain in organic dye-doped polymeric waveguides," Appl. Phys. Lett. **88**, 161114 (2006).
26. D. Pisignano, E. Mele, L. Persano, A. Athanassiou, C. Fotakis, and R. Cingolani, "Optical gain from the Open Form of a Photochromic Molecule in the Solid State," J. Phys. Chem. B **110**, 4506-4509 (2006).
27. M. Kawasaki and S. Mine, "Novel lasing Action in Dye-Doped Polymer Films Coated on large Pseudotabular Ag Islands," J. Phys. Chem. B **110**, 15052-15054 (2006).
28. H. Goudket, T. H. Nhung, B. Ea-Kim, G. Roger, and M. Canva, "Importance of dye host on absorption, propagation losses, and amplified spontaneous emission for dye-doped polymer thin films," Appl. Opt. **45**, 7736-7741 (2006).
29. Z. Yu, W. Li, J. A. Hagen, Y. Zhou, D. Klotzkin, J. G. Grote, and A.J. Steckl, "Photoluminescence and lasing from deoxyribonucleic acid (DNA) thin films doped with sulforhodamine," Appl. Opt. **46**, 1507-1513 (2007).
30. A. Büttner and U. D. Zeitner, "Experimental realization of Monolithic Diffractive Broad-Area polymeric Waveguide Dye Lasers," IEEE J. Quantum Electron. **43,** 545-551 (2007).
31. P. Yang, G. Wirnsberger, H. C. Huang, S. R. Cordero, M. D. McGehee, B. Scott, T. Deng, G. M. Whitesides, B. F. Chmelka, S. K. Buratto, and G. D. Stucky, "Mirrorless Lasing from Mesostructured Waveguides Patterned by Soft Lithography," Science **287**, 465-467 (2000).
32. X. Zhu and D. Lo, "Sol-gel glass distributed-feedback waveguide laser," Appl. Phys. Lett. **80,** 917-919 (2002).
33. D. Lo, L. Shi, J. Wang, G.-X. Zhang, and X. Zhu, "Zirconia and zirconia-organically modified silicate distributed feedback waveguide lasers tunable in the visible," Appl. Phys. Lett. **81**, 2707-2709 (2002).
34. J. Wang, G.-X. Zhang, L. Shi, D. Lo,and X. Zhu, "Tunable multiwavelength distributed-feedback zirconia waveguide lasers," Opt. Lett. **28**, 90-92(2003).
35. D. Lo, C. Ye, and J. Wang, "Distributed feedback laser action by polarization modulation," Appl. Phys. B **76,** 649-653(2003).
36. C. J. Oton, D. Navarro-Urrios, N. E. Capuj, M. Ghulinyan, L. Pavesi, S. González-Pérez, F. Lahoz, and I. R. Martin, "Optical gain in dye-impregnated oxidized porous silicon waveguides," Appl. Phys. Lett. **89**, 011107 (2006).
37. X. Peng, L. Liu, J. Wu, Y. Li, Z. Hou, L. Xu, W. Wang, F. Li, and M. Ye, "Wide-range amplified spontaneous emission wavelength tuning in a solid-state dye waveguide," Opt. Lett. **25,** 314-316 (2000).
38. M. Casalboni, F. De Matteis, V. Merlo, P. Prosposito, R. Russo, and S. Schutzmann, "1.3 μm light amplification in dye-doped Irbid sol-gel channel waveguides," Appl. Phys. Lett., **83**, 416-418 (2003).

39. T. Saraidarov, R. Reisfeld, M. Kazes, and U. Banin, "Blue laser dye spectroscopic properties in sol-gel inorganic-organic hybrid films," Opt. Lett. **31,** 356-358 (2006).
40. T. G. Pavlopoulos, "Scaling of dye lasers with improved laser dyes," Prog. Quantum Electron. **26,** 193-224 (2002).
41. D. B. Hall and C. Yeh, "Leaky waves in a heteroepitaxial film," J. Appl. Phys. **44,** 2271-2274 (1973).
42. T.-N. Ding and E. Garmire, "Measuring refractive index and thickness of thin films: a new technique," Appl. Opt. **22**, 3177-3181 (1983).
43. K. Sasaki, T. Fukao, T. Saito, and O. Hamano, "Thin-film waveguide evanescent dye laser and its gain measurement," J. Appl. Phys. **51**, 3090-3092 (1980).
44. V. M. Arutuyan, G. P. Djotyan, A. V. Karmenyan, T. E. Melicksetyan, and E. M. Sarkissyan, "Thin-film narrowband tunable dye laser," Opt. Commun. **36,** 227-228 (1981).
45. D. Shamrakov and R. Reisfeld, "Superradiant film laser operation in red perylimide dye doped silica-polymethylmethacrylate," Chem. Phys. Lett. **213,** 47-53 (1993).
46. G. S. He, C. F. Zhao, C.-K. Park, P. N. Prasad, and R. Burzynski, "Dye film leaky waveguide laser," Opt. Commun. **111,** 82-85 (1994).
47. C. Lowe, *Surface Coatings Technology* (John Wiley&Sons, London, 1997), vol. 5, Chap. VI, p.60-62.
48. M. D. McGehee, R. Gupta, S. Veenstra, E. K. Miller, M. A. Díaz-García, and A. J. Heeger, "Amplified spontaneous emission from photopumped films of a conjugated polymer," Phys. Rev. B **58,** 7035-7039 (1998).
49. L. W. Casperson and A. Yariv, "Spectral narrowing in High-Gain Lasers," IEEE J. Quantum Electron. **QE-8**, 80-85 (1972).
50. A. Penzkofer, W. Holzer, H. Tillmann, and H.-H. Hörhold, "Leaky-mode emission of luminescent thin films on transparent substrates," Opt. Commun. **229**, 279-290 (2004).

1. Introduction

The development of tunable solid-state dye lasers, in which an organic dye is incorporated into a suitable solid matrix, is an area of active research [1,2]. While retaining the versatility of liquid dye lasers, these solid-state systems present a low-cost gain medium and are compact and easy to operate and maintain. On the other hand, active and passive waveguides are key components in a variety of photonic applications. Thus, the development of dye-doped thin films or waveguides, making use of the processing flexibility of these materials and combining the tunability and high efficiency of laser dyes with the high power density that can be easily achieved in waveguide structures, makes devices based on dye-doped waveguides very attractive and promising for optoelectronic applications.

Over the last years, amplified spontaneous emission (ASE) and lasing action have been achieved from organic [3-30], inorganic [31-36], and organic-inorganic [33,37-39] hybrid thin films and planar waveguides. A large amount of these studies have been carried out with dyes of the rhodamine family, mainly with the well known Rhodamine 6G (Rh6G) dye, and their properties as gain medium in thin films and waveguides have been thoroughly assessed [8-12,14-16,31-35]. Over the last decade, laser dyes of the pyrromethene family (4,4-difluor-3a,4a-diaza-4-boro-*s*-indacene dyes, also known as dipyrromethene.BF_2 (PM) dyes), with emission covering a spectral range wider than that of rhodamines, have become standard laser dyes for emission in the green-yellow to red regions of the spectrum because of their high efficiency and photostability in both liquid and solid gain media [1,40]. In spite of this, no reports on the optical gain properties of PM dyes in waveguides have appeared, apart from a few studies dealing with the importance of dye host on absorption, losses and ASE emission of Pyrromethene 597-doped polymer thin films [28], or with some characteristics of the laser output from Pyrromethene 567-doped plastic waveguides with distributed feedback structures [11].

In this paper, we present a systematic study on the properties of the ASE emission from thin films of poly(methyl methacrylate) (PMMA) doped with dye Pyrromethene 567 (PM567). Pump thresholds for the onset of ASE emission, gain coefficients and losses are determined for thin films of different thicknesses deposited onto quartz and glass substrates. For proper waveguiding operation the refractive index of the dye-doped polymer film has to be higher than that of the substrate. This condition is fulfilled when the PMMA-based films are deposited onto quartz slabs. When the substrate was glass, the refractive index of the dye-

doped polymer film was lower than that of the substrate, and a leaky waveguide or quasi-waveguide was obtained, where light is no longer fully confined: no total internal reflection takes place at the polymer film – glass substrate interface and light leaks into the substrate [41-46]. It has been pointed out that this feature could be a useful output coupling mechanism in an active-waveguide laser device [44-46], and a technique for measuring refractive indices and thicknesses of thin films based on leaky waveguides has been reported [42]. Our results seem to indicate a stronger self-mode-restriction capability in the quasi-waveguides as compared to the conventional total internal reflection waveguides.

2. Experimental

Planar waveguides consisting of dye-doped polymer films deposited onto quartz and glass substrates (0.88 mm and 0.98 mm thick, respectively) were produced by two different procedures: spin coating and extender roller. PMMA of 25,000 molecular weight (Polysciences, Inc.) in proportion 200 mg/mL was added to a solution of Toluene (Merck) containing PM567 (laser grade, from Exciton) at a concentration (with respect to polymer) of 5×10^{-2} M. Although the dye concentration was rather high, photophysical studies did not show any evidence of aggregation of the dye molecules. Films with thickness around 5 μm and 17 μm were produced depending on the technique used. The thicker films were obtained by using the extender roller technique [47]. In this case, a few drops of the solution were placed on a standard glass microscope slide or quartz slide and extended along the slide with a calibrated rod (endless screw with calibrated thread). After solvent evaporation at room temperature, polymeric films of 17± 2 μm of thickness were obtained. Films with thickness of 5.5 ± 0.5 μm were obtained by spin coating (2000 rpm, 10s + 4000 rpm, 1s + 6000 rpm, 1s). In all cases, the thickness of the films was determined by using a gravimetric method (accuracy of balance, 10^{-4} g), taking into account the density of the polymeric film (1.19 g/mL).

The resulting quartz/glass – doped polymer – air structure defines an asymmetric slab optical waveguide. In the quartz-doped polymer-air structure, the measured refractive index of the dye-doped polymer layer (n_1 = 1.4900) is higher than the measured index of the quartz substrate (n_2 = 1.4583). Thus, total internal reflection at the film-quartz interface confines and guides the light along the film, and emission from the edge of the film is obtained. When the substrate is glass (measured index, n_2 = 1.5176), with higher refractive index than the doped polymer film, no total internal reflection takes place at the film-substrate interface and emitted light leaks into the substrate. A leaky waveguide or quasi-waveguide is obtained, where light is confined by the film-air interface while the reflection at the film-substrate boundary is leaky.

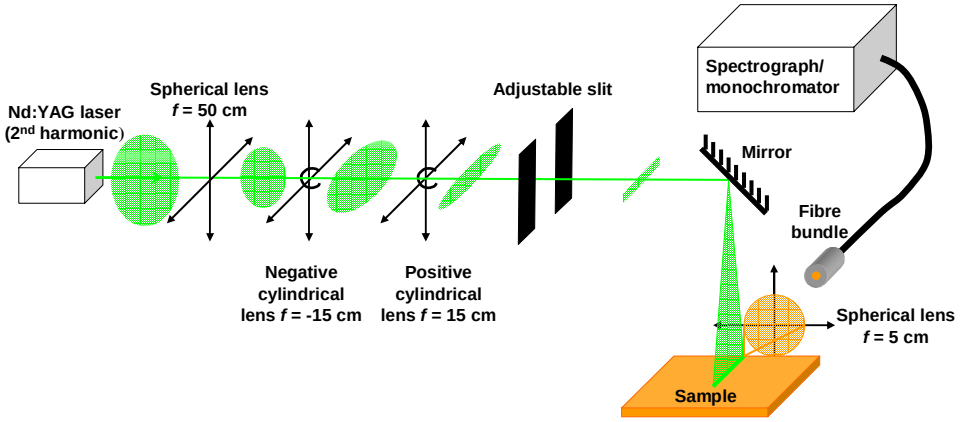

Fig. 1. Schematic of the experimental setup

The waveguides were optically pumped at 532 nm with 6 ns full width at half maximum (FWHM) pulses from a frequency-doubled *Q*-switched Ng:YAG laser (Monocrom OPL-10). The laser was typically operated at 1 Hz repetition rate, and the pulse energy was controlled by insertion of calibrated neutral density filters into the beam path. Pump energy was measured with a calibrated pyroelectric energy meter (ED200, GenTec). A schematic of the experimental setup is shown in Fig. 1. A combination of one spherical (f = 50 cm) and two cylindrical quartz lenses (f = −15 cm and +15 cm, respectively) perpendicularly arranged focused the pump beam to a narrow horizontal line onto the surface of the film. An adjustable slit was used to select only the central portion of the pump beam. The incident light was perpendicular to the substrate surface, and the excitation stripe on the sample was ~150 μm × 3 mm, with one end placed right up to the edge of the film. The edge emission from the sample was collected with a 5-cm focal length spherical lens, focused onto a fibre bundle and detected with a spectrograph/monochromator (SpectraPro-300i, Acton Research) equipped with a thermoelectrically cooled CCD detector (SpectruMM:GS 128B). A shortwave cutoff filter (OptoSigma, cutoff at 540 nm), placed before the fibre bundle avoids any scattered 532 nm light entering the spectrograph. At excitation intensities above a certain threshold value, the spontaneously emitted photons are amplified by stimulated emission as they travel along the stripe-shaped gain region and amplified spontaneous emission (ASE) occurs.

The net gain of the doped polymer film was measured by using the variable stripe length (VSL) method [48], which consists basically in pumping optically the sample with a stripe of variable length and measuring the intensity of the edge-emitted ASE as a function of stripe length. The stripe length was controlled by varying the width of the adjustable slit by means of a micrometer.

In an unsaturated amplifier having a length much greater than the diameter, the growth of intensity is governed by [49]:

$$\frac{dI(\lambda,z)}{dz} = g'(\lambda)I(\lambda,z) - \alpha\, I(\lambda,z) + \eta g'(\lambda), \tag{1}$$

where g' is the gain coefficient and α is the loss coefficient. The second term on the right side of (1) represents distributed losses, and the third term is the spontaneous emission, which has the same frequency dependence $g'(\lambda)$ as the gain coefficient. The coefficient η is then proportional to the spontaneous emission rate and to a geometrical factor that depends on the amplifier dimensions. In the recent literature on waveguides, spontaneous emission proportional to pump intensity is usually described by a term $A(\lambda)P_0$ [3], and Eq. (1) is written with the substitution $\eta g'(\lambda) = A(\lambda)P_0$.

Integration of Eq. (1) with no input intensity ($I(\lambda,0) = 0$) leads to:

$$I(\lambda) = \frac{\eta\, g'(\lambda)}{g(\lambda)}\left(e^{g(\lambda)l} - 1\right), \tag{2}$$

where $g(\lambda)$ is the net gain coefficient, $g(\lambda) = g'(\lambda) - \alpha$, and l is the length of the pumped stripe.

Eq. (2) represents the output intensity from one end of the stripe in the small-signal regime. Thus, in the absence of saturation, g can be determined by plotting the intensity of the ASE emission as a function of the pumped stripe length and fitting the resulting curve to the expected dependence given by Eq. (2).

If the ASE intensity reaches the saturation level, Eq. (1) is no longer appropriate. This Eq. implies that the excited state population is always the same regardless of the ASE intensity. In order to take saturation effects into account, a term has to be included which accounts for the depletion of the excitation density. Consequently, Eq.(1) has to be replaced by [49]:

$$\frac{dI(\lambda,z)}{dz} = \frac{g'(\lambda)I(\lambda,z)}{1 + s\, I(\lambda,z)} - \alpha\, I(\lambda,z) + \eta g'(\lambda), \tag{3}$$

where s is a saturation parameter ($s = 1/I_{sat} = \sigma\tau/h\upsilon$, where σ is the emission cross section, τ is the fluorescence lifetime, and υ is the frequency of the ASE emission). Integration of this Eq. gives the behaviour of $I(\lambda)$ in both the small-signal and gain saturation regime.

The waveguide losses were characterized by measuring the optical loss coefficient by performing experiments where the stripe was gradually translated away from the edge of the sample while keeping the pumped stripe length constant (l = 3mm). Assuming that the ASE emission from the end of the excitation stripe I_0 is constant, the emission from the edge of the sample should decrease as the stripe is displaced as a result of waveguide losses (absorption and scattering) following the Beer-Lambert law:

$$I = I_0 e^{-\alpha x}, \tag{4}$$

where x is the length of the unpumped region between the end of the pump stripe and the edge of the sample. The loss measurements were performed by mounting the sample on a micrometric stage.

All the measurements were carried out at least three times at each pump intensity and an average value obtained. When quoted, the error is the standard deviation from the mean.

Table 1. Characteristics of the thin films studied and estimated threshold pump intensity (I_{th}) for ASE emission.

Sample	Composition/solvent of initial solution	Method of preparation	Substrate	Thickness (μm)	I_{th} (MW/cm^2)
1	PMMA(200 mg/mL) + PM567/toluene	Extender roller	Quartz	15	1.85
2	PMMA(200 mg/mL) + PM567/toluene	Spin coating	Quartz	5	1.3
3	PMMA(200 mg/mL) + PM567/toluene	Extender roller	Glass	19	2.0
4	PMMA(200 mg/mL) + PM567/toluene	Spin coating	Glass	6	1.0

3. Results and discussion

3.1 Wave-guided ASE emission

PM567 doped PMMA films deposited onto quartz substrates with the composition and thickness indicated in Table 1 (samples 1 and 2) were first prepared and studied.

Figure 2 shows the dependence of the full width at half maximum (open squares) and the intensity (filled squares) of the light emitted from the edge of the film with the pump intensity for sample 1. Pump intensity was varied from 0.21 MW/cm^2 up to 7.9 MW/cm^2. It can be estimated that at the lowest pump intensity 17% of the ground state population is excited whereas at the highest pump intensity the excited population was 88%. Fig. 3 shows the actual evolution of the emission spectra collected at various pump intensities for sample 2. Spectral narrowing of the spectra and a distinct change in the slope of the output emission intensity are observed with increasing pump intensity. The collapse of the FWHM in the emission spectrum and the change in the slope in the emission intensity are a signature of the onset of amplified spontaneous emission (ASE) above a certain pump threshold. Below threshold, the emission spectrum consists of a broad band characteristic of spontaneous emission which collapses to a FWHM of about 12 nm at pump intensities above threshold. The edge-emitted ASE showed a divergence of ~ 30 mrad in sample **1**, and of ~ 13 mrad in sample 2.

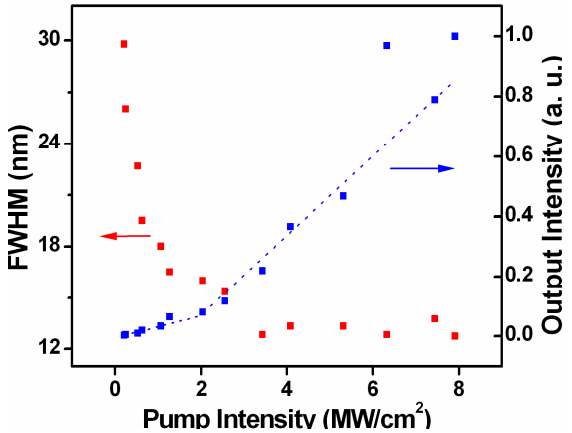

Fig. 2. Dependence of the FWHM of the emission spectra (open squares) and intensity of the output emission (full squares) on pump intensity for sample **1**. The dotted lines are a guide to the eye.

From the data in Fig. 2, a pump threshold for ASE emission of about 50 μJ (corresponding to a pump intensity of about 1.85 MW/cm^2) can be estimated for sample **1**. Up to this pump energy, the emission intensity increases slowly with pump intensity. Above threshold, the emission intensity increases sharply with pump intensity, and the FWHM of the emission levels off to values typical of ASE.

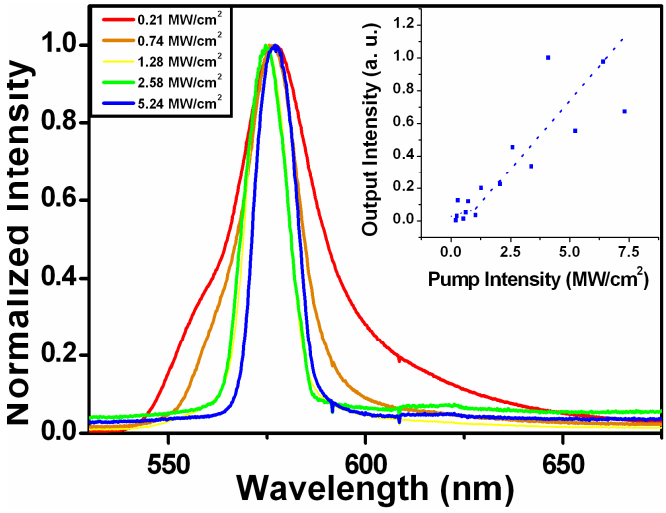

Fig. 3. Normalized emission spectra of sample **2** at different pump intensities. The inset represents the intensity of the output emission as a function of pump intensity. The dotted lines in the inset are a guide to the eye

Figure 4 shows the output intensity at the peak of the emission spectrum as a function of pump stripe length for sample **1**. Each point is an average of three measurements. The dashed line in Fig. 4 is a fit of the data to Eq. (2), which yields a net gain of 18.5 ± 4.1 cm^{-1} at a pump intensity of 3.4 MW/cm^2. In Fig. 5, the output intensity of the ASE emission from sample **1** is plotted as a function of the distance of a 3 mm-length pump stripe to the edge of the sample, at a pump intensity of 3.4 MW/cm^2. Fitting the experimental data to Eq. (4) yields a loss coefficient of $\alpha = 3.8 \pm 0.4$ cm^{-1}. The first two points in the plot, corresponding to distances to

the edge of the sample shorter than half millimetre, do not fit in the exponential behaviour predicted by Eq. (4). Probably, some irregularity in the film near the edge precludes an effective pumping of this region.

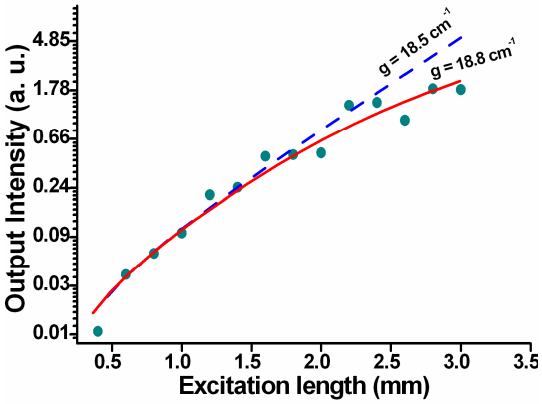

Fig. 4. Dependence of the emission intensity on excitation length for sample **1** at pump intensity of 3.4 MW/cm^2. The dashed line is a fit to the data using Eq.(2). The solid line is a fit to the data using Eq.(6).

The results obtained with sample 2 exhibit more scattering than those obtained with sample 1 (see inset in Fig. 3), probably due to the smaller thickness of sample **2**. At a PM567 concentration 5×10^{-2} M, a sample 15 μm thick absorbs about 82% of the incoming pump radiation at 532 nm, whereas a sample 5 μm thick only absorbs 44% of the pump radiation, being thus more sensitive to pump conditions and fluctuations. Threshold for ASE emission is at a pump intensity of about 1.3 MW/cm^2. By fitting Eq. (2) to the experimental data of output intensity as a function of pump stripe length (Fig. 6, dashed line), a net gain of 15.7 ± 4.6 cm^{-1} is estimated at 3.4 MW/cm^2 pump intensity. Fig. 7 shows the variation of the output intensity when the pump stripe was gradually translated away from the edge of the sample when the pump intensity was 3.4 MW/cm^2. The solid line is a fitting of the data to Eq. (4), yielding a loss coefficient of 6.1 ± 1.3 cm^{-1}.

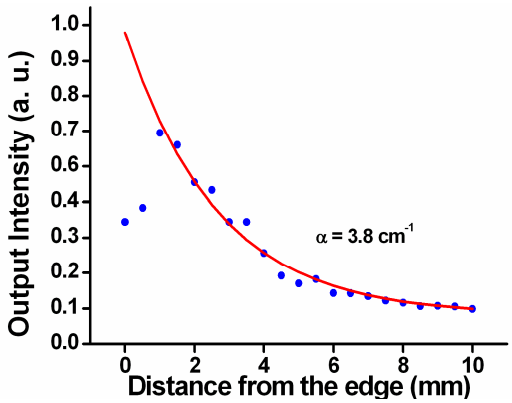

Fig. 5. Intensity of the light emitted from the edge of the waveguide as a function of the distance between the pump stripe and the edge of the sample for sample **1** at 3.4 MW/cm^2 pump intensity. The solid line is a fit to the data using Eq.(4).

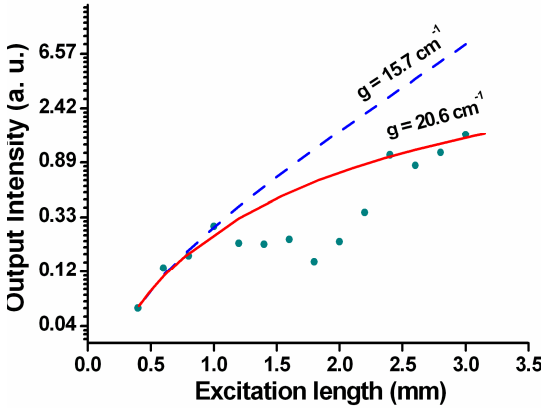

Fig. 6. Dependence of the emission intensity on excitation length for sample **2** at pump intensity of 3.4 MW/cm^2. The dashed line is a fit to the data using Eq.(2). The solid line is a fit to the data using Eq.(6).

3.2 Leaky-mode emission

Next, ASE emission from quasi-waveguides, where the gain medium was deposited onto a substrate with higher value of the refractive index, was studied. At the doped-polymer – air interface, light propagating at angles greater than the critical angle $\theta_c = 42$ ° will be totally reflected, while at the doped-polymer – glass interface no total reflection takes place at any angle, and light leaks into the substrate. Nevertheless, even in this case, where the refractive index of the film is smaller than the substrate refractive index, the large reflectivity occurring at grazing incidence leads to significant confinement of the light [42]. The different transverse modes propagating within the gain layer have different reflectivity losses due to the Fresnel law. The fundamental mode is the one with lower losses and, thus, light is amplified preferably in this mode, which means that in a quasi-waveguide there is much stronger self-mode-restriction capability than in a conventional total internal-reflection waveguide. However, when the thickness of the gain layer is large compared with the wavelength of the light, several low-loss leaky modes may exist [41].

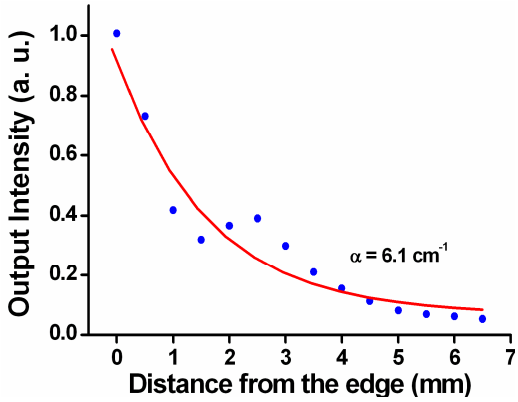

Fig. 7. Intensity of the light emitted from the edge of the waveguide as a function of the distance between the pump stripe and the edge of the sample for sample **2** at 3.4 MW/cm^2 pump intensity. The solid line is a fit to the data using Eq.(4).

Divergence of the edge-emitted ASE was ~ 100 mrad for both samples **3** and **4**. The fact that the ASE divergence is the same in both samples, independently of their thickness,

whereas in the waveguides (samples 1 and 2) the divergence of the light emitted by the thinner waveguide is lower than that of the light emitted by the thicker one is a confirmation of the quasi-waveguiding character of the light emitted when the films were deposited onto glass substrate, as it has been shown that in the emission from conventional waveguides there is a strong dependence of the properties of the emitted light on the thickness of the film [50].

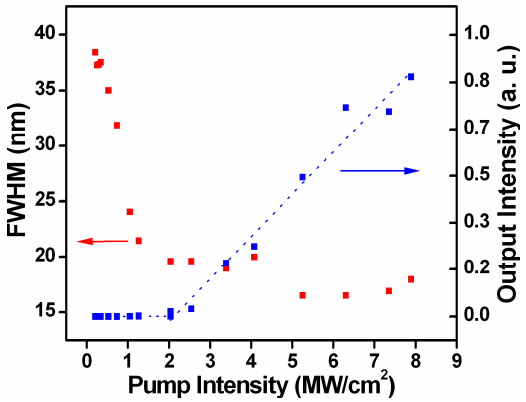

Fig. 8. Dependence of the FWHM of the emission spectra (open squares) and intensity of the output emission (full squares) on pump intensity for sample **3**. The dotted lines are a guide to the eye.

Figures 8 and 9 show the dependence of the FWHM of the emission spectra and intensity of the output emission on pump intensity for samples 3 and 4, respectively. Threshold pump intensities for the onset of ASE emission are clearly discernable in those plots and are found to be about 2.0 MW/cm^2 and 1.0 MW/cm^2, respectively. In this case reducing the film thickness results in a significant decrease in ASE threshold, whereas in the waveguides over quartz substrate this decrease is not so important.

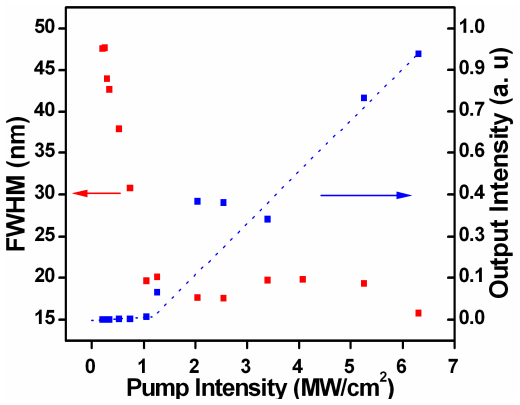

Fig. 9. Dependence of the FWHM of the emission spectra (open squares) and intensity of the output emission (full squares) on pump intensity for sample **4**. The dotted lines are a guide to the eye.

In Fig. 10 and 11, the emitted light intensity for samples 3 and 4 is plotted as a function of excitation length for different pump intensities. In the derivation of Eq. (2) gain saturation was not considered; thus, when using this Eq. to estimate the net gain coefficients only those subsets of data for which gain saturation is not evident should be used in the fitting procedure. The dashed lines in Fig. 10 and 11 are the fitting of the data using Eq. (2), leading to the net gain values collected in Table 2. Gain saturation, which is clearly evident in some of the plots

in those Fig., occurs because the light travelling in the sample is so strongly amplified that it depleted a substantial fraction of the excitation. As gain saturation sets in, the gain coefficient is reduced and light is no exponentially amplified further as the length of the pumped stripe is increased. Sample degradation can be ruled out as the cause of saturation seen in Fig. 10 and 11 because each point was obtained by pumping a fresh region. From close inspection of both Fig., it can be appreciated that gain saturation onsets at $gl \approx 4$. This is not surprising since spontaneous emission that is amplified by a factor exp(4) is most likely intense enough to significantly depopulate the excitation density, as has been pointed out by McGehee *et al.*[48].

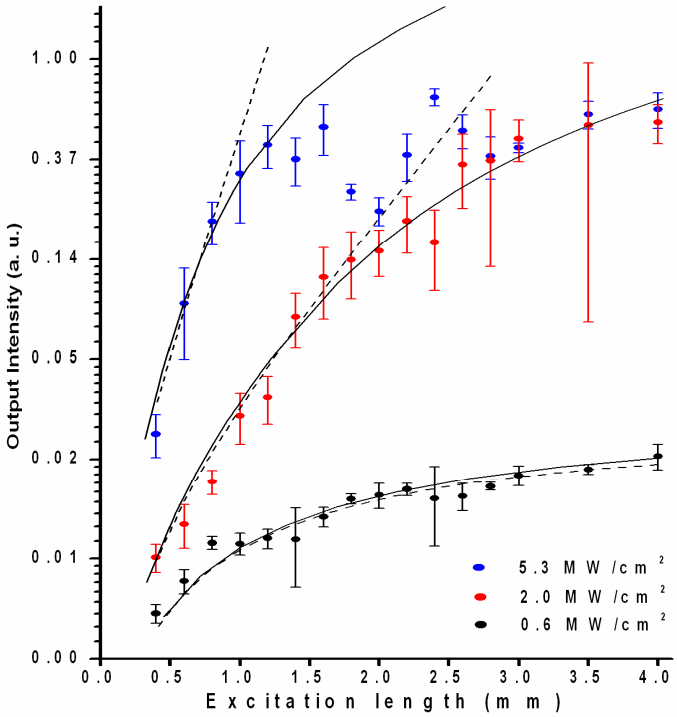

Fig. 10. Dependence of the emission intensity on excitation length at various pump intensities for sample **3**. The dashed lines are fits to the data using Eq.(2). The solid lines are fits to the data using Eq. (6).

As saturation effects are important except at the lower pump energies in these plots, using Eq. (2), even restricted to the subsets of data apparently free of saturation effects, could lead to appreciable errors in the calculated gain coefficients. Thus, to obtain a better estimation of the gain coefficients Eq.(3), which includes saturation effects, should be used as starting point.

In our experimental conditions, and supposing loss coefficients of the order of those obtained in the waveguide studies reported in the previous section, the product $\alpha s I$ is small compared to the gain coefficient $g(\lambda)$. Thus, we can replace Eq. (3) with the approximate expression:

$$\frac{dI(\lambda,z)}{dz} = \frac{\eta g'(\lambda) + [\eta g'(\lambda) s + g(\lambda)] I(\lambda,z)}{1 + s\, I(\lambda,z)}, \tag{5}$$

which, integrated between 0 and $I_t(\lambda)$ (total intensity) and between 0 and l, leads to:

$$l = s\, I_t(\lambda) + \frac{1 - \eta g'(\lambda) s}{g(\lambda) + \eta g'(\lambda)} \ln \left| \frac{\eta g'(\lambda) + [\eta g'(\lambda) + g(\lambda)] I_t(\lambda)}{\eta g'(\lambda)} \right|, \tag{6}$$

which can be used to fit the data in Fig. 10 and 11. Thus, g can be determined by plotting the pumped stripe length as a function of the intensity of the ASE emission and fitting the resulting curve to the expected dependence given by Eq. (6). As this Eq. depends on three parameters, the fit is very sensitive to the initialization values. In order to get a univocal fitting, it is convenient to use the value of ηg' calculated with Eq. (2) as a fixed parameter, since it should not be affected by saturation.

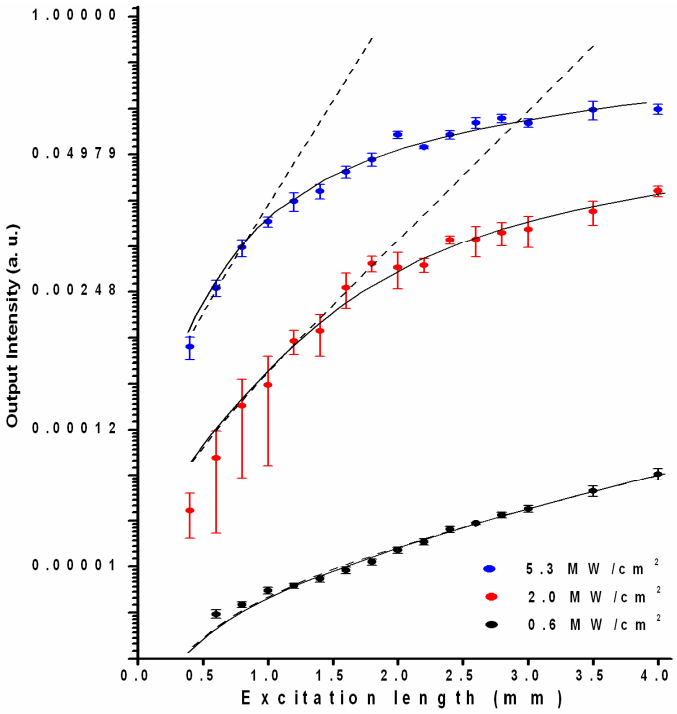

Fig. 11. Dependence of the emission intensity on excitation length at various pump intensities for sample **4**. The dashed lines are fits to the data using Eq.(2). The solid lines are fits to the data using Eq. (6).

Table 2. Net gain coefficients g at different pump intensities I_p for waveguides and quasi-waveguides obtained by using Eq. (2) (upper values) and Eq. (6) (lower values, in italic)

I_p	g (cm^{-1})			
(MW/cm^2)	Sample **1**	Sample **2**	Sample **3**	Sample **4**
5.3			42.4±5.4	45.1±4.3
			51.7± 8.4	*56*± 9
3.4	18.5±4.1	15.7±4.6		
	18.8± 2.0	*20.6*± 0.7		
2.0			17.4±2.4	28.1±1.7
			20.1± 2.5	*29.9± 1.9*
0.6			–4.2±0.7	6.7±0.2
			–4.1± 0.1	*6.9± 0.9*

The solid lines in Fig. 10 and 11 are the fitting of the data using Eq. (6).Using the same Eq. with the data of the waveguides, the solid lines in Fig. 4 and 6 are obtained. In Table 2 are collected the net gain coefficients g at different pump intensities I_p for both waveguides and quasi-waveguides, obtained by using both Eq. (2) and (6). The numbers in italics are the net gain coefficients estimated by using the more complete Eq. (6). It is seen that when saturation effects results are taken into account the net gain coefficients obtained are higher than those estimated using the small-gain expression. As expected, the differences in the values between the two sets of net gain coefficients are more important at high pump intensities, where saturation sets in earlier.

To put our results in perspective is useful to compare the net gain values obtained in this study with previous gain measurements performed on dye doped polymer films. Some authors use fluence (mJ/cm^2) instead of intensity (W/cm^2) to characterize the incident pump radiation. In our case, the intensities in Table 2 correspond to fluences in the range 3.7 mJ/cm^2 (intensity of 0.63 MW/cm^2) to 32 mJ/cm^2 (intensity of 5.3 MW/cm^2).

With pumping at 532 nm, gains of up to 40 cm^{-1} were obtained with optical waveguides based on polystyrene films doped with dye 4-(di-cyanomethylene)-2-*t*-butyl-6(1,1,7,7-tetramethyljulolidyl-9-enyl)-4*H*-pyran (DCJTB) and pumped with pulses of 0.13 mJ (Lu *et al.*[29]); the net gain increased to 52.71 cm^{-1} when a mixture of dyes DCJTB and 10-(2-benzothiazolyl)-1,1,7,7-tetramethyl-2,3,6,7-tetrahydro-1*H*,5*H*,11*H*-[1] benzopyrano [6,7,8-*ij*]quinolizin-11-one (C545T) codoped in polystyrene films was used at a pump energy of 0.08 mJ/pulse (Zhang *et al.*[18]). In both cases no pump fluence nor intensity was given. Oton *et al.*[36], obtained net gain coefficients of 8.7 cm^{-1} when pumping at fluences of 27.0 mJ/cm^2 with dye Nile blue (LC 6900) incorporated into oxidized porous silicon planar waveguides, and Calzado *et al.*[21] reported gain coefficients up to 10 cm^{-1}, at a pump intensity of 74 kW/cm^2 with perylenediimide derivatives in polystyrene films. Pumping with 100 mW of continuous radiation at 488 and 514 nm, Manaa *et al.*[4] obtained net laser gains of up to 53 cm^{-1} in plastic slab doped with perylimide dyes. In the near infrared region, Casalboni *et al.*[38] estimated an optical gain of about 11 cm^{-1} for polymethine dye IR1051 in hybrid sol-gel channel waveguides with a pump intensity of 300 W/cm^2 at 1064 nm.

With pumping at 355 nm, Kretsch *et al.*[3] obtained net optical gains of g = 15-20 cm^{-1} at pump intensity of 0.87 MW/cm^2 on stilbenoid and perylene vinylene derivative in polystyrene waveguides; Tsutsumi *et al.*[13] observed optical gain of up to 13.8 cm^{-1} for 1,4-Bis[2-[4-[N,N-di(p-tolyl)amino]phenyl] vinyl]benzene (BTAPVB) dye incorporated into different polymers with pump fluences higher than 20 mJ/cm^2; Jordan *et al.*[25] reported gains of 84 cm^{-1} on substituted stilbene-dye-doped polymer waveguide under pumping with pulses of 1.1 mJ/cm^2; Saraidarov *et al.*[39] obtained a gain factor of 14 cm^{-1} for blue laser dye Direct White in sol-gel inorganic-organic hybrid films at a pump intensity of 5 MW/cm^2, and Pisignano *et al.*[26] found a maximum gain coefficient of 5.6 cm^{-1} with photochromic molecule indolinospiropyran (1',3'-dihydro-1',3',3'-trimethyl-6-nitrospiro [2H-1-benzopyran-2,2'-(2H)-indole]) (6-nitro-BIPS) doped in polymer matrix at a pump fluence of 0.5 mJ/cm^2.

From the above comparison it is seen that the values of the net gains measured in this work compare well or are higher than those obtained in similar systems reported in the bibliography.

It is seen in Table 2 that whereas in the waveguides decreasing the film thickness results in a small variation in the gain, in the quasi-waveguides the net gain coefficient increases significantly when the thickness of the film is reduced from 19 to 6 μm. This could be understood in terms of the stronger self-mode-restriction capability in the quasi-waveguides. In the thicker quasi-waveguide (sample 3), more guided modes are allowed to propagate than in the thinner films. The higher-order modes have greater losses than the fundamental and lower-order ones, because light emitted in those modes leaks preferentially to the substrate and is no longer amplified. In the thinner quasi-waveguide (sample **4**), a lower number of modes are allowed and more pump energy appears as amplified light in the fundamental and low-loss lower-order leaky modes, which results in increased gain. In the waveguides (samples **1** and **2**), the modes are not leaky, there are no losses to the substrate, and in both

thick and thin films the light in all the allowed modes is amplified so that the gain is close in both cases. The same effect could explain the much higher decrease in the threshold for ASE emission observed in the quasi-waveguides as compared with the waveguides.

4. Summary and conclusions

We have studied the amplified spontaneous emission and gain characteristics of planar waveguides and quasi-waveguides consisting of PM567-doped PMMA films deposited onto quartz or glass substrates, respectively. Two different methods of preparation were tried: spin-coating and extender roller, leading to films with thicknesses of about 5 μm and 17 μm, respectively.

By following the evolution of the spectral FWHM and the intensity of the light emitted from the edge of the film with increasing the pump intensity, the threshold for ASE emission, characterized by the collapse of the FWHM in the emission spectrum and the change in the slope of the emission intensity, was determined and found to be lower in the thinner films. Threshold values were about 1.0 MW/cm^2 for the thinner films and about 2.0 MW/cm^2 for the thicker ones.

The study of the dependence of the intensity of the ASE emission with the length of the pump stripe at different pump intensities allowed estimating net gain coefficients by fitting the experimental points with appropriate theoretical expressions. The usual approach of considering a one-dimensional amplifier in the small-signal regime leads to an expression widely used to estimate optical gain in thin films, but that is only appropriate when saturation effects are not present. We show that a modification of the small-signal expression incorporating saturation effects allows obtaining an analytic solution in the intermediate saturation regime which leads to a better fitting of our experimental results. In this way, we estimated net gain coefficients of up to 56 ± 9 cm^{-1} at a pump intensity of 5.3 MW/cm^2 for quasi-waveguides and up to 20.6 ± 2.7 cm^{-1} at a pump intensity of 3.4 MW/cm^2 for waveguides. Loss coefficients in the waveguides were estimated to be 3.8 ± 0.4 cm^{-1} and 6.1 ± 1.3 cm^{-1} for the thicker and the thinner films, respectively.

The results obtained seem to indicate a stronger self-mode-restriction capability in the quasi-waveguides that in the waveguides based in the increased losses in the higher-order leaky modes in the quasi-waveguides, where the large reflectivity occurring at grazing incidence leads to significant confinement of the light in the lower-order modes.

Acknowledgments

This work was supported by Projects MAT2004-04643-C03-01 and MAT2007-65778-C02-01 of the Spanish CICYT.

Amplified spontaneous emission and optical gain measurements from pyrromethene 567 – doped polymer waveguides and quasi-waveguides: erratum

A. Costela [1,*], O. García [2], L. Cerdán [1], I. García-Moreno [1], and R. Sastre [1]

[1] *Instituto de Química Física "Rocasolano", C.S.I.C., Serrano 119, 28006 Madrid, Spain*
[2] *Instituto de Ciencia y Tecnología de Polímeros, C.S.I.C., Juan de la Cierva 3, 28006 Madrid, Spain*
[*] *Corresponding author: acostela@iqfr.csic.es*

Abstract: An erratum is presented to correct Eq. (6) in [Opt. Express **16**, 7023-7036 (2008)]

OCIS codes: (140.2050) Dye lasers; (140.3380) laser materials; (230.7390) Waveguides, planar; (230.310) Thin films; (250.2080) Polymer active devices; (250.5460) Polymer waveguides.

References and links

1. A. Costela, O. García, L. Cerdán, I. García-Moreno, and R. Sastre, "Amplified spontaneous emission and optical gain measurements from pyrromethene 567-doped polymer waveguides and quasi-waveguides," Opt. Express **16**, 7023-7036 (2008).

A mistake was made when writing Eq. (6) in Ref. [1], which has to be written as follows:

$$l = \frac{s\, I_t(\lambda)}{g(\lambda)+\eta g'(\lambda)s} + \frac{g(\lambda)}{\left[g(\lambda)+\eta g'(\lambda)s\right]^2} \ln\left|\frac{\eta g'(\lambda)+\left[\eta g'(\lambda)s+g(\lambda)\right]I_t(\lambda)}{\eta g'(\lambda)}\right|. \qquad (6)$$

The authors regret this mistake, which does not affect any numerical result presented or conclusions reached in Ref. [1].

Paper B3: Appl. Phys. B 97, 73–83 (2009)

Waveguides and Quasi-Waveguides based on pyrromethene 597-doped poly(methyl methacrylate)

L. Cerdán, A. Costela, I. García-Moreno, O. García, and R. Sastre

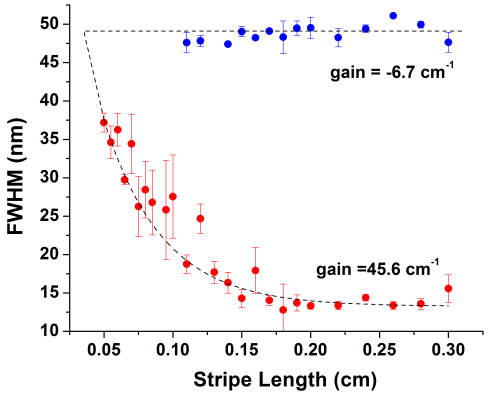

Dependence of the FWHM of the emission spectra on excitation length at two different pump intensities, below (triangles) and above threshold (circles), respectively, for the quasi-waveguide 5 μm thick. The dotted lines are a guide to the eye.

Appl Phys B (2009) 97: 73–83
DOI 10.1007/s00340-009-3518-8

Applied Physics B
Lasers and Optics

Waveguides and quasi-waveguides based on pyrromethene 597-doped poly(methyl methacrylate)

L. Cerdán · A. Costela · I. García-Moreno · O. García · R. Sastre

Received: 30 January 2009 / Revised version: 25 March 2009 / Published online: 2 May 2009

Abstract The characteristics of amplified spontaneous emission (ASE) from asymmetric planar waveguides and quasi-waveguides consisting of thin films of poly(methyl methacrylate) incorporating lasing dye pyrromethene 597 deposited onto quartz and glass substrates, respectively, are investigated. The variable stripe length and moving constant stripe methods, together with appropriate theoretical expressions which take into account gain saturation and a simple model based on a four-level laser, allow for obtaining the net gain coefficients as a function of pump intensity, losses, pump thresholds for the onset of ASE, effective stimulated emission cross sections, pump saturation intensities, and saturation lengths. Net gain coefficients of up to 84 ± 3 cm^{-1} at a pump intensity of 404 kW/cm^2 (28 μJ/pulse) for quasi-waveguides and up to 59 ± 6 cm^{-1} at a pump intensity of 360 kW/cm^2 (25 μJ/pulse) for waveguides were obtained, with pump thresholds of 15.7 kW/cm^2 (1.1 μJ/pulse) and 6.3 kW/cm^2 (0.43 μJ/pulse), respectively. When waveguides 8 μm thick were irradiated with pulses of 200 kW/cm^2 at 10 Hz repetition rate, the ASE remained at 79% of its initial value after 1000 pump pulses in the same position of the sample. In quasi-waveguides 10 μm thick, the emission remained at 82% of the initial value under the same conditions.

L. Cerdán · A. Costela (✉) · I. García-Moreno
Instituto de Química Física "Rocasolano", C.S.I.C., Serrano 119, 28006 Madrid, Spain
e-mail: acostela@iqfr.csic.es
Fax: +34-91-5642431

O. García · R. Sastre
Instituto de Ciencia y Tecnología de Polímeros, C.S.I.C., Juan de la Cierva 3, 28006 Madrid, Spain

PACS 42.55.Mv · 42.70.Jk · 42.79.Gn · 42.82.Et · 78.20.-e · 78.66.Qn

1 Introduction

The development of organic lasers based on dyes incorporated into appropriate polymer materials is an active field of research, because of the wavelength tunability, easiness of processing, high efficiency, and low fabrication cost that these media offer [1, 2]. In particular, the utilization of dye-doped materials in the form of thin films incorporated into waveguiding structures has raised much interest because the use of planar structures allows for integration of various optical components on a single substrate, and opens the door to the fabrication and development of light sources based on structures suitable for integration in optoelectronic devices.

Over the last decade, numerous studies have been reported on the properties of dye-doped organic thin films and planar waveguides from the point of view of their behavior as generators of amplified spontaneous emission (ASE) and laser action [3–32]. Although a variety of dyes have been considered for this application, it is surprising that not much attention has been paid to laser dyes of the pyrromethene family (4,4-difluoro-3a,4a-diaza-4-bora-*s*-indacene dyes), generally named dipyrromethene. BF_2 dyes (PM dyes for short). These are highly efficient and photostable laser dyes, with emission in the green-yellow to red spectral region, which outperform the laser behavior of the well known rhodamine dyes [33–39]. In spite of the PM dyes having demonstrated excellent lasing properties in solid matrix [1, 2, 40], only a few studies have appeared on their emission properties in thin films apart from a recent report of us on ASE from pyrromethene 567-doped polymer waveguides

and quasi-waveguides [41, 42]. Goudket et al. [26] considered the importance of dye host on absorption, losses and ASE of Pyrromethene 597-doped polymer thin films, and a couple of studies reported on some characteristics of the laser output from Pyrromethene 567-doped plastic and hybrid waveguides with distributed feedback structures [11, 43].

In this paper, we consider ASE from thin films of poly(methyl methacrylate) (PMMA) doped with the dye pyrromethene 597 (PM597). Asymmetric waveguides and quasi-waveguides (characterized by having substrates with refractive indices lower and higher than those of the thin film deposited on top, respectively) with different thicknesses were prepared and their properties as ASE emitters were assessed. In this study we have refined and systematized both the experimental approach and the theoretical analysis as a follow-up of our previous work with the related dye PM567. In particular, we have implemented an experimental routine which allows for obtaining in a systematic way the losses and net gain coefficients for thin films of different thicknesses at increasing pump intensities. A simple theoretical model based on a four-level laser system applied to the net gain and loss data so obtained provides information on pump threshold for the onset of ASE, effective stimulated emission cross sections, and pump saturation intensity. Although quasi-waveguides are characterized by the light not being fully confined into the waveguide channel but leaking into the substrate, it has been pointed out that the leaky waveguides could provide a useful output coupling mechanism in an active-waveguide laser device [44–46]. Our results indicate a higher net gain capability in the quasi-waveguides than in the waveguides, albeit with a higher pump threshold intensity. This is consistent with our previous studies [41, 42], where the results obtained indicated a stronger self-mode restriction capability in the quasi-waveguides than in the waveguides. The increased losses in the higher-order leaky modes in the quasi-waveguides combined with the large reflectivity occurring at grazing incidence led to significant confinement of the light in the lower-order modes.

2 Experimental

Asymmetric slab optical waveguides consisting of dye-doped polymer films deposited onto quartz and glass substrates (0.88 and 0.98 mm thick, respectively) were prepared using an extender roller technique [47]. PMMA of 25,000 molecular weight (Polysciences, Inc.) in proportion 100–200 mg/mL, depending on the desired thickness, was added to a solution of chloroform (Merck) containing PM597 (laser grade, from Exciton) at a concentration (with respect to polymer) of 5×10^{-2} M. Photophysical studies did not show any evidence of dye aggregation at this rather high dye concentration. A few drops of the solution were placed on a standard glass microscope slide or quartz slide and extended along the slide with a calibrated rod (endless screw with calibrated thread). After solvent evaporation at 50°C for 15 min, films with thickness between 5 and 13 μm were produced. In all cases the thickness of the films was determined by using a gravimetric method (accuracy of balance: 10^{-4} g), taking into account the density of the polymeric film (1.19 g/mL).

In the quartz/doped polymer/air structure, the measured refractive index of the dye-doped polymer layer ($n_1 = 1.4900$) is higher than the measured index of the quartz substrate ($n_2 = 1.4583$). Thus, total internal reflection at the film/quartz interface confines and guides the light along the film, and edge emission is obtained. When the substrate is glass, its refractive index (measured to be $n_2 = 1.5176$) is higher than that of the doped polymer film. Thus, no total internal reflection takes place at the film/substrate interface and the emitted light leaks into the substrate. A leaky waveguide or quasi-waveguide is obtained, where light is confined by the film/air interface while the reflection at the film/substrate boundary is leaky.

The waveguides were optically pumped at 532 nm with 30 ns full width at half maximum (FWHM) pulses from a frequency-doubled Q-switched Nd:YAG laser (Lotis TII SL-2132). The laser was operated at 1.5 Hz repetition rate, and the pulse energy was controlled by insertion of calibrated neutral density filters in the beam path. Pump energy was measured with a calibrated Laser Energy Meter (QE 12LP-S-MB-DO, Gentec). The experimental setup is shown schematically in Fig. 1. A combination of negative and positive cylindrical quartz lenses ($f = -15$ cm and $f = +15$ cm, respectively), perpendicularly arranged, focused the pump beam to a narrow horizontal line onto the surface of the film. An adjustable slit was used to select only the central portion of the pump beam. A micrometer screw allows one to precisely select the width of the slit. The light incident on the sample was perpendicular to the film surface, defining an excitation stripe of ∼150 μm ×3 mm, with an end placed right up to the edge of the film. The edge emission from the sample was collected with a 5-cm focal length spherical lens, focused onto a fibre bundle and detected with a spectrograph/monochromator (SpectraPro-300i Acton Research) equipped with a thermoelectrically cooled CCD detector (SpectruMM:GS 128B). The sample was placed on a XY-translation stage with micrometer screws to allow for precise positioning.

3 Theory

When the samples are pumped at excitation intensities above a certain threshold value, the spontaneously emitted photons

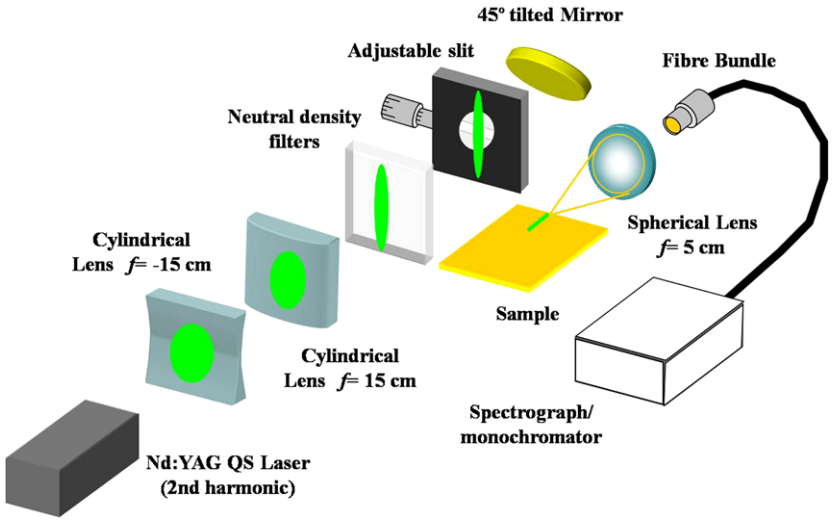

Fig. 1 Schematic of the experimental setup

are amplified by stimulated emission as they travel along the stripe-shaped gain region and amplified spontaneous emission (ASE) occurs. The net gain of the doped polymer film can be measured by using the variable stripe length (VSL) method [48], which consists basically in pumping optically the sample with a stripe-shaped beam of variable length at constant intensity and measuring the intensity of the edge-emitted ASE as a function of stripe length. Considering the pumped region as an unsaturated amplifier having a length much greater than the diameter, the ASE intensity collected at the waveguide edge varies with the pump stripe length as [41]

$$I(\lambda) = \frac{\eta g'(\lambda)}{g(\lambda)}\left(e^{g(\lambda)l} - 1\right), \tag{1}$$

where $g'(\lambda)$ is the internal gain coefficient due to stimulated emission processes, $g(\lambda)$ is the net gain coefficient, $g(\lambda) = g'(\lambda) - \alpha$, with α being the loss coefficient, l is the length of the pumped stripe, and η is a coefficient proportional to the spontaneous emission rate and to a geometrical factor that depends on the amplifier dimensions.

Equation (1) represents the output intensity from the end of the stripe in the small-signal regime. Thus, in the absence of saturation, g can be determined by plotting the intensity of the ASE as a function of the pumped stripe length and fitting the resulting curve to the expected dependence given by (1). If the ASE intensity reaches the saturation level, (1) is no longer appropriate, and it should be replaced by [41, 42]

$$l = \frac{sI(\lambda)}{g(\lambda) + \eta g'(\lambda)s} + \frac{g(\lambda)}{[g(\lambda) + \eta g'(\lambda)s]^2} \times \ln\left|\frac{\eta g'(\lambda) + [\eta g'(\lambda)s + g(\lambda)]I(\lambda)}{\eta g'(\lambda)}\right|, \tag{2}$$

where s is a gain saturation parameter ($s = 1/I_{sg} = \sigma_e \tau / h\upsilon$, where σ_e is the emission cross section, τ is the fluorescence lifetime, and υ is the frequency of the ASE). Plotting the intensity of the ASE as a function of the length of the pumped stripe and fitting the resulting curve to the expected dependence given by (2) allows for determining the net gain coefficient g.

A lasing dye can be considered as a four-level laser system [49], with the population inversion Δn between upper and lower laser levels given by [50]

$$\Delta n \approx n_t \frac{I_p/I_{sp}}{1 + I_p/I_{sp}}, \tag{3}$$

where n_t is the total population density or density of active centers, I_p is the pump intensity, and I_{sp} the pump saturation intensity. Thus, the net gain can be written as [50]

$$g = \sigma_e \Delta n - \alpha \approx \sigma_e n_t \frac{I_p/I_{sp}}{1 + I_p/I_{sp}} - \alpha. \tag{4}$$

Defining the threshold intensity I_{th} for ASE as the pump intensity for which $g = 0$, we obtain from (4)

$$I_{th} = I_{sp} \frac{\alpha/(\sigma_e n_t)}{1 - \alpha/(\sigma_e n_t)}. \tag{5}$$

As we have prepared waveguides with different thicknesses, it would be useful in the analysis of the results obtained to have an estimation of the number of modes supported for a waveguide with a given thickness. Following the treatment of Saleh and Teich [51], the number of modes M allowed in an asymmetric planar dielectric waveguide consisting of a dielectric slab of width d and refractive index n_1 placed on a substrate of lower refractive index n_2 and

covered with a medium of refractive index $n_3 < n_2 < n_1$ is given by

$$M \doteq \frac{\sin\bar{\theta}_{c12}}{\lambda/(2d)} - \frac{1}{\pi}\tan^{-1}\left(\frac{\sin^2\bar{\theta}_{c13}}{\sin^2\bar{\theta}_{c12}} - 1\right)^{1/2}, \quad (6)$$

where λ is the wavelength of the light propagating inside the waveguide, and $\bar{\theta}_{cij} = \pi/2 - \theta_{cij} = \pi/2 - \sin^{-1}(n_j/n_i)$ is the complement to the critical angle of incidence in the interface between media i and j. The symbol $\doteq$ denotes that the number of modes is the smallest integer greater than the figure given by the right hand term in (6). Using (6) in our case, it is estimated that the number of modes supported for light of 590 nm propagating in waveguides of thickness 5, 8, 11, and 13 μm is 6, 10, 13, and 15, respectively.

4 Results and discussion

4.1 ASE from quasi-waveguides

When the gain medium was deposited onto glass substrate a quasi-waveguide is obtained, where light propagating at angles greater than the critical angle $\theta_c = 42°$ will be totally reflected at the film/air interface, while at the doped polymer/glass interface no total reflection takes place at any angle, and light leaks into the substrate. Nevertheless, significant confinement of the light still takes place because of the high reflectivity occurring at grazing incidence [52]. The different transverse modes propagating within the gain layer have different reflectivity losses due to the Fresnel law. Although several low-loss leaky modes may exist when the thickness of the gain layer is large compared with the wavelength of the light [53], the fundamental mode is the one with lower losses and, thus, light is amplified preferably in this mode [54]. As a result, a quasi-waveguide provides a much stronger self-mode restriction capability than conventional total internal-reflection waveguides.

Six different quasi-waveguides with film thicknesses of 5, 6, 9, 10, 11, and 13 μm were prepared. In all cases, at low pump intensities the light emitted from the edge of the film exhibited a broad emission spectrum, with a FWHM in the range 40–50 nm, which decreased to 10–15 nm at pump intensities above a certain threshold value. The intensity of the emitted light grew linearly with the pump intensity but with a distinct change in slope at pump threshold (Fig. 2). As is well known, the collapse of the FWHM in the emission spectrum and the change in the slope in the emission intensity with increasing pump intensity are a signature of the onset of ASE above a certain pump threshold [48]. Further evidence of the ASE character of the emission above threshold can be obtained by varying the length of the pump stripe [48]. As seen in Fig. 3, below the ASE threshold ($g < 0$) the emission spectrum remains broadband

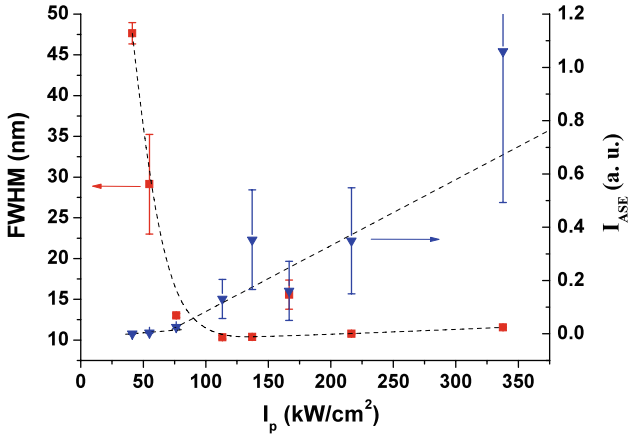

Fig. 2 Dependence of the FWHM of the emission spectra (*squares*) and intensity of the output emission (*triangles*) on pump intensity for a 3 mm length pumped stripe on the quasi-waveguide sample 5 μm thick. The *dotted lines* are a guide to the eye

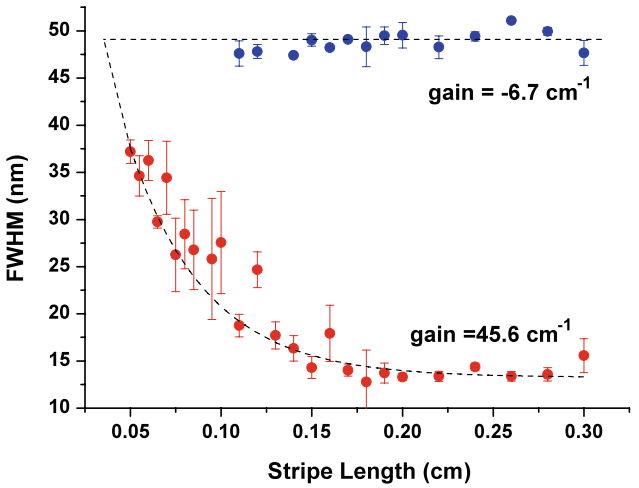

Fig. 3 Dependence of the FWHM of the emission spectra on excitation length at two different pump intensities, below (*triangles*) and above threshold (*circles*), respectively, for the quasi-waveguide 5 μm thick. The *dotted lines* are a guide to the eye

for any excitation length, but above threshold ($g > 0$) gain sets in and the spectrum becomes narrower as the excitation length increases. Another important parameter is the ASE peak wavelength, which for the quasi-waveguides was centered at about 584 nm (Fig. 4). It can be noticed that below a certain threshold intensity the emission peak wavelength jumps slightly from the ASE (584 nm) to the fluorescence peak wavelength (588 nm).

For each quasi-waveguide, systematic measurements were carried out of the intensity of the ASE peak wavelength as a function of excitation length for different pump intensities. Typically nine different pump intensities were tried with every sample, from 40 kW/cm^2 up to 450 kW/cm^2. Figure 5 shows an example of the variation of the emitted light at the ASE peak wavelength with the length of the

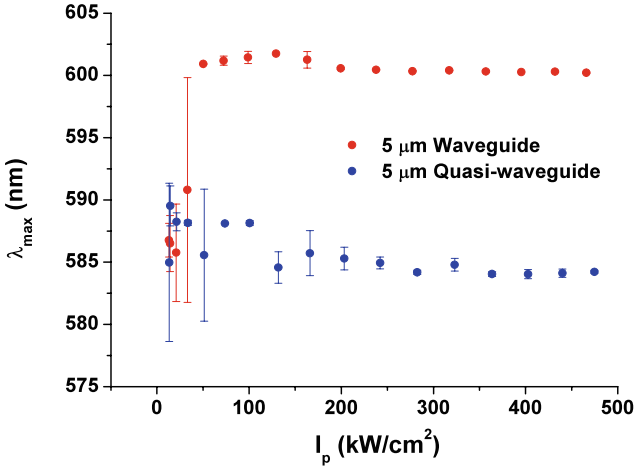

Fig. 4 Dependence of the peak wavelength of the ASE with pump intensity

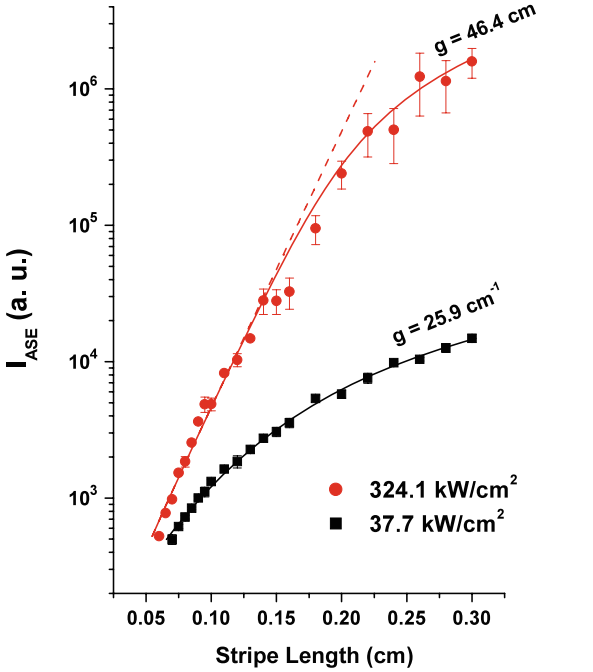

Fig. 5 Dependence of the emission intensity on the excitation length at two different pump intensities for the quasi-waveguide sample of 13 μm thick. The *dashed line* is a fit to the data using (1). The *solid lines* are fits to the data using (2)

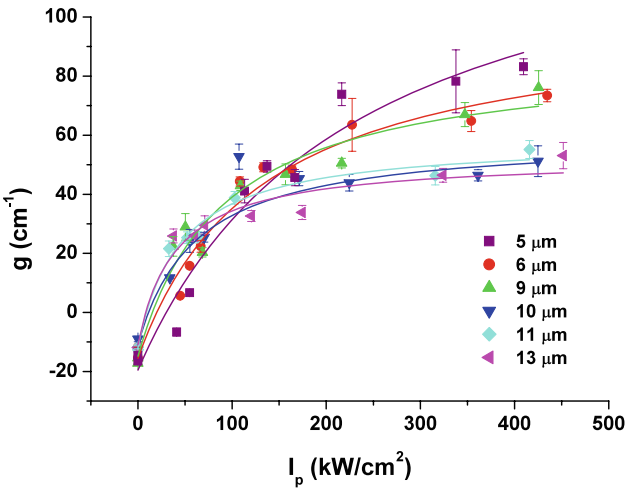

Fig. 6 Variation of the net gain coefficient with pump intensity for the quasi-waveguides. The *solid lines* are fits to the data using (4)

pumped stripe for the quasi-waveguide with 13 μm thickness and two different pump intensities. Similar plots are obtained for the other samples. Each point in the graph is an average of four measurements. If (1) is used to fit the lower subset of experimental data the dashed line is obtained, which departs from the experimental behavior at high stripe lengths because of gain saturation, an effect not considered in the derivation of (1). Gain saturation occurs because the light travelling in the sample is so strongly amplified that it depletes a substantial fraction of the excitation. As gain saturation sets in, the gain coefficient is reduced and light is not exponentially amplified further as the length of the pumped stripe is increased. To ensure that saturation is not caused by sample degradation, each point was obtained by pumping a fresh region.

The solid lines in Fig. 5 are obtained by fitting the experimental data to the expected dependence as given by (2). In this way, the net gain coefficients for the different samples are obtained for increasing pump intensities.

In Fig. 6 are presented the results obtained for the net gain coefficients for the different quasi-waveguides as a function of the pump intensities. Formally, according to (4) at zero pump intensity, $g = -\alpha$. Thus, in Fig. 6 the points at $I_p = 0$ have been experimentally determined by using the moving constant stripe method, where the pumped stripe is gradually translated away from the edge of the sample while keeping the stripe length constant ($l = 2$ mm) and the ASE is measured as a function of the distance x between the end of the pump stripe and the edge of the sample. Assuming that the ASE from the end of the excited stripe I_0 is constant, the emission from the edge of the sample should decrease as the stripe is displaced as a result of waveguide losses (absorption and scattering) following the Beer-Lambert law:

$$I = I_0 e^{-\alpha x}. \tag{7}$$

Thus, plotting the output intensity of the ASE as a function of the distance x, and using (7) to fit the experimental data, the loss coefficients α are obtained for the different samples.

The solid lines in Fig. 6 are the best fits obtained using (4). The parameters that produce those best fits are collected in Table 1, together with the values of the pump threshold intensity obtained by incorporating those parameters into (5).

Table 1 Parameters derived from the characterization of the net optical gain

Substrate	Film thickness (μm)	α (cm^{-1})	I_{sp} (kW/cm^2)	$\sigma_e \times 10^{18}$ (cm^2)	I_{th} (kW/cm^2)
Glass (quasi-waveguides)	5	15.7 ± 3.9	117 ± 9	4.4 ± 0.3	15.7 ± 1.7
	6	15.5 ± 3.7	131 ± 30	3.9 ± 0.3	20.0 ± 4.6
	9	14.8 ± 4.5	90 ± 26	3.4 ± 0.3	15.3 ± 4.3
	10	11.1 ± 1.9	61 ± 10	2.4 ± 0.1	11.4 ± 1.9
	11	11.9 ± 2.4	45 ± 9	2.3 ± 0.1	9.1 ± 1.8
	13	10.9 ± 5.2	40 ± 14	2.1 ± 0.2	8.3 ± 3.0
Quartz (waveguides)	5	6.6 ± 4.0	72 ± 24	2.7 ± 0.3	6.3 ± 2.2
	8	10.2 ± 2.4	37 ± 8	2.4 ± 0.1	6.2 ± 1.3
	11	3.6 ± 1.4	125 ± 9	1.3 ± 0.1	12.5 ± 11.0
	13	5.8 ± 0.5	155 ± 30	0.8 ± 0.06	50.6 ± 9.7

The values for the stimulated emission cross sections in Table 1 require an explanation. The stimulated emission cross section is a characteristic of the dye molecule and thus, should be independent of the thickness of the sample. The apparent decrease of the value of σ_e as the thickness of the sample increases is the result of one of the simplifying assumptions implicit in the derivation of (3) and (4), which were obtained assuming constant and homogeneous pumping through the whole film depth. In fact, the pumping is inhomogeneous both temporally and spatially. In particular, the pump intensity varies with the depth of the sample because the incident pump pulse is being absorbed as it travels down the thickness of the sample. This results in a variation of the population inversion in time and with depth. A rigorous treatment of this problem is complex, but nevertheless it is possible to obtain a qualitative understanding of the actual behavior of the system by using a simplified two-level model based on two premises: (i) there is no excited state population depletion due to stimulated emission, and (ii) neither reabsorption of the emitted radiation nor intersystem crossing takes place. With these assumptions one could write for the evolution of pump and population (taking the z-axis as the direction of the incident pump beam)

$$\frac{dn}{dt} = -\sigma_a n I_p + \frac{n_t - n}{\tau}, \tag{8}$$

$$\frac{dI_p}{dz} = -\sigma_a n I_p, \tag{9}$$

where n is the population of the ground state, σ_a is the absorption cross section at the pump wavelength, and τ is the fluorescence lifetime. Solving numerically the above equations assuming a 30 ns FWHM Gaussian pump pulse, the population inversion $\Delta n = n_t - n$ as a function of pump intensity and sample thickness is obtained (Fig. 7).

It is seen in Fig. 7 that the inhomogeneity of the pump radiation in the z-direction results in a decrease of Δn along

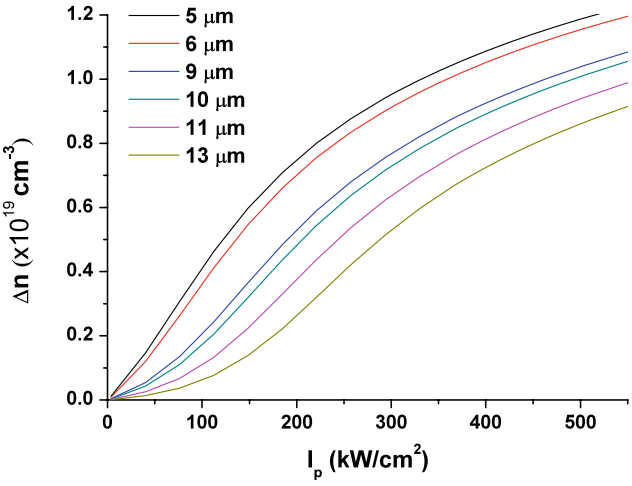

Fig. 7 Population inversion Δn as a function of pump intensity and sample thickness as predicted by (8) and (9)

the thickness of the film. Thus, the gain that we are measuring experimentally is an average number reflecting the spatial and temporal average of the population inversion along the thickness of the different samples. Equations (3) and (4) were obtained with no consideration of the pump inhomogeneity, and in them Δn is considered to be constant. Thus, when we use those equations to fit experimental results such as those plotted in Fig. 6, we are forcing Δn to be constant and the fitting procedure translates the variation in Δn to a variation in σ_e.

The above reasoning indicates that the σ_e values in Table 1 should be considered as a kind of *effective* values, reflecting the pumping inhomogeneity. These values allow for obtaining in first approximation comparative conclusions on the best media from the point of view of the effectiveness of the ASE.

The gain saturation effect can be accounted for in terms of saturation length l_s, defined as the excitation length for

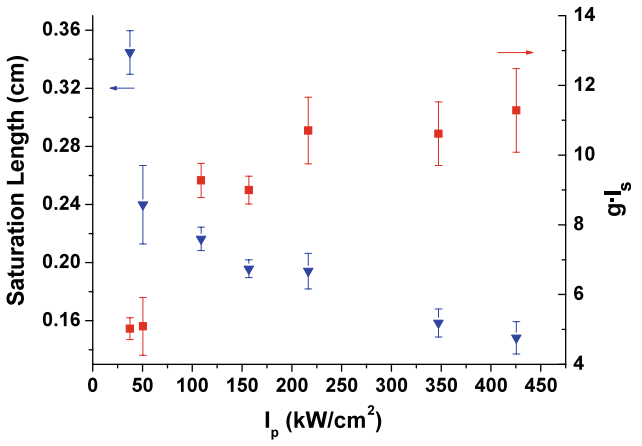

Fig. 8 Dependence of the saturation length (*triangles*) and the net gain–saturation length product (*squares*) on the pump intensity for the 9 μm thick quasi-waveguide

which the emitted intensity equals the gain saturation intensity. Thus, setting in (2) $I(\lambda) = I_{sg} = 1/s$ and using the parameters provided by fits such as that in Fig. 5, a value of l_s can be estimated for the different values of g, that is, for the different pump intensities. Figure 8 shows the saturation lengths and the corresponding net gain–saturation length products for different pump intensities for the quasi-waveguide with 9 μm thickness. It is seen in Fig. 8 that the product gl_s levels at a value of about 10 once the pump intensity is in the range 150–200 kW/cm^2, in which case the plot in Fig. 8 indicates a saturation length of about 2 mm. When gain saturation occurs, the gain coefficient is reduced and light is not amplified further as the length of the stripe is increased [55]. Thus, plots such as those in Fig. 8 provide information on the useful pump intensities and pump stripe lengths to optimize ASE. Plots similar to those shown in Fig. 8 have been obtained empirically by Kobayashi et al. [56] in a luminescent polymer gain medium, where the gl_s product levels at a value of about 4. A value of $gl \approx 4$ for the onset of gain saturation was also obtained by McGehee et al. [48] in thin-film planar waveguides of a conjugate polymer. In our previous work on quasi-waveguides, where the gain medium was the dye PM567 [41, 42], the gain saturation also onsets at $gl \approx 4$. In all those previous works the gl value for which saturation sets in was obtained empirically, from visual inspection of plots of the ASE output intensity *vs.* excitation length, which involves a certain degree of subjectivity. The procedure we propose here to estimate gl_s allows for an objective determination of this important parameter, and it takes into account its dependence on the pump power. In Fig. 8 it is seen that, although at low pump powers the gl_s product has a value of about 5, similar to those quoted in the previous works, there is room to increase this number by increasing the pump power up to a certain value which determines the best experimental conditions to optimize ASE. In a recent VSL study on silicon nanocrystal waveguides, Dal Negro et al. [57] obtained results consistent with those reported above. On the basis of a simple saturation model in a four-level amplifier they predicted a gain-length product for the onset of gain saturation in VSL experiments of about 10.

4.2 ASE from waveguides

When the PM597 doped PMMA thin films were deposited onto quartz substrates, total reflection takes place at the polymer film–substrate interface for light incident at angles higher than the critical one (76.6° in our case) and waveguiding results.

Waveguides with film thickness of 5, 8, 11, and 13 μm were prepared. In all of them, ASE, characterized by an important decrease in the spectral width and a change in the slope of the output emission intensity at pump intensities above a certain threshold, was observed. The ASE peak wavelength was centered at about 600 nm (Fig. 4). It can be noticed again that below a certain threshold intensity the emission peak wavelength jumps abruptly from the ASE (600 nm) to the fluorescence peak wavelength (588 nm).

Following the procedure described in the previous section, the VSL method provided data on the intensity of the emitted light at the ASE peak wavelength as a function of excitation length for different pump intensities, and net gain coefficients were obtained by using (2) to fit the data (Fig. 9). Plotting the gain coefficients so obtained as a function of the pump intensities and fitting those values to the behavior predicted by (4) (Fig. 10, solid lines) gives the parameters collected in Table 1. As explained in the previous section, the points at zero pump intensity in Fig. 10 correspond to $g = -\alpha$, and they are obtained by using (7) to fit the data on the output emission intensity as a function of the displacement of the pump stripe from the edge of the sample. The values of I_{th} in Table 1 are obtained by using (5). Saturation lengths and net gain–saturation length products for different pump intensities for the waveguide with 8 μm thickness are plotted in Fig. 11.

As in the case of the quasi-waveguides, there is a difference in the evolution of the net gain coefficient as a function of the pump intensity (Fig. 10) between films with thickness below and over 10 μm, resulting in net gain values of up to 59 cm^{-1} for pump intensities in the range 360–380 kW/cm^2 for the waveguides with thicknesses of 5 and 8 μm, whereas in the waveguides with thickness of 11 and 13 μm the net gain coefficients are of 10–12 cm^{-1} at the same pump intensity. In addition to the different behavior regarding gain evolution, the waveguides with thickness above 10 μm exhibit also some peculiarities in their parameters, which complicate the analysis of their properties. Thus, we are to center first in the waveguides thinner than 10 μm and the comparison of their properties with those of the corresponding quasi-waveguides.

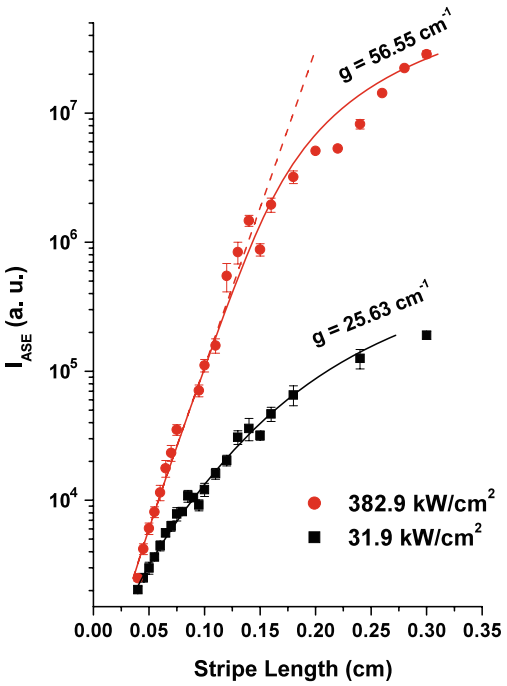

Fig. 9 Dependence of the emission intensity on the excitation length at two different pump intensities for the 8 μm thick film deposited on quartz substrate. The *dashed line* is a fit to the data using (1). The *solid lines* are fits to the data using (2)

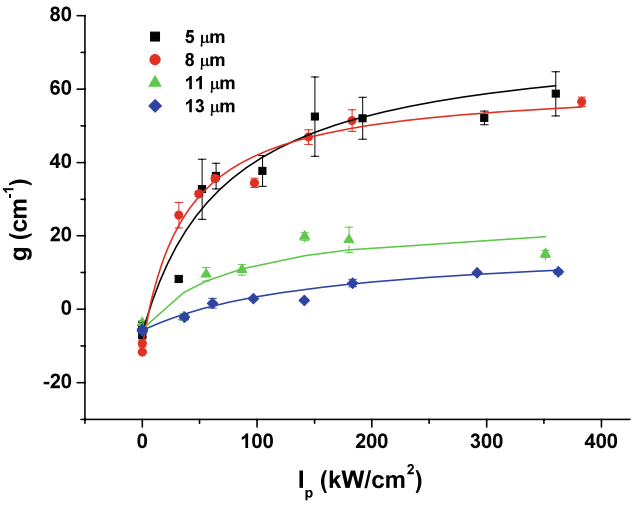

Fig. 10 Variation of the net gain coefficient with pump intensity for the waveguides. The *solid lines* are fits to the data using (4)

The differences of behavior between waveguides and quasi-waveguides with thickness below 10 μm are not difficult to understand. Close inspection in Figs. 6 and 10 shows that at pump intensities below ∼200 kW/cm^2 the net gain of the films deposited on quartz substrate is always higher than that of the quasi-waveguides. At a pump intensity of 200 kW/cm^2, gain saturation is well set up in the waveguides whereas in the quasi-waveguides there is still

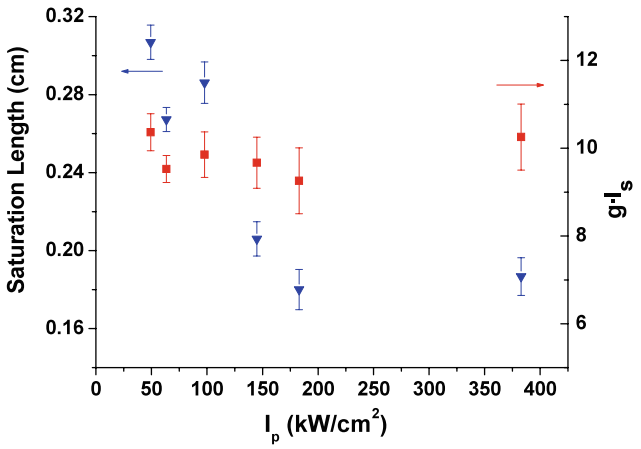

Fig. 11 Dependence of the saturation length (*triangles*) and the net gain–saturation length product (*squares*) on the pump intensity for the 8 μm thick waveguide

some room for further increase of the gain with the pump intensity. This behavior can also be inferred from Figs. 8 and 11, where it is seen that the gain–saturation length product for the 8 μm waveguide has a value slightly lower than 10 for all the pump intensities, whereas in the case of the 9 μm quasi-waveguide the value of gl_s increases with the pump intensity until finally reaching a plateau, with value slightly over 10, for pump intensities over 250 kW/cm^2. Intrinsically, the quasi-waveguides or leaky waveguides have higher losses than the waveguides, and this is reflected in Table 1. As a result, the net gain coefficients before saturation are higher in the waveguides than in the quasi-waveguides. This same effect makes the onset of gain saturation in quasi-waveguides take place at higher pump intensities than in the waveguides. As in the quasi-waveguides a large fraction of the emission goes to the substrate, stronger pumping is necessary for having an intensity of the emission travelling along the active medium similar to that in the waveguides. This fact is also clearly reflected in Table 1, where it is seen that for films of similar thickness pump saturation happens at much higher intensity in the quasi-waveguides that in the waveguides. The same reason explains the lower threshold for ASE observed in the waveguides.

The behavior of the waveguides thicker than 10 μm follows a different pattern, and it is more difficult to understand. The gain is always much lower than those of the corresponding quasi-waveguides and saturates at pump intensities of about 70 kW/cm^2. This gain saturation intensity is much lower than those which saturate both the thinner waveguides and all the studied quasi-waveguides. The pump threshold for the onset of ASE also increases considerably, being especially high in the 13 μm waveguide. A tentative qualitative explanation for this behavior could be obtained by taking into account the inhomogeneity of the pump radiation along the thickness of the samples that we have discussed in the previous section. This inhomogeneity results

in lower effective population inversion as the thickness of the film increases, which results in lower gain and higher threshold. In addition, the higher the thickness of the film is, the higher the number of allowed modes in the waveguide. We have already seen in Sect. 3 that the number of allowed modes in an 11 μm waveguide is twice those allowed in the 5 μm waveguide. The higher modes have higher thresholds and as all the modes compete for the available population inversion, in the thicker waveguides the ASE photons are distributed among more modes, which means less photons per mode for a given pump intensity. Thus, higher pump intensity is required in the thicker waveguides to reach threshold and pump saturation.

In the quasi-waveguides, there is a discrimination against the higher-order modes in that the light emitted in those modes leaks preferentially to the substrate and is no longer amplified. Thus, increasing the thickness does not result in the available population inversion being shared with higher modes and, thus, pump threshold does not increase.

The stability of the different samples was assessed by pumping them repeatedly in the same position with an intensity of 200 kW/cm^2 at 10 Hz repetition rate. After 1000 pump pulses in the same position of the sample, the emission output decreased to 45 and 63% of the initial value in the 5 μm thick films deposited onto glass and quartz substrates, respectively. When the thickness of the films was increased to 10 μm (quasi-waveguide) and 8 μm (waveguide), the intensity of the ASE remained at 82 and 79%, respectively, of the initial value.

The results here reported improve significantly those obtained in our previous work using dye PM567 [41, 42]. The highest net gain coefficients then obtained were 56 and 21 cm^{-1} for quasi-waveguides and waveguides, respectively, with pump intensities in the MW/cm^2 range. In the present case, use of PM597 as active medium results in higher net gains with pump intensities lower by one order of magnitude. Threshold pump intensities, which with PM567 were in the range 1–2 MW/cm^2, are now lower by two orders of magnitude.

Although in the literature on ASE from waveguides the pump radiation incident onto the sample is usually characterized by its intensity (in units of watts per square centimeter), some authors use fluence (energy per square centimeter) or just energy per pulse. To facilitate comparison of our results with previous ones in the literature, we present in Table 2 the highest net gain coefficients obtained in this work with both quasi-waveguides and waveguides, together with pump and threshold values in kW/cm^2, mJ/cm^2 and μJ per pulse.

With pumping at 532 nm, Lu et al. [16] obtained ASE with a threshold of 0.16 mJ/cm^2 and gains of up to 40 cm^{-1} with optical waveguides based on polystyrene films doped with dye 4-(di-cyanomethylene)-2-*t*-butyl-6(1,1,7,7-tetramethyljulolidyl-9-enyl)-4*H*-pyran (DCJTB) and pumped with pulses of 0.13 mJ. The net gain increased to 52.71 cm^{-1} when a mixture of dyes DCJTB and 10-(2-benzothiazolyl)-1, 1, 7, 7-tetramethyl-2,3,6,7-tetrahydro-1*H*,5*H*,11*H*-[1]benzopyrano [6,7,8-*ij*]quinolizin-11-one (C545T) codoped in polystyrene films was used at a pump energy of 0.08 mJ/pulse (Zhang et al. [17]). Threshold in this case was 0.016 mJ/pulse. Djiango et al. [29] obtained net gain coefficients of 37.2 cm^{-1} with near-infrared-emitting dye LDS821 incorporated into poly(4-vinyl)-phenol at a pump fluence of 1.57 mJ/cm^2 (314 kW/cm^2) with threshold for ASE of 0.14 mJ/cm^2 (28 kW/cm^2).

With pumping at 355 nm, Kretsch et al. [3] obtained net optical gains of $g = 15$–20 cm^{-1} at pump intensity of 0.87 MW/cm^2 on stilbenoid and perylene vinylene derivative in polystyrene waveguides; Zhang et al. [31] observed thresholds of 0.072 mJ/pulse and net optical gain of up to 36.3 cm^{-1} for DCJTB doped poly(9,9-diocylfluorene) (PFO) polymer thin films pumped with 0.09 mJ/pulse, and Jordan et al. [23] reported gains of 84 cm^{-1} on substituted stilbene-dye-doped polymer waveguide under pumping with pulses of 1.1 mJ/cm^2, with threshold being reached at an intensity of 0.36 MW/cm^2. With pumping at 337 nm, Yuyama et al. [30] obtained a gain of 14 cm^{-1} from 9.3 μm thick planar waveguides of fluorinated-polyimide doped with LDS950 dye with 0.74 mJ/cm^2 pumping. The lasing threshold was observed to be 0.22 mJ/cm^2.

From the above comparison, it is seen that the values of the net gains measured in this work compare well with or are higher than those obtained in similar systems reported in the literature. The observed thresholds for the onset of ASE are of the order of or lower than those reported in previous work.

5 Summary and conclusions

Asymmetric planar waveguides and quasi-waveguides consisting of PM597-doped PMMA films deposited onto quartz or glass substrates, respectively, have been prepared, and the characteristics of the ASE from the dye-doped polymer films under pumping with nanosecond pulses at 532 nm have been studied in detail.

By using the VSL method, where the intensity of the emitted light is registered as a function of the excitation length at different pump intensities, net gain coefficients could be obtained by fitting the experimental data with appropriate theoretical expressions which take into account gain saturation. A simple theoretical model based on a four-level laser system provides expressions which can be used to fit the data in plots of the net gain coefficients as a function of pump intensity, rendering estimations on pump thresholds, effective stimulated emission

Table 2 Net gain coefficients g and pump threshold for selected quasi-waveguides and waveguides

Substrate	Film thickness (μm)	Pump			g (cm^{-1})	Threshold		
		Intensity/fluence/energy per pulse				Intensity/fluence/energy per pulse		
		kW/cm^2	mJ/cm^2	μJ		kW/cm^2	mJ/cm^2	μJ
Glass (quasi-waveguides)	5	404	12.1	28	84 ± 3	15.7	0.47	1.1
	9	425	12.8	29	76 ± 6	15.3	0.46	1.1
Quartz (waveguides)	5	360	10.8	25	59 ± 6	6.3	0.19	0.43
	8	383	11.5	26	57 ± 1	6.2	0.19	0.43

cross sections, and pump saturation intensities. A proper interpretation of the results obtained requires taking into account the inhomogeneity of the pump radiation along the thickness of the samples, which results in lower effective population inversion as the thickness of the film increases.

Our procedure also allows for an objective estimation of the saturation length l_s, defined as the excitation length for which the emitted intensity equals the gain saturation intensity, and takes into account its dependence on the pump power. This is an important parameter because plots of l_s and gl_s *versus* pump intensity provide information on the useful pump intensities and pump stripe lengths to optimize ASE.

Net gain coefficients of up to 84 and 59 cm^{-1} were obtained for quasi-waveguides and waveguides, respectively. These values compare well to or are higher than previous ones reported in the literature for similar systems. Pump thresholds for the onset of ASE as low as 1.1 μJ (15.3 kW/cm^2) and 0.43 μJ (6.2 kW/cm^2) were demonstrated for quasi-waveguides and waveguides, respectively. The higher net gain capability, albeit with higher pump threshold intensity for the onset of ASE, exhibited by the quasi-waveguides as compared with the waveguides is consistent with our previous studies [41, 42], where evidence was presented indicating a stronger self-mode restriction capability in the quasi-waveguides than in the waveguides.

From a practical point of view, the stability of the ASE output under long time operation is an important parameter. In our case, upon pumping with 200 kW/cm^2 pulses at 10 Hz repetition rate, the ASE from the 5 and 8 μm thick waveguides decreased to 63 and 79% of its initial value, respectively, after 1000 pump pulses in the same position of the sample. In the quasi-waveguides the corresponding drop was to 45 and 82% of the initial output for films with thickness 5 and 10 μm, respectively.

Acknowledgements This work was supported by Project MAT2007-65778-C02-01 of the Spanish CICYT. L.C. thanks MCIIN for a predoctoral scholarship (FPI, cofinanced by Fondo Social Europeo).

References

1. A. Costela, I. García-Moreno, R. Sastre, in *Handbook of Advanced Electronic and Photonic Materials and Devices*, vol. 7, ed. by H.S. Nalwa (Academic Press, San Diego, 2001), p. 161, Chap. 4
2. A. Costela, I. García-Moreno, R. Sastre, Phys. Chem. Chem. Phys. **5**, 4745 (2003)
3. K.P. Kretsch, C. Belton, S. Lipson, W.J. Blau, F.Z. Henari, H. Rost, S. Pfeiffer, A. Teuschel, H. Tillmann, H.-H. Hörhold, J. Appl. Phys. **86**, 6155 (1999)
4. H. Manaa, S.M. Al-Alawi, J. Lumin, **94–95**, 55 (2001)
5. M.C. Castex, C. Olivero, A. Fischer, S. Mousel, J. Michelon, D. Adês, A. Siove, Appl. Surf. Sci. **197–198**, 822 (2002)
6. Y. Kawabe, L. Wang, T. Nakamura, N. Ogata, Appl. Phys. Lett. **81**, 1372 (2002)
7. A.K. Sheridan, A.R. Buckley, A.M. Fox, A. Bacher, D.D.C. Bradley, I.D.W. Samuel, J. Appl. Phys. **92**, 6367 (2002)
8. S.-S. Yap, W.-O. Siew, T.-Y. Tou, S.-W. Ng, Appl. Opt. **41**, 1725 (2002)
9. Y. Oki, S. Miyamoto, M. Maeda, N.J. Vasa, Opt. Lett. **27**, 1220 (2002)
10. Y. Oki, T. Yoshiura, Y. Chisaki, M. Maeda, Appl. Opt. **41**, 5030 (2002)
11. Y. Oki, S. Miyamoto, M. Tanaka, D. Zuo, M. Maeda, Opt. Commun. **214**, 277 (2002)
12. Y. Oki, M. Tanaka, Y. Ogawa, H. Watanabe, M. Maeda, IEEE J. Quantum Electron. **42**, 389 (2006)
13. N. Tsutsumi, T. Kawahira, W. Sakai, Appl. Phys. Lett. **83**, 2533 (2003)
14. M.A. Reilly, C. Marinelli, C.N. Morgan, R.V. Penty, I.H. White, M. Ramon, M. Ariu, R. Xia, D.D.C. Bradley, Appl. Phys. Lett. **85**, 5137 (2004)
15. M.A. Reilly, B. Coleman, E.Y.B. Pun, R.V. Penty, I.H. White, M. Ramon, R. Xia, D.D.C. Bradley, Appl. Phys. Lett. **87**, 231116 (2005)
16. W. Lu, B. Zhong, D. Ma, Appl. Opt. **43**, 5074 (2004)
17. D. Zhang, D. Ma, Appl. Opt. **46**, 2996 (2007)
18. E.V. Calzado, J.M. Villalvilla, P.G. Boj, J.A. Quintana, R. Gómez, J.L. Segura, M.A. Díaz García, J. Phys. Chem. **111**, 13595 (2007)
19. E.V. Calzado, J.M. Villalvilla, P.G. Boj, J.A. Quintana, R. Gómez, J.L. Segura, M.A. Díaz García, Appl. Opt. **46**, 3836 (2007)
20. R. Kumar, A.P. Singh, A. Kapoor, K.N. Tripathi, J. Mod. Opt. **10**, 1471 (2005)
21. K. Sakai, T. Tsuzuki, Y. Itoh, M. Ichikawa, Y. Taniguchi, Appl. Phys. Lett. **86**, 081103 (2005)
22. K. Geetha, M. Rajesh, V.P.N. Nampoori, C.P.G. Vallabhan, P. Radhakrishnan, J. Opt. A, Pure Appl. Opt. **8**, 189 (2006)
23. G. Jordan, M. Flämmich, M. Rüther, T. Kobayashi, W.J. Blau, Appl. Phys. Lett. **88**, 161114 (2006)
24. D. Pisignano, E. Mele, L. Persano, A. Athanassiou, C. Fotakis, R. Cingolani, J. Phys. Chem. B **110**, 4506 (2006)

25. M. Kawasaki, S. Mine, J. Phys. Chem. B **110**, 15052 (2006)
26. H. Goudket, T.H. Nhung, B. Ea-Kim, G. Roger, M. Canva, Appl. Opt. **45**, 7736 (2006)
27. Z. Yu, W. Li, J.A. Hagen, Y. Zhou, D. Klotzkin, J.G. Grote, A.J. Steckl, Appl. Opt. **46**, 1507 (2007)
28. A. Büttner, U.D. Zeitner, IEEE J. Quantum Electron. **43**, 545 (2007)
29. M. Djiango, T. Kobayashi, W.J. Blau, B. Cai, K. Komatsu, T. Kaino, Appl. Phys. Lett. **92**, 083306 (2008)
30. S. Yuyama, T. Nakajima, K. Yamashita, K. Oe, Appl. Phys. Lett. **93**, 023306 (2008)
31. D. Zhang, Z. Chen, D. Ma, Appl. Phys. Lett. **103**, 123103 (2008)
32. A.K. Bansal, W. Holzer, A. Penzkofer, E.B. Kley, Opt. Commun. **281**, 3806 (2008)
33. T.G. Pavlopoulos, J.H. Boyer, M. Shah, K. Thangaraj, M.-L. Soong, Appl. Opt. **29**, 3885 (1990)
34. T.G. Pavlopoulos, J.H. Boyer, T. Thangaraj, G. Sathyamoorthi, M.P. Shah, M.-L. Soong, Appl. Opt. **31**, 7089 (1992)
35. J.H. Boyer, A.M. Haag, G. Sathyamoorthi, M.-L. Soong, K. Thangaraj, T.G. Pavlopoulos, Heteroat. Chem. **4**, 39 (1993)
36. S.C. Guggenheimer, J.H. Boyer, K. Thangaraj, M. Shah, M.-L. Soong, T.G. Pavlopoulos, Appl. Opt. **32**, 3942 (1993)
37. M.P. O'Neil, Opt. Lett. **18**, 37 (1993)
38. W.P. Partridge Jr., N.M. Laurendeau, C.C. Johnson, R.N. Steppel, Opt. Lett. **19**, 1630 (1994)
39. T.G. Pavlopoulos, Prog. Quantum Electron. **26**, 193 (2002)
40. A. Costela, I. García-Moreno, D. del Agua, O. García, R. Sastre, J. Appl. Phys. **101**, 073110 (2007)
41. A. Costela, O. García, L. Cerdán, I. García-Moreno, R. Sastre, Opt. Express **16**, 7023 (2008)
42. A. Costela, O. García, L. Cerdán, I. García-Moreno, R. Sastre, Opt. Express **16**, 7587 (2008)
43. Y. Yang, G. Lin, H. Xu, M. Wang, G. Qian, Opt. Commun. **281**, 5218 (2008)
44. V.M. Arutuyan, G.P. Djotyan, A.V. Karmenyan, T.E. Melicksetyan, E.M. Sarkissyan, Opt. Commun. **36**, 227 (1981)
45. D. Shamrakov, R. Reisfeld, Chem. Phys. Lett. **213**, 47 (1993)
46. G.S. He, C.F. Zhao, C.-K. Park, P.N. Prasad, R. Burzynski, Opt. Commun. **111**, 82 (1994)
47. C. Lowe, *Surface Coatings Technology*, vol. 5 (Wiley, London, 1997), p. 60, Chap. VI
48. M.D. McGehee, R. Gupta, S. Veenstra, E.K. Miller, M.A. Díaz-García, A.J. Heeger, Phys. Rev. B **58**, 7035 (1998)
49. L.W. Hillman, in *Dye Laser Principles*, ed. by F.J. Duarte (Academic, San Diego, 1990), p. 20, Chap. 2
50. A. Siegman, *Lasers* (University Science Books, Mill Valley, 1986), pp. 248, 293
51. B.E.A. Saleh, M.C. Teich, *Fundamentals of Photonics* (Wiley, New York, 1991), pp. 248–258, Chap. 7
52. T.-N. Ding, E. Garmire, Appl. Opt. **22**, 3177 (1983)
53. D.B. Hall, C. Yeh, J. Appl. Phys. **44**, 2271 (1973)
54. A. Kumar, V. Rastogi, K.S. Chiang, App. Phys. B **90**, 507 (2008)
55. A. Yariv, *Quantum Electronic*, 2nd edn. (Wiley, New York, 1975), pp. 286–291, Chap. 12
56. T. Kobayashi, M. Flämmich, G. Jordan, R. D'Arcy, M. Rüther, W.J. Blau, Y. Suzuki, T. Kaino, Appl. Phys. Lett. **89**, 131119 (2006)
57. L. Dal Negro, P. Bettoti, M. Cazzanelli, D. Pacifici, L. Pavesi, Opt. Commun. **229**, 337 (2004)

Paper B4: Macromol. Chem. Phys. 210, 1624–1631 (2009)

High-gain long-lived amplified spontaneous emission from dye-doped fluorinated polyimide planar waveguides

L. Cerdán, A. Costela, I. García-Moreno, O. García, R. Sastre, M. Calle, D. Muñoz and J. de Abajo

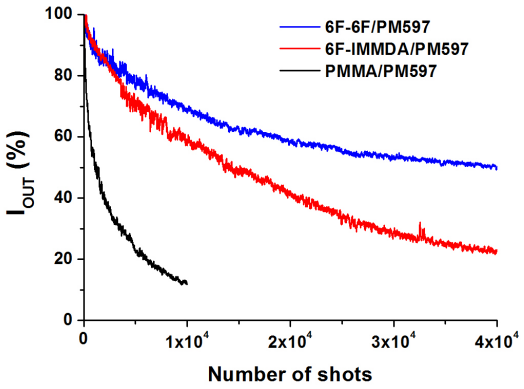

Evolution of the normalized ASE emission as a function of the number of pump pulses in the same position of the sample for polyimide-based and PMMA-based PM597 waveguides. Pump intensity and repetition rate are 220 kW/cm^2 and 5 Hz, respectively.

High-Gain Long-Lived Amplified Spontaneous Emission from Dye-Doped Fluorinated Polyimide Planar Waveguides

Luis Cerdán, Angel Costela,* Inmaculada García-Moreno, Olga García, Roberto Sastre, Mariola Calle, Dulce Muñoz, Javier de Abajo

Long-lived amplified spontaneous emission (ASE) action is demonstrated in waveguides based in transparent newly synthesized fluorinated polyimides (FPI) doped with laser dye Pyrromethene 597. Relevant parameters to optimize the lasing performance of the guides are the polymer chain density and fluorine content. The guide with the higher fluorine content was the most stable, with the ASE emission remaining at 50% of its initial value after 40 000 pump pulses of ≈220 kW · cm^{-2} delivered at a repetition rate of 5 Hz. Net gains of up to 93 cm^{-1} were obtained at a pump intensity of about 500 kW · cm^{-2} (34 μJ pulse^{-1}).

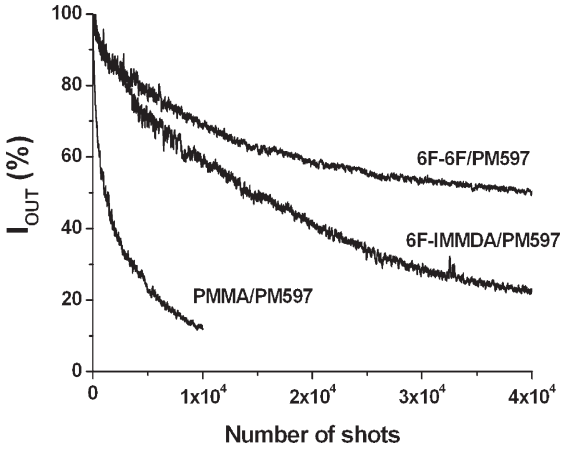

Introduction

Development of organic waveguide lasers based on dye-doped polymers has attracted much attention over the last decade for their potential applications in integrated photonics.[1–23] These gain media assure wide wavelength tunability and high efficiency with potentially very low cost, which makes them very attractive as the basis for very compact and versatile laser systems. A major drawback of these devices is their limited operational lifetime due to dye degradation, and any realistic application passes for extending it.

L. Cerdán, A. Costela, I. García-Moreno
Instituto de Química Física "Rocasolano", CSIC, Serrano 119, 28006 Madrid, Spain
Fax: (+34) 915642431; E-mail: acostela@iqfr.csic.es
O. García, R. Sastre, M. Calle, D. Muñoz, J. de Abajo
Instituto de Ciencia y Tecnología de Polímeros, CSIC, Juan de la Cierva 3, 28006 Madrid, Spain

It is known that improvement in polymer thermal conductivity reduces dye degradation and increases the device's lifetime.[24,25] Thus, any progress in the development of polymeric materials which combines adequate optical properties with improved thermal resistance could result in significant improvements in the lasing performance of devices based on dye-doped organic waveguides.

In past decades usage of imide polymers has increased considerably, and a huge number of contributions, both technical and scientific, have been made in a wide variety of applications.[26–29] Aromatic polyimides have gained a prominent position among high performance polymers because of their excellent balance of properties, in particular the very favorable combination of mechanical, electrical, and thermal resistance. Increase in the demand and technological advances are fostering a growing interest in these special polymers, and research efforts are focusing on developing and modifying aromatic polyimides to accommodate their chemical composition to fulfill technical requirements.

Macromol. Chem. Phys. **2009**, *210*, 1624–1631

DOI: 10.1002/macp.200900212

Fluorine containing polyimides have proved to be specially suitable for these modern applications, and fluorine-containing dianhydrides and diamines have provided new opportunities for chemical manipulation and development of new materials.[30,31] Possibly the most important fluorine containing dianhydride is hexafluoroisopropylidene diphthalic anhydride (6FDA) which exhibits a special potential to impart a low dielectric constant in polymers as well as outstanding solubility in organic media.[32,33] Processing is very difficult for heterocyclic polymers, such as aromatic polyimides, due to the fact that they do not melt before decomposing and are virtually insoluble in organic solvents. Thus, the use of solubilizing monomers, such as 6FDA, is an attractive approach to develop novel polyimides. However, 6FDA and fluorinated diamines are very expensive reactants, and their utilization as condensation monomers is, therefore, limited to the development of materials for special applications.

Only some fluorinated polyimides (FPI) offer a balance of properties very favorable to be used as host materials for lasing chromophores, combining excellent thermal properties with good optical transparency at the wavelengths of interest, which is perhaps the most outstanding property for a polyimide in this application. Nevertheless, although various FPIs have already been used as passive[1,34] and dye-doped active waveguides,[21,35,36] mostly in the infrared (IR) region, to the best of our knowledge there have been no previous studies on their photostability properties under laser irradiation.

In this paper, we demonstrate that long-lived amplified spontaneous emission (ASE) action can be achieved in two transparent newly synthesized FPI waveguides (**6F-6F** and **6F-IMMDA**, Scheme 1) doped with laser dye Pyrromethene 597 (PM597, Scheme 1) under 532 nm pumping. PM597 dye was chosen because it had been demonstrated to lase efficiently and with good stability in bulk solid-state dye lasers.[37–41] The procedure followed to prepare the two FPIs is described in some detail and the new materials are fully characterized.

Thin films of **6F-6F** and **6F-IMMDA** doped with PM597 were deposited onto the glass substrate. The refractive indices of polyimides **6F-6F** and **6F-IMMDA** are higher than that of glass substrate, and thus asymmetric planar waveguides resulted. In a waveguide, total reflection takes place at the polymer film – substrate interface for light incident at angles higher than the critical one, and waveguiding results. The performance of the ASE emission from the FPI-based active media is compared with that of the same dye PM597 incorporated into the more usual polymer poly(methyl methacrylate) (PMMA).

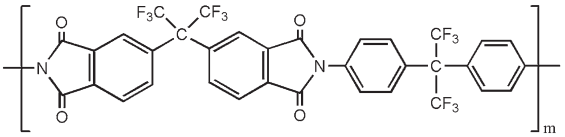

6F-6F

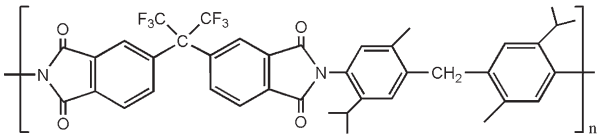

6F-IMMDA

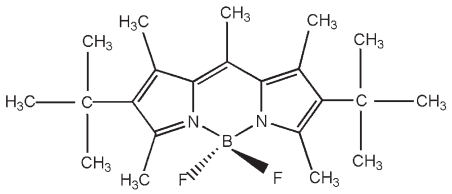

PM597

Scheme 1. Repetition unit of the synthesized polyimides and PM597 dye structure.

Experimental Part

Polymer Synthesis and Film Preparation

Polyimides **6F-6F** and **6F-IMMDA** were prepared from hexafluoroisopropylidene diphthalic anhydride (6FDA) and the corresponding diamine, i.e., hexafluoroisopropylidenedianiline (6F) and 4,4′-methylenebis(2-isopropyl-6-methyl aniline) (IMMDA), respectively. Equimolar amounts of dianhydride and diamine were first made to react at low temperature (0 °C/1 h and for 5 h at room temperature) to attain a solution of polyamic acid, which was then converted into the fully imidized polyimide by treatment with a mixture of acetic anhydride/pyridine for 3 h at room temperature and 3 h at 60 °C. Both polyimides were isolated by precipitation on water, and purified by washing with ethanol several times. The polymers were then dissolved and precipitated once more to remove traces of solvent and oligomers, extracted in boiling ethanol for 12 h and dried overnight under vacuum at 120 °C. Yields were quantitative.

For thermal measurements, films were prepared from polyimide solutions in tetrahydrofuran (THF), with a 7.5% w/w polymer concentration. These solutions were cast on glass plates, and solvent was removed at 25 °C for 24 h. After peeling off the membranes from the glass, they were heated at 180 °C under vacuum for one day.

For optical measurements, asymmetric slab optical waveguides consisting of thin films of polyimides **6F-6F** and **6F-IMMDA** doped with laser dye PM597 and deposited onto the glass substrates, were prepared using the extender roller technique from chloroform solutions of both polyimides (100 mg · mL^{-1}) and the dye ((1–5) × 10^{-2} M).[42] The substrate was 0.98 mm thick, the film thicknesses were 9 μm, and the dye concentration was 2.5 × 10^{-2} M. For comparison, thin films of PMMA doped with PM597 with the same dye concentration and film thickness were also prepared.

Methods

Thermal properties were investigated by differential scanning calorimetry (DSC) and thermogravimetric analysis (TGA). DSC experiments were carried out in N_2 at 20° min^{-1} on a Perkin-Elmer DSC-7 analyzer. Two scans were recorded on each sample, the first one from 50 to 200 °C, to eliminate any residual solvent or water absorbed, and the second one from 50 to 400 °C, to determine the range of glass transition temperature (T_g). TGA curves were recorded at 10° min^{-1} in N_2, from 50 to 800 °C with a Perkin-Elmer TGA-7 analyzer on 2–3 mg samples. Inherent viscosities were measured on filtered 0.5 $g \cdot dL^{-1}$ polymer solutions in *N*-methyl-2-pyrrolidinone (NMP) at 25.0 ± 0.1 °C, in an automated Ubbelohde viscometer.

The refractive indices of polyimides **6F-6F** and **6F-IMMDA** were measured using the Variable Angle Spectroscopic Ellipsometry (VASE) technique (ellipsometer *M*-2000DI from A. Woollam Co., Inc.), and found to be 1.5606 and 1.5523, respectively, at the dye emission wavelength. The refractive indices of PMMA and the glass substrate were measured at room temperature using an Abbe refractometer (Atago) employing 1-bromonaphtalene as sample-support interphase and a sodium lamp as monochromatic light at 589 nm, and found to be 1.4900 and 1.5176, respectively, at the dye emission wavelength.

Amplified Spontaneous Emission Measurements

The thin film samples were optically pumped at 532 nm with 20 ns full width at half maximum (FWHM) pulses from a frequency-doubled *Q*-switched Nd:YAG laser (Lotis TII SL-2132). The laser was operated at 1.5 Hz repetition rate except in the stability studies, where the repetition rate was 5 Hz. The pump radiation was horizontally polarized, which allowed controlling the pulse energy incident onto the sample by insertion into the pump beam path of a half-wave plate (HWP) and a linear polarizer (LP) set with its polarization axis horizontal. By rotating the HWP the linear polarization of the input beam is rotated out of the horizontal, and the pump beam is blocked more or less by the LP, depending on the rotation angle introduced by the HWP. Pump energy was measured with a calibrated Laser Energy Meter (QE 12LP-S-MB-DO, Gentec). The light incident on the sample was perpendicular to the film surface and focused onto that surface in stripe shape of ≈150 μm width by a combination of negative and positive cylindrical quartz lenses ($f = -15$ and $+15$ cm, respectively), perpendicularly arranged. An adjustable slit was used to select only the central portion of the pump beam. A micrometer screw allowed to precisely selecting the width of the slit. Excitation stripes of up to 2 mm length were defined, with an end placed right up to the edge of the film. The edge emission from the sample was collected with a 5 cm focal length spherical lens, focused onto a fiber bundle and detected with a spectrograph/monochromator (SpectraPro-300i Acton Research) equipped with a thermoelectrically cooled CCD detector (SpectruMM:GS 128B). The sample was placed on a XY Motorized Translation Stage, computer controlled, to allow precise positioning.

Results and Discussions

As mentioned in the Experimental Part, FPI were prepared from a fluorinated dianhydride (6FDA) and two diamines by a two-step general procedure, which involves the formation of an intermediate polyamic-acid in a first step and the attainment of the final polyimide in a second step, through a chemical cyclodehydration reaction promoted by a mixture pyridine-acetic anhydride. In this way, polyimides **6F-6F** and **6F-IMMDA** were obtained with high yield and high molecular weight, as it could be stated by measuring their inherent viscosity, η_{inh} (Table 1). Diamine IMMDA was chosen for this work as it is a non-planar monomer which bears side methyl and isopropyl groups, which in principle should provide a comparatively high free volume and, consequently, good solubility. The difference observed in the value of η_{inh} is consistent with the reactivity of the diamines against dianhydrides, and it confirmed that diamine 6F is much less nucleophilic than diamine IMMDA. Relevant properties of the prepared polyimides are collected in Table 1.

Both polymers were soluble in suitable organic media, such as THF and chloroform, which helped in the preparation of dense films by traditional casting methods. The thermal properties of the polyimides, as evaluated by DSC and TGA, were actually very good, with T_g's around 300 °C, much higher than traditional polymers such as acrylics or polycarbonates. Their resistance to high temperature was also outstanding, with initial decomposition temperatures around 500 °C, measured by dynamic TGA.

Thin films of polyimides **6F-6F** and **6F-IMMDA** doped with laser dye PM597 were deposited onto glass substrates,

Table 1. Properties of Polyimides (T_g, Glass transition temperature; T_d, decomposition temperature; η_{inh}, inherent viscosity; ρ, and density; n, refractive index).

Key	T_g [a]	T_d [b]	Char yield [c]	η_{inh}	ρ [d]	n
	°C	°C	%	$dL \cdot g^{-1}$	$g \cdot cm^{-3}$	
6F-IMMDA	281	510	57	1.24	1.2053	1.5523
6F-6F	310	510	50	0.66	1.4660	1.5606

[a] From the second trace of DSC measurements. [b] Initial decomposition temperature as measured by TGA (N_2, 10°min^{-1}). [c] Weight residue at 800 °C measured by TGA. [d] Density was measured on film samples, using a density balance.

Macromol. Chem. Phys. **2009**, *210*, 1624–1631

Macromolecular Journals

DOI: 10.1002/macp.200900212

defining an asymmetric structure consisting of the polymeric slab with refractive index n_1 surrounded by media of different refractive indices: air as the upper media with refractive index 1, and glass as the lower media with refractive index $n_2 = 1.5176$ at the dye emission wavelength. The refractive indices of polyimides **6F-6F** and **6F-IMMDA** at the dye emission wavelength are $n_1 = 1.5606$ and 1.5523, respectively, and total reflection takes place at the interface FPI/PM597-glass for light incident at angles greater than the critical angle $\theta_c = \sin^{-1} n_2/n_1 \approx 76$ and 78°, respectively. Thus, the air-FPI/PM597-glass structure defines an optical waveguide, where light incident at the film-glass interface at angles greater than ≈76 or 78° is totally reflected and guided along the length of the film. For comparison, thin films based on PMMA were also prepared. As the refractive index of PMMA ($n_1 = 1.4900$) is lower than that of glass, in this case no total reflection takes place at the film/substrate interface, and light leaks into the substrate. A leaky waveguide or quasi-waveguide is obtained, where light is confined by the film/air interface while the reflection at the film/substrate boundary is leaky. Although the optical properties of waveguides and leaky waveguides are not directly comparable, it is still possible to compare the photostability of the materials under laser irradiation.[43]

Amplified spontaneous emission measurements were carried out as described in the Experimental section. When pumped at low intensities, the light emitted from the edge of the films exhibited a broad emission spectrum, with a FWHM in the range 35–40 nm and peak wavelengths of ≈593 and ≈590 nm for **6F-6F**/PM597 and **6F-IMMDA**/PM597, respectively. At pump intensities above a certain threshold value, the spectral width of the emitted light first decreases fast and then sets in at a value of about 10 nm (Figure 1). The intensity of the emission grows linearly with the pump intensity but with a distinct change in slope at

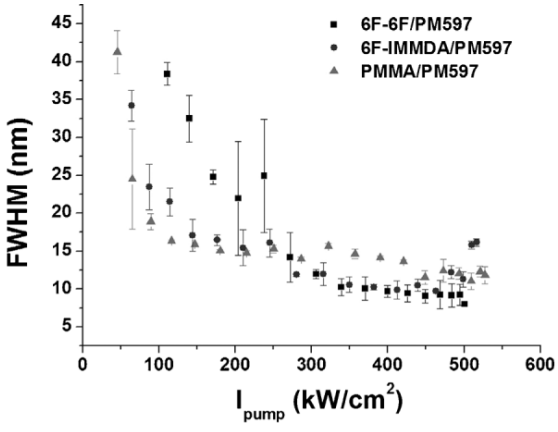

Figure 1. Dependence of the FWHM of the output emission spectra on pump intensity for a 2 mm length pumped stripe.

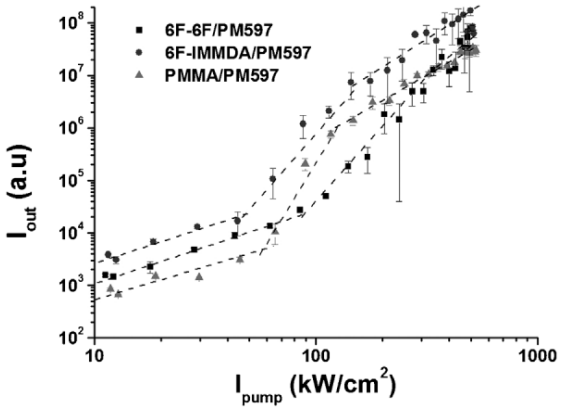

Figure 2. Dependence of the intensity of the output emission on pump intensity for a 2 mm length pumped stripe. The dotted lines are a guide to the eye.

pump threshold (Figure 2). As it is well known, the collapse of the FWHM in the emission spectrum and the change of the slope in the emission intensity with increase in the pump intensity are a signature of the onset of ASE emission above a certain pump threshold.[44,45]

In Figure 2 we have used a log-log scale to better distinguish the different behaviors in the emission as a function of the pump intensity. From the data in Figure 2, it can be estimated a pump threshold for the onset of ASE emission of 90, 55, and 58 kW · cm^{-2} for the waveguides based on polyimide **6F-6F**, polyimide **6F-IMMDA**, and PMMA, respectively. It can also be appreciated in Figure 2 a second change in slope in the emission from the films based on PMMA and polyimide **6F-IMMDA** at pump intensities above 100 kW · cm^{-2} indicating gain saturation. The pump intensity for the onset of saturation can be estimated to be 122 kW · cm^{-2} for PMMA/PM597 and 147 kW · cm^{-2} for **6F-IMMDA**/PM597. For the waveguide **6F-6F**/PM597, saturated behavior is not clear yet at pump fluences as high as 356 kW · cm^{-2}.

Amplified spontaneous emission gain measurements were carried out using the variable stripe length (VSL) method, which consists basically in pumping optically the sample with a stripe-shaped beam of variable length at constant intensity and measuring the intensity of the edge-emitted ASE as a function of stripe length.[45] In the small-signal regime, the ASE intensity collected at the waveguide edge varies with the pump stripe length as:[46]

$$I(\lambda) = \frac{\eta g'(\lambda)}{g(\lambda)}\left(e^{g(\lambda)l} - 1\right) \quad (1)$$

where $g'(\lambda)$ is the internal gain coefficient due to stimulated emission processes, $g(\lambda)$ is the net gain coefficient, $g(\lambda) = g'(\lambda) - \alpha$, with α being the loss coefficient, l is the length of the pumped stripe, and η is a coefficient

proportional to the spontaneous emission rate and to a geometrical factor that depends on the amplifier dimensions. Thus, g can be determined by plotting the intensity of the ASE emission as a function of the pumped stripe length and fitting the resulting curve to the expected dependence given by Equation (1).

Although Equation (1) is a common expression used in the literature to analyze the gain behavior of waveguides, its use should be restricted to pump energies low enough for saturation effects not being important. A usual approach consists in using Equation (1) to fit only those subsets of experimental data apparently free of saturation effects, but this procedure can led to appreciable errors in the calculated gain coefficients.[46] If the ASE intensity reaches the saturation level, as is often the case, a better estimation of the gain coefficients is obtained by using the equation:[46,47]

$$l = \frac{sI(\lambda)}{g(\lambda) + \eta g'(\lambda)s} + \frac{g(\lambda)}{[g(\lambda) + \eta g'(\lambda)s]^2} \times \ln\left|\frac{\eta g'(\lambda) + [\eta g'(\lambda)s + g(\lambda)]I(\lambda)}{\eta g'(\lambda)}\right| \quad (2)$$

where s is a gain saturation parameter ($s = 1/I_s = \sigma_e \tau/h\upsilon$, where σ_e is the emission cross section, τ is the fluorescence lifetime, and υ is the frequency of the ASE emission).

The polyimide-based samples were subjected to systematic measurements of the intensity of the emitted light as a function of excitation length for nine different pump intensities, from 11 to 530 kW · cm^{-2}. The data obtained are plotted in Figure 3, where each point in the graph is an average of four measurements. By fitting the experimental data to the expected dependence as given by Equation (2) (solid lines), the net gain coefficients at increase in the pump intensities are obtained. In Figure 4 are plotted the results obtained for the net gain coefficients as a function of the pump intensities. It can be appreciated that at pump intensities below ≈300 kW · cm^{-2} the gain of the quasi-waveguide **6F-IMMDA**/PM597 is higher than that of the waveguide **6F-6F**/PM597. The situation reverses at higher pump intensities, where net gains of up to 93 ± 4 cm^{-1} are obtained for the **6F-6F**/PM597 waveguide, whereas in the **6F-IMMDA**/PM597 quasi-waveguide the net gain coefficient levels off at about 68 ± 3 cm^{-1}.

As indicated above, plots such as those in Figure 2 allow for an estimation of the pump threshold for the onset of ASE emission. Nevertheless, the data in Figure 2 corresponds to a stripe of a given length, and thus, strictly speaking the estimated threshold values are just valid for that specific stripe length. A more accurate estimation of threshold values, independent of the pumped stripe length, can be obtained from the plots in Figure 4. Defining the threshold intensity for ASE emission as the pump intensity for which

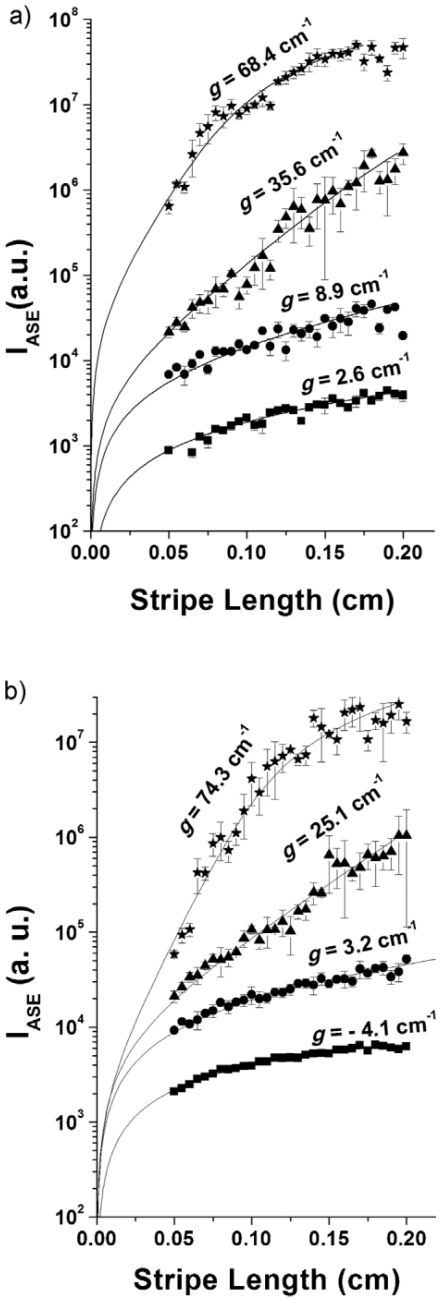

Figure 3. Dependence of the emission intensity on the excitation length at different pump intensities for (a) the waveguide **6F-IMMDA**/PM597 and (b) the waveguide **6F-6F**/PM597. The solid lines are fits to the data using Equation (2).

$g = 0$, we obtain from the data in Figure 4 threshold intensities of 65 and 30 kW · cm^{-2} for **6F-6F**/PM597 and **6F-IMMDA**/PM597, respectively.

From a practical point of view, an important parameter in the behavior of the waveguides is the stability of the ASE emission under long time operation. For successful

Macromol. Chem. Phys. **2009**, *210*, 1624–1631

Macromolecular Journals

DOI: 10.1002/macp.200900212

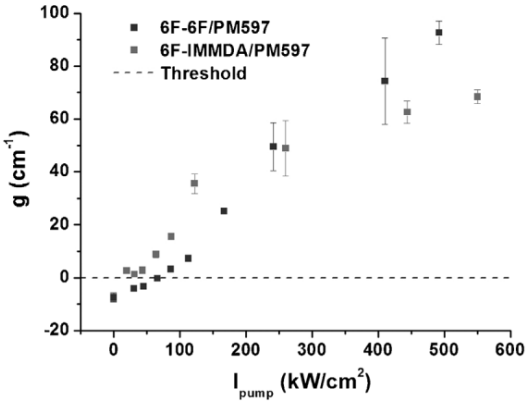

Figure 4. Variation of the net gain coefficient with pump intensity.

operation and good performance, high resistance to dye degradation under repeated pumping is required. Dye degradation rate was assessed by pumping the samples at a fixed position with an intensity of 220 kW · cm^{-2} at 5 Hz repetition rate. The actual evolution of the intensity of the ASE emission of both polyimide waveguides as a function of the number of pump pulses is presented in Figure 5. For reference, it is also included in Figure 5 the evolution of the ASE emission from a waveguide with the same thickness and dye concentration but based on PMMA.

An important fact evident in Figure 5 is that the dye photostability is substantially greater in the polyimide-based films than when the host material was PMMA: after 40 000 pump pulses in the same position of the sample the emission output decreased to 50 and 23% of the initial value in the **6F-6F**/PM597 and **6F-IMMDA**/597 films, respectively, whereas in the PMMA-based film the emission dropped to 10% of the initial value after just 10 000 pulses. The relative stability of the different films can be better appreciated by

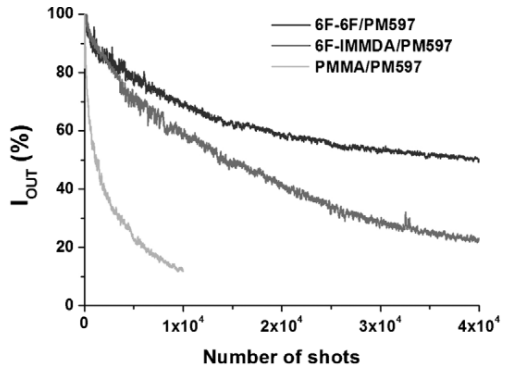

Figure 5. Evolution of the normalized ASE emission as a function of the number of pump pulses in the same position of the sample for polyimide-based and PMMA-based PM597 waveguides. Pump intensity and repetition rate are 220 kW · cm^{-2} and 5 Hz, respectively.

considering the number of pump pulses necessary for the ASE emission dropping by 50%. In this regard, it is obtained that the ASE output drops to 50% of its initial value after 40 000, 14 100, and 1 160 pulses for the waveguides based on **6F-6F**, **6F-IMMDA**, and PMMA, respectively. This means that the **6F-6F**-based waveguide is three times more stable than the **6F-IMMDA**-based guide and 34 times more stable than the PMMA-based guide.

The improvement in photostability of the two FPI films with respect to the PMMA waveguide can be attributed mostly to differences in thermal properties between both polymer families. The thermal stability of the FPIs at least doubles that of the PMMA;[40] hence, the heat transferred from the dye molecule to the matrix is more rapidly dissipated in FPI films, avoiding early thermal degradation of the dye.[25] We have already seen this effect in bulk solid-state dye lasers, where the laser action of pyrromethene chromophores incorporated into methacrylic and acrylic polymers was greatly enhanced by the presence of fluorine atoms into the structure of the organic monomers.[38,41] Important increases in photostability due to enhancement of the thermal dissipation in the matrix provided by the presence of silica have also been observed in bulk solid-state dye lasers, when dye PM597 was incorporated into silicon-modified and organic-inorganic hybrid matrices.[37,40]

To explain the differences between the two FPIs, additional aspects such as polymer chain density and fluorine content must be considered. The polyimide **6F-6F** is denser than **6F-IMMDA** (Table 1); thus, the polymeric free volume is lower and the average distance between dye molecules and polymeric chains is shorter in **6F-6F** than in **6F-IMMDA**. A higher proximity to the polymeric chains facilitates nonradiative energy transfer from the dye molecules to the polymeric chains decreasing thermal and photochemical (dye molecule radicalization via triplet states) degradation. An improvement in dye photostability when the polymeric free volume is reduced has already been seen in previous studies on dyes incorporated into polymeric bulk materials.[25] On the other hand, pyrromethene dyes incorporate fluorine atoms in their structure. This increases the compatibility of the dye molecules with the fluorinated matrix and favors the interactions between dye molecules and polymer. Polyimide **6F-6F** incorporates more fluorine atoms than polyimide **6F-IMMDA**, which should favor the stability of PM597 in the **6F-6F**. Taken together, these mechanisms could explain the better performance of PM597 when incorporated into polyimide **6F-6F**.

In a previous paper,[43] we had obtained gains of up to 57 cm^{-1} for waveguides based on PM597 incorporated into PMMA. The thickness of the films was the same as in the present work but the dye concentration was doubled (5×10^{-2} M). That gain is considerably lower than those obtained in the present work with the FPI-based thin films.

Under 532 nm pumping, gains of up to 40 cm^{-1} have been reported by Lu et al.,[10] with optical waveguides based on polystyrene films doped with dye DCJTB pumped with pulses of 0.13 mJ. Gain of 52.71 cm^{-1} was obtained by Zhang et al.,[11] with waveguides based in a mixture of dyes DCJTB and C545T in polystyrene films, with a pump energy of 0.08 $mJ \cdot pulse^{-1}$. Djiango et al.,[20] obtained net gain coefficients of 37.2 cm^{-1} with near-infrared-emitting dye LDS821 incorporated into poly(4-vinyl)-phenol, with 314 $kW \cdot cm^{-2}$ pumping. Recently, Yuyama et al.,[21] obtained gains of 14 cm^{-1} from FPI waveguides obtained from fluorinated-poly(amic-acids) precursors and doped with IR dye LDS950 dye under pumping at 337 nm with a fluence of 0.74 $mJ \cdot cm^{-2}$. More than a decade ago, Weiss et al.,[35] obtained a gain coefficient of 5.5 cm^{-1} from waveguides based on Probimine 414 polyimide (benzophenone tetracarboxylic dianhydridealkylated polyimide) doped with cresyl violet 670 dye when the system was pumped at 590 nm with pulses of 190 μJ. No assessment of photostability was carried out in any of these previous studies.

The net gains reported in the present work, of 68 and 93 cm^{-1} for waveguides **6F-6F**/PM597 and **6F-IMMDA**/PM597, respectively, were obtained at pump intensity of about 500 $kW \cdot cm^{-2}$, which corresponds to 34 μJ $pulse^{-1}$ or 15 $mJ \cdot cm^{-2}$. Thus, the gains exhibited by our FPI-based waveguides compare well or are higher than those obtained in similar systems reported in the literature.

Conclusion

In this paper, we demonstrate that replacing PMMA with FPI as host material for lasing dyes in active asymmetric planar waveguides improves substantially the photostability of the dye under laser operation. Relevant parameters to optimize the lasing performance of the guides are the polymer chain density and fluorine content. The guide with the higher fluorine content (**6F-6F**), demonstrated to be the most stable because 40 000 pump pulses of ≈220 $kW \cdot cm^{-2}$ delivered at a repetition rate of 5 Hz were necessary for the ASE output dropping to 50% of its initial value. When the material in the thin film was based on PMMA, the ASE emission dropped to 50% of its initial value after just 1 160 pulses.

The observed thresholds for the onset of ASE emission in the FPI waveguides are of the order or higher than those reported in PMMA-based waveguides, but the much higher photostability exhibited by the FPI guides makes them very attractive from the point of view of practical applications. In addition to the higher photostability, the FPI waveguides also exhibit higher gains than those based on non-fluorinated polymers, with net gain coefficients of up to 93 cm^{-1}.

Acknowledgements: This work was supported by *Project MAT2007-65778-C02-01 of the Spanish MICINN*. L. C. thanks *MICINN* for a predoctoral scholarship (FPI, cofinanced by Fondo Social Europeo). We thank *Y. Wang* and *G. Tsiminis*, from the *Organic Semiconductor Center at the University of St-Andrews* for their help in the measurement of refractive indices of the FPI.

Received: May 8, 2009; Revised: July 10, 2009; Published online; September 1, 2009; DOI: 10.1002/macp.200900212

Keywords: optics; photonics; polyimides; thin films

[1] J. Kobayashi, T. Matsuura, S. Sasaki, T. Maruno, *Appl. Opt.* **1998**, *37*, 1032.
[2] K. P. Kretsch, C. Belton, S. Lipson, W. J. Blau, F. Z. Henari, H. Rost, S. Pfeiffer, A. Teuschel, H. Tillmann, H.-H. Hörhold, *J. Appl. Phys.* **1999**, *86*, 6155.
[3] S.-S. Yap, W.-O. Siew, T.-Y. Tou, S.-W. Ng, *Appl. Opt.* **2002**, *41*, 1725.
[4] Y. Oki, S. Miyamoto, M. Maeda, N. J. Vasa, *Opt. Lett.* **2002**, *27*, 1220.
[5] Y. Oki, T. Yoshiura, Y. Chisaki, M. Maeda, *Appl. Opt.* **2002**, *41*, 5030.
[6] Y. Oki, S. Miyamoto, M. Tanaka, D. Zuo, M. Maeda, *Opt. Commun.* **2002**, *214*, 277.
[7] Y. Oki, M. Tanaka, Y. Ogawa, H. Watanabe, M. Maeda, *IEEE J. Quantum Electron.* **2006**, *42*, 389.
[8] N. Tsutsumi, T. Kawahira, W. Sakai, *Appl. Phys. Lett.* **2003**, *83*, 2533.
[9] M. A. Reilly, C. Marinelli, C. N. Morgan, R. V. Penty, I. H. White, M. Ramon, M. Ariu, R. Xia, D. D. C. Bradley, *Appl. Phys. Lett.* **2004**, *85*, 5137.
[10] W. Lu, B. Zhong, D. Ma, *Appl. Opt.* **2004**, *43*, 5074.
[11] D. Zhang, D. Ma, *Appl. Opt.* **2007**, *46*, 2996.
[12] E. V. Calzado, J. M. Villalvilla, P. G. Boj, J. A. Quintana, R. Gómez, J. L. Segura, M. A. Díaz García, *J. Phys Chem. C* **2007**, *111*, 13595.
[13] R. Kumar, A. P. Singh, A. Kapoor, K. N. Tripathi, *J. Mod. Opt.* **2005**, *10*, 1471.
[14] K. Sakai, T. Tsuzuki, Y. Itoh, M. Ichikawa, Y. Taniguchi, *Appl. Phys. Lett.* **2005**, *86*, 081103.
[15] K. Geetha, M. Rajesh, V. P. N. Nampoori, C. P. G. Vallabhan, P. Radhakrishnan, *J. Opt. A: Pure Appl. Opt.* **2006**, *8*, 189.
[16] G. Jordan, M. Flämmich, M. Rüther, T. Kobayashi, W. J. Blau, *Appl. Phys. Lett.* **2006**, *88*, 161114.
[17] M. Kawasaki, S. Mine, *J. Phys. Chem. B* **2006**, *110*, 15052.
[18] H. Goudket, T. H. Nhung, B. Ea-Kim, G. Roger, M. Canva, *Appl. Opt.* **2006**, *45*, 7736.
[19] A. Büttner, U. D. Zeitner, *IEEE J. Quantum Electron.* **2007**, *43*, 545.
[20] M. Djiango, T. Kobayashi, W. J. Blau, B. Cai, K. Komatsu, T. Kaino, *Appl. Phys. Lett.* **2008**, *92*, 083306.
[21] S. Yuyama, T. Nakajima, K. Yamashita, K. Oe, *Appl. Phys. Lett.* **2008**, *93*, 023306.
[22] D. Zhang, Z. Chen, D. Ma, *Appl. Phys. Lett.* **2008**, *103*, 123103.
[23] A. K. Bansal, W. Holzer, A. Penzkofer, E. B. Kley, *Opt. Commun.* **2008**, *281*, 3806.

[24] R. Duchowicz, L. B. Scaffardi, A. Costela, I. García-Moreno, R. Sastre, A. U. Acuña, *Appl. Opt.* **2003**, *42*, 1029.
[25] A. Costela, I. García-Moreno, R. Sastre, *Phys. Chem. Chem. Phys.* **2003**, *5*, 4745.
[26] M. K. Ghosh, K. L. Mittal, *Polyimides: Fundamentals and Applications*, Marcel Dekker, New York, USA 1996.
[27] G. Rabilloud, *High Performance Polymers*, Technip, Paris, France 1997.
[28] J. de Abajo, J. G. de la Campa, *Adv. Polym. Sci.* **1999**, *140*, 23.
[29] A. Sagisaka, H. Daido, A. S. Pirozkhov, J. Ma, A. Yogo, K. Ogura, S. Orimo, M. Mori, M. Nishiuchi, T. Kawachi, S. V. Bulanov, T. Zh. Esirkepov, Y. Oishi, T. Nayuki, T. Fujii, K. Nemoto, H. Nagatomo, *IEEE Trans. Plasma Sci.* **2008**, *36*, 1812.
[30] Y. Woo, S. Y. Oh, Y. S. Kang, B. Jung, *J. Membr. Sci.* **2003**, *220*, 31.
[31] A. E. Lozano, J. de Abajo, J. G. de la Campa, C. Guillén, J. Herrero, M. T. Gutiérrez, *J. Appl. Polym. Sci.* **2007**, *103*, 3491.
[32] Z. Y. Yang, *J. Fluorine Chem.* **2001**, *111*, 247.
[33] C. Staudt, W. Koros, *J. Membr. Sci.* **2000**, *170*, 205.
[34] W. Jiang, D. Wang, S. Guan, H. Gao, Y. Zhao, Z. Jiang, W. Gao, D. Zhang, D. Zhang, *J. Photochem. Photobiol. A: Chem.* **2008**, *197*, 426.
[35] M. N. Weiss, R. Srivastava, R. R. B. Correia, J. F. Martins-Filho, C. B. de Araujo, *Appl. Phys. Lett.* **1996**, *69*, 3653.
[36] A. Quaranta, S. Carturan, G. Maggi, oni, G. Della Mea, M. Ischia, R. Campostrini, *Appl. Phys. A* **2001**, *72*, 671.
[37] I. García-Moreno, A. Costela, A. Cuesta, O. García, D. del Agua, R. Sastre, *J. Phys. Chem.* **2005**, *109*, 21618.
[38] O. García, R. Sastre, D. del Agua, A. Costela, I. García-Moreno, *Chem. Mater.* **2006**, *18*, 601.
[39] M. Álvarez, F. Amat-Guerri, A. Costela, I. García-Moreno, M. Liras, R. Sastre, *Opt. Commun.* **2006**, *267*, 469.
[40] A. Costela, I. García-Moreno, D. del Agua, O. García, R. Sastre, *J. Appl. Phys.* **2007**, *101*, 073110.
[41] O. García, R. Sastre, D. del Agua, A. Costela, I. García-Moreno, F. López Arbeloa, J. Bañuelos Prieto, I. Lópes Arbeloa, *J. Phys. Chem. C* **2007**, *111*, 1508.
[42] C. Lowe, *Surface Coatings Technology*, Vol. 5, John Wiley&-Sons, London, UK 1997, Ch. VI p. 60.
[43] L. Cerdán, A. Costela, I. García-Moreno, O. García, R. Sastre, *Appl. Phys. B* **2009**, DOI 10.1007/s00340-009-3518-8.
[44] U. Ganiel, A. Hardy, G. Neumann, D. Treves, *IEEE J. Quantum Electron.* **1975**, *QE-11*, 881.
[45] M. D. McGehee, R. Gupta, S. Veenstra, E. K. Miller, M. A. Díaz-García, A. J. Heeger, *Phys. Rev. B* **1998**, *58*, 7035.
[46] A. Costela, O. García, L. Cerdán, I. García-Moreno, R. Sastre, *Opt. Express* **2008**, *16*, 7023.
[47] A. Costela, O. García, L. Cerdán, I. García-Moreno, R. Sastre, *Opt. Express* **2008**, *16*, 7587.

Paper B5: Opt. Express 18, 10, 10247–10256 (2010)

Laser emission from mirrorless waveguides based on photosensitized polymers incorporating POSS

L. Cerdán, A. Costela, I. García-Moreno, O. García and R. Sastre

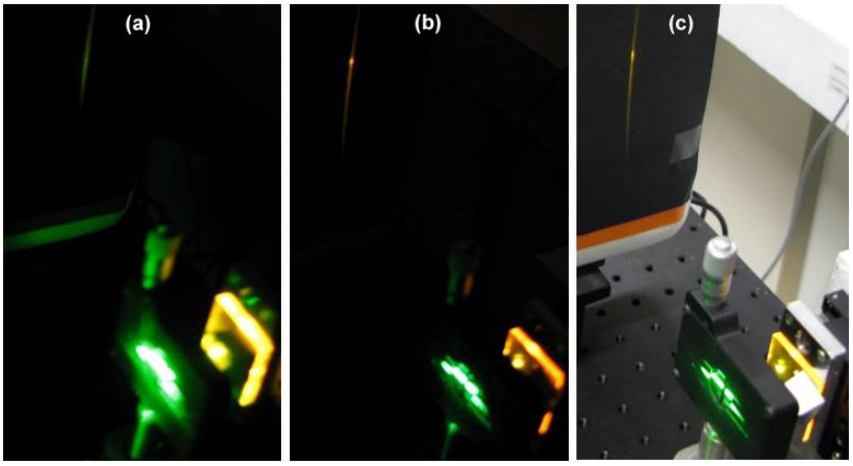

Emission from a sample without POSS (a) and with 50 wt % content of 8MMAPOSS (b) at 20 cm from the waveguide edge. In (c) the picture is as in (b) but with the room fully lighted.

Laser emission from mirrorless waveguides based on photosensitized polymers incorporating POSS

L. Cerdán,[1] A. Costela, [1,*] I. García-Moreno,[1] O. García, [2] and R. Sastre [2]

[1]*Instituto de Química Física "Rocasolano", C.S.I.C., Serrano 119, 28006 Madrid, Spain*
[2]*Instituto de Ciencia y Tecnología de Polímeros, C.S.I.C., Juan de la Cierva 3, 28006 Madrid, Spain.*
**acostela@iqfr.csic.es*

Abstract: Laser emission from leaky waveguides based in dye-doped organic gain media incorporating Polyhedral Oligomeric Silsesquioxanes (POSS) nanoparticles is reported. The samples consist of thin film gain media deposited onto glass substrate defining a planar asymmetric slab waveguide, which does not incorporate any resonant substructure. The presence of POSS results in additional amplified spontaneous emission (ASE) spectral narrowing, and conditions have been found for which directional multimode laser emission is achieved. The spectral narrowing is ascribed to the photon path enlargement caused by a non-resonant feedback mechanism provided by individual scatterers, which enhances incoherently the magnitude of the amplification process. On the contrary, the appearance of multimode lasing is attributed to coherent random lasing from a many scatterers collective effect.

OCIS codes: (230.7390) Waveguides, planar; (160.4236) Nanomaterials; (310.6628) Subwavelength structures, nanostructures; (250.2080) Polymer active devices; (250.5460) Polymer waveguides; (140.2050) Dye lasers; (140.3380) Laser materials.

References and links

1. A. Costela, I. García-Moreno, L. Cerdán, V. Martín, O. García, and R. Sastre, "Dye-Doped POSS Solutions: Random Nanomaterials for Laser Emisión," Adv. Mater. **21**(41), 4163–4166 (2009).
2. M. A. Noginov, *Solid-State Random Lasers* (Springer, New York, 2005).
3. S. Takeda and M. Obara, "Extremely selective modal oscillation of random lasing induced by strong multiple scattering," Appl. Phys. B **94**(3), 443–450 (2009).
4. K. P. Kretsch, C. Belton, S. Lipson, W. J. Blau, F. Z. Henari, H. Rost, S. Pfeiffer, A. Teuschel, H. Tillmann, and H.-H. Hörhold, "Amplified spontaneous emission and optical gain spectra from stilbenoid and phenylene derivative model compounds," J. Appl. Phys. **86**(11), 6155–6159 (1999).
5. P. Yang, G. Wirnsberger, H. C. Huang, S. R. Cordero, M. D. McGehee, B. Scott, T. Deng, G. M. Whitesides, B. F. Chmelka, S. K. Buratto, and G. D. Stucky, "Mirrorless lasing from mesostructured waveguides patterned by soft lithography," Science **287**(5452), 465–467 (2000).
6. S.-S. Yap, W.-O. Siew, T.-Y. Tou, and S.-W. Ng, "Red-green-blue laser emissions from dye-doped poly(vinyl alcohol) films," Appl. Opt. **41**(9), 1725–1728 (2002).
7. Y. Oki, S. Miyamoto, M. Maeda, and N. J. Vasa, "Multiwavelength distributed-feedback dye laser array and its application to spectroscopy," Opt. Lett. **27**(14), 1220–1222 (2002).
8. M. A. Reilly, C. Marinelli, C. N. Morgan, R. V. Penty, I. H. White, M. Ramon, M. Ariu, R. Xia, and D. D. C. Bradley, "Rib waveguide dye-doped polymer amplifier with up to26 dB optical gain at 625 nm," Appl. Phys. Lett. **85**(22), 5137–5139 (2004).
9. W. Lu, B. Zhong, and D. Ma, "Amplified spontaneous emission and gain from optically pumped films of dye-doped polymers," Appl. Opt. **43**(26), 5074–5078 (2004).
10. R. Kumar, A. P. Singh, A. Kapoor, and K. N. Tripathi, "Effect of dye doping in poly(vinyl alcohol) waveguides," J. Mod. Opt. **52**(10), 1471–1483 (2005).
11. K. Geetha, M. Rajesh, V. P. N. Nampoori, C. P. G. Vallabhan, and P. Radhakrishnan, "Laser emission from transversely pumped dye-doped free-standimg polymer film," J. Opt. A, Pure Appl. Opt. **8**(2), 189–193 (2006).
12. G. Jordan, M. Flämmich, M. Rüther, T. Kobayashi, W. J. Blau, Y. Suzuki, and T. Kaino, "Light amplification at 501 nm and large nanosecond optical gain in organic dye-doped polymeric waveguides," Appl. Phys. Lett. **88**(16), 161114 (2006).

#125643 - $15.00 USD Received 18 Mar 2010; revised 20 Apr 2010; accepted 21 Apr 2010; published 30 Apr 2010

13. E. M. Calzado, J. M. Villalvilla, P. G. Boj, J. A. Quintana, R. Gómez, J. L. Segura, and M. A. Díaz García, "Amplified spontaneous emission in polymer films doped with a perylenediimide derivative," Appl. Opt. **46**(18), 3836–3842 (2007).
14. H. Goudket, T. H. Nhung, B. Ea-Kim, G. Roger, and M. Canva, "Importance of dye host on absorption, propagation losses, and amplified spontaneous emission for dye-doped polymer thin films," Appl. Opt. **45**(29), 7736–7741 (2006).
15. M. Djiango, T. Kobayashi, W. J. Blau, B. Cai, K. Komatsu, and T. Kaino, "Near-infrared luminescent polymer waveguide with a 20 dB small-signal gain," Appl. Phys. Lett. **92**(8), 083306 (2008).
16. S. Yuyama, T. Nakajima, K. Yamashita, and K. Oe, "Solid state organic laser emission at 970 nm from dye-doped fluorinated-polyimide planar waveguides," Appl. Phys. Lett. **93**(2), 023306 (2008).
17. D. Zhang, Z. Chen, and D. Ma, "White light emission on amplified spontaneous emission with dye content controlled polymer system," J. Appl. Phys. **103**(12), 123103 (2008).
18. L. Cerdán, A. Costela, I. García-Moreno, O. García, and R. Sastre, "Waveguides and quasi-waveguides based on pyrromethene 597-doped poly(methyl methacrylate)," Appl. Phys. B **97**(1), 73–83 (2009).
19. C. Liu, J. Liu, J. Zhang, and K. Dou, "Random lasing with scatterers of diameters 20 nm in an active medium," Opt. Commun. **244**(1-6), 299–303 (2005).
20. A. Tulek, R. C. Polson, and Z. V. Vardeny, "Naturally occurring resonators in random lasing of π-conjugated polymer films," Nat. Phys. **6**(4), 303–310 (2010), doi:10.1038/NPHYS1509.
21. G. Kranzelbinder, and G. Leising, "Progress in organic solid state lasers," Rep. Prog. Phys. **63**(5), 729–762 (2000).
22. Y. Oki, S. Miyamoto, M. Maeda, and N. J. Vasa, "Multi-wavelength distributed-feedback dye laser array and its application to spectroscopy," Opt. Lett. **44**, 4965–4971 (2002).
23. X. Zhu, and D. Lo, "Sol-gel glass distributed-feedback waveguide laser," Appl. Phys. Lett. **80**(6), 917–920 (2002).
24. D. Lo, L. Shi, J. Wang, G. X. Zhang, and X. Zhu, "Zirconia and zirconia-organically modified silicate distributed feedback waveguide lasers tunable in the visible," Appl. Phys. Lett. **81**(15), 2707–3181 (2002).
25. D. Schneider, S. Hartmann, T. Bernsten, T. Dobbertin, D. Heithecker, D. Metzdorf, E. Becker, T. Riedl, H.-H. Johannes, W. Kowalsky, T. Weimann, J. Wang, and P. Hinze, "Wavelength-tunable organic solid-state distributed-feedback laser," Appl. Phys. B **77**(4), 399–402 (2003).
26. J. Wang, G.-X. Zhang, L. Shi, D. Lo, and X.-L. Zhu, "Tunable multiwavelength distributed-feedback zirconia waveguide lasers," Opt. Lett. **28**(2), 90–92 (2003).
27. F. Chen, J. Wang, C. Ye, W. Ni, J. Chan, Y. Yang, and D. Lo, "Near infrared distributed feedback lasers based on LDS dye-doped zirconia-organically modified silicate channel waveguides," Opt. Express **13**(5), 1643–1650 (2005).
28. H. Sakata, and K. Natsume, "Distributed-feedback vertical cavity structures for optically pumped solid-state organic lasers," Opt. Quantum Electron. **39**(7), 577–583 (2007).
29. M. Lu, B. T. Cunningham, S.-J. Park, and J. G. Eden, "Opt. Commun, "Vertically emitting, dye-doped polymer laser in the green (λ ~ 536 nm) with a second order distributed feedback grating fabricated by replica molding," Opt. Commun. **281**(11), 3159–3162 (2008).
30. Y. Yang, G. Lin, H. Xu, M. Wang, and G. Qian, "Distributed feedback laser actions in zirconia-ORMOSIL waveguides based on energy transfer between co-doped laser dyes," Opt. Commun. **281**(20), 5218–5221 (2008).
31. K. Yamashita, M. Arimatsu, N. Takeuchi, M. Takayama, K. Oe, and H. Yanagi, "Multilayerd solid-state organic laser for simultaneous multiwavelength oscillations," Appl. Phys. Lett. **93**(23), 233303 (2008).
32. C. Lowe, *Surface Coatings Technology* (John Wiley & Sons, London 1997), vol.5, Chap. VI, p.60–62.
33. R. Sastre, V. Martín, L. Garrido, J. L. Chiara, B. Trastoy, O. García, A. Costela, and I. García-Moreno, "Dye-Doped Polyhedral Oligomeric Silsesquioxane (POSS)-Modified Polymeric Matrices for Highly Efficient and Photostable Solid-State Lasers," Adv. Funct. Mater. **19**(20), 3307–3316 (2009).
34. T.-N. Ding and E. Garmire, "Measuring refractive index and thickness of thin films: a new technique," Appl. Opt. **22**(20), 3177-3181(1983).
35. D. B. Hall, and C. Ye, "Leaky waves in a heteroepitaxial film," J. Appl. Phys. **44**(5), 2271-2274 (1973).
36. A. Kumar, V. Rastogi, and K. S. Chiang, "Large-core single-mode channel waveguide based on geometrically shaped leaky cladding," Appl. Phys. B **90**(3-4), 507–512 (2008).
37. F. J. Duarte and R. O. James, "Tunable solid-state lasers incorporating dye-doped, polymer-nanoparticle gain media," Opt. Lett. **28**(21), 2088–2090 (2003).
38. L. Cerdán, A. Costela, I. García-Moreno, O. García, R. Sastre, M. Calle, D. Muñoz, and J. de Abajo, "High-Gain Long-Lived Amplified Spontaneous Emission from Dye-Doped Fluorinated Polyimide Planar Waveguides," Macromol. Chem. Phys. **210**(19), 1624–1631 (2009).
39. R. C. Polson, G. Levina, and Z. V. Vardeny, "Spectral analysis of polymer microring lasers," Appl. Phys. Lett. **76**(26), 3858–3860 (2000).

1. Introduction

In a recent paper [1] we demonstrated for the first time that, under certain conditions, addition of nanometer-sized particles based on polyhedral oligomeric silsesquioxanes (POSS) to liquid and solid solutions of organic dyes can scatter light in a way that increases the efficiency of the material's laser action. The POSS particles act as weak scattering centres in the Rayleigh limit (particle size much smaller than the emission wavelength), and the photon path

#125643 - $15.00 USD Received 18 Mar 2010; revised 20 Apr 2010; accepted 21 Apr 2010; published 30 Apr 2010

enlargement caused by multiple scattering provides an extra feedback which enhances incoherently the magnitude of the amplification process, in what has been called "Non-Resonant Feedback Lasing (NRFL)" or "Incoherent Random Lasing" [2,3].

Waveguiding structures have attracted much attention over the last years for their potential applications in integrated photonics [4–18]. In a conventional planar waveguide, amplified spontaneous emission (ASE) is obtained when the gain medium is pumped above a certain threshold value. ASE is a type of mirrorless lasing strongly directional but broadband, which appears when there is a population inversion but there are no structures providing resonant feedback. Although ASE may be used in applications where good spatial coherence is required but low temporal coherence suffices, coherent laser emission is needed in more demanding optoelectronic applications. Thus, it would be of much interest to study if a NRFL effect similar to that observed in bulk liquid and solid dye solutions could also act in waveguiding thin films.

Although random lasing of structureless π-conjugated polymer thin films containing TiO_2 nanoparticles has been observed [19,20], lasing action in organic materials structures has been mainly obtained by using different feedback designs, such as microcavities, distributed feedback structures, or ring microlaser structures [21]. Of these, distributed feedback resonators (DFB), which offer periodic modulation of either the gain or refractive index of the medium, have been generally preferred for solid state dye lasers, principally because of the compact design, high degree of spectral selection, edge-on or out-of-plane emission, narrow linewidth, and broad tunability [22–31]. In this paper we explore the effect of the presence of POSS nanoparticles in dye-doped organic media in the form of thin films deposited onto glass substrates to define a waveguiding structure. We demonstrate, for the first time to the best of our knowledge, that the presence of POSS in photosensitized polymeric planar waveguides allows obtaining laser emission without the need of incorporating complex resonant substructures in the material.

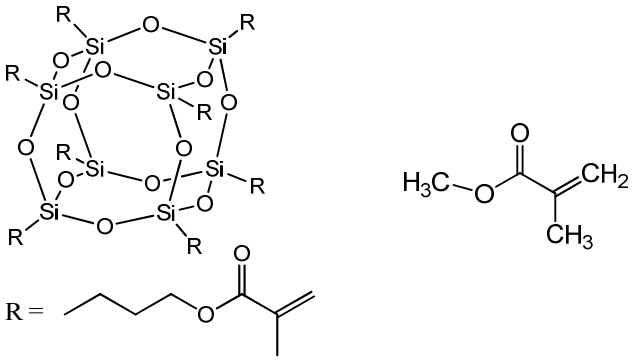

Fig. 1. Molecular structures of octa(propyl-methacryl)-POSS (8MMAPOSS) and methyl methacrylate monomer (MMA).

2. Experimental

Asymmetric slab optical waveguides consisting of dye-doped polymer films deposited onto glass substrates (standard glass microscope slides with thickness of 0.98 mm) were prepared by spin coating (2000-4000 rpm, 20 s). The polymer films consisted of poly(methyl methacrylate) (PMMA) of 25,000 molecular weight (Polysciences, Inc) in proportion 100-200 mg/mL, depending on the desired thickness, containing octa(propyl methacryl)-POSS (8MMAPOSS, Fig. 1) (Hybrid Plastics) in weight proportions from 0 to 50 wt%, and dye pyrromethene 597 (PM597) (laser grade from Exciton) at a concentration (with respect to total polymer) of 2.5 $x10^{-2}$M. Although the PM597 concentration was rather high, the dye was

#125643 - $15.00 USD Received 18 Mar 2010; revised 20 Apr 2010; accepted 21 Apr 2010; published 30 Apr 2010

completely solved and photophysical studies did not show any evidence of aggregation of the dye molecules. The casting solvent for spin-coating was chloroform (Merck).

After solvent evaporation at 50°C for 5min films with 2.1 ± 0.1 μm and 5.5 ± 0.1μm were obtained. The thickness of the films was determined by gravimetric method, taking into account the density of the polymeric film mixture (between 1.19 g/mL for pure PMMA and 1.218 g/mL for PMMA/8MMAPOSS-50 wt%). Films of 9 μm thickness were prepared by using the extender roller technique, where a few drops of the solution were first placed onto the substrate and then extended along it by using a calibrated rod (endless screw with calibrated thread) [32].

The thin film samples were pumped at 532 nm with 20 ns full width at half maximum (FWHM) pulses from a frequency-doubled *Q*-switched Nd:YAG laser (Lotis TII SL-2132). The pump radiation was horizontally polarized and the pulse energy incident onto the sample was controlled by insertion in the beam path of a half-wave plate (HWP) and a linear polarizer (LP) set with its polarization axis horizontal. By rotating the HWP the linear polarization of the input beam is rotated out of the horizontal, and the pump beam is blocked more or less by the LP, depending on the rotation angle introduced by the HWP. A combination of negative and positive cylindrical quartz lenses (f = −15 and + 15 cm, respectively), perpendicularly arranged, focused the pump beam to a narrow horizontal line onto the surface of the film. An adjustable slit was used to select only the central portion of the pump beam. A micrometer screw allowed to precisely selecting the width of the slit. The light incident on the sample was perpendicular to the film surface, defining an excitation stripe of ~150 μm × 2 mm. The sample was placed on a XY Motorized Translation Stage (MTS50XY, Thorlabs), computer controlled, to allow precise positioning. Measurements were performed with the excitation stripe end placed right up to the edge of the film or translated away from the edge of the sample in 2 mm steps, while keeping the pumped stripe length constant (Fig. 2). The distance between the end of the pump stripe and the edge of the waveguide from where the emission is collected, is denoted as z. The edge emission from the sample was collected by a fibre bundle and directed to a spectrograph/monochromator (SpectraPro-300i Acton Research) equipped with a thermoelectrically cooled CCD detector (SpectruMM:GS 128B). Emission spectra averaged over 15 pulses for values of z between 0 and 16 mm were recorded.

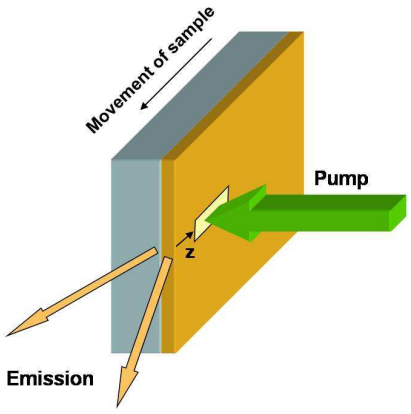

Fig. 2. Film excitation and emission geometry.

#125643 - $15.00 USD Received 18 Mar 2010; revised 20 Apr 2010; accepted 21 Apr 2010; published 30 Apr 2010

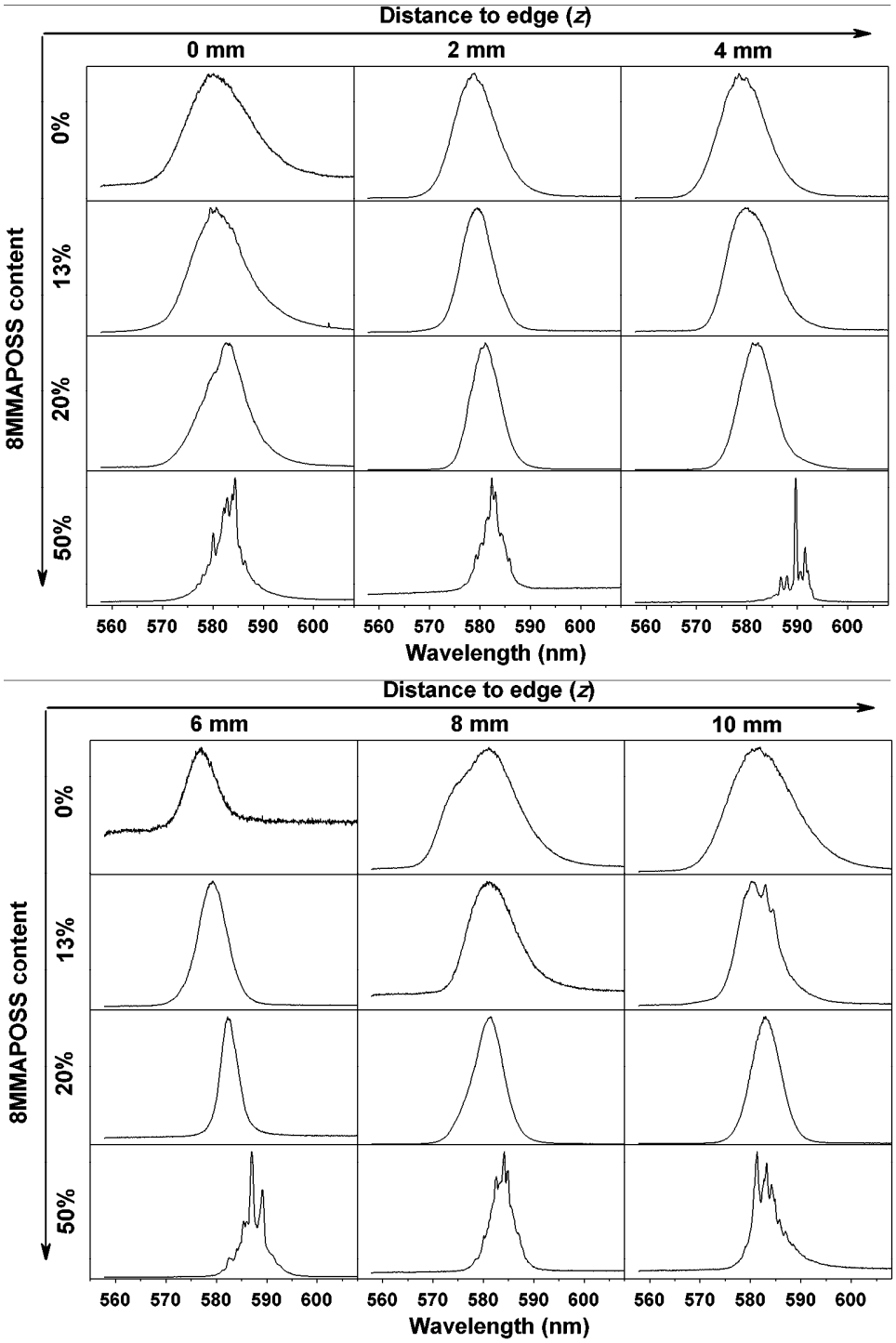

Fig. 3. Normalized emission spectra recorded for different values of z from 5.5 μm thick films onto glass with different wt% content of 8MMAPOSS at a pump intensity of 500 kW/cm^2.

#125643 - $15.00 USD Received 18 Mar 2010; revised 20 Apr 2010; accepted 21 Apr 2010; published 30 Apr 2010

2. Results and discussion

The refractive index of the film material increased linearly with the content of 8MMAPOSS, from n_1 = 1.4883 (MMA homopolymer, 0% 8MMAPOSS) up to n_1 = 1.4977 (8MMAPOSS content of 50 wt%) [33]. As the refractive index of the polymer layer is lower than that of the glass substrate (measured refractive index, n_2 = 1.5176), no total internal reflection takes place at the film/substrate interface, and the emitted light leaks into the substrate. A leaky waveguide or quasi-waveguide is obtained, where light is confined by the film/air interface while the reflection at the film/substrate boundary is leaky. Nevertheless, significant confinement of the light still takes place because of the high reflectivity occurring at grazing incidence [34]. The different transverse modes propagating within the gain layer have different reflectivity losses due to the Fresnel law. Although several low-loss leaky modes may exist when the thickness of the gain layer is large compared with the wavelength of the light [35], the fundamental mode is the one with the lower losses and, thus, light is amplified preferably in this mode [36]. As a result, a quasi-waveguide provides a much stronger self-mode restriction capability than conventional total internal-reflection waveguides.

Figure 3 shows the normalized emission spectra recorded for different values of z from 5.5 μm thin films with different wt% content of 8MMAPOSS at a pump intensity of 500 kW/cm^2. In the waveguides with no POSS, the emission is just ASE with linewidths in the range 9-15 nm FWHM. The presence of 8MMAPOSS in 13 wt% proportion results in a slight decrease in the emission linewidth, now in the range 7-13 nm FWHM, a moderate increase in the intensity, and a red shift of the peak of the emission of about 2 nm. Increasing the proportion of 8MMAPOSS in the material to 20 wt% results in a further increase of the intensity, narrowing of the emission to 4-10 nm, and a red shift of the peak of the emission of about 5 nm with respect to the emission from the material with no POSS. In the three cases, the emission with the narrowest linewidth is observed at a distance z = 6 mm between the end of the pumped stripe and the waveguide edge from which emission is collected. This behavior could be indicating a transition from ASE emission to broadband laser emission.

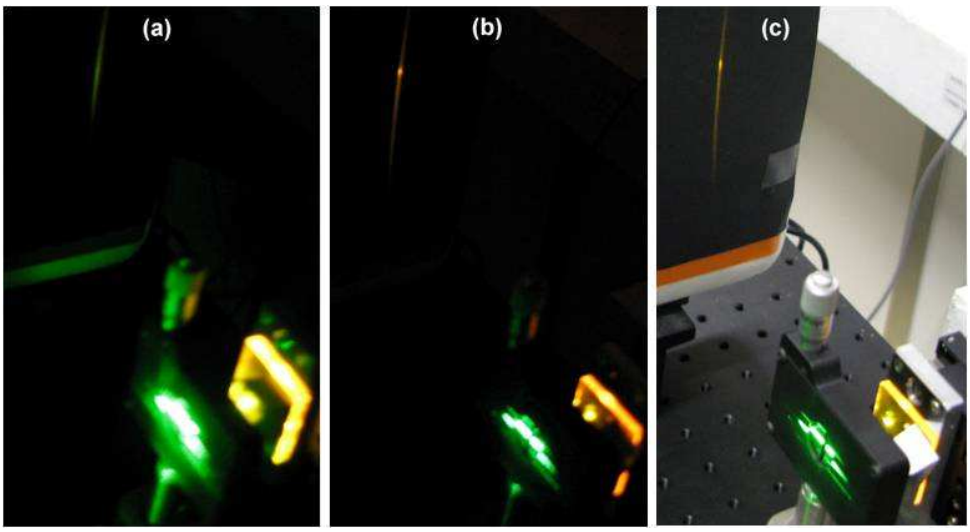

Fig. 4. Emission from a sample without POSS (a) and with 50 wt% content of 8MMAPOSS (b) at 20 cm from the waveguide edge. In (c) the picture is as in (b) but with the room fully lighted.

The characteristics of the emission change dramatically when the content of 8MMAPOSS in the polymer increases to 50 wt%. In this case, multimode emission with narrow peaks on top of a globally narrowed ASE spectrum does appear (Fig. 3), the intensity of the emission increases by more than tenfold, and in the centre of the previous fringe shaped emission does appear a bright spot. The multimode emission is best established for z distances of 4 and 6

#125643 - $15.00 USD Received 18 Mar 2010; revised 20 Apr 2010; accepted 21 Apr 2010; published 30 Apr 2010

mm and is displaced to the red for up to 10 nm with respect to the emission from the material with no POSS. The linewidth of the peaks is smaller than 0.1 nm, which is the resolution of our detection system.

Illustrative photographs of the emission from 5.5 μm films with no POSS and with 50 wt% content of 8MMAPOSS are presented in Fig. 4. Figure 4(a) shows the fringe shape emission from a sample without POSS particles at a distance of 20 cm from the sample. This image should be compared with Fig. 4(b), where the emission from a sample with 50 wt% of 8MMAPOSS at the same distance from the sample is presented. In this case a bright spot in the middle of the fringe appears, resembling laser emission. To better appreciate the brightness of the emission, Fig. 4(c) is a photograph of the same emission taken with the room fully lighted. The divergence of the emission was measured to be about 10 mrad and 6 mrad in the planes parallel and perpendicular to the film, respectively.

In Fig. 5 we have represented the evolution of the intensity of the main narrow peak in the emission from a sample with 50 wt% 8MMAPOSS with the pump intensity when the pumped spot was placed at z = 4mm from the waveguide edge. A clear pump threshold for the narrowband emission to appear is evident in the figure. Taken together, the narrow linewidth of the peaks in the multimode emission, the small divergence of the emission, and the existence of a pump threshold are evidences of the laser nature of the narrow emission lines.

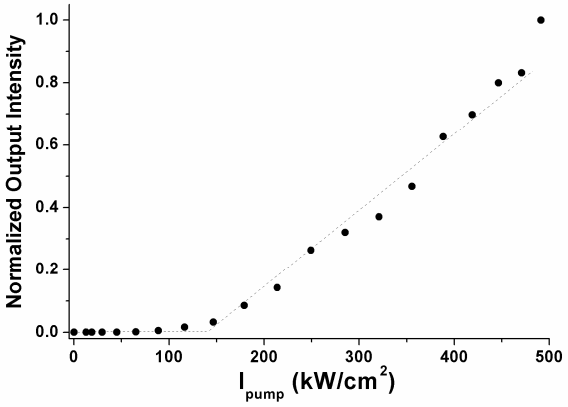

Fig. 5. Dependence on pump intensity of the intensity of the main peak in the multimode emission from a 5.5 μm thick film with 50 wt% 8MMAPOSS for a pumped stripe placed at position z = 4mm.

Some years ago, Duarte and James [37] demonstrated an improvement in the beam divergence of the laser emission from a dye-doped organic medium incorporating silica nanoparticles, and explained this effect as due to the improved thermal characteristics of the medium resulting from the presence of the nanoparticles. Although the thermal conductivity of the materials here studied was determined to increase linearly with the amount of POSS [33], going from 0.182 $Wm^{-1}K^{-1}$ for PMMA up to 0.233 $Wm^{-1}K^{-1}$for PMMA/8MMAPOSS-30 wt%, with an estimated value of 0,252 $Wm^{-1}K^{-1}$for PMMA/8MMAPOSS-50 wt%, the effects observed cannot be attributed to just the improvement of the thermal properties, since no narrowband laser emission was observed in waveguides based in newly synthesized fluorinated polyimides doped with the same dye PM597 [38], whose thermal conductivity at least doubles that of the PMMA.

#125643 - $15.00 USD Received 18 Mar 2010; revised 20 Apr 2010; accepted 21 Apr 2010; published 30 Apr 2010

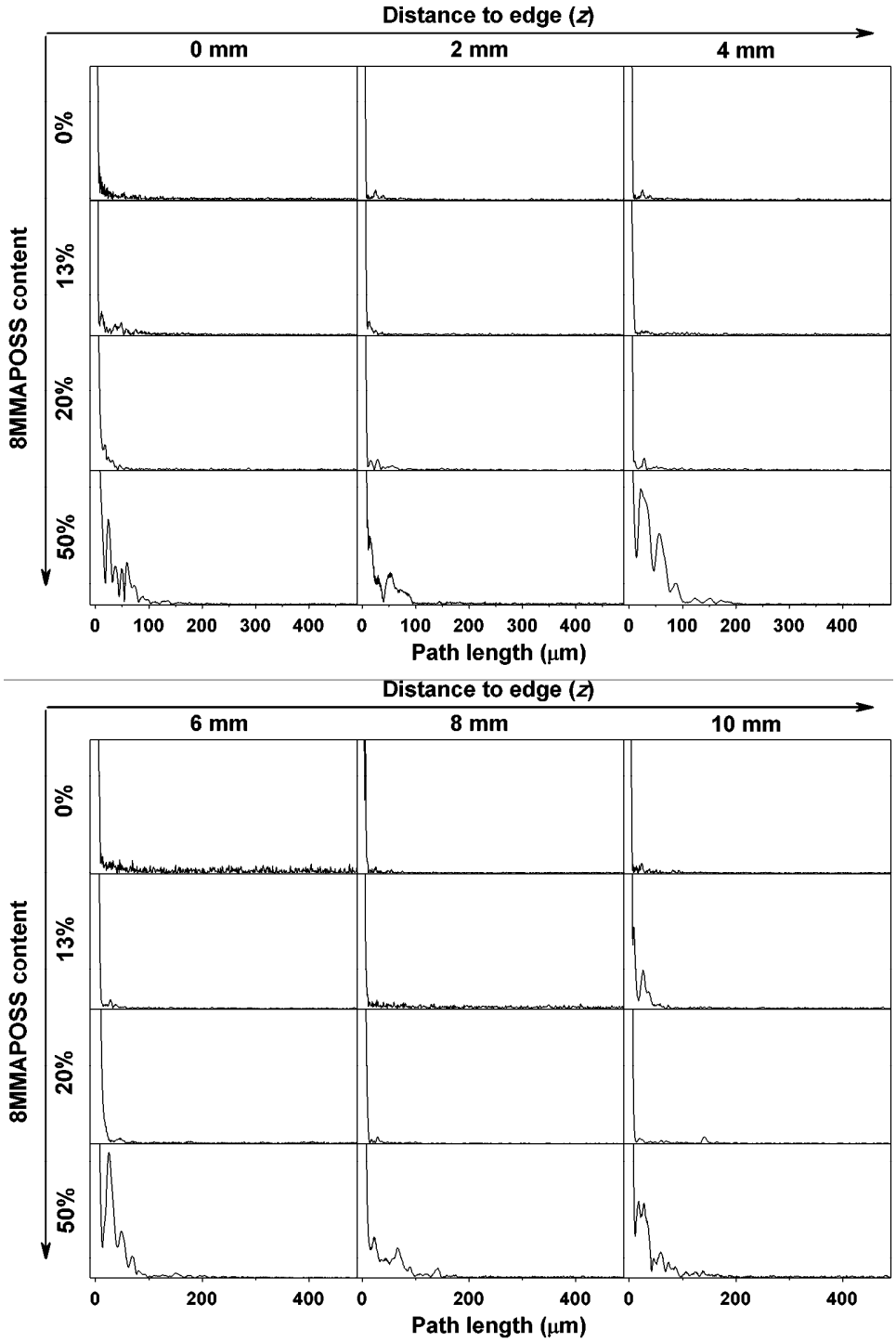

Fig. 6. Ensemble-averaged PFT spectra of the emission spectra shown in Fig. 3. Amplitude of PFT (ordinates) in arbitrary units.

#125643 - $15.00 USD Received 18 Mar 2010; revised 20 Apr 2010; accepted 21 Apr 2010; published 30 Apr 2010

We ascribe the observed spectral narrowing and red shift to an effect of Non-Resonant Feedback (NRF) lasing present in weakly scattering systems [2], where diffusive photons experience multiple scattering. Each scatterer contributes incoherently to this feedback, elongating the light path inside the gain medium and, above a certain pump threshold, results in an additional spectral narrowing. According to this the higher the scatterer density (8MMAPOSS content), the narrower the emission spectrum. This dependence can be noticed in Fig. 3. In addition, the increasing red shift in the emission with 8MMAPOSS content can be understood as being due to two related effects: on the one hand, the self-absorption of the emitted radiation is bigger due to the increased photon path, and on the other hand, the scattering losses are higher for the shorter wavelengths.

Another feature of this multimode laser emission is the randomness of the peak wavelengths when moving the sample. This fact leads us to ascribe the multimode emission to a mechanism of coherent random lasing [3]. That is, the distribution of scatterers within the excited region, that conform random ring cavities, changes in a random fashion when the sample is moved, leading to different oscillation conditions (random cavities) in each sample region.

To gain insight into the excited random cavities we calculated the Power Fourier Transform (PFT) of the spectra in Fig. 3. The PFT of the emission spectrum (in $\kappa = 2\pi/\lambda$ space) from a well-defined laser cavity shows peaks at Fourier components $p_m = mL_C \cdot n/\pi$, where m is the order of the Fourier harmonic, L_C is the cavity path length, and n is the refractive index of the gain medium [39]. Figure 6 shows the calculated ensemble-averaged PFT spectra of the emission spectra shown in Fig. 3. It is clearly seen that whenever sharp lines appear in the emission spectrum, clear peaks can be found in the PFT. In the case of 50 wt% 8MMAPOSS the first sharp peaks in the PFT spectra, corresponding to the fundamental Fourier component $m = 1$, give a mean cavity path length $L_C \approx 45$ μm (assuming $n = 1.4977$). The fact that L_C is much shorter than the scattering length ($\ell_{SC} = 56$ cm for 50 wt% 8MMAPOSS [1]) implies that only a very small amount of the scattered light is confined in the random cavity. This small confinement could explain the fact that multimode emission only appears under certain conditions of gain and scatterer concentrations.

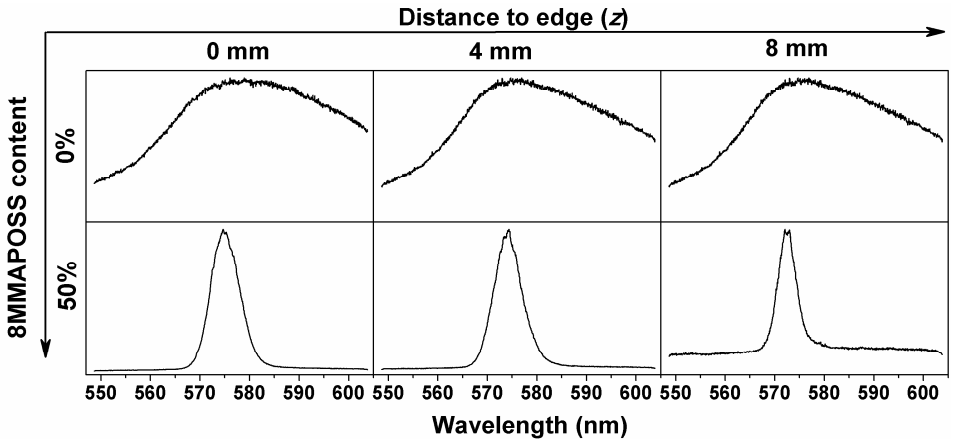

Fig. 7. Normalized emission spectra recorded for selected values of z from 2.1 μm thick films onto glass with different wt% content of 8MMAPOSS at a pump intensity of 500 kW/cm^2.

To assess the dependence of the studied phenomenon on the film thickness, samples with 2.1 μm and 9 μm thin films were prepared. When the volume of the gain region was reduced by decreasing the thickness of the films to 2.1 μm, the overall gain seen by the photons was reduced and as a result only fluorescence was detected in the samples without POSS (Fig. 7). Addition of 8MMAPOSS up to 50 wt% was not able to compensate for the lower overall gain in these thinner films, and only narrowed ASE emission was detected, albeit with some

#125643 - $15.00 USD Received 18 Mar 2010; revised 20 Apr 2010; accepted 21 Apr 2010; published 30 Apr 2010

indication of incipient peaks (Fig. 7). Increasing the thickness of the films to 9 μm resulted in well established multimode emission from 13 wt% 8MMAPOSS content.

An explanation of the different behavior of the multimode emission in films with different thicknesses is suggested from a close analogy to conventional lasing. The threshold condition in usual lasers depends coarsely on the overall medium gain and the cavity reflectivity: the higher the gain and reflectivity, the lower the threshold. On the other hand, a lower value in one of these parameters can be compensated by a higher value in the other. In our system, the effective medium gain depends directly on film thickness, and the effective cavity reflectivity is determined by the amount of 8MMAPOSS nanoparticles. In the thinner films the pump radiation is not efficiently absorbed, and consequently the effective gain is low; hence, a higher amount of 8MMAPOSS nanoparticles (reflectivity) is needed to achieve lasing. Content of more than 50 wt% of 8MMAPOSS cannot be achieved because of solubility problems, and thus, for the 2 μm thick films the multimode emission regime cannot be reached (Fig. 7). The opposite is true for the thicker films, and a small content of 8MMAPOSS (13wt% for 9 μm thick films) is enough to excite multimode emission. For the 5.5 μm thick films an intermediate situation happens and a moderate amount of 8MMAPOSS is enough for multimode lasing to occur (Fig. 3).

3. Summary and conclusion

The emission under 532 nm pumping from quasi-waveguides based in PM597-doped organic gain media incorporating 8MMAPOSS nanoparticles has been studied. Thin films with thickness between 2 and 9 μm and with weight proportions of 8MMAPOSS varying from 0 to 50% were prepared. The presence of 8MMAPOSS in the thin film composition resulted in a narrowing and red shift of the ASE emission from the samples. In the 5.5 μm films the presence of 8MMAPOSS in 50 wt% proportion resulted in multimode laser emission. When the thickness of the films was increased to 9 μm, laser emission was obtained with 8MMAPOSS content above 13 wt%. In the films 2 μm thick spectral narrowing was observed but multimode emission could not be obtained.

The spectral narrowing has been ascribed to a mechanism of Non-Resonant Feedback, where the photon path enlargement caused by multiple scattering provides an intensity feedback which enhances incoherently the magnitude of the amplification process. The presence of multimode laser emission without the need to modulate the substrate to obtain feedback can be understood in terms of coherent random lasing. The calculated mean cavity path length indicates that only a small amount of scattered light is confined within the random cavity, which entails that certain gain conditions must be met for multimode laser to appear.

Acknowledgements

This work was supported by the Spanish CICYT, Project MAT2007-65778-C02-01. L. C. thanks MICINN for a Predoctoral scholarship (FPI, cofinanced by Fondo Social Europeo).

#125643 - $15.00 USD Received 18 Mar 2010; revised 20 Apr 2010; accepted 21 Apr 2010; published 30 Apr 2010

Paper B6: J. Mater. Chem. 22, 8938–8947 (2012)

New perylene-doped polymeric thin films for efficient and long-lasting lasers

L. Cerdán, A. Costela, G. Durán-Sampedro, I. García-Moreno, M. Calle, M. Juan-y-Seva, J. de Abajo, and G. A. Turnbull

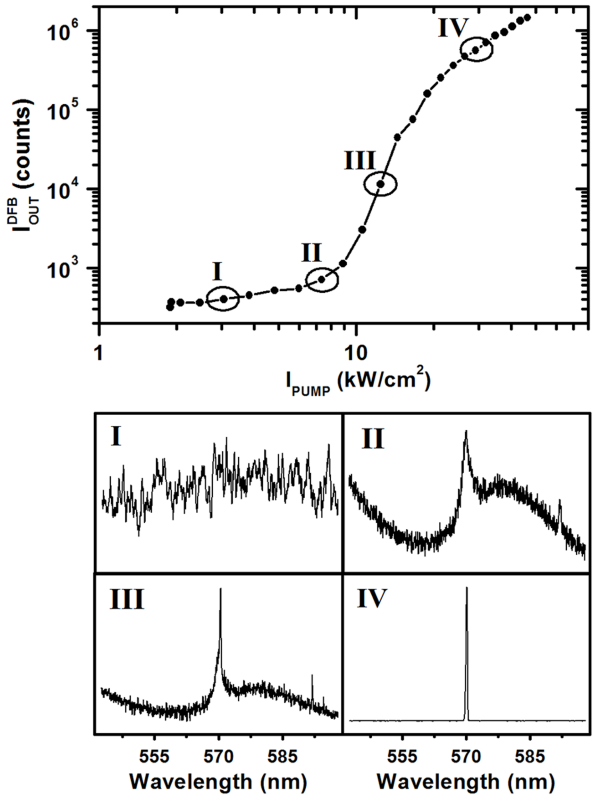

Upper panel: dependence of the DFB laser output intensity on pump intensity for PO (1×10^{-2}M) in PMMA. Lower panel: evolution of the DFB laser emission spectrum over the pumping region.

Journal of Materials Chemistry

Dynamic Article Links

Cite this: J. Mater. Chem., 2012, 22, 8938

www.rsc.org/materials

PAPER

New perylene-doped polymeric thin films for efficient and long-lasting lasers

Luis Cerdán,*[a] Angel Costela,[a] Gonzalo Durán-Sampedro,[a] Inmaculada García-Moreno,[a] Mariola Calle,[b] Marta Juan-y-Seva,[b] Javier de Abajo[b] and Graham A. Turnbull[c]

Received 21st December 2011, Accepted 29th February 2012
DOI: 10.1039/c2jm16745j

We establish an efficient strategy to optimize the performance of dye-doped host materials consisting of analyzing in a systematic way the dependence of their Amplified Spontaneous Emission (ASE) efficiency and photostability on the composition and structure of the matrices, selected to specifically avoid the thermal and/or chemical (photooxidation) processes, main mechanisms of dye photodegradation. For this study, a number of experimental polyimides have been chosen as a host matrix and their behavior has been compared with that of poly(methyl methacrylate) (PMMA). We correlate the optical properties with the oxygen permeation and thermal properties of the different polymeric hosts doped with perylene dyes to deepen the understanding of the photodegradation mechanism predominant in these dyes and to minimize its influence. We demonstrate high efficiency and photostable ASE from waveguides based on polymeric materials doped with Perylene Orange (PO), Perylene Red (PR), and mixtures of both. This enhancement in the optical properties allows reaching high gain and long-lasting distributed feedback (DFB) laser emission based on PO doped polymer matrices, even when operating in an unoptimised resonator.

1. Introduction

Over the last few years there has been significant work exploring the development of waveguiding structures based on dye doped polymers because of their potential applications in integrated photonics.[1,2] These gain media exhibit wide wavelength tunability and high efficiency, which combined with their potentially very low cost makes them attractive candidates for their exploitation as compact and versatile laser systems.[3–15] One significant challenge is to address the limited operational lifetime of these devices due to dye photodegradation, to enable use of these sources in a range of applications.

Dye degradation is generally caused by thermal and/or chemical (photooxidation) processes, and different routes must be followed in order to avoid each of them while keeping the desired efficiency in the final device. It is known that an improvement in the polymer thermal conductivity reduces dye thermal degradation through a more efficient dye-to-polymer heat transfer.[16] Chemical photodegradation, meanwhile, can be reduced by decreasing the amount of oxygen dissolved in the polymer matrix, which is responsible for dye photooxidation. Hence, polymers with a low oxygen permeability and solubility should be used as host materials for these laser dyes. Alternatively, an encapsulation layer could be used as an oxygen barrier.[17]

For most laser dyes, the dominant mechanism, or even the partial contribution of various mechanisms, to their final photodegradation is not well-established. Then, an efficient strategy to optimize the performance of dye-doped host materials consists of analyzing in a systematic way the dependence of its Amplified Spontaneous Emission (ASE) efficiency and photostability on the composition and structure of the matrices, selected to specifically avoid one or another mechanism. If the photostability increases when the oxygen permeability is reduced, then the photodegradation mechanism may be considered mainly chemical, but if the photostability increases when the thermal stability increases, the dominant mechanism will be thermal.

Organic polymers are attractive media for laser dyes since they exhibit good chemical compatibility with organic dyes as well as high optical homogeneity. In addition, and most important, they offer the possibility of easily modifying their structure and composition, allowing the introduction of controlled changes to avoid each of the various photodegradation paths. On the side of the polymers suitable to avoid thermal photodegradation one can use fluorinated polyimides (FPIs). Some FPIs offer a balance of properties very favorable to be used as host materials for lasing chromophores, combining excellent thermal properties with good optical transparency at the wavelengths of interest. Various FPIs have already been used as passive[18,19] and dye-doped active waveguides.[12,20,21] In a previous work,[22] we demonstrated that replacing the commonly used polymer poly(methyl methacrylate) (PMMA) with FPIs as host material for

[a]*Instituto de Química Física "Rocasolano", CSIC, Serrano 119, 28006 Madrid, Spain. E-mail: lcerdan@iqfr.csic.es; Fax: +34915642431; Tel: +34915619400*
[b]*Instituto de Ciencia y Tecnología de Polímeros, CSIC, Juan de la Cierva 3, 28006 Madrid, Spain*
[c]*Organic Semiconductor Centre, SUPA School of Physics & Astronomy, University of St. Andrews, St Andrews KY16 9SS, UK*

the pyrromethene 597 (PM597) dye in planar waveguides resulted in substantial improvement in the dye photostability under laser operation.

Another advantage of these FPIs is that, unlike classical aromatic polyimides, the FPIs are soluble in common non-polar organic solvents, *e.g.*, chloroform, tetrahydrofuran or dioxane, so that films doped with non-polar dyes can readily be fabricated by casting and controlled elimination of solvent.

On the side of the polymers suitable to avoid photochemical degradation, one can use the very well known PMMA which has very low oxygen permeability (0.16 Barrers[23] compared with 18–40 Barrers in FPIs), apart from being a commercial, very cheap and highly transparent polymer. For these last reasons, PMMA is the most used polymer in dye-doped polymer thin film lasers, and has been doped even with polar dyes, in spite of being a non-polar material.

Although there is an ample variety of available dyes, most of the reported work in dye doped polymer thin film lasers has used fluorophores derived from xanthene and dipyrromethene cores. Much less work has been carried out using commercial perylene dyes or perylenediimide derivatives,[9,10,24–29] in spite of these dyes having demonstrated laser emission with reasonable efficiency and good photostability when incorporated into bulk solid matrices.[30–38]

In this paper, we present a systematic study on the properties of the Amplified Spontaneous Emission (ASE) from thin films of a number of polymeric materials doped with Perylene Orange (PO), Perylene Red (PR), and mixtures of both. The molecular structures of these dyes as well as the repetition unit of the monomers selected in the present work are shown in Fig. 1. For the first time to the best of our knowledge, we have correlated these results with the oxygen permeation and thermal properties of the polymeric hosts in order to deepen the understanding of the photodegradation mechanism predominant in these dyes with the aim to optimize both the efficiency and photostability of distributed feedback (DFB) lasers based on perylene-doped polymer thin films.

2. Experimental

2.1 Materials and film preparation

Perylene Orange (BASF Lumogen F Orange) freely provided by BASF with a purity higher than 99% (checked by spectroscopic and chromatographic methods) was used as received. Perylene Red (Exciton) was purified using a chromatography column packed with flash silica gel (silica gel 60, MERCK 230–400 mesh), using hexane/dichloromethane (90/10 to 80/20) as the eluent. The pure product was recovered as a dark red solid. The structure of both dyes is represented in Fig. 1.

Polymers used were commercial PMMA of 25 000 molecular weight (Polysciences, Inc) and four FPIs synthesized in our laboratories: 6F-DDM, 6F-4M, 6F-6F, and 6F-IMM (Fig. 1). The synthesis of FPIs 6F-6F and 6F-IMM and their performance as dye host has been published previously.[22] FPIs 6F-DDM and 6F-4M have been newly synthesized for this work. The precursors for the four FPIs were: hexafluoroisopropylidene diphthalic anhydride (6FDA from Chriskev), purified by sublimation just before use; hexafluoroisopropylidene dianiline (6F from Chriskev); 4,4′-diamino-diphenylmethane (DDM from Aldrich); 4,4′-diamino-3,3′,5,5′-tetramethyl-diphenylmethane (4M from Aldrich) and 4,4′-diamino-3,3′-dimethyl-5,5′-diisopropyl-diphenylmethane (IMM from Aldrich), purified by recrystallization from suitable solvents and sublimation just before use.

The FPIs were prepared following the classical method in two steps:[39] equimolar amounts of dianhydride and diamine in a solution of *N*,*N*-dimethylacetamide (DMA) were polycondensed at low temperature to yield the corresponding polyamic-acid intermediate. To the viscous solution of the intermediate, a mixture of acetic anhydride/pyridine was added, and the imidation reaction was allowed to proceed for 24 h at 50 °C. The polymers were isolated by precipitation in an excess of water/ethanol, and then purified by thoroughly washing with ethanol and subsequent extraction in a Soxhlet apparatus with ethanol for 20 h. Yields were virtually quantitative in every case.

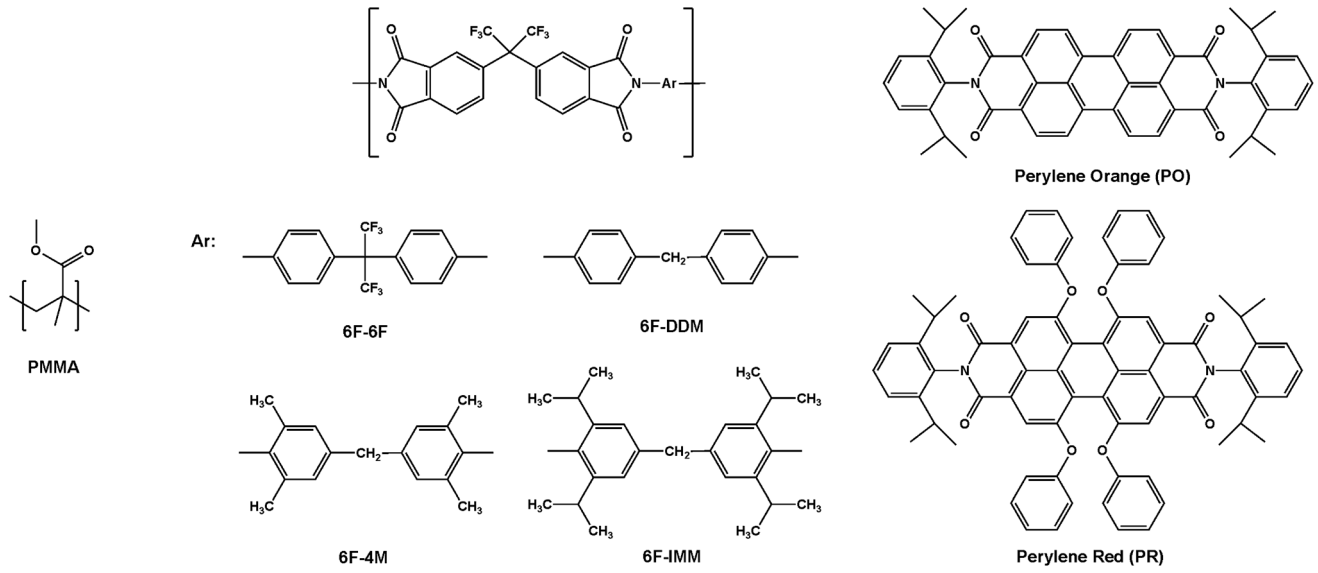

Fig. 1 Repetition unit of PMMA and the synthesized FPIs and chemical structure of PO and PR dyes.

Films of these polymers were nearly colourless to slightly yellow and showed good mechanical resistance.

Solvents used for the preparation of films were chloroform (for PMMA, 6F-6F and 6F-IMM) and tetrahydrofuran (for 6F-DDM and 6F-4M). Polymers in proportion 100–200 mg mL^{-1} and dyes at concentration (with respect to the polymer) in the range 1–10 $\times$ 10^{-3} M were added to the organic solvents. Optimal polymer proportion and dye concentration for each selected material are detailed in Table 1. For the spin coated films, solutions of 50 mg mL^{-1} of PMMA in chloroform were used.

For thermal measurements, films were prepared from polyimide solutions in tetrahydrofuran (THF), with a 7.5% w/w polymer concentration. These solutions were cast on glass plates, and solvent was removed at 25 °C for 24 h. After peeling off the membranes from the glass, they were heated at 180 °C under vacuum for one day.

For the emission characterization, polymer solutions incorporating perylene dyes were deposited onto quartz substrates by using two different procedures depending on the desired thickness: extender roller and spin coating. For the ASE measurements the extender roller technique[40] was used. In this technique, a few drops of the solution are deposited on a quartz slide and extended along the substrate with a calibrated rod (endless screw with calibrated thread). After solvent evaporation at room temperature for several minutes films of thickness of ~9 μm were obtained. The studies on DFB laser emission were carried out in films of ~1.5 μm thickness deposited by spin coating (1000 rpm, 30 seconds) onto quartz substrates. For PO based lasers, a quartz substrate with sinusoidal grating engraved in the surface by holographic photolithography with period Λ = 386 nm and depth d = 150 nm was used.

2.2 Methods

Spectroscopic methods (FTIR and ^{1}H NMR) were used to identify the synthesised polymers, and their molecular weights were indirectly estimated by viscometry. Inherent viscosities (η_{inh}) of about 1.0 dL g^{-1}, determined in an automated Ubbelohde viscometer using 0.5% (w/v) DMA solutions at 25 ± 0.1 °C, indicated average molecular weights (M_w) over 5 $\times$ 10^4 g mol^{-1}.[41]

Glass transition temperatures for the polyimides were determined by differential scanning calorimetry with a Perkin-Elmer DSC-7 at a heating rate of 20 °C min^{-1} under N_2, from 50 to 400 °C. The samples were scanned twice and the midpoint of the endothermal displacement of the second run was taken as the T_g. No endothermal peak of melting was detected in any case, which indicated that polymers were essentially amorphous, as it is usual for polyimides from 6f dianhydride. Thermogravimetric analyses (TGA) were performed using a Perkin-Elmer TGA-7 thermobalance at 10 °C min^{-1} under N_2.

A barometric permeation method was used to determine steady state pure oxygen (purity 99.5%) permeability at 30 °C on polyimide films. The downstream pressure was kept below 10^{-2} mbar while the upstream pressure was maintained at 3 bar. Permeability P was determined from the slope of downstream pressure *vs.* time plotted once steady state had been achieved, according to the expression $P = K(B \times L)/P_0$, where K is an apparatus constant which includes parameters such as temperature, cell permeation area and volume of the system, B is the slope of the downstream pressure *vs.* time, L is the film thickness and P_0 is the oxygen upstream pressure. Data for PMMA were obtained from the literature.

The refractive indices of the polymer films were measured using the Variable Angle Spectroscopic Ellipsometry technique (ellipsometer M-2000DI from A. Woollam Co., Inc.). The refractive index of the quartz substrate was measured using an Abbe refractometer (Arago) employing 1-bromonaphthalene as sample support interphase and a sodium lamp as monochromatic light at 589 nm.

The thickness of the films was measured by using a Digital Comparator (Mahr Extramess 2001) with a resolution of up to 0.2 μm.

2.3 ASE and DFB laser measurements

The thin film samples were optically pumped at 532 nm with 20 ns full width at half maximum (FWHM) pulses from a frequency-doubled Q-switched Nd:YAG laser (Lotis TII SL-2132), operated at 15 Hz repetition rate. The pump radiation was horizontally polarized, which allowed controlling the pulse energy incident on the sample by insertion into the pump beam path of a half-wave plate (HWP) and a linear polarizer (LP) set with its polarization axis horizontal. By rotating the HWP the linear polarization of the input beam is rotated out of the horizontal, and the pump beam is blocked more or less by the LP, depending on the rotation angle introduced by the HWP. Pump energy was measured with a calibrated Laser Energy Meter (QE 12LP-S-MB-DO, Gentec).

In the ASE measurements, the light incident on the sample was perpendicular to the film surface and focused onto that surface in

Table 1 ASE properties of Perylene Orange incorporated into 9 μm thick thin films of selected polymers

Polymer	n^a	$[PO]^b$/M	$[Polymer]^c$/mg ml^{-1}	$I_{40000}{}^{ASE d}$ (%)	$\Delta\lambda^e$/nm	$I_{th}{}^{ASE f}$/kW cm^{-2}	$\lambda_{peak}{}^{ASE g}$/nm	g^h/cm^{-1}	$L_{th}{}^i$/cm	$L_{sat}{}^j$/cm
PMMA	1.4979	1×10^{-2}	200	83	35/3.4	98	581.5	33.6	0.037	0.23
6F-DDM	1.5300	9×10^{-3}	120	71	34/8.7	67	582.8	37.7	0.035	0.20
6F-4M	1.5352	1×10^{-2}	150	68	37/8.7	88	581.5	—	—	—
6F-6F	1.5695	1×10^{-2}	120	68	32/14.4	118	576.8	—	—	—
6F-IMM	1.5523	1×10^{-2}	120	69	34/12.6	85	579	—	—	—

[a] Refractive index at 580 nm. [b] Perylene Orange concentration. [c] Polymer proportion in solvent. [d] ASE intensity after 40 000 pump pulses of 190 kW cm^{-2} in the same position of the sample referred to the initial intensity. [e] Max/min ASE linewidth. [f] ASE threshold intensity. [g] ASE peak. [h] Optical gain at 190 kW cm^{-2}. [i] ASE threshold length at 190 kW cm^{-2}. [j] ASE saturation length at 190 kW cm^{-2}.

a stripe shape of ~150 μm width by a combination of negative and positive cylindrical quartz lenses ($f = -15$ and +15 cm, respectively), perpendicularly arranged. An adjustable slit was used to select only the central portion of the pump beam. A micrometer screw allowed to precisely select the width of the slit. Excitation stripes of up to 2 mm length were defined, with an end placed right up to the edge of the film. The sample and the adjustable slit were placed on vertical and horizontal, respectively, motorized translation stages (MTS50, Thorlabs), computer controlled, to allow precise positioning.

In the DFB laser measurements, the two cylindrical lenses are substituted by one spherical lens ($f = +15$ cm), the adjustable slit is removed, and the sample is rotated so that the pump beam arrives at the surface at an angle of about 34° from the normal to that surface. The pumped spot at the surface is elliptical in shape with major and minor axis of about 245 μm and 185 μm, respectively.

The edge ASE and the normal to the film DFB laser emission were collected with a 5 cm focal length spherical lens, focused onto a fiber bundle and detected with a spectrograph/monochromator (Spectrapro-300i Acton Research) equipped with a thermoelectrically cooled CCD detector (SpectruMM:GS 128B). Neutral density filters were used to avoid CCD detector saturation. All the measurements are averaged over 15 pulses.

3. Results and discussion

3.1 Perylene Orange (PO)

3.1.1 Thermal stability. Perylene Orange was used as the model dye, and then we extended its results to Perylene Red, since they belong to the same family of dyes and have similar photophysical and laser properties.[37,38]

As a preliminary study on the photodegradation mechanism involved in perylene dyes, we first proceeded to evaluate the thermal stability of PO by Thermogravimetric Analyses (TGA) and compared it with that of PM597, which is known to suffer mainly thermal photodegradation.[22] The TGA (Fig. 2) indicate that PO is much more thermostable than PM597, with PO beginning to decompose at about 170 °C above the temperature at which the decomposition of PM597 begins. This fact implies that PO is a thermally robust dye and that would be, *a priori*, mainly affected by chemical photodegradation.

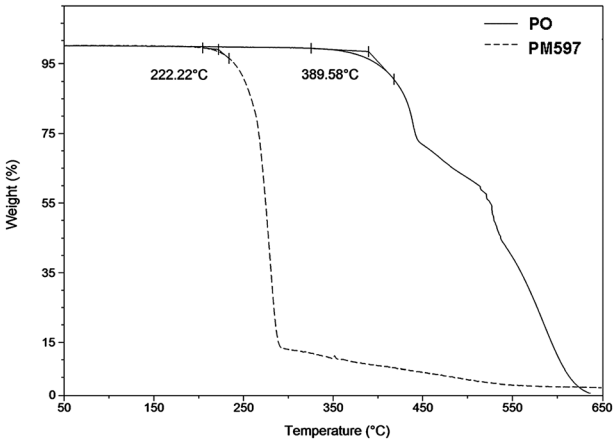

Fig. 2 TGA curves for Perylene Orange (PO) and pyrromethene 597 (PM597).

3.1.2 ASE. To confirm this statement, the ASE from waveguides based on PO incorporated into different polymers (Fig. 1), chosen to avoid one or another mechanism, were assessed. Since PO is a non-polar dye, it can be solved in PMMA and FPIs, which may avoid the chemical and thermal photodegradation, respectively. Thin films with a thickness of 9 μm, as measured by a digital comparator, were deposited onto quartz substrates. The dye concentration in each of the polymeric formulations was optimized to render the highest emission efficiency (Table 1).

As the measured refractive index of the quartz substrate ($n_2 = 1.4583$) was lower than that of the dye-doped polymer layer (see Table 1), the resulting quartz-doped polymer–air structure defines an asymmetric slab optical waveguide, where total internal reflection confines and guides the light along the film so that edge emission is obtained.

The dye degradation rate in the different materials was assessed by pumping the samples at a fixed position with an intensity of 190 kW cm^{-2}, which is well above ASE threshold, and with 15 Hz repetition rate. As mentioned above, if the photostability scales up when the oxygen permeability is reduced, then the photodegradation mechanism may be considered mainly chemical, but if the photostability scales up when the thermal stability increases, the dominant mechanism will be thermal. Fig. 3 presents the measured evolution of the normalized ASE in the different materials as a function of the number of pump pulses. It can be observed that the degradation in all the samples based on FPIs is quite similar, whereas the degradation is clearly smaller in the sample based on PMMA (Table 1). These results exclude the thermal photodegradation as the main bleaching process in PO dye, because the thermal stability in the FPIs is higher than that of PMMA which should result in lower degradation in the FPI based samples if thermal degradation was dominant. On the other hand, the permeability to oxygen $P(O_2)$ of the different materials follows the order PMMA

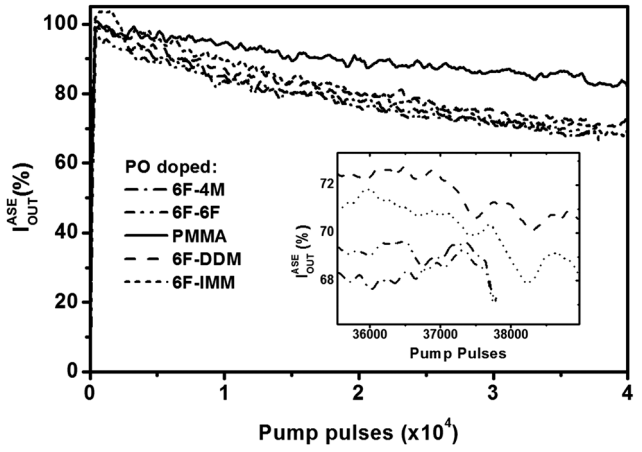

Fig. 3 Evolution of the normalized PO ASE intensity as a function of the number of pump pulses in the same position of the sample for the different host materials. Pump intensity and repetition rate were 190 kW cm^{-2} and 15 Hz, respectively. Inset: detail of the photostability traces corresponding to the FPIs in the final part of the experiment.

$\ll$ 6F-4M < 6F-DDM < 6F-6F < 6F-IMM (Table 2). Thus, the fact that the lower photodegradation is achieved in PMMA, which is the material with lower permeability to oxygen, indicates that in perylenes photodegradation is mainly caused by photooxidation processes, as could be foreseen from the TGA measurements. Further insight into the photodegradation process could be obtained through a study of the photoluminescence lifetime under similar pumping conditions, but this study is beyond the scope of the present work.

To compare the emission efficiency of PO in the different materials we made used of the ASE threshold since, unlike the output relative intensity, it is independent of the collecting efficiency of the detection system. The ASE threshold was assessed by pumping the samples with increasing pump intensities and looking for the change in slope in the ASE relative intensity. In all cases, the intensity of the emission grows linearly with the pump intensity but with a distinct change in slope at the ASE threshold as can be seen in Fig. 4, where a log–log scale is used to better distinguish the different behaviors of the emission (fluorescence, ASE and saturation) as a function of the pump intensity. At low pump intensities the light emitted from the edge of the films exhibited the broad emission spectrum characteristic of fluorescence, with a full width at half maximum (FWHM) in the range 30–40 nm, which decreased to a typical ASE FWHM of 3–10 nm (Table 1), at pump intensities above a certain threshold value (Fig. 5). As is well known, the collapse of the FWHM in the emission spectrum and the change of the slope in the emission intensity as the pump intensity increases are a signature of the onset of ASE above a certain pump threshold.[42] From the data in Fig. 4, a pump threshold for the onset of ASE in the range 70–120 kW cm^{-2} can be estimated, depending on the given matrix (Table 1), the sample based on 6F-DDM being the one with the lowest ASE threshold and the highest efficiency. All of the samples emitted close to 580 nm, but with slight shifts resulting from the different "environments" seen by the dye molecules (Table 1).

The results reported in Fig. 3–5 show that the highest ASE efficiency of PO is recorded in the sample based on the polyimide 6F-DDM, whereas the best photostability is obtained when the host material is PMMA. In order to choose the most appropriate material for PO, we carried out a more detailed study of the performance of the ASE in these two materials.

ASE gain measurements were carried out by using the variable stripe length (VSL) method, which consists basically of pumping optically the sample with a stripe-shaped beam of variable length at constant intensity and measuring the intensity of the edge-emitted ASE as a function of stripe length.[43,44] A simple fit of an appropriate expression to the resulting data gives the optical gain as an output parameter. It can be shown that the relationship

Table 2 Permeation and thermal properties of the selected polymers

Polymer	η_{inh}[a]/dl g^{-1}	T_g[b]/°C	T_d[c]/°C	Char yield[d] (%)	P(O_2)[e]/Barrers
PMMA	—	105	200	2	0.16
6F-DDM	0.85	310	510	49	17.0
6F-4M	0.92	301	515	43	4.7
6F-6F	1.03	317	511	42	17.8
6F-IMM	1.15	290	510	40	38.4

[a] Inherent viscosity measured in *N*-methyl-2-pyrrolidone, 0.5% at 25 °C. [b] Glass transition temperature. [c] Onset of the first decomposition step. [d] Carbonaceous residue at 800 °C (%). [e] Permeability coefficient in Barrers (1 Barrer = 10^{-10} cm^3 (STP) cm cm^{-2} s^{-1} cmHg^{-1}).

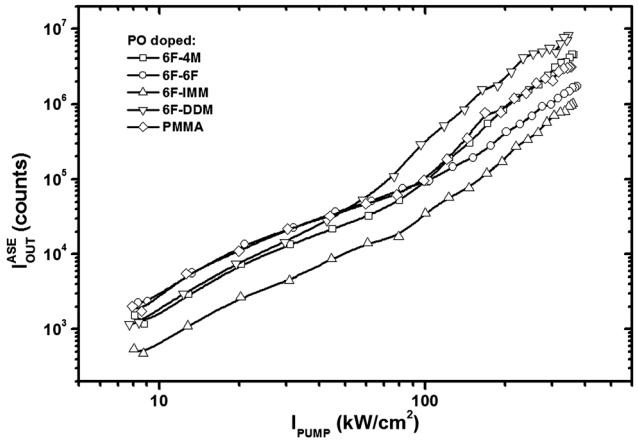

Fig. 4 Dependence of the ASE peak output intensity of the PO emission spectra on pump intensity for the different host materials. The lines are a guide to the eye.

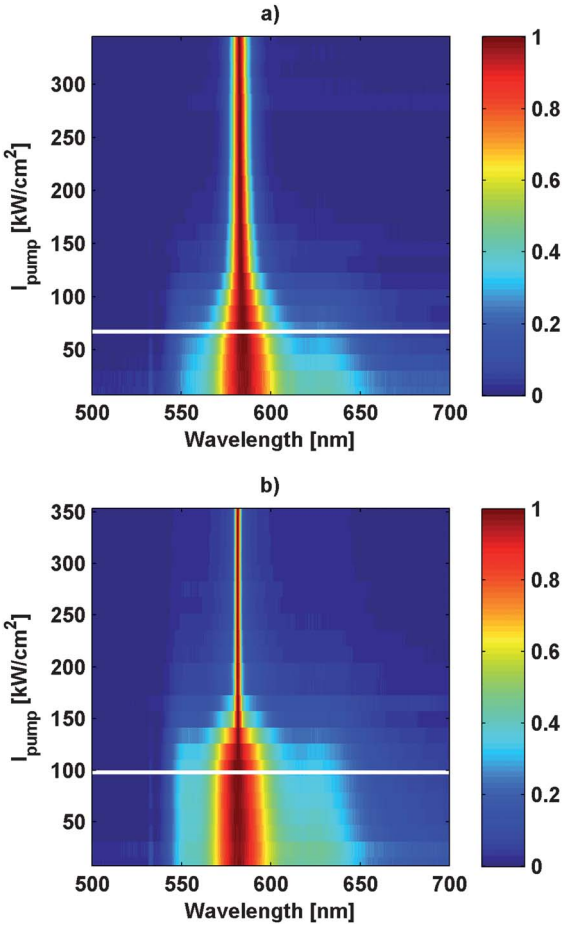

Fig. 5 Dependence of the PO normalized ASE spectra on pump intensity for (a) 6F-DDM and (b) PMMA. The white lines mark the ASE threshold intensity.

between pumped stripe length and edge-emitted ASE intensity can be written as:[44]

$$L = \frac{I_{ASE}/I_s}{g + \Omega/I_s} + \frac{g}{(g + \Omega/I_s)^2} \ln \left| \frac{\Omega + (g + \Omega/I_s) I_{ASE}}{\Omega} \right|, \quad (1)$$

where g is the net gain, I_s is the saturation intensity, and Ω is a fluorescence growing parameter. Once the VSL measurements have been performed, g, I_s, and Ω can be determined by plotting the pumped stripe length as a function of the ASE peak intensity and fitting eqn (1) to the resulting curve.

Samples of PMMA and 6F-DDM doped with PO were subjected to systematic measurements of the intensity of the emitted light as a function of the excitation length at a pump intensity of 190 kW cm^{-2}, corresponding to the one used in the photostability experiments. By fitting the expected dependence as given by eqn (1) to the experimental data, the net gain coefficients collected in Table 1 are obtained. The fitting procedure also provides values for the parameters I_s and Ω. Thus, by using the expressions:[44]

$$gL_{th} \approx 1.256, \quad (2)$$

$$gL_{sat} \approx 1 + \ln\left(\frac{gI_s}{\Omega}\right), \quad (3)$$

the values for the threshold (L_{th}) and saturation (L_{sat}) lengths, which establish the range for which the pump to ASE conversion rate is most efficient,[44] can be calculated. It is seen in Table 1 that PO waveguides exhibit ASE parameters (gain and characteristic lengths) similar for both materials, PMMA and 6F-DDM. Thus, taking into account that the waveguide based on PMMA renders the highest photostability, which in turn is the most important property, together with the fact that PMMA is much cheaper that FPIs, which would reduce the future production costs, we considered PO/PMMA as the best combination that guarantees both high efficiency and photostability. Consequently, DFB laser emission studies were performed in the sample PO/PMMA, with a dye concentration of 1×10^{-2} M.

3.1.3 DFB laser emission. In DFB lasers, light propagating in a waveguide mode of the organic film is scattered from the periodic structure on the substrate to create a diffracted wave propagating in the counterpropagating waveguide mode at a wavelength satisfying the Bragg condition, $m\lambda = 2n_{eff}\Lambda$, where m is an integer that represents the order of the diffraction, and n_{eff} is the effective refractive index of the waveguide, which represents a geometrical average of the refractive indices of the three layers of the waveguide.[1] Working with the second order $m = 2$, the resonant wavelength is equal to $n_{eff}\Lambda$, and light is diffracted out of the surface of the film perpendicular to the plane of the waveguide. That is, the second-order structure provides a surface-emitted output coupling of the laser light *via* first-order diffraction while providing in-plane feedback *via* second-order diffraction.[1]

Using samples consisting of a substrate engraved with 386 nm period sinusoidal grating onto which a 1.5 μm film of PMMA doped with PO in the concentration 1×10^{-2} M was spin coated, DFB laser emission was obtained at a wavelength of 570.1 nm, determined by the Bragg condition in second order. The upper panel of Fig. 6 shows the dependence of the DFB emission intensity on pump intensity in the region of pump intensities

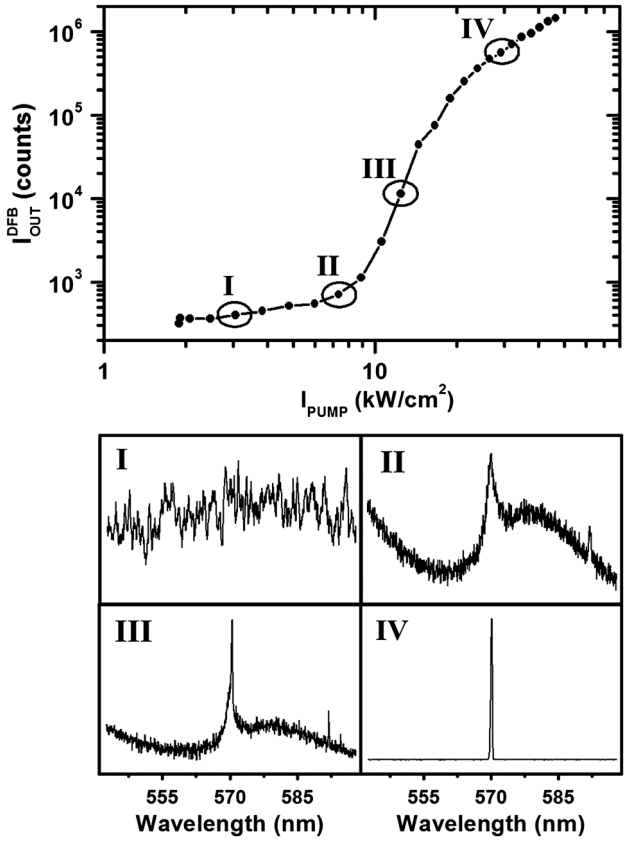

Fig. 6 Upper panel: dependence of the DFB laser output intensity on pump intensity for PO (1×10^{-2} M) in PMMA. Lower panel: evolution of the DFB laser emission spectrum over the pumping region.

around the threshold. The log–log scale of the plot allows to better appreciate the threshold region, which can be considered to be the stepped one. The behavior observed in Fig. 6 is the one expected for a laser. At low pump energies there is just fluorescence. Once the threshold is reached, the intensity of the emission increases suddenly and the FWHM of the emission collapses to a mere 0.33 nm. The lower panel in Fig. 6 shows the DFB spectra before step (I), at the beginning of step (II), at mid-step (II), and at a point where the DFB laser emission is fully established (IV). At the point corresponding to the first spectrum (pump intensity 3 kW cm^{-2}), only fluorescence is observed. At the beginning of the threshold step (pump intensity 7.5 kW cm^{-2}), an amplified emission is clearly emerging from the fluorescence background. This peak can be understood as sub-threshold ASE in the cavity mode being out coupled by the first diffraction order. The mid-step point (III), corresponding to a pump intensity 12.5 kW cm^{-2} (350 nJ), shows that the DFB emission is clearly growing out from the ASE background, and consequently this point is taken as the laser threshold. At higher pump intensities (point IV), the DFB emission is fully established, having a FWHM of 0.33 nm, very close to the resolution limit of our detection system. The Bragg gap, showing the forbidden photonic band associated with the periodic structure, cannot be observed in the fluorescence regime, because the refractive index contrast between each side of the grating (active film and substrate) is small and the waveguide is thick (1.5 μm) compared with the grating depth (150 nm).

These two facts result in the stop band being too narrow to be observed with our detection system.

Once again, an important parameter in any DFB device from the application point of view is its operational lifetime. We assessed the photostability of the PO/PMMA DFB laser developed in this work by pumping the samples at a fixed position with an intensity of 51 kW cm^{-2} (energy per pulse: 1.44 mJ), four times above the threshold, at 15 Hz repetition rate. The actual evolution of the DFB laser emission as a function of the number of pump pulses is presented in Fig. 7. It is seen that the intensity of the DFB laser emission drops to 50% of its initial intensity after 54 000 pulses (60 min) and to 20% of its initial intensity after 126 600 pulses (141 min). Higher photostability in perylenediimide derivatives has been reported by Navarro-Fuster *et al.*,[28] who demonstrated a photostability half-life of 3.1 × 10^5 pump pulses, but the pump energy (4 μJ/pulse) was only 2.2 times above the threshold and their repetition rate was 10 Hz. When they increased the pump intensity to 52.5 kW cm^{-2} (6 μJ per pulse, 3.3 times above threshold), which are pump conditions closer to ours, they obtained a photostability half-time of about 150 000 pulses, albeit at the repetition rate of 10 Hz. In this regard, it should be noticed that photodegradation in dye-doped solid matrices is affected by the repetition rate: the higher the rate, the quicker the photodegradation.[16]

The emission photostability of the PO/PMMA device, despite being acceptable, has been obtained in an unfavorable scenario, *i.e.*, in non-optimized experimental and technological conditions. Hence, it could be dramatically improved by optimizing both the deposition conditions and the resonant cavity. Thus, depositing the active film on the substrate in an oxygen free environment and encapsulating the resulting device with an oxygen impermeable film[17] would avoid the oxygen diffusion within the polymer matrix and the subsequent chemical photodegradation. Another complementary way of reducing dye degradation would consist of lowering the laser threshold and increasing the laser efficiency. In this way, less pump energy would be needed to achieve the same output intensity. This efficiency improvement has been demonstrated in edge-emitting first order DFB lasers and surface-emitting second order DFB lasers with 2D or circular gratings.[1] In addition, the use of square-profile gratings instead of sinusoidal ones would be also preferable,[45] since the duty cycle (groove width/period ratio) can be controlled and the laser threshold reduced. Finally, it has been recently shown that a 22x reduction in laser pump threshold and a 23x enhancement in energy conversion can be achieved by using a resonant pumping technique.[46]

3.2 Perylene Red (PR)

The emission of these devices can be extended to longer wavelengths by using perylene red (PR), which emits close to 610 nm. Since PO and PR are very similar in nature and chemical structure, we extrapolated the previous results with PO to PR and chose PMMA as the polymer matrix for PR.

In films based on PR-doped PMMA deposited onto quartz substrates, high gain ASE was not obtained at any of the dye concentrations tried, since the absorption at 532 nm is weak (maximum absorption at 580 nm). At high dye concentrations ((1–1.5) × 10^{-2} M), reabsorption of the emission and the presence of aggregates results in the absence of gain and in a red shifted emission with a prominent shoulder in the long-wavelength side (Fig. 8). Lowering of the dye concentration (down to 1 × 10^{-3} M) reduces the presence of aggregates and their corresponding emission and reabsorption effects, which is translated into a narrower blue-shifted band, but the absorption of pump radiation is not high enough and there is no net gain. Trying to overcome these problems, we proceeded to prepare mixtures of PO and PR in PMMA, with the idea of using the process of energy transfer from PO to PR favored by the overlapping between the emission band of PO (donor) and the absorption band of PR (acceptor)[47] (Fig. 9). In this way, it would be possible to use a concentration of PR low enough to avoid aggregation, but nonetheless to have enough excited PR molecules through the energy transfer process as to assure net gain in the PR active medium.

3.3 Mixtures of Perylene Orange and Perylene Red

To find the most adequate PO/PR proportion, ASE measurements were performed in waveguides based on ~1.5 μm thin

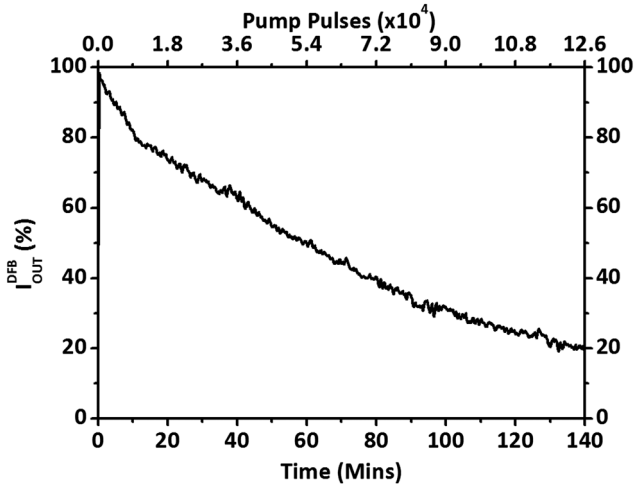

Fig. 7 Normalized DFB laser output intensity as a function of the number of pump pulses for PO (1 × 10^{-2} M) in PMMA. Pump intensity: 51 kW cm^{-2} (energy per pulse: 1.44 mJ). Repetition rate: 15 Hz.

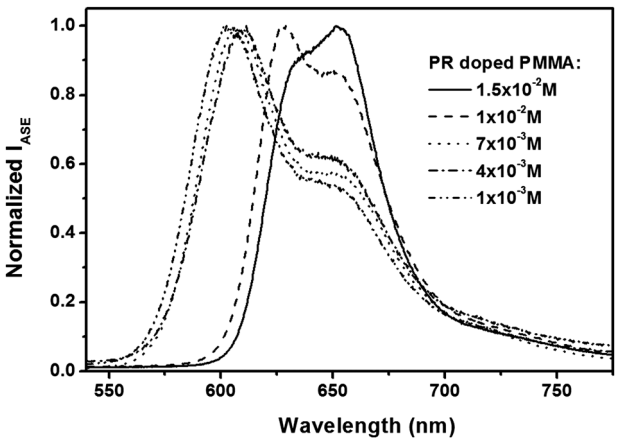

Fig. 8 Emission spectra from PR-doped PMMA thin films deposited onto quartz substrates with different dye concentrations, pumped at 460 kW cm^{-2}.

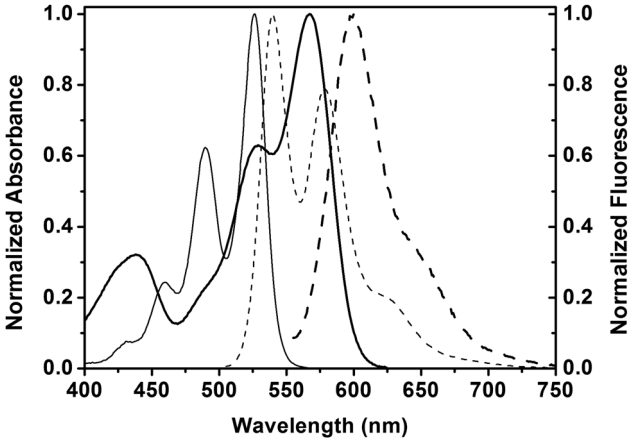

Fig. 9 Absorbance (solid lines) and fluorescence (dashed lines) spectral overlap of PO (thin lines) and PR (thick lines).

films of PO/PR mixtures in PMMA spin coated onto quartz substrates. The total concentration of dye in the films was kept at 7.5×10^{-3} M. Mixtures of PO and PR dyes were prepared with different v/v proportions in the initial solution: (9 : 1), (8.5 : 1.5), (6.6 : 3.3), (5 : 5), and (3.3 : 6.6). The mixture containing 50% of each dye produced the best combination of emission efficiency and linewidth collapse when pumped at 350 kW cm^{-2} (Fig. 10). Hence, it was chosen to carry out a detailed analysis of the ASE. The results of the assessment of the ASE as a function of the pump intensity are summarized in Fig. 11. From these data a pump threshold of 115 kW cm^{-2} for the onset of the ASE can be estimated. This threshold value is somewhat higher than that obtained for films with only PO, but much lower than the one corresponding to the PR alone, since there is always some loss of efficiency in the energy transfer process. The peak wavelength of the ASE is at about 620 nm, with a linewidth of 8 nm in the best of the cases, also somewhat higher than that obtained with just PO in the sample (compare Fig. 5 and 11b). The complex behavior shown by the peak wavelength (Fig. 11b) and by the output intensity (Fig. 11a) at low pump intensities, can be ascribed to the many competing processes present in the excited medium: first, the excited state of both dyes is being populated by

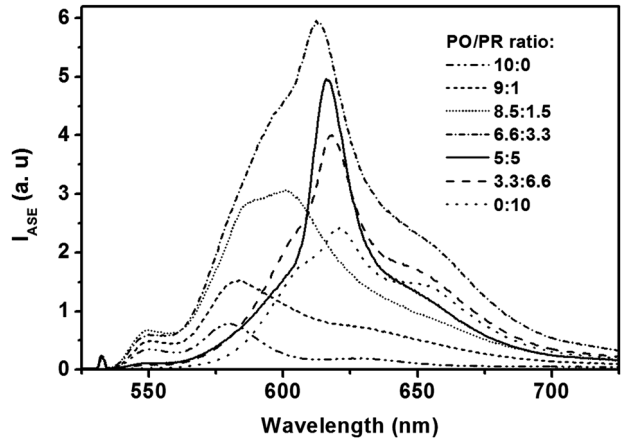

Fig. 10 ASE spectra from different mixtures of PO and PR dyes doped in PMMA thin films deposited onto quartz substrates, pumped at 350 kW cm^{-2}.

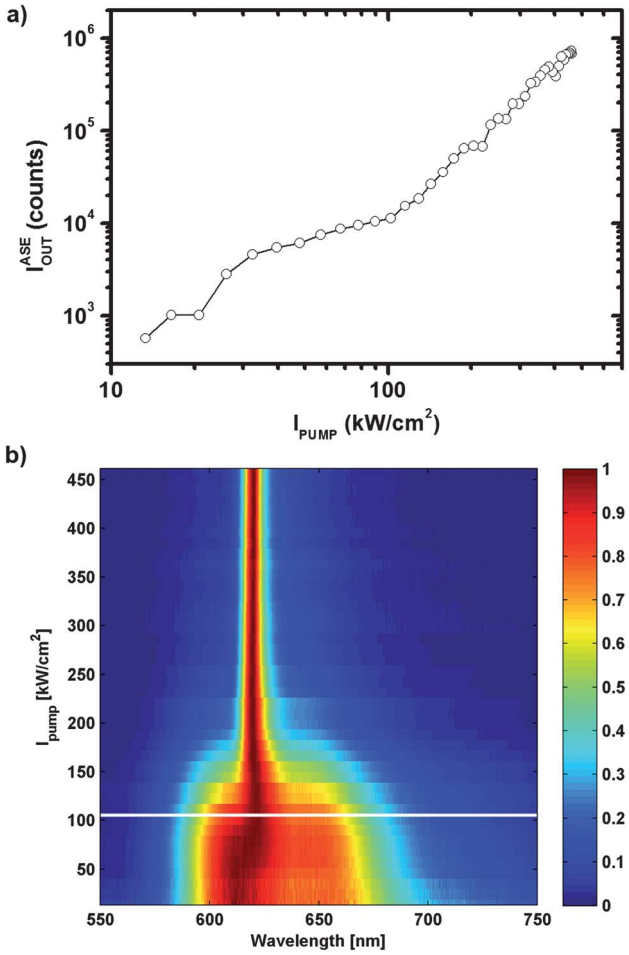

Fig. 11 Dependence on pump intensity of (a) the ASE peak output intensity and (b) the normalized ASE spectra for the 5 : 5 mixture of PO and PR dyes in PMMA. The lines are a guide to the eye. The white line in (b) marks the ASE threshold intensity.

the pump radiation, secondly, there is Förster energy transfer between PO and PR, and finally spontaneous and stimulated emission of PR, and probably of PO which is later reabsorbed by the PR, is taking place. VSL measurements were carried out on this sample, but the gain could not be extracted, since eqn (1) could not be fitted to the data, probably because it cannot cope with the many processes aforementioned.

The evolution of the ASE with the number of pump pulses in the same position of the sample, under 190 kW cm^{-2} pumping at 15 Hz repetition rate, is presented in Fig. 12. The photostability is very similar to that obtained with PO in PMMA (Fig. 7). The shape of the spectra corresponding to the first and last (56 000) emission pulses, shown in the inset in Fig. 12, seems to indicate that the degradation affects mainly PO, because the spectrum corresponding to the 56 000th pulse still keeps the emission peak at 620 nm, and the spectral broadening shows that there is a decrease of efficiency in the energy transfer due to the disappearance of the PO dye. The leveling off or even slight recuperation of the emission after about 40 000 pulses could be reflecting that, after destruction of a number of molecules of PO, the proportion PO/PR in the mixture is somewhat more efficient than the initial 5 : 5.

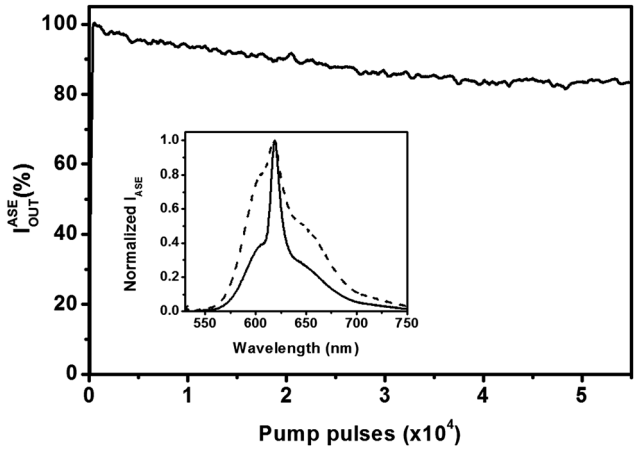

Fig. 12 Evolution of the normalized ASE as a function of the number of pump pulses in the same position of the sample for a film of a 5 : 5 mixture of PO and PR in PMMA. Pump intensity and repetition rate were 190 kW cm^{-2} and 15 Hz, respectively. Inset: ASE spectra of first (solid line) and last (dashed line) emission pulses.

It has to be pointed out that, up to now, there are very few papers on ASE from PR doped polymer waveguides;[24,25] in these reports photostability is not assessed, and when emission efficiency experiments are performed, the pumping area is not specifically stated, so that we cannot compare their threshold intensity with ours.

In view of these results, efficient and photostable DFB laser emission could be expected for the mixtures of PO and PR when deposited on substrates with a grating engraved on them whose resonant wavelength matched the corresponding emission window.

4. Conclusions

We have correlated, for the first time to the best of our knowledge, the optical properties (ASE efficiency and photostability) of thin films based on perylene dye doped polymeric hosts with their oxygen permeation and thermal properties in order to deepen the understanding of the photodegradation mechanism predominant in these dyes, and, consequently, to optimize distributed feedback (DFB) lasers based on perylene-doped polymer thin films. To this aim we have designed and synthesized thin films of PO, PR and mixtures of both incorporated into PMMA and four FPIs, two of them newly synthesized for this work. We have observed that perylene dyes mainly suffer from chemical photodegradation, since the photostability increases when the oxygen permeability is reduced. Although highly efficient and photostable ASE is recorded from waveguides based on PMMA and 6F-DDM polyimide doped with PO, we have found that PMMA is the most suitable host material for both PO and PR, since it avoids the oxygen diffusion in the final material, and the subsequent chemical photodegradation, maintains the desired ASE efficiency, and is much cheaper than 6F-DDM. In fact, we have demonstrated highly efficient and photostable ASE from waveguides based on PMMA doped with mixtures of PO and PR dyes.

When thin films of PMMA incorporating PO were deposited onto substrates engraved with surface sinusoidal gratings, long-lived DFB lasing has been obtained at a wavelength of 570.1 nm with a linewidth of 0.33 nm. The threshold energy for the onset of DFB lasing was 350 nJ per pulse (12.5 kW cm^{-2}). Upon pumping with pulses of 1.44 mJ at 15 Hz repetition rate (pump intensity of 51 kW cm^{-2}), the DFB laser emission from PO/PMMA dropped by 50% after 54 000 pump pulses and by 80% after 125 600 pump pulses in the same position of the sample. The efficiency and photostability of these DFB lasers could be further improved by optimizing the deposition process, the cavity configuration, and the pumping scheme, making these devices promising candidates for future photonic technologies.

Acknowledgements

This work was supported by Projects MAT2010-20646-C04-01, MAT2010-20668 and TRACE2009-0144 of the Spanish MICINN. L.C. thanks MICINN for a predoctoral scholarship (FPI, cofinanced by Fondo Social Europeo). The authors thank M.E. Pérez-Ojeda for performing the TGA measurements and A. Barranco for the refractive index measurements of FPIs 6F-DDM and 6F-4M.

Notes and references

1 I. D. W. Samuel and G. A. Turnbull, *Chem. Rev.*, 2007, **107**, 1272–1295.
2 E. M. Calzado, P. G. Boj and M. A. Díaz-García, *Int. J. Mol. Sci.*, 2010, **11**, 2546–2565.
3 K. P. Kretsch, C. Belton, S. Lipson, W. J. Blau, F. Z. Henari, H. Rost, S. Pfeiffer, A. Teuschel, H. Tillmann and H.-H. Hörhold, *J. Appl. Phys.*, 1999, **86**, 6155–6159.
4 S.-S. Yap, W.-O. Siew, T.-Y. Tou and S.-W. Ng, *Appl. Opt.*, 2002, **41**, 1725–1728.
5 Y. Oki, S. Miyamoto, M. Maeda and N. J. Vasa, *Opt. Lett.*, 2002, **27**, 1220–1222.
6 M. A. Reilly, C. Marinelli, C. N. Morgan, R. V. Penty, I. H. White, M. Ramon, M. Ariu, R. Xia and D. D. C. Bradley, *Appl. Phys. Lett.*, 2004, **85**, 5137–5139.
7 W. Lu, B. Zhong and D. Ma, *Appl. Opt.*, 2004, **43**, 5074–5078.
8 G. Jordan, M. Flämmich, M. Rüther, T. Kobayashi and W. J. Blau, *Appl. Phys. Lett.*, 2006, **88**, 161114 (3).
9 E. M. Calzado, J. M. Villalvilla, P. G. Boj, J. A. Quintana, R. Gómez, J. L. Segura and M. A. Díaz García, *Appl. Opt.*, 2007, **46**, 3836–3842.
10 H. Goudket, T. H. Nhung, B. Ea-Kim, G. Roger and M. Canva, *Appl. Opt.*, 2006, **45**, 7736–7741.
11 M. Djiango, T. Kobayashi, W. J. Blau, B. Cai, K. Komatsu and T. Kaino, *Appl. Phys. Lett.*, 2008, **92**, 083306 (3).
12 S. Yuyama, T. Nakajima, K. Yamashita and K. Oe, *Appl. Phys. Lett.*, 2008, **93**, 023306.
13 D. Zhang, Z. Chen and D. Ma, *J. Appl. Phys.*, 2008, **103**, 123103 (4).
14 L. Cerdán, A. Costela, I. García-Moreno, O. García and R. Sastre, *Appl. Phys. B: Lasers Opt.*, 2009, **97**, 73–83.
15 L. Cerdán, A. Costela, I. García-Moreno, O. García and R. Sastre, *Opt. Express*, 2010, **18**, 10247–10256.
16 R. Duchowicz, L. B. Scaffardi, A. Costela, I. Garcia-Moreno, R. Sastre and A. U. Acuña, *Appl. Opt.*, 2003, **42**, 1029–1035.
17 S. Richardson, O. P. M. Gaudin, G. A. Turnbull and I. D. W. Samuel, *Appl. Phys. Lett.*, 2007, **91**, 261104 (3).
18 J. Kobayashi, T. Matsuura, S. Sasaki and T. Maruno, *Appl. Opt.*, 1998, **37**, 1032–1037.
19 W. Jiang, D. Wang, S. Guan, H. Gao, Y. Zhao, Z. Jiang, W. Gao, D. Zhang and D. Zhang, *J. Photochem. Photobiol., A*, 2008, **197**, 426–433.
20 M. N. Weiss, R. Srivastava, R. R. B. Correia, J. F. Martins-Filho and C. B. de Araujo, *Appl. Phys. Lett.*, 1996, **69**, 3653–3655.
21 A. Quaranta, S. Carturan, G. Maggioni, G. Della Mea, M. Ischia and R. Campostrini, *Appl. Phys. A: Mater. Sci. Process.*, 2001, **72**, 671–677.

22 L. Cerdán, A. Costela, I. García-Moreno, O. García, R. Sastre, M. Calle, D. Muñoz and J. de Abajo, *Macromol. Chem. Phys.*, 2009, **210**, 1624–1631.
23 W.-H. Yang, V. F. Smolendo and N. A. Peppas, *J. Membr. Sci.*, 1981, **9**, 53–67.
24 D. Shamrakov and R. Reisfeld, *Chem. Phys. Lett.*, 1993, **213**, 47–53.
25 H. Manna and S. M. Al-Alawi, *J. Lumin.*, 2001, **94–95**, 55–58.
26 E. M. Calzado, J. M. Villalvilla, P. G. Boj, J. A. Quintana, R. Gómez, J. L. Segura and M. A. Díaz García, *J. Phys. Chem. C*, 2007, **111**, 13595–13605.
27 Y. Yang, G. Lin, H. Xu, M. Wang and G. Qian, *Opt. Commun.*, 2008, **281**, 5218–5221.
28 V. Navarro-Fuster, E. M. Calzado, P. G. Boj, J. A. Quintana, J. M. Villalvilla, M. A. Díaz-García, V. Trabadelo, A. Juarros, A. Retolaza and S. Merino, *Appl. Phys. Lett.*, 2010, **97**, 171104 (3).
29 M. G. Ramirez, P. G. Boj, V. Navarro-Fuster, I. Vragovic, J. M. Villalvilla, I. Alonso, V. Trabadelo, S. Merino and M. A. Diaz Garcia, *Opt. Express*, 2011, **19**, 22443–22454.
30 M. Canva, P. Georges, J.-F. Perelgritz, A. Brum, F. Chaput and J.-P. Boilot, *Appl. Opt.*, 1995, **34**, 428–431.
31 M. D. Rahn and T. A. King, *Appl. Opt.*, 1995, **34**, 8260–8271.
32 A. Dubois, M. Canva, A. Brun, F. Chaput and J.-P. Boilot, *Appl. Opt.*, 1996, **35**, 3193–3199.
33 M. D. Rahn and T. A. King, *J. Mod. Opt.*, 1998, **45**, 1259–1267.
34 W. J. Wadsworth, I. T. McKinnie, A. D. Woolhouse and T. G. Haskell, *Appl. Phys. B: Lasers Opt.*, 1999, **69**, 163–165.
35 Y. Yang, M. Wang, G. Qian, Z. Wang and X. Fan, *Opt. Mater.*, 2004, **24**, 621–628.
36 Y. Yang, J. Zou, H. Rong, G. D. Qian, Z. Y. Wang and M. Q. Wang, *Appl. Phys. B: Lasers Opt.*, 2007, **6**, 309–313.
37 I. García-Moreno, A. Costela, M. Pintado-Sierra, V. Martín and R. Sastre, *Opt. Express*, 2009, **17**, 12777–12784.
38 I. García-Moreno, A. Costela, V. Martín, M. Pintado-Sierra and R. Sastre, *Adv. Funct. Mater.*, 2009, **19**, 2547–2552.
39 J. de Abajo and J. G. de la Campa, *Adv. Polym. Sci.*, 1999, **140**, 23–59.
40 C. Lowe, in *Surface Coatings Technology*, John Wiley & Sons, London, UK, 1997, vol. 5, ch. VI, p. 60.
41 J. de Abajo and J. G. de la Campa, in *Polyimidesin Handbook of Polymer Synthesis*, ed. H. R. Kricheldorf, Marcel Dekker, New York, USA, 2005.
42 M. D. McGehee, R. Gupta, S. Veenstra, E. K. Miller, M. A. Díaz-García and A. J. Heeger, *Phys. Rev. B: Condens. Matter*, 1998, **58**, 7035–7039.
43 A. Costela, O. García, L. Cerdán, I. García-Moreno and R. Sastre, *Opt. Express*, 2008, **16**, 7023–7036; and Erratum, *Opt. Express*, 2008, **16**, 7087.
44 L. Cerdán, A. Costela and I. García-Moreno, *J. Opt. Soc. Am. B*, 2010, **27**, 1874–1877.
45 G. A. Turnbull, A. Carleton, G. F. Barlow, A. Tahraouhi, T. F. Krauss, K. A. Shore and I. D. W. Samuel, *J. Appl. Phys.*, 2005, **98**, 023105 (7).
46 C. Ge, M. Lu, Y. Tan and B. T. Cunningham, *Opt. Express*, 2011, **19**, 5086–5092.
47 A. K. Sheridan, A. R. Buckley, A. M. Fox, A. Bacher, D. D. C. Bradley and I. D. W. Samuel, *J. Appl. Phys.*, 2002, **92**, 6367–6371.

Paper B7: Appl. Phys. B 108, 839–850 (2012)

Random lasing from sulforhodamine dye doped polymer films with high surface roughness

L. Cerdán, A. Costela, G. Durán-Sampedro and I. García-Moreno

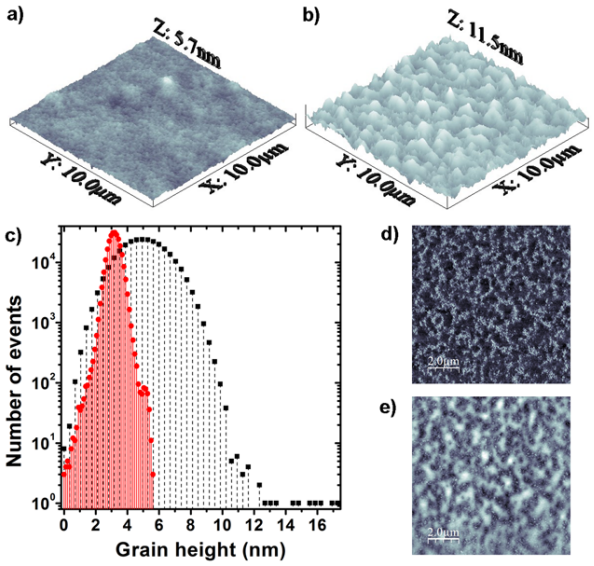

Tapping mode AFM surface analysis of 8OH-POSS/pHEMA 1 μm thick waveguides: Topography images (3D-view, 10 μm $\times$ 10 μm) of samples without (a) and with (b) 8OH-POSS (25 %). c) Grain height histogram of image a) (circles) and of image b) (squares). Phase (d) and topography (e) images (top view, 10 μm $\times$ 10 μm) of the sample with 25 % wt. 8OH-POSS.

Appl. Phys. B (2012) 108:839–850
DOI 10.1007/s00340-012-5120-8

Applied Physics B
Lasers and Optics

Random lasing from sulforhodamine dye-doped polymer films with high surface roughness

Luis Cerdán · Angel Costela · Gonzalo Durán-Sampedro · Inmaculada García-Moreno

Received: 5 March 2012 / Revised: 12 June 2012 / Published online: 16 September 2012

Abstract Active waveguides with high surface roughness due to phase separation in polymer blends can sustain wave-guided coherent random lasing, paving way to the development of integrated devices technologically and economically more favorable that the ones based on nanopatterning. In spite of the vast amount of work on organic thin film lasers carried out, the orange-red spectral region (600–700 nm) has not received much attention in this context, albeit it is of interest in biophotonic applications. In this paper, wave-guided coherent random lasing (RL) at 610 nm (Sulforhodamine B) and 630 nm (Sulforhodamine 640) is achieved by incorporating silsesquioxane nanoparticles into dye-doped polymer films. An AFM analysis concludes that the RL emission originates due to the scattering induced by the high surface roughness coming from the polymer/silsesquioxane phase separation. The reported results demonstrate that it is possible to get efficient and photostable laser emission from dye-doped thin films in the wavelength region over 600 nm by incorporating into the polymeric material appropriate nanoparticles which induce structural changes.

Electronic supplementary material The online version of this article (doi:10.1007/s00340-012-5120-8) contains supplementary material, which is available to authorized users.

L. Cerdán (✉) · A. Costela · G. Durán-Sampedro · I. García-Moreno
Instituto de Química Física "Rocasolano" (CSIC), Serrano 119, 28006 Madrid, Spain
e-mail: lcerdan@iqfr.csic.es

1 Introduction

Waveguiding structures based on dye-doped polymeric materials have attracted much attention over the last years for their potential applications in integrated photonics [1–4 and references therein]. These materials provide low-cost gain media with wide wavelength tunability and high emission efficiency which, together with their processing flexibility, makes them very attractive for the fabrication and the development of light sources suitable for integration in optoelectronic devices.

Although the development of organic lasers based on dyes incorporated into appropriate polymer materials is an active field of research [5], most of the work has been carried out with dyes emitting in the green-yellow spectral region, and few results have been published on bulk dye-doped solid-state lasers emitting in the orange-red part of the visible spectrum (>600 nm). Some more work has been reported with the dye-doped organic material cast as a thin film. In these works, laser and amplified spontaneous emission (ASE) efficiency as well as dye photostability was assessed [6–9]; gain and loss measurements were carried out [10–17], and narrow linewidth laser emission based on distributed feedback (DFB) resonator designs, where a periodic modulation of the refractive index incorporated into the gain material waveguide causes that the emitted light is Bragg reflected, was demonstrated [18–23]. The dyes used as active media were mainly DCM [9, 16, 21], Rhodamine B [6, 12, 19], and Rhodamine 640 [7, 11, 20]. Surprisingly, very few works can be found in which commercial sulforhodamine dyes are used in dye-doped polymer thin film emitting devices [23–25], in spite of these dyes having demonstrated laser action with high efficiency and good photostability when incorporated into bulk solid matrices [26, 27].

On the other hand, in the biophotonic related fields, long wavelength (>600 nm) fluorescence dyes have a clear advantage over shorter wavelength ones because long wavelength light can penetrate deeper into tissues [28]. In addition, for future biotechnological applications based on disposable lab-on-chip platforms [29] in which a high spectral purity is not strictly necessary, the use of new materials capable of sustaining laser emission in the red-edge spectral range would be needed to allow the development of integrated lasers technologically and economically more favorable that the ones based on nanopatterning (DFB, DBR, etc.). In this regard, in a previous paper [30], we demonstrated that the presence of nanometer-sized particles based on polyhedral oligomeric silsesquioxanes (POSS) in photosensitized polymeric planar waveguides could result in coherent random lasing under appropriate conditions. Hence, given the need of red-emitting cheap laser devices and the good laser performance shown by sulforhodamine dyes in this spectral range led us to explore the emission properties of these dyes in polymeric thin films incorporating adequate POSS molecules.

In this paper, we begin by studying in depth the ASE properties such as thresholds, gains and spectral fingerprints of slab waveguides consisting of poly(2-hydroxyethyl methacrylate) (pHEMA) doped with Sulforhodamine B (SRhB) and Sulforhodamine 640 (SRh640) dyes in order to serve as a guide to the subsequent laser emission measurements. To achieve laser emission rather than ASE, we follow the same approach than in the previous study [30], where incorporation of silsesquioxane nanoparticles (POSS) to the dye-doped thin film resulted in coherent random lasing (RL) under appropriate conditions. Optimization of POSS content and film thickness to achieve RL has been carried out. RL emission spectral fingerprints, thresholds and, for the first time, photostabilities are assessed and insights into the RL origin and characteristics are obtained from AFM measurements, and Power Fourier Transforms (PFT) of the emission spectra.

2 Experimental methods

2.1 Materials and film characterization

Dyes Sulforhodamine B (SRhB) and Sulforhodamine 640 (SRh640) were laser grade and purchased from Exciton. Polymer poly(2-hydroxyethyl methacrylate) (pHEMA) and octa(hydroxypropyldimethylsilyl)-POSS (8OH-POSS), purchased from Aldrich, were used as received. The polymer chosen for incorporating the dyes was pHEMA, in which both dyes, due to their polar character, exhibit high lasing efficiency in bulk samples [26, 27]. Dynamic light scattering measurements of POSS solutions showed a mean size of 1.2 nm with a log-normal distribution falling to zero at 0.5 and 4 nm [31].

Solvent used for the preparation of films was ethanol (analytical grade, Merck). Polymer in proportion 67–200 mg/mL, depending on the desired thickness of the films, and dyes at concentration (with respect to the polymer) in the range $(0.8–5) \times 10^{-2}$ M were added to the organic solvent and stirred for 24 h to fully solve dye and polymer. Films used in the random lasing measurements also incorporated 8OH-POSS nanoparticles in weight proportions of up to 25 %. It was not possible to prepare films with higher proportions of 8OH-POSS.

Polymer solutions incorporating the dyes were deposited onto quartz substrates using two different procedures depending on the desired thickness: extender roller and spin coating. In the extender roller technique [32], a few drops of the solution are deposited on a quartz slide and extended along the substrate with a calibrated rod (endless screw with calibrated thread). After solvent evaporation at room temperature for several minutes films with thickness of 9 and 4.5 μm were obtained. Films of 1 μm thickness were prepared by spin coating (1,000 rpm, 30 s). The thickness of the films was measured using a Digital Comparator (Mahr Extramess 2001) with a resolution of up to 0.2 μm.

The refractive index of the quartz substrate was measured using an Abbe refractometer (Arago) employing 1-bromonaphtalene as sample support interphase and a sodium lamp as monochromatic light at 589 nm, and found to be 1.4583. We have found no way to measure directly the refractive index of the hybrid matrix since the film surface is rough and this leads to errors when using, for example, variable angle spectroscopic ellipsometry (VASE). We have estimated it taking into account that the refractive index of pHEMA is 1.51, and the one of 8OH-POSS must be close to 1.5, as we have shown previously [33]. Then, we have assumed a refractive index of $\sim$1.51 for the mixture of both materials. The prepared samples are then asymmetric slab optical waveguides, where total internal refraction confines and guides the light along the film.

The topography of the polymer films was examined via tapping mode AFM (Molecular Imaging PicoSPM). The raw AFM data were analyzed with the software WSxM 5.0 (Nanotec) [34].

2.2 ASE and random lasing measurements

The thin film samples were optically pumped at 532 nm with 20 ns full width at half maximum (FWHM) pulses from a frequency-doubled *Q*-switched Nd:YAG laser (Lotis TII SL-2132), operated at 15 Hz repetition rate. The

pump radiation was vertically polarized, which allowed controlling the pulse energy incident on the sample by insertion into the pump beam path of a half-wave plate (HWP) and a linear polarizer (LP) set with its polarization axis vertical. By rotating the HWP the linear polarization of the input beam is rotated out of the vertical, and the pump beam is blocked more or less by the LP, depending on the rotation angle introduced by the HWP. Pump energy was measured with a calibrated Laser Energy Meter (QE 12LP-S-MB-DO, Gentec).

The light incident on the sample was perpendicular to the film surface and focused onto that surface in a stripe shape spot of $\approx$150 μm width by a combination of negative and positive cylindrical quartz lenses ($f = -15$ and $+15$ cm, respectively), perpendicularly arranged. An adjustable slit was used to select only the central portion of the pump beam. A micrometer screw allowed to precisely select the width of the slit. Excitation stripes of up to 2 mm length were defined, with an end placed right up to the edge of the film (Fig. 1). Sample and adjustable slit were placed on vertical and horizontal, respectively, motorized translation stages (MTS50, Thorlabs), computer controlled, to allow precise positioning.

The edge ASE and random laser emission was collected with a 5-cm focal length spherical lens, focused onto a fiber bundle and detected with a spectrograph/monochromator (Spectrapro-300i Acton Research) equipped with a thermoelectrically cooled CCD detector (SpectruMM:GS 128B). Neutral density filters were used to avoid CCD detector saturation. The integration time in the CCD was set at 333 ms so that all the measurements were averaged over five pulses.

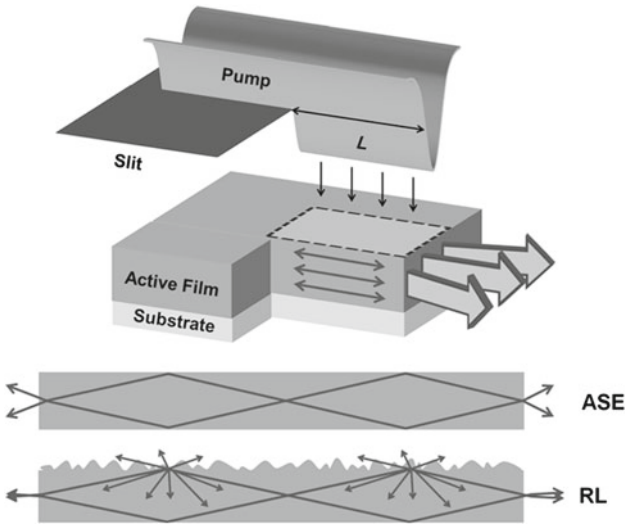

Fig. 1 Waveguides pumping scheme and ray propagation picture in ASE and RL experiments

3 Results and discussion

3.1 Sulforhodamine B-doped waveguides

3.1.1 Amplified spontaneous emission

First, waveguides with film thickness of 9 μm and SRhB dye concentration in the range $(0.8–5) \times 10^{-2}$ M were prepared and their emission characteristics at pump intensities ranging from 10 up to 430 kW/cm^2, with a stripe length of 2 mm, were recorded. In all cases, ASE, characterized by an important decrease in the spectral width and a change in the slope of the output emission intensity above a certain threshold, was observed. In particular, the concentration 1×10^{-2} M exhibited good overall performance, and this was the dye concentration selected to carry out a detailed study of the ASE and lasing properties of the SRhB-doped polymer films. We chose 9-μm thick films because we had seen in a previous work [3] that the thicker the films were, the lower the gain became, but the higher the signal was. In order to perform the gain study at the lowest pump intensities and the shortest stripe lengths, we needed enough signal-to-noise ratio to acquire the data. Given the detection limitation in our system, we decided to sacrifice the gain in favor of the signal.

In Fig. 2a, it is represented the dependence of the FWHM (circles) and the intensity of the emission at 609 nm from the edge of the film (squares) with the pump intensity. From Fig. 2a, it can be estimated an ASE threshold (indicated by the collapse of the FWHM and the corresponding change of slope in the I_{max} vs. I_{pump} plot) of 90 kW/cm^2 and a minimum FWHM of 15 nm, with the emission being centered at 609 nm. For completeness we have represented in Fig. 2b the normalized spectra as a function of pump intensity. It is interesting to see that as one approaches the threshold the FWHM increases (seen in Fig. 2a as well) but in the moment the threshold was crossed the spectral fingerprints change dramatically, with the emission peak red shifting by more than 10 nm and the FWHM rapidly decreasing. The increase in the FWHM below threshold takes place because the ASE band does not perfectly overlap with the fluorescence band, and close to threshold both contribute similarly, widening the final spectrum. This effect can be very well observed in Fig. 2b.

To better characterize the stimulated emission processes, ASE gain measurements were carried out using the variable stripe length (VSL) method, which consist basically in pumping optically the sample with a stripe-shaped beam of variable length at constant intensity and measuring the intensity of the edge-emitted ASE as a function of the excitation stripe length [2]. In the small-signal regime, the ASE intensity collected at the waveguide edge varies with the pump stripe length as [2]:

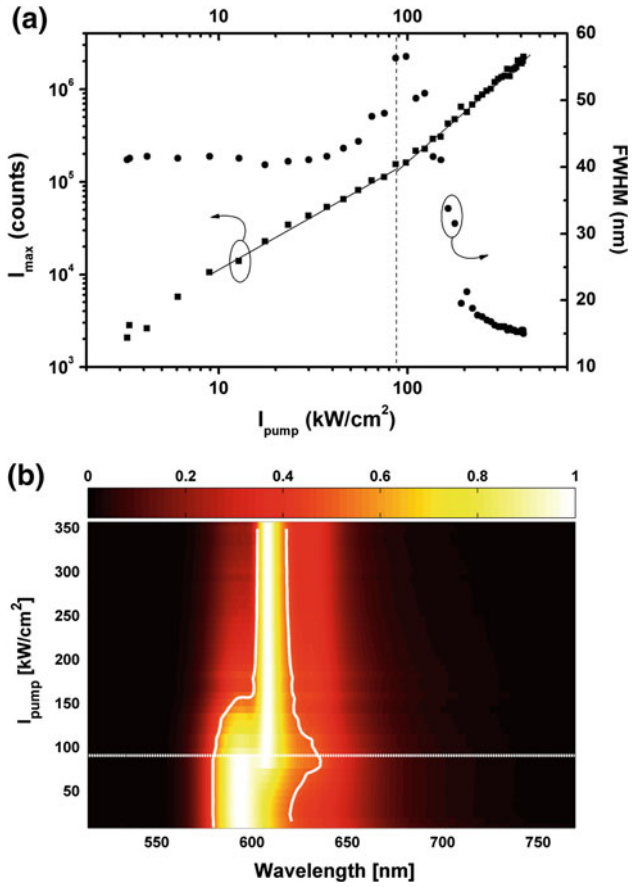

Fig. 2 ASE measurements from SRhB/pHEMA 9 μm thick waveguides: **a** peak intensity (*squares*) and FWHM (*circles*) as a function of pump intensity. *Solid* and *dashed lines* are a guide to the eye and ASE threshold marker, respectively. **b** Normalized ASE output spectra as a function of pump intensity. *Solid* and *dotted lines* represent the half maximum evolution (*FWHM*) and ASE threshold, respectively

$$I_{\mathrm{ASE}}^{S-S}(L) = \frac{\Omega}{g}(e^{gL} - 1), \tag{1}$$

where Ω is a fluorescence growing parameter, g the net gain coefficient, and L is the stripe length. Thus, g can be determined by plotting the ASE intensity as a function of the pumped stripe length and fitting the resulting curve to the expected dependence given by Eq. (1). It should be remarked that using Eq. (1) is only appropriate when saturation effects are not important. If saturation is appreciable, Eq. (1) should be modified accordingly to account for these effects [2]. In the present studies, saturation does not set in over the range of pump intensities used, as can be appreciated in Fig. 2a and, thus, use of Eq. (1) is adequate. On the other hand, information about the ASE threshold length L_{th} is obtained using the simple expression [35]

$$gL_{\mathrm{th}} = 1.256. \tag{2}$$

The results from the ASE gain analysis are depicted in Fig. 3. In Fig. 3a, the ASE intensity at 609 nm is plotted as a function of the excitation stripe length for three representative pump intensities: well below threshold, near threshold, and well above threshold. The solid lines in Fig. 3a were obtained by fitting the experimental data to the expected dependence as given by Eq. (1). It is evident from Fig. 3a that even for the highest pump intensity used in these experiments, gain saturation was not yet established, which justifies the use of Eq. (1). As seen in Fig. 3b, c, below the ASE threshold ($g < 0$) the emission spectrum remained broad for any excitation length (Fig. 3b), but above threshold ($g > 0$) a gain set in and the spectrum became narrower as the excitation length increased (Fig. 3c). Nevertheless, in the experiment well below the threshold (Fig. 3b), the spectra broadened as the excitation stripe increased from the lowest length until the FWHM reached a steady value. This could be ascribed to the presence of reabsorption/reemission processes which populate less energetic levels. At short excitation stripes the light path inside the excited medium is not long enough as to populate lower levels and the spectrum remains unchanged. Once certain light path length is reached the reabsorption/reemission processes became important and the output spectra are broadened.

In Fig. 3d is represented the dependence on the pump intensity of the net gain coefficients and threshold lengths obtained with Eqs (1) and (2), respectively, from fits such as those presented in Fig. 3a. This plot gives the value of the threshold pump intensity for the onset of ASE using the objective criterion that defines the threshold intensity I_{th} for ASE as the pump intensity for which $g = 0$ [3]. Thus, from Fig. 3d it was obtained $I_{\mathrm{th}} \sim 81$ kW/cm^2, which is a value somewhat smaller than that estimated from Fig. 2 because it corresponds to the case in which $L_{\mathrm{th}} \to \infty$ [35], and represents the minimum pump intensity for which the ASE threshold can be reached. The plot in Fig. 3d also allows estimating the losses, because when $I_{\mathrm{p}} \to 0$ then $g \to -\alpha$, with α being the loss coefficient [3]. Thus, from Fig. 3d, a value of $\alpha \sim 12$ cm^{-1} was estimated.

3.1.2 *Non-resonant feedback lasing*

Trying to achieve laser emission rather than ASE, we followed the same approach than in a previous study [30], where incorporation of 8MMA-POSS nanoparticles (Fig. 4) in waveguides composed of poly(methyl methacrylate) (PMMA) doped with dye PM597 resulted in coherent random laser emission. In the present case we used 8OH-POSS (Fig. 4), which is a POSS compound

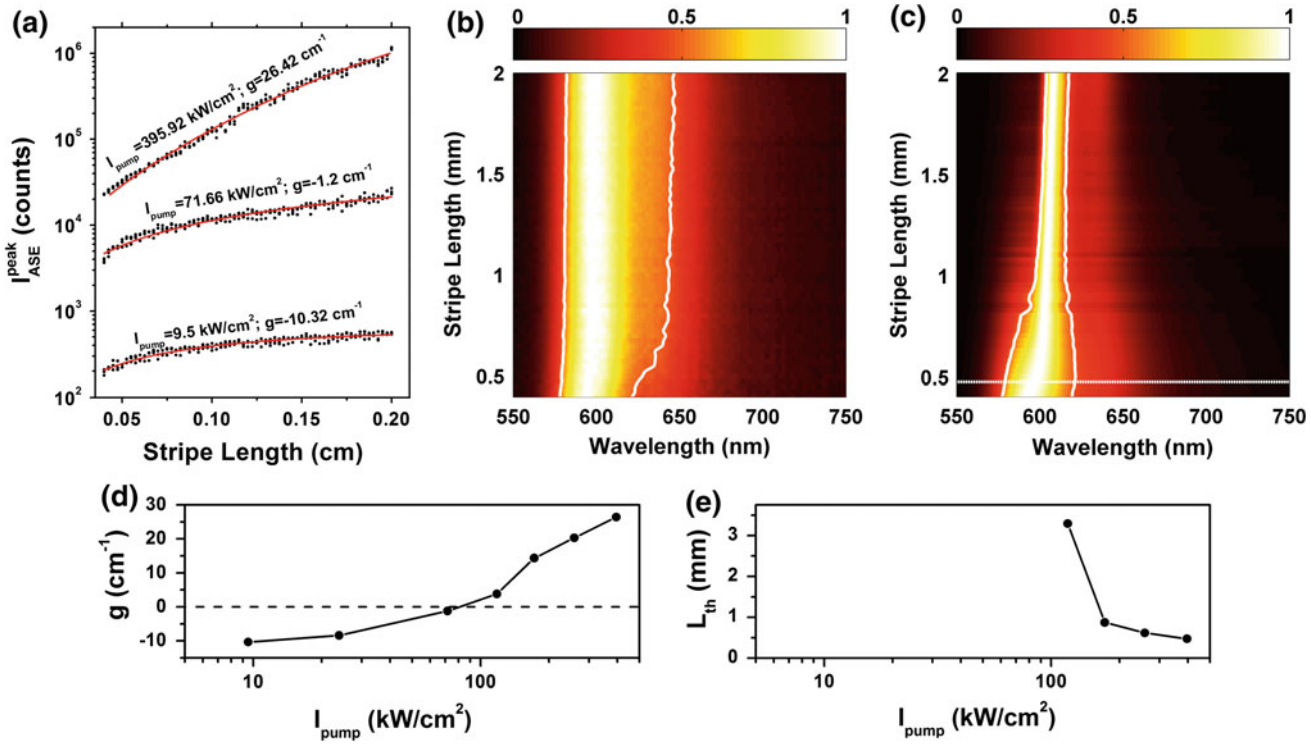

Fig. 3 ASE gain analysis in SRhB/pHEMA 9 μm thick waveguides: **a** ASE intensity at 609 nm as a function of stripe length for three representative pump intensities (well below threshold, near threshold and well below threshold). *Solid lines* are best fits of Eq. (1) to the experimental data. **b** Normalized ASE output spectra as a function of stripe length for $I_{pump} = 9.5$ kW/cm^2. **c** Normalized ASE output spectra as a function of stripe length for $I_{pump} = 396$ kW/cm^2. *Solid* and *dotted lines* represent the half maximum evolution (*FWHM*) and ASE threshold length, respectively. **d** Calculated ASE gain g and threshold length L_{th} at 609 nm as a function of pump intensity. The gain fit error ranges from 0.4 to 0.8 cm^{-1}, with a coefficient of determination R^2 from 0.91, for the lowest pump intensities (lower signal-to-noise ratio), to 0.99 for the highest intensities (higher signal-to-noise ratio)

soluble in polar solvents, chosen to match the polar nature of the polymer pHEMA used in the present studies. The waveguides first prepared for these studies were composed of SRhB-doped films of pHEMA/8OH-POSS, with 10 and 25 % weight proportion of 8OH-POSS nanoparticles, deposited onto quartz substrate and with thickness of 4.5 μm. This thickness for the films was chosen because in our previous study films with thickness of about 5 μm demonstrated to be a good compromise in order to obtain laser emission [30]. Films with 4.5 μm thickness with no 8OH-POSS in their composition were also prepared for comparison.

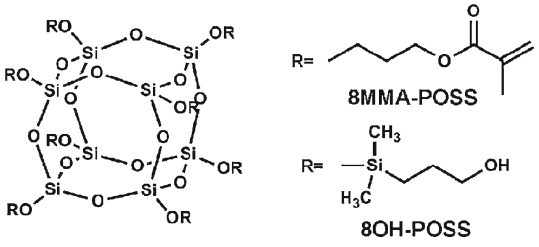

Fig. 4 Molecular structures of octa(propyl-methacryl)-POSS (8MMA-POSS) and octa(hydroxypropyldimethylsilyl)-POSS (8OH-POSS)

Figure 5a shows the normalized emission spectra for the 4.5 μm films with 0, 10 and 25 % of 8OH-POSS in weight under 490 kW/cm^2 pumping. The excitation region was a stripe of 2 mm length, obtained by selecting the central part of the Gaussian pump beam with the adjustable slit. The spectrum obtained with the 9 μm film used in the ASE studies under the same conditions is also included for comparison.

The stimulated emission threshold for the samples 9-μm thick without 8OH-PSS and 4.5 μm thick with 0, 10 and 25 % 8OH-PSS were 90, 60, 80 and 125 kW/cm^2, respectively. This indicates that at 490 kW/cm^2, the stimulated emission is fully established in all the samples and, consequently, the following spectral comparison is objective. It can be appreciated in Fig. 5a that the emission was quite similar for the 4.5 μm films with 10 and 0 % 8OH-POSS and for the 9 μm film with 0 % 8OH-POSS, consisting of a main ASE peak at 609 nm and a shoulder at around 635 nm. Nevertheless, the FWHM of the main peak was somewhat narrower for the sample with 8OH-POSS: 14 nm for the film with 10 % 8OH-POSS and 17 nm for

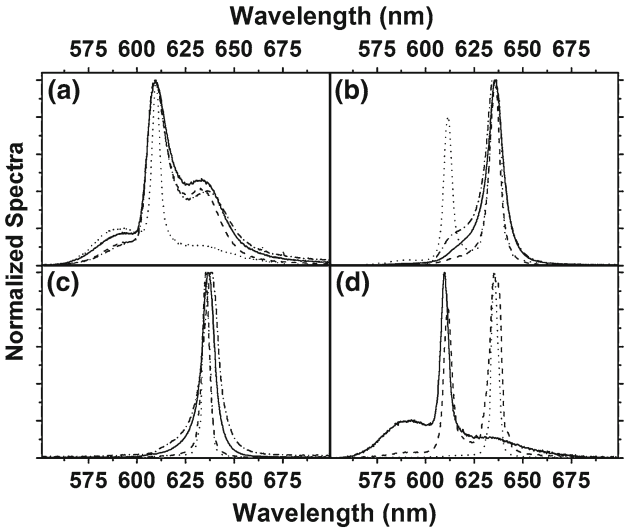

Fig. 5 Non-resonant feedback (NRF) laser measurements from SRhB/8OH-POSS/pHEMA 4.5 μm thick waveguides: output spectra for excitation stripes of **a** 2 mm, **b** 1 cm, and **c** 1.5 cm. *Solid*, *dashed* and *dotted lines* correspond to waveguides with 0, 10 and 25 % content of 8OHPOSS, respectively. *Dash-dotted line* corresponds to the 9-μm thick waveguide with 0 % wt. 8OH-POSS. **d** NRF laser output spectra from the 4.5-μm thick waveguide with 25 % wt. 8OH-POSS for excitation stripes of 2 mm (*solid line*), 1 cm (*dashed line*) and 1.5 cm (*dotted line*)

the film with no 8OH-POSS. When the proportion of 8OH-POSS in the 4.5 μm film was raised to 25 %, the shoulder at 635 nm disappeared and the main peak at 609 nm collapsed to a linewidth of just 5 nm. This collapse could be indicating a transition from ASE to broadband laser emission caused by non-resonant feedback (NRF) due to weak Rayleigh scattering induced by the 8OH-POSS nanoparticles [36].

As it was no possible to increase the proportion of 8OH-POSS in the samples (increasing the amount of 8OH-POSS above 25 % in weight resulted in the excess of 8OH-POSS being exuded from the sample), we tried increasing the length of the pumped region. Thus, we removed the slit and used two configurations: an excitation stripe of about 1 cm length and 150 μm width in the central region (with this central region placed just on the edge of the sample), and the same excitation stripe placed so that its central region was in the center of the sample, resulting in the whole 1.5 cm length of the sample being pumped. The results obtained in this approach are shown in Fig. 5b, c, respectively.

When the pumped region was 1 cm in length (Fig. 5b), the peak of the emission was shifted to 635 nm in the samples with no 8OH-POSS as well as in the sample with 10 % weight proportion of 8OH-POSS, with FWHM of 10 and 6 nm, respectively. When the 8OH-POSS proportion was increased to 25 %, simultaneous emission at 611 and 635 nm was obtained, with FWHM of 5 and 7 nm, respectively. Increasing the length of the pumped region to 1.5 cm resulted in single-peaked emission in all cases (Fig. 5c), centered at 635 nm and with the FWHM decreasing to 4 nm when there was 8OH-POSS in the sample and to 8 nm in the samples with no 8OH-POSS. The relative intensity of the two peaks at 611 and 635 nm, observed in the sample with 25 % 8OH-POSS when the pumped region was 1 cm in length, could be varied by decreasing or increasing the length of the pumped region: going to shorter pump lengths did result in an increase of the 611 nm peak and a decrease of the 635 nm peak; on the contrary, going to longer pump lengths resulted in a decrease of the 611 nm peak and an increase of the 635 nm, until the total disappearance of the first peak when the length of the pumped region reached 1.5 cm. It is worth noticing that collapsed bichromatic emission was only observed in the sample with 25 % 8OH-POSS. The sample with 10 % wt. proportion showed bichromatic emission, but being both bands very broad.

Bichromatic laser emission from dye solutions containing randomly distributed scattering particles has been observed [37] and explained in terms of the coexistence of monomers and dimers in the active media [38–40]. Under appropriate conditions, simultaneous lasing emission of monomers and dimers takes place, with monomers being responsible for the short-wavelength emission and dimers causing the long wavelength emission.

It is well known that for xanthene dyes aggregates are formed at concentrations greater than 10^{-4} M at room temperature [41, 42]. In the present studies we are using dye concentrations of 10^{-2} M and, thus, we are well in the dye concentration region where aggregates form. As the monomer emission partially overlaps the dimer absorption band [38], there is energy transfer from monomers to dimers. In these conditions, the appearance or not in the lasing spectrum of both emission peaks depends on the amount of scatterers in the medium as well as on the optical path followed by the photons inside the sample. When there is no 8OH-POSS at all, the bands corresponding to monomers and dimers are quite broad do to the limited gain, and so it is quite difficult to resolve both bands simultaneously. As the 8OH-POSS content is increased the scattering level increases, which enhances the amplification process and so both bands are more collapsed [36]. This way, the monomer and dimer bands are better distinguished. In the sample with the highest load of nanoparticles (25 %), the collapse is maximum, and so both bands are more easily resolved. On the other hand, the larger the optical path the more the emission from the monomers is absorbed by the dimers, which leads to activation of the dimers laser action. Figure 5d, in which the normalized spectra obtained with the sample with 25 % 8OH-POSS at the different pump lengths are shown, is

particularly useful to understand the behavior of the samples. When the whole length of the sample (1.5 cm) is pumped, most of the excitation ends in the dimers, which results in laser action only at the long wavelength characteristic of the emission from the dimers. When the pumped region is shortened to 1 cm, not all the emission from the monomers is absorbed by the dimers, and two peaks are observed, the short-wavelength one due to the monomers, and the long wavelength one from the dimers. When the length of the pumped region is shortened more, to 2 mm, there is no enough excitation transferred to the dimers, and the short-wavelength emission from the monomers dominates. This is a clear indication that the energy transfer from monomer to dimer is mainly radiative.

3.1.3 Random lasing

In the measurements reported above, we observed spectral collapse when there was 8OH-POSS in the material, which indicated the onset of NRF lasing. What we did not observe was coherent random lasing (RL), characterized by multimode emission with narrow peaks on top of a globally narrowed ASE spectrum [30]. As we had already seen that decreasing the thickness of the film lowers the threshold for ASE and increases the gain [3], we decided to prepare films with 1 μm thickness and a 25 % content in weight of 8OH-POSS. Films with the same thickness but without 8OH-POSS were also prepared for comparison.

Figure 6a shows the normalized emission spectra of 1-μm thick samples with and without 8OH-POSS, pumped at 380 kW/cm^2 and an excitation stripe of 2 mm. While the emission from the sample with no 8OH-POSS is just ASE, the emission from the sample with 25 % 8OH-POSS exhibited a narrower ASE with very narrow peaks on top of it, with a linewidth smaller than 0.3 nm, close to the resolution of our detection system (0.1 nm). In other words, the sample with 8OH-POSS presented coherent RL emission. It is worth noticing that some peaks timidly appeared in the ASE spectrum of the sample without 8OH-POSS. These components could be ascribed to roughness in the sample surface which could cause some random lasing by themselves. In fact, coherent RL due to naturally occurring resonators from planar waveguides with granular surfaces has been already demonstrated [43].

In Fig. 6b it is represented the dependence of the output intensity integrated over the whole spectrum with the pump intensity for samples with and without 8OH-POSS. The estimated thresholds were 50 and 35 kW/cm^2 for the samples with and without 8OH-POSS. The output spectra for the sample without 8OH-POSS remained smooth irrespective of the pump intensity (Fig. 6c), whereas in the sample with 8OH-POSS, narrow peaks superposed onto the

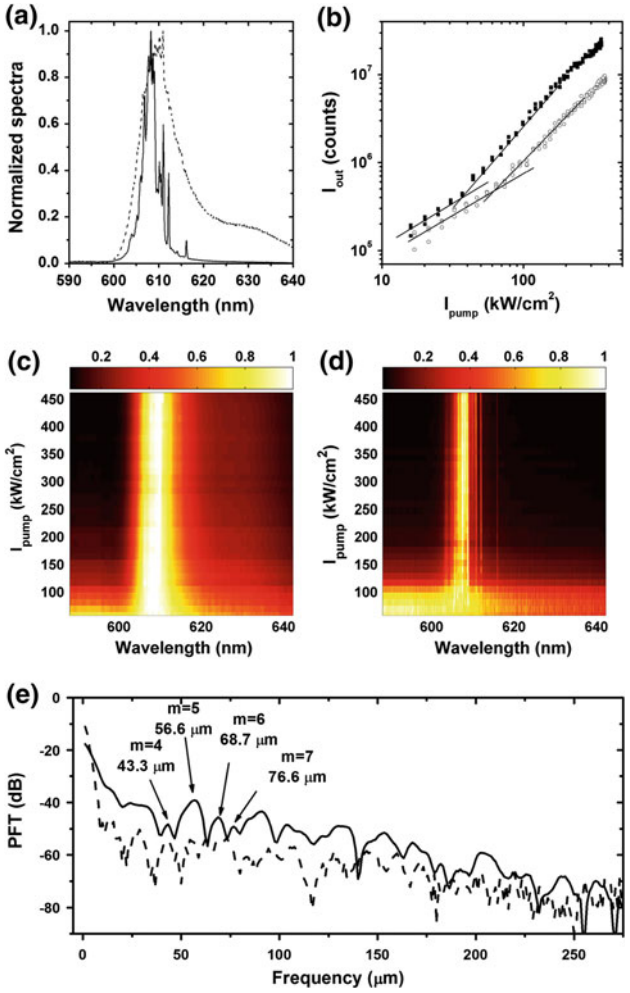

Fig. 6 ASE (0 % 8OH-POSS) and RL (25 % 8OH-POSS) measurements from SRhB/8OH-POSS/pHEMA 1 μm thick waveguides: **a** normalized RL (*solid line*) and ASE (*dashed line*) output spectra at $I_{pump} = 380$ kW/cm^2. **b** ASE (*solid squares*) and RL (*open circles*) output intensity (integrated over all wavelengths) as a function of pump intensity. *Solid lines* are a guide to the eye. **c** Normalized ASE output spectra as a function of pump intensity. **d** Normalized RL output spectra as a function of pump intensity. **e** Power Fourier Transform (PFT) in decibels of RL (*solid line*) and ASE (*dashed line*) spectra shown in **a**

ASE were always seen for pumping intensities above threshold (Fig. 6d).

It is possible to gain insight into the excited random cavities by calculating the PFT of the emission spectra. As it is well known, the PFT of the emission spectrum (in $k = 2\pi/\lambda$ space) from a well-defined laser cavity exhibits peaks at Fourier components with frequency $p_m = mL_C n/\pi$, where m is the order of the Fourier harmonic, L_C the cavity path length, and n is the refractive index of the gain medium [44]. Figure 6e shows the calculated PFT spectra of the emission spectra shown in Fig. 6a. It can be appreciated that in the PFT of the emission spectrum of the

sample without 8OH-POSS there are some Fourier components, corresponding to the peaks that timidly appear in the ASE spectrum (Fig. 6a). On the other hand, in the PFT of the sample with 8OH-POSS the Fourier components are much more pronounced and defined. Due to the presence of some residual noise, the Fourier components corresponding to $m = 1$, 2, and 3 were not very well resolved. Thus, we made use of the higher orders, $m = 4$–7, to calculate the cavity path length, which resulted to be $L_C \sim 23$ μm. This path length is much longer than the waveguide thickness, meaning that, as expected, the feedback is taking place in the waveguide plane.

To assess whether the peaks that timidly appear in the ASE spectrum were due to surface roughness and to find out whether the RL emission in the sample with 8OH-POSS had the same origin, we performed an AFM analysis (Fig. 7) of the sample surfaces. As it is clearly evident from Fig. 7a, b, which show the topography of the samples with and without 8OH-POSS, the roughness of the surfaces was highly affected by the addition of 8OH-POSS. The sample with neat pHEMA (Fig. 7a) presented a quite smooth surface, with an average grain height of 3.2 nm and standard deviation $\sigma = 0.4$ nm, whereas the topography of the sample with 8OH-POSS showed a much rougher surface (Fig. 7b) with island type nanostructures, with average height of 5 nm and standard deviation $\sigma = 1.5$ nm, as can be seen in the height histograms of Fig. 7c. The phase image of the sample with only pHEMA (not shown) revealed a single domain, as expected for a neat material. Nevertheless, the phase image of the sample with 8OH-POSS (Fig. 7d) shows a clear superficial phase separation. When comparing the topography in 2D (Fig. 7e) with the phase image (Fig. 7d) in this sample, a clear correlation between the topography white regions (island structures) and phase image dark regions could be observed. On the other hand, as seen in Fig. 7d, the proportion of material corresponding to the dark regions was higher than the material corresponding to the clear ones. Taking into account that pHEMA is in a higher proportion than 8OH-POSS (75/25), the dark regions in the phase image and, consequently, the island nanostructures in the surface corresponded to pHEMA. The phase separation may have the origin in the different solvent solubilities of pHEMA and 8OH-POSS. In this case pHEMA would have a higher solubility in ethanol than 8OH-POSS and, then, 8OH-POSS would be more quickly depleted from the solvent, whereas pHEMA would tend to stay longer in the liquid phase, thus giving place to the granular surface structure.

With this analysis we concluded that the RL emission in the samples with 8OH-POSS originates due to the scattering induced by the high surface roughness coming from the pHEMA/8OH-POSS phase separation. As illustrated in Fig. 1, the waveguiding structure confines and guides the

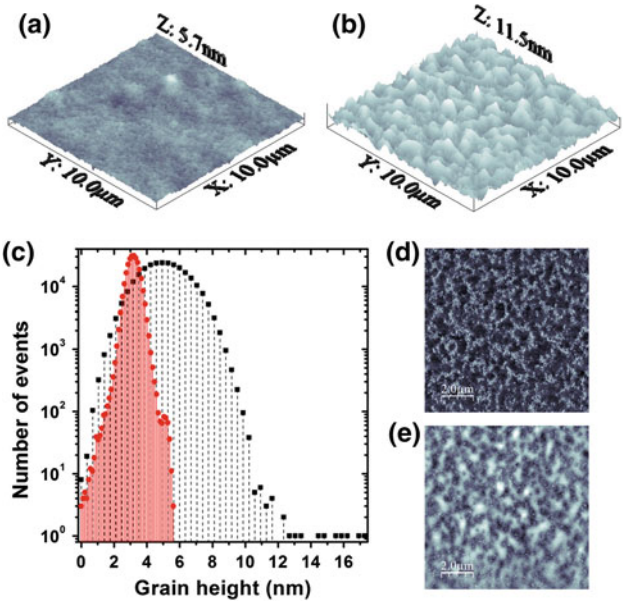

Fig. 7 Tapping mode AFM surface analysis of 8OH-POSS/pHEMA 1 μm thick waveguides: topography images (3D-view, 10 μm × 10 μm) of samples without (**a**) and with (**b**) 8OH-POSS (25 %). **c** Grain height histogram of images **a** (*circles*) and **b** (*squares*). Phase (**d**) and topography (**e**) images (*top view* 10 μm × 10 μm) of the sample with 25 % wt. 8OH-POSS

light, and RL emission is obtained due to scattering feedback in the direction defined by the pumping stripe, and consists of overlapped RL and waveguide modes [45, 46]. Given the excitation region dimensions, 2 mm × 150 μm × 1 μm, many modes may exist but, even so, there are distinguishable modes that emerge in the RL spectra. In fact, RL from planar waveguides with granular surface due to solvent evaporation phase separation of the dye-doped polystyrene/poly-methylmethacrylate blend has been recently reported [47].

The increase in the emission threshold intensity when adding scattering with respect to the case without scattering (Fig. 6b) has been observed before in thin films based on conjugated polymers containing TiO_2 nanoparticles [43] and has been explained in terms of an increase disorder (losses). In addition, the surface roughness present in our samples outcouples the laser light out of the excitation region, and supposes an additional contribution to these losses, which in turn increases the laser threshold further. This could explain as well, to some extent, the differences in the overall output emission intensity observed in Fig. 6b.

From a practical point of view, an important parameter in the behavior of the waveguides is the stability of the emission under long time operation, which implies high resistance to dye degradation under repeated pumping. It is worth noticing that, as far as we know, no photostability measurements have been performed on SRhB-doped waveguides so far. We assessed this stability by pumping

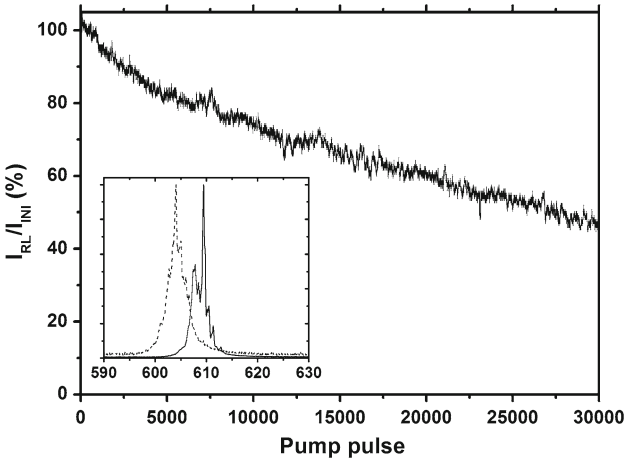

Fig. 8 RL photostability measurement: evolution of the RL emission normalized to the first shot intensity as a function of the number of pump pulses in the same position from SRhB/25 % wt. 8OH-POSS/pHEMA 1 μm thick waveguide. Pump intensity and repetition rate were 550 kW cm^{-2} and 15 Hz, respectively. *Inset*: RL spectra of first (*solid line*) and last (*dashed line*) emission pulses

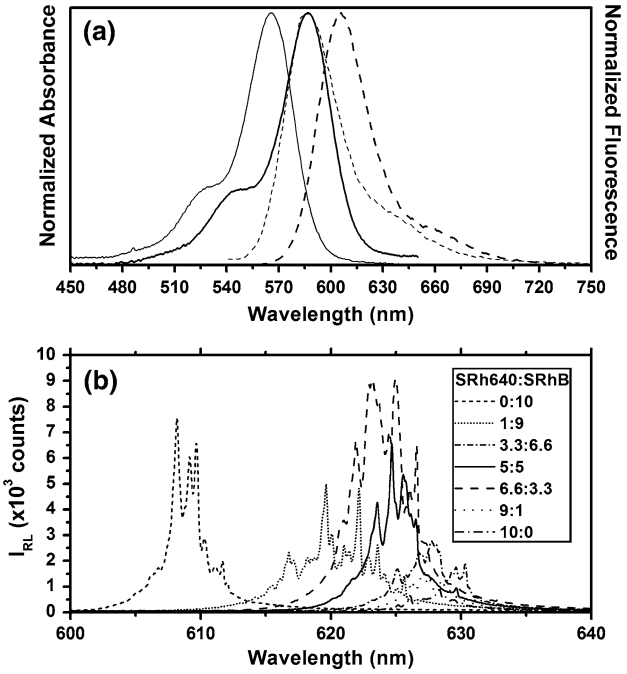

Fig. 9 **a** SRhB (*thin lines*)/SRh640 (*thick lines*) spectral overlap. Absorbance in solid lines and fluorescence ($\lambda_{ex} = 532$ nm) in *dashed lines*. **b** RL spectra at $I_{pump} = 380$ kW/cm^2 from SRhB + SRh640/25 % wt. 8OH-POSS/pHEMA 1 μm thick waveguides as a function of donor(SRhB)/acceptor(SRh640) molar ratio

the samples at a fixed position in very demanding conditions: the pump intensity was 550 kW/cm^2 (ten times over RL threshold) and the repetition rate was 15 Hz. The actual evolution of the emission from 1 μm films with 25 % in weight of 8OH-POSS is presented in Fig. 8. It was observed that in the films exhibiting RL emission the output decreased to 50 % of the initial intensity after 24,000 pump pulses (27 min) and that after 30,000 pump pulses (33 min) it remained at 41 % of its initial value. In addition to the reduction in the output intensity, the emission spectrum (inset Fig. 8) was progressively blue shifted as dye photodegradation was running up, since the disappearance of dye molecules reduces the reabsorption/reemission processes, responsible of the red shift observed in the initial spectra. Furthermore, the RL peaks were less prominent for the last spectra than for the initial ones, since the overall efficiency is lowered due to photodegradation.

3.2 Sulforhodamine 640-doped waveguides

3.2.1 Amplified spontaneous emission

With the aim to extend the emission to longer wavelengths, we also prepared waveguides based on dye SRh640, which were characterized following the same procedures described above for SRhB. At the optimum dye concentration of 1×10^{-2} M, ASE centered at 631 nm with FWHM of 14 nm was obtained from 9-μm thick films pumped above threshold. From plots similar to those presented in Figs. 2 and 3 for SRhB (see Figs. SI to SII), and using the same arguments and reasoning than when discussing the results obtained with waveguides based on SRhB, we determined a threshold for the onset of ASE of 106 kW/cm^2, net gain coefficient of 14.2 cm^{-1} at the pump intensity of 396 kW/cm^2, and estimated loss coefficient $\alpha = 17$ cm^{-1}.

3.2.2 Random lasing

Following the same approach than with dye SRhB, we investigated RL emission in waveguides based on SRh640 by preparing films with 1-μm thickness and a 25 % content in weight of 8OH-POSS. When these films were pumped at 532 nm, with an excitation stripe of 2 mm length, RL was equally excited, but the emission was clearly weaker than that obtained with SRhB, due to the lower absorption of SRh640 at 532 nm (Fig. SIII). To overcome this problem, we made use of the perfect overlap of the emission spectrum of SRhB and absorption spectrum of SRh640 (Fig. 9a), and prepared samples containing mixtures of SRhB and SRh640. Thus, the pump radiation absorbed by SRhB was transferred via Förster resonance energy transfer (FRET) and/or via radiative energy transfer (RET) [48] to the acceptor SRh640 molecules. In Fig. 9b, the emission from 1-μm thin films with mixtures of SRhB and SRh640 in different proportions is presented. It is seen that the presence of just 10 % of SRh640 inhibited completely the emission from SRhB, indicating a complete transfer of energy from SRhB to SRh640. Increasing the amount of

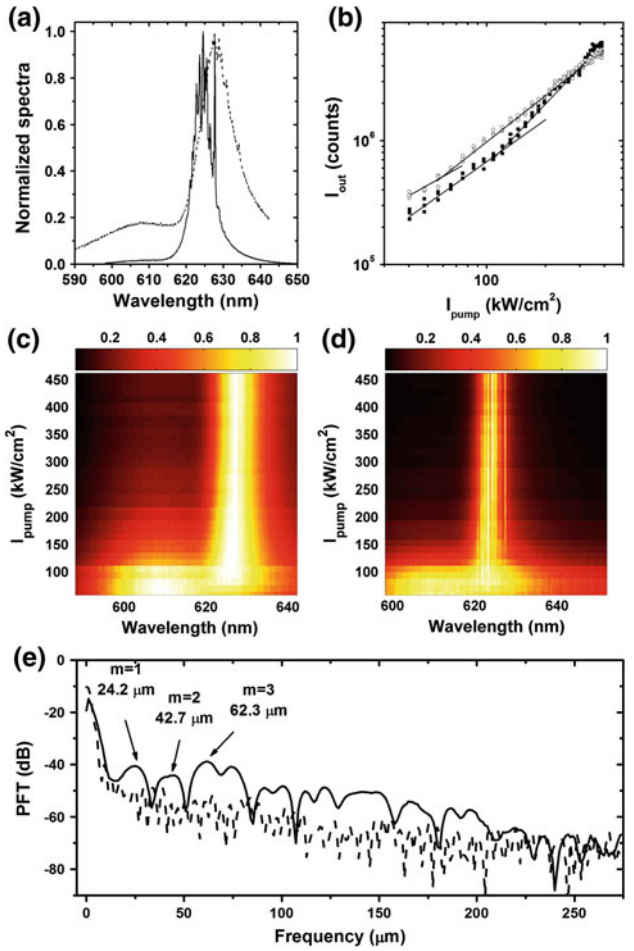

Fig. 10 ASE (0 % 8OH-POSS) and RL (25 % 8OH-POSS) measurements from SRh640/8OH-POSS/pHEMA 1 μm thick waveguides: **a** normalized RL (*solid line*) and ASE (*dashed line*) output spectra at $I_{pump} = 380$ kW/cm^2. **b** ASE (*solid squares*) and RL (*open circles*) output intensity (integrated over all wavelengths) as a function of pump intensity. *Solid lines* are a guide to the eye. **c** Normalized ASE output spectra as a function of pump intensity. **d** Normalized RL output spectra as a function of pump intensity. **e** Power Fourier Transform (PFT) in decibels of RL (*solid line*) and ASE (*dashed line*) spectra shown in **a**

SRh640 in the mixture shifts the emission to the red due to reabsorption/reemission effects from the acceptor. The highest collapse in the FWHM of the emission was obtained with a mixture of SRhB/SRh640 in proportion 1:1, and this was the composition that we used in our study. Films with SRhB/SRh640 in proportion 1:1 but without 8OH-POSS in their composition were also prepared for comparison.

Figure 10a shows the normalized emission spectra of 1-μm thick samples, with and without 8OH-POSS, pumped at 380 kW/cm^2 and an excitation stripe of 2 mm. The behavior is similar to that observed with SRhB; the sample with 25 % 8OH-POSS exhibited a narrower ASE with superposed peaks with linewidth 0.3 nm. Interestingly, the ASE spectrum of the sample without 8OH-POSS presented residual emission close to 610 nm coming from SRhB even at the highest pump intensities, whereas the spectrum of the sample with 8OH-POSS showed no evidence of SRhB emission, meaning that the energy transfer is complete when RL emission takes place. In addition, this indicates that the FRET process is not strong enough as to provide the complete energy transfer, and that both FRET and RET are taking place in this particular system.

In Fig. 10b, the dependence of the output intensity integrated over the whole spectrum with the pump intensity for samples with and without 8OH-POSS is represented. The estimated thresholds were now slightly higher than those obtained with SRhB: 60 kW/cm^2 in the sample with no 8OH-POSS, and 70 kW/cm^2 when the sample contains 25 % in weight of 8OH-POSS. Again, the output spectra for the sample without 8OH-POSS remained smooth irrespective of the pump intensity (Fig. 10c), whereas in the sample with 8OH-POSS, narrow peaks superposed onto the ASE were always seen for pumping intensities above threshold (Fig. 10d). It is worth noticing that both samples presented residual emission from SRhB at low pump intensities (Fig. 10c, d) but, unlike in the sample without 8OH-POSS, when the RL emission threshold was reached all the emission from the SRhB was transferred to SRh640, as was previously stated. Once again this is an indicative of the presence of both FRET and RET in this waveguides.

The PFT of the emission spectra in Fig. 10a is shown in Fig. 10e. In this case, the Fourier components were better resolved than in the case of the SRhB-doped samples, and we could use the lower orders $m = 1$–3 to calculate the cavity path length, which in this case resulted to be $L_C = 44$ μm, near the double than in the samples with SRhB. This difference in the path length could be ascribed to differences in the sample roughness, which changes along the sample and from sample to sample, and to the fact that the resonant conditions depend on the spectral range, which is different in SRhB and SRh640.

Finally, the photostability of this sample was similar to that obtained with SRhB in analogous pumping conditions (see Fig. SIV); in the films with 8OH-POSS, exhibiting RL, the output emission decreased by 50 % of the initial value after 25,400 pump pulses (28 min) at 15 Hz repetition rate at pump intensity of 550 kW/cm^2 (eight times over RL threshold), and it remained at 45 % of the initial value after 30,000 pump pulses (33 min). It is worth noticing that the addition of SRhB as a donor increases significantly the photostability of the sample with SRh640, since it has been shown that SRh640 is intrinsically less photostable that SRhB in solid matrices [27], fact that is not obvious in these results. To conclude, the final spectra were as well blue shifted, slightly broader and with RL peaks less prominent than in the initial spectra, all of which is due to

the reduction in efficiency and reabsorption/reemission processes. As in the case of SRhB, as far as we know, no photostability measurements have been performed on SRh640-doped waveguides so far.

4 Summary and conclusion

Here, we present RL emission from asymmetric slab optical waveguides based on red-emitting organic dyes incorporated into polymer films deposited onto quartz substrates. A systematic study of the ASE properties helps select the material composition and experimental conditions needed to optimize the RL emission. Using the VSL method, where the intensity of the light emitted from the edge of the film is registered as a function of the excitation length at different pump intensities and the experimental points are fitted with appropriate theoretical expression, net gain coefficients could be obtained and loss coefficients and pump threshold for the onset of ASE could be estimated. In films with 9-μm thickness, pHEMA films doped with SRhB rendered emission at 609 nm with ASE threshold of 81 kW/cm^2, loss coefficient of 12 cm^{-1} and net gain coefficients of up to 26.4 cm^{-1} for pumping at 396 kW/cm^2. SRh640 rendered emission at 631 nm with ASE threshold of 106 kW/cm^2, loss coefficient of 17 cm^{-1} and net gain coefficients of up to 14.2 cm^{-1} for pumping at 396 kW/cm^2.

Addition of 8OH-POSS nanoparticles to the polymeric medium resulted in narrowing of the FWHM of the ASE emission. Upon pumping 4.5-μm thick films of SRhB/pHEMA at 490 kW/cm^2, the ASE FWHM collapsed from 17 to 5 nm when the proportion of 8OH-POSS in weight in the film was 25 %, indicating the transition from ASE to broadband laser emission caused by non-resonant feedback (NRF) due to weak Rayleigh scattering induced by the 8OH-POSS nanoparticles. In these conditions, lengthening the pumping stripe from 2 to 10 mm resulted in simultaneous NRF laser emission at 611 and 635 nm. Further increase in length of the pumped region results in a progressive disappearance of the shorter wavelength peak so that at a pumped length of 15 mm only emission at 635 nm remained. The shorter wavelength peak of this bichromatic emission is ascribed to SRhB monomer emission, while dimers are responsible for the emission of the 635 nm peak.

By reducing the thickness of the films to 1 μm, the presence of 8OH-POSS in the material gave place to the apparition of very narrow peaks, with linewidth smaller than 0.3 nm, on top of a globally narrowed ASE spectrum, which is a signature of coherent RL. With the help of an AFM analysis we concluded that this RL emission originates due to the scattering induced by the high surface roughness coming from the pHEMA/8OH-POSS phase separation. By calculating the PFT of the emission spectra the path length of these cavities L_C was estimated to be $L_C = 23$ μm when the dye was SRhB and $L_C = 44$ μm when the active medium was a mixture 1:1 of SRhB and SRh640. In both cases, the path length was much longer than the waveguide thickness, meaning that, as expected, the feedback is taking place in the waveguide plane.

Finally, we have measured for the first time the photostability of SRhB and SRh640 in polymer waveguides, obtaining a good photostability for both dyes under very demanding pump conditions (about ten times over RL threshold, and 15 Hz repetition rate), with the emission remaining at 50 % of the initial output after about 25,000 pump pulses ($\sim$28 min) in the same position of the sample.

The reported results demonstrate that it is possible to get efficient, photostable, and narrowband laser emission from dye-doped thin films in the wavelength region over 600 nm by incorporating in the polymeric material appropriate nanoparticles which induce structural changes.

Acknowledgments This work was supported by Projects MAT2010-20646-C04-01 and TRACE2009-0144 of the Spanish Ministerio de Economía y Competitividad (MINECO). L.C. thanks MINECO for a predoctoral scholarship (FPI, cofinanced by Fondo Social Europeo). The authors thank A. Cuesta (IQFR-CSIC) for conducting the AFM measurement. L.C. thanks V. Martín (IQFR) for fruitful discussion on phase separation.

References

1. S. Chénais, S. Forget, Polym. Int. **61**, 390 (2012). doi: 10.1002/pi.3173
2. A. Costela, O. García, L. Cerdán, I. García-Moreno, R. Sastre, Opt. Express **16**, 7023 (2008)
3. L. Cerdán, A. Costela, I. García-Moreno, O. García, R. Sastre, Appl. Phys. B **97**, 73 (2009)
4. L. Cerdan, A. Costela, I. García-Moreno, O. García, R. Sastre, M. Calle, D. Muñoz, J. de Abajo, Macromol. Chem. Phys. **210**, 1624 (2009)
5. A. Costela, I. García-Moreno, R. Sastre, in *Solid-State Dye Lasers*, ed. by F.J. Duarte. Tunable laser applications, 2nd edn. (CRC Press, Boca Raton, 2009)
6. A.V. Deshpande, E.B. Namdas, J. Lumin. **91**, 25 (2000)
7. S.S. Yap, T.T. Tou, S.W. Ng, Jpn. J. Appl. Phys. **39**, 5855 (2000)
8. Y. Kawabe, L. Wang, T. Nakamura, N. Ogata, Appl. Phys. Lett. **81**, 1372 (2002)
9. Y. Huang, S.-T. Wu, Opt. Express **18**, 27697 (2011)
10. H. Manaa, S.M. Al-Alawi, J. Lumin. **94–95**, 55 (2001)
11. M.A. Reilly, B. Coleman, E.Y.B. Pun, R.V. Penty, I.H. White, M. Ramon, R. Xia, D.D.C. Bradley, Appl. Phys. Lett. **87**, 231116 (2005)
12. H. Goudket, T.H. Nhung, B. Ea-Kim, G. Roger, M. Canva, Appl. Opt. **45**, 7736 (2006)
13. D. Pisignano, E. Mele, L. Persano, A. Athanassiou, C. Fotakis, R. Cingolani, J. Phys. Chem. B **110**, 4506 (2006)
14. D. Zhang, D. Ma, Appl. Opt. **46**, 2996 (2007)

15. D. Zhang, Z. Deng, Q. Wang, B. Li, S. Chen, Y. Wang, Y. Liu, D. Ma, Appl. Opt. **49**, 315 (2010)
16. M. Leonetti, R. Sapienza, M. Ibisate, C. Conti, C. López, Opt. Lett. **34**, 3764 (2009)
17. L. Sznitko, J. Mysliwiec, P. Karpinsky, K. Palewska, K. Parafiniuk, S. Bartkiewicz, I. Rau, F. Kajzar, A. Miniewicz, Appl. Phys. Lett. **99**, 031107 (2011)
18. W.J. Wadsworth, I.T. McKinnie, A.D. Woolhouse, T.G. Haskell, Appl. Phys. B **69**, 163 (1999)
19. T. Voss, D. Scheel, W. Schade, Appl. Phys B **73**, 105 (2001)
20. K. Yamashita, N. Takeuchi, K. Oe, H. Yanagi, Opt. Lett. **35**, 2451 (2010)
21. N. Tsutsumi, M. Takeuchi, Opt. Commun. **281**, 2179 (2008)
22. J. Wang, H. Dong, J. Fan, R. Li, L. Zhang, K.Y. Wong, Appl. Opt. **50**, 6248 (2011)
23. Z. Yu, W. Li, J.A. Hagen, Y. Zhou, D. Klotzkin, J.G. Grote, A.J. Steckl, Appl. Opt. **46**, 1507 (2007)
24. Y. Kakegawa, Y. Kobayashi, S. Muto, Y. Kurokawa, Nippon Kagaku Kaishi **10**, 1257 (1992)
25. I. Finkelstein, S. Ruschin, Y. Sorek, R. Reisfeld, Opt. Mat. **7**, 9 (1997)
26. V. Martín, A. Costela, M. Pintado-Sierra, I. García-Moreno, J. Photochem. Photobiol. A Chem. **219**, 265 (2011)
27. I. García-Moreno, A. Costela, M. Pintado-Sierra, V. Martín, R. Sastre, J. Phys. Chem. B **113**, 10611 (2009)
28. A. Gómez-Hens, M.P. Aguilar-Caballos, Trends Anal. Chem. **23**, 127–136 (2004)
29. C. Vannahme, S. Klinkhammer, U. Lemmer, T. Mappes, Opt. Express **19**, 8179–8186 (2011)
30. L. Cerdán, A. Costela, I. García-Moreno, O. García, R. Sastre, Opt. Express **18**, 10247 (2010)
31. A. Costela, I. García-Moreno, L. Cerdán, V. Martín, O. García, R. Sastre, Adv. Mat. **21**, 4163 (2009)
32. C. Lowe, *Test Methods for UV and EB Curable systems* (Wiley, London, 1997)
33. R. Sastre, V. Martín, L. Garrido, J.L. Chiara, B. Trastoy, O. García, A. Costela, I. García-Moreno, Adv. Funct. Mat. **19**, 3307 (2009)
34. I. Horcas, R. Fernandez, J.M. Gomez-Rodriguez, J. Colchero, J. Gomez-Herrero, A.M. Baro, Rev. Sci. Instrum. **78**, 013705 (2007)
35. L. Cerdán, A. Costela, I. García-Moreno, J. Opt. Soc. Am. B **27**, 1874 (2010)
36. L. Cerdán, A. Costela, I. García-Moreno, V. Martín, M.E. Pérez-Ojeda, IEEE J. Quant. Electron. **47**, 907 (2011)
37. R.M. Balachandran, N.M. Lawandy, Opt. Lett. **21**, 1603 (1996)
38. P. Vaveliuk, A.M. de Brito Silva, P.C. de Oliveira, Phys. Rev. A **68**, 013805 (2003)
39. W.L. Sha, C.-H. Liu, F. Liu, R.R. Alfano, Opt. Lett. **21**, 1277 (1996)
40. C. Tolentino Domínguez, E. de Lima, P.C. de Oliveira, F. López Arbeloa, Chem. Phys. Lett. **464**, 245 (2008)
41. O. Valdés-Aguilera, D.C. Neckers, Acc. Chem. Res. **22**, 171 (1989)
42. F. López Arbeloa, Y. Rodrígues Liebana, E. Cordero Fernández, I. López Arbeloa, Spectrochim. Acta Part A **45**, 1201 (1989)
43. A. Tulek, R.C. Polson, Z.V. Vardeny, Nat. Phys. **6**, 303 (2010)
44. R.C. Polson, G. Levina, Z.V. Vardeny, Appl. Phys. Lett. **76**, 3858 (2000)
45. Q. Song, L. Liu, S. Xiao, X. Zhou, W. Wang, L. Xu, Phys. Rev. Lett. **96**, 033902 (2006)
46. S. Kéna-Cohen, P.N. Stavrinou, D.D.C. Bradley, S.A. Maier, Appl. Phys. Lett. **99**, 041114 (2011)
47. X. Zhao, Z. Wu, S. Ning, S. Liang, D. Wang, X. Hou, Opt. Express **19**, 16126 (2011)
48. B. Valeur, *Molecular Fluorescence* (Wiley, Weinheim, 2001)

Supporting information to:

Random lasing from sulforhodamine dye doped polymer films with high surface roughness

Luis Cerdán,* Angel Costela, Gonzalo Durán-Sampedro,

and Inmaculada García-Moreno

Instituto de Química Física "Rocasolano" (CSIC), Serrano 119, 28006 Madrid, Spain

*lcerdan@iqfr.csic.es

Complementary figures:

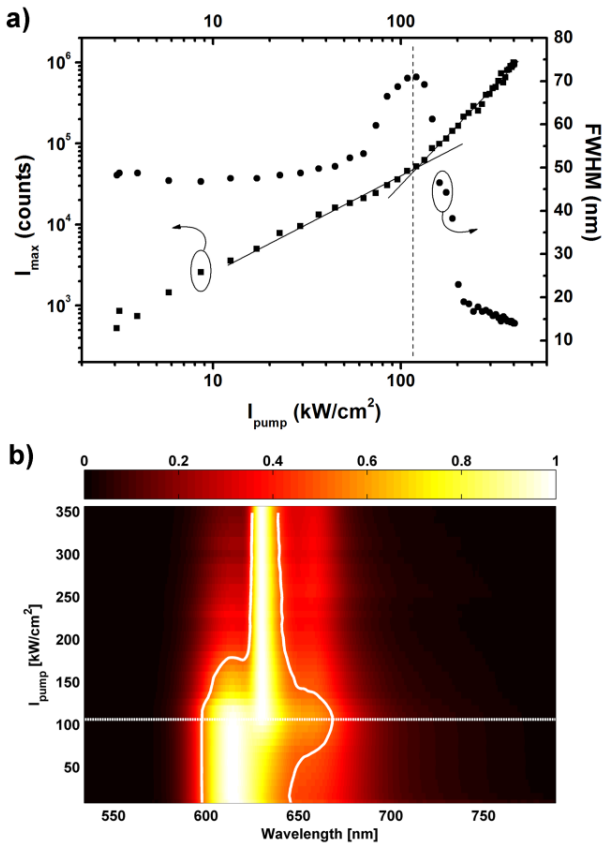

Fig. SI ASE measurements from SRh640/pHEMA 9 µm thick waveguides: a) Peak intensity (squares) and FWHM (circles) as a function of pump intensity. Solid and dashed lines are a guide to the eye and ASE threshold marker, respectively. b) Normalized ASE output spectra as a function of pump intensity. Solid and dotted lines represent the half maximum evolution (FWHM) and ASE threshold, respectively.

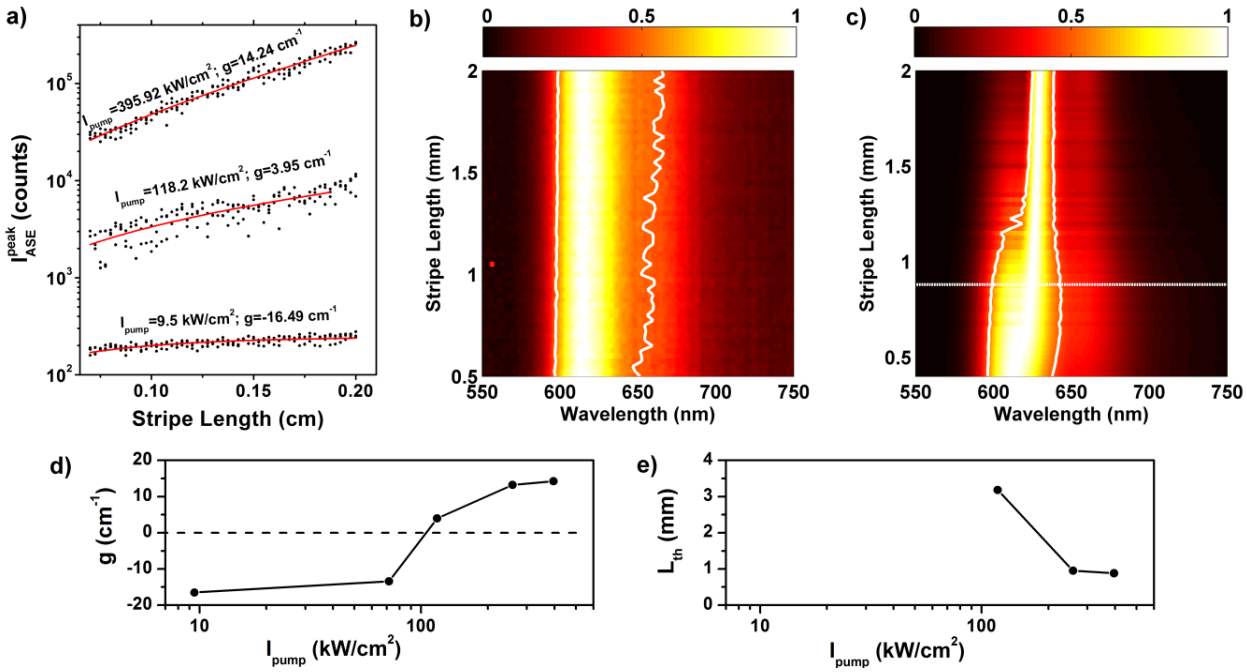

Fig. SII ASE gain analysis in SRh640/pHEMA 9 μm thick waveguides: a) ASE intensity at 631 nm as a function of stripe length for three representative pump intensities (well below threshold, near threshold and well below threshold). Solid lines are best fits of Eq. (1) to the experimental data. b) Normalized ASE output spectra as a function of stripe length for Ipump=9.5 kW/cm^2. c) Normalized ASE output spectra as a function of stripe length for Ipump=396 kW/cm^2. Solid and dotted lines represent the half maximum evolution (FWHM) and ASE threshold length, respectively. d) Calculated ASE gain *g* and threshold length L_{th} at 631 nm as a function of pump intensity.

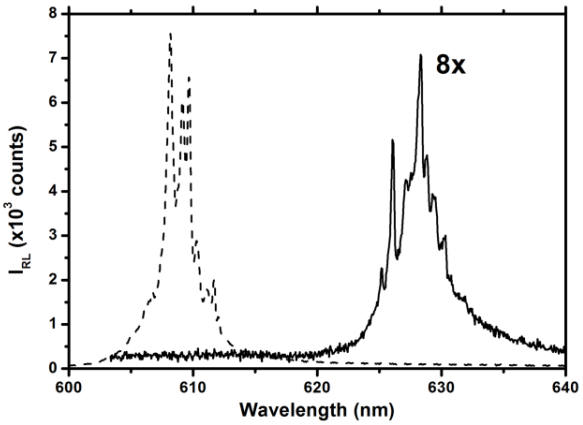

Fig. SIII a) Comparison between RL emission at I_{pump}=380 kW/cm^2 in SRhB/25% wt. 8OH-POSS/pHEMA (dashed line) and SRh640/25% wt. 8OH-POSS/pHEMA (solid line) 1 μm thick waveguides.

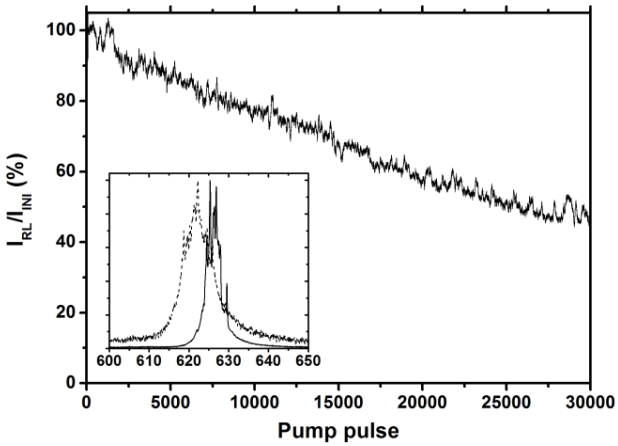

Fig. SIV RL Photostability measurement: Evolution of the RL emission normalized to the first shot intensity as a function of the number of pump pulses in the same position from SRh640/25% wt. 8OH-POSS/pHEMA 1 μm thick waveguide. Pump intensity and repetition rate were 550 kW cm^{-2} and 15 Hz, respectively. Inset: RL spectra of first (solid line) and last (dashed line) emission pulses.

Paper B8: Org. Electron. 13, 1463–1469 (2012)

Waveguided random lasing in red-emitting-dye-doped hybrid polymer thin films

L. Cerdán, A. Costela, and I. García-Moreno

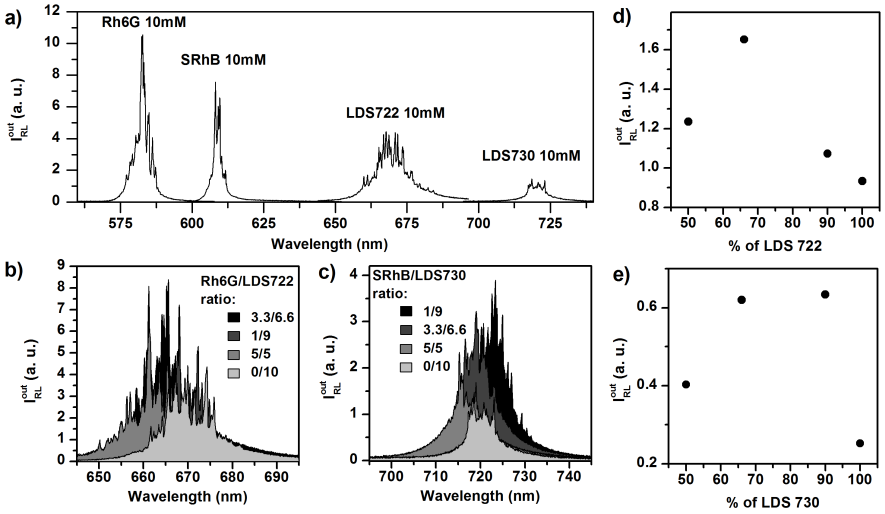

RL emission spectra from waveguides based on pHEMA/8OH-POSS(25 %) pumped at $I_{pump} = 380$ kW/cm^2: (a) doped with donor and acceptor dyes alone, (b) as a function of donor/acceptor molar ratio for the pair Rh6G/LDS722, and (c) as a function of donor/acceptor molar ratio for the pair SRhB/LDS730, (d) and (e) RL output intensity integrated over the whole spectral range as a function of percentage of LDS 722 and LDS 730, respectively.

Organic Electronics 13 (2012) 1463–1469

Contents lists available at SciVerse ScienceDirect

Organic Electronics

journal homepage: www.elsevier.com/locate/orgel

Waveguided random lasing in red-emitting-dye-doped organic–inorganic hybrid polymer thin films

Luis Cerdán *, Angel Costela, Inmaculada García-Moreno

Instituto de Química Física "Rocasolano" (CSIC), Serrano 119, 28006 Madrid, Spain

ARTICLE INFO

Article history:
Received 31 January 2012
Received in revised form 11 April 2012
Accepted 22 April 2012
Available online 5 May 2012

Keywords:
Hybrid polymer
Waveguides
Dye lasers
Energy transfer
Random lasing

ABSTRACT

Long-wavelength (660–740 nm) coherent random lasing (RL) in slab waveguides consisting of poly(2-hydroxyethyl methacrylate) (pHEMA) incorporating silsesquioxane nanoparticles (POSS) doped with the red-emitting dyes LDS722 and LDS730 is presented. Energy transfer from a donor dye is used to overcome the inherent low pump (532 nm) absorption of these dyes and to enhance the lasing efficiency of the samples. Rhodamine 6G is used as donor for LDS722 and Sulforhodamine B as donor for LDS730, in donor/acceptor molar proportions 3.3/6.6 and 1/9, respectively. RL emission spectral fingerprints and thresholds are studied in depth and insights into the RL characteristics are obtained from the Power Fourier Transforms of the emission spectra. Finally, photostabilities of LDS722 and, for the first time, of LDS730 doped into polymer slab waveguides are assessed.

1. Introduction

Over the last few years laser scientists have been exploring the development of wave guiding structures based on organic materials since they are promising candidates for future applications in integrated photonics [1–5]. These materials, either organic semiconductors or dye-doped polymers, exhibit wide wavelength tunability and high efficiency, which combined with their potentially very low cost makes them attractive candidates for their exploitation as compact and versatile laser systems.

Most of the work on organic thin film lasers has been carried out with dyes emitting in the green–yellow spectral region [1–5], and few results have been published on thin film devices emitting in the deep red part of the visible spectrum (660–740 nm), even though this spectral region is of interest in biophotonic applications. Leaving apart specifically synthesized dyes, commercial dyes such as Rhodamine 640 [6], Nile Blue [7] and Oxazine 725 [8] have been used as dopants for active polymer waveguides with emission in the red. Surprisingly, well known hemicyanine dyes, which emit in the deep red spectral region [9,10] and are characterized by very broad absorption and emission bands and huge Stokes shifts [11], have not received much attention in this context.

On the other hand, it has been demonstrated [12–14] that active waveguides with high surface roughness due to phase separation in polymer blends may sustain waveguided coherent random lasing (RL), paving the way to the development of integrated devices technologically and economically more favorable that the ones based on nanopatterning (distributed feedback, Bragg reflectors, etc.).

In previous papers [12,14] we demonstrated that the presence of nanometer-sized particles based on polyhedral oligomeric silsesquioxanes (POSS) in dye-doped polymer slab waveguides could result in coherent RL due to the scattering induced by the high surface roughness coming from the polymer/POSS phase separation obtained after solvent evaporation. With the aim to obtain RL emission into the red spectral edge (660–730 nm), in the present work we have followed the same approach than the one described in Ref. [14], but using this time the commercial

* Corresponding author. Tel.: +34 915619400; fax: +34 915642431.
E-mail addresses: lcerdan@iqfr.csic.es (L. Cerdán), acostela@iqfr.csic.es (A. Costela), iqrfm84@iqfr.csic.es (I. García-Moreno).

1566-1199/$ - see front matter © 2012 Elsevier B.V. All rights reserved.
http://dx.doi.org/10.1016/j.orgel.2012.04.017

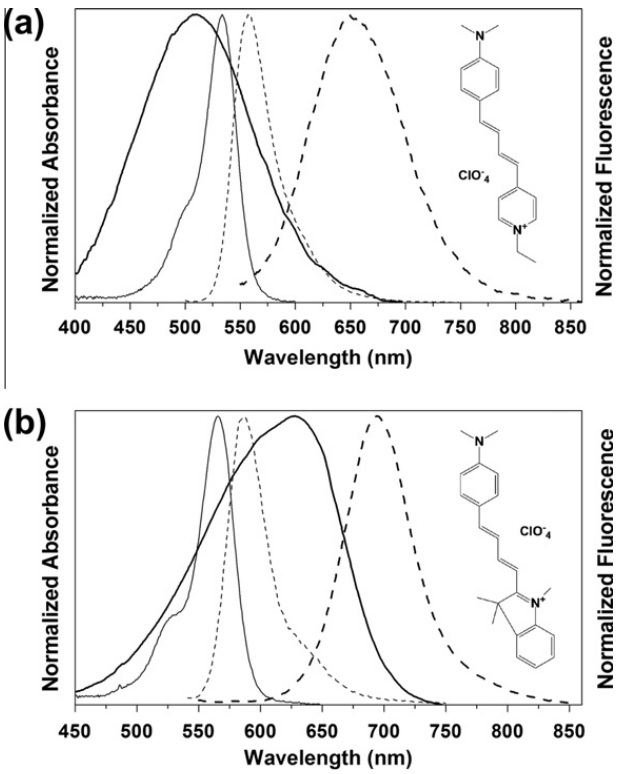

Fig. 1. Absorbance (solid lines) and fluorescence (dashed lines) spectral overlap of (a) Rh6G (thin lines)/LDS722 (thick lines) and (b) SRhB (thin lines)/LDS730 (thick lines), respectively. Insets show molecular structure of LDS722 and LDS730.

dyes LDS722 (also known as Pyridin 2) and LDS730 (also known as Styryl 6), which are charge transfer dyes belonging to the hemicyanine family with emission covering this spectral range (Fig. 1). It has been shown before [10,11] that LDS722 may sustain efficient and tunable DFB laser emission, but there are no reports of LDS730 being used in waveguide laser devices so far, which makes the results on LDS730 here presented a very novelty of the present work.

In this paper we report RL emission spectral fingerprints, thresholds and, for the first time, photostabilities from red-emitting dyes (LDS722 and LDS730) incorporated into asymmetric slab optical waveguides based on pHEMA/8OH-POSS (25%) polymer blends. An energy transfer approach is used to increase the final device efficiency. Insights into the RL characteristics are obtained from the Power Fourier Transforms of the emission spectra.

2. Materials and methods

Dyes LDS722 and LDS730 were laser grade and purchased from Exciton. Polymer poly(2-hydroxyethyl methacrylate) (pHEMA) and octa(hydroxypropyldimethylsilyl)-POSS (8OH-POSS), purchased from Aldrich, were used as received. The polymer chosen as dye host was pHEMA because the HEMA monomer mimics ethanol, which is a solvent in which hemicyanine dyes, due to their polar character, exhibited high lasing efficiency [11,15]. The POSS compound 8OH-POSS, which is soluble in polar solvents, was chosen to match the polar nature of pHEMA.

pHEMA (75 wt.%; 50 mg/mL), 8OH-POSS (25 wt.%; 16,7 mg/mL), and dye (10 mM with respect to the polymer) were added to ethanol and stirred for 24 h to fully solve dye and polymer. Increasing the amount of 8OH-POSS above 25% in weight resulted in the excess of 8OH-POSS being exuded from the sample. Films 1 m thick were obtained by spin coating (1000 rpm, 30 s) the polymer solution onto quartz substrates and left at room temperature for several minutes to remove the remaining solvent. We have found no way to measure directly the refractive index of the hybrid matrix since the film surface is rough and this leads to errors when using, for example, variable angle spectroscopic ellipsometry (VASE). We have estimated it taking into account that the refractive index of pHEMA is 1.51, and the one of 8OH-POSS is close to this value, as we have shown previously [16]. Then, the mixture of both must have a refractive index ~1.51. As this refractive index is higher than that of the quartz substrate ($n = 1.456$), the prepared samples defined asymmetric slab optical waveguides, where total internal refraction confines and guides the light along the film.

The absorbance and front face fluorescence spectra of the dye doped thin films were measured with a diode array spectrograph (Analytik Jena SPECORD 600) and a spectrofluorimeter (HORIBA Jobin Yvon Fluoromax-4), respectively.

The thin film samples were optically pumped at 532 nm with 20 ns full width at half maximum (FWHM) pulses from a frequency-doubled Q-switched Nd:YAG laser, operated at 15 Hz repetition rate. The pump radiation was vertically polarized, which allowed controlling the pulse energy incident on the sample by insertion into the pump beam path of a half-wave plate (HWP) and a linear polarizer (LP) set with its polarization axis vertical. By rotating the HWP the linear polarization of the input beam is rotated out of the vertical, and the pump beam is blocked more or less by the LP, depending on the rotation angle introduced by the HWP.

The light incident on the sample was perpendicular to the film surface and focused onto that surface in a stripe shape spot of ~150 microns width by a combination of negative and positive cylindrical quartz lenses ($f = -15$ and +15 cm, respectively), perpendicularly arranged. An adjustable slit was used to select only the central portion of the pump beam. Excitation stripes 2 mm long were defined, with an end placed right up to the edge of the film.

The RL emission was collected in the axis defined by the pumping stripe with a 5-cm focal length spherical lens, focused onto a fiber bundle and detected with a spectrograph/monochromator equipped with a thermoelectrically cooled CCD detector. Neutral density filters were used to avoid CCD detector saturation. The integration time in the CCD was set at 333 ms so that all the measurements were averaged over five pulses.

3. Results and discussion

We began the study by preparing samples doped with LDS722 (10 mM) alone and LDS730 (10 mM) alone. When these films were pumped at 380 kW/cm^2, RL was excited (Fig. 2a), but the emission was clearly weaker than that

obtained with sulforhodamines, partially due to the inherent lower efficiency and partially due to the lower absorption at 532 nm of LDS722 and LDS730 (Table 1). One approach to overcome the later is using mixtures of dyes in a system based on energy transfer, which is a physical phenomenon where excitation energy from an excited donor is radiatively (re-absorption/re-emission) and/or non-radiatively (Förster type via dipole–dipole coupling) transferred to a ground-state acceptor [20]. Thus, what is needed is a system consisting of two dyes, of which one (donor) should absorb efficiently the pump radiation at 532 nm and should be able to transfer the excitation energy to the second, low-absorbing long-wavelength emitting dye (acceptor). The energy transfer requires good overlap between donor emission and acceptor absorption bands, and depends strongly on the host medium and on the distance between donor and acceptor molecules. At the dye concentration used in this work (10 mM), the average intermolecular distance is approximately 7 nm, a value which is close to the typical Förster radius [20], meaning that the non-radiative transfer would be, a priori, efficient. Following this approach we tried Rhodamine 6G (Rh6G), Pyrromethene 567, Pyrromethene 597 and Sulforhodamine B (SRhB) as candidate donors for LDS722 and LDS730 due to the good overlap of their emission spectra with the absorption spectra of LDS722 and LDS730. We found that the best compromise between energy transfer and RL efficiency and photostability was obtained for the donor/acceptor pairs Rh6G/LDS722 and SRhB/LDS730. The good spectral overlap of the pairs Rh6G/LDS722 and SRhB/LDS730 can be appreciated in Fig. 1. The donor dyes by themselves exhibit good RL emission performance (efficiency and photostability, see Appendix A for Rh6G and Ref. [14] for SRhB) in their respective emission regions when placed alone into 8OH-POSS/pHEMA waveguides.

Table 1
Molar extinction coefficient at λ_{pump} (ε_A) and photoluminescence quantum yield (ϕ) of dyes used in this work.

	Rh6G	SRhB	LDS 722	LDS 730
ε_A (532 nm) [10^4 M^{-1} cm^{-1}]	7.7	2.6	2.3	1.4
ϕ	0.62[a]	0.61[b]	0.41[c]	0.59[b]

[a] Ref. [17].
[b] Ref. [18].
[c] Ref. [19].

The RL spectra from 1 m thin films with mixtures of Rh6G/LDS722 and SRhB/LDS730 in different molar proportions are shown in Fig. 2b and c, respectively. The highest output intensity (Fig. 2d and e) and collapse in the full width half maximum (FWHM) of the emission was obtained with mixtures of Rh6G/LDS722 in molar proportion 3.3/6.6 and SRhB/LDS730 in molar proportion 1/9. From now on every time we refer to samples Rh6G/LDS722 and SRhB/LDS730 it should be understood that the relative dye proportions are the optimal (3.3/6.6) and (1/9), respectively. The RL spectra from Rh6G/LDS722 and SRhB/LDS730 is overall much less collapsed that the RL spectra from Rh6G and SRhB alone. Although this could be a result of the lower efficiency of the formers, it is worth noticing that

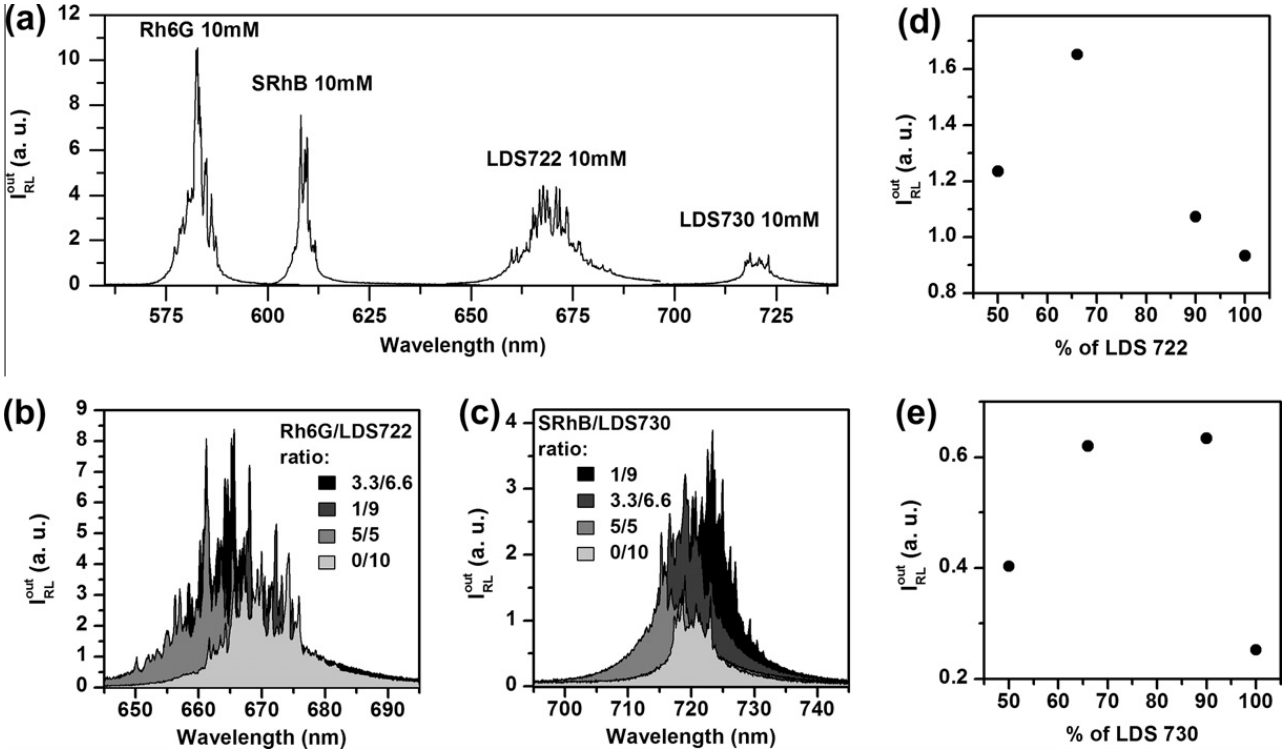

Fig. 2. RL emission spectra from waveguides based on pHEMA/8OH-POSS(25%) pumped at I_{pump} = 380 kW/cm^2: (a) doped with donor and acceptor dyes alone, (b) as a function of donor/acceptor molar ratio for the pair Rh6G/LDS722, and (c) as a function of donor/acceptor molar ratio for the pair SRhB/LDS730, (d) and (e) RL output intensity integrated over the whole spectral range as a function of percentage of LDS 722 and LDS 730, respectively.

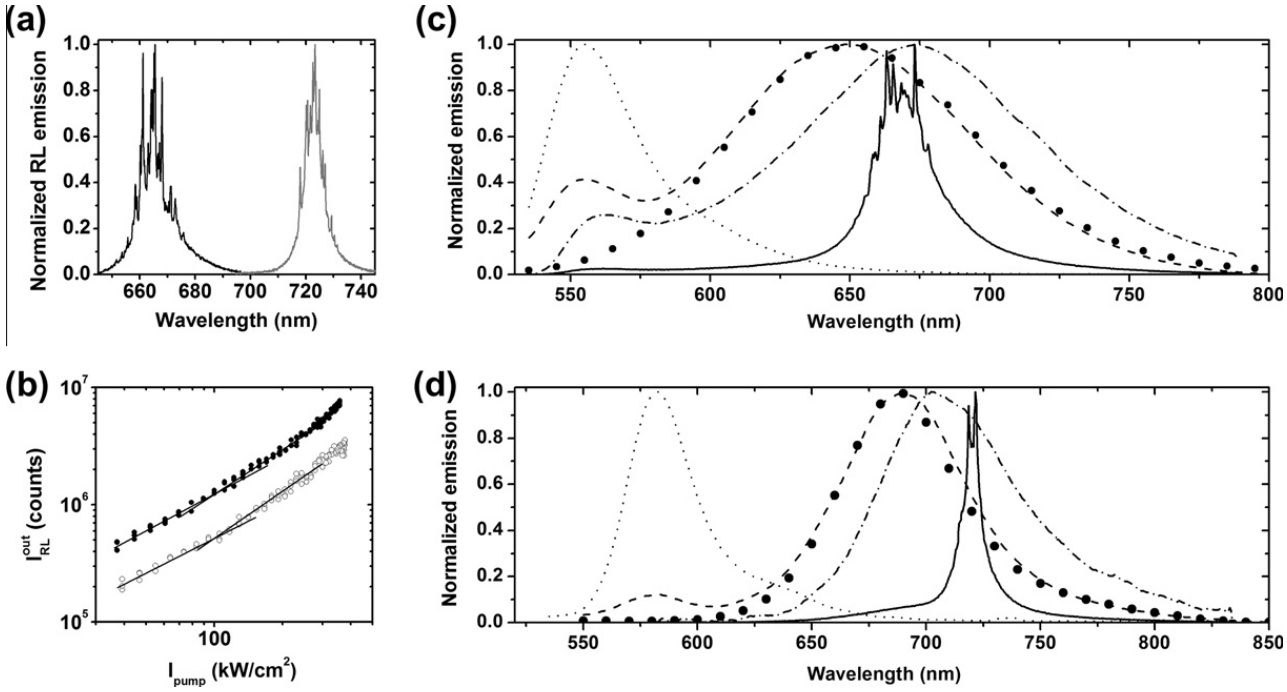

Fig. 3. RL and fluorescence measurements from waveguides based on pHEMA/8OH-POSS(25%): (a) Normalized RL output spectra at I_{pump} = 380 kW/cm^2 from samples Rh6G/LDS722 (black line) and SRhB/LDS730 (gray line). (b) RL output intensity (integrated over all wavelengths) as a function of pump intensity in the samples Rh6G/LDS722 (filled circles) and SRhB/LDS730 (hollow circles). Solid lines are a guide to the eye. (c) Front-face fluorescence (λ_{exc} = 532 nm) from samples doped with Rh6G 3.3 mM (dotted line), LDS722 6.6 mM (thick dots), Rh6G/LDS722 (3.3/6.6) 10 mM (dashed line) and fluorescence in RL set up at 30 kW/cm^2 in sample Rh6G/LDS722 (3.3/6.6) 10 mM (dash-dotted line) as compared with RL emission at 380 kW/cm^2 (solid line) of the last. (d) Front-face fluorescence (λ_{exc} = 532 nm) from samples doped with SRhB 1 mM (dotted line), LDS730 9 mM (thick dots), SRhB/LDS730 (1/9) 10 mM (dashed line) and fluorescence in RL set up at 30 kW/cm^2 in sample SRhB/LDS730 (1/9) 10 mM (dash-dotted line) as compared with RL emission at 380 kW/cm^2 (solid line) of the last.

the fluorescence FWHM (Fig. 1) of LDS722 and LDS730 reaches 100 and 63 nm, respectively, against the 41 and 37 nm of Rh6G and SRhB, respectively. In view of this fact, it could be concluded that the degree of collapse was greater in the hemicyanines (LDS722 and LDS730) than in the xanthenes (Rh6G and SRhB).

Fig. 3a shows the normalized RL emission spectra of the samples Rh6G/LDS722 and SRhB/LDS730, pumped at 380 kW/cm^2 with an excitation stripe of 2 mm. Both spectra exhibit a narrow ASE centered around 665 nm (Rh6G/LDS722) and 725 nm (LDS730) with very narrow peaks on top of it, with a linewidth smaller than 0.3 nm. As we had already concluded [14] the RL emission in the samples with 8OH-POSS originates in closed-loop random cavities formed in the medium due to the scattering induced by the high surface roughness coming from the pHEMA/8OH-POSS phase separation. Then, the waveguiding structure confines and guides the light, and the scattering feedback is obtained in the direction defined by the pumping stripe and the waveguide plane, with the emission consisting of overlapped RL and waveguide modes [21].

In Fig. 3b it is represented the dependence of the output intensity integrated over the whole spectrum with the pump intensity for both dyes. The estimated RL thresholds were in both cases close to 100 kW/cm^2, somewhat higher than the ones in the samples with Rh6G (60 kW/cm^2) and SRhB (50 kW/cm^2) alone. It is worth noticing at this point that the sample Rh6G/LDS722 presented some residual emission from Rh6G in the whole range of pump intensities used, meaning that the energy transfer was not complete. It is as well true that the residual emission from Rh6G was reduced as the pump intensity increased, indicating that there is a non-vanishing contribution of radiative transfer [20] to the overall energy transfer process. Nevertheless, the close proximity (~7 nm) and the good spectral overlap of donor and acceptor molecules (Fig. 1) suggest that non-radiative (FRET) energy transfer should have an important contribution to the overall energy transfer.

In order to estimate the weight of the FRET on the overall energy transfer in these donor/acceptor systems we had to minimize at maximum the effects of the radiative transfer processes. The steady-state front face measurement helps to minimize these processes since it reduces the optical path within the active medium, although it cannot remove them completely, since there will be always some optical path. As has been shown before [22], to reduce significantly the re-absorption/re-emission phenomena in these measurements, the optical path must be as short as possible. In the present samples the optical path in the front face measurement is determined by the sample thickness (~1 μm), which is short enough, less than two emitted wavelengths, as to minimize to a large extent the reabsorption/reemission effects, even at the high concentrations used in this work. In fact, we have compared the fluorescence emission obtained in the RL set-up at

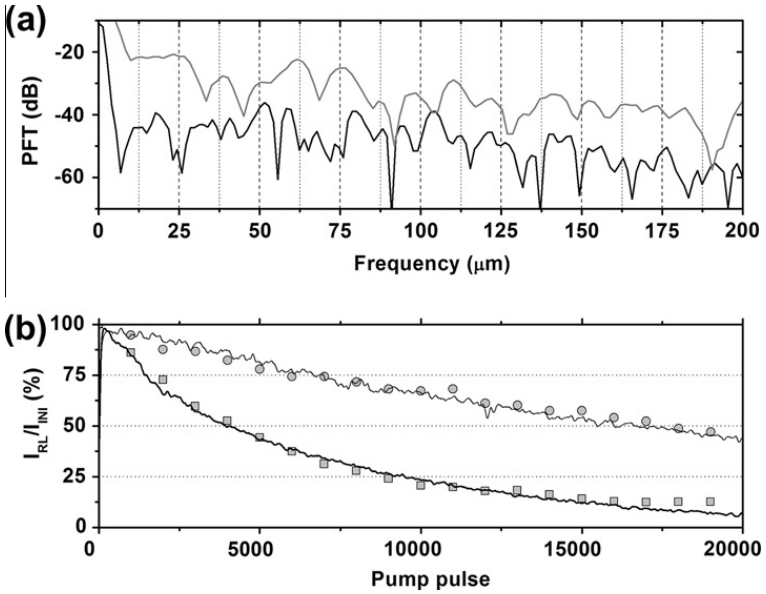

Fig. 4. (a) Power Fourier Transform (PFT) in decibels of RL spectra shown in Fig. 3a (Rh6G/LDS722 in black line and SRhB/LDS730 in gray line). (b) Evolution of the RL emission normalized to the first shot intensity as a function of the number of pump pulses in the same position for samples doped with Rh6G/LDS722 10 mM (filled squares), SRhB/LDS730 10 mM (filled circles), LDS722 10 mM (thick line) and LDS730 10 mM (thin line). Pump intensity and repetition rate were 550 kW cm^{-2} and 15 Hz, respectively.

the lowest pump intensity (30 kW/cm^2), in which the radiative transfer effects are enhanced due to the long optical path (2 mm), and the fluorescence (excited at 532 nm to compare the results with the RL measurements) in front-face configuration. The presence of homo radiative transfer (both from donor to donor and from acceptor to acceptor) should result in a red-shift of donor and acceptor emission peaks with respect to its fluorescence band, whereas the presence of hetero radiative transfer (from donor to acceptor) should result in a lower donor emission. It can be seen in the Fig. 3c and d that these two different radiative effects are minimized in the front-face fluorescence since the emission peaks are blue-shifted with respect to the RL set-up fluorescence and the donor emission is enhanced.

Fig. 3c and d show the fluorescence spectra of the donor alone, the acceptor alone and of the optimized mixtures from the pairs Rh6G/LDS722 and SRhB/LDS730, respectively. It can be observed in Fig. 3c that the energy transfer is not complete in the sample Rh6G/LDS722, since its spectrum clearly shows the band corresponding to the emission of Rh6G. On the contrary, the energy transfer is more favorable in the pair SRhB/LDS730, since the emission corresponding to SRhB is nearly negligible (Fig. 3d). It is possible to obtain an estimation of the FRET processes efficiency from the spectra shown in Fig. 3c and d. The FRET quantum yield ϕ_{FRET} is given by [20]:

$$\phi_{FRET} = 1 - \frac{I_F^{D+A}(\lambda_D^{peak})}{I_F^{D}(\lambda_D^{peak})}, \quad (1)$$

where $I_F^{D+A}(\lambda_D^{peak})$ and $I_F^{D}(\lambda_D^{peak})$ are the fluorescence intensity at the donor emission peak in the presence and absence of acceptors, respectively. According to Eq. (1) and to the spectra shown in Fig. 3c and d (without normalization), it is found $\phi_{FRET}^{Rh6G/LDS722} \leqslant 0.9$ and $\phi_{FRET}^{SRhB/LDS730} \leqslant 0.98$. It is worth noticing that these values may be affected somewhat by radiative processes, and thus we have presented an upper-limit ($\leqslant$) instead of a full equality (=). Nevertheless, in the RL measurements the radiative transfer processes are activated thanks to the length traveled by the photons in the active medium and by the population inversion situation, which is translated into a less pronounced contribution of the donor emission to the final spectra, as can be observed as well in Fig. 3c and d. Whereas the sample SRhB/LDS730 shows no evidence of donor emission in its RL spectrum (Fig. 3d), the sample Rh6G/LDS722 still presents some contribution of the emission from Rh6G (Fig. 3c), as has been already mentioned. Then, the energy transfer in these systems is dominated by FRET and is reinforced by radiative transfer processes. As a final remark, time-resolved studies would provide more accurate information on the FRET phenomenon, but these measurements are beyond the scope of this work.

It is possible to gain insight into the excited random cavities by calculating the Power Fourier Transform (PFT) of the emission spectra. As it is well known, the PFT of the emission spectrum (in $k = 2\pi/\lambda$ space) from a well-defined laser cavity exhibits peaks at Fourier components with frequency $p_m = mL_C n/\pi$, where m is the order of the Fourier harmonic, L_C is the cavity path length, and n is the refractive index of the gain medium [23]. Fig. 4a shows the calculated PFT spectra of the emission spectra shown in Fig. 3a. The cavity path lengths resulted to be 21 and 23 μm for Rh6G/LDS722 and SRhB/LDS730, respectively. These path lengths are much longer than the waveguide thickness, meaning that, as expected, the feedback is taking place in the waveguide plane. The slight difference in the path length between the two samples can be ascribed to differences in the sample roughness, which changes along the sample and from sample to sample, and to the fact that the resonant conditions depend on the spectral

range, which is different in the samples Rh6G/LDS722 and SRhB/LDS730.

From a practical point of view, an important parameter in the behavior of the waveguides is the stability of the emission under long time operation, which implies high resistance to dye degradation under repeated pumping. It is worth noticing that, as far as we know, no photostability measurements have been performed on waveguides doped with LDS730. We assessed this stability by pumping the samples at a fixed position with a pump intensity of 550 kW/cm^2 (five times over RL threshold) and a repetition rate of 15 Hz. The actual evolution of the output emission integrated over a window of 10 nm around the emission peak is presented in Fig. 4b for both Rh6G/LDS722 and SRhB/LDS730. It can be observed that the RL emission decreased to 50% of the initial intensity after 4300 pump pulses in the sample Rh6G/LDS722 and after 18,000 pump pulses in the sample SRhB/LDS730. Then, SRhB/LDS730 is much more photostable that Rh6G/LDS722, fact that has been previously observed in bulk materials [15]. In Ref. [24] a much longer durability for LDS 722 was reported, with the emission falling to half of its initial value after 45,000 shots, instead of the 4300 measured in the present work. However, to properly compare both results it is necessary to consider the experimental conditions selected to carry out each particular experiment, since factors such as dye concentration, pump repetition rate, pump configuration and pump energy strongly affect the devices life-time. In fact, the particular thin film DFB laser presented in Ref. [24] had a thickness of 5 μm and a dye concentration of up to 38 mM, and was pumped at 160 μJ (267 kW/cm^2). Our thin film random laser has a thickness of 1 μm, a dye concentration of 10 mM and was pumped, for the photostability measurements, at 550 kW/cm^2. On the one hand, both a thicker film and a higher dye concentration may increase the measured photostability since, after all, there are more dye molecules to be destroyed. This effect is nicely reproduced in Fig. 4 of Ref. [24]. On the other hand, the lower the pump intensity is, the lower the degradation rate becomes. Then, with a thicker film, a higher concentration and a lower pump intensity the device in Ref. [24] was operated in better conditions to obtain a longer durability than our device. Therefore, once the experimental conditions are considered, the durability of our samples is not as short as could initially appear. Finally, to assess the effect that the energy transfer process might have on the devices operational lifetime, we measured the photostability of samples of LDS722 (10 mM) and LDS730 (10 mM) without donor, and found that the photostabilities of the samples with and without donor molecules were the same (Fig. 4b). This result suggests that the photostability of the mixture is limited by the intrinsic higher photodegradation rate of the emitting dye, which means that the improvement in the photostability should come from chemical modifications of dye, host or both.

4. Conclusions

We have studied in depth RL emission from red-emitting dyes (LDS722 and LDS730) incorporated into asymmetric slab optical waveguides based on pHEMA/8OH-POSS (25%) polymer blends. To circumvent the inherent low absorption of these dyes we have made use of energy transfer processes, both FRET and radiative transfer, by using mixtures of LDS722 with Rh6G and LDS730 with SRhB in donor/acceptor proportions 3.3/6.6 and 1/9, respectively. In the absence of time-resolved measurements, the fluorescence spectra study helps estimate that the FRET process reaches efficiencies of $\phi_{FRET}^{Rh6G/LDS722} \leqslant 0.9$ and $\phi_{FRET}^{SRhB/LDS730} \leqslant 0.98$. The sample with Rh6G/LDS722 gave RL emission centered at 665 nm whereas the emission from the sample SRhB/LDS730 was centered at 725 nm, both systems presenting a threshold close to 100 kW/cm^2. By calculating the Power Fourier Transform of the emission spectra the path length of the random cavities was estimated to be $L_C = 21$ m when the dye was Rh6G/LDS722 and $L_C = 23$ μm when the active medium was based on SRhB/LDS730. In both cases, the path length was much longer than the waveguide thickness, meaning that, as expected, the feedback is taking place in the waveguide plane.

Finally, we have measured the photostability of Rh6G/LDS722 and, for the first time, of SRhB/LDS730 in polymer waveguides, and have observed that the RL emission decreased to 50% of the initial intensity after 4300 pump pulses in the sample Rh6G/LDS722 and after 18,000 pump pulses in the sample SRhB/LDS730 when pumped at intensities five times above threshold.

In conclusion, it is possible to obtain efficient and photostable laser emission from dye-doped thin films in the deep red spectral range (660–730 nm) without the need of using complicated and expensive nanopatterned structures by incorporating in the polymeric material appropriate nanoparticles which induce structural changes.

Acknowledgments

This work was supported by projects MAT2010-20646-C04-01 and TRACE2009-0144 of the Spanish Ministerio de Economía y Competitividad (MINECO). L.C. thanks MINECO for a predoctoral scholarship (FPI, cofinanced by Fondo Social Europeo). We would like to thank the reviewers for their careful reading of the manuscript, which has allowed us to improve it significantly.

Appendix A. RL measurements from waveguides based on pHEMA/8OH-POSS (25%) doped with Rh6G

Fig. A1 shows the results on RL measurements from Rh6G (10 mM) doped waveguides. The RL emission was centered at 582 nm (Fig. A1a), characteristic of Rh6G, and had the threshold at 60 kW/cm^2 (Fig. A1b). From the spectrum shown in Fig. A1a a cavity path length of 23 μm was calculated (Fig. A1c). Photostability measurements were performed in this sample, and we found that the RL emission decreased to 50% of the initial intensity after 4700 pump pulses when pumped in a fixed position at 550 kW/cm^2 (ten times over RL threshold) with a repetition rate of 15 Hz.

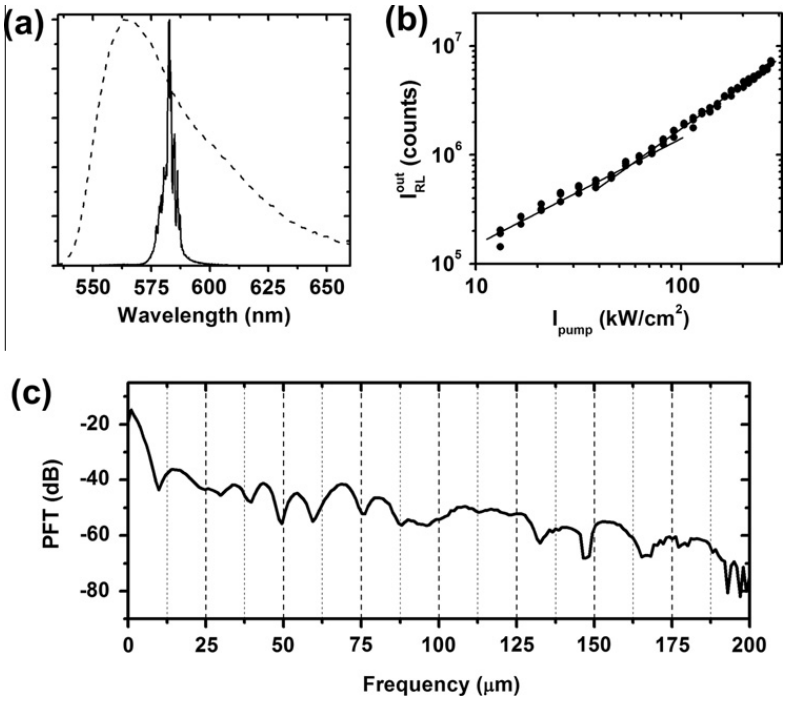

Fig. A1. RL results from Rh6G 10 mM doped pHEMA/8OH-POSS(25%) waveguides: (a) normalized fluorescence (dashed line) and RL output spectra at I_{pump} = 380 kW/cm^2 (solid line). (b) RL output intensity (integrated over all wavelengths) as a function of pump intensity. Solid line is a guide to the eye. (c) Power Fourier Transform (PFT) in decibels of RL spectrum shown in (a).

References

[1] E.M. Calzado, P.G. Boj, M.A. Díaz García, Amplified spontaneous emission properties of semiconducting organic materials, Int. J. Mol. Sci. 11 (2010) 2546–2565.

[2] S. Chénais, S. Forget, Recent advances in solid-state organic lasers, Polym. Int. DOI: http://dx.doi.org/10.1002/pi.3173.

[3] A. Costela, O. García, L. Cerdán, I. García-Moreno, R. Sastre, Amplified spontaneous emission and optical gain measurements from pyrromethene 567-doped polymer waveguides and quasi-waveguides, Opt. Express 16 (2008) 7023–7036.

[4] L. Cerdán, A. Costela, I. García-Moreno, O. García, R. Sastre, Waveguides and quasi-waveguides based on pyrromethene 597-doped poly(methyl methacrylate), Appl. Phys. B 97 (2009) 73–83.

[5] L. Cerdan, A. Costela, I. García-Moreno, O. García, R. Sastre, M. Calle, D. Muñoz, J. de Abajo, High-gain long-lived amplified spontaneous emission from dye-doped fluorinated polyimide planar waveguides, Macromol. Chem. Phys. 210 (2009) 1624–1631.

[6] S.S. Yap, W.O. Siew, T.T. Tou, S.W. Ng, Red-green-blue laser emission from dye-doped poly(vinyl alcohol) films, Appl. Opt. 41 (2002) 1725–1728.

[7] C.J. Oton, D. Navarro-Urrios, N.E. Capuj, M. Ghulinyan, L. Pavesi, S. González-Pérez, F. Lahoz, I.R. Martín, Optical gain in dye-impregnated oxidized porous silicon waveguides, Appl. Phys. Lett. 89 (2006) 011107.

[8] C. Ye, J. Wang, L. Shi, D. Lo, Polarization and threshold energy variation of distributed feedback lasing of oxazine dye in zirconia waveguides and in solutions, Appl. Phys. B 78 (2004) 189–194.

[9] Y. Oki, S. Miyamoto, M. Maeda, N.J. Vasa, Multiwavelength distributed-feedback dye laser array and its application to spectroscopy, Opt. Lett. 27 (2002) 1220–1222.

[10] Y. Oki, S. Miyamoto, M. Tanaka, D. Zuo, M. Maeda, Long lifetime and high repetition rate operation from distributed feedback plastic waveguide dye lasers, Opt. Commun. 214 (2002) 277–283.

[11] U. Beckmann, Lambdachorme Laser Dyes, first ed., Lambda Physik AG, Göttingen, 2000.

[12] L. Cerdán, A. Costela, I. García-Moreno, O. García, R. Sastre, Laser emission from mirrorless waveguides based on photosensitized polymers incorporating POSS, Opt. Express 18 (2010) 10247–10256.

[13] X. Zhao, Z. Wu, S. Ning, S. Liang, D. Wang, X. Hou, Random lasing from granular surface of waveguide with blends of PS and PMMA, Opt. Express 19 (2011) 16126–16131.

[14] L. Cerdán, A. Costela, G. Durán-Sampedro, I. García-Moreno, Random lasing from polymer slab waveguides doped with sulforhodamine dyes, Submitted elsewhere.

[15] I. García-Moreno, A. Costela, V. Martín, M. Pintado-Sierra, R. Sastre, Materials for a reliable solid-state dye laser at the red spectral edge, Adv. Funct. Mater. 19 (2009) 2547–2552.

[16] R. Sastre, V. Martín, L. Garrido, J.L. Chiara, B. Trastoy, O. García, A. Costela, I. García-Moreno, Dye-doped polyhedral oligomeric silsesquioxane (POSS)-modified polymeric matrices for highly efficient and photostable solid-state lasers, Adv. Funct. Mater. 20 (2009) 3307–3316.

[17] F. López-Arbeloa, T. López-Arbeloa, I. López-Arbeloa, A. Costela, I. García-Moreno, J.M. Figuera, F. Amat-Guerri, R. Sastre, Relations between photophysical and lasing properties of rhodamines in solid polymeric matrices, Appl. Phys. B 64 (1997) 651–657.

[18] I. López-Arbeloa, Private communication.

[19] L. Cerdán, A. Costela, I. García-Moreno, J. Bañuelos, I. López-Arbeloa, Singular laser behavior of hemicyanine dyes: unsurpassed efficiency and finely structured spectrum in the near-IR region, Laser. Phys. Lett. http://dx.doi.org/10.1002/lapl.2012.100.19.

[20] J.R. Lakowicz, Principles of Fluorescence Spectroscopy, Kluwer Academic/Plenum Publishers, New York, 1999.

[21] S. Kéna-Cohen, P.N. Stavrinou, D.D.C. Bradley, S.A. Maier, Random lasing in low molecular weight organic thin films, Appl. Phys. Lett. 99 (2011) 041114.

[22] I. López-Arbeloa, Fluorescence quantum yield evaluation: corrections for re-absorption and re-emission, J. Photochem. 14 (1980) 97–105.

[23] R.C. Polson, G. Levina, Z.V. Vardeny, Spectral analysis of polymer microring lasers, Appl. Phys. Lett. 76 (2000) 3858–3860.

[24] Y. Oki, K. Aso, D. Zuo, N.J. Vasa, M. Maeda, Wide-wavelength-range operation of a distributed-feedback dye laser with a plastic waveguide, Jpn. J. Appl. Phys. 41 (2002) 6370–6374.